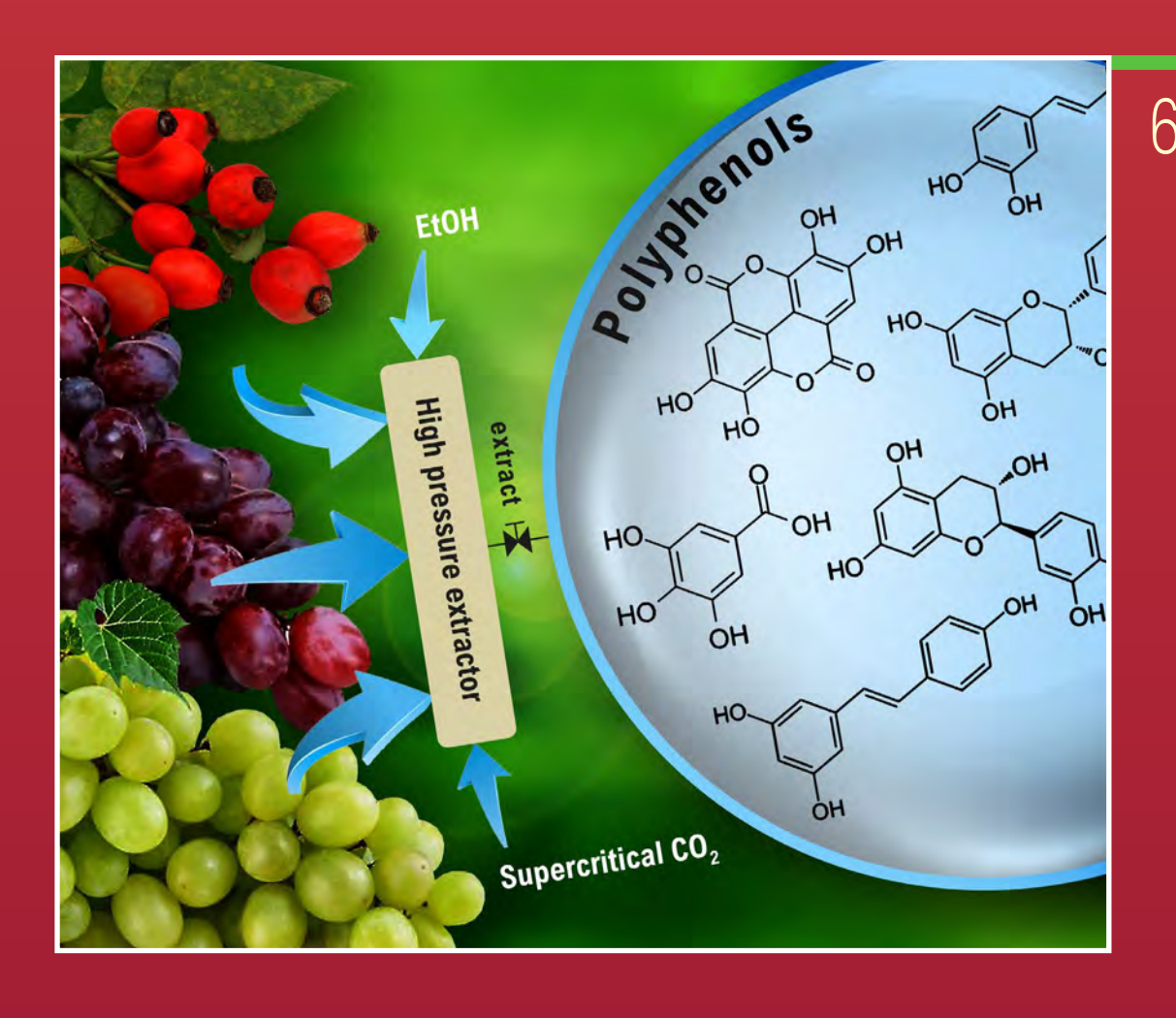




ActaChimicaSla Acta Chimica Slo Slovenica Acta

66/2019



EDITOR-IN-CHIEF

KSENIIA KOGEI

Slovenian Chemical Society, Hajdrihova 19, SI-1000 Ljubljana, Slovenija, E-mail: ACSi@fkkt.uni-li.si, Telephone: (+386)-1-479-8538

ASSOCIATE EDITORS

Janez Cerkovnik, University of Ljubljana, Slovenia Krištof Kranjc, University of Ljubljana, Slovenia Ksenija Kogej, University of Ljubljana, Slovenia Franc Perdih, University of Ljubljana, Slovenia Aleš Podgornik, University of Ljubljana, Slovenia Helena Prosen, University of Ljubljana, Slovenia Damjana Rozman, University of Ljubljana, Slovenia Melita Tramšek, Jožef Stefan Institute, Slovenia Irena Vovk, National Institute of Chemistry, Slovenia

ADMINISTRATIVE ASSISTANT

Marjana Gantar Albreht, National Institute of Chemistry, Slovenia

EDITORIAL BOARD

Wolfgang Buchberger, Johannes Kepler University, Austria
Alojz Demšar, University of Ljubljana, Slovenia
Stanislav Gobec, University of Ljubljana, Slovenia
Marko Goličnik, University of Ljubljana, Slovenia
Günter Grampp, Graz University of Technology, Austria
Wojciech Grochala, University of Warsaw, Poland
Danijel Kikelj, Faculty of Pharmacy, Slovenia
Janez Košmrlj, University of Ljubljana, Slovenia
Blaž Likozar, National Institute of Chemistry, Slovenia
Mahesh K. Lakshman, The City College and
The City University of New York, USA

Janez Mavri, National Institute of Chemistry, Slovenia Friedrich Srienc, University of Minnesota, USA Walter Steiner, Graz University of Technology, Austria Jurij Svete, University of Ljubljana, Slovenia Ivan Švancara, University of Pardubice, Czech Republic Jiri Pinkas, Masaryk University Brno, Czech Republic Gašper Tavčar, Jožef Stefan Institute, Slovenia Christine Wandrey, EPFL Lausanne, Switzerland Ennio Zangrando, University of Trieste, Italy

ADVISORY EDITORIAL BOARD

Chairman

Branko Stanovnik, Slovenia

Members

Josef Barthel, Germany Udo A. Th. Brinkman, The Netherlands Attilio Cesaro, Italy Dušan Hadži, Slovenia Vida Hudnik, Slovenia Venčeslav Kaučič. Slovenia Željko Knez, Slovenia Radovan Komel, Slovenia Janez Levec, Slovenia Stane Pejovnik, Slovenia Anton Perdih, Slovenia Slavko Pečar, Slovenia Andrej Petrič, Slovenia Boris Pihlar, Slovenia Milan Randić, Des Moines, USA Jože Škerjanc, Slovenia Miha Tišler, Slovenia Đurđa Vasić-Rački, Croatia Marjan Veber, Slovenia Gorazd Vesnaver, Slovenia Jure Zupan, Slovenia Boris Žemva, Slovenia Majda Žigon, Slovenia

Acta Chimica Slovenica is indexed in: Academic Search Complete, Central & Eastern European Academic Source, Chemical Abstracts Plus, Chemical Engineering Collection (India), Chemistry Citation Index Expanded, Current Contents (Physical, Chemical and Earth Sciences), Digitalna knjižnica Slovenije (dLib.si), DOAJ, ISI Alerting Services, PubMed, Science Citation Index Expanded, SciFinder (CAS), Scopus and Web of Science. Impact factor for 2017 is IF = 1.104.



Articles in this journal are published under the Creative Commons Attribution 4.0 International License

Izdaja - Published by:

SLOVENSKO KEMIJSKO DRUŠTVO - SLOVENIAN CHEMICAL SOCIETY

Naslov redakcije in uprave – Address of the Editorial Board and Administration Hajdrihova 19, SI-1000 Ljubljana, Slovenija

Tel.: (+386)-1-476-0252; Fax: (+386)-1-476-0300; E-mail: chem.soc@ki.si

Izdajanje sofinancirajo – Financially supported by: Slovenian Research Agency, Ljubljana, Slovenia National Institute of Chemistry, Ljubljana, Slovenia Jožef Stefan Institute, Ljubljana, Slovenia

Faculty of Chemistry and Chemical Technology at University of Ljubljana, Slovenia Faculty of Chemistry and Chemical Engineering at University of Maribor, Slovenia

Faculty of Pharmacy at University of Ljubljana, Slovenia

University of Nova Gorica, Nova Gorica, Slovenia



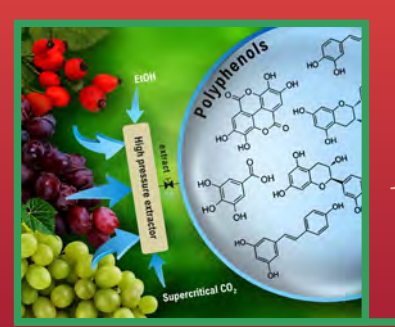
Acta Chimica Slovenica izhaja štirikrat letno v elektronski obliki na spletni strani http://acta.chem-soc.si. V primeru posvečenih številk izhaja revija tudi v tiskani obliki v omejenem številu izvodov.

Acta Chimica Slovenica appears quarterly in electronic form on the web site http://acta.chem-soc.si. In case of dedicated issues, a limited number of printed copies are issued as well.

Transakcijski račun: 02053-0013322846 Bank Account No.: SI56020530013322846-Nova Ljubljanska banka d. d., Trg republike 2, SI-1520 Ljubljana, Slovenia, SWIFT Code: LJBA SI 2X

Oblikovanje ovitka - Design cover: KULT, oblikovalski studio, Simon KAJTNA, s. p. Grafična priprava za tisk: Majanafin, d. o. o.

Graphical Contents



ActaChimicaSlo ActaChimicaSlo SlovenicaActaC

Year 2019, Vol. 66, No. 4

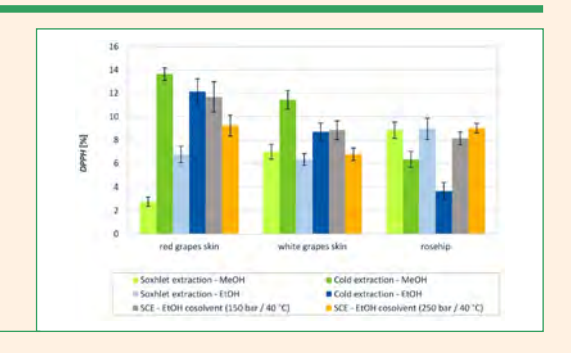
FEATURE ARTICLE

751–761

Chemical, biochemical and environmental engineering

Extracts of White and Red Grape Skin and Rosehip Fruit: Phenolic Compounds and their Antioxidative Activity

Maša Knez Hrnčič, Darija Cör, Petra Kotnik and Željko Knez



REVIEW

762–776

Applied chemistry

Amperometric Biosensors for Glucose and Lactate with Applications in Food Analysis: A Brief Review

Totka Dodevska, Yanna Lazarova and Ivan Shterev



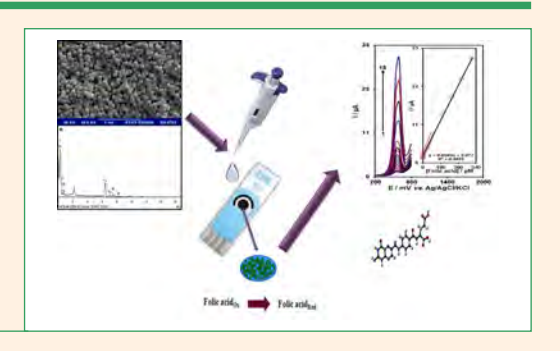
SCIENTIFIC PAPER

777-783

Analytical chemistry

Modified Screen Printed Electrode for Selective Determination of Folic Acid

Mohadeseh Safaei, Hadi Beitollahi and Masoud Reza Shishehbore

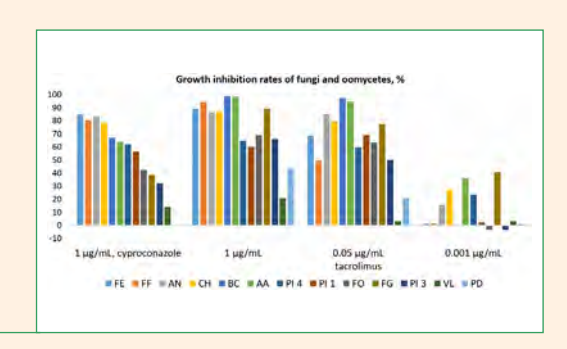


784-791

Biomedical applications

Tacrolimus as Antifungal Agent

Lyudmyla Antypenko, Zhanar Sadykova, Fatuma Meyer, Leif-Alexander Garbe and Karl Steffens



792-801 Analytical chemistry

A Simple and Highly Sensitive Turn-on Schiff Base Type Naked-eye Fluorescent Sensor for Aluminum Ion in Living Cells

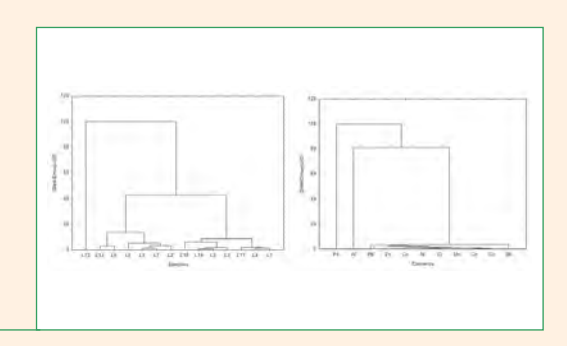


Sedat Keskin and Mevlut Bayrakci

802-813 Analytical chemistry

The Evaluation of ICP OES for the Determination of Potentially Toxic Elements in Lipsticks: Health Risk Assessment

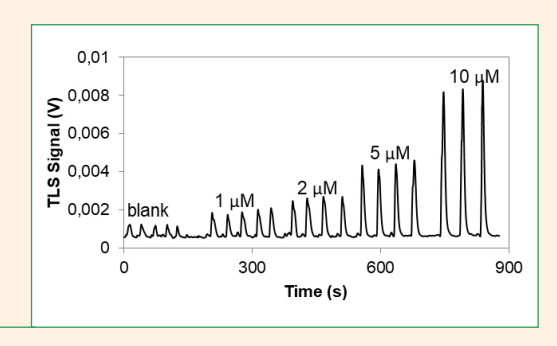
Jelena Mrmošanin, Aleksandra Pavlović, Snežana Miti, Snežana Tošić, Emilija Pecev-Marinković, Jovana Krstić and Milena Nikolić



814-820 Analytical chemistry

Determination of Iron in Environmental Water Samples by FIA-TLS

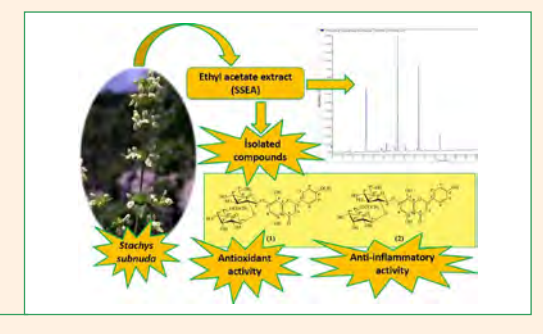
Gaja Tomsič, Leja Goljat, Hana Budasheva, Dorota Korte Arne Bratkič and Mladen Franko



821-830 Biomedical applications

Methodological Aspects of Extraction, Phytochemical Characterization and Molecular Docking Studies of *Salix* caprea L. Bark and Leaves

Emilia Gligorić, Ružica Igić, Ljiljana Suvajdžić, Branislava Teofilović, Maja Turk-Sekulić, and Nevena Grujić-Letić



831–838 Analytical chemistry

Two Acylated Isoscutellarein Glucosides with Anti-Inflammatory and Antioxidant Activities Isolated from Endemic *Stachys Subnuda* Montbret & Aucher ex Benth Ethyl actiate entrett (SSIA)

Isolated compounds

Compounds

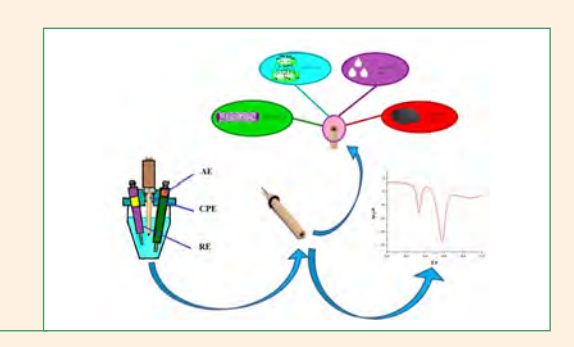
Studye Antionidant Anti-infammatory activity

Ali Sen, Fatih Goger, Ahmet Dogan and Leyla Bitis

839–849 Analytical chemistry

Fabrication and Application of a New Modified Electrochemical Sensor Using Newly Synthesized Calixarene-Grafted MWCNTs for Simultaneous Determination of Cu(II) and Pb(II)

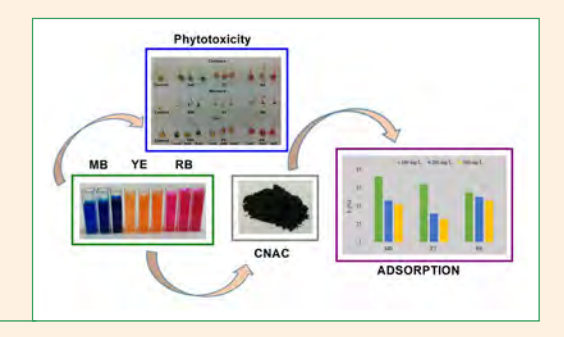
Semahat Kucukkolbasi, Serkan Sayin and Mustafa Yilmaz



850–858 Chemical, biochemical and environmental engineering

Kinetic, Equilibrium and Phytotoxicity Studies for Dyes Removal by Low Cost Natural Activated Plant-Based Carbon

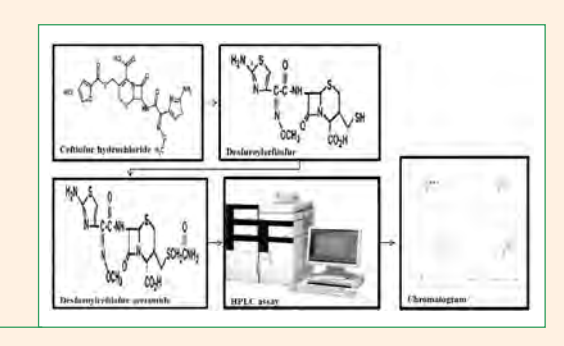
Emilia Neag, Ana Moldovan, Vanda Băbălău-Fuss, Anamaria Török, Oana Cadar and Cecilia Roman



859–864 Analytical chemistry

Isocratic High Performance Liquid Chromatography Assay for Quantification of Ceftiofur Hydrochloride in Bubaline Plasma

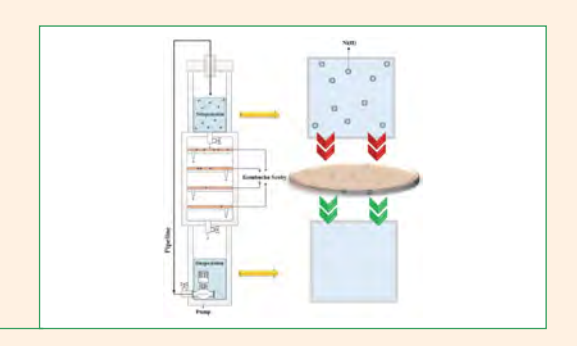
Muhammad Adil, Muhammad Ovais Omer, Aqeel Javeed, Aamir Ghafoor, Muhammad Ashraf and Abdul Muqeet Khan



865-873 Applied chemistry

Separation of Ni (II) from Industrial Wastewater by Kombucha Scoby as a Colony Consisted from Bacteria and Yeast: Kinetic and Equilibrium Studies

Seyyed Mojtaba Mousavi, Seyyed Alireza Hashemi, Aziz Babapoor, Amir Savardashtaki, Hossein Esmaeili, Yaghoub Rahnema, Fatemeh Mojoudi, Sonia Bahrani, Sara Jahandideh and Marziyeh Asadi

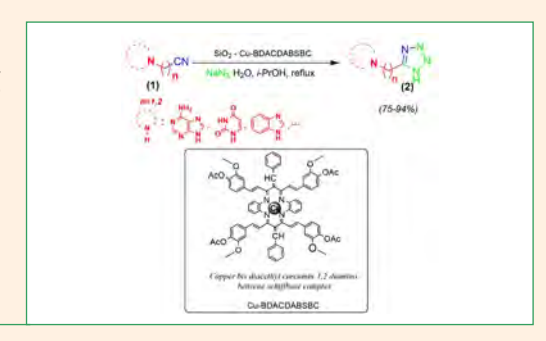


874-887

Organic chemistry

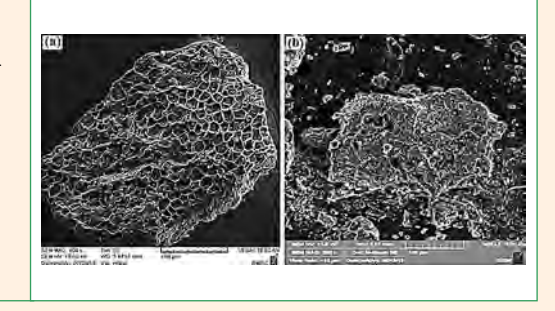
Synthesis, Antifungal Evaluation and Molecular Docking Studies of Some Tetrazole Derivatives

Mohammad Hosein Afsarian, Mojtaba Farjam, Elham Zarenezhad, Somayeh Behrouz and Mohammad Navid Soltani Rad



888–898 Chemical, biochemical and environmental engineering

Sulfate Ion Removal from Water Using Activated Carbon Powder Prepared by Ziziphus Spina-Christi Lotus Leaf

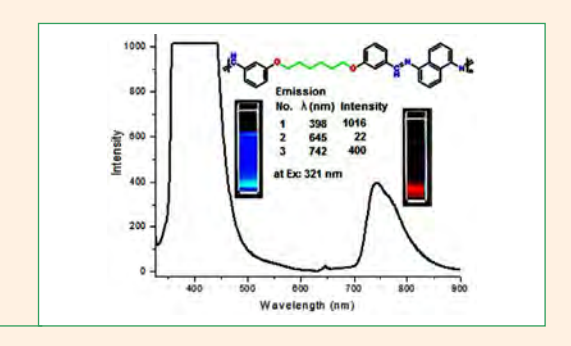


Morteza Rahmati, Golan Yeganeh and Hossein Esmaeili

899–912 Materials science

New Fluorescent, Thermally Stable and Film Forming Polyimines Containing Naphthyl Rings

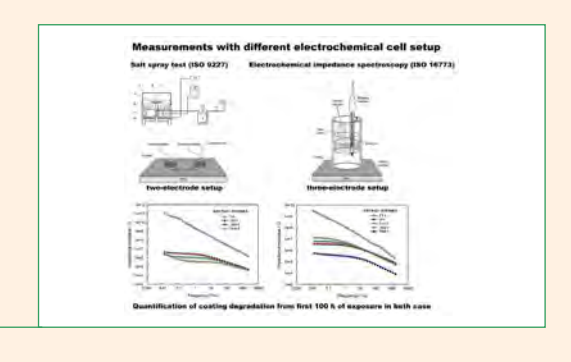
Farah Qureshi, Muhammad Yar Khuhawar and Taj Muhammad Jahangir



913–522 Materials science

A Novel Application of EIS for Quantitative Coating Quality Assessment During Neutral Salt Spray Testing of High-Durability Coatings

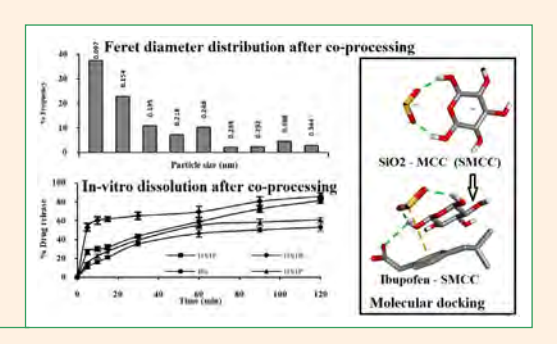
Marina Mrđa Lalić and Sanja Martinez



923–933 Materials science

Interactions between Ibuprofen and Silicified-MCC: Characterization, Drug Release and Modeling Approaches

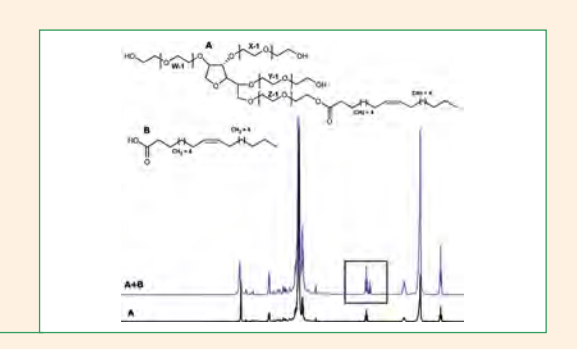
Rudra Narayan Sahoo, Ashirbad Nanda, Arunima Pramanik, Souvik Nandi, Rakesh Swain, Sukanta Kumar Pradhan and Subrata Mallick



934–943 Analytical chemistry

Comparison of the NMR and the Acid Value Determination Methods for Quality Control of Input Polysorbates

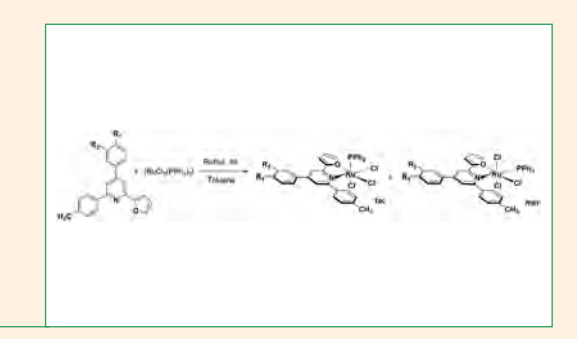
Ema Valentina Brovč, Stane Pajk, Roman Šink and Janez Mravljak



944–949 Inorganic chemistry

DNA Interaction, *in vitro* Antibacterial and Cytotoxic Activities of Ru(III) Heterochelates

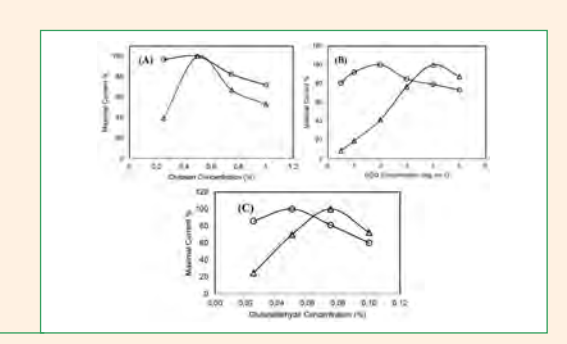
Parag S. Karia, Pankaj A. Vekariya, Anshul P. Patidar, Darshana N. Kanthecha, Bhupesh S. Bhatt and Mohan N. Patel



950–957 Physical chemistry

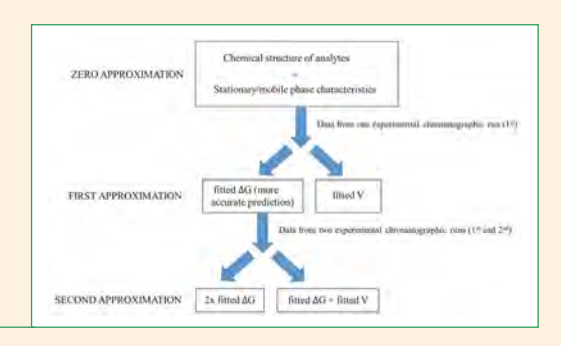
Amperometric Glucose Biosensor Based on Homopolymer-Chitosan Double Layered Glucose Oxidase Electrode Modified with Zinc Oxide Nanoparticles

Gul Ozyilmaz, Ali Tuncay Ozyilmaz, Esiye Irem Bayram and Ragibe Hulya Akyürekoğlu



958–970 Analytical chemistry

Application of Solvatic Model for Prediction of Retention at Gradient Elution in Reversed-Phase Liquid Chromatography

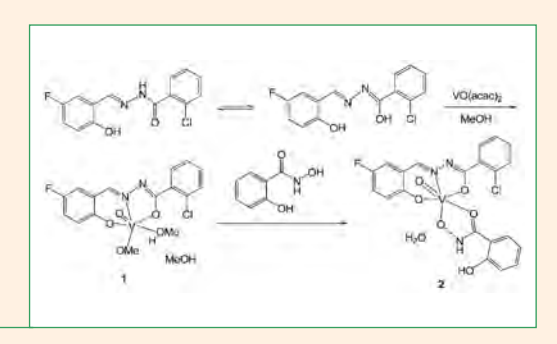


Tina Snoj Ekmečič and Irena Kralj Cigić

971–977 Inorganic chemistry

Synthesis, Spectroscopic Characterization, Crystal Structures and Antibacterial Activity of Vanadium(V) Complexes of Fluoro- and Chloro-Substituted Benzohydrazone Ligands

En-Cheng Liu, Wei Li and Xiao-Shan Cheng

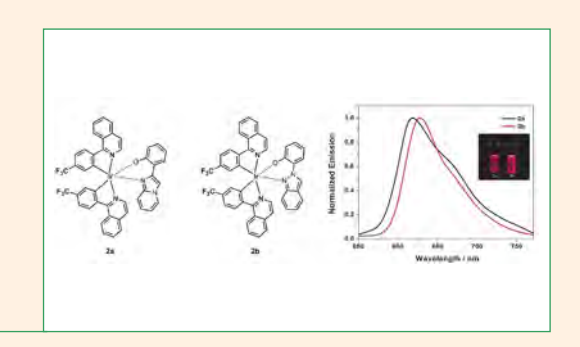


978-986

Organic chemistry

Synthesis and Characterization of High-Efficiency Red Phosphorescent Iridium(III) Complexes with 1-(4-(Trifluoromethyl)phenyl)isoquinoline Ligand

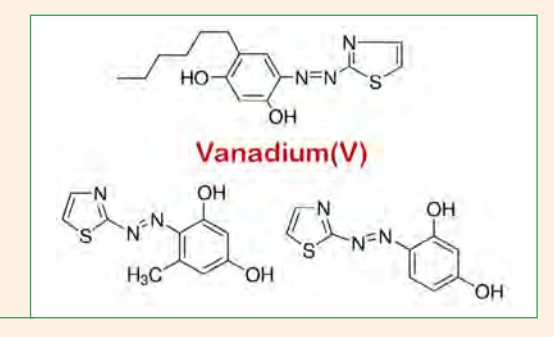
Zheng Zhao, Xiao-Han Yang, Zi-Wen Tao, Han-Ru Xu, Kai Liu, Guang-Ying Chen, Zheng-Rong Mo, Shui-Xing Wu, Zhi-Gang Niu, and Gao-Nan Li



987_994

Inorganic chemistry

Extraction-Chromogenic Systems for Vanadium(V)
Based on Azo Dyes and Xylometazoline Hydrochloride

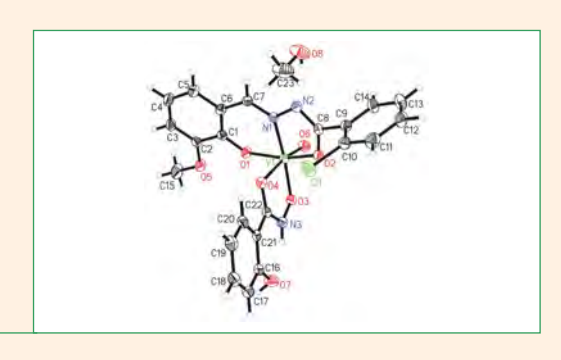


Danail G. Hristov, Nikolina P. Milcheva and Kiril B. Gavazov

995-1001

Inorganic chemistry

Synthesis, Characterization, X-Ray Crystal Structures and Antibacterial Activities of Oxidovanadium(V) Complexes with Hydrazone and Hydroxamate Ligands

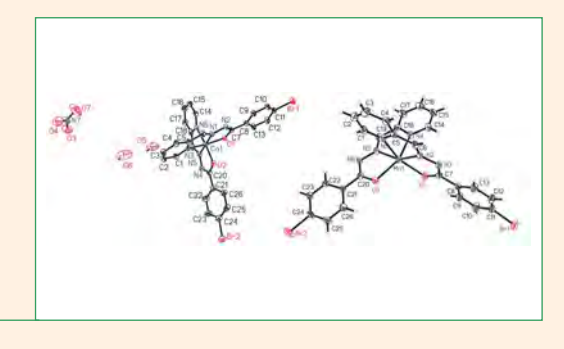


Heng-Yu Qian

1002-1009

Inorganic chemistry

Syntheses, Characterization, Crystal Structures and Antimicrobial Activity of 4-Bromo-N'-(pyridin-2-ylmethylene)benzohydrazide and Its Cobalt(III) and Manganese(II) Complexes

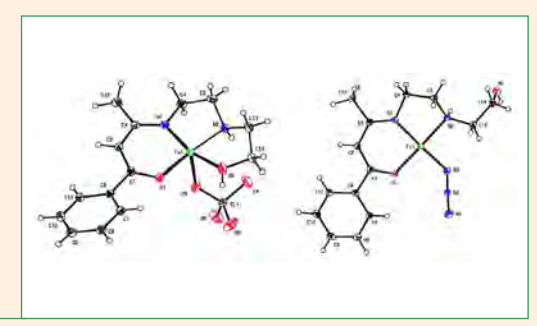


Yao Tan

1010-1018

Inorganic chemistry

Anion Modulated Structural Variations in Copper(II) Complexes with a Flexidentate Ligand Derived from 2-((2-Aminoethyl)Amino)Ethan-1-ol: Synthesis and Spectroscopic and X-ray Structural Characterization



Rasoul Vafazadeh, Abolghasem Kazemi-nasab and Anthony C. Willis

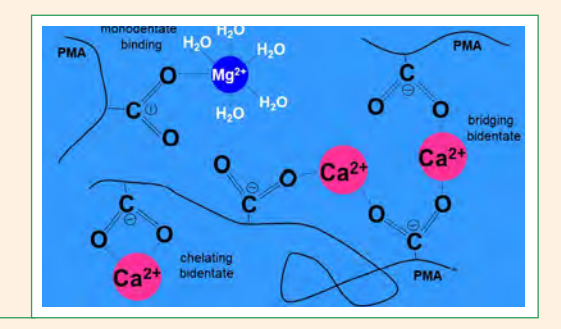
1019–1025 Inorganic chemistry

Copper(II) Coordination Compounds with Methanoato and Pyridine Ligands: Conversion from Mononuclear to Polynuclear in the Presence of Moisture

Amalija Golobič, Fedja Marušič, Primož Šegedin and Marta Počkaj

1026-1037 Physical chemistry

Temperature Dependent Behavior of Isotactic and Atactic Poly(Methacrylic Acid) in the Presence of MgCl₂ and CaCl₃

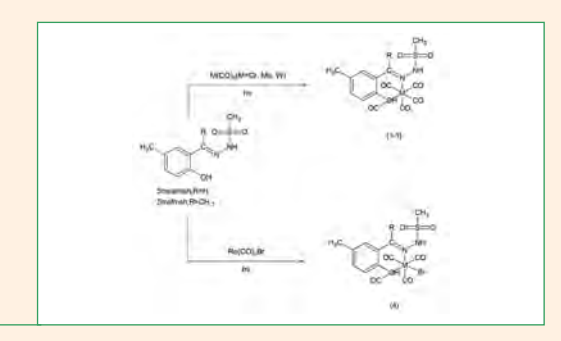


Patricija Hriberšek and Ksenija Kogej

SHORT COMMUNICATION

1038-1042 Inorganic chemistry

Investigation of Photochemical Reactions of some Metal Carbonyls with N'-(2-Hydroxy-6-Methylbenzylidene)Methanesulfonohydrazide and 5-Methyl-2-Hydroxyacetophenonemethanesulfonylhydrazone



Sema Sert

Feature article

Extracts of White and Red Grape Skin and Rosehip Fruit: Phenolic Compounds and their Antioxidative Activity

Maša Knez Hrnčič,^{1,*} Darija Cör,¹ Petra Kotnik^{1,2} and Željko Knez^{1,2}

¹ University of Maribor, Faculty of Chemistry and Chemical Engineering, Smetanova 17, SI-2000 Maribor, Slovenia,

² University of Maribor, Faculty of Medicine, Taborska ulica 8, SI-2000 Maribor, Slovenia,

* Corresponding author: E-mail: masa.knez@um.si Phone: +386 2 2294477, fax:+38622527774

Received: 05-09-2019

Abstract

The current work concerns solid liquid extraction from red and white grapes skin and the rosehip (*Rosa canina*) to obtain extracts with a high phenolic content. Extracts have been acquired using conventional extraction techniques and extraction with supercritical fluids (SCFs). The effect of extraction method and experimental parameters (time, pressure, temperature and solvent mixture) mostly believed to affect the extraction process was undertaken. The quantitative parameters studied are: total phenolic compounds, proanthocyanin content, and the phenolic constituent profile. The qualitative parameter analyzed is antioxidant capacity. The results demonstrate that the contents of the major constituents significantly varied among the different types of materials. The highest content of total phenolics was determined in the extract from the white grape skin, macerated with MeOH (26.7 mg GA/g extract), and similar, 25.6 mg GA/g extract in the MeOH extract attained by Soxhlet. Ellagic acid (0.650 mg/100 g extract), catechin (0.164 mg/100 g extract), gallic acid (0.133 mg/100 g extract) as well as caffeic acid (0.038 mg/100 g extract) are the major compounds present in the rosehip extracts attained by maceration using MeOH as solvent. The presence of epictechin, hesperidin/neohesperidin, rutin, and chlorogenic acid was also confirmed. Aspects of each type of processing were correlated with the chemistry of the material. The obtained extracts could be used as natural bioactive compounds in several industrial applications.

Keywords: Phenolic compounds; Conventional extraction; Supercritical fluid extraction; LC-MS; DPPH.

1. Introduction

Increasing pressure on natural resources and the problems caused by unhealthy eating habits have brought along an enlarged incidence of different types of cancer. Besides, the worldwide population is aging and countries are facing ongoing challenges in caring for their elderly. Consequently, the demand for different types of high quality products is increasing. Substantial investigation has been concentrated on fruits and crops containing antioxidant bioactive compounds. A bioactive compound is known as a substance that beneficially influences the health of living organisms. These extra nutritional constituents are present in both plant and animal products, and typically occur in low quantities in foods. High ingestion of fruits has consequently been associated with low incidence of chronic-degenerative diseases, probably due to the presence of bioactive compounds, considered to enhance or boost the immune system.¹ Here, extraction is an

important process to isolate the bioactive compounds. Biological activities of the extract highly depends on the extraction procedure and this releases a gateway for selection of appropriate extraction methods. A great deal of interest has been devoted to the extraction of active components from natural sources, aiming at satisfying the increasing request of natural products not only for therapeutic use but also as preventing and protecting agents.² Among the large number of active substances in the focus, polyphenols have received particular attention in the last decade.3 The identification and development of phenolic compounds or extracts from different plants has become a major area of food, health- and medical-related research.4 Divided into two major groups (nonflavonoid and flavonoids), phenolic compounds show antioxidant and radical scavenging activities possibly responsible for many health benefit effects⁵ and for the yellow, orange and red pigments in a large variety of plants and animal kingdoms. Extracts containing these natural ingredients are incorporated into

different food, therapeutic and cosmetic products. Nutritional composition, colour and antioxidant activity of such products depends on the total composition of the extract. The development of such novel functional products emphasizes the bioactive and preservation potential of phenolic compounds. Most of the compounds were extracted using Soxhlet and conventional solvent extraction methods. However, conventional solvent extraction has certain disadvantages such as application of large amount of solvents, long extraction times, and the presence of toxic organic solvents in the final products.8 Those can lead to deterioration of the quality of the extracts and can cause thoughtful health difficulties.9 Indeed, conventional techniques have been widely accepted, mainly because of the ease of procedure, effectiveness, and widespread applicability.10,11

Processes based on SCFs are an environment-friendly alternative to traditional solvent extraction techniques. 12 Supercritical carbon dioxide (SC CO₂) is the most prominent amongst various solvents used in this method because of the low critical temperature (31.18 °C) and pressure (7.4 MPa), inexpensiveness, nontoxicity, non-flammability, recyclability and environmental benignity. 13 The extraction with SC CO2 was used to acquire extracts from over 300 plant species. 14,15 This technique has already been used to isolate health-promoting compounds from the pomace of a various plants, inter alia, grapes, ¹⁶ tomatoes, ¹⁷ olives,¹⁸ sour cherries,¹⁹ and the guelder-rose²⁰ and the quality of the extracts has been evaluated. In view of the bio-refinery concept, the nutrient extraction from agrofood industry waste such as skins, stalks and seeds represent a recent challenge. Valorization of by-products for the recovery of oil, phenolic compounds, and fibers by the means of sustainable extraction procedures has gained an increased interest.²¹ Grape is one of the most popular and widely cultivated fruits in the world, but are usually discarded in regular dietary intake and the winery and grape juice industry. Grape seeds and skin are rich in polyphenols,²² traditionally, extracted by using organic solvents.²³ In recent years, according to the biorefinery concept suband supercritical fluid extraction has been utilized as an alternative extraction technique of both polar and non-polar compounds²⁴ for processing of a spectrum of marketable products. Extraction efficiency is predisposed by numerous factors such as polarity and concentration of solvent, material-solvent ratio, duration, temperature, pH, etc... Extensive research has been carried out to improve the supercritical fluid extraction (SC extraction) technique to optimize a specific target compound extraction. This research comprises kinetic modelling, 25 sample preparation and pre-treatment by using pressing,²⁶ ultrasonication,²⁷ microwave irradiation,²⁸ enzyme-assistance²⁹ or, within the extraction vessel, ultrasonic-assistance,³⁰ and a hydrothermal approach.³¹ Despite there are many review publications on the subject of this review, however, most studies discuss the influence of a single factor has been discussed,

while the relations between the factors on the extract yield and composition have not been studied comprehensively.32 As process efficiency depends on polarity of the solvent(s) being employed, in SC extraction, polarity of CO₂ can be manipulated by process temperature and pressure. Moisture content of the plant raw material also sometimes hinders the product yield, apart from particle size, solvent flow rate, separation conditions employed at separation vessel(s). Besides factors such pressure, temperature, flowrate, sample particle size and moisture content in the material, subjected to the extraction process, addition of co-solvent or modifier enhances extraction efficiency. Particularly if polar compounds are among target ones, co-solvent/modifier could be any polar solvent such as MeOH or EtOH. However, if safety of the extract is of importance, EtOH with less polarity, though compared to MeOH could be the option.³³ Consideration of the optimal processing parameters is extremely important due to the high manufacturing costs associated with SC extraction, resulting from high initial investment costs (associated with high pressure operation/equipment costs) which have been the major limitation preventing its use in industrial processes. The relatively high pressures required to achieve the supercritical point could make the process energy-intensive and economically non-viable which often restricts the use of SC extraction. On the other hand, if SC extraction is utilized as part of a biorefinery rather than as a stand-alone technology, this could lead to a positive effect on the downstream processing of biomass.³⁴

Recent investigation has been oriented towards utilization of fruits and their specific parts with a high bioactive compounds content. The main aims of the present study were to maximize the recovery of phenolic compounds in the extracts by application of different extraction methods and variation of experimental parameters. ^{35,36} We have been focused mainly on materials that are available in the phytogeographical regions of Slovenia (eg *Rosa canina* L.) or even constitute waste in processing (grape skin) and have been relatively poorly studied so far.

Due to the low polarity of CO₂ EtOH-modified SC CO₂ extraction has been performed to obtain extracts with a high phenolic content. Alteration of operating pressure has been assumed to influence the extraction rate of phytochemicals. In the frame of the present research EtOH-modified SC CO₂ extraction has been carried out at 40 °C and pressures of 150 bar and 250 bar by using EtOH as an entrainer. Conventional extraction methods, such as Soxhlet and maceration have been performed as the reference methods to compare success of the applied methodology. Soxhlet extraction and extraction with cold solvent have been carried out by using EtOH and MeOH as solvents since substantial number of scientific reports exist where non-conventional methods using EtOH and MeOH as extraction media contributed to the high phenolic recovery.³⁷ The effect of extraction technique, temperature, pressure, and solvent on the extraction yield, phenolic content and profile along with the estimation of the scavenging activity against the artificial radical DPPH* (2,2-diphenyl-1-picrylhydrazyl) has been considered. Phenolic profile varied significantly in the extracts obtained from different materials. The highest net content of identified phenolic compounds determined by LC-MS/MS analysis has been determined in the MeOH extracts of white grapes skin (1,55 mg/g extract), rosehip extract attained by cold extraction with MeOH (100 mg /100 g extract), whilst in red grape skin extract the content of phenolic compounds was only about 30 mg/100 g extract.

2. Experimental

2. 1. Materials

All solvents/chemicals used were of analytical/HPLC grade and obtained from Merck, Germany. Folin–Ciocalteu reagent, DPPH, and chemical HPLC-grade standards (purity ≥ 95%) of ellagic acid, gallic acid, chlorogenic acid, (+)-catechin, (−)-epicatechin, hesperidin/neohesperidin, myricetin, resveratrol, rutin and caffeic acid were purchased from Sigma-Aldrich (St. Louis, MO, USA).

Lyophilized material was milled and stored in a dry, dark place. Materials were further subjected to extraction experiments.

2. 2. Methods

Extraction

Soxhlet extraction: Approximately 20 g of material was weighed in a filter bag, which was inserted into the cylindrical part of the apparatus. 180 mL of solvent was heated to reflux. After 240 min of extraction at a temperature above the solvent boiling point, the solvent was removed from the extract solution by means of a rotary evaporator, yielding the extracted compound, which was later dried and weighed. The samples were stored in a dark and cool place until analyzes.

Cold solvent extraction: Red and white grapes skin were purchased by the local suppliers, the rosehip fruits were donated by Frutarom Etol d.o.o.(Slovenia). The powdered materials (20 g) were extracted by stirring using a magnetic stirrer with 180 mL of MeOH at 25 °C for 4 h. The extract was filtered for removal of solid particles. The extracts were cooled to room temperature and concentrated under vacuum at 40 °C.

EtOH-modified SC extraction: SC extraction (SCE) experiments were performed on extraction unit previously described in the literature.³⁸ The high pressure vessel was loaded with 10 g of material and placed in a water bath heated to the desired temperature (40 °C). EtOH was pumped continuously using a high pressure pump with a flow rate of 2 mL / min. Pressurized CO₂ has been introduced in the autoclave from the gas cylinder using a HPLC pump and was kept constant during the entire experiment.

The extract and the solvent were collected in the tubes. The total time of extraction was 100 minutes. Solution was transferred to evaporation flask and the solvent was evaporated using a rotary vacuum evaporator. The mass of the extract was determined gravimetrically and the extraction efficiency was calculated. The extract was stored in a freezer at -10 °C until the analyses.

2. 3. Spectrophotometric Analyses

Determination of total phenolic content, proanthocyanidin concentration in extracts and antioxidant activity was done using UV-visible spectrophotometer (CARY 50 UV-VIS).

Determination of total phenolic content

Total phenolic content in extracts was determined using Folin-Ciocalteu reagent as described in the literature.³⁹ Briefly, the Folin-Ciocalteu reagent solution has been prepared by diluting the basic Folin-Ciocalteu reagent solution with distilled water in a ratio of 1:10. Na₂CO₃ solution has been prepared by weighing approximately 3.75 g of Na₂CO₃ in a 50 mL volumetric flask, diluted with distilled water to the mark and sonicated until total dissolution of Na₂CO₃ was obtained. Approximately 50 mg of the extract was weighted in a 10 mL volumetric flask and diluted with MeOH. 2.5 mL of the Folin-Ciocalteu reagent solution and 2 ml of Na₂CO₃ were added to 5 mL of the prepared extract solution. The mixture was left for 30 min at room temperature (25 \pm 2 °C), then the absorbance of the solution was measured at 765 nm using a UV-visible spectrophotometer. The total phenolic compounds was determined in triplicate for each sample. The calibration curve of gallic acid was used for quantification of total phenolic compounds and the amount of phenolic compounds in the samples was expressed as gallic acid equivalents, in mg of gallic acid / g of material.

Determination of proanthocyanidin content

The proanthocyanidins were determined by UV spectrophotometry method (Varian-UV-VIS Spectrophotometer) based on acid hydrolysis and colour formation.⁴⁰ The reagent was prepared by weighing 77 mg of Fe(SO₄) \times 7 H₂O and adding 500 mL of HCl: butanol solution (200 mL HCl and 300 mL of butanol). 50 mg of the extract was weighted into a 10 mL volumetric flask and filled with MeOH to the mark. After the entire extract is dissolved, 1.0 mL of the extract solution was mixed with 10 mL of iron sulphate solution. At the same time, a control sample was prepared; instead of the extract solution, the same amount of MeOH was added to iron sulphate solution. The samples were thermostated for 15 minutes at a water bath at 95 °C. The solutions were cooled and the absorbance was measured at 540 nm. The concentration of proanthocyanidins (PAC) in the extract solution is expressed as mg PAC /mL of extract solution.

DPPH Radical Scavenging Assay

Radical scavenging activity of extracts was measured using the stable radical DPPH (2,2-diphenyl-picryl-hydrazil) reagent. 50 μ L of extract solution in MeOH was added to 1.95 mL of the MeOH solution of DPPH (0.025 g/L). In parallel, a negative control was prepared by mixing 50 μ L of MeOH with 1.95 mL of the MeOH solution of DPPH. After 15 min of incubation in the dark at room temperature, the absorbance was measured at 517 nm against a blank sample. An ascorbic acid was used as positive control of an antioxidant reference, measured at the same conditions as samples. For each concentration, the test is repeated 3 times. The absorbance is measured by the UV-Vis spectrophotometer.

2. 4. Chromatographic Analyses

LC-MS/MS analysis: For identification and quantification of detected phenolic compounds, the Agilent 1200 HPLC in tandem with Agilent 6460 QQQ with JetStream ionization was used. The HPLC apparatus was equipped by quaternary HPLC high pressure pump, automatic sampler and column thermostat. The chromatographic separation of the compounds was performed on analytical column Agilent Eclipse Plus, 150 mm \times 4.6 mm i.d., 1.8 µm particle size. The column was maintained at 35 °C. The elution gradient consisted of mobile phase A (water with addition of 0.1 vol.% of formic acid) and mobile phase B

(acetonitrile with addition of 0.1 vol.% of formic acid). The flow rate was 0.5 mL/min using gradient program as follows: 0 min 5% B, 5 min 18% B, 10 min, 30% B, 15 min 35% B, 20 min 50% B, 21 min 70% B and at 25 min back to 5% of B. Samples, subjected to the analyses, were prepared by weighing approximately 100 mg of the extract in a 10 mL volumetric flask and diluted with MeOH up to 10 mL. Prepared samples were filtered through 0.2 µm syringe filter and injected (volume of 5 µL) into the system. The multiple reaction monitoring (MRM) mode was used to quantify the analytes, where the assay of was performed following two transitions per compound, the first one for quantitative purposes and the second for confirmation. The optimum ESI conditions were determined: gas temperature 300 °C, gas flow 6 L/min, nebulizer 45 psi (nitrogen), sheath gas temperature 250 °C, sheath gas flow 11 L/ min, capillary 3500 V and nozzle voltage 500 V at delta EMV 200 in negative ionization.

3. Results and Discussion

3. 1. Conventional and SC Extraction

Results in Figure 1 indicate that MeOH was an efficient solvent for extraction of red grapes skin using Soxhlet apparatus. Soxhlet extraction with MeOH gave the total mass yield of approx. 72%, while cold solvent extraction with MeOH gave a yield of approx. 50%. In general

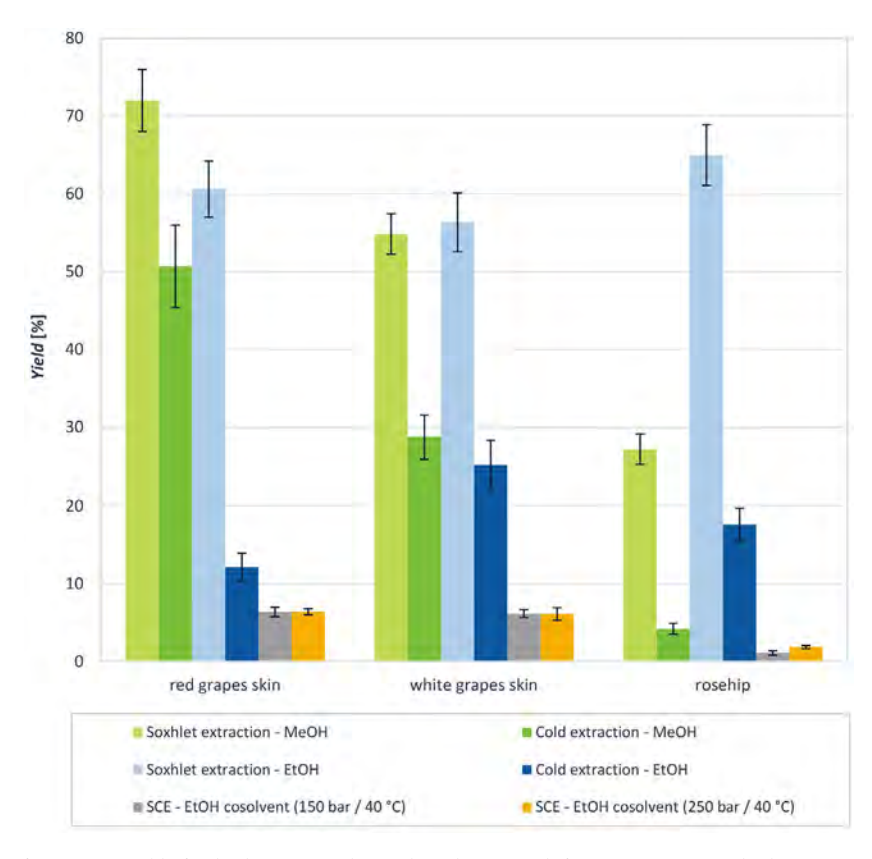


Figure 1: Comparison of extraction yield of red, white grapes skin and rosehip using different extraction methods.

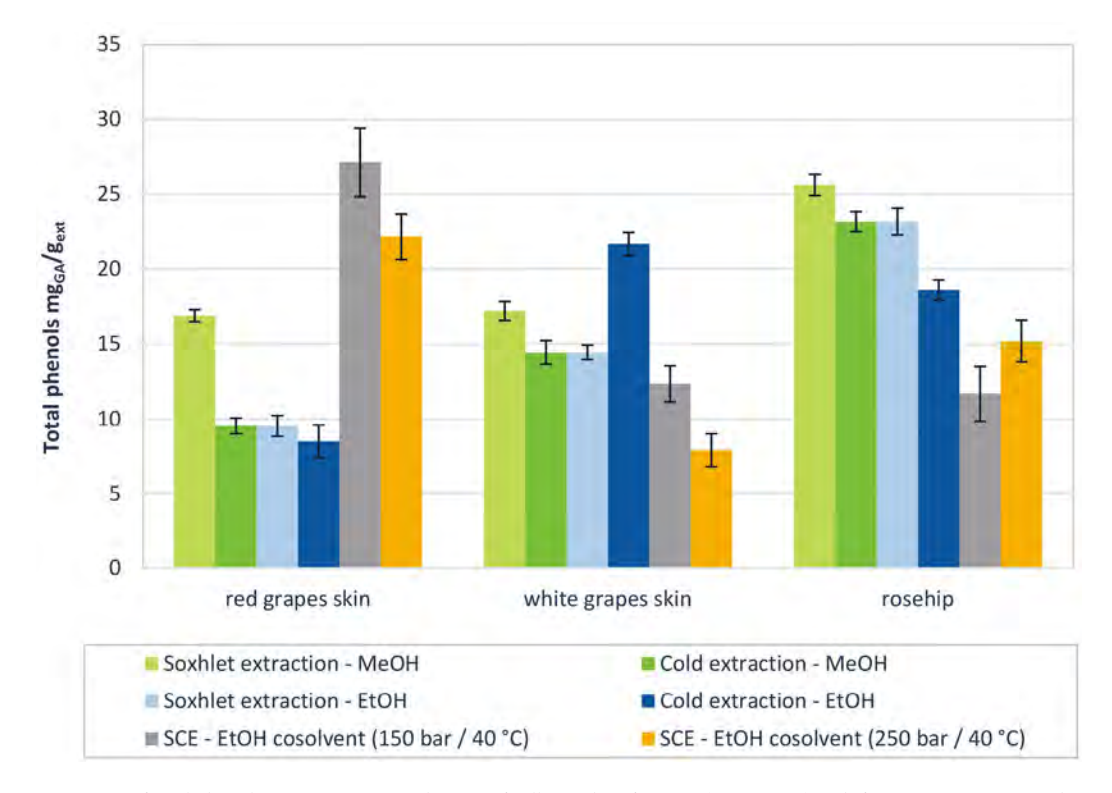
the extraction yield decreased with decreasing solvent temperature. Likewise, for the extraction of white grapes skin and rosehip, the MeOH was more efficient extraction media at elevated temperatures. For white grapes skin, the total extraction yield was 54.9% by using Soxhlet extraction and only 28.8% by cold extraction. Rosehip extraction by MeOH gave relatively low yields, about 27.5% by Soxhlet and only 4.2% by cold extraction. Higher solvent temperature apparently contributed to a higher extraction yield. EtOH was demonstrated as a less efficient solvent considering the total mass yield for both kinds of grapes skin. However, the yields were higher when utilizing hot solvent for all of the examined materials. Soxhlet extraction gave yields ranging from 56.4% for white grape skin and up to 65% for rosehip. Cold extraction of white grape skin gave a maximum yield approx. 25%.

In addition, Figure 1 demonstrates that the extractions of grape skin (red and white) gave high yields with MeOH and EtOH. Consequently, it can be confirmed that MeOH and EtOH are a good choice for the solvent in the extraction of grapes, because they have high polarity and are therefore very good solvents for polyphenolic components, including resveratrol. The temperature has a significant effect in the extraction process. For instance, for red and white grape skin, it can be noticed that cold extraction yielded twice as low of extract as Soxhlet's extraction, regardless of solvent used. The same applies to rosehip, as this material also gets lower extraction efficiency than in extraction with higher temperatures. The relative polarity of the MeOH is higher than polarity of EtOH, due to this

extraction efficiency of white and red grapes is higher when MeOH was used as a solvent media. In that case, the polarity of the solvent influences the extraction yields. Higher temperatures usually lead to higher yields of extraction. SC extraction gave lower mass yields compared to conventional extraction methods, despite the use of EtOH as entrainer. Beside the low solvent polarity, low extraction temperature may have also contributed to the low extraction yield. The highest yield, approx. 6.4% has been attained by red grapes skin extraction at 250 bar, similar as for the white grape skin, where the yield was about 6.2%. Supercritical extraction (SC extraction) of the rosehip gave yields only somewhat higher than 1.86%. The effect of pressure has also been investigated and it was considered that the pressure does not have a tremendous effect on the extraction efficiency, since very similar yield have been attained at 150 and 250 bar for the same materials, except for the rosehip, where higher pressure gave higher yield.

3. 2. Total Phenolic Content in Extracts

Comparison of total phenolic content, expressed as mg of gallic acid/g of extract (mgGA/gEXT) at different extraction procedures is given in Figure 2. The concentration of total phenolic compounds in extracts ranged from 8.49 mg of gallic acid per g of extract to 21.66 mg of gallic acid per g of extract for grape skin, depending on solvent selection and temperature during the extraction process. The highest concentration of phenolic compounds for conventional extraction procedure was 25.61 mg of gallic



 $\textbf{Figure 2}: \textbf{Comparison of total phenolic content, expressed as mg of gallic acid/g of extract (mg_{GA}/g_{EXT}) at different extraction procedures.}$

acid per g of extract in red grape extract. In general, Soxhlet extraction with MeOH gave higher concentrations of phenolic compounds in comparison with EtOH.

In extracts obtained with SC extraction method, the concentration of total phenolic compounds ranged from 7.9 mg of gallic acid per g of extract to 27.12 mg of gallic acid per g of extract. The highest content was determined in extracts from red grape skin, attained at 150 bar and 40 °C. The content varied depending on pressure during the extraction process; the content in the extract, attained at 250 bar and 40 °C was 22.15 mg of gallic acid per g of extract.

The concentration of phenolic compounds in white grape skin extract was 8.83 mg of gallic acid per g of extract at 150 bar and 40 °C, whilst at higher extraction pressure the concentration decreased to 6.77 mg of gallic acid per g of extract. In general, from both grape skin, higher concentrations of phenolic compounds have been attained at lower extraction pressure. On the contrary, in case of rosehip, the content increased with elevation of extraction pressure from 8.13 mg of gallic acid per g of extract at 150 bar and 40 °C up to 9.01 mg of gallic acid per g of extract at 250 bar and 40 °C.

Also, the influence of temperature during the extraction process on the total amount of phenols in extracts was noticed. Extraction of both grape skin and rosehip with MeOH at its boiling point resulted higher amount of phe-

nolic compounds compared to the amount of phenolics in case of cold extraction with MeOH. In general, higher extraction temperature contributed to higher concentration of phenolic compounds except in case of cold extraction of white grape skin with EtOH, which was more efficient for extraction of phenolic compounds. White grape skin extract contains more phenolic compounds in comparison with red grapes skin.

3. 3. Proanthocyanins in Extracts

The amount of proanthocyanins (PAC) in the extracts obtained by Soxhlet, cold and SC extraction is presented in Figure 3. The highest concentration of proanthocyanins was obtained in white grapes skin by cold extraction with MeOH (2.02 mg PAC /mL). It can be observed that white grapes have higher amount of proanthocyanins in comparison with red grapes skin, where the content of proanthocyanins was highest in the extract attained by Soxhlet extraction with MeOH (1.34 mg PAC / mL). The concentration of proanthocyanins in rosehip extracts was the lowest, up to 0.96 mg/mL PAC in the extract obtained by cold extraction with MeOH.

The highest concentration of proanthocyanins obtained by modified SC extraction was determined in rose-hip extracts attained at 250 bar and 40 °C; approximately 0.69 mg PAC/mL. The amount of extracted proanthocya-

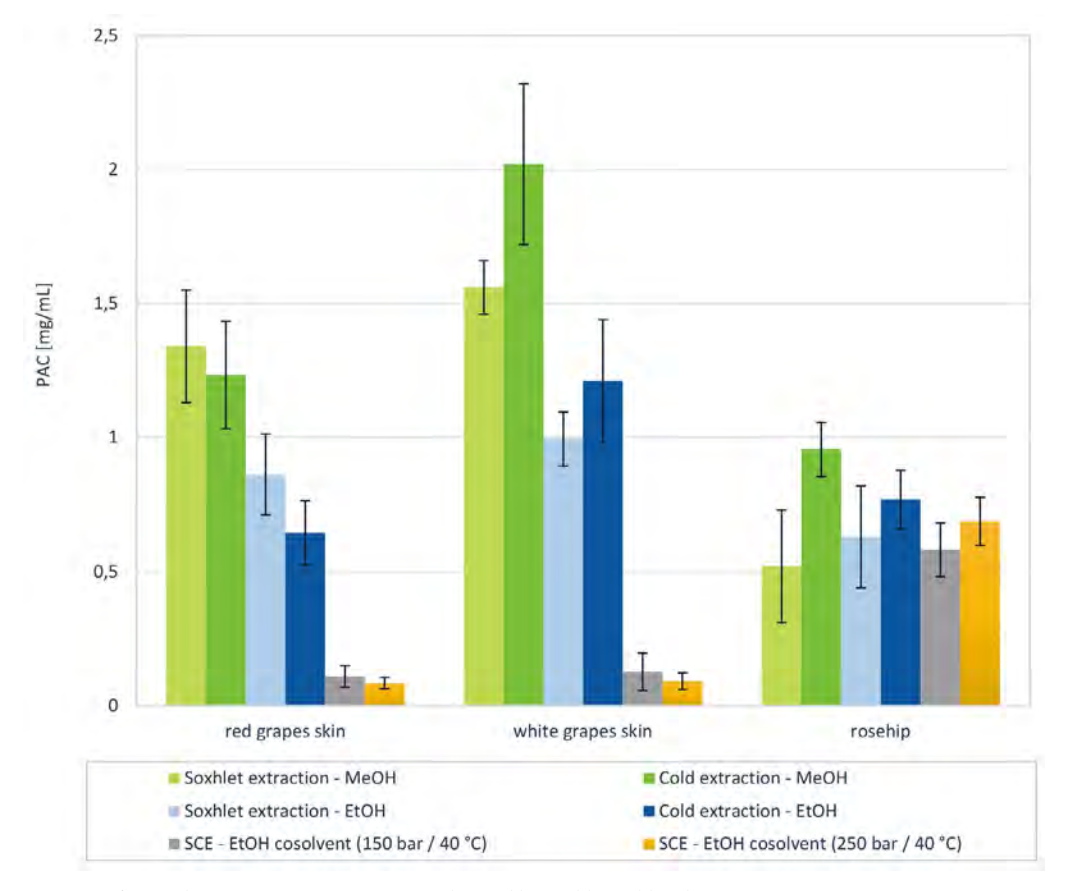


Figure 3: Comparison of proanthocyanins content in extracts obtained by Soxhlet, cold and SC extraction.

nins in rosehip extracts decreased with decreasing extraction pressure to 0.583 mg PAC /mL).

It was found, that white grapes have slightly higher amount of proanthocyanins in comparison with red grapes skin. The content of proanthocyanins was highest in the white grape skin extract attained at 150 bar and 40 °C; approximately 0.13 mg PAC /mL and about 0.09 mg PAC /mL in extract attained at 250 bar and 40 °C. The concentration of proanthocyanins in red grapes skin extracts was the lowest, up to 0.11 mg PAC /mL at 150 bar and 40 °C and only 0.085 mg PAC /mL at 250 bar and 40 °C. Almost three times higher concentration of proanthocyanins was obtained in white grapes skin obtained by cold extraction with MeOH (2.02 mg PAC /mL).

3. 4. LC/MS Analysis

The phenolic compounds were analyzed using LC-MS/MS analytical method. The identification and quantification of individual phenolic compound was done using analytical standards of each compound and the calculation was done using calibration curves, as described in section 2.4.

The content of phenolic compounds in extracts is shown in Table 1. The highest content of the identified phenolic compounds was present in MeOH extracts of white grape skin, whereas the major compound was catechin (0.980 µg/mg extract). EtOH extracts gave lower phenolics recovery, apparently by decreasing solvents polarity less phenolics were dissolved. EtOH white grape skin extract contained approximately a half of the identified compounds when utilizing Soxhlet procedure, again, catechin was the major compound (0.438 µg/mg extract), whilst the cold solvent extract contained only 0.085 µg/mg extract, which is ten times lower than in case of MeOH extracts. Gallic acid was the major compound in SC extracts of white grapes skin (0.080 µg/mg extract), higher pressure contributed to somewhat higher content. The major compound in red grape skin extract was ellagic acid (0.050 µg/ mg extract), its recovery increased with increasing solvent polarity, whilst effect of temperature was not explicit. Caffeic acid was also identified, the highest content was present in the MeOH extract. Gallic, ellagic acid and resveratrol were identified in SC extracts. Likewise, rosehip extracts mainly contained caffeic, gallic, ellagic acid and resveratrol, although the highest recovery of ellagic acid was analyzed in MeOH extract. Resveratrol was detected only in SC extracts. However, the highest recovery of resveratrol was observed in SC extract of white grape skin attained at 250 bar and the macerated white grape skin extracts (0.03 µg/mg extract). Rutin and hesperidin were present in lower concentration, however, 0.068 µg/mg extract of rutin was analyzed in MeOH extract of red grapes skin, whereas the content of hesperidin/neohesperidin

Table 1: Content of phenolic compounds in the extracts of white and red grape skin and rosehip at different extraction conditions.

Compound	caffeic acid	cate- chin	chloroge- nic acid	ellagic acid	epica- techin	gallic acid	hesperidin/ neohespe- ridin	resve- ratrol	rutin	sum
sample	ug/mg	ug/mg	ug/mg	ug/mg	ug/mg	ug/mg	ug/mg	ug/mg	ug/mg	mg/100 g
White grapes skin, Cold – MeOH	0.013	0.838	0.001	0.043	0.340	0.074	0.015	0.030	0.015	1.370
White grape skin, Soxhlet – MeOH	0.016	0.980	0.007	0.044	0.346	0.096	0.012	0.027	0.023	1.550
White grape skin Soxhlet – EtOH	0.011	0.438	0.002	0.025	0.212	0.050	0.008	0.015	0.012	0.773
White grapes skin, Cold – EtOH	0.012	0.085	0.002	0.019	0.038	0.034	0.003	0.011	0.002	0.207
White grapes skin – 150 bar	0.014	0.028	0.006	0.027	0.015	0.071	0.009	0.020	0.009	0.199
White grapes skin – 250 bar	0.015	0.056	0.002	0.022	0.024	0.080	0.003	0.029	0.000	0.230
Red grapes skin, Cold – MeOH	0.025	0.009	0.001	0.050	0.009	0.016	0.033	0.007	0.100	0.249
Red grapes skin, Cold – EtOH	0.012	0.003	0.001	0.013	0.004	0.014	0.008	0.006	0.022	0.084
Red grapes skin, Soxhlet – MeOH	0.019	0.090	0.006	0.018	0.021	0.027	0.038	0.014	0.068	0.301
Red grapes skin, Soxhlet – EtOH	0.029	0.019	0.004	0.022	0.005	0.023	0.012	0.011	0.032	0.157
Red grapes skin, 250 bar	0.038	0.000	0.001	0.014	0.002	0.016	0.001	0.012	0.000	0.083
Rosehip, HT, MeOH	0.014	0.164	0.017	0.650	0.021	0.133	0.003	/	0.000	1.003
Rosehip, 150 bar	0.019	0.012	0.011	0.373	0.004	0.116	0.003	0.022	0.000	0.560
Rosehip, 250 bar	0.014	0.014	0.005	0.145	0.004	0.106	0.002	0.015	0.001	0.306

was about 0.03 μ g/mg extract in the same extract. All extraction procedures gave similar yield of epicatechin (up to 0.346 μ g/mg). Chlorogenic acid was present in traces, up to 0.02 μ g/mg extract in MeOH and SC extract of rosehip.

Among all the extracts, the highest content of caffeic acid (0.038 ug/mg_{raw material}) has been present in red grapes skin extract, attained at 250 bar and 40 °C. Rosehip extract attained at 150 bar contained up to 0.373 ug/mg_{raw material} ellagic acid. The content of resveratrol was low in all samples, however, the highest contents were present in the MeOH extracts and white grapes skin extracts, attained by SC extraction at 250 bar, up to 0.030 ug/mg_{raw material}.

3. 5. DPPH Activity of Extracts

The results of DPPH* radical scavenging activities of conventional extracts obtained using Soxhlet or cold extraction are presented on Figure 4 and vary between 2.75% to 13.64%, depending on solvent and method used. The highest DPPH* radical scavenging inhibitory activity 13.64% was observed for red grapes skin extract prepared by cold extraction with MeOH as solvent. DPPH* radical scavenging inhibitory activity for white grape skin were slightly lower, but trend is similar. In general, for grape skin solvent MeOH resulted higher DPPH* radical scavenging. Results obtained for grape skin show that extracts, attained by the cold extraction method exhibited higher DPPH* radical scavenging comparison to extracts attained by Soxhlet extraction. In case of rosehip extraction, Sox-

hlet extraction gave extracts with higher DPPH* radical scavenging activity regardless of the solvent used. Higher extraction yield does not necessarily mean higher biological activity of the extracts. The use of different solvents can result in the extraction of various types of metabolites from extracted material, with varying radical scavenging activities. Furthermore, increased temperatures during the extraction process may result in denaturation and a reduction of the loss of ability to act as an antioxidant.

The results of DPPH* radical scavenging activities of extracts obtained using modified SC extraction vary between 6.67% and 11.68%, depending on the material. The highest DPPH* radical scavenging inhibitory activity was observed for red grapes skin extract, attained at 150 bar and 40 °C. The activity is lower in the extract, attained at 250 bar and 40 °C; 9.23%.

DPPH* radical scavenging inhibitory activities for white grape skin were slightly lower in both extracts compared to the red grape skin extracts. Lower extraction pressure again resulted in somewhat higher scavenging activity of the extract; approximately 8.83%, whilst the extract attained at 250 bar showed somewhat lower inhibition ability, approximately 6.67%.

Rosehip extracts showed similar scavenging inhibitory activity as the extracts of white grape skin. However, in this case higher extraction pressure contributed to somewhat higher scavenging activity (9.01%), whilst the extract attained at 150 bar showed lower inhibition ability, approximately 8.13%. The use of different process condi-

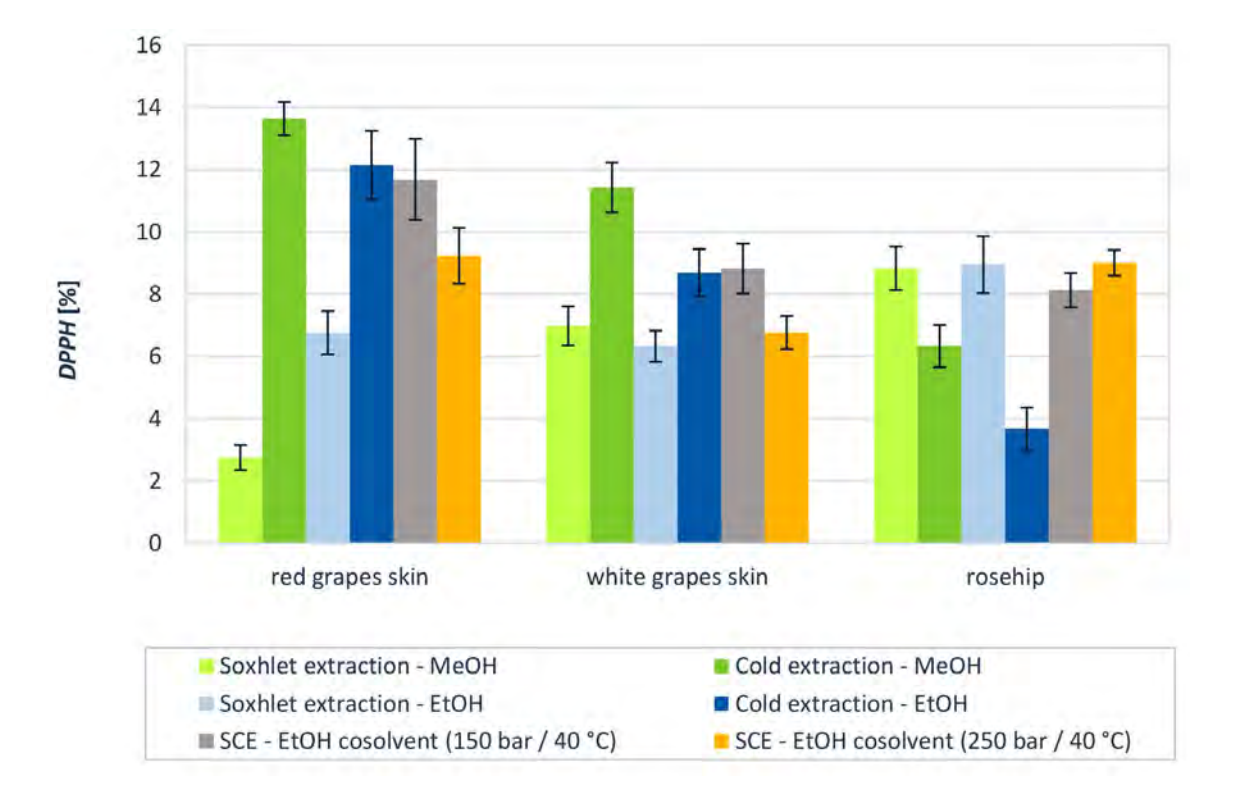


Figure 4: Comparison DPPH activity in % using different extraction procedures.

tions can result in the extraction of various types of metabolites from extracted material, with varying radical scavenging activities. In general, the amount of proanthocyanins and the total phenolic content is not directly related to the radical scavenging inhibitory activities. Red grapes skin extracts prepared by cold extraction and SC extraxtion exhibited similar scavenging inhibitory activities (ranging from 9% up to nearly 14%), whilst the contents of proanthocyanins and the total phenolics ranged from 0.085 mg PAC /mL in extract attained by SC extraction at 250 bar and 40 °C up to 1.233 mg PAC /mL in cold MeOH extract, which exhibited highest inhibitory activity. Meanwhile, the concentration of total phenolic compounds in that extract was 9.53 mg of gallic acid per g of extract. Amongst all red grape skin extracts the lowest DPPH* was determined for Soxhlet extract prepared with MeOH, where the contents of proanthocyanins was the highest (1.34 PAC /mL).

Amongst all white grape skin extracts the highest DPPH* (11.43%) was determined for MeOH extract prepared by cold extraction; the concentration of proanthocyanins was high, 2.02 mg PAC /mL, and the total phenolics content was about 14.41 mg of gallic acid per g of extract. Both Soxhlet extracts of rosehip exhibited similar scavenging activities (about 9%). Similar value was measured for extract, attained at 250 bar and 40 °C. The concentration of proanthocyanins was the highest for MeOH extract prepared by cold extraction; 0.956 PAC /mL, whilst total phenolics content was about 24 mg of gallic acid per g of extract.

4. Conclusion

The obtained results confirm earlier findings that rosehip, white and red grape skin are potentially good sources of natural antioxidants. Although, the content of total phenolics differs depending on the type of material, isolation method and applied solvent. Besides, anthocyanin content in grape skin can depends on the variety and the harvest year.

According to the previous research,⁴¹ the conventional extraction methods involving organic solvents and increased temperature yielded more total phenols. The present results show that the amount of anthocyanins depends on the plant material and extraction solvent. Regardless of the method and solvent used, the highest content of total phenolic compounds (27.12 mg_{GA}/g_{EXT}) has been determined in the extracts from red grape skin, obtained at 150 bar and 40 °C. High content of total phenolic compounds was, according to their polar nature, determined also in extracts, obtained by conventional extraction with MeOH; up to 25.61 mg_{GA}/g of red grape skin extract. In general, Soxhlet extraction using MeOH gave higher concentrations of phenolic compounds in comparison to extractions using EtOH. In addition, the higher

extraction temperatures contributed to higher concentration of phenolic compounds. The content of proanthocyanins in extracts obtained by modified SC extraction was the lowest in all extracts.

According to the analyses, the yield of phenolic compounds in extracts attained by SC extraction was lower than in the extracts attained by the conventional solvent extraction. This may be explained by the fact that CO₂ usually yields good recoveries for nonpolar compounds, but polar compounds may remain partially unextracted because of their lower solubility in this fluid. For this reason, EtOH as organic modifier has been added as cosolvent to the primary fluid to boost the extraction effectiveness. The extraction output considering mass yield was higher in case of conventional extraction methods, but the amount of anthocyanins and phenols successfully extracted with supercritical solvent is considerable. The results show, that generally SC CO₂ in combination with a polar entrainer, represents a good extraction media for isolation of total phenols, while the amount of extracted anthocyanins is low. LC-MS/MS analyses show that gallic, ellagic acid and resveratrol were identified in SC extracts. Therefore, we could consider that SC extraction with CO₂ therefore provides an alternative method to replace extractions with organic solvents for the recovery of phenolic compounds. In general, SC extraction was less efficient due to the limited solvent polarity. Despite the lower total mass yield and the proportion of total phenols in extracts compared to the conventionally obtained extracts, the method was efficient for isolation of caffeic acid, galic and elagic acid.

DPPH* radical scavenging activities of extracts obtained using modified SC extraction and conventional extraction are similar and depend on the type of material. Highest DPPH* radical scavenging inhibitory activity was observed for red grapes skin using cold extraction and MeOH as solvent (about 13%), where the content of total phenols was 9.53 mg of gallic acid per g of extract. The activity of supercritical extract attained at 150 bar and 40 °C was only slightly lower, about 12%, whilst the content of total phenols was the highest, 27.12 mg of gallic acid per g of extract.

The primary aim of this work was utilization of SC extraction for isolation of phenolic compounds as a sustainable method which involves lower consumption of organic solvents. Besides, SCFs are generally cheap, simple, and comparatively safe solvents which is of special attractiveness for industrial processes (especially in food and pharmaceutical applications). Toxic hazards from solvent manipulation are greatly reduced as well as disposal costs. Another motivation for developing processes involving SCFs as solvents SC extraction processes is the reduction or even complete elimination of residual solvents in the products, lower operating temperatures and prevention of oxidation during processing. In contrast to various organic solvents, SCFs can be more simply recycled which signifi-

cantly reduces the cost of any analytical procedure. The union between economic feasibility and safety are getting more consideration and indeed, safer and less harmful solvents that are easy to remove, or recover, are gaining in popularity in the favor of SC extraction. If certain parameters (absence of organic solvents, lower processing temperatures, shorter processing times, no need for further purification of the extract) are taken into account, a high value product can be obtained for a relatively low price. Laboratory-scale data can be safely used to develop economic evaluations of the SC extraction process, as the tendency of the process is to improve yield with increasing scale.

In terms of product quality and environmental issues, compared to conventional extraction processes, SC extraction can be regarded as a more suitable alternative for processing heat-sensitive materials, providing appropriate conditions to maintain the functional properties of the extract.

Acknowledgements

The authors would like to acknowledge the Slovenian Research Agency (ARRS) for financing this research in the frame of Program P2-0046 (Separation processes and production design) and Project J2-1725.

Author biographies

Dr. Maša Knez Hrnčič holds a PhD in Chemical Engineering from the Faculty of Chemistry and Chemical Engineering, University of Maribor, where she is employed as an Assistant Professor. Her past work experience include research work at several foreign universities (University of Alabama at Birmingham, Graz University of Technology, University of Fresno). She has also established herself as a research project leader. Her main areas of research are separation processes, phase equilibria, green chemistry.

Dr. **Darija Cör** is a Researcher Assistant with a PhD obtained at the Faculty of Chemistry and Chemical Engineering, University of Maribor. During her PhD her research was focused on extraction of biological materials using subcritical and supercritical fluids. She has wide experience in high pressure technologies and analytical techniques (gas and liquid chromatography, UV-VIS spectroscopy, Differential scanning calorimetry...)

Dr. **Petra Kotnik** received her PhD in 2014 at the Faculty of Chemistry and Chemical Engineering, University of Maribor, where she works as an Assistant with PhD in the Laboratory for Separation Processes and Product Design. Her main research activity covers extraction with high pressure technologies, supercritical chromatography,

analytical techniques (liquid and gas chromatography with mass spectrometry, UV/VIS spectroscopy).

Professor Dr. **Željko Knez** earned his PhD in Chemical Engineering in 1984 at the University of Maribor, where he currently works as a Vice dean for research at the Faculty of Chemistry and Chemical Engineering. His expertise are separation processes and product design using sub- and supercritical fluids. He has published over a 295 articles in scientific journals, and his bibliography also includes 25 patents and patent applications. He was president and a member of WP "High pressure technologies" of EFCE and a head of several research projects.

5. References

- E. Brglez Mojzer, M. Knez Hrnčič, M. Škerget, Ž. Knez, U. Bren, *Molecules*, 2016, 21, 901.
 DOI:10.3390/molecules21070901
- C. Negro, L. Tommasi, A. Miceli, Bioresour. *Technol.*, 2003, 87, 41–44. DOI:10.1016/S0960-8524(02)00202-X
- 3. P. Thangaraj, in Pharmacological Assays of Plant-Based Natural Products, Springer, Cham, Switzerland, **2016**, pp. 11–13. **DOI:**10.1007/978-3-319-26811-8_3
- 4. Altemimi, N. Lakhssassi, A. Baharlouei, D. Watson, D. Lightfoot, *Plants*, **2017**, *6*, 42. **DOI:**10.3390/plants6040042
- W. I. Haminiuk, G. M. Maciel, M. S. V. Plata-Oviedo and R. M. Peralta, *Int. J. Food Sci. Technol.*, 2012, 47, 2023–2044.
 DOI:10.1111/j.1365-2621.2012.03067.x
- M. Hojnik, M. Škerget, Ž. Knez, LWT-Food Sci. Technol., 2008, 41, 2008-2016. DOI:10.1016/j.lwt.2007.11.017
- M. Boukroufa, C. Boutekedjiret, L. Petigny, N. Rakotomanomana, F. Chemat, *Ultrason. Sonochem.*, 2015, 24, 72–79.
 DOI:10.1016/j.ultsonch.2014.11.015
- 8. F. J. Barba, N. Grimi, E. Vorobiev, *Food Eng. Rev.*, **2015**, *7*, 45–62. **DOI:**10.1007/s12393-014-9095-6
- Khoddami, M. A. Wilkes, T. H. Roberts, *Molecules*, 2013, 18, 2328–2375. DOI:10.3390/molecules18022328
- V. Camel, Analyst, 2001, 126, 1182–1193.
 DOI:10.1039/b008243k
- F. Chemat, M. A. Vian and G. Cravotto, *Int. J. Mol. Sci.*, 2012, 13, 8615–8627. DOI:10.3390/ijms13078615
- 12. M. E. Wagner, J. French, S. S. H. Rizvi, *J. Food Eng.*, **2013**, *118*, 100–107. **DOI:**10.1016/j.jfoodeng.2013.03.023
- 13. M. M. R. de Melo, A. J. D. Silvestre, C. M. Silva, *J. Supercrit. Fluids*, **2014**, 92, 115–176. **DOI:**10.1016/j.supflu.2014.04.007
- M. Solana, I. Boschiero, S. Dall'Acqua and A. Bertucco, *J. Supercrit. Fluids*, 2015, 100, 201–208.
 DOI:10.1016/j.supflu.2015.02.014
- Capuzzo, M. E. Maffei, A. Occhipinti, Molecules, 2013, 18, 7194–7238. DOI:10.3390/molecules18067194
- M. Pinelo, A. Ruiz-Rodríguez, J. Sineiro, F. J. Señoráns, G. Reglero, M. J. Núñez, *Eur. Food Res. Technol.*, 2007, 226, 199–205. DOI:10.1007/s00217-006-0526-3
- 17. W. Huang, Z. Li, H. Niu, D. Li, J. Zhang, J. Food Eng., 2008,

- 89, 298-302. DOI:10.1016/j.jfoodeng.2008.05.006
- S. Stavroulias, C. Panayiotou, Chem. Biochem. Eng. Q., 2005, 19, 373–381.
- Ł. Woźniak, K. Marszałek, S. Skąpska, Sep. Sci. Technol., 2016, 51, 1472–1479.
- P. Kraujalis, V. Kraujalienė, R. Kazernavičiūtė, P. R. Venskutonis, J. Supercrit. Fluids, 2017, 122, 99–108.
 DOI:10.1016/j.supflu.2016.12.008
- E. Zondervan, M. Monsanto and J. Meuldijk, Chem. Eng. Trans., 2015, 5, 61–66.
- K. S. Duba, A. A. Casazza, H. B. Mohamed, P. Perego, L. Fiori, Food Bioprod. Process., 2015, 94, 29–38.
 DOI:10.1016/j.fbp.2015.01.001
- M. Latoui, B. Aliakbarian, A. A. Casazza, M. Seffen, A. Converti, P. Perego, *Food Bioprod. Process.*, 2012, 90, 748–754.
 DOI:10.1016/j.fbp.2012.01.003
- A. Casazza, B. Aliakbarian, S. Mantegna, G. Cravotto, P. Perego, *J. Food Eng.*, **2010**, *100*, 50–55.
 DOI:10.1016/j.jfoodeng.2010.03.026
- Z. Zeković, B. Pavlić, A. Cvetanović, S. Đurović, *Ind. Crops Prod.*, 2016, 94, 353–362.
 DOI:10.1016/j.indcrop.2016.09.008
- K. Aladić, K. Jarni, T. Barbir, S. Vidović, J. Vladić, M. Bilić, S. Jokić, *Ind. Crops Prod.*, 2015, 76, 472–478.
 DOI:10.1016/j.indcrop.2015.07.016
- 27. C. Da Porto, A. Natolino, D. Decorti, *LWT Food Sci. Tech-nol.*, **2015**, *61*, 98–104. **DOI:**10.1016/j.lwt.2014.11.027
- 28. C. Da Porto, D. Decorti, A. Natolino, *J. Supercrit. Fluids*, **2016**, *107*, 38–43. **DOI**:10.1016/j.supflu.2015.08.006
- M. S. Lenucci, M. De Caroli, P. P. Marrese, A. Iurlaro, L. Rescio, V. Böhm, G. Dalessandro, G. Piro, *Food Chem.*, **2015**, *170*, 193–202. **DOI**:10.1016/j.foodchem.2014.08.081

- H. Kawamura, K. Mishima, T. Sharmin, S. Ito, R. Kawakami, T. Kato, M. Misumi, T. Suetsugu, H. Orii, H. Kawano, K. Irie, K. Sano, K. Mishima, T. Harada, S. Mustofa, F. Hasanah, Y. D. I. Siregar, H. Zahroh, L. S. E. Putri, A. Salim, *Ultrason. Sono-chem.*, 2016, 29, 19–26. DOI:10.1016/j.ultsonch.2015.08.016
- K. Chhouk, A. T. Quitain, D. G. Pag-asa, J. B. Maridable, M. Sasaki, Y. Shimoyama, M. Goto, *J. Supercrit. Fluids*, 2016, 110, 167–175. DOI:10.1016/j.supflu.2015.11.016
- N. Ćujić, K. Šavikin, T. Janković, D. Pljevljakušić, G. Zdunić,
 S. Ibrić, Food Chem., 2016, 194, 135–142.
 DOI:10.1016/j.foodchem.2015.08.008
- K.-Y. Khaw, M.-O. Parat, P. N. Shaw, J. R. Falconer, *Molecules*, 2017, 22, 1186. DOI:10.3390/molecules22071186
- 34. J. M. Prado, I. Dalmolin, N. D. D. Carareto, R. C. Basso, A. J. A. Meirelles, J. Vladimir Oliveira, E. A. C. Batista, M. A. A. Meireles, *J. Food Eng.*, **2012**, *109*, 249–257. **DOI:**10.1016/j.jfoodeng.2011.10.007
- M. Herrero, A. Cifuentes, E. Ibañez, Food Chem., 2006, 98, 136–148. DOI:10.1016/j.foodchem.2005.05.058
- K. M. Sharif, M. M. Rahman, J. Azmir, A. Mohamed, M. H.
 A. Jahurul, F. Sahena and I. S. M. Zaidul, *J. Food Eng.*, 2014, 124, 105–116. DOI:10.1016/j.jfoodeng.2013.10.003
- G. Brusotti, I. Cesari, A. Dentamaro, G. Caccialanza, G. Massolini, *J. Pharm. Biomed. Anal.*, 2014, 87, 218–228.
 DOI:10.1016/j.jpba.2013.03.007
- 38. M. Hadolin, M. Škerget, Z. Knez, D. Bauman, *Food Chem.*, **2001**, *74*, 355–364. **DOI**:10.1016/S0308-8146(01)00152-2
- 39. G. K. Jayaprakasha, R. P. Singh, K. K. Sakariah, *Food Chem.*, **2001**, *73*, 285–290. **DOI**:10.1016/S0308-8146(00)00298-3
- 40. L. J. Porter, L. N. Hrstich, B. G. Chan, *Phytochemistry*, **1985**, 25, 223–230. **DOI:**10.1016/S0031-9422(00)94533-3
- 41. T. Vatai, M. Škerget, Ž. Knez, J. *Food Eng.*, **2009**, 90, 246–254. **DOI:**10.1016/j.jfoodeng.2008.06.028

Povzetek

Določali smo vsebnost fenolnih spojin v ekstraktih, pridobljenih iz tropin rdečega in belega grozdja ter lupin šipka (*Rosa canina*). Ekstrakti so bili pridobljeni s konvencionalnimi tehnikami ekstrakcije z uporabo organskih topil in ekstrakcijo z nadkritičnimi tekočinami (SCFs). Proučevali smo učinek topila, vrste ekstrakcije in eksperimentalnih parametrov (čas, tlak, temperatura) na kvaliteto ekstraktov. Kvantitativno je bila ovrednotena vsebnost skupnih fenolnih spojin in proantocianidinov. S tekočinsko kromatografijo z masno spektrofotometrijo je bil določen profil fenolnih sestavin. Vsem ekstraktom je bila izmerjena antioksidativna učinkovitost. Rezultati kažejo, da je vsebnost posamičnih fenolnih spojin v ekstraktih, pridobljenih iz različnih vrst materialov, znatno variirala. Najvišja vsebnost skupnih fenolov je bila določena v ekstraktih iz tropin belega grozdja, pridobljenih z maceriranjem z MeOH (26,7 mg GA / g ekstrakta). Podobna vsebnost, 25,6 mg GA / g ekstrakta, je bila določena v ekstraktu, pridobljenem s Soxhletovo ekstrakcijo z MeOH. Elagna kislina (0,650 mg / 100 g ekstrakta), katehin (0,164 mg / 100 g ekstrakta), galna kislina (0,133 mg / 100 g ekstrakta) ter kofeinska kislina (0,038 mg / 100 g ekstrakta) da so ekstrakti spojine, ki so v višjem deležu prisotne v maceriranem ekstraktu šipkove lupine; kot topilo je bil uporabljen MeOH. Potrjena je bila tudi prisotnost epitehina, hesperidina / neohepersidina, rutina in klorogenske kisline. Ugotovili smo, da ekstrakti iz naravnih materialov bogat vir fenolnih spojin, njihova vsebnost pa je odvisna od izbire ekstrakcijskega postopka glede na vrsto materiala, vrste topila in obratovalnih pogojev.



Except when otherwise noted, articles in this journal are published under the terms and conditions of the Creative Commons Attribution 4.0 International License

@creative

Review

Amperometric Biosensors for Glucose and Lactate with Applications in Food Analysis: A Brief Review

Totka Dodevska*, Yanna Lazarova and Ivan Shterev

Department of Organic Chemistry and Inorganic Chemistry, University of Food Technologies, 26, Maritsa Boulevard, Plovdiv 4002, Bulgaria

> * Corresponding author: E-mail: dodevska@mail.bg Tel.: +359 32 603 679; Fax: +359 32 644 102

> > Received: 05-15-2019

Abstract

Over the past two decades, electrochemical biosensor devices have received great attention in the field of food analysis owing to their attractive performances. In the food industry the quality control during manufacturing process and final products requires quick and reliable analytical methods. A promising alternative to the traditional analytical techniques are the electrochemical enzymatic biosensors – devices that combine the robustness of electrochemical techniques with the specificity of biological recognition processes and offer great advantages due to size, cost, sensitivity, selectivity, and fast response. This brief review has attempted to summarise the literature on the recent progress in the development of enzyme biosensors with amperometric detection for quantitative analysis of glucose and lactate in various food samples. The review concludes with an outlook on the future challenges and perspectives in this area.

Keywords: Biosensors, Glucose, Lactate, Food analysis

1. Introduction

In food quality control, the development of reliable, sensitive and selective methods for fast, precise sensing and quantification of food ingredients and supplements, 1-4 toxicants, 5-9 antibiotics, and allergens, 10 is an issue of constantly increasing importance. 11-16 Recently, as a new direction of the analytical technology is distinguished the development of electrochemical enzymatic biosensors complex systems that include an immobilised enzyme (bioelement) and a physical transducer of the signal which may be potentiometric or amperometric, as well as a device for signal reading and processing. The amperometric biosensors have a superior sensitivity and better linear range than potentiometric devices and are the most successful commercially. In particular, in food analysis the majority of the electrochemical biosensors are based on the amperometric electrodes in combination with oxidases enzymes and it seems that these systems will continue to dominate the technology of commercial biosensors.

The electrochemical biosensing systems provide the opportunity for an accurate, highly selective, sensitive and susceptible to automatisation analysis, and are a promising alternative of the traditional analytical techniques, that are time-consuming and often require specific expensive

equipment or multi-step painstaking procedures for sample preparation. Not at least, the electrochemical biosensors offer the possibility of miniaturisation and potential for development of portable hand-held devices for real time monitoring. Fully automated biosensor systems are being developed and adapted for continuous on-line or periodic monitoring of various processes in food industry.

The amperometric enzyme-based biosensors are dominant in the food sector since they have a number of advantages in determining submilimolar levels of the analyte: extremely low detection limit, high sensitivity, wide linear range, fast response and relatively low cost of analysis. Generally, biosensors do not require extensive sample preparation and in most cases only a suitable dilution is needed; the high specificity and the wide linear dynamic range allow direct quantification of the target analyte. The results are obtained within minutes, which is particularly important as it allows corrective actions during manufacturing process.

Amperometry is based on the measurement of the current resulting from the electrochemical oxidation or reduction of an electroactive species. The resulting steady-state current is proportional to the bulk concentration of the analyte. Three-electrode set-up has to be used for am-

perometric measurements – a working electrode (electrically conductive material combined with an immobilised enzyme), that is maintained under constant potential, reference and auxiliary electrode. The working electrode is either metal (usually Pt, Au) or carbon-based material (glassy carbon, graphite, screen-printed or carbon paste electrode). As the immobilisation of enzymes on the electrode surface is a necessary and critical step in the design of biosensors, the transducer should provide a stable surface for immobilisation of biomolecules while retaining their structure, mobility and biocatalytic activity.

In order to enhance the sensitivity of biosensors, nanomaterials like metal and metal oxide nanoparticles, 17-20 carbon nanotubes (CNTs),²⁰⁻²² graphene and its derivates, 22-27 are used in the construction of transducers for increasing the electrode surface area. As a result the nanostructured electrodes possess unique characteristics such as large surface-to-volume value and extremely high catalytic efficiency. Nanomaterials not only accelerate the electron transfer and so improve the response characteristics of the transducers, but also act as immobilisation matrices. The immobilisation of enzymes on nanomaterials enhanced the amount of the enzyme loading, supported the retention of biocatalytic activity and therefore improved the sensitivity of the biosensor device. Electrochemical biosensors incorporating enzymes with nanomaterials, which combine the recognition and catalytic properties of enzymes with the electronic properties of various nanomaterials, are new materials with synergistic properties and they have excellent prospects for interfacing biological recognition events by electronic signal transduction with extremely high sensitivity and stability.²⁸

Within the family of nanomaterials, CNTs are arousing growing interest, mainly due to their exceptional structural, electronic and chemical properties. CNTs have a unique tubular structure, good biocompatibility and modifiable sidewall, making them ideal candidates for the construction of biosensors with high performances. CNTbased biosensors generally have higher sensitivities, lower limits of detection, and faster electron transfer kinetics than traditional carbon electrodes, but to fully explore the potential of the complex enzyme/CNTs, it is essential to find optimal methods for enzyme immobilisation.²⁹ CNTs can be functionalised with hydroxyl, carboxyl, carbonyl or amino groups. Functionalised CNTs exhibit increased solubility, catalytic activity and biocompatibility, since enhance the immobilisation of biorecognition molecules on the electrode surface facilitating covalent bonding. Combination of CNTs with other nano-sized materials such as metal nanoparticles for surface modification of electrodes has proved to be feasible and more effective than using either nanomaterial alone in biosensing design. Several quality review papers, published in the past decade, comprehensively discussed the uses of novel functional nanomaterials as key components of various electrochemical biosensors, some of which were successfully applied in food analysis, and provided trends in biosensing strategies based on nanomaterials.^{30–37}

For biosensing purposes, the immobilisation procedure must be reproducible and stable to ensure extended working and long-time storage stability. Factors such as accuracy of measurements, sensor-to-sensor reproducibility and operational lifetime are drastically influenced by enzyme stability, i.e. the enzyme immobilisation appears as a key factor to develop efficient biosensors with appropriate analytical performances.³⁸ Moreover, the immobilisation matrix may function only as a support or may also be concerned with mediation of the signal transduction mechanism.31 A variety of enzyme immobilisation methods are applied including physical adsorption (van der Waals interactions or hydrogen bonding), covalent attachment, physical entrapment in polymer matrices, cross-link formation (the process uses bifunctional agent forming a "bridge" between protein and electrode surface; most often used cross-linker is glutaraldehyde), and self-assembly formed monolayer (long-chain alkylthiols, amines, or disulphides are used). As a promising strategy, sol-gels also have been used to immobilise enzymes - the technique provides an environment similar to that of the enzyme in solution.³⁹ The choice of an appropriate immobilisation method is strongly individual and depends on the nature of the enzyme used, transducer type, physicochemical properties of the analyte, and biosensor's operating conditions.40

Amperometric biosensors can be classified into three categories in accordance with the principle of the response generation: 41

- 1/ first generation biosensors the signal corresponds to electrochemical reaction of an active reagent or product, involved in the biochemical transformation of the target compound; they are also called "mediator-less" amperometric biosensors;
- 2/ second generation biosensors the response results from the oxidation/reduction of the redox mediator (freely diffusing low molecular weight compound that effectively shuttles electrons between the electrode surface and the enzyme's active centre);
- 3/ third generation biosensors the enzyme's active centre has a direct electrical connection to the transducer and the concentration of the analyte is directly proportional to the redox current generated at the polarised electrode.

As a general rule, designing electrochemical biosensors requires consideration of both the target analyte and the complexity of the sample in which the analyte has to be quantified. Enzymatic electrochemical biosensors are based on biological recognition – enzyme macromolecules have binding "pockets" with unique hydrogen bonding and electrostatic biorecognition patterns to achieve extremely high specificity to the substrate. In order to operate, the enzyme must be stable and available to catalyse a

specific biochemical reaction under the operating conditions of the biosensor. However, in electrochemical biosensing the detecting device is directly in contact with the analysed sample and interferents are a serious problem. Food/beverage samples contain a number of low- and high-molecular weight interfering compounds: oxidisable acids (ascorbic acid, citric acid, caffeic acid, vanillic acid, etc.) and bases (amines, etc.), sugars, proteins, lipids, polyphenols, pigments, pesticides, etc. Some of these compounds are electroactive and capable to produce current signal, while others may cause electrode passivation/biofouling by adsorption. In particular, at a suitable applied potential phenolic compounds polymerise to form a polymeric film on the electrode surface, thereby decreasing biosensor signal.

In order to minimise the contribution of interfering species, several approaches have been proposed in development of glucose and lactate biosensors. The use of artificial electron transferring agent (mediator) in the construction of biosensors leads to lowering the operating potential and so reduces the interference effects of other electrochemically active species. The most commonly used mediators are ferrocene derivates, Meldola blue, Prussian blue, toluidine blue, methylene green, and osmium complex redox polymers.

The other approach is to use permselective membrane to restrict the access of the interfering substances. Different types of polymeric membranes serving as a barrier, ensuring the selective penetration of the substrate being determined into the layer with immobilised enzyme, have been introduced in biosensor design. Permselective membranes such as cellulose acetate, polyaniline, and polypyrrole are based on size exclusion, whereas membranes such as Nafion and polyvinylpyridine are based on charge exclusion. The polymeric films used for this purpose are usually solvent-cast or electropolymerised. In contrast to solvent-cast films, where it is difficult to obtain uniform thickness coating, electropolymerisation offers advantages with respect to thickness control, reproducibility, and uniformity of the polymer film on the electrode surface.

Cellulose acetate and polypyrrole (PPy) membranes have been reported to have a good interference effect and they are one of the first polymers used to improve biosensor's selectivity. The polymer structure is distinguished by small-sized pores and allows only small molecules to pass through. Overoxidised PPy rejects proteins and acts as an ion-exchange membrane – forms an ultra-thin film that is ion-selective against anions. Recently, successfully applied in construction of selective electrochemical biosensors is Nafion – sulphonated tetrafluoroethylene copolymer. Nafion membranes possess excellent mechanical stability, low swelling capability in aqueous media, and high cation-conductive properties. The negative charge of Nafion prevents the diffusion of anionic components through polymer film, coated on the electrode surface, and acts as a

highly effective barrier for various interferences, significantly enhancing biosensor selectivity. Polystyrene and polyurethanes with phospholipid polar groups have also been used as membrane coatings.

Using amperometric biosensors, various analytes such as alcohols, sugars, pesticides, etc. can be determined quantitatively in food samples with extremely high selectivity and sensitivity. Biosensor arrays save time as they offer the possibility for detecting multiple target analytes simultaneously. Single enzyme-based and multi-enzyme-based biosensor systems are developed and successfully applied in food processing for monitoring food quality and safety. 30,31,42-44 In this review, we have summarised and discussed the recent development of enzyme-based amperometric biosensors for glucose and lactate and their applications in food industry. Finally, future trends in amperometric biosensor development are briefly discussed. Despite the clear advantages of electrochemical biosensor systems, compared to classical analytical techniques, there is a long way to emerge from the research laboratory to the marketplace. Considerable efforts should be focused on the development of commercially available highly sensitive, miniaturised, and portable devices for fast and reliable analysis. In this context, the synergy between nanotechnology, biotechnology, and electronics, will have a pronounced influence on the development of new electrochemical biosensing devices in the foreseeable future.

2. Amperometric Glucose Biosensors

Information about glucose content of foods and beverages is essential for both producers and consumers. Glucose monitoring is crucial in tracing the fermentation processes in the wine, brewing and dairy industries. In food control, the accurate evaluation of the glucose content in foods is extremely important for the maintenance of its physiological level in blood of diabetic individuals. According to the World Health Organisation (WHO),⁴⁵ the number of people with diabetes has risen from 108 million in 1980 to 422 million in 2014; WHO predicts that the diabetes will be the seventh leading cause of death in 2030.

In the field of product authentication, the determination of glucose content in honey or wine can prove their originality and even help to identify the region of the world from which the product originates. 46,47

The enzyme glucose oxidase (GOx) (EC 1.1.3.4), frequently used for glucose detection, is unusually sustainable towards environmental influences, and is relatively inexpensive. GOx is a homodimeric enzyme (flavoprotein) with an FAD molecule non-covalently bound at the active site of each 80 kDa subunit. GOx catalyses oxidation of β -D-glucose, utilizing molecular oxygen as an electron acceptor, to produce D-gluconic acid and hydrogen peroxide (H₂O₂):

$$\beta - D - Glucose + O_i \xrightarrow{GOx} D - gluconic acid + H.O.$$

This reaction allows quantitative determination of glucose by detecting the amount of oxygen, consumed during the reaction, or detecting the amount of H₂O₂, product of the reaction. The first method has significant drawbacks: the concentration of oxygen in aqueous solutions is high, making it difficult to determine low concentrations of the analyte; moreover, in the real samples the oxygen concentration is not constant and may vary. Quantitatively glucose can be determined by measuring the current generated from the oxidation or reduction of H_2O_2 . Hydrogen peroxide can be oxidised at a conventional Pt-electrode, but the direct electrooxidation of H₂O₂ requires high overpotential and quantification suffers from interference of other compounds. The process is accompanied by co-oxidation of interfering species that are present in the real samples. For instance, food samples usually contain a high concentration of ascorbic acid and/or citric acid. Both species are classical interferents in the electrochemical analysis. As a result, the registered signal is higher and does not correspond to the real concentration of the analyte. The problem can be solved partially by using permselective barrier (membrane) to block the access of this type of interfering species at the electrode surface.

Conventional amperometric glucose biosensor that includes a cellulose acetate membrane, treated with amylamine and glutaraldehyde, is described. The system operates at a potential of 0.65 V (vs. Ag/AgCl, 3 M KCl) with linearity of the signal up to 320 mM glucose. This type of biosensor has been tested successfully for glucose determination in orange juice and tonic samples, and the results are similar to those obtained with the conventional measurement method (spectrophotometry).

In order to improve the electrochemical response of $\rm H_2O_2$ (resp., the selectivity of glucose detection), the applied potential should be efficiently lowered. The low-potential detection of $\rm H_2O_2$ is one of the most successful strategies for oxidase-based biosensors providing both sensitivity and extremely high selectivity in the presence of easily oxidisable compounds. A number of researches confirm that the optimal potentials for biosensor applications are close to 0.0 V (vs. Ag/AgCl) where, depending on the type of the electrode material, the current of $\rm H_2O_2$ reduction may be several hundred times higher than the current of oxygen reduction. At such low potentials the interference of electroactive substances in the real samples is reduced or totally eliminated.

Recently, there are a numerous studies on the development of effective electrocatalysts for reduction of $\rm H_2O_2$ by modifying the surface of the bare electrode with suitable electrocatalytic active phase that facilitates electron-transfer process – metal or metal oxide particles, bimetallic nanomaterials, conducting polymer films, metal

complexes, etc. In this connection, new carbonaceous electrodes modified with microquantities of noble metals (Pd, Pd+Pt, Pd+Au) have been proven to be promising transducers for the development of biosensors. On their basis, improved model biosensor systems for glucose^{49–51} and xanthine^{50,52,53} analysis have been developed.

In some cases, electrodes modified with horseradish peroxidase (HRP) as an efficient biocatalyst for reduction of $\rm H_2O_2$ are used. The development of bienzymatic systems that include both GOx and HRP, leads to a significant increase in the selectivity of the analysis, but also considerably complicates the architecture of the biosensor.

A number of research groups have used Prussian Blue (ferric hexacyanoferrate) as an "artificial peroxidase". At an optimal potential for sensor/biosensor applications 0.0 V (vs. Ag/AgCl) Prussian Blue (PB) has been shown to be highly active and selective catalyst in $\rm H_2O_2$ electroreduction in the presence of oxygen (the current of $\rm H_2O_2$ reduction was several hundred times higher than of oxygen reduction). ⁵⁴ Here it should be noted that the stability associated with limited working pH-range of the PB-based transducers is a crucial point commonly raised by referees as an objection against their practical applications.

Carbon film resistor electrodes have been evaluated as transducers for the development of oxidase-based enzyme biosensors.55 The electrodes were first modified with PB and then covered by a layer of covalently immobilised oxidase enzymes. These enzyme electrodes were used to detect the substrate of the oxidase (glucose, ethanol, lactate, glutamate) via reduction of hydrogen peroxide at 0.05 V vs. Ag/AgCl in the low micromolar range at response time within 2 min. Finally, the glucose, ethanol, and lactate electrochemical biosensors were used to analyse complex food matrices - must, various wines, and yoghurt. Data obtained by the single standard addition method were compared with a spectrophotometric reference method and showed good correlation, indicating that the electrodes are suitable for food analysis. However, the lifetime of the enzyme electrodes, stored 1 month in 0.1 M phosphate buffer pH 7.0 at temperature of 4 °C, evaluated by running two calibration curves per week, was unsatisfactory - glucose biosensor retained 50-60% of its initial activity, while the activity of lactate biosensor was in the 20-40% range.

For industrial control, the use of automated methods is desirable and the flow injection analysis (FIA) is worthwhile. In this connection, the combination of the FIA system with amperometric biosensors became attractive due to its versatility, simplicity, and suitability for large-scale analyses. Biosensor developed on the basis of glassy carbon with electrodeposited Prussian Blue, immobilised GOx, and coating of a Nafion polymer layer, was used for industrial routine measurements of glucose in instant coffee samples. The linear concentration range is from 0.15 to 2.5 mM glucose (RSD < 1.5%) with detection limit of 0.03 mM. The system has a high operational stability and

fast response which enables the measurement of 60 samples per hour and is suitable for automated monitoring of glucose in commercial soluble coffee.

An amperometric biosensor system with ferrocene as a mediator and a Nafion protective film operating at 0.25 V (vs. Ag/AgCl, 3 M KCl) was used to determine the glucose content in wine.⁵⁷ Neutral Red⁵⁸ and osmium polymers⁵⁹ were also successfully used as mediators for glucose analysis in wines and alcoholic beverages.

The support material, used for enzyme immobilisation, should possess mechanical stability and rigidity, as well as high affinity to proteins. Recently, in biosensor design chitosan has been widely used as a support for enzyme immobilisation. 60,61 Chitosan is a natural linear amine-rich polysaccharide, non-toxic biocompatible polymer, distinguished by its ability to form flexible, transparent membranes with sufficient mechanical strength, high adhesive consistency and protein-binding capacity. The common drawback of the direct entrapment of enzyme in the polymer is relatively low efficacy of enzyme loading. This results in inconsistency in amperometric response and reduced sensitivity during long-term operation of the biosensor. Therefore, for better enzyme loading cross-linking agents (glutaraldehyde GA, thiol linkers) have been combined with polymer layers. An amperometric enzyme electrode based on GOx immobilised on chitosan membrane via cross-linking showing the highest response to glucose utilised 0.21 ml cm⁻² thick chitosan membrane.⁶⁰ Under optimal experimental conditions (pH 6.0, temperature of 35 °C, and applied potential of 0.6 V vs. Ag/AgCl) detection limit of 0.05 mM was reached. The performance of the biosensor was evaluated by determining the glucose content in fruit homogenates; the accuracy was compared to that of a commercial glucose assay kit and results indicated that the present immobilisation method and measurement procedure are reliable and have potential for commercial application.

An amperometric biosensor, distinguished by its simplicity and relative low cost, based on GOx, hydrogel, of chitosan and highly ordered titanium dioxide nanotube arrays (TiO₂NTAs) has been evaluated by Artigues et al.⁶² In the recent years, TiO₂NTAs has been extensively studied and proved as material suitable as an electrochemical interface for biosensor applications. TiO2NTAs offer excellent biocompatibility, high active area that allows immobilisation of a high number of enzyme molecules, and remarkable ability to promote charge transfer processes. The GOx-Chitosan/TiO2NTAs biosensor showed a sensitivity of 5.46 μA mM⁻¹ with a linear range from 0.3 to 1.5 mM; no significant interferences from fructose, ascorbic acid, and citric acid were obtained. Measurements done with the studied biosensor showed high repeatability (RSD equal to 0.8%) and reproducibility (RSD equal to 2.5%). The biosensor has good storage stability - after 30 days 85% of its initial current response was retained. Glucose content of different food samples - soft drinks, milk, yoghurt, fried tomato, and ketchup, was measured using the biosensor and compared with the respective HPLC value. In all the cases, the glucose concentration was determined with sufficient accuracy (deviation less than 10%) regardless of the matrix composition.

Conducting (poly)thiophene films were also applied as support material in designing glucose biosensors. The development of biosensors by electrochemical polymerisation of (poly)thiophenes, namely 2,2'-bithiophene (2,2'-BT) and 4,4'-bis(2-methyl-3-butyn-2-ol)-2,2'-bithiophene (4,4'-bBT), followed by immobilisation of GOx on the films, is described.⁶³ *N*-cyclohexyl-*N*'-(2-morpholinoethyl) carbodiimide metho-*p*-toluenesulphonate (CMC) was used as a condensing agent, and *p*-benzoquinone (BQ) was used as a redox mediator. The enzyme electrodes based on films of 2,2'-BT and 4,4'-bBT were tested for their ability to detect glucose in synthetic and real samples – pear, apricot, and peach fruit juices.

A simple inexpensive paper-based amperometric glucose biosensor based on Prussian Blue-modified screen-printed carbon electrode (SPCE) was developed. The use of cellulose paper proved to be a simple, "ideal", and green biocompatible immobilisation matrix for GOx. The glucose biosensor allowed a small amount (0.5 μ L) of sample solution for glucose analysis and had a linear calibration range from 0.25 to 2.00 mM with a detection limit of 0.01 mM glucose. Its analytical performance was demonstrated in analysis of selected commercial glucose beverages. Despite the simplicity of the immobilisation method, the biosensor retained 72% of its activity after a storage period of 45 days.

Glucose biosensor based on GOx, poly(3,4-ethylene-dioxythiophene) (PEDOT) and anthranilic acid (AA) doped with poly(4-styrenesulphonic acid) (PSSH) was successfully applied for determination of glucose concentration in food samples such as grape juice and honey. After a careful examination of the experimental data, it can be stated that the presented biosensor will be an appropriate tool for measurement of glucose concentration in food samples, provided that the concentration of ascorbic acid in such samples remains below the level of 0.1 mM.

Glucose oxidase was immobilised in conducting copolymers of three different types of poly(methyl-methacrylate-co-thienyl-methacrylate). Immobilisation of enzyme was carried out by entrapment in conducting polymers during electrochemical polymerisation of pyrrole on the copolymer electrodes. The amount of glucose in orange juices was investigated by using the developed enzyme electrodes.

In biosensors development, incorporation of biocatalyst within the bulk of carbon matrix offers some advantages such as: high stability, possibility to incorporate other components, and a renewable surface.⁶⁷ Glucose and sucrose concentrations were determined with < 3% errors with an amperometric method by using FIA technique.⁶⁸ A carbon paste electrode containing GOx, HRP, and ferro-

Table 1. Electrochemical biosensors for glucose analysis in food samples.

Electrode modifier	Method (Potential, V)	Sensitivity	Linear range, M (Detection limit, M)	Samples
GOx + cellulose acetate membrane + GA ⁴⁸	Amp (0.65 V)	-	up to 3.2×10^{-1}	orange juice, soft drinks
${\text{GOx} + \text{PB} + \text{GA}^{55}}$	Amp (0.05 V)	8 μA mM ⁻¹	$1 \times 10^{-5} - 8 \times 10^{-4}$ (1×10^{-6})	wine
GOx + PB + Nafion ⁵⁶	FIA, Amp (-0.05 V)	25.13 nA mM ⁻¹	$1.5 \times 10^{-4} - 2.5 \times 10^{-3}$ (3×10^{-5})	instant coffee
${\text{GOx + PNR + GA}^{58}}$	Amp (-0.35 V)	3.5 μA mM ⁻¹ cm ⁻²	$9 \times 10^{-5} - 1.8 \times 10^{-3}$ (2.2 × 10 ⁻⁵)	wine
GDH + diaphorase + CNTs + Os-polymer + NAD+ 59	Amp (0.2 V)	13.4 μA mM ⁻¹ cm ⁻²	$1 \times 10^{-5} - 8 \times 10^{-4}$ (1×10^{-5})	sweet wine
$\overline{\text{GOx} + \text{CS}^{60}}$	Amp (0.6 V)	$0.0597~\mu A~m M^{-1}$	$1 \times 10^{-5} - 1.3 \times 10^{-1}$ (5×10^{-5})	fruit homogenates
$\overline{\text{GOx} + \text{CS}^{61}}$	Amp (0.6 V*)	21 mA M ⁻¹ cm ⁻²	$5 \times 10^{-5} - 1.5 \times 10^{-2}$ (1×10^{-5})	mixed fruit juice, orange juice, sport drink, cola
$\overline{\text{GOx} + \text{CS} + \text{TiO}_2\text{NTAs}^{62}}$	Amp (-0.4 V)	5.46 μA mM ⁻¹	$0.3 \times 10^{-3} - 1.5 \times 10^{-3}$ (7×10^{-5})	soft drinks, milk, yoghurt, fried tomato, ketchup
$\overline{\text{GOx + poly(2,2'-BT)} + \text{BQ}^{63}}$ $\overline{\text{GOx + poly(4,4'-bBT)} + \text{BQ}^{63}}$	Amp (0.4 V*)	-	$9 \times 10^{-5} - 5.2 \times 10^{-3}$ (3×10^{-5}) $1.5 \times 10^{-4} - 5.2 \times 10^{-3}$ (5×10^{-5})	fruit juice (pear, apricot, peach)
GOx + PB + cellulose paper ⁶⁴	Amp (-0.3 V)	2.14 μA mM ⁻¹	$2.5 \times 10^{-4} - 2 \times 10^{-3}$ (1×10^{-5})	glucose beverages
GOx + PEDOT + PAA + PSSLi ⁶⁵		$2.74 \times 10^{-4} \text{ A M}^{-1}$	$9.6 \times 10^{-4} - 3 \times 10^{-2}$	
GOx + PEDOT + AA + PSSH ⁶⁵	Amp (0.6 V)	$2.57 \times 10^{-4} \text{ A M}^{-1}$	(2.9×10^{-4}) $1.86 \times 10^{-3} - 3 \times 10^{-2}$ (5.6×10^{-4})	grape juice, honey
GOx + HRP + Fc ⁶⁸	FIA, Amp (0.0 V)	10.7 nA mg ⁻¹ L	25 – 80 mg L ⁻¹	fruit juices
GOx + CMC + ferricyanide ⁶⁹	Amp (0.4 V)	-	$1 \times 10^{-3} - 1 \times 10^{-1}$ (1×10^{-3})	lactic fermenting beverages
$RhO_2 + GOx + Nafion^{70}$	Amp (-0.2 V)	$0.098~\mu A~mg^{-1}~L$	$1 - 250 \text{ mg L}^{-1}$ (0.2 mg L ⁻¹)	instant tea, honey
$GOx + GA^{71}$	Amp (0.2 V)	-	$4 \times 10^{-5} - 2.5 \times 10^{-3}$ (4×10^{-5})	wine and must
GOx + HMDA + GA ⁷²	FIA, Amp (0.7 V)	$505 \pm 55 \ \mu A \ mM^{-1}$	up to 1.5×10^{-5} (1×10^{-6})	pineapple and orange juice
$\overline{\text{GOx} + \text{PPy}^{73}}$	Amp (0.7 V)	3.5 μA mM ⁻¹ cm ⁻²	$5 \times 10^{-4} - 2.4 \times 10^{-2}$ (2.69 × 10 ⁻⁵)	fruit juices, non-alcoholic beverages

The potential value is referred vs. Ag/AgCl, 3 M KCl; *vs. saturated calomel electrode (SCE); Amp – amperometry; FIA – flow injection analysis; GOx – glucose oxidase; GDH – glucose dehydrogenase; CNTs – carbon nanotubes; NAD – nicotinamide adenine dinucleotide; GA – glutaraldehyde; PB – Prussian Blue; CS – chitosan; NTAs – nanotube arrays; PNR – poly(neutral red); HRP – horseradish peroxidase; Fc – ferrocene; PEDOT – poly(3,4-ethylenedioxythiophene); PAA – polyacrylic acid; PSSLi – poly(4-lithium styrenesulphonic acid); AA – anthranilic acid; PSSH – poly(4-styrenesulphonic acid); 2,2'-BT – 2,2'-bithiophene; 4,4'-bis(2-methyl-3-butyn-2-ol)-2,2'-bithiophene; BQ – *p*-benzoquinone; CMC – carboxymethyl cellulose; HMDA – hexamethylenediamine; PPy – polypyrrole.

cene was used in combination with the soluble enzymes invertase and mutarotase. The effect of invertase, mutarotase, and ascorbic acid on the electrode response was examined. The proposed method for glucose and sucrose measurements was validated in real samples of fruit juices.

An amperometric biosensor system based on screen-printed electrodes for simultaneously detection of glucose and L-lactate has been developed and applied for simple and rapid monitoring of their levels in lactic fermenting beverages. Using the proposed method, assays were completed within 5 min and a good agreement with high-performance liquid chromatography results was obtained. The system was based on three-dimensionally layered electrodes and ferricyanide as a mediator. A linear relationship between steady-state current and concentration was found over a range of 1–100 mM (glucose) and 1–50 mM (lactate). The stability of the proposed system was examined – after storage in a freezer at temperature of –30 °C under dry conditions, the biosensor response was stable for at least 10 months.

Table 1 summarises applications of various types of electrochemical glucose biosensors in food analysis.

In the literature, third-generation biosensors based on direct electrochemistry of GOx have been reported. $^{74-79}$ These biosensors operate close to the redox potential of the enzyme, eliminating the need of redox mediator or peroxidase. The devices have significant advantages such as simpler design and independence from $\rm O_2$ content in the solution (the electron acts as a second substrate for the enzymatic reaction). However, analytical results for glucose detection in real food samples with third-generation biosensors are not reported yet.

3. Amperometric Lactate Biosensors

Lactate is a key metabolite of the anaerobic glycolytic pathway. In food industry the lactate level is an indicator of the fermentative processes and is related to the freshness, stability, and storage quality of various foods and beverages such as wine, beer, cider and diary products (milk, cheese, yoghurt, butter). In wine industry the malolactic fermentation is monitored by following the decreasing level of L-malic acid, and increasing level of L-lactic acid – conversion that leads to deacidification and softening of the wine taste. Contamination of milk, fruit juices, canned fruits/vegetables, and eggs with lactic acid bacteria during production or storage leads to increased level of L-lactate – marker of spoilage. In meat processing it can be taken as an indicator of pre-mortem stress imparting the deficiency in the meat quality.

On the other hand, L-lactic acid (E 270) is used as a preservative and food supplement; it is added as an acidulant to foods and beverages, where a tart flavour is desired (jams, jellies, candy, soft drinks, etc.) and also as emulsifying agent in bakery products. Moreover, in clinical analysis

and sport medicine analysis of lactate is relevant for diagnostic of ischemic conditions and cystic fibrosis; blood lactate level correlates to the status of anaerobic metabolism during muscle work and is an indicator for training status at athletes. As an alternative to the conventional analytical methods (chromatographic and spectrophotometric) for lactate monitoring, amperometric biosensors, which provide reliable, direct and rapid measurements, are successfully used. Most of the commercial biosensors for lactate utilise lactate oxidase as a biorecognition element.

Lactate oxidase (LOx) (EC 1.13.12.4) is a globular flavoenzyme, mostly used in amperometric biosensor applications. The quantitative determination of L-lactate, using LOx, is based on the following catalytic reaction:

$$L-Lactate + O_2 \xrightarrow{LOx} pyruvate + H_2O_2$$

LOx catalyses the oxidation of L-lactate to pyruvate in the presence of dissolved oxygen and forms H_2O_2 . The produced H_2O_2 can be reduced or oxidised electrochemically to give a current proportional to the concentration of L-lactate.

Raw milk and dairy products are among the most important foods, and their quality is of great importance for human health. Bienzyme amperometric biosensors for lactate analysis in milk and dairy products have been reported. Biosensor system, reported by Torriero et al., is based on a glassy carbon electrode with immobilised LOx and HRP with a mediator osmium redox polymer. The working potential of 0.0 V (vs. Ag/AgCl, 3 M KCl) eliminates the interference of the electroactive substances in milk samples and allows detection of extremely low lactate concentrations (5 nM). Analysis is rapid, highly selective, and sensitive and there is a good correlation with the results obtained by standard spectrophotometric method.

L-lactic acid was determined in cow's milk, goat's milk and whey protein concentrate (WPC)-enriched goat's milk yoghurts by using an amperometric biosensor involving a bienzyme graphite–Teflon–LOx–HRP–ferrocene composite electrode. The correlation between the L-lactic acid results obtained at the same applied potential (0.0 V vs. Ag/AgCl) using the bienzyme biosensor method and a standard colorimetric enzymatic method was 0.95. One-and two-way analyses of variance indicated that the biosensor method was able to discriminate between WPC supplemented and non-supplemented yoghurts, whereas this discrimination could not be accomplished with the colorimetric enzymatic method.⁸¹

To overcome interference of electroactive substances such as polyphenols and ascorbic acid, some research groups used mediators, redox polymers, and membranes, that serve as a selective barrier for easily oxidisable species: poly(5-hydroxy-1,4-naphthoquinone-co-5- hydroxy-3-acetic acid-1,4-naphthoquinone),⁸² polyvinylimidazole-Os,⁸³ polyaniline-co-fluoroaniline film,⁸⁴ chitosan membrane with ferrocyanide,⁸⁵ polysulphone membrane/

MWCNTs with ferrocene,⁸⁶ overoxidised polypyrrole (PPYox).⁸⁷

The advantages of covalent immobilisation techniques were coupled with the excellent interference-rejection capabilities of PPYox and a bilayer disposable lactate biosensor able to operate in FIA was developed by Palmisano et al.⁸⁷ The biosensing layer, obtained by glutaraldehyde co-cross-linking of LOx with bovine serum albumin (BSA), was cast on an underlying electropolymerised layer of PPYox. In this work co-cross-linking of enzyme with BSA by GA is preferred as a simple procedure mainly because it allows a higher degree of intermolecular bonding, a lower extent of enzyme crowding and enzyme deactivation, and results in an immobilised enzyme layer showing high enzyme stability and good mechanical properties. When integrated in a FIA system, a linear response up to 1 mM and detection limit of 2 µM were obtained; the introduction of a microdialysis membrane-based sampler extended the linear range up to 50 mM lactate. The anti-interference characteristics of the biosensor permitted lactate determination in untreated milk and diluted yoghurt samples.

A similar immobilisation technique has been applied in the development of an interference and cross-talk-free dual electrode amperometric biosensor for simultaneous monitoring of glucose and lactate by FIA.⁸⁸ The potential of the biosensor system was demonstrated by simultaneous determination of lactate and glucose in untreated tomato juice samples.

In order to improve the sensitivity of lactate biosensors, nanomaterials are used to increase the working surface of the electrode. Amperometric biosensors based on a gold planar electrode and two types of nanocomposites, derived from different MWCNTs, were used to determine lactate in foods (apple juice, tomato paste, olive brine, probiotic drink), in red and white wines. 85 Biosensors are constructed by immobilizing LOx and HRP in a layer of chitosan onto the electrode surface and ferrocyanide was used as a mediator. The protein affinity of chitosan prevents enzyme denaturalisation, thus offering an enzyme-friendly environment. Amperometric measurements were performed at -0.05 V (vs. Ag/AgCl, 3 M KCl). The linear concentration range of biosensor, based on a gold electrode, was from 5 to 244 µM with a limit of detection 0.96 µM. The analytical system shows satisfactory stability (no loss of sensitivity after 60 consecutive measurements) and excellent stability after 15 months storage at room temperature (retained 90% of its initial sensitivity).

Bienzymatic biosensor with LOx, HRP, and redox mediator ferrocene, included in graphite-Teflon composite matrix, was developed.⁸⁹ Lactate content in red wine and yoghurt was determined at potential of 0.0 V (vs. Ag/AgCl, 3 M KCl). The composite bioelectrode exhibits long-term stability – reproducible amperometric signal was achieved with no significant loss of enzyme activity after storage for 6 months at 4 °C. Detection limit of 90 nM has

been determined and excellent selectivity of analysis in real samples has been demonstrated. The sensor developed can be applied for monitoring and optimizing the fermentation process, and for controlling the quality of fermented products.

An amperometric bienzymatic biosensor based on incorporation of LOx and HRP into a CNTs/polysulphone membrane by the phase inversion technique onto screen-printed electrodes has been developed by Perez and Fabregas. ⁸⁶ In order to improve the sensitivity and to reduce the working potential, experimental conditions are optimised and ferrocene as a redox mediator has also been incorporated into the membrane. The biosensor response time to L-lactate was 20 s and showed an excellent reproducibility (RSD 2.7%); at an applied potential of –0.1 V (vs. Ag/AgCl) the detection limit of 0.05 mg L⁻¹ L-lactate with a linear range from 0.1 to 5 mg L⁻¹ were determined. The system has been successfully applied for quantitative detection of L-lactic acid in different wine and beer samples.

Lactate biosensors based on various types of transducers and immobilised LOx were developed, and lactate determination during fermentation process was performed in wine and must samples.^{71,90-93} Commercially available screen printed electrodes SensLab are preferred as transducers from research groups of Shkotova and Goriushkina. Appropriate function of the electrochemical biosensor requires effective coverage of the transducer with enzyme. In this connection, Shkotova and co-authors present two ways for immobilisation of LOx onto the working electrode surface: 1/ physical adsorption into a Residrol polymer layer, and 2/ immobilisation in poly 3,4-ethylenedioxythiophene applying electropolymerisation.90 Electrochemical measurements with both biosensor systems were performed at potential of 0.3 V (vs. Ag/ AgCl) in phosphate buffer, pH 7.2. The first type biosensor is characterised by a shorter linear dynamic range (0.004 - 0.5 mM) and higher sensitivity (320 nA mM⁻¹) as compared with the second type biosensor (0.05 -1.6 mM and sensitivity of 60 nA mM⁻¹). The immobilisation method has been shown to have no effect on the stability and the pH-optimum. Both biosensors are applied for analysis of lactate in wine and must. Due to their good analytical characteristics and operational stability, the use of these biosensors in wine quality control is recommended.

With same application are the amperometric biosensors based on platinum printed electrode and immobilised enzymes alcoholoxidase (AOx), GOx, and LOx, developed by Goriushkina et al. Their application is shown in quantitative detection of ethanol, glucose, and lactate with a linear concentration range of 0.3 – 20 mM ethanol, 0.04 – 2.5 mM glucose, and 0.008 – 1 mM lactate. The operational stability of both ethanol and glucose biosensors remains for two months, whereas for the lactate biosensor this time is only 4 days. The developed biosensors show high selectivity with respect to the substrates and have been successfully applied for the analysis of complex mixtures.

Biosensors based on sol-gel approach are distinguished by improved activity and stability of the bioelement. One advantage of sol-gel immobilisation is that the enzyme is entrapped within the matrix without covalent bonding involved, hereby the enzyme activity is better preserved and the sensitivity of the biosensor is higher. The porous 3-D structure of sol-gel matrix favours the diffusion of substrate molecules and facilitates the specific interaction with the enzyme's active centre. A lactate biosensor with an appropriate stability, suitable for food quality control and clinical analysis (including non-invasive diagnostics), is developed on the basis of LOx immobilised in gel membranes formed from alkoxysilanes on the top of Prussian Blue modified electrode. 93 Operational stability of the elaborated lactate biosensor was tested in flow-injection mode by injecting 0.1 mM of lactate. It was found that after 500 injections the current response remained 85% of its initial value. The biosensor remained not less than 90% of its initial activity after 6 months of storage in a waterproof package at 4 °C. The authors do not state data on the reproducibility of the biosensor. A main disadvantage of the sol-gel immobilisation approach is that it is not uniform - the thickness of the layer, the amount, and the distribution of loaded enzyme may vary a lot, affecting the sensor-to-sensor reproducibility.

A lactate oxidase amperometric biosensor was developed and optimised for malolactic fermentation monitoring during wine-making process. 94 LOx was immobilised on Prussian Blue modified screen-printed carbon electrode in order to reduce the electrochemical interferences. The biosensor showed high sensitivity (852 $\mu A~M^{-1}$) and a detection limit for lactic acid of 0.005 mM (0.45 mg L^{-1}). The operational stability and the lifetime of the biosensor were also evaluated and were equal to 8 h and 30 days, respectively. In flow injection system the biosensor was used for lactic acid analysis during malolactic fermentation of a red wine and the results were compared with those obtained by ion chromatography with good agreement.

An amperometric lactate biosensor with LOx immobilised into a Prussian Blue modified electrode was fabricated.95 The advantage of using cetyltrimethylammonium bromide (CTAB) in the electrodeposition step of PB films onto glassy carbon surfaces was confirmed taking into account both the stability and sensitivity of the measurements. The biosensor was used in the development of a FIA amperometric method for lactate determination. Under optimal conditions (pH 6.9 and applied potential of -0.1 V vs. Ag/AgCl, NaCl sat.), the repeatability of the method for injections of 0.28 mM lactate was 2.2% (n = 18). Due to the near-zero working potential, high catalytic activity and selectivity of Prussian Blue towards the cathodic reduction of hydrogen peroxide, the biosensor system exhibited a practically interference-free response towards the target analyte. The usefulness of the developed biosensor was demonstrated by determining lactate level in beer samples and the results were in good agreement

with those obtained by using a reference spectrophotometric enzyme method.

Polypyrrole (PPy) is a conductive polymer with positive charges that can be formed onto electrode surface through electropolymerisation using cyclic voltammetry. As advantages of PPy can be specified: 1/ the thickness of the PPy layer can be quantitatively controlled by controlling the number of cycles applied during cyclic voltammetry, and 2/ enzymes with negative charges can be absorbed into PPy layers via electrostatic forces. However, some authors note that the enzyme loading capability of PPy is low which may results in a reduced biosensor sensitivity. Further, PPy layer is most stable at pH range of 5.5 – 6.0, which limits the type of the used enzyme.

Biosensor system based on LOx, immobilised on the surface of planar electrode modified with Prussian Blue and electropolymerised polypyrrole film, was applied in quality control of kvass (traditional Russian yeast drink). 96 The analytical characteristics of the resulting biosensor are as follows: a sensitivity of 190 ± 14 mA M^{-1} cm $^{-2}$, a linear dynamic range from 0.5 to 500 μM , and high operational stability. Due to the low working potential (0.0 V vs. Ag/AgCl) the biosensor is indifferent to species that present in the analysed samples and included in FIA system allows an express assessment of the quality of food products.

Marzouk and co-authors present an analytical FIA system by amperometric simultaneous detection of glucose and lactate.⁹⁷ The enzyme-generated H₂O₂ is measured by a working platinum electrode with deposited layer of *m*-phenylenediamine. The system is applicable for quantitative analysis of glucose and lactate in dairy products.

An amperometric biosensor system based on screen-printed electrode and ferricyanide as a mediator has been used for simultaneous detection of glucose and lactate in dairy drinks. ⁶⁹ The linear range is from 1.0 to 100 mM glucose and from 1.0 to 50 mM lactate. The duration of the analysis is only 5 min. An excellent agreement of the results with those obtained by HPLC has also been demonstrated.

Integrated amperometric biosensors for the determination of L-malic and L-lactic acids in wine during fermentation were developed by co-immobilisation of the enzymes L-malate dehydrogenase (MDH) and diaphorase (DP), or LOx and HRP, respectively, together with the redox mediator tetrathiafulvalene (TTF), on a 3-mercaptopropionic acid (MPA) self-assembled monolayer-modified gold electrode by using a dialysis membrane.⁹¹ After 7 days of continuous use, the MDH/DP biosensor still exhibited 90% of the original sensitivity, while the LOx/HRP biosensor yielded 91% of the original response after 5 days. Calibration graphs were obtained with linear range from 0.52 to 20 µM for L-malic acid, and from 0.42 to 20 μM for L-lactic acid, respectively. The experimental results obtained with both biosensors exhibited a very good correlation when plotted against those obtained by using commercial enzymatic kits.

Rahman et al. developed an amperometric lactate biosensor based on a conducting polymer poly-5,2'-5',2"-terthiophene-3'-carboxylic acid (pTTCA) and MWCNTs composite on a gold electrode. ⁹⁸ Lactate dehydrogenase (LDH) and the oxidised form of nicotinamide adenine dinucleotide (NAD+) were subsequently immobilised onto the pTTCA/MWCNTs composite film. The detection signal was amplified by the pTTCA/MWCNTs assembly with immobilised enzyme. The applicability of the biosensor was demonstrated successfully in commercial milk and human serum samples.

Polyethyleneimine (PEI), a cationic polymer, was also used to immobilise LOx⁹⁹ and LDH¹⁰⁰ to the surface of a screen-printed carbon electrodes, which were subsequently applied to the determination of lactate in yoghurt samples. PEI possesses a strong positive charge in aqueous solutions enabling electrostatic binding of the enzymes to the electrode surface.

It should be noted that the use of charged protective layers like Nafion in design of lactate biosensors influences the response characteristics of the sensor as well, and in particular obviously reduces the sensitivity of the resulting

biosensor device because the analyte is negatively charged. Such effect was observed by Patel et al. in developing of disposable-type lactate oxidase biosensors for dairy products and clinical analysis.⁹⁹ It was established that the biosensor without coating of Nafion showed naturally higher response than that coated with Nafion and the current signal was dramatically attenuated by increasing the total amount of Nafion on the electrodes.

Table 2 gives an overview for applications of amperometric lactate sensors in the food analysis.

Biosensors are not only objects of fundamental and applied research but they are also important commercial products. Depending on application, the biosensor could be a laboratory stand, portable, or hand-held device. Several commercial instruments based on electrochemical amperometric biosensor are available – Fuji Electric Co. (Japan), IBA GmbH (Germany), Yellow Springs Instruments (USA), Nova Biomedical (USA), Analox Instruments (UK-USA), Sensolytics GmbH (Germany), Tectronik (Italy), BioFutura s.r.l. (Italy), Biosentec (France), and Chemel AB (Sweden) produce glucose and lactate biosensor devices applicable in bioprocess control and food analysis.

Table 2. Electrochemical biosensors for lactate analysis in food samples.

Electrode modifier	Method (Potential, V)	Sensitivity	Linear range, M (Detection limit, M)	Samples
$\overline{LOx + PB + GA^{55}}$	Amp (0.05 V)	10.4 μA mM ⁻¹	$1 \times 10^{-5} - 5 \times 10^{-4}$ (1×10^{-6})	wine, yoghurt
LOx + CMC + ferricyanide ⁶⁹	Amp (0.4 V)	1.7124 μA mM ⁻¹	$1 \times 10^{-3} - 5 \times 10^{-2}$ (1×10^{-3})	lactic fermenting beverages
LOx + PEDOT ⁷¹	Amp (0.2 V)	-	$8 \times 10^{-6} - 1 \times 10^{-3}$ (8×10^{-6})	wine and must
LOx + HRP + Os-PAA ⁸⁰	FIA, Amp (0.0 V)	-	$1 \times 10^{-5} - 2.5 \times 10^{-3}$ (5 × 10 ⁻⁹)	fresh milk, skimmed milk, acidophilus milk, skimmed yoghurt, fruit yoghurt
${\text{LOx + HRP + Fc}^{81}}$	Amp (0.0 V)	-	$5 \times 10^{-6} - 1 \times 10^{-4}$	yoghurts
LOx + poly(JUG-co-JUGA) ⁸²	$\begin{array}{c} \text{Amp} \\ (-0.1 \text{ V}^*) \end{array}$	$70 \pm 10 \; \mu A \; M^{-1} \; cm^{-2}$	$5 \times 10^{-5} - 1.5 \times 10^{-3}$ (5 × 10 ⁻⁵)	yoghurt
${\text{LOx + HRP + Fc + CS}^{85}}$	Amp (-0.05 V)	3.47 nA μM ⁻¹	$5 \times 10^{-6} - 2.44 \times 10^{-4}$ (9.6 × 10 ⁻⁷)	wine
LOx + HRP + CNTs + Fc + polysulphone membrane ⁸⁶	Amp (-0.1 V)	1168.8 μA M ⁻¹ mm ⁻²	$1.1 \times 10^{-6} - 5.6 \times 10^{-5}$ (5.6×10^{-7})	wine and beer
LOx + GA + BSA + PPyox ⁸⁷	FIA, Amp (0.65 V)	300 ± 10 nA mM ⁻¹ L	up to 5×10^{-2} (1×10^{-3})	untreated milk, yoghurt
LOx + Resydrol ⁹⁰		320 nA mM ⁻¹	$4 \times 10^{-6} - 5 \times 10^{-4}$	
LOx + PEDOT ⁹⁰	Amp (0.3 V)	$60~\mathrm{nA~mM^{-1}}$	$5 \times 10^{-5} - 1.6 \times 10^{-3}$	wine, must
LOx + HRP + TTF + MPA ⁹¹	Amp (-0.05 V)	$2711 \pm 190 \ \mu A \ M^{-1}$	$4.2 \times 10^{-7} - 2 \times 10^{-5}$ (4.2×10^{-7})	wine

LOx + APTS + PB ⁹³	FIA, Amp (0.0 V)	0.18 A M ⁻¹ cm ⁻²	$5 \times 10^{-7} - 1 \times 10^{-3}$ (1×10^{-7})	beverages
LOx + PB + CTAB ⁹⁵	FIA, Amp (-0.1 V)	-	$4 \times 10^{-6} - 2.8 \times 10^{-4}$ (8.4×10^{-7})	beer
LOx + PPy + PB%	Amp (0.0 V)	$190 \pm 14 \text{ mA M}^{-1} \text{ cm}^{-2}$	$5 \times 10^{-7} - 5 \times 10^{-4}$ (5 × 10 ⁻⁷)	kvass
LDH + pTTCA + MWCNTs + NAD+98	3 Amp (0.3 V)	$0.0106~\mu A~\mu M^{-1}$	$5 \times 10^{-6} - 9 \times 10^{-5}$ (1×10^{-6})	milk
LOx + PEI + PCS + Nafion ⁹⁹	Amp (0.6 V)	0.682 nA μM ⁻¹	up to 1×10^{-3} (5 × 10 ⁻⁷)	yoghurt, buttermilk
${\text{LOx + PtNPs + GCNF + PEI + GA}^{100}}$	Amp (0.3 V)	41.3 μA M ⁻¹ cm ⁻²	$1 \times 10^{-5} - 2 \times 10^{-3}$ (6.9×10^{-6})	wine, cider
LOx + laponite-organosilasesquioxane	101 Amp (0.4 V)	$0.33 \pm 0.01 \text{ A M}^{-1} \text{ cm}^{-2}$	$3 \times 10^{-6} - 3 \times 10^{-4}$ (1×10^{-6})	yoghurt, fermented milk, red wine
LOx + laponite/CS hydrogels + FcMe ¹⁰	² Amp (0.4 V)	$0.326 \pm 0.003 \text{ A M}^{-1} \text{ cm}^{-2}$	$1 \times 10^{-5} - 7 \times 10^{-4}$ (3.8×10^{-6})	white wine, fermented milk, beer
LOx (SIRE-technology) ¹⁰³	Amp (0.65 V)	-	up to 1×10^{-4} (3.3 × 10 ⁻⁵)	tomato paste, baby food
LDH + PyrOx ¹⁰⁴	EIS (0.0 V)	-	$1 \times 10^{-5} - 2.5 \times 10^{-4}$ (1.7 × 10 ⁻⁵)	yoghurt
LOx + HRP + PPy ¹⁰⁵	Amp (0.075 V)	$13500 \pm 600 \ \mu A \ M^{-1} \ cm^{-2}$	$1 \times 10^{-6} - 1 \times 10^{-4}$ (5.2 × 10 ⁻⁷)	red wine
LOx + natural protein membrane ¹⁰⁶	FIA, Amp (0.59 V)	81.2 μA mM ⁻¹	$1 \times 10^{-4} - 1 \times 10^{-3}$ (5×10^{-5})	milk, cheese, kefir
LOx + HRP ¹⁰⁷	Amp (0.0 V)	$0.84~\mathrm{nA}~\mu\mathrm{M}^{-1}\mathrm{L}$	$1 \times 10^{-5} - 1.8 \times 10^{-4}$ (1×10^{-5})	yoghurt, cheese, milk
LDH + SWCNTs + VB + Nafion ¹⁰⁸	Amp (0.2 V)	=	$2 \times 10^{-4} - 1 \times 10^{-3}$	probiotic yoghurt
LOx + DTSP ¹⁰⁹	Amp (0.3 V*)	$0.77 \pm 0.08 ~\mu A ~m M^{-1}$	up to 3×10^{-4} (1×10^{-5})	wine, beer
LOx + MnO ₂ + nanoCoPc ¹¹⁰	Amp (0.5 V*)	$3.98~\mu A~mM^{-1}~cm^{-2}$	$2 \times 10^{-5} - 4 \times 10^{-3}$	milk
LOx + 3,4DHS-AuNPs ¹¹¹	Amp (0.3 V**)	$5.1 \pm 0.1 \; \mu A \; mM^{-1}$	up to 8×10^{-4} (2.6 × 10 ⁻⁶)	wine, beer, yoghurt
LOx + PB ¹¹²	Amp (0.0 V)	11.7± 0.5 nA mM ⁻¹	up to 5×10^{-2} (1×10^{-3})	fermented milk products
LDH + GONPs ¹¹³	Amp (0.7 V)	-	$5 \times 10^{-3} - 5 \times 10^{-2}$ (1×10^{-7})	beer, wine, milk, curd, yoghurt
LOx + DNPs + MPTS + HMF ¹¹⁴	CV	2.6 μA mM ⁻¹	$5.3 \times 10^{-5} - 1.6 \times 10^{-3}$ (1.6×10^{-5})	wine

BSA – bovine serum albumin; PPyox – overoxidised polypyrrole; EIS – electrochemical impedance spectroscopy; LOx – lactate oxidase; LDH – lactate dehydrogenase; FcMe – ferrocene-methanol; TTF – tetrathiafulvalene; MPA – 3-mercaptopropionic acid; CTAB – cetyltrimethylammonium bromide; CMC – carboxymethyl cellulose; Os-PAA – [Os(bpy)2ClPyCH2NHpoly(allylamine)]; poly(JUG-co-JUGA) – poly(5-hydroxy-1,4-naphthoquinone-co-5-hydroxy-3-thioacetic acid-1,4-naphthoquinone); PEI – polyethyleneimine; PCS – poly(carbamoyl)sulphonate hydrogel; pTTCA – poly-5,2'-5',2''-terthiophene-3'-carboxylic acid; MWCNTs – multi-wall carbon nanotubes; SIRE – sensors based on injection of the recognition element; PyrOx – pyruvate oxidase; NPs – nanoparticles; GCNF – graphitised carbon nanofibers; APTS – γ -aminopropyl triethoxysiloxane; SWCNTs – single-wall carbon nanotubes; VB – Variamine Blue; DTSP – 3,3'-dithiodipropionic acid di(N-succinimidyl ester); CoPc – cobalt phthalocyanine; GO – graphene oxide; DNPs – diamond nanoparticles; MPTS – (3-mercaptopropyl)-trimethoxysilane; HMF – hydroxymethyl-ferrocene; **vs. silver pseudoreference electrode. Other abbreviations are the same as Table 1.

4. Conclusions and Perspectives

Over the two last decades phenomenal growth has been observed in the field of electrochemical biosensors for analysis of food and beverages. Amperometric enzyme-based biosensors have been developed and widely used due to their well-understood bio-interaction and detection process. The high affinity of the enzyme molecules for their target analytes allowed the development of extremely sensitive and selective biosensor systems applicable in complex and variable samples. In electrochemical biosensor design precise selection of the enzyme type, suitable working electrode, as well as suitable, robust, and reproducible immobilisation methodology play a crucial role in order to achieve better selectivity and stability of biosensors. This brief review has highlighted the strategies that have been introduced to successfully improve the operational parameters of amperometric enzyme-based biosensors for glucose and lactate detection in food samples. The analytical performances in terms of high sensitivity, wide linear range and low detection limit of some of the reviewed biosensors evidence that these systems have the potential to radically change food analysis. However, despite the variety of electrochemical biosensors for glucose and lactate monitoring, 35,115-125 limited number of devices successfully applied for quality and safety assessment of foods and beverages testifies that the food sample matrices present significant challenges and there is still a need to improve analytical performances, both selectivity and operational stability of the immobilised biocomponent and shelf-life of biosensor systems. Moreover, designing novel reliable and commercially available biosensors that are capable to detect nanomolar levels of analytes, as well as biosensors for reliable analysis of multiple analytes using a single device, 126,127 are required in the field of food industry and have become an important topic in electroanalysis.

Electrochemical biosensors offer the possibility of rapid and on-site monitoring, thus providing real-time information essential in the control of production processes. The great advantage of real-time monitoring in food manufacture, particularly of dairy and winemaking industries, will motivate the commercialisation and widespread usage of these devices. Generally, the driving force for commercialisation of biosensor systems is the market/hand-held size, simplicity of operation and the instrument cost. Transforming electrochemical biosensor system into a simple, easy-to-use, cheap and portable commercial product from lab-scale research is complicated and still remains a challenge due to its high cost, stability issues, and complex instrumentation design. The fabrication of hand-held biosensor devices can be complex due to the difficulty in ensuring the operational stability and reproducibility of the sensor; in most cases the stability of the enzyme immobilised on the electrode surface is not maintained in real sample analysis conditions. It should also be taken into account that the sophisticated sensing device fabrication also may incur more cost which affects its commercialisation.

Current trends toward miniaturisation of biosensor systems have led researchers to use screen-printed electrodes (SPE). The printing of electrodes is one of the most promising technologies in transducers elaboration because it is economic, enables easy integration, improves portability, and drastically reduces contamination. Screen-printing technology is well established, reproducible, and easily incorporated in miniaturised portable devices, so SPEs belong to the most suitable electrodes for biosensing purposes. SPEs can be modified in the same way as conventional electrodes through surface chemistry modification or directly modifying the composition of the ink. Moreover, with the discovery of new nano-sized materials with superior electrocatalytic properties, we expect research groups to explore novel advanced SPEs.

Development of sensor networks and wireless signal transmitters for remote sensing is relevant in the field of biosensor technologies. Nowadays, fabrication of portable potentiostats is not a scientific challenge. In fact, small (pocket size) portable potentiostats powered by a USB connection, combined with a simple notepad, and conveniently designed to fit SPEs for on-field use, are available in the electrochemical equipment market. Particularly, for mobile sensor/biosensor applications several companies offer potentiostats with integrated Bluetooth, using a smartphone for control. Such portable potentiostat with wireless connectivity to smartphones would facilitate analysis at the point-of-use and in the field, where access to a computer is impossible.

Future trend in biosensors engineering is development of "smart" sensors which are capable of measuring, analysing, and adjusting the appropriate parameters of the analyte. The potential of this technology is enormous and should revolutionise analysis and control, because it will not only improve the food quality/safety, but will also provide much more effective control with less employment, time and energy saving.

5. References

- C. Ozdemir, F. Yeni, D. Odaci, S. Timur, Food Chem. 2010, 119, 380–385. DOI:10.1016/j.foodchem.2009.05.087
- G. Xu, M. Zhang, X. Yu, Acta Chim. Slov. 2018, 65, 502–511.
 DOI:10.17344/acsi.2017.3974
- 3. S. Malhotra, Y. Tang, P. Varshney, *Acta Chim. Slov.* **2018**, *65*, 687–697. **DOI**:10.17344/acsi.2018.4386
- 4. D. Durovic, B. Milisavljevic, M. Nedovic-Vukovic, B. Potkonjak, S. Spasic, M. Vrvic, *Acta Chim. Slov.* **2017**, *64*, 276–282. **DOI**:10.17344/acsi.2016.2582
- G. Nikoleli, D. Nikolelis, C. Siontorou, S. Karapetis, T. Varzakas, *Adv. Food Nutr. Res.* 2018, 84, 57–102.
 DOI:10.1016/bs.afnr.2018.01.003
- 6. J. Kos, E. Hajnal, I. Jajic, S. Krstovic, J. Mastilovic, B. Saric, P. Jovanov, *Acta Chim. Slov.* **2016**, *63*, 747–756.

- 7. J. Vichapong, Y. Santaladchaiyakit, R. Burakham, S. Srijaranai, *Acta Chim. Slov.* **2017**, *64*, 590–597.
 - DOI:10.17344/acsi.2017.3336
- N. Temell, R. Gurkan, Acta Chim. Slov. 2018, 65, 138–149.
 DOI:10.17344/acsi.2017.3724
- 9. Y. Santaladchaiyakit, J. Bunchamnan, D. Tongsa, S. Srijaranai, *Acta Chim. Slov.* **2017**, *64*, 849–857.
 - DOI:10.17344/acsi.2017.3413
- R. Pilolli, L. Monaci, A. Visconti, TRAC Trends Analyt. Chem.
 2013, 47, 12–26. DOI:10.1016/j.trac.2013.02.005
- X. Lu (Ed.): Sensing Techniques for Food Safety and Quality Control, Royal Society of Chemistry, 2017, pp. 1–358.
 DOI:10.1039/9781788010528
- M. Mutlu, Biosensors in Food Processing, Safety, and Quality Control, CRC Press, New York, USA, 2017, pp. 1–385.
 ISBN 9781138116009
- D. Correa, A. Pavinatto, L. Mercante, L. Mattoso, J. Oliveira, A. Riul Jr, in: A. Grumezesco (Ed.): Nanobiosensors, Elsevier, Amsterdam, Netherlands, 2016, pp. 205–244.
 DOI:10.1016/B978-0-12-804301-1.00006-0
- A. Cifuentes, ISRN Anal. Chem. 2012, Article ID 801607, 16 pages. DOI:10.5402/2012/801607
- G. Bülbül, A. Hayat, S. Andreescu, Sensors, 2015, 15, 30736–30758. DOI:10.3390/s151229826
- 16. C. Adley, *Foods* **2014**, *3*, 491–510. **DOI**:10.3390/foods3030491
- H. Malekzad, P. Zangabad, H. Mirshekari, M. Karimi, M. Hamblin, *Nanotechnol. Rev.* 2016, 6, 301–329.
 DOI:10.1515/ntrev-2016-0014
- 18. J. Wang, *Microchim. Acta* **2012**, *177*, 245–270. **DOI:**10.1007/s00604-011-0758-1
- P. Solanki, A. Kaushik, V. Agrawal, B. Malhotra, NPG Asia Mater. 2011, 3, 17–24. DOI:10.1038/asiamat.2010.137
- M. Holzinger, A. Le Goff, S. Cosnier, Front. Chem. 2014, 2, 63 (10 pages). DOI:10.3389/fchem.2014.00063
- S. Alim, J. Vejayan, M. Yusoff, A. Kafi, *Biosens. Bioelectron*.
 2018, 121, 125–136. DOI:10.1016/j.bios.2018.08.051
- 22. Z. Zhu, *Nano-Micro Lett.* **2017**, *9*, 25 (24 pages). **DOI:**10.1007/s40820-017-0128-6
- A. Lawal, Biosens. Bioelectron. 2018, 106, 149–178.
 DOI:10.1016/j.bios.2018.01.030
- C. Justino, A. Gomes, A. Freitas, A. Duarte, T. Rocha-Santos, *TrAC Trends Anal. Chem.* 2017, 91, 53–66.
 DOI:10.1016/j.trac.2017.04.003
- P. Suvarnaphaet, S. Pechprasarn, Sensors 2017, 17, 2161 (24 pages). DOI:10.3390/s17102161
- Y. Shao, J. Wang, H. Wu, J. Liu, I. A. Aksay, Y. Lin, *Electro-analysis* 2010, 22, 1027–1036. DOI:10.1002/elan.200900571
- 27. M. Zhou, Y. Zhai, S. Dong, *Anal. Chem.* **2009**, *81*, 5603–5613. **DOI:**10.1021/ac900136z
- H. Li, S. Liu, Z. Dai, J. Bao, X. Yang, Sensors 2009, 9, 8547–8561. DOI:10.3390/s91108547
- W. Feng, P. Ji, *Biotechnol. Adv.* 2011, 29, 889–895.
 DOI:10.1016/j.biotechadv.2011.07.007
- B. Perez-Lopez, A. Merkoci, Trends Food Sci. Technol. 2011,
 625–639. DOI:10.1016/j.tifs.2011.04.001

- L. Mello, L. Kubota, Food Chem. 2002, 77, 237–256.
 DOI:10.1016/S0308-8146(02)00104-8
- 32. W. Putzbach, N. Ronkainen, *Sensors (Basel)*. **2013**, *13*, 4811–4840. **DOI**:10.3390/s130404811
- K. Warriner, S. Reddy, A. Namvar, S. Neethirajan, *Trends Food Sci. Technol.* 2014, 40, 183–199.
 DOI:10.1016/j.tifs.2014.07.008
- 34. Y Zeng, Z. Zhu, D. Du, Y. Lin, *J. Electroanal. Chem.* **2016**, *781*, 147–154. **DOI**:10.1016/j.jelechem.2016.10.030
- 35. C. Chen, Q. Xie, D. Yang, H. Xiao, Y. Fu, Y. Tan, S. Yao, *RSC Adv.* **2013**, *3*, 4473–4491. **DOI**:10.1039/c2ra22351a
- 36. V. Scognamiglio, *Biosens. Bioelectron.* **2013**, *47*, 12–25. **DOI:**10.1016/j.bios.2013.02.043
- 37. A. Hayat, G. Catanante, J. L. Marty, *Sensors* **2014**, *14*, 23439–23461. **DOI:**10.3390/s141223439
- 38 A. Sassolas, J. Blum, B. Leca-Bouvier, *Biotechnol. Adv.* **2011**, *30*, 489–511. **DOI**:10.1016/j.biotechadv.2011.09.003
- 39. N. Demirkıran, E. Ekinci, *Acta Chim. Slov.* **2012**, *59*, 302–306. http://acta-arhiv.chem-soc.si/59/59-2-302.pdf
- 40. R. Săndulescu, M. Tertiş, C. Cristea, E. Bodoki, in: T. Rinken (Ed.): Biosensors Micro and Nanoscale Applications, IntechOpen, London, UK, 2015.
 DOI:10.5772/60510. Available from: https://www.intechopen.com/books/biosensors-micro-and-nanoscale-applications/new- materials-for-the-construction-of-electrochemical-biosensors
- 41. N. Ronkainen, H. Halsall, W. Heineman, *Chem. Soc. Rev.* **2010**, *39*, 1747–1763. **DOI:**10.1039/b714449k
- 42. H. Schnerr, in: R. Marks, D. Cullen, I. Karube, C. Lowe, H. Weetall (Ed.): Handbook of Biosensors and Biochips, Part Eight Biosensor Applications, John Wiley & Sons, Ltd., USA, **2008**. **DOI**:10.1002/9780470061565.hbb118
- 43. M. Thakur, K. Ragavan, *J. Food Sci. Technol.* **2013**, *50*, 625–641. **DOI:**10.1007/s13197-012-0783-z
- 44. E. Korotkaya, *Foods and Raw Mater.* **2014**, *2*, 161–171. **DOI:**10.12737/5476
- 45. World Health Organization. Diabetes, http://www.who.int/news-room/fact-sheets/detail/ diabetespp, (assessed: October 30, 2018)
- 46. S. Bogdanov, P. Martin, *Swiss Bee Research Centre* **2002**, 1–20. http://www.bee-hexagon.net/files/fileE/Honey/ AuthenticityRevue_Internet.pdf
- 47. G. Rapeanu, C. Vicol, C. Bichescu, *Innov. Rom. Food Biotech-nol.* **2009**, 5, 1–9. http://www.bioaliment.ugal.ro/revista...
- 48. B. Alp, S. Multu, M. Mutlu, Food Res. Int. **2000**, *33*, 107–112. **DOI**:10.1016/S0963-9969(00)00013-2
- T. Dodevska, E. Horozova, N. Dimcheva, *Anal. Bioanal. Chem.* 2006, 386, 1413–1418.
 DOI:10.1007/s00216-006-0682-0
- E. Horozova, T. Dodevska, N. Dimcheva, *Bioelectrochemistry* 2009, 74, 260–264.
 DOI:10.1016/j.bioelechem.2008.09.003
- E. Horozova, T. Dodevska, N. Dimcheva, R. Mussarlieva, *Int. J. Electrochem. Sci.* 2011, Article ID 697698, 8 pages.
 DOI:10.4061/2011/697698

- E. Horozova, T. Dodevska, N. Dimcheva, J. Chem. Technol. Metall. 2008, 43, 59–64.
 - http://dl.uctm.edu/journal/node/j2008-1/8_Horozova_ Dodevska-59-64.pdf
- 53. T. Dodevska, E. Horozova, N. Dimcheva, *Cent. Eur. J. Chem.* **2010**, *8*, 19–27. **DOI:**10.2478/s11532-009-0102-3
- 54. A. Karyakin, *Electroanalysis* **2001**, *13*, 813–819. **DOI**:10.1002/1521-4109(200106)13:10<813::AID-ELAN813>3.0.CO;2-Z
- S. de Luca, M. Florescu, M. Ghica, A. Lupu, G. Palleschi, C. Brett, D. Compagnone, *Talanta* 2005, 68, 171–178.
 DOI:10.1016/j.talanta.2005.06.017
- I. de Mattos, M. Areias, *Talanta* 2005, 66, 1281–1286.
 DOI:10.1016/j.talanta.2005.01.044
- M. Ghica, C. Brett, Anal. Lett. 2005, 38, 907–920.
 DOI:10.1081/AL-200054036
- M. Ghica, C. Brett, *Electroanalysis* 2006, 18, 748–756.
 DOI:10.1002/elan.200503468
- R. Antiochia, L. Gorton, *Biosens. Bioelectron.* 2007, 22, 2611–2617. DOI:10.1016/j.bios.2006.10.023
- L. Ang, L. Por, M. Yam, *PLoS ONE* **2015**, *10*, e0111859.
 DOI:10.1371/journal.pone.0111859
- 61. M. Yang, Y. Yang, B. Liu, G. Shen, R. Yu, Sens. Actuat. B Chem. **2004**, 101, 269–276. **DOI:**10.1016/j.snb.2004.01.003
- M. Artigues, J. Abella, S. Colominas, Sensors 2017, 17, 2620– 2635 DOI:10.3390/s17112620
- 63. M. Pilo, R. Farre, J. Lachowicz, E. Masolo, A. Panzanelli, G. Sanna, N. Senes, A. Sobral, N. Spano, J. Anal. Methods Chem. 2018, Article ID 1849439, 7 pages DOI:10.1155/2018/1849439
- N. Sekar, S. Mousavi, S. Sum, H. Ng, L. Ge, S. Tan, Sens. Actuat. B Chem. 2014, 204, 414–420.
 DOI:10.1016/j.snb.2014.07.103
- 65. P. Krzyczmonik, E. Socha, S. Skrzypek, *Electrocatalysis* **2018**, *9*, 380–387. **DOI:**10.1007/s12678-017-0442-2
- H. Yildiz, S. Kiralp, L. Toppare, Y. Yagci, *Int. J. Biol. Macromol.* 2005, 37, 174–178. DOI:10.1016/j.ijbiomac.2005.10.004
- 67. P. Erden, S. Pekyardımcı, E. Kılıç, *Acta Chim. Slov.* **2012**, *59*, 824–832. http://acta-arhiv.chem-soc.si/59/59-4-824.pdf
- 68. Y. Guemas, M. Boujtita, N. El Murr, *Appl. Biochem. Biotechnol.* **2000**, *89*, 171–181. **DOI**:10.1385/ABAB:89:2-3:171
- 69. N. Sato, H. Okuma, *Anal. Chim. Acta* **2006**, 565, 250–254. **DOI:**10.1016/j.aca.2006.02.041
- P. Kotzian, P. Brazdilova, S. Rezkova, K. Kalcher, K. Vytras, *Electroanalysis* 2006, 18, 1499–1504.
 DOI:10.1002/elan.200503549
- 71. T. Goriushkina, A. Soldatkin, S. Dzyadevych, *J. Agric. Food Chem.* **2009**, *57*, 6528–6535. **DOI:**10.1021/jf9009087
- 72. M. Portaccio, M. Lepore, J. *Sensors* **2017**, Article ID 7498945, 8 pages. **DOI:**10.1155/2017/7498945
- 73. J. Ayenimo, S. Adeloju, *Food Chem.* **2017**, *229*, 127–135. **DOI:**10.1016/j.foodchem.2017.01.138
- 74. Y. Wang, L. Liu, M. Li, S. Xu, F. Gao, *Biosens. Bioelectron.* **2011**, *30*, 107–111. **DOI**:10.1016/j.bios.2011.08.038
- J. Li, Z. Yang, Y. Tang, Y. Zhang, X. Hu, Biosens. Bioelectron.
 2013, 41, 698-703. DOI:10.1016/j.bios.2012.09.059

- Y. Bai, T. Xu, J. Luong, H. Cui, Anal. Chem. 2014, 86, 4910–4918. DOI:10.1021/ac501143e
- M. Wooten, S. Karra, M. Zhang, W. Gorski, *Anal. Chem.* 2014, 86, 752–757. DOI:10.1021/ac403250w
- 78. S. Su, H. Sun, F. Xu, L. Yuwen, C. Fan, L. Wang, *Microchim. Acta* 2014, 181, 1497–1503.
 DOI:10.1007/s00604-014-1178-9
- 79. N. Ridhuan, K. Razak, Z. Lockman, *Sci. Rep.* **2018**, *8*, Article number: 13722. **DOI:**10.1038/s41598-018-32127-5
- 80. A. Torriero, E. Salinas, F. Battaglini, J. Raba, *Anal. Chim. Acta* **2003**, *498*, 155–163. **DOI:**10.1016/S0003-2670(03)00897-3
- A. Herrero, T. Requena, A. Reviejo, J. Pingarrón, Eur. Food Res. Technol. 2004, 219, 557–560.
 DOI:10.1007/s00217-004-0973-7
- 82. J. Haccoun, B. Piro, V. Noe, M. Pham, *Bioelectrochemistry* **2006**, 68, 218–226. **DOI**:10.1016/j.bioelechem.2005.09.001
- 83. X. Li, J. Zang, Y. Liu, Z. Lu, Q. Li, C. Li, Anal. Chim. Acta 2013, 771, 102–107. DOI:10.1016/j.aca.2013.02.011
- S. Suman, R. Singhal, A. Sharma, B. Malthotra, C. Pundir, Sens. Actuat. B Chem. 2005, 107, 768–772.
 DOI:10.1016/j.snb.2004.12.016
- 85. R. Monosik, M. Stredansky, G. Greif, E. Sturdik, *Food Control* **2012**, *23*, 238–244. **DOI**:10.1016/j.foodcont.2011.07.021
- 86. S. Perez, E. Fabregas, *Analyst* **2012**, *137*, 3854–3861. **DOI:**10.1039/c2an35227c
- 87. F. Palmisano, M. Quinto, R. Rizzi, P. Zambonin, *Analyst* **2001**, *126*, 866–870. **DOI:**10.1039/b010180j
- F. Palmisano, R. Rizzi, D. Centonze, P. Zambonin, *Biosens. Bioelectron.* 2000, *15*, 531–539.
 DOI:10.1016/S0956-5663(00)00107-X
- B. Serra, A. Reviejo, C. Parrado, J. Pingarron, *Biosens. Bioelectron.* 1999, 14, 505–513.
 DOI:10.1016/S0956-5663(99)00022-6
- L. Shkotova, T. Goriushkina, C. Tran-Minh, J. Chovelon, A. Soldatkin, S. Dzyadevych, *Mater. Sci. Eng. C* 2008, 5-6, 943–948. DOI:10.1016/j.msec.2007.10.038
- M. Gamella, S. Campuzano, F. Conzuelo, J. Curiel, R. Munos,
 A. Reviejo, J. Pingarrón, *Talanta* 2010, 81, 925–933.
 DOI:10.1016/j.talanta.2010.01.038
- 92. M. Albareda-Sirvent, A. Hart, Sens. Actuators B Chem. 2002, 87, 73–81. DOI:10.1016/S0925-4005(02)00219-8
- 93. E. Yashina, A. Borisova, E. Karyakina, O. Shchegolikhina, M. Vagin, D. Sakharov, A. Tonevitsky, A. Karyakin, *Lett. Anal. Chem.* **2010**, *82*, 1601–1604. **DOI**:10.1021/ac9027615
- 94. A. Sannini, D. Albanese, F. Malvano, A. Crescitelli, M. Di Matteo, *Chem. Eng. Trans.* 2015, 44, 283–288. DOI:10.3303/CET1544048
- D. Lowinsohn, M. Bertotti, J. Brazil. Chem. Soc. 2008, 19, 637–642. DOI:10.1590/S0103-50532008000400005
- L. Korneyeva, A. Borisova, Y. Yashina, E. Karyakina, O. Voronin, S. Cosnier, A. Karyakin, *Mosc. Univ. Chem. Bull.* 2010, 65, 49–55. DOI:10.3103/S0027131410010074
- 97. S. Marzouk, H. Sayour, A. Ragab, W. Cascio, S. Hassan, *Electroanalysis* **2000**, *12*, 1304–1311.
 - **DOI:**10.1002/1521-4109(200011)12:16<1304::AID-ELAN1304>3.0.CO;2-B

- 98. M. Rahman, M. Shiddiky, M. Rahman, Y. Shim, *Anal. Biochem.* **2009**, *384*, 159–165. **DOI:**10.1016/j.ab.2008.09.030
- 99. N. Patel, A. Erlenkotter, K. Cammann, G. Chemnitius, Sens. Actuat. B Chem. 2000, 67, 134–141.
 - **DOI:**10.1016/S0925-4005(00)00410-X
- 100. O. Loaiza, P. Lamas-Ardisana, L. Añorga, E. Jubete, V. Ruiz, M. Borghei, G. Cabañero, H. Grande, *Bioelectrochemistry* 2015, 101, 58–65. DOI:10.1016/j.bioelechem.2014.07.005
- 101. V. Zanini, B. Mishima, P. Labbe, V. Solis, *Electroanalysis* **2010**, *22*, 946–954. **DOI**:10.1002/elan.200900416
- V. Zanini, B. Mishima M. Solis, Sens. Actuat. B Chem. 2011, 155, 75–80. DOI:10.1016/j.snb.2010.11.026
- 103. K. Kriz, L. Kraft, M. Krook, D. Kriz, *J. Agric. Food Chem.* **2002**, *50*, 3419–3424. **DOI**:10.1021/jf0114942
- 104. D. Chan, M. Barsan, Y. Korpan, C. Brett, *Electrochim. Acta* 2017, 231, 209–215. DOI:10.1016/j.electacta.2017.02.050
- 105. P. Gimenez-Gomez, M. Gutierrez-Capitan, F. Capdevila, A. Puig-Pujol, C. Fernandez-Sanchez, C. Jimenez-Jorquera, Anal. Chim. Acta 2016, 905, 126–133.
 DOI:10.1016/j.aca.2015.11.032
- 106. Z. Bori, G. Csiffáry, D. Virág, M. Tóth-Markus, A. Kiss, N. Adányi, *Electroanalysis* 2012, 24, 158–164.
 DOI:10.1002/elan.201100409
- 107. F. Ghamouss, S. Ledru, N. Ruillé, F. Lantier, M. Boujtita, Anal. Chim. Acta 2006, 570, 158–164.
 DOI:10.1016/j.aca.2006.04.022
- 108. A. Radoi, D. Moscone, G. Palleschi, *Anal. Lett.* **2010**, *43*, 1301–1309. **DOI:**10.1080/00032710903518716
- 109. A. Parra, E. Casero, L. V'azquez, F. Pariente, E. Lorenzo, Anal. Chim. Acta 2006, 555, 308–315.
 DOI:10.1016/j.aca.2005.09.025
- K. Wang, J. Xu, H. Chen, Sens. Actuat. B Chem. 2006, 114, 1052–1058. DOI:10.1016/j.snb.2005.07.066
- I. Bravo, M. Revenga-Parra, F. Pariente, E. Lorenzo, Sensors
 2017, 17, 144–155. DOI:10.3390/s17010144
- 112. S. Kamanin, V. Arlyapov, V. Alferov, A. Reshetilov, *Ferment. Technol.* **2016**, *5*, 1. **DOI**:10.4172/2167-7972.1000128
- 113. B. Batra, V. Narwal, C. Pundir, *Eng. Life Sci.* **2016**, *16*, 786–794. **DOI:**10.1002/elsc.201600082

- 114. M. Briones, E. Casero, L. Vazquez, F. Pariente, E. Lorenzo,
 M.D. Petit-Dominguez, *Anal. Chim. Acta* 2016, 908, 141–
 149. DOI:10.1016/j.aca.2015.12.029
- 115. S. Yazid, I. Isa, S. Bakar, N. Hashim, S. Ghani, Anal. Lett., 2014, 47, 1821–1834. DOI:10.1080/00032719.2014.888731
- 116. R. Batool, A. Rhouati, M. Nawaz, A. Hayat, J. Marty, *Biosensors*, **2019**, 9, 46 (19 pages).
 - DOI:10.3390/bios9010046
- 117. L. Rassaei, W. Olthuis, S. Tsujimura, E. Sudholter, A. Van der Berg, *Anal. Bioanal. Chem.* **2014**, *406*, 123–137. **DOI**:10.1007/s00216-013-7307-1
- 118. K. Rathee, V. Dhull, R. Dhull, S. Singh, *Biochem. Biophys. Rep.* 2016, 5, 35–54. DOI:10.1016/j.bbrep.2015.11.010
- 119. A. Uzunoglu, J. Electrochem. Soc. 2018, 165, B436–B441. DOI:10.1149/2.0601810jes
- 120. D. Hickey, R. Reid, R. Milton, S. Minteer, *Biosens. Bioelectron*. **2016**, *77*, 26–31. **DOI:**10.1016/j.bios.2015.09.013
- 121. A. M. Parra-Alfambra, E. Casero, L. Vázquez, C. Quintana, M. del Pozo, M. D. Petit-Domínguez, *Sens. Actuat. B: Chemical* **2018**, *274*, 310–317.
 - DOI:10.1016/j.snb.2018.07.124
- 122. M. Briones, E. Casero, M.D. Petit-Dominguez, M.A. Ruiz, A.M. Parra-Alfambra, F. Pariente, E. Lorenzo, L. Vazquez, *Biosens. Bioelectron.* 2015, 68, 521–528. DOI:10.1016/j.bios.2015.01.044
- 123. D. Tu, Y. He, Y. Rong, Y. Wang, G. Li, Meas. Sci. Technol. 2016, 27, 045108 (7pp).
 DOI:10.1088/0957-0233/27/4/045108
- 124. C. Yang, S. Yu, Q. Yang, Q.Wang, S. Xie, H. Yang, J. Electrochem. Soc. 2018, 165, B665–B668.

DOI:10.1149/2.0341814jes

- 125. X. Luo, W. Shi, H. Yu, Z. Xie, K. Li, Y. Cui, Sensors 2018, 18, 3398–3415. DOI:10.3390/s18103398
- 126. J. Pilas, Y. Yazici, T. Selmer, M. Keusgen, M. Schöning, Electrochim. Acta 2017, 251, 256–262. DOI:10.1016/j.electacta.2017.07.119
- 127. J. Pilas, Y. Yazici, T. Selmer, M.Keusgen, M. Schöning, Sensors 2018, 18, 1470–1482. DOI:10.3390/s18051470

Povzetek

V preteklih dveh desetletjih so elektrokemijski biosenzorji vzbudili veliko zanimanja na področju analize živil, predvsem zaradi svojih privlačnih delovnih karakteristik. V prehrambeni industriji kontrola kvalitete med proizvodnjo ter končnih izdelkov zahteva hitre in zanesljive analizne metode. Obetavna alternativa tradicionalnim analiznim metodam so elektrokemijski encimatski biosenzorji – naprave, ki kombinirajo robustnost elektrokemijskih tehnik s specifičnostjo biološke prepoznave ter ponujajo veliko prednosti zaradi svoje velikosti, cene, občutljivosti, selektivnosti in hitrega odziva. Pričujoči kratki pregled literature poskuša povzeti objave v zadnjem obdobju na temo napredka v razvoju encimskih biosenzorjev z amperometrijsko detekcijo za kvantitativno analizo glukoze in laktata v različnih živilskih vzorcih. Pregled se zaključi z napovedjo bodočih izzivov in perspektiv na tem področju.



Except when otherwise noted, articles in this journal are published under the terms and conditions of the Creative Commons Attribution 4.0 International License



Scientific paper

Modified Screen Printed Electrode for Selective Determination of Folic Acid

Mohadeseh Safaei,*,1 Hadi Beitollahi2 and Masoud Reza Shishehbore1

¹ Department of Chemistry, Faculty of Sciences, Islamic Azad University, Yazd Branch, Yazd, Iran

² Environment Department, Institute of Science and High Technology and Environmental

* Corresponding author: E-mail: mohadeseh_safaei@yahoo.com

Received: 07-24-2018

Abstract

Folic acid (FA) as one of the water-soluble vitamins contributes to the construction of healthy cells, as FA deficiency is one of the leading causes of anaemia. Based on reports, reduced folate level can lead to development of carcinogenesis. Hence, its analysis from the clinical point of view is highly demanded. In the present work, NiFe₂O₄ nanoparticles was successfully synthesized and used for modified novel voltammetric sensor for determination of folic acid. Differential pulse voltammetry response shows the linear increment of oxidation signals with an increase in the concentration of folic acid in the range of 1.0×10^{-7} – 5.0×10^{-4} M with limit of detection 3.4×10^{-8} M. The modified electrode displays an excellent selectivity towards the determination of FA even in the presence of various interfering species. Finally, the screen printed electrode (SPE) consists of three main parts which are a graphite counter electrode, a silver pseudo-reference electrode and a graphite working electrode modified by NiFe₂O₄ nanoparticles (NFO), and was applied for FA determination folic acid in tablet and urine samples whose accuracy was attested by means of addition and recovery assays (97.0–103.5%) as well as by differential pulse voltammetry.

Keywords: Folic acid; NiFe₂O₄ nanoparticles; screen printed electrodes; voltammetry; real sample; eectrochemical sensor.

1. Introduction

Application of screen-printed electrodes (SPEs) has a main advantage of miniaturization compared to the conventional electrodes including carbon paste or glassy carbon electrodes. SPEs offer attractive advantages in electrochemical analysis featuring disposability, low cost, flexible in design, ease of chemical modification, and rapid response. ²⁻⁴

Magnetic nanoparticles (NPs) are the most popular materials in analytical biochemistry, medicine, removal of heavy metals and biotechnology, and have been increasingly applied to immobilize proteins, enzymes, and other bioactive agents due to their unique advantages. $^{5-9}\,\rm NiFe_2O_4$ nanoparticles (NiFe_2O_4 NPs) have attracted an increasing interest in construction of sensors and biosensors because of their good biocompatibility, strong super paramagnetic property, low toxicity, easy preparation and high adsorption ability. The quantitative cytotoxicity test verified that NiFe_2O_4 nanoparticles had noncytotoxicity. Moreover, NiFe_2O_4 NPs exhibit high surface area and low mass transfer resistance. $^{10-12}$

Folic acid (FA) is a kind of water-soluble vitamin and can act as coenzyme in the transfer and utilization of one-carbon groups and in the regeneration of methionine from homocysteine.¹³

This vitamin has lately received considerable attention due to its believed antioxidant activity and use for cancer prevention. While present in a wide variety of nutritions and pharmaceutical formulations, the human metabolism is unable to produce folic acid. 14-16 The decrease in concentration of folic acid can cause however serious complications such as leucopoenia, gigantocytic anemia, psychosis, devolution of mentality and increasing possibility of heart attack and stroke. Hence, the development of sensitive and fast methods for the determination of folic acid has attracted considerable attention. 17-19 Some analytical methods have been reported for the determination of FA with high performance liquid chromatography,²⁰ spectrophotometry,²¹ chemiluminescence,²² spectrofluorometric ²³ and Enzyme-linked ligand sorbent test methods.²⁴ But these techniques have many disadvantages, such as high cost from the equipments and disposable chemicals, complicated and time-consuming pretreatments, and so on. Electrochemical techniques are the most preferred ones considering their simplicity, rapid response, good stability, low cost, high sensitivity and excellent selectivity which are widely used in the field of food, drug, biological and environmental analysis.²⁵⁻²⁹

The present study is aimed at the synthesis of the NiFe $_2$ O $_4$ nanoparticles and its application in the form of the modified screen printed electrode for trace, rapid, and sensitive determination of folic acid through cyclic voltammetric and differential pulse voltammetric techniques. To our knowledge, there is no report on the voltammetric behaviour, and the determination of folic acid at the NiFe $_2$ O $_4$ nanoparticles. Low detection limit, high sensitivity, and a wide linear range of folic acid concentrations were thus obtained.

2. Experimental

2. 1. Apparatus and Chemicals

Fourier transform infrared (FT-IR) spectra were recorded in transmission mode with a Perkin Elmer BX FT-IR infrared spectrometer. FT-IR spectra in the range 4000–400 cm⁻¹ were recorded in order to investigate the nature of the chemical bonds formed. X-ray powder diffraction (XRD) analysis was conducted on a Philips analytical PC-APD X-ray diffractometer with graphite monochromatic CuK α radiation (α_1 , λ_1 = 1.54056 Å, α_2 , λ_2 = 1.54439 Å) to verify the formation of products. The X-ray diffraction pattern was indexed using Joint Committee on Powder Diffraction Standards (JCPDS) card. SEM images of the samples were collected on JSM, 6380 LV equipped with an EDX microanalysis.

The electrochemical measurements were performed with an Autolab potentiostat/galvanostat (PGSTAT 302N, Eco Chemie, the Netherlands). The experimental conditions were controlled with the General Purpose Electrochemical System software. The screen-printed electrode (DropSens, DRP-110, Spain) consists of three main parts which are a graphite counter electrode, a silver pseudo-reference electrode and a graphite working electrode, unmodified. A Metrohm 710 pH meter was used for pH measurements.

Folic acid and all other reagents were of the analytical grade, and they were obtained from Merck (Darmstadt, Germany). The buffer solutions were prepared from orthophosphoric acid and its salts over the pH range of 2.0–9.0.

2. 2. Synthesis of NiFe₂O₄ Nanoparticles

NiFe $_2$ O $_4$ nanoparticles were synthesized in the presence of urea using a hydro/solvothermal method. Solution of urea were dissolved in 60 mL of deionized water and then 20 mL polyethylene glycol was added to solution to form brown homogeneous solutions. Then 10 mL FeCl $_3$ ·

6H₂O (16 mmol) and 10 mL NiCl₂· 6H₂O (8 mmol) were added into the above solution, respectively. The mixed solutions, with stoichiometric 30 molar ratio of urea/Fe³⁺ (with excess urea that form sufficient precipitating ions for metal oxides formation), were magnetically stirred until all the starting materials were totally dissolved at 25 °C. These solutions were further homogenized in an ultrasonic water bath for 15 min and then respectively transferred into Teflon-lined stainless steel autoclave with a capacity of 200 mL in order to keep them at 200 °C for 24 h in an oven. Subsequently, the autoclaves were air cooled to room temperature. The as-obtained precipitates were centrifuged, and then washed with deionized water and absolute ethanol for several times to remove the impurities in the products. The resulting products were dried in a vacuum oven at 105 °C for 12 h.

2. 3. Preparation of the Electrode

The bare graphite screen printed electrode was coated with NiFe $_2$ O $_4$ nanoparticles, as shown in the following. A stock solution of NiFe $_2$ O $_4$ nanoparticles in 1 mL of the aqueous solution was prepared by dispersing 1 mg of NiFe $_2$ O $_4$ nanoparticles with ultra-sonication for 30 min, while 5 μ L of aliquots of the NiFe $_2$ O $_4$ suspension solution was cast on the carbon working electrodes, followed by waiting until the solvent was evaporated in room temperature.

2. 4. Preparation of Real Samples

Folic acid tablets (Ruzdarou, Iran [labelled value folic acid = 5 mg/tablet]) were perchased. The folic acid tablets were completely grounded and homogenized before preparing 10 mL of the 0.1 M stock solution. The solution was sonicated to assure complete dissolution and then filtered. The required amount of clear filtrate was then added to the electrochemical cell containing 10 mL of the 0.1 M PBS (pH 7) to record the DPV voltammogram.

Urine samples were stored in a refrigerator immediately after collection. Ten millilitres of the samples were centrifuged for 15 min at 2000 rpm. The supernatant was filtered out by using a 0.45 μm filter. Next, different volumes of the solution was transferred into a 25 mL volumetric flask and diluted to the mark with PBS (pH 7.0). The diluted urine samples were spiked with different amounts of folic acid. The folic acid contents were analysed by the proposed method by using the standard addition method.

3. Result and Discussion

3. 1. Morphology and Structure of NiFe₂O₄ Nanoparticles

The vibration frequencies in the infrared spectrum of a molecule were considered to be a unique physical

property and were a characteristic of the molecule. Fig. 1 shows two persistent absorption bands corresponding to the vibration of tetrahedral and octahedral complexes at 599 cm⁻¹ and 465 cm⁻¹, respectively. Those bands confirmed the formation of spinel nickel ferrite structure. As can be seen from FT-IR spectra the normal mode of vibration of tetrahedral cluster (599 cm⁻¹) is higher than that of octahedral cluster (465 cm⁻¹). This is due to the shorter bond length of tetrahedral cluster than the octahedral cluster. ³⁰

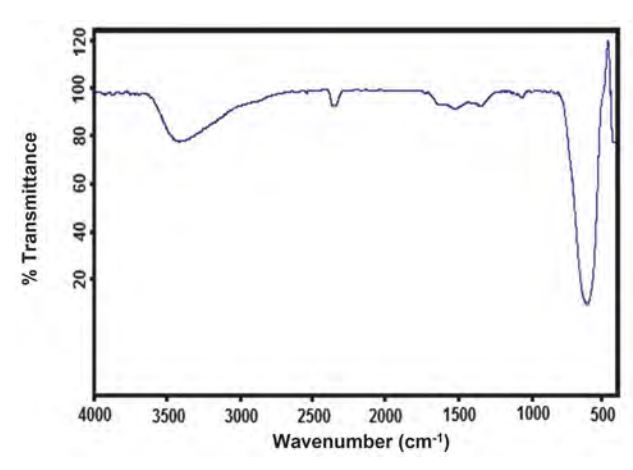


Fig. 1. FT-IR spectra of NiFe₂O₄ nanoparticles

An XRD spectrum of the NiFe₂O₄ nanoparticles is shown in Fig. 2. For the NiFe₂O₄ nanoparticles, the eleven characteristic peaks occur at 2 θ of 30.48°, 35.87°, 36.21°, 45.52°, 51.89°, 57.51°, 63.63°, 72.14°, 75.52°, 76.68°, and 79.68°, which are marked by their corresponding indices (220), (311), (222), (400), (422), (511), (440), (620), (533), (622) and (444), respectively. This reveals that the magnetic particles are pure NiFe₂O₄ with a spinel structure. No diffraction peaks of other impurities such as α -Fe₂O₃ or NiO were observed. The broadness of the diffraction peaks suggests the nano-sized nature of the product and the average crystallite size (t) of it was calculated using the De-

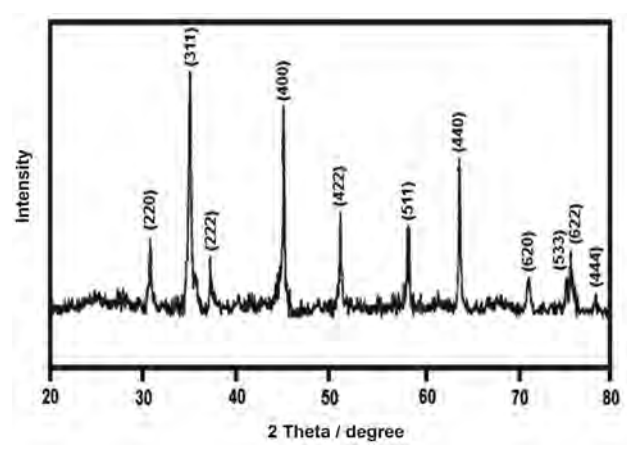


Fig. 2. X-ray diffraction patterns of the NiFe₂O₄ nanoparticles.

bye-Scherrer formula as 40.0 nm. t = 0.9 λ / β cos (θ) where λ is the wavelength of the X-ray radiation (1.54056 Å for Cu lamp), θ is the diffraction angle and β is the full width at half-maximum (FWHM). $^{30,\,31}$

The morphology of the product was examined by SEM. Fig. 3A depicts the SEM pictures of $NiFe_2O_4$ nanoparticles. From the graph, it was observed that the nanoparticles, which are nearly spherical, are not agglomerated and they are seen as less than 10 nm.

The EDX analysis was performed to further confirm the composition of the obtained products. Fig. 3B shows that the products are composed of Ni, Fe and O. The C peak in the spectrum is attributed to the electric latex of the SEM sample holder.

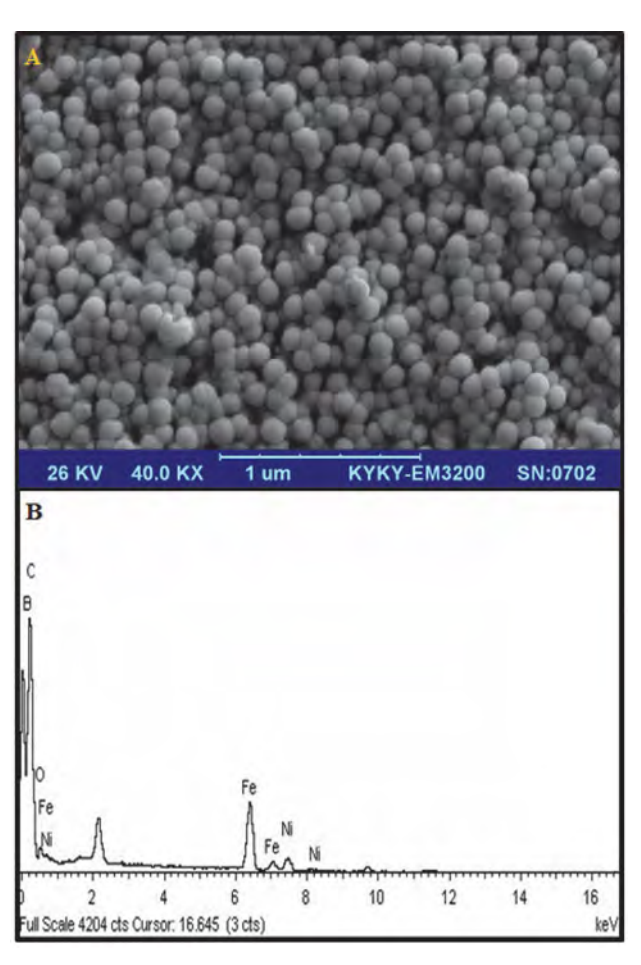


Fig. 3. (A) SEM micrographs with (B) its EDX spectra of NiFe $_2\mathrm{O}_4$ nanoparticles.

3. 2. Electrochemical Behaviour of Folic Acid at The Surface of Various Electrodes

The electrochemical behaviour of folic acid depends on the pH value of the aqueous solution. Therefore, the pH optimization of the solution seems to be necessary in order to obtain the best results for electro-oxidation of folic acid. Thus, the electrochemical behaviour of folic acid was stud-

ied in 0.1 M PBS in different pH values (2.0–9.0) at the surface of NFO/SPE by voltammetry. It was found that the electro-oxidation of folic acid at the surface of NFO/SPE was more favoured under neutral conditions than in acidic or basic medium. Here pH 7.0 was chosen as the optimum pH for electro-oxidation of folic acid at the surface of NFO/SPE.

Fig. 4 depicts the CV responses for electro-oxidation of $100.0~\mu\text{M}$ folic acid at the unmodified SPE (curve b) and NFO/SPE (curve a). The peak potential occurs at 670 mV due to the oxidation of folic acid, which is about 70 mV more negative than the unmodified SPE. Also, NFO/SPE shows much higher anodic peak currents for the oxidation of folic acid compared to the unmodified SPE, indicating that the modification of the unmodified SPE with NiFe₂O₄ nanoparticles has significantly improved the performance of the electrode towards folic acid oxidation.

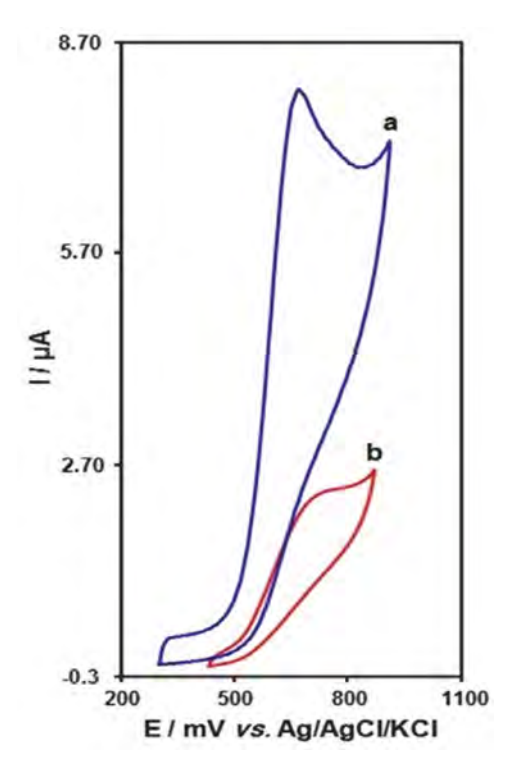


Fig. 4. CVs of a) NFO/SPE and b) unmodified SPE in the presence of 100.0 μ M folic acid at pH 7.0. In all cases, the scan rate was 50 mV s⁻¹.

3. 3. Effect of Scan Rate

Fig. 5 illustrate the effects of potential scan rates on the oxidation currents of folic acid, indicating that increasing the scan rate increased the peak currents. Also based on the fact that the plots of Ip against the square root of the potential scan rate ($v^{1/2}$) for analyte was linear, it was concluded that the oxidation processes are both diffusion controlled.

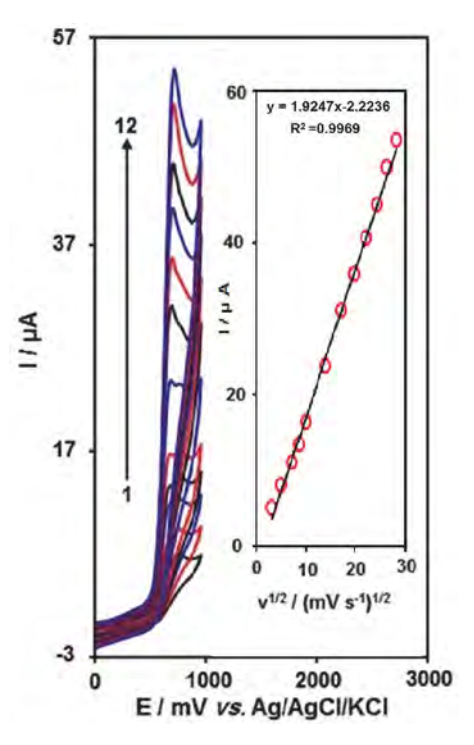


Fig. 5. CVs of NFO/SPE in 0.1 M PBS (pH 7.0) containing 150.0 μM of folic acid at various scan rates; numbers 1–12 correspond to 10, 25, 50, 75, 100, 200, 300, 400, 500, 600, 700 and 800 mV s⁻¹, respectively. Inset: Variation of anodic peak current ν s. square root of scan rate.

3. 4. Chronoamperometric Measurements

Chronoamperometric measurements of folic acid at NFO/SPE were carried out by setting the working electrode potential at 0.75 V vs. Ag/AgCl/KCl (3.0 M) for various concentrations of folic acid (Fig. 6) in PBS (pH 7.0). For electroactive materials (folic acid in this case) with a diffusion coefficient of D, the current observed for the electrochemical reaction at the mass transport limited condition is described by the Cottrell equation.³²

$$I = nFAD^{1/2}C_b\pi^{-1/2}t^{-1/2}$$
 (1)

where D and C_b are the diffusion coefficient (cm² s⁻¹) and the bulk concentration (mol cm⁻³), respectively. Experimental plots of I vs. t^{-1/2} were employed with the best fits for different concentrations of folic acid (Fig. 6A). The slopes of the resultant straight lines were then plotted against folic acid concentrations (Fig. 6B). From the resultant slope and the Cottrell equation, the mean values of D were found to be 1.3×10^{-5} cm²/s for folic acid.

3. 5. Calibration Plots and Limits of Detection

The electro-oxidation peak currents of folic acid at the surface of NFO/SPE can be used to determine folic acid in the solution. Since differential pulse voltammetry (DPV) has the advantage of having an increase in sensitivity and better characteristics for analytical applications,

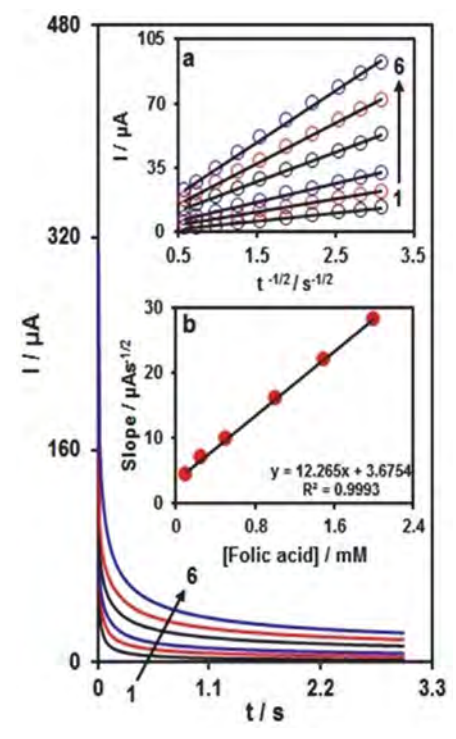


Fig. 6. Chronoamperograms obtained at NFO/SPE in 0.1 M PBS (pH 7.0) for different concentrations of folic acid. The numbers 1-6 correspond to 0.1, 0.25, 0.5, 1.0, 1.5 and 2.0 mM of folic acid. Insets: (a) Plots of I vs. $t^{-1/2}$ obtained from chronoamperograms 1-6. (b) Plot of the slope of the straight lines against folic acid concentrations.

DPV experiments were performed by using NFO/SPE in 0.1 M PBS containing various individual concentrations of folic acid (Fig. 7). The results show that the electrocatalytic peak currents of folic acid oxidation at the surface of NFO/SPE were linearly dependent on folic acid concentrations over the range of 1.0–500.0 μM , while the detection limit (3 σ) was obtained as 0.023 μM . These values are comparable with values reported by other research groups for electrocatalytic oxidation of levodopa at the surface of chemically modified electrodes (see Table 1).

3. 6. Interference Study

We investigated the effect of various interfering species on measuring 20.0 μM FA. The tolerance limit was

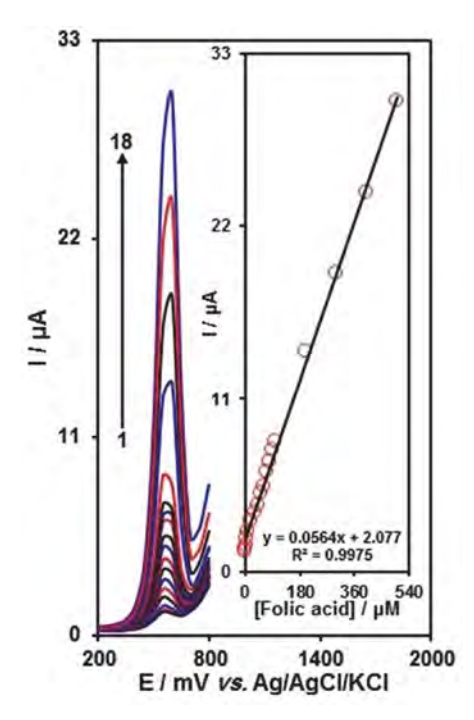


Fig. 7. DPVs of NFO/SPE in 0.1 M PBS (pH 7.0) containing different concentrations of folic acid. Numbers 1–18 correspond to 0.1, 0.5, 1.0, 5.0, 10.0, 20.0, 30.0, 40.0, 50.0, 60.0, 70.0, 80.0, 90.0, 100.0, 200.0, 300.0, 400.0 and 500.0 μM of folic acid. The inset shows the plot of the peak current as a function of the folic acid concentration in the range of 0.1–500.0 μM .

adjusted as the concentration of foreign ions causing ±5% error in the determination. Based on the obtained results, the tolerance limit for Na⁺, Cl⁻ and K⁺ was 0.1 M; for Mg²⁺ and Ca²⁺ it was 0.05 M; for L-lysine, glucose, sucrose, lactose, citric acid, fructose methanol, ethanol, L-asparagine, alanine, phenylalanine, glycine and NADH it was 0.004 M.

3. 7. Real Sample Analysis

In order to evaluate the analytical applicability of the proposed method, it was applied to determine folic acid in folic acid tablets and urine samples by using the standard addition method. The results for the determination of the folic acid in real samples are given in Table 2. Satisfactory recoveries of the experimental results were found for folic

Table 1. Comparison of analytical parameters for the determination of folic acid by various electrodes.

Electrode	Modifier	LOD (M)	LDR (M)	Ref.
Carbon paste	multiwall carbon nanotubes	1.10×10^{-6}	$4.6 \times 10^{-6} - 152.0 \times 10^{-6}$	33
Carbon paste	(DEDE) and NiO/CNTs nanocomposite	0.90×10^{-6}	$3.0 \times 10^{-6} - 550.0 \times 10^{-6}$	34
Carbon paste	ZrO ₂ nanoparticles	9.86×10^{-6}	$2.0 \times 10^{-5} - 2.5 \times 10^{-3}$	35
Glassy carbon	graphene/MWCNT nanocompositeloaded Au nanoclusters	0.09×10^{-6}	$10.0 \times 10^{-6} - 170.0 \times 10^{-6}$	36
Carbon paste	Ruthenium(II) Complex-ZnO/CNTs Nanocomposite	1.00×10^{-6}	$3.0 \times 10^{-6} - 700.0 \times 10^{-6}$	37
Screen printed	NiFe ₂ O ₄ nanoparticles	3.40×10^{-8}	$1.0 \times 10^{-7} - 5.0 \times 10^{-4}$	This Work

Sample	Spiked	Found	Recovery (%)	RSD (%)
	0	15.0	_	3.2
	2.5	17.8	101.7	1.7
Folic acid tablet	5.0	19.5	97.5	2.8
	7.5	23.3	103.5	2.2
	10.0	24.8	99.2	2.4
	0	_	-	_
	10.0	10.3	103.0	3.4
Urine	20.0	19.9	99.5	1.7
	30.0	29.1	97.0	2.3
	40.0	40.5	101.2	2.8

Table 2. Determination of folic acid in folic acid tablet and urine samples. All the concentrations are in μM (n=5).

acid. The reproducibility of the method was demonstrated by the mean relative standard deviation (RSD).

4. Conclusion

In this work, NiFe₂O₄ nanoparticles has been employed as a modifier in the modification of SPEs. A novel sensor has been developed, which provides an extremely sensitive and selective method for determination of folic acid. At the optimum pH of 7.0, the oxidation of FA occurs at a potential about 670 mV which is about 70 mV more negative than the unmodified SPE. Based on differential pulse voltammetry (DPV), the oxidation of LD exhibited a dynamic range between 1.0×10^{-7} and 5.0×10^{-4} M and a detection limit (3 σ) of 3.4×10^{-8} M. The proposed protocol demonstrated a novel, simple, portable, inexpensive, and easy-to-use fabrication method to measure folic acid concentrations in folic acid tablet and urine samples with good analytical performance.

5. References

- D. Martín-Yerga, E. Costa Rama, A. García, *J Chem Educ*, 2016, 93, 1270–1276. DOI:10.1021/acs.jchemed.5b00755
- L. Ochiai, M. D. Agustini, L. C. Figueiredo-Filho, C. E. Banks,
 L. H. Marcolino-Junior, M. F. Bergamini, Sens Actuator B,
 2017, 241, 978–984. DOI: 10.1016/j.snb.2016.10.150
- 3. F.Y. Kong, S.X. Gu, W. Li, T.T. Chen, Q. Xu, W. Wang, *Biosens Bioelectron*, **2014**, *56*, 77–82. **DOI**:10.1016/j.bios.2013.12.067
- S. Jahani, H. Beitollahi, *Electroanalysis*, 2016, 28, 2022–2028.
 DOI:10.1002/elan.201501136
- Y. Xiong, L. Fu, X. Wang, Chem. Eng. J., 2012, 195, 149–157.
 DOI:10.1016/j.cej.2012.05.007
- M. Safaeia, H. Beitollahib, M. R. Shishehbore, Russ. J. Electrochem. 2018, 54, 851–859.
 - **DOI:**10.1134/S1023193518130402
- H. Chen, J. Yan, H. Wu, Y. Zhang, S. Z. Liu, J. Power Sources, 2016, 324, 499–508. DOI:10.1016/j.jpowsour.2016.05.075

- 8. X. Sun, Y.Q. Ma, S. T. Xu, Y. F. Xu, B. Q. Geng, *Charact*, **2015**, *107*, 343–349. **DOI**:10.1016/j.matchar.2015.08.003
- 9. S. Jahani, Anal. Bioanal. Electrochem. 2018, 10, 739-750.
- M. Safaei, H. Beitollahi, M. R. Shishehbore, J. Chin. Chem. Soc. 2019, 66, 1–8. DOI:10.1002/jccs.201900073
- A. A. Ensafi, B. Arashpour, B. Rezaei, A. R. Allafchian, *Mater. Sci. Eng. C* 2014, 39, 78–85. DOI:10.1016/j.msec.2014.02.024
- U. Kurtan, H. Gungunes, H. Sozeri, A. Baykal, *Ceramics Int.* 2016, 42, 7987–7992. DOI:10.1016/j.ceramint.2016.01.200
- C.M. Pfeiffer, Z. Fazili, L. McCoy, M. Zhang, E.W. Gunter, Clin. Chem., 2004, 50, 423–432.
 DOI:10.1373/clinchem.2003.026955
- 14. W. Shi, Y. Wang, H. Zhang, Z. Liu, Z. Fei, *Food Chem.*, **2017**, 226, 128–134. **DOI:**10.1016/j.foodchem.2017.01.054
- M. Dervisevic, M. Senel, T. Sagir, S. Isik, *Biosens. Bioelectron*,
 2017, 91, 680–686. DOI:10.1016/j.bios.2017.01.030
- B.N. Chandrashekar, B. E. Kumara Swamy, K.J. Gururaj, C. Cheng, *J. Mol. Liq.*, 2017, 231, 379–385.
 DOI:10.1016/j.molliq.2017.02.029
- 17. L. Zhang, C. Xiong, H. Wang, R. Yuan, Y. Chai, Sens. Actuators B, 2017, 241, 765–772. DOI:10.1016/j.snb.2016.10.138
- K. Vimala, K. Shanthi, S. Sundarraj, S. Kannan, J. Colloid Interface Sci., 2017, 488, 92–108.
 DOI:10.1016/j.jcis.2016.10.067
- C. Santos, P. Gomes, J. A. Duarte, M. M. Almeida, M. E. V. Costa, M. H. Fernandes, *Int. J. Pharm.*, **2017**, *516*, 185–195.
 DOI:10.1016/j.ijpharm.2016.11.035
- R. H. F. Cheung, P. D. Morrison, D. M. Small, P. J. Marriott, *J. Chromatogr. A.* 2008, *1213*, 93–99.
 DOI:10.1016/j.chroma.2008.09.098
- 21. M. R. Shishehbore, A. Sheibani, A. Haghdost, *Spectrochim. Acta A*, **2011**, *81*, 304–307. **DOI:**10.1016/j.saa.2011.06.015
- 22. B.T. Zhang, L. X. Zhao, J. M. Lin, Talanta, **2008**, *74*, 1154–1159. **DOI:**10.1016/j.talanta.2007.08.027
- 23. J. L. Manzoori, A. Jouyban, M. Amjadi, J. Soleymani, *Luminesence*, **2011**, *26*, 106–111. **DOI:**10.1002/bio.1191
- 24. J. Arcot, A. K. Shrestha, U. Gusanov, Food Control, **2002**, 13, 245–252. **DOI**:10.1016/S0956-7135(02)00018-X
- 25. M. Najafi, M. A. Khalilzadeh, H. Karimi-Maleh, *Food Chem.*, **2014**, *158*, 125–131. **DOI**:10.1016/j.foodchem.2014.02.082

- M. Elyasi, M. A. Khalilzadeh, H. Karimimaleh, Food Chem., 2013, 141, 4311–4317.
 - DOI:10.1016/j.foodchem.2013.07.020
- 27. M. Bijad, H. Karimi-Maleh, M. A. Khalilzadeh, *Food Anal. Methods*, **2013**, *6*, 1639–1647.
 - DOI:10.1007/s12161-013-9585-9
- S. Gheibi, H. Karimi-Maleh, M. A. Khalilzadeh, H. Bagheri, J. Food Sci. Technol., 2015, 52, 276–284.
 DOI:10.1007/s13197-013-1026-7
- J. B. Raoof, N. Teymoori, M. A. Khalilzadeh, Food Anal. Methods, 2015, 8, 885–892. DOI:10.1007/s12161-014-9962-z
- A. A. Ensafi, B. Arashpour, B. Rezaei, A. R. Allafchian, *Mater. Sci. Eng. C*, 2014, 39, 78–85. DOI:10.1016/j.msec.2014.02.024
- U. Kurtan, H. Gungunes, H. Sozeri, A. Baykal, *Ceramics Int.*,
 2016, 42, 7987–7992. DOI:10.1016/j.ceramint.2016.01.200

- A. J. Bard, L. R. Faulkner, Electrochemical Methods Fundamentals and Applications, 2001, second ed, (Wiley, New York).
- 33. A. A. Ensafi, H. Karimi-Maleh, *J. Electroanal. Chem.*, **2010**, 640, 75–83. **DOI**:10.1016/j.jelechem.2010.01.010
- 34. H. Karimi-Maleh, P. Biparva, M. Hatami, *Biosens. Bioelectron.*, **2013**, *48*, 270–275. **DOI**:10.1016/j.bios.2013.04.029
- 35. M. Mazloum-Ardakani, H. Beitollahi, M. K. Amini, F. Mirkhalaf, M. Abdollahi-Alibeik, *Sens. Actuators B*, **2010**, *151*, 243–249. **DOI**:10.1016/j.snb.2010.09.011
- A. A. Abdelwahab, Y. B. Shim, Sens. Actuators B, 2015, 221, 659–665. DOI:10.1016/j.snb.2015.07.016
- H. Karimi-Maleh, F. Tahernejad-Javazmi, M. Daryanavard,
 H. Hadadzadeh, A. A. Ensafi, M. Abbasghorbani, *Electroa-nalysis*, 2014, 26, 962–970. DOI:10.1016/j.snb.2015.07.016

Povzetek

Sintetizirali smo nanodelce NiFe $_2$ O $_4$ in jih uporabili za izdelavo novega voltametričnega senzorja za določanje folne kisline. Odziv diferencialne pulzne voltametrije je pokazal linearno zvišanje oksidacijskih signalov s povečanjem koncentracije folne kisline v območju $1.0 \times 10^{-7} - 5.0 \times 10^{-4}$ M, z mejo zaznave 3.4×10^{-8} M. Elektroda ima odlično selektivnost za določanje folne kisline tudi v primeru prisotnosti različnih motenj. SPE sestavljajo trije deli: grafitna protielektroda, srebrna psevdo referenčna elektroda in grafitna delovna elektroda modificirana z nanodelci NiFe $_2$ O $_4$. Senzor smo uspešno uporabili za določanje folne kisline v vzorcih tablet in urina.



Except when otherwise noted, articles in this journal are published under the terms and conditions of the Creative Commons Attribution 4.0 International License

Scientific paper

Tacrolimus as Antifungal Agent

Lyudmyla Antypenko,* Zhanar Sadykova, Fatuma Meyer, Leif-Alexander Garbe and Karl Steffens

Department of Agriculture and Food Science, Neubrandenburg University Brodaer Str. 2, 17033, Neubrandenburg, Germany

* Corresponding author: E-mail: antypenkol@gmail.com

Received: 09-18-2018

Abstract

Tacrolimus (FK506) is an immunosuppressant drug widely used to avoid organ rejection in transplant patients. It has a profound influence on the cellular stress response by interfering with the calmodulin-calcineurin signaling pathway. In this context FK506 also became a valuable antifungal drug in medical care. Here it is shown *in vitro* that tacrolimus has a potent growth inhibition activity against 11 fungi and 3 oomycetes of agricultural importance. The significance of this finding is discussed with respect to crop protection. The *in silico* molecular docking to 6 major antifungal enzymes determined UDP-N-acetylmuramoyl-L-alanine: D-glutamate ligase (MurD) as the main target by the best affinity score.

Keywords: Tacrolimus, Antiphytofungal activity

1. Introduction

Presently azoles, echinocandines, pyrimidine analogs and polyenes are among the most common antifungals in human medical care and crop protection. The search for new potent antifungal agents will remain an urgent task at the background of an ongoing emergence of drug resistance.1 Especially resistant pathogenic fungi rise concerns human medical care. For instance, immunocompromised patients after HIV infection or organ transplantation, who have overcome cryptococcal meningitis infection, may need a life-time fluconazole prophylaxis.² Here, management of infections become extremely difficult if azole resistant pathogens get involved. Also the arise of fluconazole-resistant mutants among Cryptococcus neoformans clinical isolates was observed.³ In search for new targets for antifungals the calmodulin-calcineurin signaling cascade came into focus. A stress response of a fungal cell starts by the uptake of Ca²⁺, which then binds to the four binding sites of calmodulin. After a conformational change Ca²⁺ occupied calmodulin forms a ternary complex together with calcineurin subunits CnA and CnB, thereby gaining a phosphatase activity; in turn the complex dephosphorylates transcription factor Crz1. Genes activated by dephosphorylized Crz1 are involved in drug resistance, growth and cell wall integrity. Generally, calcineurin is an important part of the stress response of fungal cells.4

Searching for novel immunosuppressive agents a 822-kD 23-membered macrolide lactone named tacrolim-

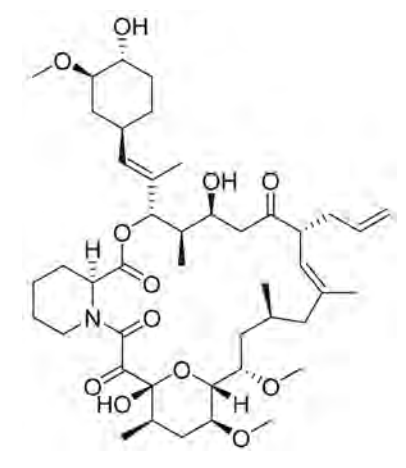


Figure 1. Chemical structure of tacrolimus (FK506).

us (FK506, Fujimycin, etc.) was isolated and characterized from *Streptomyces tsukubaensis* (Fig. 1).⁵

Tacrolimus in capsules for oral intake and as solution for injection is used for prophylaxis against organ rejection in patients receiving liver, kidney or heart transplants. As a topical ointment it is applied as a second-line therapy for the short-term and non-continuous chronic treatment of moderate to severe atopic dermatitis in non-immunocompromised adults and children. FK506 has a favorable toxicological profile: no evidence of mutagenicity was observed *in vitro* in the CHO/HGPRT assay (the Chinese hamster ovary cell assay). Also it did not cause unsched-

uled DNA synthesis in rodent hepatocytes. LD_{50} in rat oral test was 134 mg/kg for tacrolimus hydrate.⁷

Experimental evidence suggests that tacrolimus binds to the intracellular protein FKBP12 and thereby interferes with the calcineurin signal pathway, which is a key element in regulation of intracellular Ca²⁺ concentration.⁴ FKBP12-tacrolimus inhibits the phosphatase activity of the calmodulin-CnA-CnB complex, which in turn silences transcription factor Crz1 and corresponding stress related genes. As a consequence, inhibitors of calcineurin like tacrolimus may function as potent antifungals. In combination with standard antifungal drugs FK506 may reverse resistance against them or increase their efficacy.^{8,9} Also phytopathogenic fungi rely on the calcineurin pathway securing cell wall and membrane

integrity, virulence¹⁰ or formation of infectious appressoria.¹¹

Practically all of tacrolimus studies are related to the development of supportive antifungal therapy to improve regimes of infected patients. Here we describe novel antifungal efficacy of FK506 towards eleven pathogenic fungi and three *Phytophthora* oomycetes of agricultural importance.

2. Results and Discussion

2. 1. Known Antifungal Data

All reported antifungal literature data were summarized below (Table 1) to show its found minimum inhibitory concentrations (MIC).

Table 1. Summary of reported antifungal activity of tacrolimus (FK506)

Fungus	Reported strain name	MIC_{100} , $\mu g/mI$
	AF293, DUMC 119.00,	1.5612
	DUMC 153.90, DUMC 101.01	1.56
A at ancillus funcicatus	DUMC 165.86	6.25
Aspergillus fumigatus	DUMC 182.99	0.39
	DUMC 168.95	3.125
	DUMC 131.00	0.78
	6 strains	$0.025 \text{-} 0.4^{13}$
Aspergillus fumigantus	AF1 - AF10	>25614
	TIMM0063	$\leq 0.008^{15}$
A an augillus seigen	2 strains	$0.006 \text{-} 0.012^{13}$
Aspergillus niger	ATCC6275	$\leq 0.008^{15}$
A an ancillus flance	4 strains	$0.1 - 0.2^{13}$
Aspergillus flavus	AFL1 - AFL8	>256 ¹⁴
A:11	4 strains	0.025-0.113
Aspergillus terreus	AT1, AT2	>25614
Aspergillus ustus	3 strains	>0.414
Aspergillus versicolor	1 strain	>0.4 ¹⁴
	SC5314, echinocandin-res.:	
	Fks1 S645Y, Fks1 F641S,	
andida albicans	Fks1 S645F, Fks1 S645P;	>16 ¹⁶
	azole-res.: 2–76,	
	2–86, 12–99.	
	SC5314, cnb1/cnb1 (DAY364),	
	cnb1/cnb1 CNB1 (MCC85),	>3.121
	CNB1-1/CNB1 (YAG237),	
	rbp1/rbp1 (YAG171)	7
	azole-susc. CA5, CA8, CA12,	
	CA14, CA129; azole-res. CA10,	512 ¹⁸
	CA15, CA16, CA135, CA137.	
	TIMM1623	
Candida tropicalis	TIMM0313	>128 ¹⁵
Candida kefyr	ATCC28838	

Malassezia globose 36 strains $0.016-0.25^{22}$ Malassezia restrica 28 strains $0.016-0.25^{22}$ Malassezia sympodialis 19 strains 0.125^{22} Malassezia obtuse 7 strains 0.03^{22} Malassezia slooffiae 10 strains 0.016^{22} Malassezia japonica 2 strains 0.016^{22} Malassezia pachydermatis 6 strains 0.016^{22} Malassezia pachydermatis 6 strains $0.012 \text{ to } > 0.4^{13}$ Malassezia yamatoensis 2 strains $0.012 \text{ to } > 0.4^{13}$ Paecilomyces licasinusb 5 strains $0.012 \text{ to } > 0.4^{13}$ Paecilomyces variotib 4 strains $0.025 \text{ to } > 0.4^{13}$ Rhizomucor spp.b 2 strains $0.012 - 0.025^{13}$ Rhizomucor spp.b 5 strains $0.012 - 0.025^{13}$ Scedosporium apiospermumb 4 strains $0.05 \text{ to } > 0.4^{13}$ Scedosporium prolificansb 4 strains $0.05 \text{ to } > 0.4^{13}$ Scopulariopsis spp.b 4 strains $0.05 \text{ to } > 0.4^{13}$ YFK005 wild type YFK012 (fkr1), YFK256 (PDR) YFK257 (nkt 2), YFK259 (nkt 7) YFK257 (nkt 2), YFK258 (nkt 2	Fungus	Reported strain name	MIC ₁₀₀ , μg/mI
Part	Candida alahrata ^a		256^{19}
Cryptococcus neoformans $2015 \\ -0.09^{11}, 12.5^{20} \\ -0.09$		CG4, CG8, CG2, CG3	512
Cryptococcus neoformans H99 C20, C21 C20F1 C20F2 C20F2 C20F1 C20F1 C20F2 C21F3 C20F1 C20F3 C20F1 C20F3		EP1551	•
$ \begin{array}{c} C20, C21 \\ C20F1 \\ C20F2 \\ C20F2 \\ C20F2 \\ C21F3 \\ C21$			
$ \begin{array}{c ccccccccccccccccccccccccccccccccccc$			
	Cryptococcus neoformans		
C21F3 $AcnaI$ mutant, $AfrII$ mutant 2521 $> 25^{20}$ Cunninghamella spp.b 2 strains 0.05-0.213 Fusarium spp.b 6 strains >0.413 Lichtheimia spp.b 2 strains 0.2-0.413 Malassezia furfur 8 strains 26 strains 0.0322 0.0322 Malassezia globose 36 strains 0.016-0.2522 Malassezia globose 36 strains 0.016-0.2522 Malassezia pubuse 7 strains 0.012522 Malassezia obtuse 7 strains 0.0322 Malassezia butuse 7 strains 0.0322 Malassezia pubuse 7 strains 0.01622 Malassezia pubuse 7 strains 0.01622 Malassezia padridermatis 3 strains 0.01622 Malassezia pachydermatis 6 strains 0.012 to >0.413 Malassezia yamatoensis 2 strains 0.012 to >0.413 Paecilomyces licasinusb 5 strains 0.012 to >0.413 Paecilomyces varioti b 4 strains 0.012 to >0.413 Rhizopus spp.b 2 strains 0.01 to >0.413 Scedosporium			
Cunninghamella spp.b 2 strains $0.05-0.2^{13}$ Fusarium spp.b 6 strains $>0.4^{13}$ Lichtheimia spp.b 2 strains $0.2-0.4^{13}$ Malassezia furfur 8 strains 26 strains 0.03^{22} Malassezia globose 36 strains $0.016-0.25^{22}$ Malassezia restrica 28 strains $0.016-0.25^{22}$ Malassezia sympodialis 19 strains 0.125^{22} Malassezia obtuse 7 strains 0.03^{22} Malassezia slooffiae 10 strains 0.016^{22} Malassezia padonica 2 strains 0.016^{22} Malassezia padonica 2 strains 0.016^{22} Malassezia pachydermatis 6 strains 0.012^{22} Malassezia pachydermatis 6 strains 0.012^{22} Malassezia pachydermatis 6 strains 0.012^{22} Malassezia pachydermatis 6 strains			
Fusarium spp.b 6 strains $>0.4^{13}$ Lichtheimia spp.b 2 strains $0.2-0.4^{13}$ Malassezia furfur 8 strains 0.03^{22} Malassezia furfur 26 strains $0.016-0.25^{22}$ Malassezia globose 36 strains $0.016-0.25^{22}$ Malassezia globose 36 strains $0.016-0.25^{22}$ Malassezia sympodialis 19 strains 0.125^{22} Malassezia obtuse 7 strains 0.03^{22} Malassezia obtuse 7 strains 0.03^{22} Malassezia obtuse 10 strains 0.012^{22} Malassezia polica 10 strains 0.016^{22} Malassezia paponica 2 strains 0.016^{22} Malassezia pachydermatis 6 strains 0.016^{22} Malassezia pachydermatis 6 strains 0.012^{22} Mucor spp.b 4 strains 0.012^{22} Paecilomyces licasinusb 5 strains 0.012^{22} Paecilomyces variotib 4 strains 0.025^{22} Rhizopuc spp.b 2 strains 0.012^{22} <			
Lichtheimia spp.b 2 strains $0.2-0.4^{13}$ Malassezia furfur 26 strains 0.03^{22} Malassezia globose 36 strains $0.016-0.25^{22}$ Malassezia restrica 28 strains $0.016-0.25^{22}$ Malassezia sympodialis 19 strains 0.125^{22} Malassezia obtuse 7 strains 0.03^{22} Malassezia slooffiae 10 strains 0.016^{22} Malassezia dermatis 3 strains 0.016^{22} Malassezia ponica 2 strains Malassezia pannica 4 strains Malassezia pachydermatis 6 strains Malassezia yamatoensis 2 strains Mucor spp. b 4 strains 0.012 to $>0.4^{13}$ Paecilomyces licasinus b 5 strains 0.025 to $>0.4^{13}$ Paecilomyces varioti b 4 strains 0.012 to $>0.4^{13}$ Rhizomucor spp. b 2 strains $0.012 \cdot 0.025$ to $>0.4^{13}$ Rhizomucor spp. b 3 strains $0.012 \cdot 0.025$ to $>0.4^{13}$ Scedosporium apiospermum b 4 strains $0.012 \cdot 0.025$ to $>0.4^{13}$ Scedosporium apiospermum b 4 strains 0.05 to $>0.4^{13}$ Scedosporium prolificans b 4 strains 0.05 to $>0.4^{13}$ Scedosporium prolificans b 4 strains 0.05 to $>0.4^{13}$ Scedosporium prolificans b 5 strains 0.05 to $>0.4^{13}$ Scedosporium prolificans b 6 strains 0.05 to >0.5 to >0	Cunninghamella spp. ^b	2 strains	$0.05 - 0.2^{13}$
Malassezia furfur 8 strains 26 strains $0.03^{22} 0.5-32^{15}$ Malassezia globose 36 strains $0.016-0.25^{22}$ Malassezia restrica 28 strains $0.016-0.25^{22}$ Malassezia sympodialis 19 strains 0.125^{22} Malassezia obtuse 7 strains 0.03^{22} Malassezia dermatis 3 strains 0.016^{22} Malassezia japonica 2 strains 0.016^{22} Malassezia pachydermatis 6 strains $0.012 \text{ to } > 0.4^{12}$ Malassezia yamatoensis 2 strains $0.012 \text{ to } > 0.4^{13}$ Mucor spp. b 4 strains $0.012 \text{ to } > 0.4^{13}$ Paecilomyces licasinus b 5 strains $0.012 \text{ to } > 0.4^{13}$ Rhizomucor spp. b 4 strains $0.012 - 0.025^{13}$ Rhizomucor spp. b 2 strains $0.012 - 0.025^{13}$ Rhizopus spp. b 4 strains $0.012 - 0.025^{13}$ Scedosporium apiospermum b 4 strains $0.012 - 0.025^{13}$ Scedosporium prolificans b 4 strains $0.05 \text{ to } > 0.4^{13}$ Scedosporium prolificans b 4 strains	Fusarium spp. ^b	6 strains	>0.4 ¹³
Malassezia furfur 26 strains $0.5 \cdot 32^{15}$ Malassezia globose 36 strains $0.016 - 0.25^{22}$ Malassezia restrica 28 strains 0.0125^{22} Malassezia sympodialis 19 strains 0.125^{22} Malassezia obtuse 7 strains 0.03^{22} Malassezia slooffiae 10 strains 0.016^{22} Malassezia japonica 2 strains 0.016^{22} Malassezia pachydermatis 6 strains 0.012^{22} Malassezia pachydermatis 6 strains 0.012 to 0.04^{13} Mucor spp. b 4 strains 0.012 to 0.04^{13} Paecilomyces licasinus b 5 strains 0.012 to 0.04^{13} Paecilomyces varioti b 4 strains 0.025 to 0.04^{13} Rhizomucor spp. b 2 strains $0.012 \cdot 0.025^{13}$ Rhizopus spp. b 5 strains $0.012 \cdot 0.025^{13}$ Scedosporium apiospermumb 4 strains 0.05 to 0.04^{13} Scedosporium prolificans b 4 strains 0.05 to 0.04^{13} Scedosporium prolificans b 4 strains 0.05 to	Lichtheimia spp. ^b	2 strains	$0.2 - 0.4^{13}$
Malassezia globose 36 strains $0.016-0.25^{22}$ Malassezia restrica 28 strains $0.016-0.25^{22}$ Malassezia sympodialis 19 strains 0.125^{22} Malassezia obtuse 7 strains 0.03^{22} Malassezia alooffiae 10 strains 0.016^{22} Malassezia oponica 2 strains 0.016^{22} Malassezia paponica 2 strains 0.016^{22} Malassezia pachydermatis 6 strains 0.012^{22} Malassezia yamatoensis 2 strains 0.012^{22} Mucor spp. b 4 strains 0.012^{22} Paecilomyces licasinus b 5 strains 0.012^{23} Paecilomyces varioti b 4 strains 0.025^{22} Rhizomucor spp. b 2 strains 0.012^{24} Rhizomucor spp. b 2 strains 0.012^{24} Rhizopus spp. b 5 strains 0.015^{22} Scedosporium apiospermumb 4 strains 0.05^{24} Scedosporium prolificans b 4 strains 0.05^{24} Scopulariopsis spp. b 4 strains 0.05^{24}	Malanasia funfun	8 strains	0.03^{22}
Malassezia restrica28 strains $0.016-0.25^{22}$ Malassezia sympodialis19 strains 0.125^{22} Malassezia obtuse7 strains 0.03^{22} Malassezia slooffiae10 strains 0.016^{22} Malassezia japonica2 strains 0.016^{22} Malassezia pachydermatis6 strains $0.012 \text{ to } > 0.4^{13}$ Malassezia yamatoensis2 strains $0.012 \text{ to } > 0.4^{13}$ Mucor spp. b4 strains $0.012 \text{ to } > 0.4^{13}$ Paecilomyces licasinus b5 strains $0.025 \text{ to } > 0.4^{13}$ Paecilomyces varioti b4 strains $0.012 \text{ to } > 0.012 \text{ to } > 0.012$ Rhizomucor spp. b2 strains $0.012 \text{ co.} 0.025^{13}$ Rhizopus spp. b5 strains $0.012 \text{ co.} 0.012 \text{ co.} 0.012$ Scedosporium apiospermumb4 strains $0.05 \text{ to } > 0.4^{13}$ Scedosporium prolificans b4 strains $0.05 \text{ to } > 0.4^{13}$ Scopulariopsis spp. b4 strains $0.05 \text{ to } > 0.4^{13}$ Scopulariopsis spp. b4 strains $0.05 \text{ to } > 0.4^{13}$ Saccharomyces cerevisiae bYFK07 (pdrl-3), YFK256 (PDR) YFK014 (fkr2), YFK258 (PDR) YFK093 (fkr3) YFK093 (fkr3) YFK093 (fkr3) YFK093 (fkr3) YFK093 (fkr3) YFK093 (fkr3) YFK222-2A (pdrl-7) 35 $0.00 \text{ to } 0.00 $	Maiassezia furfur	26 strains	$0.5 - 32^{15}$
Malassezia restrica28 strainsMalassezia sympodialis19 strains 0.125^{22} Malassezia obtuse7 strains 0.03^{22} Malassezia slooffiae10 strains 0.016^{22} Malassezia paponica2 strains 0.016^{22} Malassezia paponica2 strains 0.016^{22} Malassezia pachydermatis6 strains $0.012 \text{ to } > 0.4^{13}$ Malassezia yamatoensis2 strains $0.012 \text{ to } > 0.4^{13}$ Paecilomyces licasinush5 strains $0.012 \text{ to } > 0.4^{13}$ Paecilomyces varioti b4 strains $0.025 \text{ to } > 0.4^{13}$ Rhizomucor spp. b2 strains $0.012 \text{ to } > 0.4^{13}$ Scedosporium apiospermumb4 strains $0.05 \text{ to } > 0.4^{13}$ Scedosporium prolificansb4 strains $0.05 \text{ to } > 0.4^{13}$ Scopulariopsis spp. b4 strains $0.05 \text{ to } > 0.4^{13}$ Scopulariopsis spp. b4 strains $0.05 \text{ to } > 0.4^{13}$ Scopulariopsis spp. b4 strains $0.05 \text{ to } > 0.4^{13}$ Scopulariopsis spp. b4 strains $0.05 \text{ to } > 0.4^{13}$ Scopulariopsis spp. b4 strains $0.05 \text{ to } > 0.4^{13}$ Sporonthrix schenikiiCBS 133021 1.24 Sporonthrix brasilliensisCBS 132984 2.24	Malassezia globose	36 strains	0.016_0.2522
Malassezia obtuse7 strains 0.03^{22} Malassezia slooffiae10 strains 0.016^{22} Malassezia dermatis3 strains 0.016^{22} Malassezia japonica2 strainsMalassezia pachydermatis6 strainsMalassezia yamatoensis2 strainsMucor spp. b4 strains 0.012 to $>0.4^{13}$ Paecilomyces licasinus b5 strains 0.025 to $>0.4^{13}$ Paecilomyces varioti b4 strains 0.025 to $>0.4^{13}$ Rhizomucor spp. b2 strains $0.012 - 0.025$ tisRhizopus spp. b2 strains $0.012 - 0.025$ to $>0.4^{13}$ Scedosporium apiospermum b4 strains 0.05 to $>0.4^{13}$ Scedosporium prolificans b4 strains 0.05 to $>0.4^{13}$ Scopulariopsis spp. b4 strains 0.05 to $>0.4^{13}$ Scopulariopsis spp. b4 strains 0.05 to $>0.4^{13}$ Saccharomyces cerevisiae bYFK005 wild type YFK012 (fkr1), YFK256 (PDR) YFK012 (fkr1), YFK256 (PDR) YFK014 (fkr2), YFK259 (pdrl-7) YFK014 (fkr2), YFK259	Malassezia restrica	28 strains	
Malassezia slooffiae10 strains 0.03^{22} Malassezia dermatis3 strains 0.016^{22} Malassezia japonica2 strainsMalassezia nana4 strainsMalassezia pachydermatis6 strainsMalassezia yamatoensis2 strainsMucor spp. b4 strains 0.012 to $>0.4^{13}$ Paecilomyces licasinus b5 strains 0.025 to $>0.4^{13}$ Paecilomyces varioti b4 strains 0.025 to $>0.4^{13}$ Rhizomucor spp. b2 strains $0.012 - 0.025^{13}$ Rhizopus spp. b5 strains 0.1 to $>0.4^{13}$ Scedosporium apiospermum b4 strains 0.05 to $>0.4^{13}$ Scedosporium prolificans b4 strains >0.05 to $>0.4^{13}$ Scopulariopsis spp. b4 strains >0.05 to $>0.4^{13}$ Spoulariopsis spp. b4 strains >0.05 to $>0.4^{13}$ Spoulariopsis spp. b5 strains >0.05 to $>0.4^{13}$ Spoulariopsis spp. b4 strains >0.05 to $>0.4^{13}$	Malassezia sympodialis	19 strains	0.125^{22}
Malassezia slooffiae10 strainsMalassezia dermatis3 strains 0.016^{22} Malassezia japonica2 strainsMalassezia nana4 strainsMalassezia pachydermatis6 strainsMalassezia yamatoensis2 strainsMucor spp. b4 strains 0.012 to $>0.4^{13}$ Paecilomyces licasinusb5 strains $>0.41^3$ Paecilomyces varioti b4 strains 0.025 to $>0.4^{13}$ Rhizomucor spp. b2 strains $0.012-0.025^{13}$ Rhizopus spp. b5 strains 0.1 to $>0.4^{13}$ Scedosporium apiospermumb4 strains 0.05 to $>0.4^{13}$ Scedosporium prolificansb4 strains >0.05 to $>0.4^{13}$ Scopulariopsis spp. b4 strains >0.05 to $>0.4^{13}$ YFK007 wild type 22 YFK012 (fkr1), YFK256 (PDR) YFK012 (fkr1), YFK256 (PDR) YFK093 (fkr3) YFK257 (pdrl-3), YFK259 (pdrl-7) YFK014 (fkr2), YFK258 (PDR) YFK093 (fkr3) YFK223-5C (pdrl-3) YFK222-2A (pdrl-7) 35 6 YFK222-2A (pdrl-7) 35Sporonthrix brasilliensisCBS 133021 1^{24} Sporonthrix schenckiiCBS 132984 2^{24}	Malassezia obtuse	7 strains	0.03 ²²
$ \begin{array}{c ccccccccccccccccccccccccccccccccccc$	Malassezia slooffiae	10 strains	
Malassezia japonica2 strainsMalassezia nana4 strainsMalassezia pachydermatis6 strainsMalassezia yamatoensis2 strainsMucor spp.b4 strains $0.012 \text{ to } > 0.4^{13}$ Paecilomyces licasinusb5 strains $0.025 \text{ to } > 0.4^{13}$ Paecilomyces variotib4 strains $0.025 \text{ to } > 0.4^{13}$ Rhizomucor spp.b2 strains $0.012 \text{ -} 0.025^{13}$ Rhizopus spp.b5 strains $0.1 \text{ to } > 0.4^{13}$ Seedosporium apiospermumb4 strains $0.05 \text{ to } > 0.4^{13}$ Scedosporium prolificansb4 strains $0.05 \text{ to } > 0.4^{13}$ Scopulariopsis spp.b4 strains $0.05 \text{ to } > 0.4^{13}$ Scopulariopsis spp.b4 strains $0.05 \text{ to } > 0.4^{13}$ Scopulariopsis spp.b4 strains $0.05 \text{ to } > 0.4^{13}$ YFK007 wild type YFK012 (fkr1), YFR256 (PDR) YFK257 (pdrl-3), YFK259 (pdrl-7) YFK014 (fkr2), YFR258 (PDR) YFK093 (fkr3) YFK223-5C (pdrl-3) YFK223-5C (pdrl-3) YFK222-2A (pdrl-7) 6 YFK222-2A (pdrl-7) 35Sporonthrix brasilliensisCBS 133021 1^{24} Sporonthrix schenckiiCBS 132984 2^{24}	Malassezia dermatis	3 strains	0.016^{22}
Malassezia pachydermatis6 strainsMalassezia yamatoensis2 strainsMucor spp. b4 strains $0.012 \text{ to } > 0.4^{13}$ Paecilomyces licasinus b5 strains $> 0.4^{13}$ Paecilomyces varioti b4 strains $0.025 \text{ to } > 0.4^{13}$ Rhizomucor spp. b2 strains $0.012 - 0.025^{13}$ Rhizopus spp. b5 strains $0.1 \text{ to } > 0.4^{13}$ Scedosporium apiospermumb4 strains $0.05 \text{ to } > 0.4^{13}$ Scedosporium prolificans b4 strains $0.05 \text{ to } > 0.4^{13}$ Scopulariopsis spp. b4 strains $0.05 \text{ to } > 0.4^{13}$ Scopulariopsis spp. b4 strains $0.05 \text{ to } > 0.4^{13}$ Scopulariopsis spp. b4 strains $0.05 \text{ to } > 0.4^{13}$ Scopulariopsis spp. b4 strains $0.05 \text{ to } > 0.4^{13}$ Scopulariopsis spp. b4 strains $0.05 \text{ to } > 0.4^{13}$ YFK005 wild type YFK07 wild type YFK07 (pdrl-3), YFK256 (PDR) YFK257 (pdrl-3), YFK259 (pdrl-7) YFK093 (fkr3) YFK203 (fkr3) YFK203 (fkr3) YFK222-2A (pdrl-7) 50 Sporonthrix brasilliensisCBS 133021 1^{24} Sporonthrix schenckiiCBS 132984 2^{24}	Malassezia japonica	2 strains	
Malassezia yamatoensis 2 strains Mucor spp. b 4 strains 0.012 to $>0.4^{13}$ Paecilomyces licasinusb 5 strains $>0.4^{13}$ Paecilomyces varioti b 4 strains 0.025 to $>0.4^{13}$ Rhizomucor spp. b 2 strains $0.012 \cdot 0.025^{13}$ Rhizopus spp. b 5 strains 0.1 to $>0.4^{13}$ Scedosporium apiospermumb 4 strains 0.05 to $>0.4^{13}$ Scedosporium prolificansb 4 strains >0.05 to $>0.4^{13}$ Scopulariopsis spp. b 4 strains >0.05 to $>0.4^{13}$ Scopulariopsis spp. b 4 strains >0.05 to $>0.4^{13}$ Scopulariopsis spp. b 4 strains >0.05 to $>0.4^{13}$ YFK005 wild type 1523 YFK007 wild type 22 YFK012 (fkr1), YFK256 (PDR) >80 YFK093 (fkr3), YFK259 (pdrl-7) >80 YFK093 (fkr3) 50 YFK223-5C (pdrl-3) 6 YFK222-2A (pdrl-7) 35 Sporonthrix brasilliensis CBS 133021 1^{24} Sporonthrix schenckii CBS 132984 2^{24	Malassezia nana	4 strains	
Mucor spp. b 4 strains 0.012 to $>0.4^{13}$ Paecilomyces licasinus b 5 strains $>0.4^{13}$ Paecilomyces varioti b 4 strains 0.025 to $>0.4^{13}$ Rhizomucor spp. b 2 strains $0.012 - 0.025^{13}$ Rhizopus spp. b 5 strains 0.1 to $>0.4^{13}$ Scedosporium apiospermumb 4 strains 0.05 to $>0.4^{13}$ Scedosporium prolificans b 4 strains 0.05 to $>0.4^{13}$ Scopulariopsis spp. b 4 strains 0.05 to $>0.4^{13}$ YFK005 wild type 15^{23} YFK007 wild type 22 YFK012 (fkr1), YFK256 (PDR) >80 YFK257 (pdrl-3), YFK259 (pdrl-7) >80 YFK093 (fkr3) >0 YFK093 (fkr3) >0 YFK223-5C (pdrl-3) <0 YFK222-2A (pdrl-7) <0 Sporonthrix brasilliensis CBS 133021 <0 Sporonthrix schenckii CBS 132984 <0	Malassezia pachydermatis	6 strains	
Paecilomyces licasinus ^b 5 strains $>0.4^{13}$ Paecilomyces varioti ^b 4 strains 0.025 to $>0.4^{13}$ Rhizomucor spp. ^b 2 strains $0.012 - 0.025^{13}$ Rhizopus spp. ^b 5 strains 0.1 to $>0.4^{13}$ Scedosporium apiospermum ^b 4 strains 0.05 to $>0.4^{13}$ Scedosporium prolificans ^b 4 strains $>0.4^{13}$ Scopulariopsis spp. ^b 4 strains 0.05 to $>0.4^{13}$ YFK005 wild type 15^{23} YFK007 wild type 22 YFK012 (fkr1), YFK256 (PDR) >80 YFK257 (pdrl-3), YFK259 (pdrl-7) >80 YFK093 (fkr3) 50 YFK223-5C (pdrl-3) 6 YFK225-2A (pdrl-7) 35 Sporonthrix brasilliensis CBS 132984 2^{24}	Malassezia yamatoensis	2 strains	
Paecilomyces varioti b 4 strains $0.025 \text{ to } > 0.4^{13}$ Rhizomucor spp. b 2 strains $0.012 - 0.025^{13}$ Rhizopus spp. b 5 strains $0.1 \text{ to } > 0.4^{13}$ Scedosporium apiospermum b 4 strains $0.05 \text{ to } > 0.4^{13}$ Scedosporium prolificans b 4 strains $> 0.4^{13}$ Scopulariopsis spp. b 4 strains $0.05 \text{ to } > 0.4^{13}$ YFK005 wild type 15^{23} YFK007 wild type 22 YFK012 (fkr1), YFK256 (PDR) > 80 YFK257 (pdrl-3), YFK259 (pdrl-7) > 80 YFK093 (fkr3) 50 YFK223-5C (pdrl-3) 6 YFK222-2A (pdrl-7) 35 Sporonthrix brasilliensis CBS 133021 1^{24} Sporonthrix schenckii CBS 132984 2^{24}	Mucor spp.b	4 strains	0.012 to >0.4 ¹³
Rhizomucor spp. b 2 strains $0.012 - 0.025^{13}$ Rhizopus spp. b 5 strains $0.1 \text{ to } > 0.4^{13}$ Scedosporium apiospermumb 4 strains $0.05 \text{ to } > 0.4^{13}$ Scedosporium prolificansb 4 strains $> 0.4^{13}$ Scopulariopsis spp. b 4 strains $0.05 \text{ to } > 0.4^{13}$ YFK005 wild type 15^{23} YFK007 wild type 22 YFK012 (fkr1), YFK256 (PDR) > 80 YFK014 (fkr2), YFK259 (pdrl-7) > 80 YFK093 (fkr3) 50 YFK093 (fkr3) 50 YFK223-5C (pdrl-3) 6 YFK225-2A (pdrl-7) 35 Sporonthrix brasilliensis CBS 133021 1^{24} Sporonthrix schenckii CBS 132984 2^{24}	Paecilomyces licasinus ^b	5 strains	>0.4 ¹³
Rhizopus spp. b 5 strains $0.1 \text{ to } > 0.4^{13}$ Scedosporium apiospermumb 4 strains $0.05 \text{ to } > 0.4^{13}$ Scedosporium prolificansb 4 strains $> 0.4^{13}$ Scopulariopsis spp. b 4 strains $0.05 \text{ to } > 0.4^{13}$ YFK005 wild type 15^{23} YFK007 wild type 22 YFK012 (fkr1), YFK256 (PDR) > 80 YFK257 (pdrl-3), YFK259 (pdrl-7) > 80 YFK014 (fkr2), YFK258 (PDR) 45 YFK093 (fkr3) 50 YFK223-5C (pdrl-3) 6 YFK222-2A (pdrl-7) 35 Sporonthrix brasilliensis CBS 133021 1^{24} Sporonthrix schenckii CBS 132984 2^{24}	Paecilomyces varioti ^b	4 strains	0.025 to >0.4 ¹³
Scedosporium apiospermumb 4 strains $0.05 \text{ to } > 0.4^{13}$ Scedosporium prolificansb 4 strains $>0.4^{13}$ Scopulariopsis spp.b 4 strains $0.05 \text{ to } > 0.4^{13}$ YFK005 wild type 15^{23} YFK007 wild type 22 YFK012 (fkr1), YFK256 (PDR) > 80 YFK257 (pdrl-3), YFK259 (pdrl-7) > 80 YFK014 (fkr2), YFK258 (PDR) 45 YFK093 (fkr3) 50 YFK223-5C (pdrl-3) 6 YFK222-2A (pdrl-7) 35 Sporonthrix brasilliensis CBS 133021 1^{24} Sporonthrix schenckii CBS 132984 2^{24}		2 strains	$0.012 - 0.025^{13}$
Scedosporium prolificansb 4 strains $>0.4^{13}$ Scopulariopsis spp.b 4 strains $0.05 \text{ to } > 0.4^{13}$ YFK005 wild type 15^{23} YFK007 wild type 22 YFK012 (fkr1), YFK256 (PDR) >80 YFK257 (pdrl-3), YFK259 (pdrl-7) >80 YFK014 (fkr2), YFK258 (PDR) 45 YFK093 (fkr3) 50 YFK223-5C (pdrl-3) 6 YFK222-2A (pdrl-7) 35 Sporonthrix brasilliensis CBS 133021 1^{24} Sporonthrix schenckii CBS 132984 2^{24}	Rhizopus spp.b	5 strains	$0.1 \text{ to } > 0.4^{13}$
Scopulariopsis spp. b 4 strains $0.05 \text{ to } > 0.4^{13}$ YFK005 wild type 15^{23} YFK007 wild type 22 YFK012 (fkr1), YFK256 (PDR) > 80 YFK257 (pdrl-3), YFK259 (pdrl-7) > 80 YFK014 (fkr2), YFK258 (PDR) 45 YFK093 (fkr3) 50 YFK223-5C (pdrl-3) 6 YFK222-2A (pdrl-7) 35 Sporonthrix brasilliensis CBS 133021 1^{24} Sporonthrix schenckii CBS 132984 2^{24}	Scedosporium apiospermum ^b	4 strains	0.05 to >0.4 ¹³
YFK005 wild type 15 ²³ YFK007 wild type 22 YFK012 (fkr1), YFK256 (PDR) >80 YFK257 (pdrl-3), YFK259 (pdrl-7) >80 YFK014 (fkr2), YFK258 (PDR) 45 YFK093 (fkr3) 50 YFK223-5C (pdrl-3) 6 YFK222-2A (pdrl-7) 35 Sporonthrix brasilliensis CBS 133021 1 ²⁴ Sporonthrix schenckii CBS 132984 2 ²⁴	Scedosporium prolificans ^b	4 strains	>0.4 ¹³
YFK007 wild type 22 YFK012 (fkr1), YFK256 (PDR) >80 YFK257 (pdrl-3), YFK259 (pdrl-7) >80 YFK014 (fkr2), YFK258 (PDR) 45 YFK093 (fkr3) 50 YFK223-5C (pdrl-3) 6 YFK222-2A (pdrl-7) 35 Sporonthrix brasilliensis CBS 133021 124 Sporonthrix schenckii CBS 132984 224	Scopulariopsis spp. ^b	4 strains	0.05 to >0.4 ¹³
Saccharomyces cerevisiaeb YFK012 (fkr1), YFK256 (PDR) >80 YFK257 (pdrl-3), YFK259 (pdrl-7) >80 YFK014 (fkr2), YFK258 (PDR) 45 YFK093 (fkr3) 50 YFK223-5C (pdrl-3) 6 YFK222-2A (pdrl-7) 35 Sporonthrix brasilliensis CBS 133021 124 Sporonthrix schenckii CBS 132984 224			
Saccharomyces cerevisiaeb YFK257 (pdrl-3), YFK259 (pdrl-7) >80 YFK014 (fkr2), YFK258 (PDR) 45 YFK093 (fkr3) 50 YFK223-5C (pdrl-3) 6 YFK222-2A (pdrl-7) 35 Sporonthrix brasilliensis CBS 133021 124 Sporonthrix schenckii CBS 132984 224			
Satcharomyces cerevisiae YFK014 (fkr2), YFK258 (PDR) 45 YFK093 (fkr3) 50 YFK223-5C (pdrl-3) 6 YFK222-2A (pdrl-7) 35 Sporonthrix brasilliensis CBS 133021 124 Sporonthrix schenckii CBS 132984 224			
YFK093 (fkr3) 50 YFK223-5C (pdrl-3) 6 YFK222-2A (pdrl-7) 35 Sporonthrix brasilliensis CBS 133021 124 Sporonthrix schenckii CBS 132984 224	Saccharomyces cerevisiae ^b		
YFK223-5C (pdrl-3) 6 YFK222-2A (pdrl-7) 35 Sporonthrix brasilliensis CBS 133021 1 ²⁴ Sporonthrix schenckii CBS 132984 2 ²⁴			
YFK222-2A (pdrl-7) 35 Sporonthrix brasilliensis CBS 133021 1 ²⁴ Sporonthrix schenckii CBS 132984 2 ²⁴			
Sporonthrix brasilliensisCBS 133021124Sporonthrix schenckiiCBS 132984224			
Sporonthrix schenckii CBS 132984 2 ²⁴	Sporonthrix brasilliensis	<u> </u>	1^{24}
Trichosporon asahii CBS 2479 >64 ²⁵		CBS 132984	2 ²⁴
	Trichosporon asahii	CBS 2479	>64 ²⁵

VUT-77011 VUT-97010 VUT-00001	>100 ²⁶ 0.781 ²⁶ 6.25 ²⁶
,	
VUT-00001	6.25^{26}
VUT-00002	25^{26}
VUT-00003	12.5^{26}
TIMMl189	>128 ¹⁵
EP594	15
EP596	>128 ¹⁵
	VUT-00003 TIMMl189 EP594

aMIC₈₀, bMIC₅₀

Odom at al. revealed, that in vitro FK506 was toxic to Cryptococcus neoformans at 37 °C, but not at 24 °C, because at the higher temperature growth and virulence were dependent on the protein phosphatase calcineurin.²¹ It was found, that tacrolimus inhibited CDR1 and CaM-DR1 genes in *C. albicans*, which are thought to play a role in the antifungal resistance to azole derivatives.⁸ Along with the high level of stress that was induced by an influx Ca2+ and Na+ the membrane distortion caused by the azole interference of the ergosterol metabolism gave rise to an enhanced intracellular FK506 concentration.^{9,27} In vitro studies with fluconazole-resistant C. glabrata isolates revealed a distinct synergistic effect when FK506 was combined with ketoconazole (77%), itraconazole (73%), voriconazole (63%) and fluconazole (60%).²⁸ It has also been shown that tacrolimus dramatically induced Ca2+ uptake in C. glabrata cells in the presence of fluconazole²⁹ or terbinafine and fenpropimorph.¹⁷ The addition of FK506 or the disruption of calcineurin gene CMP2 specifically reversed the β-1,3-glucan synthase Fks2-mediated resistance of C. glabrata to echinocandin³⁰ as well as to posaconazole in C. albicans. 16 Li et al. 19 mentioned the decrease in ERG11 and SNQ2 gene expression levels and the inhibition of fluconazole efflux by FK506 in Candida glabrata. Poeta et al.20 demonstrated that it exhibits marked synergistic activity with the H+ATPase inhibitor bafilomycin A₁ and pneumocandin MK-0991/caspofungin acetate in C. neoformans cells. Steinbach et al. 12 confirmed that FK506 and cyclosporin exhibit an inherent activity against Aspergillus fumigatus, generally delaying filamentation and producing smaller hyphae. Borba-Santos²⁴ observed an increase of itraconazole and fluconazole efficiency when applied in combination with FK506 in therapy regime for sporotrichosis, which is caused by pathogenic fungi Sporonthrix brasiliensis or S. schenckii. Ozawa et al.²⁶ also revealed synergistic activity of tacrolimus with itraconazole against Trichophyton mentagrophytes. In contrast FK506 showed no high activity against Trichosporon asahii strains (MIC > 64.0 μg/mL).²⁵ However, a larger synergistic interaction was observed by the combinations FK506 + amphotericin B (96.67%) and FK506 + caspofungin (73.33%) against fluconazole-susceptible isolates of Trichosporon asahii. The activity of

FK506 in combination with azole antifungals against *Malassezia* species was investigated too. 15,22

Also FK506 was thoroughly tested against fungal biofilms of A. fumigatus¹⁴ and 60 selected clinical fungal isolates:¹³ A. flavus, A. terreus, A. ustus, A. niger, A. versicolor, Purpureocillium lilacinus, Paecilomyces variotii, Scopulariopsis spp., Rhizopus spp., Mucor spp., Rhizomucor spp., Lichtheimia spp., Cunninghamella spp., Fusarium spp., Scedosporium apiospermum and S. prolificans. Besides FK506 was reported to effect growth of Paecilomyces variotii,¹³ Cryptococcus neoformans,²¹ Neurospora crassa³¹ and Coccidioides immitis.³²

2. 2. Antifungal Studies

Considering the above-mentioned data, we decided to investigate antifungal activity of tacrolimus in concentrations of 1, 0.05 and 0.001 µg/mL against not studied before ten phytopathogenic fungi and three *Phytophthora* oomycetes: *A. alternata*, *F. graminearum*, *B. cinerea*, *C. higginsianum*, *F. equiseti*, *F. fujikuroi*, *F. oxysporum*, *P. digitatum*, *V. lecanii*, *M. indicus*, *P. infestans* p-4, GC-1 and p-3. (Table 2). And also *A. niger*, that to our knowledge was the only one fungus treated earlier with FK506 (Table 1).¹³

So, it was found that at 1 µg/mL all fungi were susceptible to FK506, except M. indicus. A near complete inhibition of 99.0 % was detected with B. cinerea. Whereas lowest effect (21.1%) was observed with V. lecanii. Moreover, FK506 was always more active against any strain than the strong antifungal reference cyproconazole (2-(4-chlorphenyl)-3-cyclopropyl-1-(1H-1,2,4-triazol-1-yl)butan-2-ol)³³ in the same concentration. And the results against the different strains of the same specie had the similar inhibition zones when treated with 1 µg/mL of tacrolimus.

Lowering the concentration to 0.05 µg/mL still conferred an inhibition of all strains. *A. alternata*, *F. graminearum*, *B. cinerea*, *C. higginsianum* and *A. niger* were the most sensitive ones and were effected more than 70%.

Even at a 1000 times lower concentration (0.001 μg/ mL) moderate effects were still observed against *F. graminearum* (41.0 %), *A. alternata* (36.1%), *C. higginsianum* (27.1%), *P. infestans* p-4 (23.7%) and *A. niger* (15.9 %), showing high efficiency of FK506 antifungal activity.

Numbers represent means of experiments carried out in triplicate. Cyproconazole was used as positive control. Experimental procedures were as described in materials and methods. The strains are
 Table 2. Growth inhibition rates (%) of tacrolimus (FK506)

presented in columns according decrease of average activity of tacrolimus in 1 μg/mL

#	Dosage					Growt	Growth inhibition rates of fungi or oomycetes, % ± SD	rates of fung	ti or oomyce	tes, % ± SD				
	(µg/mL)	BC	AA	FF	FG	FE	СН	AN		PI 4	PI 3	PI 1	PD	ΛΓ
	1	99.0 ± 0	98.5 ± 2.1 94.4 ± 1.1	94.4 ± 1.1	89.4 ± 1.0	89.4 ± 2.1	87.8 ± 0	86.5 ± 1.1	69.2 ± 1.1	69.2 ± 1.1 64.8 ± 2.3 66.4 ± 1.0 60.5 ± 1.2 44.2 ± 6.5	66.4 ± 1.0	60.5 ± 1.2		21.1 ± 0
*	0.05	97.6 ± 1.0	94.6 ± 2.8	49.8 ± 1.2	77.7 ± 1.0	68.9 ± 4.1	79.8 ± 1.2	85.1 ± 1.1	63.4 ± 2.2	59.9 ± 0.9	50.2 ± 2.5 69.2 ± 2.2 21.1 ± 6.5	69.2 ± 2.2	21.1 ± 6.5	3.5 ± 5.0
	0.001	0.0	36.4 ± 0.9	1.6 ± 3.2	41.0 ± 2.1	1.5 ± 2.9	27.1 ± 2.5	15.9 ± 2.9	-3.4 ± 4.4	23.7 ± 0.7	-3.3 ± 1.2 2.2 ± 0	2.2 ± 0	1.3 ± 0.9	3.5 ± 5.0
C	1	67.3 ± 1.9	67.3 ± 1.9 64.0 ± 3.1	80.7 ± 0.5	38.8 ± 1.0	84.8 ± 0.2	78.4 ± 1.4 83.5 ± 2.4	83.5 ± 2.4	42.8 ± 7.7	$42.8 \pm 7.7 62.0 \pm 1.4 32.4 \pm 1.0 56.8 \pm 5.6$	32.4 ± 1.0	56.8 ± 5.6	0.0	14.0 ± 5.0
Į.	tacrolimus, C	- cyproconazole	*T - tacrolimus, C- cyproconazole, B. cinerea (BC), A. alternata (AA), (FF), F. graminearum (FG), F. equiseti (FE), C. higginsianum (CH), A. niger (AN), F. oxysporum (FO), P. infestans GC-1 (PI 1), p-4 (PI	'), A. alternata ((AA), (FF), F. g	raminearum (F	G), F. equiseti	(FE), C. higgin	sianum (CH),	A. niger (AN),	F. oxysporum ((FO), P. infest	ans GC-1 (PI	.), p-4 (PI

4) and p-3 (PI 3), P. digitatum (PD) and V. lecanii (VL). M. indicus was insensitive to all tested substances (0%

2. 3. Molecular Docking Studies

In order to propose unstudied antifungal activity mechanism *in silico* molecular docking was done³⁴. The found affinity scores of tacrolimus and reference cyproconazole³³ to common antifungal targets³⁵ are presented in Table 3.

As it was expected the 14α -demethylase (CYP51) has shown the best affinity with triazole derivative cyproconazole according to its best score (-7.9 Kcal/Mol) (Table 3).

An interesting result was found for tacrolimus, because it fitted into the active sites of secreted aspartic proteinase (SAP2) and UDP-*N*-acetylmuramoyl-*L*-alanine: *D*-glutamate ligase (MurD) better then cyproconazole, and its affinity scores were much higher (–8.5 and –9.8 Kcal/Mol correspondingly).

The visualization of interaction (Figure 2) with the best target indicates that tacrolimus binds to MurD by four conventional hydrogen and three carbon hydrogen bonds. Also five hydrophobic alkyl and π -alkyl bonds are formed with LEU15, LEU416, ARG186 and PHE422 residues of enzyme (Table 4).

3. Experimental

The mycelial growth rate assay was used for antifungal studies.³⁶ Strains of filamentous fungi were obtained from the following sources: Aspergillus niger DSM 246, Altenaria alternata DSM 1102, Fusarium equiseti DSM 21725, F. graminearum DSM 1095, F. fujikuroi DSM 893, Verticillium lecanii, Penicillium digitatum DSM 2731 from DSMZ (Braunschweig, Germany); Fusarium oxysporum 39/1201 St. 9336 and Botrytis cinerea from the Technische Universität Berlin (Germany); Colletotrichum higginsianum MAFF 305635, originally isolated in Japan, via the Department of Biology, Friedrich-Alexander-Universität (Erlangen, Germany); Phytophthora infestans GL-1 01/14 wild strain, p-3 (4/91; R+) and p-4 (4/91; R-) strains were kindly donated by Julius Kühn-Institut (Quedlinburg, Germany). Potato Dextrose Agar (PDA) were purchased from C. Roth (Karlsruhe, Germany). Cyproconazole (99%) was obtained from (Sigma Aldrich, Germany). Tacrolimus (99 %) was purchased from Huaian Ruanke Trade, Ltd. (Huaian, China). Strains were cultivated on PDA for 6 d at 25 °C. Spores from each strain were gently harvested with a sterile glass rod from plate surfaces with deionized water. Spore concentration numbers in suspension were determined microscopically and adjusted to 7.5*106 spores/mL. The clear stock solutions of 1 mg/mL were made of 0.01 g of cyproconazole and tacrolimus in 10 mL of deionized sterile water as solvent. 10 mL of these stock solutions were mixed in situ into 99 mL of PDA prior to solidification to obtain a final concentration of 1 µg/mL. Additionally, from the same stock solution PDA solutions with final concentration of 0.05 and 0.001 µg/mL were made appropriately. 9 mL of each mixture were poured

Table 3. Affinity to binding sites

The calculated affinity of substances to binding sites of sterol 14α-demethylase (CYP51) 5TZ1, *N*-myristoyltransferase (NMT) 1IYL, secreted aspartic proteinase (SAP2) 1EAG, UDP-*N*-acetylmuramoyl-*L*-alanine: *D*-glutamate ligase (MurD) 1UAG, topoisomerase II (Topo II) 1Q1D, and *L*-glutamine: *D*-fructose-6-phosphate amidotransferase (GlcN-6-P) 1XFF.

Substance				Kcal/Mol			
	Co	andida albica	ans		Escherichia coli	Sacchromyces cerevisiae	Escherichia coli
	5TZ1	1IYL	1EAG		1UAG	1Q1D	1XFF
Cyproconazole	-7.9	-7.8	-6.3		-6.9	-6.1	-5.5
Tacrolimus	-6.0	-6.7	-8.5		-9.8	-6.1	-5.4

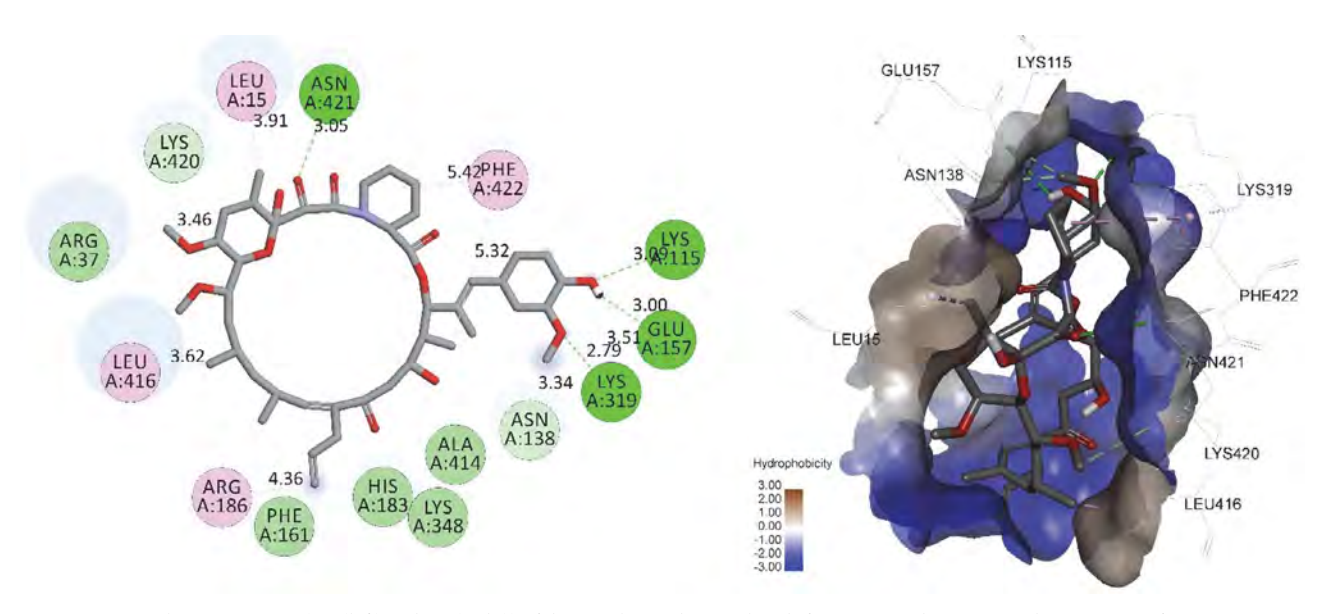


Figure 2. Visual representation (2D (left) and 3D (right)) of the tacrolimus showing bonds formation and position in the active site of UDP-N-acetylmuramoyl-L-alanine: D-glutamate ligase (MurD) 1UAG. Pale green – van der Waals interaction, green – classical conventional hydrogen bond, light green – non classical carbon hydrogen bond, pink – hydrophobic alkyl and π -alkyl bonds.

Table 4. The list of in silico calculated bonds formed between tacrolimus and UDP-N-acetylmuramoyl-L-alanine: D-glutamate ligase (MurD) active site

Name	Distance, Å	Category	Type
A:LYS115:NZ - :UNL1:O	3.09159	Hydrogen	Conventional
A:LYS319:NZ - :UNL1:O	2.78738	Hydrogen	Conventional
A:ASN421:ND2 - :UNL1:O	3.0506	Hydrogen	Conventional
:UNL1:H - A:GLU157:OE2	2.99646	Hydrogen	Conventional
:UNL1:C - A:LYS420:O	3.45662	Hydrogen	Carbon
:UNL1:C - A:ASN138:O	3.33652	Hydrogen	Carbon
:UNL1:C - A:GLU157:OE2	3.51104	Hydrogen	Carbon
:UNL1:C - A:LEU15	3.90689	Hydrophobic	Alkyl
:UNL1:C - A:LEU416	3.6241	Hydrophobic	Alkyl
:UNL1:C - A:ARG186	4.36225	Hydrophobic	Alkyl
A:PHE422 - :UNL1	5.42448	Hydrophobic	π-Alkyl
A:PHE422 - :UNL1:C	5.32047	Hydrophobic	π-Alkyl

into 6 cm diameter petri dishes. A central hole (diameter: 2.5 mm) was cut out and inoculated with 6.5 μ L spore suspension. Plates were incubated at 25°C (+/-1°C) for 6 d. Control plates containing only PDA and DMSO were prepared in the same way. Inhibitory effects (1%) were deter-

mined by analyzing growth zone diameters and calculated as described³⁶: I % = [(C-T)/(C-2.5 mm)])*100, where C (mm) represents the growth zone of control PDA, and T (mm) the average growth zone in presence of tacrolimus. All growth experiments were carried out in triplicate.

Means and standard deviations were calculated with software "Excel 2016" (Microsoft, USA). The strong antifungal agent was used as positive control.

Molecular docking. Macromolecular data of crystal structures were downloaded from the Protein Data Bank (PDB):³⁷ sterol 14α-demethylase (CYP51) 5TZ1, topoisomerase II (Topo II) 1Q1D, L-glutamine: D-fructose-6-phosphate amidotransferase (GlcN-6-P) 1XFF, secreted aspartic proteinase (SAP2) 1EAG, *N*-myristoyltransferase (NMT) 1IYL, and UDP-*N*-acetylmuramoyl-L-alanine: D-glutamate ligase (MurD) 1UAG; taken from *Candida albicans* (CYP51, NMT, SAP2), *Escherichia coli* (MurD, GlcN-6-P) and *Sacchromyces cerevisiae* (Topo II).³⁵ As reference cyproconazole (2-(4-chlorphenyl)-3-cyclopropyl-1-(1*H*-1,2,4-triazol-1-yl)butan-2-ol) was chosen.³³

Ligand preparation. Substances were drawn using MarvinSketch 6.3.0 and were saved in mol format. They were optimized by program Chem3D using molecular dynamics MM2 algorithm and saved as pdb-files. Molecular mechanics was used to produce more realistic geometry values for the majority of organic molecules owing to the fact of being highly parameterized. By using AutoDock-Tools-1.5.6 pdb-files were converted to PDBQT, and number of active torsions was set as default.

Protein preparation. Discovery Studio 4.0 was used to delete water molecules and ligand from crystal structures. The proteins were saved as pdb-files. In AutoDock-Tools-1.5.6 polar hydrogens were added and saved as PD-BQT. The Grid boxes were set as following: 5TZ1 center_x = 70.728, center y = 65.553, center z = 3.865, size x = 35, $size_y = 35$, $size_z = 35$; 1Q1D center_x = 28.5, center_y = 34.4, center_z = 32.7, size_x = 30, size_y = 30, size_z = 30; $1XFF center_x = 5$, $center_y = 28$, $center_z = 26$, $size_x = 26$ 30, size $_y = 30$, size $_z = 30$; 1UAG center $_x = 47$, center $_y = 47$ = -1.5, center_z = 15, size_x = 30, size_y = 30, size_z = 30, $1IYL center_x = 31$, $center_y = 74.5$, $center_z = 57$, $size_x$ = 30, size_y = 30, size_z = 30, 1EAG center_x = 42, cen $ter_y = 26$, $center_z = 11$, $size_x = 30$, $size_y = 30$, $size_z = 20$ 30. Vina was used to carry out docking. For visualization Discovery Studio Visualizer v17.2.0.16349 was used.

4. Conclusion

Considering a substantial role of FK506 in crop protection due to its distinct activity against phytopathogenic fungi, the availability in bulk quantities at affordable costs have to be taken into account.³⁸ For the development of a formulation for agricultural usage purity standards may be much less demanding than for immunosuppressant manufacturing. Furthermore, quantities necessary of tacrolimus may be reduced if advantages of synergistic effects in blends with conventional antifungal agrochemicals (e.g. triazoles) can be generated as it is already described for medical care of patients infected with *C. albicans*.⁸ Investi-

gations to further explore the potential benefits of FK506 in agriculture must be accompanied by studies covering emergence of resistance, toxicity and environmental friendliness of this compound.

5. Acknowledgements

Authors gratefully acknowledge German Federal Ministry of Education and Research (Grant: FKZ 03FH025IX4) for financial support of this work; Federal Research Centre for Cultivated Plants (Quedlinburg, Germany) for presenting the strain *Phytophthora infestans*; Department of Biology, Friedrich Alexander University, Erlangen, Nürnberg, Germany for the strain *Colletotricum higginsianum*.

6. References

- A. H. Fairlamb, N. A. Gow, K. R. Matthews, A. P. Waters. *Nat. Microbiol.* 2016, 1, 1–14. DOI:10.1038/nmicrobiol.2016.92
- A. Paugam, J. Dupouy-Camet, P. Blanche, J. P. Gangneux, C. Tourte-Schaefer, D. Sicard. Clin. Infect. Dis. 1994, 19, 975–976. DOI:10.1093/clinids/19.5.975-a
- M. L. Cameron, W. A. Schell, S. Bruch, J. Bartlett, H. A. Waskin, J. R. Perfect. *Antimicrob. Agents Chemother.* 1993, 37, 2449–2453. DOI:10.1128/AAC.37.11.2449
- 4. P. R. Juvvadi, F. Lamoth, W. J. Steinbach. *Fungal Biol. Rev.* **2014**, *28* (2-3), 56–69. **DOI:**10.1016/j.fbr.2014.02.004
- H. Tanaka, A. Kuroda, H. Marusawa, H. Hatanaka, T. Kino,
 T. Goto, M. Hashimoto, T. Taga. *J. Am. Chem. Soc.* 1987, 109 (16), 5031–5033. DOI:10.1021/ja00250a050
- TOXNET U.S. National Library of Medicine TOXICOL-OGY DATA NETWORK https://toxnet.nlm.nih.gov/cgi-bin/ sis/search2/r?dbs+hsdb:@term+@rn+@rel+104987-11-3 (accessed: August 17, 2018).
- R. J. Sr. Lewis (Ed.): Sax's Dangerous Properties of Industrial Materials. 11th Edition. Wiley-Interscience, Wiley & Sons, Inc. Hoboken, NJ, 2004, p. 3344.
- 8. S. Maesaki, P. Marichal, M. A. Hossain, D. Sanglard, H. ven Bossche, S. J. Kohno. *Antimicrob. Chemother.* **1998**, 42 (6), 747–753. **DOI:**10.1093/jac/42.6.747
- P. Uppuluri, J. Nett, J. Heitman, D. Andes. *Antimicrob. Agents Chemother.* 2008, 52 (3), 1127–1132.
 DOI:10.1128/AAC.01397-07
- J. Schumacher, I. F. de Larrinoa, B. Tudzynski. *Eukaryot. Cell* 2008, 7 (4), 584-601. DOI:10.1128/EC.00426-07
- 11. J. H. Choi, Y. Kim, Y. H. Lee. *J. Microbiol. Biotechnol.* **2009**, 19 (1), 11-6.
- W. J. Steinbach, W. A. Schell, J. R. Blankenship, C. Onyewu, J. Heitman, J. R. Perfect. *Antimicrob. Agents Chemother.* 2004, 48 (5), 1664–1669. DOI:10.1128/AAC.48.5.1664-1669.2004
- F. Lamoth, B. D. Alexer, P. R. Juvvadi, W. J. Steinbach. *J. Anti*microb. Chemother. 2014, 70 (5), 1408–1411.
 DOI:10.1093/jac/dku549

- L. Gao, Y. Sun. Antimicrob. Agents Chemother. 2015, 59 (11), 7097–7099. DOI:10.1128/AAC.01510-15
- H. Nakagawa, T. Etoh, Y. Yokota, F. Ikeda, K. Hatano, N. Teratani, K. Shimomura. *Clin. Drug Invest.* 1996, 12 (5), 244–250.
 DOI:10.2165/00044011-199612050-00003
- Y. L. Chen, V. N. Lehman, A. F. Averette, J. R. Perfect, J. Heitman. *PLoS One* 2013, 8 (3), e57672.
 - **DOI:**10.1371/journal.pone.0057672
- C. Onyewu, J. R. Blankenship, M. Del Poeta, J. Heitman. *Antimicrob. Agents Chemother.* 2003, 47 (3), 956.
 DOI:10.1128/AAC.47.3.956-964.2003
- S. Sun, Y. Li, Q. Guo, C. Shi, J. Yu, L. Ma. Antimicrob Agents Chemother. 2008, 52 (2), 409–417.
 DOI:10.1128/AAC.01070-07
- H. Li, Z. Chen, C. Zhang, Y. Gao, X. Zhang, S. Sun. J. Med. Microbiol. 2015, 64 (1), 44–52.
 DOI:10.1099/jmm.0.081760-0
- M. Del Poeta, M. C. Cruz, M. E. Cardenas, J. R. Perfect, J. Heitman. *Antimicrob. Agents Chemother.* 2000, 44 (3), 739–746. DOI:10.1128/AAC.44.3.739-746.2000
- A. Odom, M. Del Poeta, J. Perfect, J. Heitman. Antimicrob. Agents Chemother. 1997, 41 (1), 156–161.
 DOI:10.1128/AAC.41.1.156
- T. Sugita, M. Tajima, T. Ito, M. Saito, R. Tsuboi, A. Nishikawa.
 J. Clin. Microbiol. 2005, 43 (6), 2824–2829.
 DOI:10.1128/JCM.43.6.2824-2829.2005
- L. Brizuela, G. Chrebet, K. A. Bostian, S. A. Parent, Mol. Cell. Biol. 1991, 11 (9), 4616–4626. DOI:10.1128/MCB.11.9.4616
- L. P. Borba-Santos, L. F. Reis de Sá, J. A. Ramos, A. M. Rodrigues, Z. P. de Camargo, S. Rozental, A. Ferreira-Pereira. Front. Microbiol. 2017, 8, 1–9. DOI:10.3389/fmicb.2017.01759
- T. F. Kubiça, L. B. Denardi, M. I. Azevedo, V. Oliveira, L. C. Severo, J. M. Santurio, S. H. Alves. *Brazilian J. Infect. Dis.* 2016, 20 (6), 539–545. DOI:10.1016/j.bjid.2016.08.008

- H. Ozawa, K. Okabayashi, R. Kano, S. Watanabe, A. Hasegawa.
 J. Vet. Med. Sci. 2005, 67, 629–630. DOI:10.1292/jvms.67.629
- J. R. Blankenship, J. Heitman. *Infect. Immun.* 2005, 73, 5767-5774. DOI:10.1128/IAI.73.9.5767-5774.2005
- L. B. Denardi, D. A. N. Mario, É. S. Loreto, J. M. Santurio, S. H. Alves. *Brazilian J. Microbiol.* 2015, 46 (1), 125–129.
 DOI:10.1590/S1517-838246120120442
- 29. R. Kaur, I. Castan o B. P. Cormack. *Antimicrob. Agents Chemother.* **2004**, 48, 1600–1613.
 - **DOI:**10.1128/AAC.48.5.1600-1613.2004

 O. S. K. Katiyar, A. Alastruey-Izquierdo, K. R.
- S. K. Katiyar, A. Alastruey-Izquierdo, K. R. Healey, M. E. Johnson, D. S. Perlin, T. D. Edlind. *Antimicrob. Agents Chemother.* 2012, 56, 6304–6309. DOI:10.1128/AAC.00813-12
- 31. M. Tropschug, I. B. Barthelmess, W. Neupert. *Nature* **1989**, 342, 953–955. **DOI:**10.1038/342953a0
- 32. Kirkl, T. N. J. Fierer. Antimicrob. Agents Chemother. 1983, 24, 921–924. DOI:10.1128/AAC.24.6.921
- 33. PPDB: Pesticide Properties DataBase. Cyproconazol. http://sitem.herts.ac.uk/aeru/ppdb/en/Reports/198.htm (accessed: August 21, 2019).
- 34. J. Alvarez, B. Shoichet, PART V: Docking Strategies and Algorithms, Virtual Screening in Drug Discovery. CRC Press, Taylor & Francis: Boca Raton, FL, 2005, pp. 301–348.
 DOI:10.1201/9781420028775
- A.Siwek, P.Staczek, A. Strzelczyk, J. Stefanska. Lett. Drug. Design. Discov. 2013, 10, 2–10. DOI:10.2174/157018013804142393
- R. Tang, L. Jin, C. Mou, J. Yin, S. Bai, D. Hu, J. Wu, S. Yang, B. Song. *Chem. Cent. J.* 2013, 7, 1–8.
 DOI:10.1186/1752-153X-7-30
- 37. Worldwide Protein Data Bank. http://www.pdb.org (accessed: April 12, 2018).
- 38. C. Barreiro, M. Martínez-Castro. *Appl. Microbiol. Biotechnol.* **2014**, 98 (2): 497–507. **DOI**:10.1007/s00253-013-5362-3

Povzetek

Takrolimus (FK506) je imunosupresivno zdravilo, ki se pogosto uporablja za preprečevanje zavrnitve organov pri bolnikih s presaditvijo. Ima močan vpliv na celični stresni odziv z vmešavanjem v signalno pot kalmodulin-kalcinevrin. V tem kontekstu je FK506 postal tudi dragoceno protiglivično zdravilo v zdravstveni negi. Tu je *in vitro* prikazano, da ima takrolimus močan učinek zaviranja rasti proti 11 glivam in 3 oomicetom kmetijskega pomena. Pomen te ugotovitve je obravnavan v zvezi z zaščito pridelkov.



Except when otherwise noted, articles in this journal are published under the terms and conditions of the Creative Commons Attribution 4.0 International License

@creative

Scientific paper

A Simple and Highly Sensitive Turn-on Schiff Base Type Naked-eye Fluorescent Sensor for Aluminum Ion in Living Cells

Sedat Keskin and Mevlut Bayrakci*

Karamanoglu Mehmetbey University, Faculty of Engineering, Department of Bioengineering 70200, Karaman/TURKEY

> * Corresponding author: E-mail: mevlutbayrakci@gmail.com Tel.: +90 338 2262200 fax: +90 338 2262214

> > Received: 09-28-2018

Abstract

Six different Schiff bases to be used as turn-on fluorescent probes based on photoinduced electron transfer (PET) mechanism for the recognition of aluminum ions were successfully synthesized and characterized. The binding abilities of synthesized compounds with different metal cations were investigated by absorption and emission spectra. From the spectrophotometric experiments, it were seen that compound **SK-1** displayed an excellent fluorescence response towards targeted aluminum ions probably due to its suitable chelating structure. Furthermore, such compound **SK-1** also showed high sensitivity and selectivity response towards aluminum ions over other competing ions. In addition, the potential biological applications of **SK-1** to detect aluminum ions in living cells were also investigated and results showed that fluorescence sensor **SK-1** could be a promising probe for determining and/or monitoring aluminum ions in both biological and/or chemical samples.

Keywords: Schiff Base, fluorescent probe, cell imaging, aluminum, PET.

1. Introduction

Aluminum is one of the most abundant metal elements in the Earth's crust and has an important place in our live. 1 Due to different reasons such as both ecological system and human activities, high quantities of aluminum are found in the environment.² The presence of excess amount of aluminum in nature life affects the living beings. Consequently, some natural products containing large amount of aluminum in food chain are slowly consumed by human beings and this consumption causes many toxic effects towards human health and this toxicity leads to different diseases such as cancer, neurotoxicity, dialysis disease, Alzheimer's and Parkinson's diseases.³⁻⁶ With respect to the World Health Organization, desired concentration of aluminum in drinking water must be limited to 7.4 µM.7 Therefore, it is important topic to design and develop effective analytical methods or instruments for detection of aluminum ions in environmental and/or biological systems. Although many different and sophisticated analytical techniques including inductively coupled plasma emission (ICP-OES) or mass spectrometry (ICP-MS), and atomic absorption spectrometry have been used extensively for the detection of aluminum ions, 8,9 most of these techniques have some disadvantages such as time consuming, qualified personal and high cost. 10 But among them, fluorescence spectroscopy is most popular analytical instrument for the detection of metal ions and it is preferred intensively by scientists in analytical applications owing to its easy operation, comparatively low cost, and high sensitivity, etc.11 Thus, many different fluorescence based chemosensors specific for metal ions have been designed and developed. Compared to these metal ions, just a few fluorescent probes have been reported for detection of trace amount of aluminum ions. Some limitations such as poor coordination ability and lack of spectroscopic characteristics have always been problematic for the detection of aluminum ions.12 In addition to these limitations, both complicated synthesis and solubility properties of new fluorescent probes are also other restrictions in the point of design of aluminum sensors.¹³ Therefore, it is necessary and important to design and synthesis of aluminum sensors that can be easily prepared and dissolved. Many sensitive and selective fluorescent sensors

for metal cations have been reported based on fluorescence resonance energy transfer (FRET),14 chelation- enhanced fluorescence (CHEF), 15 internal charge transfer (ICT), ¹⁶ photoinduced electron transfer (PET), ¹⁷ and excimer/exciplex formation mechanisms. 18 However, although photoinduced electron transfer (PET)-based fluorogenic sensors have many advantages, 19 their synthesis and application are not common in the literature. Although there are very interesting literature reports about photoinduced electron transfer (PET)-based fluorogenic sensors for different analytes, ^{20–22} synthesis of Schiff base type probes are very inspirational owing to their easily preparation, faster response and high selectivity towards specific analytes of interest. Schiff bases are the most popular class of synthetic compounds in organic, medicinal and pharmaceutical chemistry due to their unique biochemical properties such as antitumor, anti-HIV, antibacterial, antioxidant, anti-inflammatory, antifungal, pesticidal, anthelmintic and antihypertensive, activitie. 23-25 Although, there are appropriate literature reports showing their biological applications of Schiff base compounds, recently, limited number of literature results about using of Schiff base derivatives as fluorescent probe for the detection of metal ions in living cell have been existed.^{26–30} In the light of these literature, here, we presented the design, synthesis and biological applications of a series of Schiff base based fluorescent sensors containing ortho, meta and para hydroxy units which could detect aluminum ions by the 'naked eye'.

2. Experimental

2. 1. General

2,3-dihydroxybenzaldehyde, 3,4-dihydroxybenzaldehyde, *ortho*, *meta* and *para* aminophenol and all metal

salts were of analytical grade and purchased from Sigma-Aldrich or Merck and was further used without any purification. 1H NMR spectra was recorded on Agilent Premium Compact spectrometer operating at 600 MHz. Chemical shifts were reported as δ values (ppm). Peak multiplicities were expressed as follows: s, singlet; bs, broad singlet; d, doublet; t, triplet and m, multiplet. Bruker Vertex FT-IR spectrometer (ATR) was used for FT-IR spectra. UV-vis absorbance spectra were collected by a Shimadzu UV-1800 and the fluorescence measurements were obtained by Hitachi F-7100.

2. 2. General Procedure for the Synthesis of Schiff Base Probes

To a stirred solution of corresponding *ortho*, *meta* or *para* aminophenol compounds (1.5 mmol) in 20 mL absolute ethanol was added 1.5 mmol of 2,3-dihydroxybenzaldehyde (for **SK-1**, **SK-2** and **SK-3**, respectively) or 1.5 mmol of 3,4-dihydroxybenzaldehyde (for **MK-2**, **MK-3** and **MK-4**, respectively); the reaction mixture was stirred under reflux for 18 h. After completion of the reaction, excess amount of solvent was removed under reduced pressure and the solid residue was washed with 1 N HCl, brine and excess amount of water. The crude product was crystallized from CH₂Cl₂-C₂H₅OH (1:1) solvent system (Scheme 1).

SK-1: Red solid with 68% yields, FT-IR (ATR cm⁻¹): 1616 (C=N stretching). ¹H NMR (600 MHz DMSO): δ 14.21 (bs, 1H, OH) 9.88 (bs, 1H, OH), 9.02 (bs, 1H, OH), 8.91 (s, 1H, CH=N), 7.38 (d, J= 8.3 Hz, 1H, Ar-H), 7.10 (m, 1H, Ar-H), 7.02 (m, 1H, Ar-H), 6.95 (m, 1H, Ar-H), 6.87 (m, 1H, Ar-H), 6.77 (m, 1H, Ar-H), 6.69 (m, 1H, Ar-H). Anal. calcd. For C₁₃H₁₁O₃N: C, 68.11; H, 4.84; N, 6.11. Found: C, 68.09; H, 4.90; N, 6.19%.

Scheme 1. The synthetic route of Schiff base compounds (SK-1, SK-2, SK-3, MK-2, MK-3, and MK-4)

SK-2: Dark red solid with 70% yields, FT-IR (ATR cm⁻¹): 1623 (C=N stretching). 1 H NMR (600 MHz DMSO): δ 14.18 (bs, 1H, OH) 9.87 (bs, 1H, OH), 9.03 (bs, 1H, OH), 8.89 (s, 1H, CH=N), 7.35 (d, J= 8.4 Hz, 1H, Ar-H), 7.13 (m, 1H, Ar-H), 7.03 (m, 1H, Ar-H), 6.92 (m, 1H, Ar-H), 6.85 (m, 1H, Ar-H), 6.74 (m, 1H, Ar-H), 6.65 (s, 1H, Ar-H). Anal. calcd. For C₁₃H₁₁O₃N: C, 68.11; H, 4.84; N, 6.11. Found: C, 68.03; H, 4.80; N, 6.07%.

SK-3: Dark red solid with 70% yields, FT-IR (ATR cm⁻¹): 1621 (C=N stretching). 1 H NMR (600 MHz DMSO): δ 14.17 (bs, 1H, OH) 9.88 (bs, 1H, OH), 9.06 (bs, 1H, OH), 8.91 (s, 1H, CH=N), 7.34 (d, J= 8.4 Hz, 1H, Ar-H), 7.17–7.11 (m, 3H, Ar-H), 6.83 (m, 1H, Ar-H), 6.34 (m, 1H, Ar-H), 6.21 (m, 1H, Ar-H). Anal. calcd. For $C_{13}H_{11}O_3N$: C, 68.11; H, 4.84; N, 6.11. Found: C, 68.03; H, 4.88; N, 6.15%.

MK-2: Red solid with 71% yields, FT-IR (ATR cm⁻¹): 1635 (C=N stretching). ¹H NMR (600 MHz DMSO): δ 9.84 (bs, 1H, OH) 9.48 (bs, 1H, OH), 9.03 (bs, 1H, OH), 8.87 (s, 1H, CH=N), 7.27 (m, 2H, Ar-H), 7.18 (m, 2H, Ar-H), 7.10–7.04 (m, 3H, Ar-H). Anal. calcd. For C₁₃H₁₁O₃N: C, 68.11; H, 4.84; N, 6.11. Found: C, 68.09; H, 4.90; N, 6.19%.

MK-3: Red solid with 65% yields, FT-IR (ATR cm⁻¹): 1634 (C=N stretching). ¹H NMR (600 MHz DMSO): δ 9.81 (bs, 1H, OH) 9.52 (bs, 1H, OH), 9.11 (bs, 1H, OH), 8.91 (s, 1H, CH=N), 7.33 (m, 2H, Ar-H), 7.25 (m, 1H, Ar-H), 7.09 (m, 1H, Ar-H), 6.88 (m, 2H, Ar-H), 6.57 (m, 1H, Ar-H). Anal. calcd. For $C_{13}H_{11}O_3N$: C, 68.11; H, 4.84; N, 6.11. Found: C, 68.03; H, 4.80; N, 6.07%.

MK-4: Dark red solid with 58% yields, FT-IR (ATR cm⁻¹): 1620 (C=N stretching). ¹H NMR (600 MHz DMSO): δ

9.81 (bs, 1H, OH) 9.47 (bs, 1H, OH), 9.16 (bs, 1H, OH), 8.90 (s, 1H, CH=N), 7.34–7.29 (m, 2H, Ar-H), 7.17 (m, 2H, Ar-H), 7.03 (m, 3H, Ar-H). Anal. calcd. For $C_{13}H_{11}O_3N$: C, 68.11; H, 4.84; N, 6.11. Found: C, 68.03; H, 4.88; N, 6.15%.

2. 3. Uv-Vis and Fluorescence Studies

The stock solutions of SK-1, SK-2, SK-3, MK-2, MK-3 and MK-4 (1 mM), the guest nitrate salts of metal cations (Li+, Na+, Ag+, Ca2+, Ba2+, Co2+, Cs+, Cu2+, Mg2+, Hg²⁺, Mn²⁺, Pb²⁺, Ni²⁺, Sr²⁺, Zn²⁺ and Al³⁺) (1 mM) in DMF were prepared. In absorption and emission experiments, the volume of studied solutions was adjusted as 2.0 mL. Titration experiments were performed by addition of corresponding amount of metal cation solutions to a DMF solution of targeted fluorescent probe (SK-1). The absorption spectra of SK-1, SK-2, SK-3, MK-2, MK-3 and MK-4 in the presence and absence of metal cations were recorded in the range of 200-600 nm. All emission spectra were obtained at room temperature under the excitation of 400–430 nm. The solutions were scanned (1200 nm/min) with 400 watt of PMT voltage in a spectrofluorometer with the range of 400-750 nm. The widths of the slit for the both excitation and emission were adjusted at 5 nm. The best fluorescence intensity at 530 nm was determined under the excitation at the wavelength of 430 nm.

2. 4. Biological Applications

The living MCF7 cells were provided by ATCC (American Type Culture Collection, Rockville, MD, USA). MCF7 cells were incubated with 10 μ M of Al³+ ions in the culture medium at 37 °C for 1 h and washed with phos-

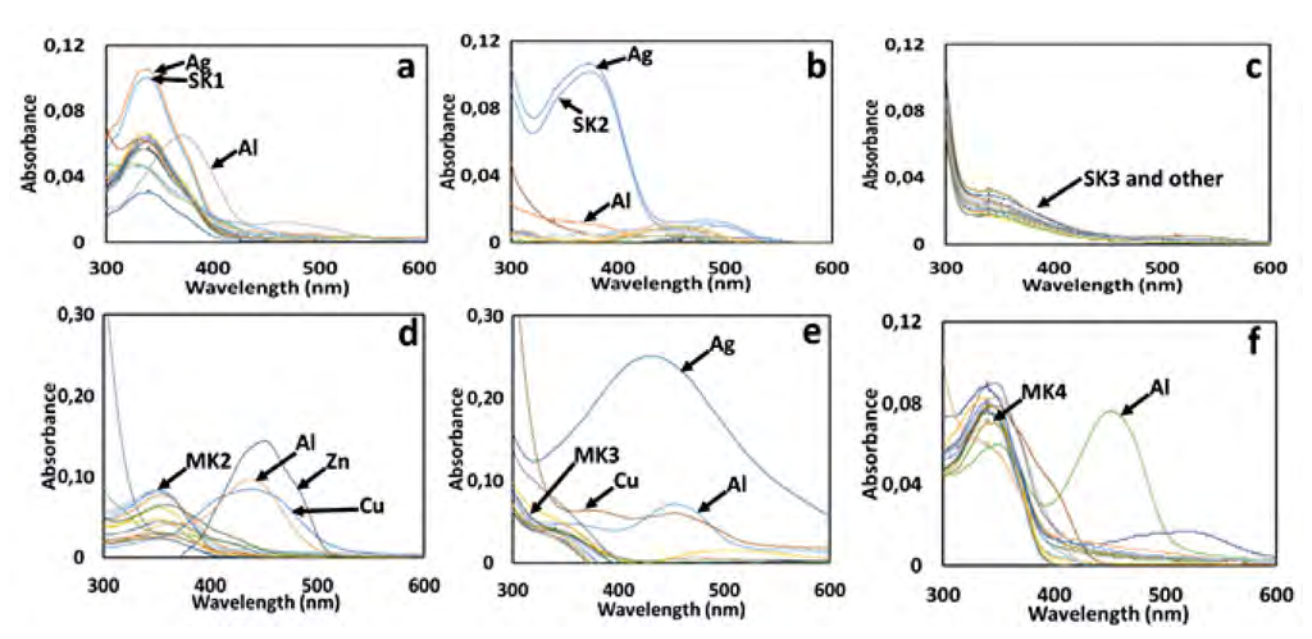


Fig. 1. UV-vis absorption spectra of $(1\mu M)$; (a) SK-1, (b) SK-2, (c) SK-3, (d) MK-2, (e) MK-3, and (f) MK-4 in the presence of several metal ions such as Li⁺, Na⁺, Ag⁺, Ca²⁺, Ba²⁺, Co²⁺, Cs⁺, Cu²⁺, Mg²⁺, Mg²⁺, Mn²⁺, Pb²⁺, Ni²⁺, Sr²⁺, Zn²⁺ and Al³⁺ (10 eq. for each metal ion).

phate buffered saline (PBS) followed by the addition of 10 μ M of **SK-1**. Bright field and fluorescent images were taken from Leica DM3000 fluorescence microscopy.

3. Results and Discussion

3. 1. UV-vis Absorption Studies

The absorption spectrum of the Schiff bases SK-1, SK-2, SK-3, MK-2, MK-3 and MK-4 was investigated by the absence and/or presence of 10 equiv. of metal cations such as Li⁺, Na⁺, Ag⁺, Ca²⁺, Ba²⁺, Co²⁺, Cs⁺, Cu²⁺, Mg²⁺, Hg²⁺, Mn²⁺, Pb²⁺, Ni²⁺, Sr²⁺, Zn²⁺ and Al³⁺. As seen in Fig. 1, the absorption spectrum of all Schiff bases, exhibited a broad absorption band attributable to π - π * transition of the imine moiety at around 342 nm. The absorption band positions generally remained unchanged over the various metal ions except Al³⁺ ions. After the addition of Al³⁺, the appreciable bathochromic or hypochromic changes at around 342 nm for SK-1, SK-2, MK-2, MK-3 and MK-4 was observed owing to the imine nitrogen (CH=N) was involved in coordination with Al3+ ion. However, considerable changes in the absorption spectra of the SK-3 was not observed over the various metal ions (Fig. 1c). Furthermore, new absorption bands at around 470 nm (for SK-1, and SK-2) and 450 nm (for MK-2, MK-3 and MK-4) were seen probably due to the complexation capabilities of these molecules with Al3+ ions. Since absorption spectroscopy is a complementary part of emission spectroscopy, fluorescence emission studies were also applied for the getting more information about the spectrophotometric results.

3. 2. Fluorescence Emission Analysis

High selectivity is necessary to define the excellent chemosensor. Therefore, to evidence the usability of the synthesized Schiff bases as a selective sensor, the fluorescence behavior of Schiff bases SK-1, SK-2, SK-3, MK-2, MK-3 and MK-4 was investigated by Hitachi F-7100 Spectrofluorometer upon addition of selected metal ions such as Li⁺, Na⁺, Ag⁺, Ca²⁺, Ba²⁺, Co²⁺, Cs⁺, Cu²⁺, Mg²⁺, Hg²⁺, Mn²⁺, Pb²⁺, Ni²⁺, Sr²⁺, Zn²⁺ and Al³⁺. The reported Schiff base probes (1 µM) showed a weak fluorescence emission spectrum at around 530 nm (for SK-1), 480 nm (for SK-2), 508 nm (for SK-3), 518 nm (for MK-2), 430 nm (for MK-3) and 518 nm (for MK-4) with an excitation of 430 (for SK-1), 400 nm (for SK-2 and SK-3,), 380 nm (for MK-3,) and 430 nm (for MK-2 and MK-4). Other metal ions (10 μM) such as Li⁺, Na⁺, Ag⁺, Ca²⁺, Ba²⁺, Co²⁺, Cs⁺, Cu²⁺, Mg²⁺, Hg²⁺, Mn²⁺, Pb²⁺, Ni²⁺, Sr²⁺, and Zn²⁺ were added to the solution of Schiff base probes, considerable decrease or increase in fluorescent intensity of probes were not observed in Fig. 2. Whereas, upon addition of Al3+ (10 μM) remarkable fluorescence increase accompanied by a red shift of 24 nm from 530 nm to 554 nm was only noticed for the Schiff base probe SK-1 (Fig. 2a). Schiff base probe SK-1 exhibited a more than 37-fold fluorescent enhancement alone in the presence of Al3+ ions. This increase in fluorescence intensity is such that the Schiff base probe SK-1 shows "OFF-ON" mode of high sensitivity for Al³⁺ ions. Furthermore, the Schiff base probe **SK-1** indicated considerable color change from colorless to brilliant turquoise fluorescence in the presence of Al³⁺ ions under UV light, and this color change was also easily detected by

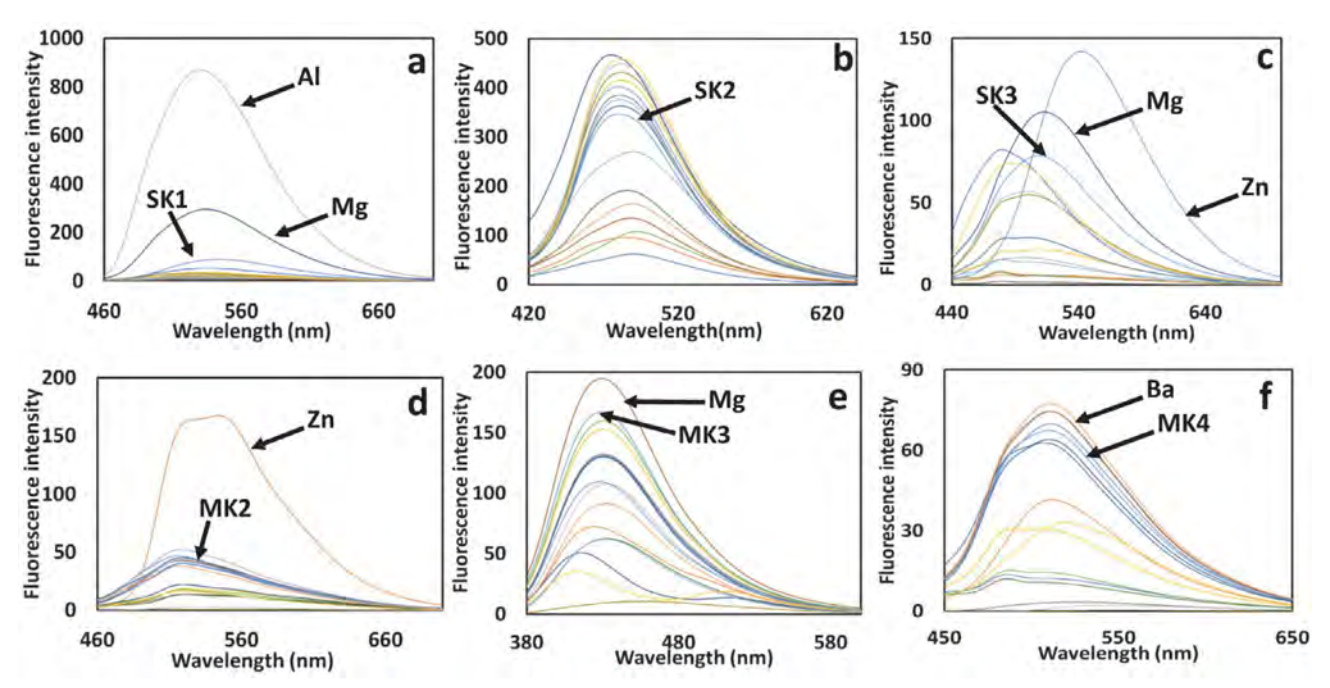


Fig. 2. Fluorescent emission spectra of (1µM); (a) SK-1, (b) SK-2, (c) SK-3, (d) MK-2, (e) MK-3, and (f) MK-4 in the presence of several metal ions such as Li⁺, Na⁺, Ag⁺, Ca²⁺, Ba²⁺, Co²⁺, Cs⁺, Cu²⁺, Mg²⁺, Hg²⁺, Mn²⁺, Pb²⁺, Ni²⁺, Sr²⁺, Zn²⁺ and Al³⁺ (10 eq. for each metal ion).

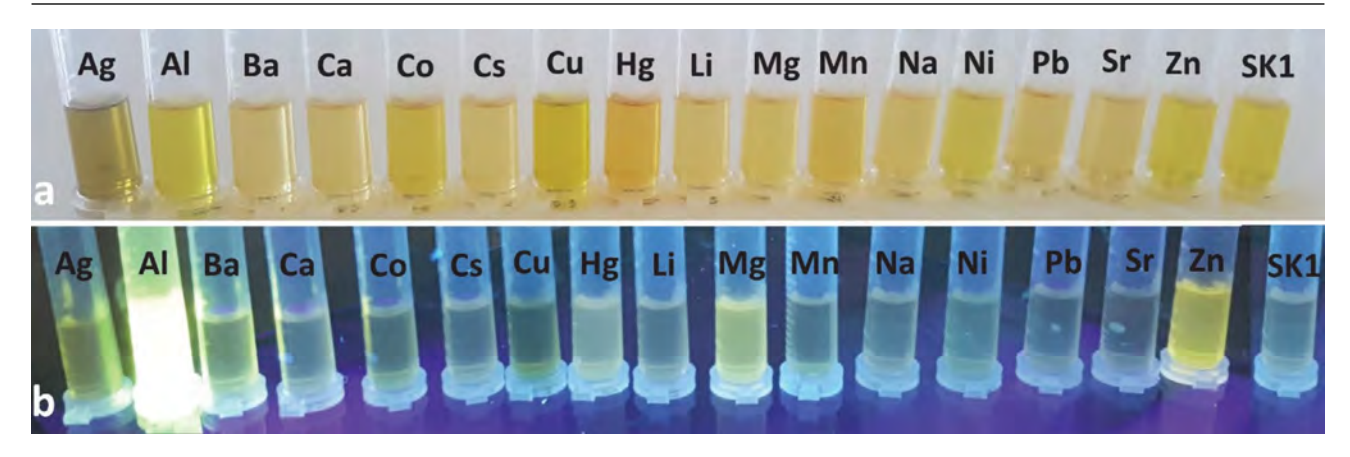


Fig. 3. Images showing the corresponding (a) visible color and (b) fluorescence color changes of SK-1 with and without metal cations (10 equiv. of Li⁺, Na⁺, Ag⁺, Ca²⁺, Ba²⁺, Co²⁺, Cs⁺, Cu²⁺, Mg²⁺, Hg²⁺, Mn²⁺, Pb²⁺, Ni²⁺, Sr²⁺, Zn²⁺ and Al³⁺) under day light and UV light.

the naked eye (Fig. 3). As a results, this Schiff base probe **SK-1** can be evaluated to determine Al³⁺ ions in solution visually.

Photoinduced electron transfer (PET) mechanism includes the deactivation of the excited-state of fluorescent compounds by adding an electron to its frontier orbital. This electron addition to one of frontier orbital of excited-state causes a non-emissive state for fluorophore structures. For instance, the presence of one or more functional groups having free pair of electrons attached to the fluorescent molecule may quench its fluorescent intensity intramolecularly due to photoinduced electron transfer (PET) mechanism. However, a possible interaction of these electron donor groups with electron acceptor metal ions reduces efficient electron donor capabilities of these groups. thereby disconnecting the photoinduced electron transfer (PET) mechanism and increase the fluorescence output via chelation-enhanced fluorescence (CHEF). 31,32 Herein, the emission intensity of SK-1 was very low because of the quenching by the lone pair electrons of imine group through a PET mechanism. However, with increasing of Al^{3+} (0–10 equiv.), the fluorescence emission intensity of SK-1 (1.0 μ M) at 530 nm increased gradually (Fig. 4b). The complexation of the imine group (-C=N) with Al3+ ion given rise to the PET mechanism was suppressed, the fluorescence of the complex structure was restored. 33,34

3. 3. Titration and Competition Studies

The binding properties of SK-1 with Al³⁺ ions were studied by both UV-vis and fluorescent titration experiments (Fig. 4a and 4b). Firstly, we explored the UV-vis titration spectra of SK-1 with increasing concentrations of Al3+ in DMF. As shown in Fig. 4a, upon addition of increasing amounts of Al3+ (0.0 to 2.0 equiv.), absorption bands of SK-1 appeared at around 360 nm was gradually decreased with increasing amount of Al3+, while the intensities of absorption SK-1 at around 434 nm increased. Furthermore, the absorbance at around 434 nm reached maximum in the presence of 1.0 equiv. of Al³⁺ and showed nearly no change with further addition of metal ion. The titration configuration of SK-1 with Al³⁺ in Fig. 4a indicated 1 equiv. of Al³⁺ reacting with same equiv. of SK-1 could quickly reached an equilibrium, showing complex formation between SK-1 and Al³⁺ with 1:1 stoichiometry. To further examine the sensing properties of SK-1, sensitivity of SK-1 as a probe toward Al³⁺ ions was investigated by the fluorescence titration experiments by increasing concentration of Al³⁺ ions (0-10 equiv.) at 530 nm (Fig. 4b). Upon excitation at 430 nm, SK-1 in the absence of any Al3+ showed practically no emission signal between the range of 460 and 700 nm which was probably due to PET process.35 However, a clear enhancement in fluorescence in-

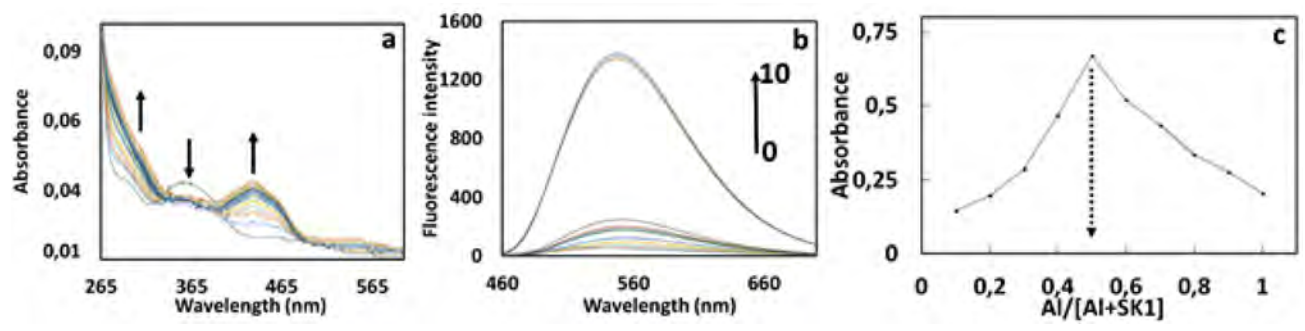


Fig. 4. (a) UV-Vis, (b) fluorescence titration spectra of compound SK-1 (1 μ M) respectively, upon addition of Al³+ (from 0 to 10 equiv.) at room temperature ($\lambda_{ex} = 430 \text{ nm}$; $\lambda_{em} = 530 \text{ nm}$) and (c) Job's plot for the determination of stoichiometry of SK-1-Al³+ system.

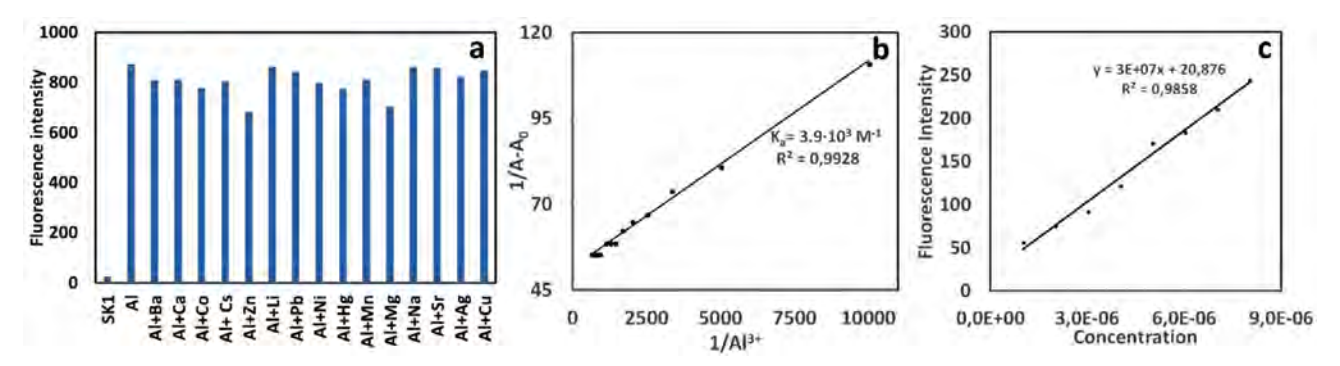


Fig. 5. Fluorescent selectivity of SK-1 (1 μ M) at 530 nm upon addition of various metal ions (10 μ M) Li⁺, Na⁺, Ag⁺, Ca²⁺, Ba²⁺, Co²⁺, Cs⁺, Cu²⁺, Mg²⁺, Hg²⁺, Mn²⁺, Pb²⁺, Ni²⁺, Sr²⁺, and Zn²⁺, λ_{ex} = 430 nm. (b) Calculation of binding constant between SK-1 and Al³⁺. A₀ is the absorbance of free SK-1 solution (1 μ M); A is the absorbance of compound SK-1 solution (1 μ M) upon addition of different amounts of Al³, (c) Calculation of detection limit of SK-1 for Al³⁺ with excitation at 430 nm and emission at 530 nm by addition of different amounts of Al³⁺ to SK-1 solution (1 μ M)

tensity of SK-1 was observed gradually at around 530 nm with increasing concentrations of Al³⁺ as shown in Fig 4b. This increase in fluorescent intensity was probably due to the chelation-enhanced fluorescence (CHEF) effect that inhibiting the PET process by complexation of SK-1 with Al3+.36 Furthermore, the detection limit of Al3+ was estimated based on the fluorescence titration profile (Fig. 5c). The detection limit of SK-1 in recognizing Al³⁺ was found to be $4.85 \cdot 10^{-7}$ M which was lower than some reported literature results regarding Al3+ selective chemosensors.^{37,38} This result was shown that this sensor could be used for both detection and monitoring of sub-micromolar concentration of aluminum ions in biological and environmental systems. To verify the practical application of **SK-1** as an Al³⁺ selective and sensitive fluorescent sensor. competition experiments were also performed by adding of Al3+ into SK-1 solution mixed with other coexisting metal ions such as Li⁺, Na⁺, Ag⁺, Ca²⁺, Ba²⁺, Co²⁺, Cs⁺, Cu²⁺, Mg²⁺, Hg²⁺, Mn²⁺, Pb²⁺, Ni²⁺, Sr²⁺, and Zn²⁺. As depicted in Fig. 5a, relatively low interference was seen for the detection of Al³+ in the presence of other competing metal ions. Although, the slightly decreasing in emission intensity of **SK-1** at around 530 nm was observed in the presence of Zn²+, and Mg²+, fluorescent response was relatively detectable. However, upon addition of other competing metal ions under same conditions, it was seen that the fluorescence emission intensity at around 530 nm did not change considerably and **SK-1** still have an efficient "turn-on" rate for the detection of Al³+. Consequently, it was concluded that **SK-1** could be a promising selective and sensitive fluorescent sensor for the detection of Al³+ in the presence of competing metal ions.

3. 4. Binding Studies

To determine the binding stoichiometry of **SK-1** with Al³⁺, the method of continuous variations known as Job's plot was used.³⁹ In this method, each experiment per-

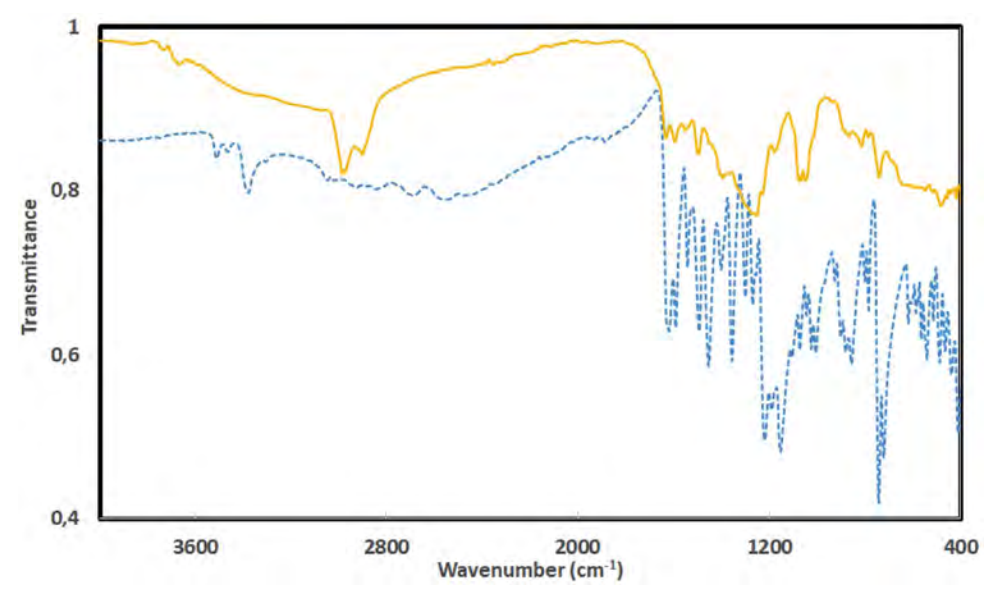


Fig. 6. The FT-IR (ATR) spectra of SK-1 with (1.0 equiv of Al³⁺) and without Al³⁺.

formed with different concentrations of SK-1 and Al3+ with maintaining the total concentration at 10 µM. The plot obtained by measuring the fluorescence intensity at 530 nm for nine experiments with molar fraction of SK-1 (0.1 to 0.9). In this experiment, the maximum absorbance value was observed when the molar fraction was 0.5 (Fig. 4c) and it was consistent well with the UV-vis titration spectra (Fig. 4a). This data showed that 1 mole of **SK-1** and Al³⁺ participated in the complex formation and binding mode was determined as 1:1 stoichiometry. Furthermore, the binding constant of the probe **SK-1** with Al³⁺ were calculated by the Benesi-Hildebrand method. 40 From curve fitting of absorbance values of probe SK-1 against the reciprocal of the Al³⁺ concentration, this plot yielded a linear fit as seen in Fig. 5b. The value of the binding constant was calculated as $3.9 \cdot 10^3 \,\mathrm{M}^{-1}$ which was within the range of those $(10^3 - 10^9)$ M⁻¹) previously reported Al³⁺ sensors.⁴¹ In addition, the linear plot also proved the 1:1 complexation behavior of **SK-1** to Al³⁺. Because, if a 1:1 metal-probe complex is formed between receptor and metal ions, Benesi-Hildebrand plot should be linear. 42 In related to stoichiometry, the binding site participated in complexation was clarified by FT-IR (ATR) and ¹H NMR experiments along with stoichiometry confirmation as presented in Fig. 6 and 7.

The IR spectra of free SK-1 and SK-1-Al³⁺ complex structure showed that the characteristics frequencies of SK-1 with 1.0 equiv. of Al3+ exhibited significant changes as compared with those of free the SK-1 (Fig. 6). The IR spectra of the free SK-1 showed the absence of bands at around 1735 and 3300 cm⁻¹ attributable to the carbonyl ν (C=O) and ν (NH₂) stretching vibrations and a clear strong new band at around 1616 cm⁻¹ due to azomethine ν(HC=N) linkage. 43-45 All these existing and disappearing signals in IR indicated that amino and aldehyde groups in starting reactants (Scheme 1) were converted into the SK-1 and synthesis of the SK-1 was successfully carried out. The comparison of IR spectra of free SK-1 and its Al³⁺ complex (Fig. 6) demonstrated that SK-1 probe was principally coordinated to the Al3+ ion. The strong band appearing at around 1616 cm⁻¹ due to azomethine group shifted to a higher frequency at 1629 cm⁻¹ in Al³⁺ complex, indicating participation of azomethine group in the complexation with the Al³⁺ ion. On the other hand, the free OH group at 3378 cm⁻¹ was completely disappeared at 1 equiv. of Al³⁺. In addition, disappearing of strong band at around 3378 cm⁻¹ indicated that phenolic hydroxy group of **SK-1** participated in the complex formation with Al³⁺.

To better understand the complexation between the probe SK-1 and Al3+, ¹H NMR experiment of SK-1 in DMSO- d_6 were examined by addition of 1 equiv. of Al³⁺. As seen in Fig. 7, three phenolic -OH signals belonging to **SK-1** was observed at around 9.88, 9.02 and 14.21 ppm. Compared the phenolic -OH signals, appearing signal at around 14.21 ppm attributed the ortho position of SK-1 is probably due to the intramolecular hydrogen bonding (Fig. 7). While the phenolic OH proton at 14.21 ppm disappeared when added of 1.0 equiv. of Al3+ to SK-1 solution, the other signal at around 9.88 and 9.02 ppm shifted to downfield. Also, it was seen that the imine (CH=N) proton of **SK-1** at 8.91 ppm was slightly shifted to some extent. This shift for the imine proton was probably due to complexation ability of the azomethine group after coordination of SK-1 with Al³⁺ · ⁴⁴ All these shifting and/or disappearing of signals showed that both phenolic OH group located in ortho position and imine group of SK-1 were efficient on complex formation between **SK-1** and Al³⁺. In the light of obtained spectroscopic data, possible complex formation mechanism was given in Fig. 8.



Fig. 8. Proposed binding mechanism between the compound SK-1 and Al^{3+}

3. 5. Biological Applications

SK-1 was successfully applied for imaging of Al^{3+} ions in human breast cancer cells, MCF7 under fluorescence microscope. Cells treated with free **SK-1** were used as controls. When MCF7 cells were incubated with **SK-1** (10 μ M), it was not seen any fluorescence response (Fig. 9e). However, after addition of Al^{3+} ions, a brilliant red fluorescence was sighted in the MCF7 cells (Fig. 9b). Merged images of fluorescence and bright-field showed that fluorescence signals were detected in the intra-cel-

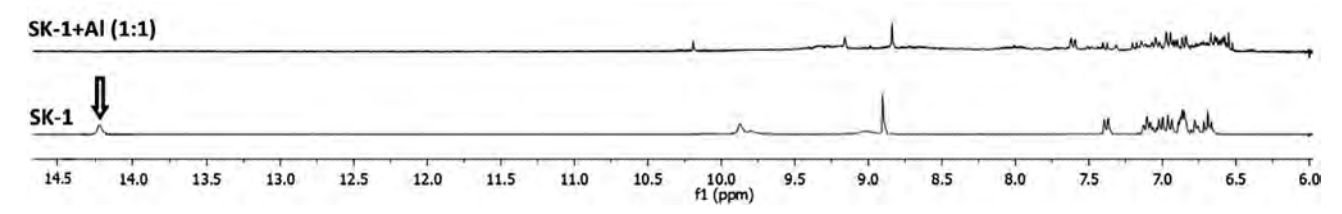


Fig. 7. ¹H NMR spectra in DMSO- d_6 of SK-1 with (1.0 equiv of Al³⁺) and without Al³⁺.

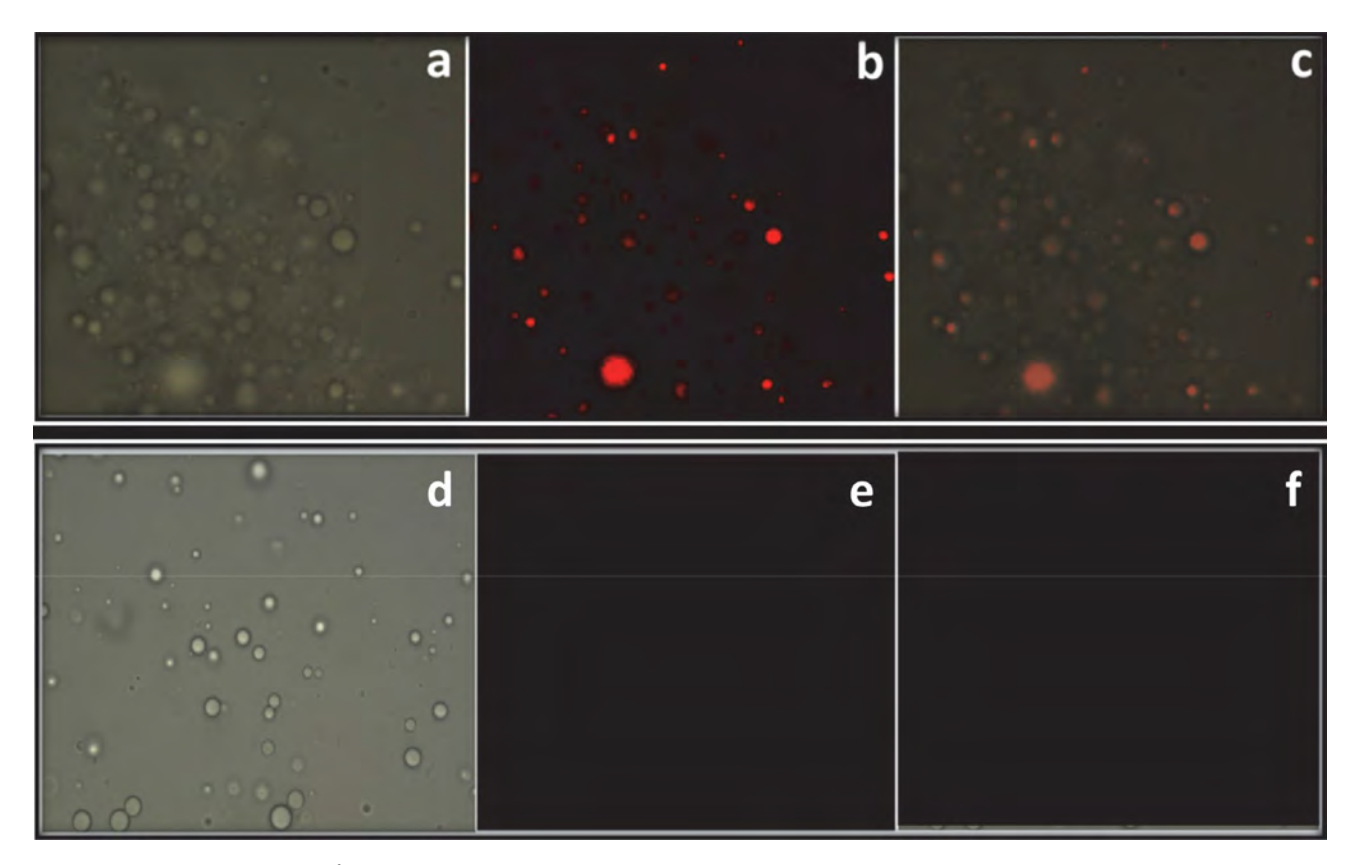


Fig. 9. Fluorescence images of Al³⁺ using probe **SK-1** in MCF7: (a) bright field image of MCF7 cells treated with probe **SK-1**; (b) fluorescence image of MCF7 cells treated with probe **SK-1** without Al³⁺; (e) fluorescence image of MCF7 cells treated with probe **SK-1** without Al³⁺; (e) fluorescence image of MCF7 cells treated with probe **SK-1** without Al³⁺; (d); (f) merged image of (d) and (e).

lular zone, showing the distribution of Al^{3+} and cell membrane permeabilities of **SK-1** molecules (Fig 9c). On the other hand, Fig. 9 indicated that **SK-1** could stain Al^{3+} ions in living cells without any harm (cells remain alive even after several hours of exposure to 10 μ M of **SK-1**), making it useful to monitor Al^{3+} in biological systems.

4. Conclusion

In conclusion, visual detection of highly selective and sensitive $\mathrm{Al^{3+}}$ ions by a very simple and low-cost fluorescence sensor (**SK-1**) based on the blocking PET process was carried out successfully. **SK-1** showed high sensitivity with the detection limit at around 4.8×10^{-7} M in the micromolar scale and selectivity response towards $\mathrm{Al^{3+}}$ over other metal ions with 37-fold fluorescence enhancement. The predicted configuration of the **SK-1-Al^{3+}** complex formation was well-characterized to be 1:1 by spectroscopic analyses. Beyond that, **SK-1** was utilized to detect sensitively the $\mathrm{Al^{3+}}$ ions in living cells by emitting visible fluorescence. Cell applications indicated that **SK-1** could be used as an excellent fluorescence probe for visualizing of $\mathrm{Al^{3+}}$ ions in cell lines.

5. Acknowledgments

The authors declare that there is no conflict of interest. This study is part of master thesis of Sedat Keskin and authors of this paper gratefully would like to thank Karamano-glu Mehmetbey University Research Foundation (BAP) and The Scientific and Technological Research Application Center (BILTEM) for the financial and technical supports.

6. References

- J. Zhu, Y. Zhang, L. Wang, T. Sun, M. Wang, Y. Wang, D. Ma, Q. Yang, Y. Tang. *Tetrahedron Lett.*, **2016**, *57*, 3535–3539.
 DOI:10.1016/j.tetlet.2016.06.112
- 2. X. Yan, H. Yang, F. Tian. *RSC Adv.*, **2015**, 107012–107019. **DOI:**10.1039/C5RA17557G
- V. K. Gupta, S. K. Shoora, L. K. Kumawat, A. K. Jain. Sensors Actuators, B Chem., 2015, 209, 15–24.
 DOI:10.1016/j.snb.2014.10.143
- 4. K. Kaur, V. K. Bhardwaj, N. Kaur, N. Singh. *Inorg. Chem. Commun.*, **2012**, *18*, 79–82. **DOI**:10.1016/j.inoche.2012.01.018
- Y. Xu, S. Mao, H. Peng, F. Wang, H. Zhang, S.O. Aderinto, H. Wu. *J. Lumin.*, 2017, 192, 56–63.
 DOI:10.1016/j.jlumin.2017.06.023

- L. Kang, Y. T. Liu, N.N. Li, Q. X. Dang, Z. Y. Xing, J. L. Li, Y. Zhang. *J. Lumin.*, 2017, 186, 48–52.
 DOI:10.1016/j.jlumin.2016.12.056
- T. Han, X. Feng, B. Tong, J. Shi, L. Chen, J. Zhi, Y. Dong. Chem. Commun., 2012, 48, 416–418. DOI:10.1039/C1CC15681K
- M. H. Nagaoka, T. Maitani. Analyst, 2000, 125, 1962–1965.
 DOI:10.1039/b006590k
- 9. M. Shellaiah, Y. H. Wu, H. C. Lin. Analyst, **2013**, *138*, 2931–2942. **DOI**:10.1039/c3an36840h
- S. Mukherjee, P. Mal, H. Stoeckli-Evans. J. Lumin., 2016, 172, 124–130. DOI:10.1016/j.jlumin.2015.11.014
- S. Das, D. Karak, S. Lohar, A. Banerjee, A. Sahana, D. Das. *Anal. Methods.*, 2012, 4, 3620–3624.
 DOI:10.1039/c2av25825k
- X. Sun, Y.-W. Wang, Y. Peng. Org. Lett., 2012, 14, 3420–3423.
 DOI:10.1021/ol301390g
- 13. C.-Y. Huang, Y. Jhong, J.-L. Chir, A.-T. Wu. *J. Fluoresc.*, **2014**, 24, 991–994. **DOI**:10.1007/s10895-014-1404-1
- H. Cheng, Y. Qian. RSC Adv., 2015, 5, 82887–82893.
 DOI:10.1039/C5RA15546K
- M. Shellaiah, Y.C. Rajan, P. Balu, A. Murugan. New J. Chem., 2015, 39, 2523–2531. DOI:10.1039/C4NJ02367F
- S. Jana, S. Dalapati, N. Guchhait. J. Phys. Chem. A, 2013, 117, 4367–4376. DOI:10.1021/jp3120463
- G. Q. Wang, J. C. Qin, L. Fan, C. R. Li, Z. Y. Yang. *J. Photo-chem. Photobiol. A Chem.*, 2016, 314, 29–34.
 DOI:10.1016/j.jphotochem.2015.08.005
- L. Wang, W. Qin, X. Tang, W. Dou, W. Liu. J. Phys. Chem. A.,
 2011, 115, 1609–1616. DOI:10.1021/jp110305k
- J. Shao, H. Lin, Z.-S. Cai, H. Lin. J. Photochem. Photobiol. B Biol., 2009, 95, 1–5. DOI:10.1016/j.jphotobiol.2008.12.007
- J. Kumar, M.J. Sarma, P. Phukan, D. K. Das. *Dalt. Trans.*, 2015, 44, 4576–4581. DOI:10.1039/C4DT03932G
- J. Wu, W. Liu, J. Ge, H. Zhang, P. Wang. Chem. Soc. Rev., 2011, 40, 3483–3495. DOI:10.1039/c0cs00224k
- T. Gunnlaugsson, H. D. P. Ali, M. Glynn, P. E. Kruger, G. M. Hussey, F. M. Pfeffer, C. M. G. Dos Santos, J. Tierney. *J. Fluoresc.*, 2005, 15, 287–299.
 DOI:10.1007/s10895-005-2627-y
- M. H. Yan, T. R. Li, Z. Y. Yang. *Inorg. Chem. Commun.*, 2011, 14, 463–465. DOI:10.1016/j.inoche.2010.12.027
- 24. S. Sen, T. Mukherjee, B. Chattopadhyay, A. Moirangthem, A. Basu, J. Marek, P. Chattopadhyay. *Analyst*, **2012**, *137*, 3975–3981. **DOI**:10.1039/c2an35560d
- C. Dohno, A. Okamoto, I. Saito. J. Am. Chem. Soc., 2005, 127, 16681–16684. DOI:10.1021/ja054618q
- L. Fan, T. R. Li, B. D. Wang, Z. Y. Yang, C. J. Liu. Spectrochim.
 Acta Part A Mol. Biomol. Spectrosc., 2014, 118, 760–764.
 DOI:10.1016/j.saa.2013.09.062

- Y. J. Lee, C. Lim, H. Suh, E. J. Song, C. Kim. Sensors Actuators B Chem., 2014, 201, 535–544. DOI:10.1016/j.snb.2014.05.035
- 28. S. Guha, S. Lohar, A. Sahana, A. Banerjee, D. A. Safin, M. G. Babashkina, M.P. Mitoraj, M. Bolte, Y. Garcia, S.K. Mukhopadhyay, D. Das. *Dalt. Trans.*, **2013**, *42*, 10198-10207. **DOI:**10.1039/c3dt51045j
- S. K. Shoora, A. K. Jain, V. K. Gupta. Sensors Actuators, B Chem., 2015, 216, 86–104. DOI:10.1016/j.snb.2015.04.038
- M. Tajbakhsh, G. B. Chalmardi, A. Bekhradnia, R. Hosseinzadeh, N. Hasani, M. A. Amiri. Spectrochim. Acta Part A Mol. Biomol. Spectrosc., 2018, 189, 22–31.
 DOI:10.1016/j.saa.2017.08.007
- P. Alaei, S. Rouhani, K. Gharanjig, J. Ghasemi. Spectrochim. Acta - Part A Mol. Biomol. Spectrosc., 2012, 90, 85–92.
 DOI:10.1016/j.saa.2012.01.008
- N. C. Lim, S. V. Pavlova, C. Brückner. *Inorg. Chem.*, 2009, 48, 1173–1182. DOI:10.1021/ic801322x
- 33. J. M. An, Z. Y. Yang, M. H. Yan, T. R. Li. *J. Lumin.*, **2013**, *139*, 79–83. **DOI**:10.1016/j.jlumin.2013.02.019
- 34. T. Gunnlaugsson, A. P. Davis, J. E. O'Brien, M. Glynn. *Org. Lett.*, **2002**, *4*, 2449–2452. **DOI**:10.1021/ol026004l
- G. Zhu, Y. Wang, H. Fu, X. Xu, Z. Cui, X. Ji, G. Wu. Spectrochim. Acta Part A Mol. Biomol. Spectrosc., 2015, 137, 148– 153. DOI:10.1016/j.saa.2014.08.021
- F. Karagöz, O. Güney, M. Kandaz, A.T. Bilgiçli. J. Lumin.,
 2012, 132, 2736–2740. DOI:10.1016/j.jlumin.2012.05.005
- D. Zhou, C. Sun, C. Chen, X. Cui, W. Li. J. Mol. Struct., 2015, 1079, 315–320. DOI:10.1016/j.molstruc.2014.09.050
- W.-H. Ding, D. Wang, X.-J. Zheng, W.-J. Ding, J.-Q. Zheng, W.-H. Mu, W. Cao, L.-P. Jin. Sensors Actuators B Chem., 2015, 209, 359–367. DOI:10.1016/j.snb.2014.11.144
- J. S. Renny, L. L. Tomasevich, E. H. Tallmadge, D. B. Collum. *Angew. Chem. Int. Ed. Engl.*, 2013, 52, 11998–2013.
 DOI:10.1002/anie.201304157
- 40. H. A. Benesi, J. H. Hildebrand. *J. Am. Chem. Soc.*, **1949**, *71*, 2703–2707. **DOI:**10.1021/ja01176a030
- 41. C. Kim, T. G. Jo, J. Lee, E. Nam, K. H. Bok, M.H. Lim. *New J. Chem.*, **2016**, *40*, 8918–8927. **DOI:**10.1039/C6NJ01544A
- 42. H. M. Kim, C. Jung, B. R. Kim, S.-Y. Jung, J. H. Hong, Y.-G. Ko, K. J. Lee, B. R. Cho. *Angew. Chemie Int. Ed.*, **2007**, 46, 3460–3463. **DOI:**10.1002/anie.200700169
- 43. İ. Kaya, E. Kartal, D. Şenol. *Des. Monomers Polym.*, **2015**, *18*, 524–535. **DOI**:10.1080/15685551.2015.1041084
- V. K. Gupta, A. Kumar, S. Lokesh, K.Kumawat. Sensors Actuators, B Chem., 2015, 195, 98-108.
 DOI:10.1016/j.snb.2013.12.092
- V. K. Gupta, B. Sethi, R. A. Sharma, S. Agarwal, A. Bhartia. j. Mol. Liq., 2013, 177, 114-118.
 DOI:10.1016/j.molliq.2012.10.008

Povzetek

Za detekcijo aluminijevih ionov na osnovi fotoinduciranega prenosa elektronov smo sintetizirali in okarakterizirali šest Schiffovih baz. Z absorpcijskimi in emisijskimi spektri smo raziskovali možnost vezave sintetiziranih spojin z različnimi kovinskimi kationi. S spektrofotometrijo smo ugotovili, da daje spojina SK-1 odličen fluorescenčni odziv na ciljne aluminijeve ione. Razlog je verjetno njena kelatna struktura. Spojina SK-1 je za aluminijeve ione pokazala večjo občutljivost in selektivnost kot za ostale ione. Rezultati raziskav možnosti uporabe SK-1 za detekcijo aluminijevih ionov v celicah so pokazali, da je lahko fluorescenčni senzor SK-1 obetavna sonda za določanje in/ali monitoring aluminijevih ionov v bioloških in/ali kemijskih vzorcih.



Except when otherwise noted, articles in this journal are published under the terms and conditions of the Creative Commons Attribution 4.0 International License

@creative

Scientific paper

The Evaluation of ICP OES for the Determination of Potentially Toxic Elements in Lipsticks: Health Risk Assessment

Jelena Mrmošanin, Aleksandra Pavlović*, Snežana Miti, Snežana Tošić, Emilija Pecev-Marinković, Jovana Krstić and Milena Nikolić

University of Niš, Faculty of Sciences and Mathematics, Department of Chemistry, Višegradska 33, P.O.Box 224, 18000 Niš, Serbia

* Corresponding author: E-mail: aleksandra.pavlovic@pmf.edu.rs *phone: +381 18 533-015, fax: +381 18 533-014

Received: 12-14-2018

Abstract

This study aimed to optimize and validate the inductively coupled plasma optical emission spectrometric method (ICP OES) for the simultaneous determination of eleven potentially toxic elements (Al, Cd, Cr, Co, Cu, Ni, Pb, Fe, Sb, Mn, and Zn) in lipstick samples. The method was evaluated by applying the standard addition method. The recoveries for all elements in lipsticks were between 90% and 110%, except for Cd and Pb they were <90% and >110%, respectively. The health risk assessment was determined by calculating the average daily intake (ADD), hazard quotient (HQ), and hazard index (HI). The highest mean value for ADD was for Fe (4.8×10^{-1} mg kg $^{-1}$ day $^{-1}$), and the lowest was for Co (9.3×10^{-6} mg kg $^{-1}$ day $^{-1}$). There was no significant toxic health risk for any of the elements (HQ < 1), except for Fe (HQ < 3) which indicates a potential health risk. Based on PCA, all potentially toxic elements have been classified in the three groups. The first group includes Fe, the second includes Al, and all other elements belong to the third group. The cluster analysis of the elements provided the identical grouping that was obtained on the basis of PCA. Two separate clusters were obtained when cluster analysis was applied to the analyzed samples. The first cluster contained the only sample that was brown. The second cluster was divided into two sub-clusters. The first sub-cluster included the samples belonging to category II and III regarding the price.

Keywords: Trace elements; makeup; inductively coupled plasma optical emission spectrometry; method development; health risk assessment

1. Introduction

Cosmetic products play an important role in human lives, being a part of routine body care. During the recent decades, these products have been used by an increasing number of people, which has influenced the increase in their production. Cosmetics include skin care creams, lotions, powders, perfumes, lipsticks, nail polish, eye makeup, hair dyes, deodorants, baby products, bathing oils, and many other types of products. Some cosmetics are benign, but others have been investigated as a possible cause of cancer. The most important are those which are directly applied to human skin, because they may produce local effects on human skin, such as allergy, irritation, sensitization, or photoreactions. Let the presence of harmful chemicals in cosmetics. Potentially

toxic elements are some of them. The sources of elements in cosmetics are raw materials which naturally contain them, the water used, the coated apparatuses during the cosmetics production, and the metal compounds used during the manufacturing of cosmetics.⁵

Toxic elements are widely diffused in colored makeup products such as lipsticks. Some of the studies conducted have shown that lipsticks contain potentially toxic elements such as Al, Cd, Co, Cr, Cu, Fe, Mn, Ni, Pb, Sb, and Zn.⁶⁻¹³ These potentially toxic elements can be classified as particularly toxic elements such as Pb, Cd, Ni, As, Sb, Al, and Hg, and toxic trace elements that are essential but dangerous in excessive amounts, such as Cr, Fe, Cu, Mn, Zn, and Co.⁵ Lipstick consumers are exposed to potentially toxic elements only in small amounts, but they expose themselves for a prolonged period of wearing time, which makes it significant in developing chronic health risk or skin damages. Nickel, chromium, cobalt, and cadmium may sensitize the immune system and produce an allergic reaction due to their cumulative effects. 14-16 It was reported that cosmetic products must contain less than 5 mg kg⁻¹, and preferably levels below 1 mg kg⁻¹ of elements such as chromium, cobalt, and nickel, in order to reduce the risk of eczema or allergic reactions. 17,18 Also, the U.S. Food and Drug Administration together with the Campaign for Safe Cosmetics¹⁹ has conducted a study and found that 61% of the 33 brands of lipsticks contained lead, with levels ranging up to 0.65 mg kg⁻¹. This research by the U.S. Food and Drug Administration²⁰ also found lead in all lipstick samples tested, with levels ranging from 0.09 mg kg⁻¹ to 3.06 mg kg⁻¹. The Health Canada²¹ reported that 81% of the lipstick samples they tested on lead had levels ranging from 0.079 to 0.84 mg kg⁻¹, and one of them contained lead in the concentration of 6.3 mg kg⁻¹. Also, some elements such as As, Sb, Cd, Pb, Cr, and Hg are banned as intentional ingredients in cosmetics in Canada.²²

Most studies determined the content of potentially toxic elements in cosmetic products, but only a couple of them determined the content of some elements and their impact on human health. Volpe et al.7 determined the content of Pb using flame-atomic absorption spectrometry (F-AAS), and contents of Cd, Cr, Co, and Ni by ICP OES in eyeshadow samples. Ullah et al.8 used F-AAS for the determination of Pb, Cd, Cu, Co, Fe, Cr, Ni, and Zn in samples of shampoo, talc powders, lipstick, surma, and cream available in the Pakistan market. Bocca et al.9 reviewed the concentrations of Sb, As, Cd, Cr, Co, Hg, Ni, and Pb in cosmetics, including lipstick samples, using different techniques. Piccinini et al.10 evaluated microwave acid digestion for the determination of the content of Pb in lip products (lipsticks and lip glosses) of different color and price using ICP-MS, and Ziarati et al.11 evaluated the wet digestion method for the determination of Pb and Cd by flame emission spectrophotometer. Zakaria and Ho¹² evaluated the potential health risks due to the daily ingestion of Pb, Cd, and Cr in lipsticks, while Batista et al.¹³ developed ICP OES method for determination of Cd, Co, Cr, Cu, and Ni and the graphite furnace atomic absorption spectrometry (GF AAS) method for the determination of Pb in lipsticks.

Because of the importance of the control and monitoring of toxic elements in cosmetics, our primary objective was to develop an effective and sensitive inductively coupled plasma atomic emission (ICP OES) method which may be applicable for a simultaneous analysis of potentially toxic elements in lipsticks. The second one was to apply the chemometric techniques of principal component analysis (PCA) and cluster analysis (CA) to the results obtained from the ICP OES determination of eleven potentially toxic elements in marketed lipsticks to assess whether there is a similarity regarding their element contents as well as to evaluate the possibility of potential health risk due to the daily ingestion of toxic elements in lipsticks among lipstick users.

2. Experimental

2. 1. Chemicals

Ultra-scientific (U.S.A.) ICP multi-element standard solutions of about 20.00 ± 0.10 mg L⁻¹ were used as a stock solution for calibration. Nitric acid (65%) (Merck, Darmstadt, Germany) and hydrogen peroxide (30%) (Fluka, Buchs, Switzerland) were both of the analytical grade.

2. 2. Instrumentation

The thermo Scientific iCAP 6000 inductively coupled plasma atomic emission spectrometer with an Echelle optical design (52.91 grooves mm⁻¹, 63.5° blaze angle) and a change injection device solid-state detector (RACID86) was used to analyze the lipstick samples. The nebulizer was glass concentric. The iTEVA operating software for iCAP 6000 series was used to control all functions of the instrument. The microwave digestion system ETHOS 1 was used for performing a digestion (Milestone, Bergamo, Italy).

2. 3. Samples

Fourteen lipstick samples (L1–L14) were purchased in local markets in Serbia. The lipstick samples were classified by price in three categories varied from "cheap" (category I) to "expensive" (category III). Every sample label contained the origin country of manufacture and was stored at room temperature until the analysis.

2. 4. Sample Preparation

The sample preparation was carried out using a microwave digester according to the method of Zakaria and Ho¹² with slight modification. 0.2 g of lipstick was weighed in a microwave vessel and 6 mL of HNO₃ (65%) and 1 mL of H_2O_2 (30%) were added. The conditions were as follows: 1800 W, 90 bar, with the temperature program: heating to 130 °C in 15 min (held for 20 min), then to 200 °C in 15 min (held for 20 min). After the second step of the programme, the vessels were cooled to 50 °C for 10 min. The extracts were filtered and then diluted with 0.5% HNO₃ to the final volume of 25 mL. The procedure was carried out in triplicate. A blank was prepared in the same way. The plastic containers used for storing the samples were cleaned to avoid the contamination of the samples with the traces of any elements. The containers were treated with 20% HNO₃ and washed with ultra-pure water 0.05 μS cm⁻¹ (MicroMed high purity water system, TKA Wasseraufbereitungssysteme GmbH, Niederelbert, Germany).

2. 5. Operating Plasma Condition

Before the metal analysis, the operating parameters were conducted to check the instrument performance. The

following ICP OES instrument performance tests should be performed: RF power, nebulizer gas flow rate, torch gas flow rate, viewing height and sample introduction rate. RF power, viewing height, and nebulizer gas flow rate are three of the parameters that have high influence on the analytical characteristics of ICP plasma.²³ In the present study, using a 27.12 MHz ICP, RF power, and nebulizer argon flow rate were varied under the constant values of other plasma conditions.^{24,25} Also, both viewing modes (axial/radial) were considered in this study. In order to eliminate the memory effect, the delay time for washing between samples and signal measurement was set to 30 s. Mermet²⁶ reported that plasma robust conditions can be represented by a Mg II 280.270 nm/Mg I 285.213 nm ratio (Mg II/Mg I) higher than 10. Under robust plasma conditions matrix effects as well as other interferences are mainly assigned to the aerosol transport.

2. 6. The selection of Analytical Lines and the Evaluation of Matrix Effect (ME)

Prior to the analysis, the line selections were performed. The spectral interferences and matrix effect in both axial and radial view modes for a total of 44 lines recommended by the ICP OES spectrometer library, corresponding to 11 determined elements, were checked. The analytical lines were evaluated according to the ratio of the slope of the calibration curve and slope of the standard addition method line (slope_{cal}/slope_{sam}).

A standard addition method was used to overcome the matrix effect. 23,26,27 A portion of the sample was spiked at a different concentration levels of the standard according to U.S. Food and Drug Administration 28 (from 0.1 mg L⁻¹ to 1.0 mg L⁻¹ for trace elements). The increase in signal was to the standard that was added, and the original signal was due to the analyte only. A ratio of two elemental signals was used to calculate the matrix effect. 29

2. 7. Validation

The instrument was calibrated at a four-point calibration curve. The linearity of each element was tested ranging from 0 mg kg $^{-1}$ to 5 mg kg $^{-1}$. The calibration curve linearity for each element was evaluated by the coefficient of determination (R^2). Each sample of lipstick was analyzed in triplicate in order to gain a more precise estimation of the data. A method blank was carried throughout the entire sample preparation and analytical process.

The detection (LOD) and quantification (LOQ) limits were calculated with three and ten times of the residual standard deviation of the regression line (3σ and 10σ criterion), divided with a slope of the calibration curve.³⁰ Both limits were expressed in ng g⁻¹.

The signal-to-background ratio (SBR) is also a figure of merit that can be correlated with the limit of detection.

$$SBR = \frac{I_{standard} - I_{blank}}{I_{blank}} \tag{1}$$

All signals were measured in the presence of some degree of background. A quantitative measure of the background level is called the background equivalent concentration (BEC), and was calculated by the following formula:

$$BEC = \frac{c_{standard}}{SBR}$$
 (2)

where $I_{standard}$ and I_{blank} are emission intensities for the multielemental standard and blank solutions, $c_{standard}$ is the concentration of the multielemental standard solution (2 mg $\rm L^{-1}$).

The recovery test was evaluated by spiking three replicates of each lipstick sample with the element standard. 2 mL of 62.5 mg L^{-1} of Al and Fe, and 2 mL of 6.25 mg L^{-1} of Mn, Ni, Sb, Cu, Zn, Cr, Cd, Co, and Pb were added to the lipstick samples. The samples were prepared as is described in the Sample preparation part.

2. 8. Human Health Risk Assessment

Regarding health risk assessment, risk level was determined using the average daily intake dose (ADD, mg kg⁻¹ day⁻¹) of ingestion, hazard quotient (HQ) and hazard index (HI).

ADD is used to quantify the oral exposure dosage for deleterious substances.³¹ This dose of the elements was calculated using the following equation:^{12,32}

$$ADD = \frac{c \times IR \times ED \times EF}{BW \times AT} \times CF \tag{3}$$

where c is the concentration of elements found in the tested lipstick samples (mg kg⁻¹); IR is the intake rate (40 mg day⁻¹);³³ ED is the exposure duration (35 years); EF is the exposure frequency (260 days year⁻¹); BW is the average body weight for an adult (57.9 kg);¹² AT is the average exposure time for non-carcinogenic effects (365 days years⁻¹ × number of exposure years (35)); CF is the conversion factor (10⁻³).

To assess the health risk associated with a potential toxic element, the hazard quotient and hazard index can be calculated using the following equations:^{12,34}

$$HQ = ADD/RfD \tag{4}$$

$$HI = \sum HQ$$
 (5)

where *RfD* is the oral reference dose (mg kg⁻¹ day⁻¹), based on the US EPA database. The RfD value is regarded as an estimate of a daily exposure to the human population that

is likely to be without a significant risk of harmful effects during a lifetime.³⁵

If value $HQ \le 1$ then no adverse health effects (no risk); if $HQ \ge 1$ then adverse health effects and $1 < HQ \le 5$ (low risk); $5 < HQ \le 10$ (medium risk); $HQ \ge 5$ (high risk).³⁶ The HI index represents the sum of the HQ index and shows the influence of toxic elements on human health.

2. 9. Statistical Analysis

Statistical multivariate methods such as principal component analysis (PCA) and cluster analysis (CA) were used for the classification of samples based on the metal content. PCA and CA were performed using a statistical package running on a computer (Statistica 8.0, StatSoft, Tulsa, Oklahoma, USA). The Tukey's test was used (significant level of p < 0.05) for the determination of the difference between the mean concentration of metal in the analyzed lipsticks.³⁷

3. Results and Discussion

3. 1. The Optimization of Plasma Operating Conditions

The Mg II/Mg I line intensity ratio was selected to evaluate the ICP operating conditions and the plasma robustness. ²⁶ Using a 27.12 MHz ICP, the RF power was varied from 750 W to 1350 W with the intervals of 200 W. The other plasma conditions were constant: flush pump rate 50 rpm, analysis pump rate 50 rpm, nebulizer gas flow rate 0.5

L/min, coolant gas flow rate 12 L/min, auxiliary gas flow rate 0.7 L/min, dual (axial/radial) viewed plasma mode and sample uptake delay 30 s. The highest Mg II/Mg I ratio was obtained for the RF power of 1150 W and was found to be 10.35 and 11.42 for the axially and radially viewed, respectively. As expected, the results showed a higher Mg II/Mg I ratio for the radially viewed configuration (Table 1).^{24,25}

Using an RF power of 1150 W, nebulizer gas flow was varied from 0.5 mL/min to 1.5 mL/min in intervals of 0.5 mL/min. The highest Mg II/Mg I ratio of 10.35 and 11.42 for axially and radially viewed ICP OES, respectively, was at the nebulizer gas flow of 0.5 L min $^{-1}$ (Table 1). This value was selected for further proceedings.

3. 2. The Selection of Analytical Lines

The best lines experimentally found in both axial and radial plasma viewing modes after the study of ratio slope_{cal}/slope_{sam} and matrix effect, are shown in Table 2. A final selection of wavelength lines also took into consideration the accuracy obtained for each line and spectral interferences. As it can be seen in Table 2, the slopes of both kinds of lines were statistically comparable, which indicates the lack of the matrix effects. The ME data up to 9.5% indicate that the method of the evaluation of the matrix effect generates reliable results.

3. 3. Validation

On the basis of the calibration curve of each metal, the selected wavelengths of the analyte lines, coefficient of

Viewing mode	RF power (W)	Relative intensity ± SD (280.270 nm)	RSD (%)	Relative intensity ± SD (285.213 nm)	RSD (%)	Intensity ratio Mg II/Mg I
Axial	750	318233 ± 4550	1.43	75120 ± 1092	1.45	4.24
	950	832600 ± 6038	0.73	109697 ± 953	0.87	7.59
	1150	1155400 ± 7779	0.67	111658 ± 872	0.78	10.35
	1350	1413317 ± 19909	1.41	141050 ± 1275	0.90	10.02
Radial	750	18685 ± 273	1.46	2454 ± 6	0.24	7.61
	950	30189 ± 509	1.69	3147 ± 35	1.11	9.59
	1150	42177 ± 377	0.89	3694 ± 27	0.73	11.42
	1350	45005 ± 435	0.97	3961 ± 30	0.76	11.36

Viewing mode	Nebulizer gas flow (l/min)	Relative intensity ± SD (280.270 nm)	RSD (%)	Relative intensity ± SD (285.213 nm)	RSD (%)	Intensity ratio Mg II/Mg I
Axial	0.5	1155400 ± 7779	0.67	111658 ± 872	0.78	10.35
	1.0	1029000 ± 9337	0.91	102286 ± 1057	1.03	10.06
	1.5	698000 ± 6902	0.99	70950 ± 395	0.56	9.84
Radial	0.5	42177 ± 377	0.89	3694 ± 27	0.73	11.42
	1.0	39209 ± 452	1.15	3573 ± 45	1.26	10.97
	1.5	32041 ± 280	0.87	3094 ± 26	0.84	10.36

Table 2. Analyte line selected with the ratio $slope_{cal}/slope_{sam}$, matrix effect (ME), BEC and SBR, as well as coefficient of determination (R^2), LOD and LOQ of the calibration for each metal determination. Plasma view mode: axial.

Element	λ (nm)	Slope _{cal} /Slope _{sam}	ME (%)	R^2	LOD (ng g ⁻¹)	LOQ (ng g ⁻¹)	BEC (ng g ⁻¹)	SBR
Al	396.152	0.976	-2.4	0.9995	85	280	109.3	18.3
Cd	226.502	1.056	5.6	0.9999	8	25	26.9	74.3
Co	228.616	1.078	7.8	0.9999	2	5	3.5	563
Cr	283.563	0.905	-9.5	0.9997	30	100	36.5	54.8
Cu	324.754	1.019	1.9	1	25	80	15.2	131.2
Fe	259.940	1.011	1.1	0.9998	25	80	63.1	31.7
Mn	257.610	0.982	-1.8	0.9997	5	15	20.5	97.7
Ni	231.604	0.983	-1.7	0.9998	20	68	17.1	116.6
Pb	220.353	0.958	-4.2	1	11	36	15.9	125.9
Sb	231.147	1.033	3.3	0.9999	17	55	14.2	104.5
Zn	213.856	0.981	-1.9	0.9998	5	15	16.8	119.3

determination, limit of detection and limit of quantification are shown in Table 2. The four-point calibration curve showed good linearity over the concentration range from 0

to 5 mg kg⁻¹, where correlation coefficients ranged from 0.9995 to 1. Table 2 also shows the parameters of merit (BEC, SBR, LOD, LOQ) obtained under robust conditions

Table 3. Spiked concentration^a (mg kg⁻¹) of elements in lipstick samples and recovery test (n = 3)

Samples	Al^{b} $c_{sr} \pm SD$	RSDc	Recoveryd	$\begin{array}{c} \text{Cd} \\ c_{\text{sr}} \pm \text{SD} \end{array}$	RSD	Recovery	$c_{\rm sr} \pm { m SD}$	RSD	Recovery
	79 ± 1	1.3	97.5	0.49 ± 0.01	2.0	88.8	1.43 ± 0.02	1.4	96.6
L2	254 ± 1	0.4	98.8	0.15 ± 0.01 0.55 ± 0.02	3.6	85.3	1.59 ± 0.02 1.59 ± 0.03	1.9	96.4
L3	164 ± 3	1.8	97.6	0.49 ± 0.01	2.1	88.5	1.39 ± 0.02	1.4	97.2
L4	26 ± 1	3.8	96.3	0.67 ± 0.02	3.0	111.4	1.43 ± 0.02	1.4	97.3
L5	226 ± 1	0.4	98.3	0.50 ± 0.01	2.0	97.9	1.42 ± 0.02	1.4	102.9
L6	361 ± 4	1.1	99.4	0.56 ± 0.01	1.8	85.6	1.77 ± 0.03	1.7	95.7
L7	112 ± 1	0.9	96.5	0.54 ± 0.01	1.9	84.8	2.43 ± 0.04	1.6	95.3
L8	113 ± 1	0.9	97.4	0.55 ± 0.01	1.8	85.4	1.76 ± 0.02	1.1	95.6
L9	139 ± 1	0.7	97.9	0.54 ± 0.01	1.8	88.1	1.54 ± 0.01	0.6	96.9
L10	488 ± 3	0.6	99.2	0.47 ± 0.01	2.1	87.7	1.37 ± 0.01	0.7	97.2
L11	9.02 ± 0.05	0.5	96.5	0.48 ± 0.01	2.1	87	1.40 ± 0.01	0.7	97.2
L12	190 ± 1	0.5	97.9	1.20 ± 0.03	2.5	85.1	3.47 ± 0.04	1.2	94.8
L13	432 ± 2	0.5	99.1	0.57 ± 0.02	3.5	87.6	1.71 ± 0.02	1.2	96.6
L14	262 ± 2	0.8	99.6	0.55 ± 0.01	1.8	88	4.94 ± 0.05	1.0	95.4

$\begin{array}{c} \text{Co} \\ c_{\text{sr}} \pm \text{SD} \end{array}$	RSD	Recovery	$Cu \\ c_{\rm sr} \pm {\rm SD}$	RSD	Recovery	$Ni c_{sr} \pm SD$	RSD	Recovery	$Pb c_{sr} \pm SD$	RSD	Recovery
0.49 ± 0.01	2.1	97.4	1.74 ± 0.05	2.9	93.8	0.78 ± 0.01	1.3	97.5	1.31 ± 0.04	3.1	88.5
0.61 ± 0.02	3.3	96.0	8.2 ± 0.1	1.2	91.5	1.07 ± 0.02	1.9	96.4	1.58 ± 0.03	1.9	87.8
0.52 ± 0.01	1.9	95.7	1.88 ± 0.05	2.7	94.2	0.84 ± 0.01	1.2	96.5	1.20 ± 0.04	3.3	88.9
0.50 ± 0.01	2.0	96.9	1.01 ± 0.02	2.0	94.9	0.72 ± 0.01	1.4	97.3	1.11 ± 0.04	3.6	88.1
0.54 ± 0.02	3.7	96.1	2.16 ± 0.04	1.8	91	0.84 ± 0.01	1.2	95.4	2.02 ± 0.05	2.5	87.8
0.52 ± 0.01	1.9	98.3	1.35 ± 0.03	2.2	92.3	0.89 ± 0.02	2.2	94.7	1.37 ± 0.04	2.9	113.2
1.00 ± 0.02	2.0	95	2.22 ± 0.04	1.8	91.8	1.77 ± 0.03	1.7	97.2	17.33 ± 0.6	3.5	85.8
0.51 ± 0.01	1.9	98.5	1.51 ± 0.04	2.6	92.1	0.84 ± 0.02	2.4	97.7	1.63 ± 0.05	3.1	88.1
0.57 ± 0.01	1.8	97.8	1.16 ± 0.03	2.6	95	0.80 ± 0.01	1.3	98.8	1.06 ± 0.03	2.8	88.3
0.52 ± 0.01	1.9	95.6	2.02 ± 0.03	1.5	90.7	0.72 ± 0.01	1.4	97.3	0.92 ± 0.02	2.2	87.6
0.74 ± 0.01	1.3	95	1.93 ± 0.02	1.0	91.1	1.34 ± 0.02	1.5	103.9	1.21 ± 0.04	3.3	89
0.88 ± 0.02	2.3	97.8	3.77 ± 0.05	1.3	90	1.41 ± 0.02	1.4	96.6	7.00 ± 0.08	1.1	86.7
0.49 ± 0.01	2.0	98.8	2.19 ± 0.04	1.8	92	1.29 ± 0.02	1.6	97.7	1.35 ± 0.03	2.2	87.1
0.62 ± 0.01	1.6	96.6	5.11 ± 0.07	1.4	93.7	1.84 ± 0.03	1.6	95.3	6.76 ± 0.07	1.0	86.3

Fe $c_{\rm sr} \pm {\rm SD}$	RSD	Recovery	$Sb c_{sr} \pm SD$	RSD	Recovery	Mn $c_{\rm sr} \pm SD$	RSD	Recovery	Z_n $c_{sr} \pm SD$	RSD	Recovery
-75 ± 1	1.3	94.9	6.34 ± 0.2	3.2	94.6	1.23 ± 0.01	0.8	93.2	3.59 ± 0.02	0.6	95
659 ± 2	0.3	99.5	7.75 ± 0.1	1.3	94.5	2.83 ± 0.05	1.8	90.4	21.7 ± 0.1	0.5	98.8
93 ± 1	1.1	95.9	1.44 ± 0.07	4.9	93.5	0.94 ± 0.01	1.1	94.9	3.07 ± 0.01	0.3	95.2
145 ± 1	0.7	98.0	2.05 ± 0.08	3.9	92.8	2.96 ± 0.07	2.4	90.5	6.15 ± 0.04	0.6	94.7
21.4 ± 0.3	1.4	95.5	1.03 ± 0.05	4.9	93.6	1.41 ± 0.03	2.1	93.4	3.37 ± 0.02	0.6	94.3
974 ± 13	1.3	99.8	8.9 ± 0.1	1.1	91.6	1.99 ± 0.03	1.5	94.3	9.68 ± 0.05	0.5	96.9
548 ± 3	0.5	98.9	7.08 ± 0.08	1.1	95	3.27 ± 0.04	1.2	91.1	6.18 ± 0.06	1.0	95
617 ± 2	0.3	101.0	7.8 ± 0.1	1.3	94.8	6.79 ± 0.02	0.3	94.1	13.8 ± 0.1	0.7	97.9
360 ± 3	0.8	100.5	4.54 ± 0.04	0.9	93.4	3.24 ± 0.04	1.2	93.9	4.85 ± 0.03	0.6	94.2
9.4 ± 0.1	1.1	94.9	5.05 ± 0.04	0.8	92.7	0.96 ± 0.01	1.0	92.3	2.41 ± 0.02	0.8	94.7
22.8 ± 0.3	1.3	96.6	3.26 ± 0.07	2.2	92.3	0.74 ± 0.01	1.3	91.4	1.84 ± 0.02	1.1	94.7
3816 ± 17	0.4	99.0	6.9 ± 0.1	1.4	94.5	5.85 ± 0.04	0.7	96.8	14.3 ± 0.1	0.7	97.3
802 ± 4	0.5	99.5	9.2 ± 0.2	2.3	95.6	1.82 ± 0.02	1.1	91.9	12.3 ± 0.1	0.8	97
50 ± 0.4	0.8	97.5	6.97 ± 0.08	1.1	95.3	1.25 ± 0.01	0.8	91.9	6.71 ± 0.02	0.3	94.8

^aMean (c_{sr}) \pm standard deviation (SD) of three replicates, ^bSpiked concentrations for Al and Fe are 62.5 mg L⁻¹ (2 mL), while for other elements are 6.25 mg L⁻¹ (2 mL), ^cRelative standard deviation (%), ^dResults obtained from recovery test (%)

and using an axially viewed configuration. High SBR values and low BEC values were obtained.

The results obtained by the standard addition method and the recovery experiments for lipstick samples are shown in Table 3. In the tested samples, the recovery for all elements was between 90% and 110%, except for Cd and Pb, they were < 90% and > 110%. The element concentrations precision ranged from 0.3% to 4.9%. Lower RSD values were obtained for Zn, higher RSD values were obtained for Pb and Sb. Nevertheless, in all cases, the accuracy and precision were within the acceptable recoveries and RSD percentages obtained from the Horwitz function³⁸⁻⁴¹ and from the AOAC Peer-Verified Methods (PVM) program on the analyte level.⁴² According to Horwitz and AOAC PVM RSDs, the maximum RSD values acceptable for the analyte level of 100 µg kg⁻¹ are 22.6% and 15%; for 1 mg kg⁻¹ they are 16% and 11%; for 10 mg kg⁻¹ they are 11.3% and 7.3%; for 100 mg kg⁻¹ they are 8% and 5.3%, respectively, and so on. The results obtained clearly demonstrate that this type of digestion and ICP measurements are suitable for all elements.

3. 4. The Concentration of Elements in Lipsticks

Potentially toxic elements concentrations, expressed as milligram per kilogram (mg kg $^{-1}$), in the lipstick samples investigated are shown in Table 4. The overall (n=14) mean concentration of potentially toxic elements was: 202 ± 2 mg kg $^{-1}$ for Al; 0.160 ± 0.003 mg kg $^{-1}$ for Cd; 1.55 ± 0.02 mg kg $^{-1}$ for Cr; 0.129 ± 0.004 mg kg $^{-1}$ for Co; 2.31 ± 0.02 mg kg $^{-1}$ for Cu; 0.61 ± 0.01 mg kg $^{-1}$ for Ni; 3.25 ± 0.08 mg kg $^{-1}$ for Pb; 584 ± 3 mg kg $^{-1}$ for Fe; 5.00 ± 0.09 mg kg $^{-1}$ for Sb; 2.20 ± 0.02 mg kg $^{-1}$ for Mn, and 7.62 ± 0.04 mg kg $^{-1}$ for Zn. Based on the mean concentrations, the potentially toxic metal contents were arranged in the following decreasing order: Fe > Al > Zn > Sb > Pb > Cu > Mn > Cr > Ni > Cd > Co.

The concentrations of Al, Cd, Cr, Co, Cu, Ni, Pb, Fe, Sb, Mn, and Zn in all analyzed lipsticks were in the interval of 4.35-487 mg kg⁻¹, 0.038-0.914 mg kg⁻¹, 0.88-4.68 mg kg⁻¹, n.d.-0.556 mg kg⁻¹, 0.56-8.5 mg kg⁻¹, 0.24-1.43 $mg\ kg^{-1}, 0.55-19.7\ mg\ kg^{-1}, 4.9-3850\ mg\ kg^{-1}, 0.6-9.1\ mg$ kg⁻¹, 0.31-6.72 mg kg⁻¹, 1.44-21.5 mg kg⁻¹, respectively. The concentration ranges of Cd, Cr, Co, Cu, Ni, Pb, Fe, Zn in lipsticks found by Ullah et al.8 were: 0.2-0.43 mg kg⁻¹, $n.d.-0.77 \text{ mg kg}^{-1}$, $0.3-0.872 \text{ mg kg}^{-1}$, 0.026-6.036 mg kg^{-1} , 0.696–1.610 mg kg^{-1} , 2.58–11.33 mg kg^{-1} , 258–1164 mg kg⁻¹, 0.696-1.610 mg kg⁻¹, respectively. Zakaria and Ho¹² found Cd, Cr, and Pb in concentration ranges n.d.-0.33 mg kg⁻¹, 0.24–2.50 mg kg⁻¹, 0.77–15.44 mg kg⁻¹, respectively. Liu, Hammond, and Rojas-Cheatham⁴³ found Al in lipsticks in the concentration interval of 4.448– 27.032 mg kg⁻¹, while Al-Qutob, Alatrash, and Abol-Ola⁴⁴ found it in the concentration range 10.98–694.5 mg kg⁻¹. As can be seen, the obtained results are consistent with the results obtained by other authors. Aluminum is added to cosmetics as white pigments in colored cosmetics. The EC Regulation⁴⁵ allowed some compounds of Al as colorants in cosmetics. According to the U.S. low (FD&C Act)46 color additives can contain lead in lipsticks as an impurity up to 10 mg kg⁻¹. On the other hand, the EC Regulation⁴⁵ banned Pb and its compounds as intentional ingredients in cosmetics. Also, The EC Regulation⁴⁵ banned the use of Cd, Ni, Sb, and Co as metallic ions or salts in the preparation of cosmetic formulations. The Health Canada sets out a list of banned or limited ingredients in cosmetics, where some elements such as As, Sb, Cd, Pb, Cr, and Hg and its compounds are banned. Also, the Health Canada determined appropriate limits for As, Cd, and Hg (3 μ g g⁻¹), for Pb (10 μ g g⁻¹), and for Sb (5 μ g g⁻¹), as impurities in cosmetic products, while Germany set a limit for Cd as an impurity of 5 mg kg⁻¹.47,48 The Cr(III) oxide green and Cr(III) hydroxide green are allowed for use as colorants in cosmetic products. 49 The EU

Table 4. Element contents* (mg kg-1) in lipstick samples

Samples ^b	Country of production	Color	Price category	$Al c_{\rm sr} \pm SD$	$Cd c_{\rm sr} \pm SD$	$Cr c_{sr} \pm SD$	$c_{\rm sr} \pm { m SD}$
L1	China	orange	I	76 ± 1	0.054 ± 0.002^{c}	0.98 ± 0.03^{b}	n.d.ª
L2	Slovenia	pink	II	252 ± 1^{b}	0.145 ± 0.007^{efg}	1.15 ± 0.02^{c}	0.131 ± 0.002^{g}
L3	France	orange	I	163 ± 4	0.050 ± 0.002^{bc}	0.93 ± 0.02^{a}	0.041 ± 0.002^{cd}
L4	Turkey	red	I	22 ± 1	0.099 ± 0.005	0.97 ± 0.01^{b}	0.019 ± 0.001^{ab}
L5	London	purple	I	225 ± 2	0.071 ± 0.002^{c}	0.88 ± 0.02^{a}	0.064 ± 0.005^{ef}
L6	Serbia	red	III	358 ± 5	0.155 ± 0.002^{g}	1.35 ± 0.04^{d}	0.030 ± 0.002^{c}
L7	Poland	pink	II	111 ± 1^{a}	0.133 ± 0.002^{e}	2.05 ± 0.03	0.556 ± 0.007
L8	Poland	pink	II	111 ± 1^{a}	0.144 ± 0.002^{ef}	1.34 ± 0.04^{d}	0.022 ± 0.000^{b}
L9	Ireland	red	III	137 ± 1	0.114 ± 0.007^{d}	1.09 ± 0.04^{c}	0.081 ± 0.006^{f}
L10	Turkey	violet	I	487 ± 2	0.038 ± 0.002^{a}	0.91 ± 0.01^{a}	0.049 ± 0.002^{de}
L11	Poland	orange	I	4.35 ± 0.04	0.047 ± 0.004^{ab}	0.94 ± 0.05^{ab}	0.28 ± 0.01
L12	China	brown	II	189 ± 1	0.914 ± 0.005	3.16 ± 0.05	0.400 ± 0.007
L13	Germany	red	II	431 ±2	0.151 ± 0.005^{fg}	1.27 ± 0.02	n.d.a
L14	Serbia	pink	I	$258\pm2^{\rm b}$	$0.124 \pm 0.002^{\mathrm{de}}$	4.68 ± 0.02	$0.14\pm0.01^{\rm g}$

Samples	$Cu \\ c_{\rm sr} \pm {\rm SD}$	$Ni c_{sr} \pm SD$	$Pb \\ c_{\rm sr} \pm SD$	Fe $c_{\rm sr} \pm {\rm SD}$	$\begin{array}{c} \text{Sb} \\ c_{\text{sr}} \pm \text{SD} \end{array}$	Mn $c_{\rm sr} \pm SD$	$\frac{\mathrm{Zn}}{c_{\mathrm{sr}} \pm \mathrm{SD}}$
L1	1.35 ± 0.01^{a}	0.30 ± 0.01^{b}	0.98 ± 0.04	74 ± 1	6.2 ± 0.2^{a}	0.82 ± 0.01^{b}	3.28 ± 0.01^{a}
L2	8.50 ± 0.1	0.61 ± 0.01	1.30 ± 0.05^{d}	657 ± 2	7.7 ± 0.1^{b}	2.63 ± 0.01^{c}	21.5 ± 0.1
L3	1.50 ± 0.06^{ab}	0.37 ± 0.01^{de}	0.85 ± 0.05^{bc}	92 ± 2	1.04 ± 0.06	0.49 ± 0.02^{a}	2.73 ± 0.02
L4	0.56 ± 0.01	0.24 ± 0.01^{a}	0.76 ± 0.05^{ab}	143 ± 1	1.71 ± 0.07	2.77 ± 0.06^{c}	5.99 ± 0.02^{b}
L5	1.87 ± 0.05^{c}	0.38 ± 0.01^{e}	1.80 ± 0.04	17.4 ± 0.2	0.60 ± 0.02	1.01 ± 0.01	3.07 ± 0.01^{a}
L6	0.96 ± 0.01	0.44 ± 0.01	0.71 ± 0.05^{ab}	971 ± 12	9.2 ± 0.2^{c}	1.61 ± 0.03	9.49 ± 0.06
L7	1.92 ± 0.01^{c}	1.32 ± 0.02	19.7 ± 0.4	549 ± 4	6.95 ± 0.06^{a}	3.09 ± 0.04^{d}	6.00 ± 0.05^{b}
L8	1.14 ± 0.01	0.36 ± 0.02^{cd}	1.35 ± 0.04^{d}	606 ± 1	7.7 ± 0.1^{b}	6.72 ± 0.01	13.6 ± 0.1
L9	0.72 ± 0.01	0.31 ± 0.02^{bc}	0.70 ± 0.04^{ab}	353 ± 3	4.36 ± 0.03	2.95 ± 0.02^{cd}	4.65 ± 0.02
L10	1.73 ± 0.01	0.24 ± 0.01^{a}	0.55 ± 0.04^{a}	4.9 ± 0.1	4.95 ± 0.04	0.54 ± 0.01^{a}	2.05 ± 0.02
L11	1.62 ± 0.02^{b}	$0.79 \pm 0.02^{\rm f}$	0.86 ± 0.03^{c}	18.6 ± 0.3	3.03 ± 0.09	0.31 ± 0.01	1.44 ± 0.01
L12	3.69 ± 0.01	0.96 ± 0.02	7.57 ± 0.06	3850 ± 17	6.8 ± 0.03^{a}	5.54 ± 0.05	14.2 ± 0.1
L13	1.88 ± 0.03^{c}	$0.82 \pm 0.01^{\rm f}$	1.05 ± 0.05	801 ± 5	9.1 ± 0.2^{c}	1.48 ± 0.01	12.17 ± 0.09
L14	4.95 ± 0.01	1.43 ± 0.02	7.33 ± 0.08	46.3 ± 0.1	6.81 ± 0.04^{a}	0.86 ± 0.01^{b}	6.58 ± 0.01

*Mean \pm standard deviation, n = 3; n.d. – not detected; values with different letters within the columns are statistically different at p < 0.05 by Tukey's test

banned Cr(VI) which can still be in these coloring agents.^{45,49} Moreover, as opposed to the other elements, Cr is not limited as a cosmetic's impurity. Also, some countries (Germany and Canada) adopted the national limits to define the maximum allowable amount of Sb as an impurity in cosmetics (5–10 mg kg⁻¹).^{47,48}

Concentrations of analyzed potentially toxic elements in lipsticks were below reported limits, but it was needed to evaluate the possibility of potential health risk (ADD, HQ, HI, and RfD) due to daily exposure of these elements through lipstick consummation.

3. 5. Health Risk Assessment

The oral reference doses (RfD) for Co, Cu, Cr, Cd, Fe, Ni, Zn, and Mn are 3×10^{-4} , 4×10^{-2} , 3×10^{-3} , 1×10^{-3} , 7×10^{-1} , 2×10^{-2} , 3×10^{-1} , 1.4×10^{-1} , respectively. So Lead, chromium, and cadmium belong to toxic and potentially carcinogenic substances. According to US EPA, it is inap-

propriate to develop an RfD value for inorganic lead because the degree of uncertainty about the health effects of lead is quite low. 12,55

The mean daily intake of potentially toxic elements for adults (ADD) and potential toxic health risk effects (HQ and HI) are given in Table 5. Since As, Pb, Cd, and Cr are classified by the US EPA^{50–52} as being carcinogenic agents, HQ of Cd and Cr were used to calculate HI.

The ADD values of Co, Cu, Fe, Ni, Zn, Mn, Cr, and Cd varied from n.d. to 2.7×10^{-4} ; 2.8×10^{-4} to 4.2×10^{-3} ; 1.9×10^{-3} to 4.8×10^{-1} ; 1.2×10^{-4} to 7.0×10^{-4} ; 7.1×10^{-4} to 1.1×10^{-2} ; 1.5×10^{-4} to 3.3×10^{-3} ; 3.7×10^{-4} to 2.3×10^{-3} ; 1.9×10^{-5} to 2.6×10^{-5} , respectively. The mean concentrations for daily intake decrease in the following order: Fe > Zn > Cu~Mn > Cr > Ni > Co > Cd.

The obtained ADD values were lower than the RfDs, which indicated that there would not be any adverse health effects. A study by Zakaria and Ho¹² also reported that there was no significant health risk due to the exposure of

Table 5. Health risk assessment for the exposure to Co, Cu, Fe, Ni, Zn, Mn, Cr, and Cd in the lipstick samples

Sample	Co		Cı	1	Fe	;	Ni	
-	ADD	HQ	ADD	HQ	ADD	HQ	ADD	HQ
L1	n.d.	n.d.	6.6×10^{-4}	0.017	3.6×10^{-2}	0.052	1.5×10^{-4}	0.007
L2	6.4×10^{-5}	0.215	4.2×10^{-3}	0.105	3.2×10^{-1}	0.462	3.0×10^{-4}	0.015
L3	2.0×10^{-5}	0.067	7.4×10^{-4}	0.018	4.5×10^{-2}	0.065	1.8×10^{-4}	0.009
L4	9.3×10^{-6}	0.031	2.8×10^{-4}	0.007	7.0×10^{-2}	0.100	1.2×10^{-4}	0.006
L5	3.1×10^{-5}	0.104	9.2×10^{-4}	0.023	8.6×10^{-3}	0.012	1.9×10^{-4}	0.009
L6	1.5×10^{-5}	0.049	4.7×10^{-4}	0.012	4.8×10^{-1}	0.683	2.2×10^{-4}	0.011
L7	2.7×10^{-4}	0.912	$9.4 imes 10^{-4}$	0.024	2.7×10^{-1}	0.386	6.5×10^{-4}	0.032
L8	1.1×10^{-5}	0.036	5.6×10^{-4}	0.014	3.0×10^{-1}	0.426	1.8×10^{-4}	0.009
L9	4.0×10^{-5}	0.133	3.5×10^{-4}	0.010	1.7×10^{-1}	0.248	1.5×10^{-4}	0.008
L10	2.4×10^{-5}	0.080	8.5×10^{-4}	0.021	2.4×10^{-3}	0.003	1.2×10^{-4}	0.006
L11	$1.4 imes 10^{-4}$	0.459	$8.0 imes 10^{-4}$	0.020	9.1×10^{-3}	0.013	3.9×10^{-4}	0.019
L12	2.0×10^{-4}	0.656	1.8×10^{-3}	0.045	1.9×10^{-3}	2.707	4.7×10^{-4}	0.024
L13	n.d.	n.d.	9.2×10^{-4}	0.023	3.9×10^{-1}	0.563	4.0×10^{-4}	0.020
L14	6.9×10^{-5}	0.230	2.4×10^{-3}	0.061	2.3×10^{-2}	0.033	7.0×10^{-4}	0.035

Sample	Zn		M	[n	C	r	Co	Cd		
-	ADD	HQ	ADD	HQ	ADD	HQ	ADD	HQ		
L1	1.6×10^{-3}	0.005	1.6×10^{-3}	0.005	4.8×10^{-4}	0.161	2.7×10^{-5}	0.027	0.188	
L2	1.1×10^{-2}	0.035	1.1×10^{-2}	0.035	5.7×10^{-4}	0.189	7.1×10^{-5}	0.071	0.260	
L3	1.3×10^{-3}	0.004	1.3×10^{-3}	0.004	$4.8 imes 10^{-4}$	0.152	2.5×10^{-5}	0.025	0.177	
L4	2.9×10^{-3}	0.010	2.9×10^{-3}	0.010	4.1×10^{-4}	0.138	4.9×10^{-5}	0.049	0.187	
L5	1.5×10^{-3}	0.005	1.5×10^{-3}	0.005	3.7×10^{-4}	0.125	3.5×10^{-5}	0.035	0.160	
L6	4.7×10^{-3}	0.016	4.7×10^{-3}	0.016	5.7×10^{-4}	0.191	7.6×10^{-5}	0.076	0.267	
L7	2.9×10^{-3}	0.010	2.9×10^{-3}	0.010	8.7×10^{-4}	0.291	6.5×10^{-5}	0.065	0.356	
L8	6.7×10^{-3}	0.022	6.7×10^{-3}	0.022	5.7×10^{-4}	0.190	7.1×10^{-5}	0.071	0.261	
L9	2.3×10^{-3}	0.008	2.3×10^{-3}	0.008	4.6×10^{-4}	0.153	5.6×10^{-5}	0.056	0.209	
L10	1.0×10^{-3}	0.003	1.0×10^{-3}	0.003	3.8×10^{-4}	0.128	1.9×10^{-5}	0.019	0.147	
L11	$7.1 imes 10^{-4}$	0.002	7.1×10^{-4}	0.002	4.0×10^{-4}	0.132	2.3×10^{-5}	0.023	0.155	
L12	7.0×10^{-3}	0.023	7.0×10^{-3}	0.023	1.6×10^{-3}	0.518	4.5×10^{-5}	0.450	0.968	
L13	6.0×10^{-3}	0.020	6.0×10^{-3}	0.020	6.2×10^{-4}	0.208	7.4×10^{-5}	0.074	0.282	
L14	3.2×10^{-3}	0.011	3.2×10^{-3}	0.011	2.3×10^{-3}	0.768	6.1×10^{-5}	0.061	0.829	

 $^{a}H I = \Sigma HQ(Cr) + HQ(Cd)$

Pb, Cd, and Cr in lipsticks from Malaysia, USA, Korea, France, and the United Kingdom.

The HQ risk value for Fe in one lipstick sample was 2.707 and indicates the potential of an adverse effect to human health, but low risk. The HQ values for other elements were below 1, indicating an acceptable level and no significant toxic health risk for lipstick users. The order of severity of the heavy metal total health risk is Fe > Cr > Co > Cd > Cu > Ni ~ Zn > Mn. The HI values for all lipsticks were below 1, which suggested that none of the analyzed potential toxic elements may pose a health risk.

3. 6. Chemometric Techniques for Correlation Analysis

To understand the connection between lipstick samples and potentially toxic elements contents, chemometric

techniques PCA and CA were used. The obtained results for PCA are given in Fig. 1.

Two significant principal components are extracted based on the Kaiser criterion. 56 The first principal component (PC1) (with an eigenvalue of 10.51) explained 75.08% of the variance and the second principal component (PC2) (with an eigenvalue of 3.46) explained 24.72% of the variance. The first two PCs are enough to explain 99.80% of the pattern variation. Based on PCA, all potentially toxic elements have been classified in three fully separated groups. Iron is located on the negative side of PC1 and on the negative side of PC2 and it is a major contributor to PC1. Aluminum is located on the negative side of the PC1 and positive side of PC2 and it is a major contributor to PC2. Other elements (Sb, Cd, Cr, Co, Cu, Ni, Pb, Zn, Mn) are located on the positive side of PC1 and the near-zero values of PC2. Such grouping of elements is probably based on the origin of elements in lipstick. The most abundant element

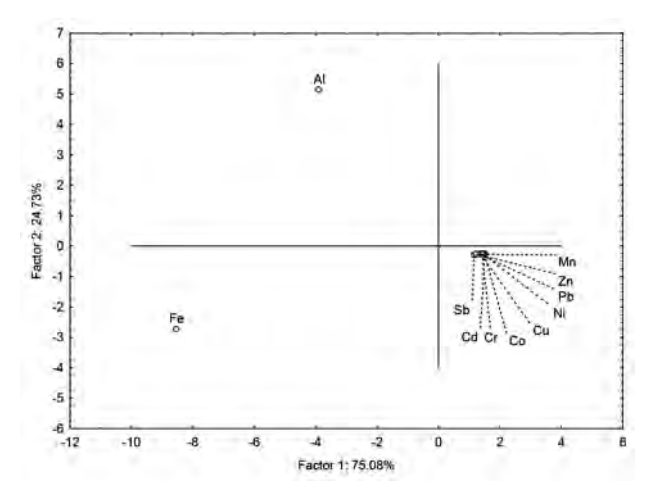


Figure 1. Principal component analysis of element contents in lipstick samples

in lipsticks is Fe, as a result of using metal-based pigments in color cosmetics such as orange, red, yellow, and black. Aluminum is the light metal and adds as a pigment in lipsticks. Other elements may be added as pigments or derivatives of oil such as mineral oils, paraffin, silicones. 9

Cluster analysis (CA), as a multivariate method, is also used to classify elements and lipsticks in clusters based on their similarities. 57,58 Ward's method with Euclidean distance was used to adopt measures. 58 The linkage distance was given as $D_{\rm link}/D_{\rm max}$, which represents the quotient between the linkage distances for a particular case divided by the maximal linkage distance. 57,58

The dendrogram of the cluster analysis of the analyzed elements is presented in Fig. 2 and shows three separated clusters at $(D_{link}/D_{max}) \times 100 < 50$.

The first cluster contained Fe, the second cluster contained Al and the third cluster involved Sb, Cd, Cr, Co, Cu, Ni, Pb, Zn, and Mn. It can be seen that the CA of the elements provided the identical grouping obtained on the basis of PCA.

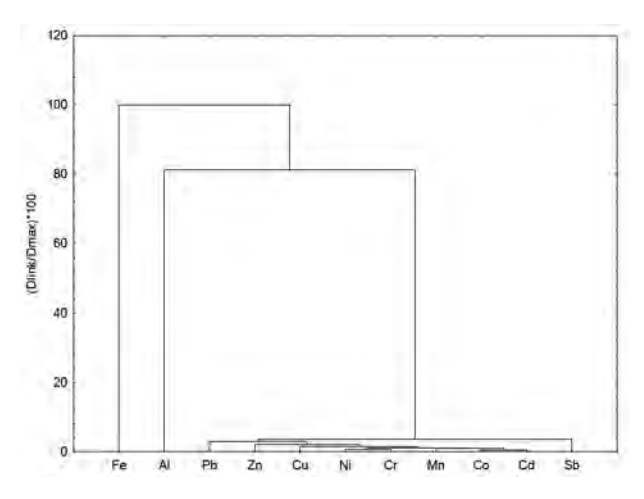


Figure 2. The dendrogram of the cluster analysis of elements based on their concentrations

The cluster analysis was applied to the analyzed samples using Ward's method, with Euclidian distances as the criterion for forming clusters of samples. Two separate clusters were obtained (Fig. 3).

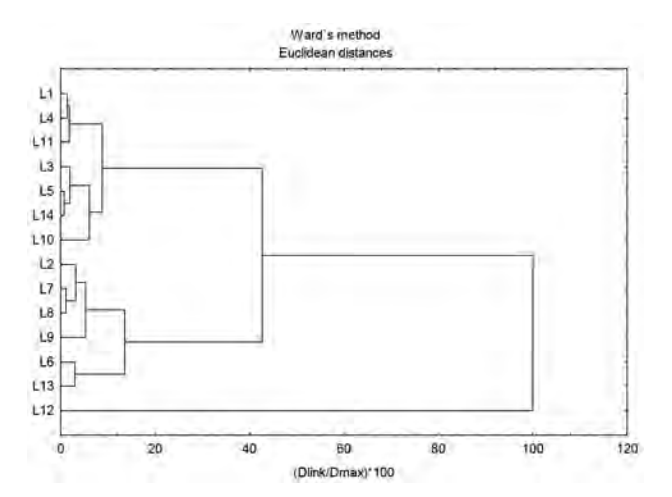


Figure 3. The dendrogram of the cluster analysis of lipsticks

The first cluster contained sample L12, which is the only one in brown color. The second cluster is divided into two sub-clusters. The first sub-cluster included samples L1 and L4 (88-Euclidean distances)/L11 which showed a close association with samples L5 and L14 (45-Euclidean distances)/L3 and L10. All lipsticks in this sub-cluster belong to category I regarding the price. The second sub-cluster included samples L7 and L8 (73-Euclidean distances)/L2 and sample L9 which showed a close association with samples L6 and L13 (185-Euclidean distances). All lipsticks in this sub-cluster belong to category II and III regarding the price.

4. Conclusion

The optimization and validation of the ICP OES method permitted an accurate and precise determination of Al, Cd, Cr, Co, Cu, Ni, Pb, Fe, Sb, Mn, and Zn in lipsticks. The recoveries for all elements in lipsticks were between 90% and 110%, except for Cd and Pb they were < 90% and > 110%, respectively. The element concentrations precision ranged from 0.3% to 4.9%. Lower RSD values were obtained for Zn, higher RSD values were obtained for Pb and Sb. Results for spike experiments in lipsticks have confirmed the suitability of the whole analytical procedure. In all samples, the concentrations of potentially toxic elements (Pb, Cd, and Cr) were within the level permitted in cosmetics. Only the sample L7 contained a higher concentration of lead compared to the acceptable and safe concentration given by the Health Canada and FDA (< 10 mg kg⁻¹), but lower than the permissible limit subscribed by German Federal Government (< 20 mg kg⁻¹) and EU

which banned lead. The concentrations of other potentially toxic elements did not exceed the permissible limits. The HQ and HI values for Co, Cu, Fe, Ni, Zn, Mn, Cr, and Cd were less than 1, except HQ value for Fe (HQ < 3). The obtained results indicate that there is no risk to human health. Based on the comparison of element concentration, the examined elements were classified into three groups by the PCA interpretation. The first group contains Fe, the second group includes Al and the third group contains the other analyzed elements (Sb, Cd, Cr, Co, Cu, Ni, Pb, Zn, and Mn). CA confirms the results obtained by PCA. The cluster analysis separated the analyzed samples into two clusters regarding the price and color.

5. Acknowledgments

This research was supported by grant No. 172047 from the Serbian Ministry of Education, Science and Environmental Protection.

6. References

- E. L. Sainio, R. Jolanki, E. Hakala, L. Kanerva, Contact Derma.
 2001, 42, 5–10. DOI:10.1034/j.1600-0536.2000.042001005.x
- G. J. Nohynek, E. Antignac, T. Re, H. Toutain, Toxicol. Appl. Pharmacol. 2010, 243, 239–259.
 - DOI:10.1016/j.taap.2009.12.001
- 3. K. Tomankova, K. Kejlova, S. Binder, A. Daskova, J. Zapletalova, H. Bendova, H. Kolarova, D. Jirova, *Toxicol. In Vitro.* **2011**, 25, 1242–1250. **DOI:**10.1016/j.tiv.2011.04.026
- R. F. Davies, G. A. Johnston, Clin. Dermatol. 2011, 29, 311–315. DOI:10.1016/j.clindermatol.2010.11.010
- S. Borowska, M. M. Brzóska, J. Appl. Toxicol. 2015, 35, 551–572. DOI:10.1002/jat.3129
- I. Al-Saleh, S. Al-Enazi, Toxicol. Environ. Chem. 2011, 93, 1149–1165. DOI:10.1080/02772248.2011.582040
- 7. M. G. Volpe, M. Nazzaro, R. Coppola, F. Rapuano, R. P. Aquino, *Microchem. J.* **2012**, *101*, 65–69.
 - DOI:10.1016/j.microc.2011.10.008
- H. Ullah, S. Noreen, Fozia, A. Rehman, A. Waseem, S. Zubair, M. Adnan, I. Ahmad, *Arab. J. Chem.* **2017**, *10*, 10–18.
 DOI:10.1016/j.arabjc.2013.09.021
- B. Bocca, A. Pino, A. Alimonti, G. Forte, Regul. Toxicol. Pharm. 2014, 68, 447–467. DOI:10.1016/j.yrtph.2014.02.003
- P. Piccinini, M. Piecha, S. F. Torrent, *J. Pharm. Biomed. Anal.* 2013, 76, 225–233. DOI:10.1016/j.jpba.2012.11.047
- P. Ziarati, S. Moghimi, S. Arbabi-Bidgoli, M. Qomi, *Int. J. Chem. Eng. Appl.* 2012, 6, 450–452.
 DOI:10.7763/IJCEA.2012.V3.241
- 12. A. Zakaria, Y. Bin Ho, Regul. Toxicol. Pharmacol. **2015**, 73, 191–195. **DOI:**10.1016/j.yrtph.2015.07.005
- É. F. Batista, A. dos Santos Augusto, E. R. Pereira-Filho, *Talanta* 2016, 150, 206–212.
 DOI:10.1016/j.talanta.2015.12.011

- C. F. Allenby, D. A. Basketter, Contact Dermat. 1993, 28, 129–133. DOI:10.1111/j.1600-0536.1993.tb03371.x
- D. A. Basketter, G. Briatico-Vangosa, W. Kaestner, C. Lally, W. J. Bontinck, *Contact Dermat.* 1993, 28, 15–25.
 DOI:10.1111/j.1600-0536.1993.tb03318.x
- 16. M. Hindsén, L. Persson, B. Gruvberger, *Contact Dermat.* **2005**, 53, 350–351. **DOI:**10.1111/j.0105-1873.2005.0592a.x
- 17. C. F. Allenby, B. F. Goodwin, *Contact Dermat.* **1983**, *9*, 491–499. **DOI**:10.1111/j.1600-0536.1983.tb04470.x
- D. A. Basketter, G. Angelini, A. Ingber, P. S. Kern, T. Menné, Contact Dermat. 2003, 49, 1–7.
 DOI:10.1111/i.0105-1873.2003.00149.x
- Campaign for Safe Cosmetics and the U.S. Food and Drug Administration (FDA), Lead in Lipstick, 2010 (accessed: April 02, 2018).
- 20. U.S. Food and Drug Administration, Lipstick and Lead: Questions and Answers, 2011, http://www.lb7.uscourts.gov/documents/110-cv-14073.pdf, (accessed: April 03, 2018).
- Health Canada, Consumer product safety Labelling of cosmetics, 2006, https://www.canada.ca/en/health-canada.html, (accessed: April 04, 2018).
- 22. Health Canada, Cosmetic Ingredient Hotlist, **2015**, https://www.canada.ca/content/dam/hc-sc/migration/hc-sc/cps-spc/alt_formats/pdf/cosmet-person/hot-list-critique/hotlist-liste-eng.pdf, (accessed: April 04, 2018).
- J. L. Todoli, L. Gras, V. Hernandis, J. Mora, J. Anal. Atom. Spectrom. 2002, 17, 142–169.

DOI:10.1039/B009570M

- 24. J. M. Mrmošanin, A. N. Pavlović, J. N. Krstić, S. S. Mitić, S. B. Tošić, M. B. Stojković, R. J. Micić, M. S. Đorđević, J. Food Comp. Anal. 2018, 67, 163–171.
 DOI:10.1016/j.jfca.2018.01.008
- M. Mitić, A. Pavlović, S. Tošić, P. Mašković, D. Kostić, S. Mitić, G. Kocić, J. Mašković, *Microchem. J.* 2018, 141, 197–203.
 DOI:10.1016/j.microc.2018.05.022
- 26. J. M. Mermet, Anal. Chim. Acta 1991, 250, 85–94. DOI:10.1016/0003-2670(91)85064-Y
- M. L. Salit, G. C. Turk, A. P. Lindstrum, T. A. Butler, C. M. Beck II, B. Norman, *Anal. Chem.* 2001, 73, 4821–4829.
 DOI:10.1021/ac0155097
- 28. US Food and Drug Administration, Guidelines for the Validation of Chemical Methods for the FDA Foods Program, Department of Health and Human Services, 2015, https://www.fda.gov/downloads/scienceresearch/fieldscience/ucm298730.pdf, (accessed April 14, 2018).
- K. E. Sharpless, J. B. Thomas, S. J. Christopher, R. R. Greenberg, L. C. Sander, M. M. Schantz, M. J. Welch, S. A. Wise, *Anal. Bioanal. Chem.* 2007, 389, 171–178.
 DOI:10.1007/s00216-007-1315-y
- 30. S. Chandran, S. P. Singh, Pharmazie 2007, 62, 4-14.
- R. M. Tripathi, R. Raghunath, T. M. Krishnamoorthy, *Sci. Total Environ.* 1997, 208, 149–159.
 DOI:10.1016/S0048-9697(97)00290-8
- US EPA, Exposure Factors Handbook: EPA/600/P-95/002F, Washington, DC: US Environmental Protection Agency, 1997.

03, 2018).

- 33. SCCP Scientific Committee on Consumer Products the SC-CP's Notes of Guidance for the Testing of Cosmetic Ingradients and Their Safety Evaluation, http://ec.europa.eu/health/scientific_committees/consumer_safety/docs/sccs_s_004.pdf, (accessed: April 21, 2018).
- 34. US EPA, Guidance for Performing Aggregate Exposure and Risk Assessments. Office of Pesticide Programs. Washington, DC: US Environmental Protection Agency, 1999.
- 35. US EPA, Integrated Risk Information System. Washington, DC: US Environmental Protection Agency, 2007.
- S. Khan, Q. Cao, Y. M. Zheng, Y. Z. Huang, Y. G. Zh, Environ. Pollut. 2008, 152, 686–692.
 - DOI:10.1016/j.envpol.2007.06.056
- J. N. Miller, J. C. Miller (Ed. 6th): Statistics and Chemometric for Analytical Chemistry, Pearson Education Limited, England. 2010.
- 38. W. Horwitz, *Anal. Chem.* **1982**, *54*, 67–76. **DOI:**10.1021/ac00238a002
- R. Wood, Trends Anal. Chem. 1999, 18, 624–632.
 DOI:10.1016/S0165-9936(99)00150-8
- M. Thompson, The amazing Horwitz function, http://www.rsc.org/images/horwitz-function-technicalbrief-17_tcm18-214859.pdf; (accessed: April 13, 2018).
- A. G. Gonzalez, M. A. Herrador, Trends Anal. Chem. 2007, 26, 227–238. DOI:10.1016/j.trac.2007.01.009
- 42. AOAC International, Method Validation Program (OMA/ PVM Department), including Appendix D: Guidelines for collaborative study procedures to validate characteristics of a method of analysis, AOAC International, Rockville, MD, 2000.
- S. Liu, K. Hammond, A. Rojas-Cheatham, Envin. Health Perspect. 2013, 121, 705–710. DOI:10.1289/ehp.1205518
- 44. M. A. Al-Qutob, H. M. Alatrash, S. Abol-Ola, *AES Bioflux* **2013**, *5*, 287–293.
- Regulation (EC) No 1223/2009 of the European parliament and of the council on cosmetic products, Official Journal of the European Union, 2009,
 - http://eur-lex.europa.eu/legal-content/EN/TXT/?uri=CEL-EX:32009R1223, (accessed: April 21, 2018).
- 46. Federal Food, Drug, and Cosmetic Act (FD&C Act sec. 721; 21 U.S.C. 379), https://www.fda.gov/ForIndustry/ColorAdditives/ColorAdditivesinSpecificProducts/InCosmetics/ ucm110032.htm, (accessed: April 27, 2018).

- 47. Health Canada, Guidance on Heavy Metal Impurities in Cosmetics, 2012, http://www.hc-sc.gc.ca/cps-spc/pubs/indust/heavy_metals-metaux_lourds/index-eng.php.2012, (accessed: April 07, 2018).
- 48. Bundesinstitut für Risikobewertung (BfR), Kosmetische Mittel: BfR empfiehlt Schwermetallgehalte über Reinheitsanforderungen der Ausgangsstoffe zu regeln, Stellungnahme Nr. 025/2006, 2006, http://www.bfr.bund.de/cm/343/kosmetische_mittel_bfr_empfiehlt_schwermetallgehalte_ueber.pdf, (accessed: April
- EU Council Directive 76/768/EEC on the approximation of the laws of the Member States relating to cosmetic products, Official Journal of the European Union, 1976.
- 50. US EPA, Guidance Manual for Assessing Human Health Risks from Chemically Contaminated, Fish and Shellfish, EPA-503/8-89-00239, Washington, DC: US Environmental Protection Agency, 1989.
- US EPA, Integrated Risk Information System: Cadmium, CASRN 7440-43-9. Washington, DC: US Environmental Protection Agency, 1991.
- 52. US EPA, Integrated Risk Information System: Chromium, CASRN 18540-29-9. Washington, DC: US Environmental Protection Agency, 1998.
- US EPA, US Environmental Protection Agency, Guidelines for Carcinogen Risk Assessment, EPA/630/P-03/001F. Washington, DC: US Environmental Protection Agency, 2005.
- 54. US EPA, Regional Screening Level Table (RSL) for Chemical Contaminants at Superfund Sites, Washington, DC: US Environmental Protection Agency, **2011**.
- 55. US EPA, Integrated Risk Information System: Lead and Compounds (Inorganic). CASRN 7439-92-1. Washington, DC: US Environmental Protection Agency, 2004.
- 56. H. F. Kaiser, Educ. and Psychol. Meas. 1960, 20, 141–151. DOI:10.1177/001316446002000116
- R. A. Johnson, D. W. Wichern, (Ed. 6th) Applied multivariate statistical analysis, New Jersey, NJ: Pearson Prentice-Hall, 2007.
- 58. R. Reghunath, T. R. Sreedhara Murthy, B. R. Raghavan, *Water Research* **2002**, *36*, 2437–2442.

DOI:10.1016/S0043-1354(01)00490-0

Povzetek

Namen te študije je bil optimizirati in validirati metodo induktivno sklopljene plazme z optično emisijsko spektrometrijo (ICP OES) za hkratno določevanje enajstih potencialno strupenih elementov (Al, Cd, Cr, Co, Cu, Ni, Pb, Fe, Sb, Mn in Zn) v vzorcih rdečila za ustnice. Metodo smo evalvirali z uporabo metode standardnega dodatka. Izkoristki so bili za vse elemente v rdečilih med 90 % in 110 %, razen za Cd in Pb, za katera sta izkoristka bila <90 % in >110 %. Oceno zdravstvenega tveganja smo naredili z izračunom povprečnega dnevnega vnosa (ADD), kvocienta tveganja (HQ) in indeksa tveganja (HI). Najvišja povprečna vrednost za ADD je bila za Fe $(4,8 \times 10^{-1} \text{ mg kg}^{-1} \text{ dan}^{-1})$ in najnižja za Co $(9,3 \times 10^{-6} \text{ mg kg}^{-1} \text{ dan}^{-1})$. Za nobenega od elementov nismo ugotovili pomembnejšega zdravstvenega tveganja (HQ < 1), razen za Fe (HQ < 3), kar kaže na potencialno zdravstveno tveganje. Glede na PCA smo vse potencialno strupene elemente klasificirali v tri skupine. V prvi skupini je Fe, v drugi je Al, vsi ostali elementi pa so v tretji skupini. Analiza skupkov (CA) je za elemente pokazala enako grupiranje, kot je bilo opaženo s PCA. Če smo CA uporabili za analizirane vzorce, smo opazili dva ločena skupka. Prvi skupek je vseboval samo en vzorec, ki je bil rjave barve. Drugi skupek se je delil na dva podskupka. Prvi podskupek je vseboval vzorce iz kategorije I glede na ceno, drugi podskupek pa vzorce iz kategorij II in III glede na ceno.



Except when otherwise noted, articles in this journal are published under the terms and conditions of the Creative Commons Attribution 4.0 International License



Scientific paper

Determination of Iron in Environmental Water Samples by FIA-TLS

Gaja Tomsič, ¹ Leja Goljat, ¹ Hana Budasheva, ¹ Dorota Korte^{1,*} Arne Bratkič ² and Mladen Franko¹

¹ University of Nova Gorica, Laboratory for Environmental and Life Sciences, Vipavska 13, SI-5000 Nova Gorica, Slovenia

² Vrije Universiteit Brussel, Boulevard de la Plaine 2, 1050 Ixelles, Bruxelles, Belgium

* Corresponding author: E-mail: Dorota.Korte@ung.si

Received: 10-30-2018

Presented at the 24th Annual Meeting of the Slovenian Chemical Society

Abstract

The determination of low concentration of iron in natural waters can be difficult due to the complexity of natural water, but primarily because it requires preconcentration of the sample with solvent extraction. In this work we report on results of thermal lens spectrometry (TLS) coupled to flow injection analysis (FIA) as a highly sensitive FIA-TLS method of iron detection. The concentration of iron redox species was determined using 1,10-phenanthroline (PHN), that forms stable complexes with Fe(II) ions which are characterized by an absorption maximum at 508 nm. The TLS system using a 633 nm probe laser and 530 nm pump laser beam was exploited for on-line detection in flow injection analysis, where a PHN solution was used as the carrier solution for FIA. The concentration of the complexing agent affects the quality of the TLS signal, and the optimal concentration was found at 1 mM PHN. The achieved limits of detection (LODs) for Fe(II) and total iron were 33 nM for Fe(II) and 21 nM for total iron concentration. The method was further validated by determining the linear concentration range, specificity in terms of analytical yield and by determining concentration of iron in a water sample from a local water stream.

Keywords: Flow injection analysis; iron concentration; thermal lens spectrometry

1. Introduction

As the fourth most frequent element in the earth's crust, iron is a geologically important element. As a trace element iron is also present in the biosphere in organisms, where it performs key life functions.

Iron can be found in various forms in water: as dissolved, colloidal or particulate, either in the elemental form or in bivalent or trivalent ion forms, and in complexes. The abundance of each species depends on the pH and Eh values of the aquatic environment. The oxidation state of iron affects the properties of the species, mobility and accessibility to organisms. At pH around 8, iron can be found as Fe(II) and Fe(OH)₃. In the reductive conditions, the prevalent oxidation state is the divalent ion form Fe(II), which is soluble in water. In oxidative conditions, however, Fe(II) is oxidized to Fe(III). It forms insoluble hydroxides, Fe(OH)₃. Due to this phenomenon, the concentration of iron in natural water is very low.

In fresh waters as rivers, lakes, groundwater and drinking water, iron is found at trace amounts. Compared with seawater, fresh water is richer in Fe(II) ions. Iron concentrations in fresh water can vary greatly depending on the source of water, its tributaries and other external circumstances. The World Health Organization, which operates within the United Nations, reports that the average iron concentration in rivers is around 14 μM.² In anaerobic conditions, iron concentrations may be higher, between 9–190 μM. The highest possible values may reach up to 893 µM. In drinking water iron concentrations are usually lower, less than 5 µM. In Slovenian rivers, the concentration of soluble iron species reaches up to 13 μM.³ The lowest concentrations are lower than the limit of quantification of methods nowadays widely used as colorimetric analysis with UV-VIS detection, atomic absorption spectroscopy, chemiluminescence. In groundwater iron concentrations are significantly lower than the concentrations measured in rivers.⁴ Generally, the concentrations of iron in groundwater are below 0.2 μ M, but sometimes can be even lower than 2 nM. As a result, lower concentrations of iron are also found in drinking water. The limit value of iron in drinking water is 4 μ M, ⁵ but this value is rarely exceeded, as iron concentrations in surface waters exploited as drinking water sources reach only up to 0.7 μ M, with a mean value of about 0.2 μ M.

In certain ocean areas dissolved iron concentrations can be as low as $20{\text -}30$ pM, so that iron represents a limiting factor in the growth of microorganisms. ⁷⁻¹¹ It was observed that already at 1.3 nM concentration of iron in water or lower, the growth of biomass is slowing down. ¹¹

Without the environmentally available iron marine and freshwater organisms cannot perform their metabolic functions, since iron participates in the photosynthetic process, cellular respiration, nitrate reduction and the synthesis of chlorophyll. The content of iron in the aquatic environment, even if it is usually low, therefore, affects the functioning of organisms, as it enables or impedes their growth. This can have an impact on the entire ecosystem. The amount of algae in marine waters can play an important role in the fixation of atmospheric carbon dioxide in sea biomass. Consequently, the increased biomass growth and photosynthesis reduces the amount of carbon dioxide in the atmosphere, which represents an important sink for this greenhouse gas.

In order to assess the status of an aquatic system, one of the key data that must be at disposal is the bioavailability of iron. Chemical analysis of natural water is a challenging task. UV-VIS spectrometry is a technique often used to determine the concentration of iron species in liquid samples after the complexation with 1,10-phenanthroline (PHN) and formation of an orange-coloured complex. This is a simple method, yet it has a major disadvantage, i.e. the limited sensitivity. Measurement of very low iron concentrations by UV-VIS is therefore impeded. For this reason, a number of other techniques for determining iron concentration in water samples were developed. The methods are as flow injection analysis coupled with spectrophotometric detection and on line preconcentration using a column filled with 8-hydroxyquinoline resin¹³ or inductively coupled plasma mass spectrometry,14,15 laser-induced breakdown spectroscopy,16 flow injection chemiluminometric method¹⁷ and for lowest concentrations rely on preconcentration. In all cases, the aim is to maximize the sensitivity of the technique while simultaneously simplifying the system. The method should be user-friendly and inexpensive, but must provide reliability, high sensitivity and good repeatability. Furthermore, an increasing emphasis is nowadays put on environmental protection by developing methods that use as little harmful chemicals as possible. Recently, TLS which is known as one of the most sensitive spectrometric methods for the analysis of liquid samples, and enables detection of absorbances as low as 10⁻⁷ absorption units, 18 was developed and optimized to provide a high throughput platform for highly sensitive

and environmentally friendly analysis of water and other samples.¹⁹

The main aim of this study was to develop an efficient, fast and reliable method for determination of low concentrations of iron species in natural water based on TLS technique coupled to flow injection analysis (FIA). The performances of FIA-TLS technique (LOD, linear range, specificity) were evaluated and the achieved LODs were compared to UV-VIS spectrometry, after establishing the optimal conditions for FIA-TLS determination of Fe(II) and Fe(III) species.

2. Experimental

2. 1. Reagents and Solutions

Double deionized ultrapure Milli-Q-water (MQ) water (18 $M\Omega$ cm $^{-1}$) was used for preparation of the initial solutions and for their dilution. The MQ water was obtained with the NANOpure double deionization system (Barnstead, Thermo Scientific). The following chemicals were used without further purification:

- Hydrochloric acid, HCl (*p.a.*, 32%, Carlo Erba reagents)
- Acetic acid, CH₃COOH (puriss. p.a., ≥ 99,8%, Sigma-Aldrich)
- Ascorbic acid, C₆H₈O₆ (reagent grade, 99%, Sigma)
- 1,10-phenanthroline (reagent grade, 99%, Alfa Aesar)
- Ferrous sulphate heptahydrate, FeSO₄ · 7H₂O (ACS grade, 99,5%, Merck)
- Ferric chloride hexahydrate, FeCl₃·6H₂O (*puriss*. p.a., ≥ 99.5%, Riedel-de Haën)

Iron detection was enabled by a colorimetric reaction with PHN, that binds Fe(II) ions and forms a stable $[Fe(PHN)_3]^{2+}$ complex with an absorption maximum at 508 nm. The total iron was determined by reducing Fe(III) ions to Fe(II) in the presence of ascorbic acid, since only the redox form of Fe(II) can form a $[Fe(PHN)_3]^{2+}$.

For the UV-VIS spectrophotometric measurements all the working standard solutions (5-100 $\mu M)$ were prepared by adding 1 mL of 30 mM PHN solution to the corresponding volume of the stock standard solution of 0.01 M Fe(II), and diluting to 10 mL by deionised water in a volumetric flask. 1 mL of 0.03 mM solution of ascorbic acid was added to the solutions containing Fe(III) ions before adding 30 mM PHN.

For the FIA-TLS measurements the working standard solutions were prepared in the range of 1–20 μM by proper dillution of stock standard solution by deionized $H_2O.$ 1 mM PHN solution, which was made 0.03 mM with respect to ascorbic acid to reduce Fe(III) was used as carrier solution for Fe determination. In optimization experiments the PHN concentrations from 30 mM to 0.5 mM were tested.

The pH of analysed solutions was found to be in the optimum pH range for the complexation reaction (between 6 and 9), thus, did not required further adjustment.

The analysed real samples were water samples from Vrtojbica creek. The samples were measured as collected without any pre-treatment.

2. 2. Measurement Techniques

2. 2. 1. UV-VIS Spectrophotometry

The PerkinElmer Lambda 650 S UV-VIS dual beam spectrometer was used to measure the absorbances of working standard solutions and for recording the absorption spectra, in the wavelengths' range between 400 nm and 650 nm. All measurements were performed in a 10 mm optical path quartz cuvette (HELLMA, model 100-QS) with respect to blank solution, that contained all added reagents to the working standard solutions except for iron.

2. 2. 2. Thermal Lens Spectrometry with Flow Injection Analysis

The scheme of the FIA-TLS experimental setup is shown in Figure 1. The sample is irradiated by laser light from Innova 70 Coherent Ar-ion laser with output wavelength of 514.5 nm, providing 150 mW power at the sample (excitation beam, EB). EB is modulated using a mechanical modulator (Scitec instruments, Control unit model 300C, chopping head model 300CD, chopping disks model 300H). The selected frequency was 30 Hz, as this ensured the maximum signal-to-noise ratio (for frequencies ≤ 10 Hz the mechanical chopper did not provide stable modulation frequency). The absorbed energy is converted into heat and as a result, the refractive index of the sample is changed, and a thermal lens (TL) is formed in the sample. The TL is detected by the use of another laser beam - the probe beam (PB) from a He-Ne laser (Uniphase, Model 1103P) with output wavelength of 633 nm and output power of 2 mW. PB is defocused by TL resulting and its intensity change is measured by a photodiode (Thorlabs, model PDA 36A-EC) and converted into voltage registered by the lock-in voltage amplifier (Stanford Research Instruments, the SR830 DSP model) and collected by Mathlab software. The recorded change in the PB intensity depends linearly on the concentration of absorbing species in the sample.

The flow injection unit (FIA) consisted of an HPLC pump (Knauer Advanced Scientific Instruments) used to deliver the carrier solution (PHN) and the sample to the detection cell. The working standard solutions and the sample (different concentration of iron ions) are injected through the metal free injection valve (RHEODYNE, model 7725) equipped with a 10 μ L peek sample loop (CHEMINERT, VICI). The carrier solution flow rate of 0.6 mL min⁻¹ is used and the TLS detection is performed in a

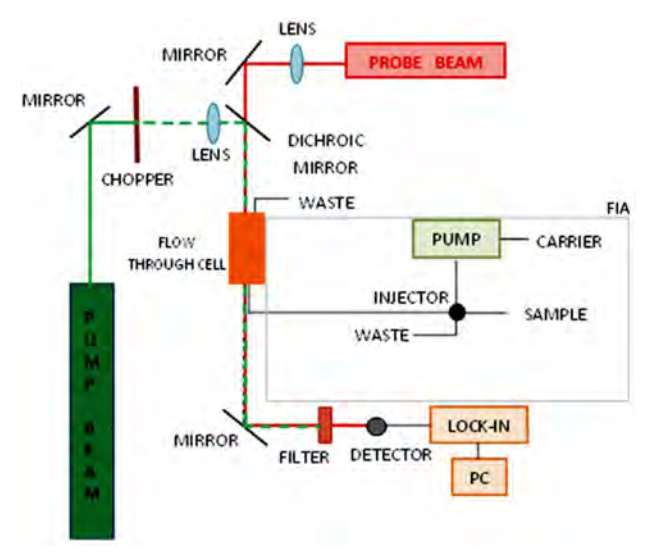


Figure 1. Scheme of the FIA-TLS experimental setup adopted from [20]

10 mm pathlength (8 μ L) flow through detection cell (HELLMA, model 178.173-QS) in which the TL was induced upon irradiation by the EB.

3. Results and Discussion

3. 1. UV-VIS Spectrophotometry

In the first step the absorption spectra of $[Fe(PHN)_3]^{2+}$ solutions were recorded at different concentrations of the complex (Figure 2). The absorption maximum was found at 508 nm.

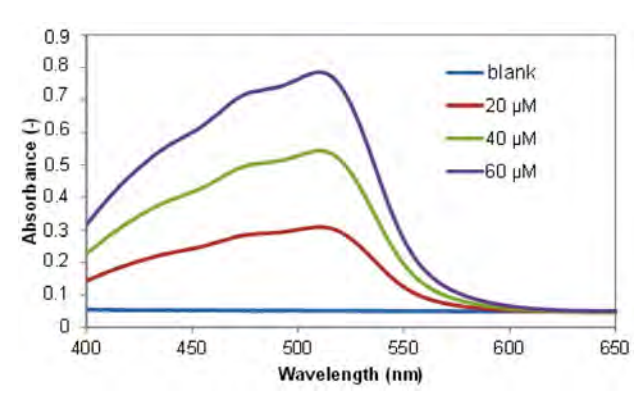


Figure 2. Absorption spectra of $[Fe(PHN)_3]^{2+}$ complex for different Fe(II) concentration

Next, the calibration curves for Fe(II) and Fe(III) determination were constructed in the 5 μ M-100 μ M concentration range (Figure 3).

The obtained relationship between absorbance and concentration shows good linearity ($R^2 > 0.995$) over the investigated concentration range (0 to 100 μ M) for Fe(II) and Fe(III) ions (Figure 3). The limit of detection (LOD) is calculated as the concentration giving a signal that is three

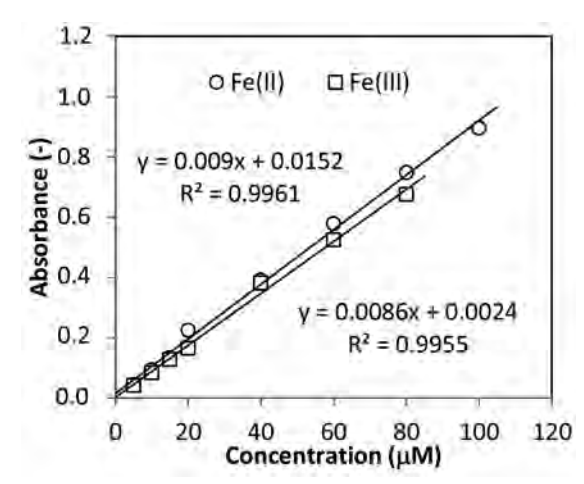


Figure 3. Calibration curves for Fe(II) and Fe(III) determination by UV-VIS spectrophotometry

times larger than the standard deviation of blank signal (Equation 1).

$$LOD = \frac{3*SD_0}{k},\tag{1}$$

Where LOD is the limit of detection, SD_0 standard deviation of blank signal and k the slope of the calibration line.

The calculated LODs were 130 nM for Fe(II) and 135 nM for Fe(total). The concentration of total iron was determined on the basis of calibration line for Fe(II), since Fe(III) was reduced to Fe(II) by ascorbic acid. The concentration of Fe(III) was then calculated as difference between the concentration of total iron and Fe(II).

3. 2. Thermal Lens Spectrometry with Flow Injection Analysis

Different concentration of the complexing agent (PHN) in the carrier were examined in the study. In case of 30 mM PHN solution (as used for the measurement by UV-VIS spectrophotometry) incomplete mixing of the

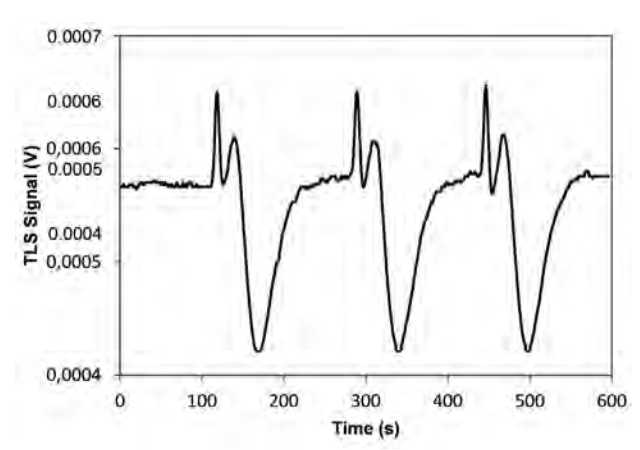


Figure 4. The shape of FIA-TLS signal peaks for 30 mM PHN used as a carrier solution

carrier and sample solutions was observed in the form of disturbance in the signal peaks which are the consequence of inhomogeneous refractive index of solution in the mixing area (Figure 4).²¹

As the problem could not be solved using a mixing coil between the injector and the sample cell, the concentration of PHN in the carrier solution was reduced to make the carrier and sample solutions as similar as possible in their composition. Thus, the PHN concentration was reduced from 30 mM to 10 mM, 5 mM, 2 mM, 1 mM and 0,5 mM.

The changes in shape of FIA-TLS signal peaks are presented in Figure 5. It is observed, that with decrease in PHN concentration the mixing problems disappear, but the height of the measured signal peak also decreases. This is related to the fact that in the case of lower reactant concentrations the reaction rate decreases, which means that in the same time interval not all Fe(II) ions are complexed by PHN to form [Fe(PHN)₃]²⁺ complex. At concentrations of PHN as low as 0.5 mM, the value of the TLS signal at its peak is 3.5 times lower compared to 2 mM PHN.

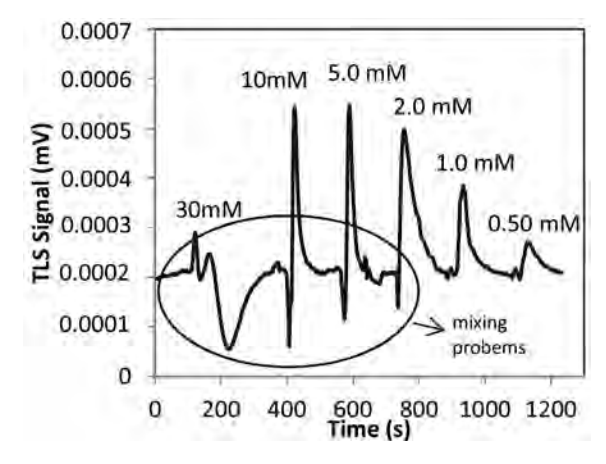


Figure 5. The shape of TLS signal peaks for different concentrations of PHN in carrier solution

Figure 5 shows, that for 1.0 and 0.5 mM PHN-related peaks mixing of the carrier and the sample have no significant effect on the peak heights, as there is no sharp decrease of the TLS signal before the peak, as observed at higher PHN concentrations. In these two cases the concentration of PHN is sufficiently low to provide similar composition of carrier solution and the sample in terms of refractive index. Unfortunately, as it is seen in Figure 5, the decrease of the TLS signal peak heights at lower PHN concentrations in the carrier decreases the sensitivity and increases the LOD of the method.

Thus, for FIA-TLS measurements, 1 mM was chosen as the optimal PHN concentration in the carrier solution, since it provided the highest sensitivity among tested carrier solutions and conditions where no effects on TLS signal due to mixing problems were observed. The peaks of TLS signal for Fe(II) and Fe(III) for 1 mM PHN solution

used as carrier are shown in Figures 6 and 7, respectively. The constructed calibration lines for Fe(II) and Fe(III) concentration are presented in Figure 8. Good agreement of the slopes confirms that the reduction of Fe(III) is quantitative under given experimental conditions.

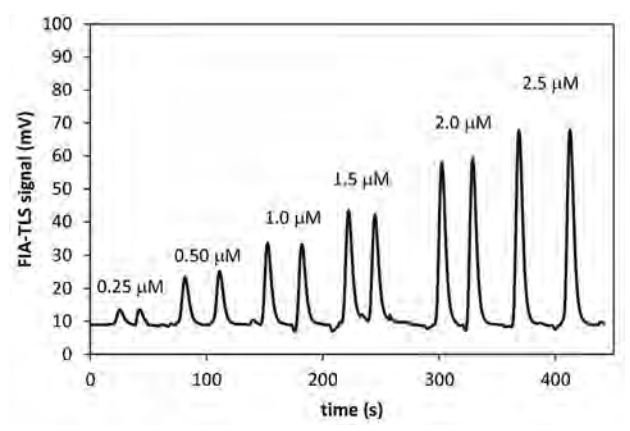


Figure 6. The TLS signal peaks of Fe(II) with 1 mM PHN as carrier solution

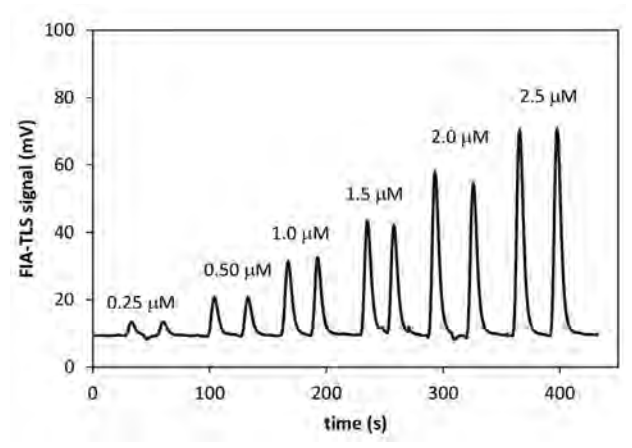


Figure 7. The TLS signal peaks of Fe(III) with 1 mM PHN as carrier solution

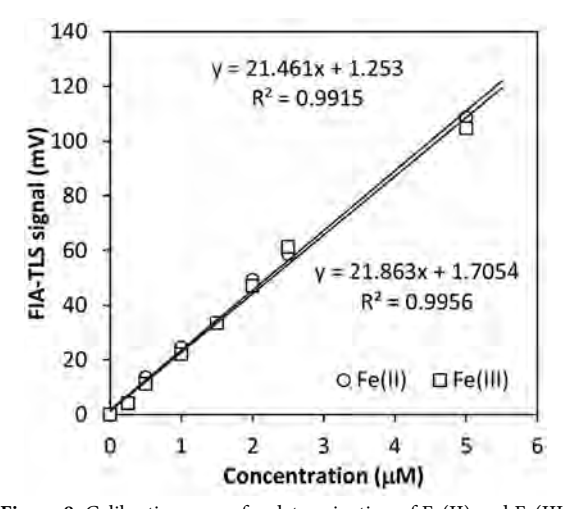


Figure 8. Calibration curve for determination of Fe(II) and Fe(III) by FIA-TLS with 1 mM PHN as carrier solution

The linear range of the method (defined as the range of independent variable for which strong linear relationship exists between the iron concentration and the FIA-TLS signal) is between 0.2–5 μ M for Fe(II) and 0.2–2.5 μ M for Fe(III) and the calculated LODs were 15 nM and 13 nM for Fe(II) and Fe(total), respectively.

The effect of PHN concentration on the sensitivity of the FIA-TLS method was investigated further by performing the complexation reaction off-line and using just water as the carrier. In this case final dilution was made to 50 mL and 30 mM PHN could be used as reagent added to the sample. The final concentration of PHN in the sample was therefore similar (0.6 mM) as used in the carrier in case of FIA-TLS to avoid mixing problems. As can be seen on Figure 9, no distortions of the peaks due to mixing are observed. Figure 9 also shows significant difference in sensitivity, as can be deduced by comparison of TLS signal peak heights to those recorded in case of FIA-TLS with on-line complexation reaction (Figures 6 and 7), which is in fact five times lower due to use of lower PHN concentration. LODs of 3 nM were achieved for Fe(II) and Fe(total) by of-line complexation of Fe(II) and TLS detection in FIA mode.

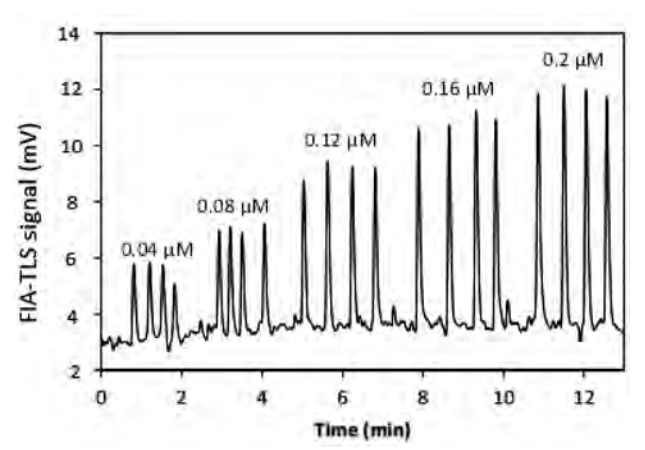


Figure 9. FIA-TLS signals for replicate injections of [Fe(PHN)₃]²⁺at different concentrations

To verify the method, concentration of iron species in real samples was determined by standard addition method. The examined sample was the water from Vrto-jbica creek, which was spiked by Fe(II) standard (for determination of Fe(II)) or by Fe(III) standard (for determination of Fe(total)) solutions at 0.5 μ M, 1 μ M, 2 μ M, 3 μ M and 4 μ M levels. Figure 10 shows the FIA-TLS signals for original water sample and signals for samples with different standard additions of Fe(III). The complexity of the medium affected the limit of detection, which was 373 nM for Fe(II) and 314 nM for Fe(III) determination. This is approximately 25 times higher than for the Fe(II) and Fe(III) in deionized water.

Vrtojbica creek contained 1.43 μM \pm 0.15 μM Fe(II), which corresponds to 80 $\mu g/L$ \pm 8 $\mu g/L$, as well as 1.90 μM

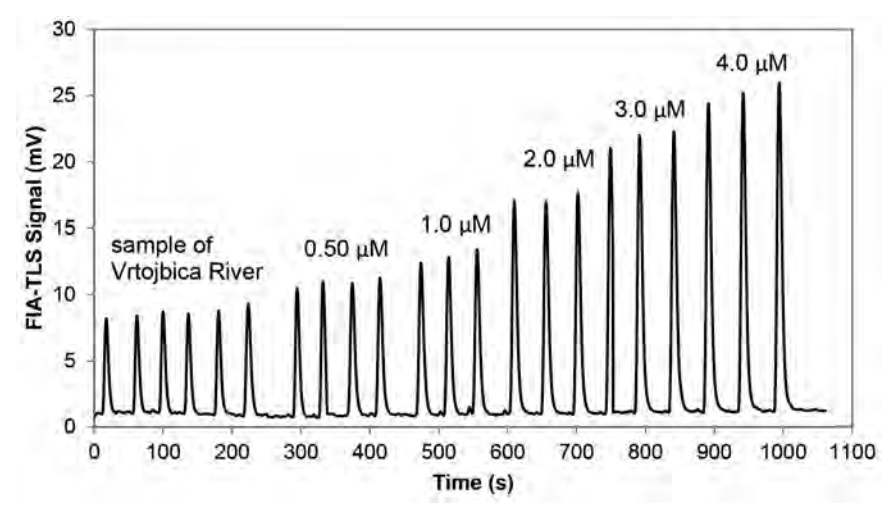


Figure 10. The TLS signal peaks of Vrtojbica creek with added proper amount of Fe(III) and 1 mM PHN as carrier solution

 \pm 0.12 μM total iron, which corresponds to 106 $\mu g/L \pm 7$ $\mu g/L$. From the subtraction of the concentration of Fe(II) from the measured value of total iron concentration, the concentration of Fe(III) was found to be 26 $\mu g/L \pm 8$ $\mu g/L$.

These results correspond within the measurements uncertainty to those determined by external calibration.

In the next step the analytical yield of the method was determined as a ratio of the measured and actually added concentration of the analyte in the examined sample solution. The results are presented in Table 1.

Table 1. The analytical yield of the FIA-TLS method for determination of total iron added as Fe(III)

Added concentration (µM)	Measured concentration (μM)	SD (µM)	Yield (%)
1.0	1.02	0.20	102 ± 10
5.0	4.37	0.28	88 ± 5
0.50	0.55	0.07	110 ± 3
3.0	3.16	0.15	105 ± 3

The results show, that the analytical yield of the method is satisfactory and in agreement with US-EPA recommendations for acceptable analytical yields in the range of 80-120% for determination of metals and trace elements in water. ²²

The results obtained by the use of FIA-TLS technique were compared to those obtained by UV-VIS spectropho-

Table 2. Comparison of LODs for determination of Fe(II) and Fe(I-II) by FIA-TLS and UV-VIS spectrophotometry

	Fe(II)	Fe(III)	
UV-VIS	130 nM	135 nM	
FIA-TLS	15 nM	13 nM	

tometry. The value of LODs achieved by these two methods are compared in Table 2. The LODs achieved by FIA-TLS are up to 10 times lower than those achieved by UV-VIS spectrophotometry.

4. Conclusion

In this study iron redox species concentration was determined by thermal lens spectrometry coupled to flow injection analysis (FIA-TLS).

The technique was optimised regarding the concentration of the complexing agent used as the carrier solution. The optimal concentration of PHN is 1 mM, as in this way we avoid mixing problems between the sample solution and the carrier.

Furthermore, the use of the FIA-TLS method significantly reduces the amount of sample consumption. By using UV-VIS spectrophotometry approximately 3 mL of the sample was used for the final measurement, while with FIA-TLS the amount was 20 μ L, what is 150 times lower.

The achieved LOD is much lower compared to those achieved for spectrophotometric method (1.07 uM; in 10 cm long sample cell), thermal lens microscopy (TLM) in batch mode (0.01uM) and compared to values achieved by TLM-uFIA (36 nM). $^{\rm 23-24}$

The applicability of FIA-TLS technique was verified by determining iron species concentrations in a real freshwater sample from Vrtojbica creek. The concentration of iron in Vrtojbica creek was determined by the standard addition method. It was found, that Vrtojbica creek contains 80 μ g/L of Fe(II) and 26 μ g/L of Fe(III). The total iron content was therefore 106 μ g/L, which fully corresponds to the values of iron in Slovenian water streams, that range from less than 1 μ g/L to 750 μ g/L.

On the basis of the presented results it was it can be concluded that the optimized FIA-TLS technique has several advantages over other methods used for determination of metals in liquid samples. These are in particular high sensitivity and low LODs without the need of sample preconcentration, low consumption of reagents and online detection, consequently reducing also the possible contamination.

5. References

- Rich, H. W., Morel, F. M. M., Limnol. Oceanogr. 1990, 35, 652–662. DOI:10.4319/lo.1990.35.3.0652
- WHO. 2003. Iron in Drinking-water; Background document for development of WHO Guidelines for Drinking-water Quality. Geneva.
- 3. ARSO. 2017. Reke- izpis podatkov za leto 2017.
- 4. ARSO. 2017. Podzemne vode- izpisi podatkov za leto 2017.
- 5. Uradni list RS, Št 19/2004. 2004. Pravilnik o pitni vodi.
- ARSO. 2017. Površinske vode, ki se odvzemajo za oskrbo s pitno vodo.
- Kuma, K. Biogeochemistry of iron in seawater. Report on Amur-Okhotsk Project No.2, 2004.
- 8. Archer, D. E., Johnson, K., *Global Biogeochem. cycles.* **2000**, 14, 269–279. **DOI**:10.1029/1999GB900053
- Anderson, M. A., Morel, F. M. M., Limnol. Oceanogr. 1982, 27, 789–813. DOI:10.4319/lo.1982.27.5.0789
- Wells, M. L., Price, N. M., Bruland, K. W., Mar. Chem. 1995, 48, 157–182. DOI:10.1016/0304-4203(94)00055-I
- 11. Boye, M., van den Berg, C. M. G., *Mar. Chem.* **2000**, *70*, 277-287. **DOI**:10.1016/S0304-4203(00)00032-3
- Kinnan, M. K. Determination of Iron(II) Concentrations in Seawater Using Flow Injection Analysis and Chemiluminescence. University of North Florida. 2003.

- Laës, A., Vuillemin, R., Leilde, B., Sarthou, G., Bournot-Marec, C., Blain, S., *Mar. Chem.* 2005, 97, 347–356.
 DOI:10.1016/j.marchem.2005.06.002
- de Jong, J., Schoemann, V., Lannuzel, D., Tison, J., Mattielli, N., *Anal. Chim. Acta.* 2008, 623, 126–139.
 DOI:10.1016/j.aca.2008.06.013
- Milne, A., Landing, W., Bizimis, M., Morton, P., Anal. Chim. Acta. 2010, 665, 200–207. DOI:10.1016/j.aca.2010.03.027
- Nakamura, S., Ito, Y., Sone, K., Hiraga, H., Kaneko, K., Anal. Chem. 1996, 68(17) 2981–2986. DOI:10.1021/ac9601167
- Worsfold, P. J., Lohan, M. C., Ussher, S. J., Bowie, A. R., *Mar. Chem.* 2014, *166*, 25–35.
 DOI:10.1016/j.marchem.2014.08.009
- Franko, M., Tran, C. D., in: R.A. Meyers (Ed.): Encyclopedia of Analytical Chemistry, John Wiley & Sons Ltd., 2010.
- Liu, M., Malovrh, S., Franko, M., Anal. Methods 2016, 8, 5053–5060. DOI:10.1039/C6AY00932H
- 20. Korte, D., Grahovac, A., Jerkič, A., Vajdle, O., Anojčič, J., Guzsvany, V., Budič, B., Franko, M., *Pharm. Anal. Acta.* **2018**, 9, 1–10.
- Madžgalj, A., Baesso, M.L., Franko, M., Eur. Phys. J. Special Topics 2008, 153, 503–506.
 DOI:10.1140/epjst/e2008-00494-4
- 22. EPA, Guidance for Methods Development and Methods Validation for the Resource Conservation and Recovery Act (RCRA) Program, 2012.
- De Assis Gonsalves A., Melo Araujo C. R., Galhardo C. X., Fonseca Goulart M. O., De Abreu F. C., *Am. J. Anal. Chem.* 2011, 2, 776–782. DOI:10.4236/ajac.2011.27089
- Cabrera H. Korte D., Franko M., Int. J. Thermophys. 2015, 36, 2434–2439. DOI:10.1007/s10765-015-1933-0

Povzetek

Določevanje železa v naravnih vodah je pogosto oteženo zaradi nizkih koncentracij analita in kompleksnosti naravne vode, kar zahteva predkoncentracijo vzorca z ekstrakcijo. V tem delu poročamo o razvoju nove, visoko občutljive FIA-TLS metode za določevanje redoks specij železa brez predkoncentracije, ki temelji na uporabi spektrometrije s toplotnimi lečami (TLS), sklopljene s pretočno injekcijsko analizo (FIA). Koncentracije železa (Fe(II), Fe-skupno) smo določali po kolorimetrični reakciji z 1,10–fenantrolinom (PHN), ki kompleksira železove Fe(II) ione v stabilen kompleks z absorpcijskim maksimumom pri 508 nm. Spektrometer TLS s tipalnim laserskim snopom valovne dolžine 633 nm in vzbujevalnim laserskim snopom valovne dolžine 530 nm smo uporabili za detekcijo v sistemu FIA, kjer je nosilna raztopina vsebovala PHN, in pri določevanju skupnega železa tudi askorbinsko kislino za redukcijo Fe(III).

Visoka koncentracija PHN v nosilni raztopini (30 mM) negativno vpliva na višino in obliko TLS signalov za injicirane vzorce. Ugotovili smo, da je optimalna koncentracija PHN 1 mM in z njo dosegli meji zaznave (LOD) 33 nM za Fe(II) in 21 nM za skupno koncentracijo železa. Metodo smo validirali še z določitvijo linearnega koncentracijskega območja, specifičnosti v smislu analitskega izkoristka in z določitvijo koncentracije železa v vzorcu naravne površinske vode.



Except when otherwise noted, articles in this journal are published under the terms and conditions of the Creative Commons Attribution 4.0 International License



Scientific paper

Methodological Aspects of Extraction, Phytochemical Characterization and Molecular Docking Studies of *Salix caprea* L. Bark and Leaves

Emilia Gligorić, Ružica Igić, Ljiljana Suvajdžić, Branislava Teofilović, Maja Turk-Sekulić, and Nevena Grujić-Letić^{1,*}

¹ University of Novi Sad, Faculty of Medicine, Department of Pharmacy, Hajduk Veljkova 3, 21000 Novi Sad, Serbia

² University of Novi Sad, Faculty of Sciences, Department of Biology and Ecology, Trg Dositeja Obradovića 3, Novi Sad, Serbia

³ University of Novi Sad, Faculty of Technical Sciences, Department of Environmental Engineering and Safety at Work, Trg Dositeja Obradovića 6, Novi Sad, Serbia

> * Corresponding author: E-mail: nevena.grujic-letic@mf.uns.ac.rs Phone: +381 21 422 760 Fax: +381 21 422 760

> > Received: 10-30-2018

Abstract

Contents of twelve selected bioactive substances and antioxidant potential of *Salix caprea* L. extracts were compared in its two vegetative organs (bark and leaves) and in terms of different ethanol/water mixtures used for extraction (30–70% aq, ethanol) and extraction time (30 min; 24, 48 and 72 h). The extracts were characterized by High Pressure Liquid Chromatography (HPLC), and total phenolics and flavonoids were determined spectrophotometrically. All secondary metabolites identified in *Salix caprea* L. extracts (gallic, chlorogenic and vanillic acid, epicatechin, rutin, quercetin and naringenin) were found more accumulated in bark. Salicin and *p*-hydroxybenzoic acid were detected in bark and ferulic, *trans*-cinnamic and *p*-coumaric acid in leaves extracts only. Rutin was most abundant bioactive compound both in bark (1.71 g/100 g of de) and leaves extracts (0.434 g/100 g of de). Bark extract with highest bioactive substances contents was obtained with 70% aq. ethanol as most suitable solvent during extraction time of 48 h. Molecular docking showed salicin to have similar affinity toward COX-2 as acetylsalicylic acid, but lower toward COX-1.

Keywords: Extraction; HPLC; molecular docking; salicin; Salix caprea

1. Introduction

Willow bark (*Salix spp.*, Salicaceae) is traditionally used herbal remedy due to its anti-inflammatory, analgesic and antipyretic properties. Salicin is usually described as the analgesic agent found in willow bark, responsible for its pharmacological effects.^{1–3} However, it was suggested that many of these effects cannot be explained by the presence of salicylic derivatives only and that other compounds such as polyphenols (flavonoids, flavan-3-ols) and simple phenols (phenolic acids) can contribute to the therapeutic effects of willow bark.^{4–8} On the other hand, leaves of many Salix species are mainly not studied and are considered as waste product after collection of bark.

Genus Salix includes about 350 different, mainly woody species. Salix caprea is a common species of wil-

low native to Europe, Western and Central Asia and it is widely distributed in the flora of Serbia. It has been reported to exhibit strong antioxidant activity in many *in vitro* systems. ^{10,11}

Solvent extraction, i.e. solid-liquid extraction, is commonly used for the isolation of phenolic compounds from plant material. Extraction procedure and solvent selection are considered to be a critical point since they dictate the amount and nature of secondary metabolites transferred to extract. Some previous studies involving different plant material showed a great impact of solvent polarity and time of extraction on total extraction yield, antioxidant activity and bioactive compounds contents in final extracts. He than ol and water mixtures are commonly used solvents for herbal extractions as they can dissolve a wide range of phenolics and are also acceptable for

human consumption.¹⁸ By far mainly used solvents for the extraction of *Salix caprea* were 80% methanol for bark, 70% acetone for leaves, 95% ethanol for flowers and 95% acetone for wood and knots.^{12,19,20} There is no available data on testing the impact of different extraction conditions and solvent concentrations on total extraction yield, chemical composition and antioxidant activity of extracts obtained from bark and leaves of *Salix caprea* L. Thus, the objective of this study was to use different ethanol/water mixtures (30–70% aq, ethanol) for extraction of two vegetative organs of *Salix caprea* L. during extraction time of 30 min; 24, 48 and 72 h in order to gain extracts with the highest amount of target compounds.

COX-1 and COX-2 are two isoforms of cyclooxygenase which has a role in conversion of arachidonic acid to prostaglandins that are involved in inflammatory processes in human body. Salicin is considered to be main compound found in willow responsible for its analgesic and anti-inflammatory properties. Salicylic acid, which is released in body from salicin, is considered to have similar affinity toward COX-2 as acetylsalicylic acid. 21,22 Therefore, the secondary goal of this paper was to elucidate the interaction and binding affinity of salicin and COX-1 and COX-2 using molecular docking, an efficient tool to get an insight into ligand-receptor interactions. These molecular docking studies could be useful in better understanding of interactions between ligand and active sites of enzymes which is of great importance in aspect of designing a novel potent inhibitors.

2. Experimental

2. 1. Plant Material

Bark and leaf of *Salix caprea* L., Salicaceae were collected from locality of Vlasina Lake, Serbia in June 2013. The plant material was air-dried and stored at room temperature. Dried willow bark and leaves were ground in a mill and particle size diameter (d = 0.35 mm) was determined by sieve set (Retsch GmbH and Co KG).

2. 2. Chemicals

The following HPLC grade compounds were used as standards for analysis by HPLC-DAD: gallic acid (purity ≥97%), chlorogenic acid (purity ≥95%), ferulic acid (purity ≥99%), rutin (purity ≥94%), naringenin (purity ≥98%), p-hydroxybenzoic acid (purity ≥99%), vanillic acid (purity ≥97%), trans-cinnamic acid (purity ≥99%), epicatechin (purity ≥98%) purchased from Sigma Aldrich; p-coumaric acid (purity ≥98%) from Fluka; quercetin (purity ≥99%) from Extrasynthese and salicin (purity ≥90%) from Carl Roth. HPLC grade acetonitrile, methanol, o-phosphoric acid, tetrahydrofuran and acetic acid were obtained from J.T. Baker. Sodium carbonate and methanol (analytical grade) were purchased from

POCH, aluminium chloride from Sigma Aldrich. Folin-Ciocalteu (FC) reagent was obtained from Merck and 2,2-diphenyl-1-pycrylhydrazil (DPPH) from Alfa Aesar. Analytical grade EtOH was obtained from Zorka pharma. Distilled deionised water (dd $\rm H_2O$) was used throughout the experiments.

2. 3. Extraction Procedure

Ethanolic extracts were prepared as following: 0.5 g of plant material (bark/leaves) was extracted with 5 ml of aqueous ethanol (30%, 40%, 50%, 60% v/v) for 30 min, 24, 48 and 72 hours at room temperature (25 °C) and by method of maceration with 70% ethanol for 30 minutes to 72 hours at room temperature, according to the procedure given in EMA.²³ After maceration, the extracts were filtered, evaporated to dryness and left in exicator for 24 hours. After measuring the weight of dry extract, the extraction yield was calculated.

2. 4. Chemical Characterization by High Performance Liquid Chromatography (HPLC)

Chemical characterization of the obtained extracts and quantification of the selected compounds was carried out by applying HPLC method.²⁴ Agilent HP 1100 HPLC-diode array detection (DAD) system equipped with an autosampler was used. The components were separated using reversed-phase Zorbax CB-C18 column (4.6 × 150 mm, 5 µm particle size) held at 25 °C. Solvent A was 0.1% aqueous CH₃COOH and solvent B was 0.1% CH₃COOH in acetonitrile. The mobile phase used was delivered in gradient mode (3,25 min 10% B; 8 min 12% B; 15 min 25% B; 15,8 min 30% B; 25 min 90% B; 25,4 min 100% B), with flow rate of 1 mL/min. The HPLC mobile phase was prepared fresh daily and filtered through a 0.45 µm nylon filter. The injection volume was 15 µL. For the quantification of the selected compounds, standards (gallic acid, chlorogenic acid, ferulic acid, rutin, naringenin, p-hydroxybenzoic acid, vannilic acid, trans-cinnamic acid, epicatechin, p-coumaric acid, quercetin) dissolved in methanol, were run under the same conditions. UV detection was set at 280 nm.

Salicin was determined by a slightly modified HPLC method described earlier, 25 using Zorbax CB-C18 column (4.6 \times 150 mm, 5 μm particle size). For quantification of salicin, the standard was dissolved in methanol and run under the same conditions.

Phenolic compounds were identified by comparing their retention time and UV/Vis spectra with those obtained from standard compounds. For quantitative analysis, a calibration curve for each standard was constructed: gallic acid (y = 41245x - 466.1, $R^2 = 0.998$); chlorogenc acid (y = 13523x - 42.854, $R^2 = 0.998$), p-hydroxybenzoic acid (y = 22708x + 12.73, $R^2 = 0.999$); vanillic acid (y = 22708x + 12.73); vanillic acid (y = 22708x +

23028x + 53.27, $R^2 = 1$); epicatechin (y = 6269 x + 23.72, $R^2 = 0.999$); p-coumaric acid (y = 67213x - 75.38, $R^2 = 0.999$); rutin (y = 9921x - 70.05, $R^2 = 0.999$); ferulic acid (y = 41992x - 508.1, $R^2 = 0.999$); trans-cinnamic acid (y = 11200x + 69.55, $R^2 = 0.999$); quercetin (y = 19129x - 103.3, $R^2 = 0.999$); naringenin (y = 52671x - 770.6, $R^2 = 0.999$) and salicin (y = 1927x - 113.4, $R^2 = 0.995$). The results were expressed in g/100 g of dried extract.

2. 5. Antioxidant Activity - DPPH Assay

The DPPH-assay was performed as previously described. 26 Different volumes (10–100 µl) of samples, dissolved in methanol, were mixed with 1ml of 90 µM DPPH solution and made up with 95% methanol to a final volume of 4 ml. After 1 h at room temperature, absorbance of the resulting solutions and the control (same chemicals without sample) were measured spectrophotometrically at 515 nm (Agilent 8453 UV-Visible Spectroscopy System). Methanol was used as a blank. For each sample, the experiment was performed in triplicate. RSC, expressed as a percentage, was calculated by the following equation:

2. 6. Determination of Total Phenolics and Flavonoids Content

Total phenolics and flavonoids content were determined spectrophotometrically by Agilent 8453 UV-Visible Spectroscopy System. The amount of total phenolic compounds in the extracts was assessed using the method described before. The concentration of total phenolics was expressed as mg of gallic acid equivalents per g of dried extract, using a standard curve of gallic acid (y = 0.2559x + 0.3345). Measurement of the total flavonoid content in the obtained extracts was evaluated using the method based on formation of flavonoid-aluminium complex with the absorptivity maximum at 430 nm. The flavonoids content was expressed as mg of quercetin equivalents per g of dried extract, using a standard curve of quercetin (y = 0.0039x + 0.012). All measurements were performed in triplicate.

2. 7. Molecular Docking Studies

Chemical structures of ligand molecules used in this research were taken from PubChem database (http://pubchem.ncbi.nlm.nih.gov/). Three dimensional crystallographic structures of proteins COX-1 in complex with flurbiprofen (1CQE)²⁹ and COX-2 in complex with indomethacin (4COX)³⁰ were retrieved from Protein Data Bank (PDB) (http://www.rcsb.org/). Ligands, chains B, C, D and molecules of water were erased, polar hydrogen atoms added and parcial atomic charge was calculated by

Gasteiger method, using AutoDock Tools. The dimension of the grid box was 60×60×60 with distance of 0.375 Å between points. Molecular docking was conducted using AutoDock 4.2.3. program package, by Lamarckian Genetic Algorithm,³¹ with standard docking procedure for rigid receptor and flexible ligand, with 25 independent runs per ligand. Other parameters were set to default. Conformations of docked structures with the lowest binding energy were considered as the most favorable docking pose. Discovery Studio Visualizer 4.5. was used to visualize the results and produce the figures.

2. 8. Statistical Analysis

Statistical analyses were performed by SPSS, version 22. Results of extraction yield, total phenolics and flavonoids amount and antioxidant activity were analyzed using Student's t-test and one-way analysis of variance (ANOVA) to determine significant differences among samples with level of significance p < 0.05.

3. Results and Discussion

3. 1. Extraction Yield, Antioxidant Activity and Total Phenolics and Flavonoids

Effects of operating conditions (extraction time and solvent polarity) on extraction yield of leaves and bark of *Salix caprea* L. are shown in Table 1.

Yield of Salix caprea L. leaves extracts ranged from 12.47 to 20.94 g/100 g of drug and bark extracts from 9.49 to 16.77 g/100 g of drug. Yield of dry extract of both leaves and bark, increased by increasing extraction time, due to longer contact between plant material and solvent. In case of leaves, differences in extraction length are significant only in 50%, 60% and 70% ethanol extracts, whereas in ethanolic bark extracts there is statistically significant difference between each time interval. Considering solvent polarity, by increasing ethanol concentration from 30% to 70% (v/v), in case of bark, yield of dry extract increased, so the highest was achieved by 70% ethanol. In case of leaves, 40% ethanol as solvent was the most selective for obtaining the highest extraction yield. In terms of prolonged extraction time leading to increase of extraction yield, our results are in agreement with other similar researches. 14,15 Also, the results obtained for S. caprea leavesare in accordance with the results of mate tea extraction from an earlier study, which revealed that the highest yield was achieved by using a more polar solvent, particularly 40% aqueous ethanol, 16 as it was in case of S. caprea leaves as well.

The DPPH radical scavenging activity of the different extracts of bark and leaves of *Salix caprea* was assessed. Concentrations of extracts inhibiting 50% of DPPH radical (IC_{50}) are shown in Table 2.

Table 1. Effects of extraction solvent on extraction yield (g dry extract /100 g drug) of leaves and bark of Salix caprea

Drug	Extraction time	30% EtOH	40% EtOH	Extraction type 50% EtOH	60% EtOH	70% EtOH
Leaves	30 min 24h 48h 72h	$17.14 \pm 1.49 a^{a}$ $19.12 \pm 0.28 a^{a}$ $19.43 \pm 0.84 a^{a}$ $20.55 \pm 2.09 a^{a}$	$19.19 \pm 1.18 a^{a}$ $19.33 \pm 0.52 a^{a}$ $20.15 \pm 0.74 a^{a}$ $19.50 \pm 0.41 a^{a}$	$17.50 \pm 3.33 \text{ a}^{a}$ $17.19 \pm 0.57 \text{ a}^{ab}$ $19.79 \pm 0.14 \text{ a}^{a}$ $20.47 \pm 1.17 \text{ a}^{ac}$	$15.89 \pm 0.71_{a}^{a}$ $18.12 \pm 0.72_{a}^{b}$ $19 \pm 0.35_{a}^{bc}$ $19.89 \pm 0.48_{a}^{c}$	$12.47 \pm 0.29_{a}^{a}$ $17.60 \pm 0.55_{a}^{bc}$ $19.23 \pm 0.52_{a}^{b}$ $20.94 \pm 0.32_{a}^{bd}$
Bark	30 min 24h 48h 72h	9.49 ± 0.02 a ^a 11.29 ± 0.04 a ^b 12.68 ± 0.03 a ^c 13.20 ± 0.03 a ^d	$10.22 \pm 0.02 \text{ a}^{\text{ a}}$ $12.72 \pm 0.03 \text{ a}^{\text{ b}}$ $13.30 \pm 0.03 \text{ a}^{\text{ c}}$ $14.23 \pm 0.03 \text{ a}^{\text{ d}}$	$10.48 \pm 0.03 \text{ ac}^{a}$ $11.76 \pm 0.04 \text{ ac}^{b}$ $14.24 \pm 0.03 \text{ ac}^{c}$ $15.15 \pm 0.02 \text{ ac}^{d}$	$13.02 \pm 0.03 _{bcd}^{a}$ $14.01 \pm 0.03 _{bcd}^{b}$ $14.72 \pm 0.03 _{bcd}^{c}$ $15.96 \pm 0.02 _{bcd}^{d}$	10.33 ± 0.03 cd ^a 14.93 ± 0.03 cd ^b 16.58 ± 0.02 cd ^c 16.77 ± 0.02 cd ^d

Data are presented as mean value of triplicate measurements \pm standard deviation; Superscript letters within the same column indicate significant (P < 0.05) differences of means within the extracting solvent; Subscript letters indicate significant (P < 0.05) differences of means between extraction types.

Table 2. Antioxidant activity of S. caprea leaves and bark extracts [µg/ml]

Drug	Extraction			Extraction type		
	time	30% EtOH	40% EtOH	50% EtOH	60% EtOH	70% EtOH
	30 min	26.82 ± 0.2 a ^a	$3.33 \pm 0.35_{\text{bcef}}^{\text{ a}}$	$2.41 \pm 0.40_{\text{ cdef}}^{a}$	1.73 ± 0.08 de ^a	1.57 ± 0.04 e ^a
т.	24h	16.04 ± 0.27 a b	$2.75 \pm 0.05_{\text{bcef}}^{\text{b}}$	$6.02 \pm 0.08_{\text{cdef}}^{\text{b}}$	$2.05 \pm 0.06_{de}^{b}$	$3.72 \pm 0.08_{e}^{b}$
Leaves	48h	$7.48 \pm 0.27_{a}^{c}$	$4.01 \pm 0.20_{\text{bcef}}^{\text{ c}}$	$3.80 \pm 0.05_{\text{cdef}}^{\text{c}}$	$2.86 \pm 0.15_{\rm de}{}^{\rm c}$	$3.42 \pm 0.18_{e}^{c}$
	72h	$60.15 \pm 0.15 \frac{d}{a}$	4.45 ± 0.05 bcef d	$2.79 \pm 0.26_{\text{ cdef}}^{\text{ d}}$	4.26 ± 0.04 de ^d	$4.24 \pm 0.05 _{e}^{d}$
	30 min	1.07 ± 0.04 af ^a	1.35 ± 0.03 acf ^a	0.99 ± 0.01 _{bcde} ^a	1.33 ± 0.01 _{cd} ^a	$0.99 \pm 0.02_{\text{de}}^{\text{ a}}$
D 1	24h	$3.03 \pm 0.08 _{af}^{b}$	$1.97 \pm 0.02_{acf}^{b}$	1.80 ± 0.03 bcde b	2.59 ± 0.03 _{cd} ^b	$1.41 \pm 0.02_{\rm de}^{\rm b}$
Bark	48h	$2.55 \pm 0.05 _{af}^{c}$	$2.49 \pm 0.04 _{\rm acf}^{\ \ c}$	$1.68 \pm 0.04_{\rm \ bcde}^{\ \ c}$	1.61 ± 0.06 _{cd} ^c	$1.60 \pm 0.06_{de}^{c}$
	72h	$3.34 \pm 0.06 _{af}^{d}$	$2.87 \pm 0.02 _{acf}^{d}$	$1.31 \pm 0.01_{\text{bcde}}^{\text{d}}$	$1.21 \pm 0.01 _{cd}^{d}$	$1.58 \pm 0.01_{\rm de}^{\ c}$

Data are presented as mean value of triplicate measurements \pm standard deviation; Superscript letters within the same column indicate significant (P < 0.05) differences of means within the extracting solvent; Subscript letters indicate significant (P < 0.05) differences of means between extraction types.

Lower IC50 values indicate higher antioxidant activity. IC₅₀ values of bark extracts ranged from 0.99 to 3.34 μg/ ml indicating strong antioxidant activity. Increasing ethanol concentration from 30% to 70%, antioxidant activity of bark extracts increased, whereas increased extraction time led to decrease of antioxidant activity. This could be explained by the fact that longer extraction time might increase the oxidation of phenolic compounds contributing to lower DPPH radical scavenging activity.³² The highest antioxidant activity of bark extracts was observed for 50% and 70% ethanol extracts after 30 min of maceration. Compared to results of antioxidant activity of Salix aegyptiaca ethanol bark extracts (19 \pm 3 μ g/ml),³³ our results indicate higher antioxidant activity. IC₅₀ values of leaves extracts were in range of 1.57 to 60.15 µg/ml, also indicating high antioxidant activity. Among leaves extracts the highest antioxidant activity was observed for 70% ethanol extract obtained after 30 min of maceration. Comparing the results of bark and leaves extracts, it can be noticed that bark extracts possess higher antioxidant activity. Compared to Salix caprea ethanol flower extract, where IC₅₀ value was 75 µg/ ml,¹² extracts of both bark and leaves exhibited stronger antioxidant activity, indicating that antioxidant potential could depend on the selected plant material.

The total phenolics content in the obtained extracts of bark and leaves of *Salix caprea* L. are presented in Table 3.

The amount of total phenolics in the investigated extracts ranged from 16.44 to 68.37 mg GAE/g de and from 4.14 to 26.16 mg GAE/g de in bark and leaves, respectively. Increasing ethanol concentration from 30% to 70%, the amount of total phenolics increased for both bark and leaves extracts and the highest amount of phenolic compounds was observed in 70% ethanol extracts. The obtained results for bark extracts are lower than results from a study (75.5 \pm 0.1 mg GAE/g de) where Salix caprea bark was extracted by 80% aqueous methanol using Ultra Turrax.¹⁹ However, results obtained for most 70% ethanol leaves extracts in our study are higher than results of total phenolics in Salix caprea leaves extracts (37.6 \pm 0.1 mg GAE/g de), where extraction was carried out by 70% aqueous acetone using magnetic mixer.¹⁹ Total phenolics content in 70% ethanol extracts of leaves is significantly higher than the amount of phenolics obtained by extraction with other concentrations of ethanol. There is a statistically significant difference between total phenolics content in bark and leaves extracts. The highest amount of phenolics in bark was achieved by extraction with 70% ethanol.

Table 3. Total phenolics content of S.caprea leaves and bark extracts [mg of gallic acid equivalents per g of dried extract]

rug Extraction Extraction Type

100/ FtOH

100/ Ft

Drug	Extraction time	30% EtOH	40% EtOH	Extraction type 50% EtOH	60% EtOH	70% EtOH
Leaves	30 min 24h 48h 72h	21.20 ± 0.07 ad ^a 8.22 ± 0.26 ad ^b 11.38 ± 0.05 ad ^c 12.09 ± 0.08 ad ^d	22.92 ± 0.13 abd ^a 14.24 ± 0.15 abd ^b 5.84 ± 0.04 abd ^c 23.44 ± 0.02 abd ^d	$23.19 \pm 0.12_{abd}^{a}$ $20.69 \pm 0.12_{abd}^{b}$ $4.14 \pm 0.08_{abd}^{c}$ $18.82 \pm 0.07_{abd}^{d}$	$17.56 \pm 0.24_{bcd}^{a}$ $30.11 \pm 0.12_{bcd}^{b}$ $26.16 \pm 0.08_{bcd}^{c}$ $22.62 \pm 0.04_{bcd}^{d}$	$25.52 \pm 0.04_{c}^{a}$ $33.98 \pm 0.02_{c}^{b}$ $45.37 \pm 0.28_{c}^{c}$ $41.14 \pm 0.02_{c}^{d}$
Bark	30 min 24h 48h 72h	$\begin{aligned} 51.12 &\pm 0.31_a{}^a \\ 17.31 &\pm 0.09_a{}^b \\ 20.16 &\pm 0.17_a{}^c \\ 23.76 &\pm 0.22_a{}^d \end{aligned}$	$\begin{array}{l} 56.12 \pm 0.23_{ac}{}^{a} \\ 16.44 \pm 0.21_{ac}{}^{b} \\ 25.42 \pm 0.16_{ac}{}^{c} \\ 27.58 \pm 0.12_{ac}{}^{d} \end{array}$	$48.89 \pm 0.18_{a}^{a}$ $45.82 \pm 0.16_{a}^{b}$ $29 \pm 0.18_{a}^{c}$ $26.84 \pm 0.12_{a}^{d}$	$52.36 \pm 0.12_{ac}{}^{a}$ $25.63 \pm 0.18_{ac}{}^{b}$ $38.16 \pm 0.11_{ac}{}^{c}$ $42.65 \pm 0.02_{ac}{}^{d}$	$42.68 \pm 0.23_{bc}^{a}$ $64.88 \pm 0.11_{bc}^{b}$ $68.37 \pm 0.08_{bc}^{c}$ $55.71 \pm 0.04_{bc}^{d}$

Data are presented as mean value of triplicate measurements \pm standard deviation; Superscript letters within the same column indicate significant (P < 0.05) differences of means within the extracting solvent; Subscript letters indicate significant (P < 0.05) differences of means between extraction types.

Total flavonoids content in the investigated bark and leaves extracts is shown in Table 4.

Increasing ethanol concentration led to the increase of total flavonoids of both bark and leaves extracts, so the highest amount of flavonoids was obtained by maceration with 70% ethanol. The amount of total flavonoids in bark extracts is significantly higher than in leaves extracts of *S. caprea*. The great impact of solvent polarity and extraction time on total flavonoid content found in this research is in agreement with other studies. ^{15,16}

3. 2. Chemical Composition of Extracts

Bioactive compounds considered to be responsible for pharmacological effects of willow were identified and quantified by HPLC analysis. The impact of different extraction conditions on chemical composition of *Salix caprea* L. bark and leaves extracts are shown in Tables 5 and 6.

Presence of active ingredients in the extracts was confirmed by comparing their retention time with the retention times of the standards, as well as comparing their UV/VIS spectra with the spectra of the standard signal.

Phenolic compounds identified in both Salix caprea L. bark and leaves extracts were gallic acid, chlorogenic acid and vanillic acid and the flavonoids identified were epicatechin, rutin, quercetin and naringenin. p-Hydroxybenzoic acid was found in bark extracts and ferulic acid, trans-cinnamic acid and p-coumaric acid were identified in leaves extracts only. The most abundant polyphenols in bark extracts was rutin (1.71 g/100 g de). Also high amounts of chlorogenic acid (0.965 g/100 g de), p-hydroxybenzoic acid (0.542 g/100 g de) and quercetin (0.603 g/100 g de) were detected in bark. Previous study of Salix aegyptiaca indicate a similar polyphenolic profile, where rutin was one of the predominant flavonols in ethanolic bark extract.33 Other published reports indicate that epicatechin is one of the most dominant flavonoids in willow bark extracted with polar solvents.³⁴ In leaves extracts, rutin was also the most abundant polyphenol (0.968 g/100 g de), followed by naringenin (0.434 g/100 g de) and quercetin (0.226 g/100 g de). Our results are in accordance with earlier published studies on polyphenol content in leaves of six different Salix species, which revealed that quercetin was one of the major flavonols.35

Table 4. Total flavonoids content of *S. caprea* leaves and bark extracts [mg of quercetin equivalents per g of dried extract]

Drug	Extraction time	30% EtOH	40% EtOH	Extraction type 50% EtOH	60% EtOH	70% EtOH
Leaves	30 min 24h 48h 72h	4.07 ± 0.09 ad ^a 1.03 ± 0.08 ad ^b 0.91 ± 0.04 ad ^b 1.28 ± 0.02 ad ^c	$1.99 \pm 0.04 _{abd}{}^{a}$ $1.72 \pm 0.04 _{abd}{}^{b}$ $1.30 \pm 0.03 _{abd}{}^{c}$ $7.01 \pm 0.03 _{abd}{}^{d}$	$2.93 \pm 0.03 a^{a}$ $2.57 \pm 0.03 a^{b}$ $2.09 \pm 0.02 a^{c}$ $1.76 \pm 0.03 a^{d}$	$4.69 \pm 0.03 _{bd} ^{a}$ $7.50 \pm 0.04 _{bd} ^{b}$ $8.14 \pm 0.05 _{bd} ^{c}$ $5.76 \pm 0.04 _{bd} ^{d}$	16.92 ± 0.01 c ^a 15.10 ± 0.07 c ^b 15.21 ± 0.04 c ^{bc} 14.86 ± 0.02 c ^{bd}
Bark	30 min 24h 48h 72h	4.45 ± 0.03 a ^a 4.08 ± 0.03 a ^b 3.91 ± 0.00 a ^b 3.75 ± 0.01 a ^c	$5.69 \pm 0.03_{b}^{a}$ $5.84 \pm 0.01_{b}^{b}$ $5.71 \pm 0.00_{b}^{ac}$ $5.76 \pm 0.06_{b}^{a}$	$5.38 \pm 0.01_{b}^{a}$ $7.28 \pm 0.01_{b}^{b}$ $6.28 \pm 0.01_{b}^{c}$ $4.42 \pm 0.03_{b}^{d}$	7.16 ± 0.06 c a 8.70 ± 0.06 c b 8.38 ± 0.05 c c 11.23 ± 0.00 c d	$15.19 \pm 0.02 \frac{d}{d}$ $15.65 \pm 0.05 \frac{d}{d}$ $18.24 \pm 0.01 \frac{d}{d}$ $17.95 \pm 0.06 \frac{d}{d}$

Data are presented as mean value of triplicate measurements \pm standard deviation; Superscript letters within the same column indicate significant (P < 0.05) differences of means within the extracting solvent; Subscript letters indicate significant (P < 0.05) differences of means between extraction types.

Table 5. Chemical composition of Salix caprea leaves extracts

Extraction	Time	GA	CHLA	VA	EPC	CA	R	FA	Q	TCA	NRG	SA
type						[g/100 g d	rug]					
	30 min	n.d.	n.d.	n.d.	n.d.	0.009	0.046	0.074	n.d.	n.d.	0.092	n.d.
200/ E4OH	24h	n.d.	n.d.	n.d.	n.d	0.014	0.047	0.077	0.035	0.0009	0.122	
30% EtOH	48h	n.d.	n.d.	0.003	n.d.	0.009	0.057	n.d.	0.043	0.0011	0.204	
	72h	n.d.	0.019	0.005	0.0004	n.d.	0.045	0.070	0.036	0.0011	0.091	
	30 min	n.d.	0.030	0.001	n.d.	n.d.	0.072	0.100	0.048	0.0009	0.136	
400/ E/OH	24h	0.071	n.d.	0.003	0.003	0.012	0.044	0.073	0.034	0.0008	0.092	
40% EtOH	48h	n.d.	n.d.	0.006	0.087	0.0008	0.052	0.072	0.044	0.005	0.160	
	72h	n.d.	n.d.	n.d.	n.d.	n.d.	0.049	n.d.	0.048	0.002	0.302	
	30 min	n.d.	n.d.	0.008	0.002	0.008	0.056	0.083	0.047	0.004	0.188	
700/ E/OH	24h	0.074	0.027	n.d.	0.013	0.011	0.058	0.084	0.052	0.007	0.131	
50% EtOH	48h	0.068	n.d.	n.d.	0.007	0.007	0.057	0.075	0.069	0.026	0.141	
	72h	n.d.	n.d.	n.d.	n.d.	n.d.	0.105	n.d.	0.066	0.006	0.330	
	30 min	0.099	n.d.	n.d.	0.021	n.d.	0.099	0.095	0.073	0.009	0.330	
con Elou	24h	0.077	0.100	n.d.	0.015	0.011	0.259	n.d.	0.060	0.023	0.113	
60% EtOH	48h	n.d.	n.d.	n.d.	n.d.	n.d.	0.968	n.d.	0.067	0.035	0.156	
	72h	n.d.	n.d.	0.017	0.009	0.007	0.054	0.076	0.068	0.043	0.136	
	30 min	0.111	0.082	0.002	0.002	0.020	0.129	n.d.	0.185	0.075	0.319	
700/ E/OH	24h	n.d.	n.d.	n.d.	0.028	0.015	0.089	n.d.	0.087	0.033	0.146	
70% EtOH	48h	n.d.	n.d.	0.013	0.015	n.d.	0.177	n.d.	0.226	0.090	0.434	
	72h	0.060	0.028	0.0002	0.055	n.d.	0.116	n.d.	0.125	0.032	0.032	

 $n.d.-not\ detected;\ GA-gallic\ acid;\ CHLA-chlorogenic\ acid;\ PHB-p-hydroxybenzoic\ acid;\ VA-vanillic\ acid;\ EPC-epicatechin;\ CA-p-coumaric\ acid;\ R-rutin;\ FA-ferulic\ acid\ Q-quercetin;\ NRG-naringenin;\ SA-salicin$

Table 6. Chemical composition of Salix caprea bark extracts

Extraction type	Time	GA	CHLA	PHB	VA	EPC	R	Q	NRG	SA
				[g	/100 g de]					
	30 min	n.d.	0.004	0.020	0.008	0.0006	0.087	0.043	n.d.	n.d.
30% EtOH	24h	n.d.	0.202	n.d.	0.027	0.093	0.329	0.091	n.d.	n.d.
30% ElOn	48h	n.d.	0.019	0.0009	0.003	0.002	0.064	0.042	n.d.	n.d.
	72h	n.d.	0.035	0.003	0.004	0.010	0.099	0.101	0.052	n.d.
	30 min	n.d.	0.093	0.111	0.047	0.050	0.428	0.074	0.078	0.789
400/ E(OH	24h	n.d.	0.050	0.007	0.009	0.007	0.128	0.066	0.061	0.250
40% EtOH	48h	0.032	0.10	0.078	0.070	0.134	0.341	0.138	0.055	0.273
	72h	0.068	0.166	0.078	0.077	0.285	0.620	0.304	0.103	0.269
	30 min	0.043	0.285	0.252	0.143	0.108	0.786	0.155	0.086	0.749
400/ E(OH	24h	0.035	0.092	0.074	0.005	0.039	0.243	0.106	0.076	0.638
40% EtOH	48h	0.030	0.165	0.107	0.082	0.218	0.783	0.139	0.082	0.469
	72h	0.057	0.536	0.307	0.302	0.699	1.470	0.429	0.153	0.530
	30 min	0.032	0.244	0.293	0.117	0.17	1.135	0.168	0.072	0.615
600/ E(OH	24h	0.029	0.294	0.135	0.098	0.412	0.980	0.244	0.074	0.628
60% EtOH	48h	n.d.	0.702	0.091	0.114	0.435	1.710	0.31	0.115	0.461
	72h	0.054	0.965	0.332	0.232	0.697	1.442	0.344	0.127	n.d.
	30 min	0.113	0.563	0.542	0.329	0.672	1.320	0.603	0.157	0.658
FOOV EVOLU	24h	n.d.	0.583	0.29	0.172	0.267	0.550	0.098	0.05	0.598
70% EtOH	48h	n.d.	0.825	0.43	0.486	0.499	1.680	0.642	0.111	0.413
	72h	0.093	0.655	0.34	0.209	0.649	1.630	0.532	0.130	0.604

 $n.d.-not\ detected;\ GA-gallic\ acid;\ CHLA-chlorogenic\ acid;\ PHB-p-hydroxybenzoic\ acid;\ VA-vanillic\ acid;\ EPC-epicatechin;\ R-rutin;\ Q-quercetin;\ NRG-naringenin;\ SA-salicin$

Gallic acid content varied from 0.029 to 0.113 g/100 g de and from 0.060 to 0.111 g/100 g de in bark and leaves, respectively. The highest amount of gallic acid in leaves was found in 70% ethanolic extract. It was not detected in either bark or leaves extracts obtained by maceration with 30% ethanol, implying that this concentration of ethanol is not selective for gallic acid isolation. The amount of chlorogenic acid was in interval of 0.004-0.965 g/100 g de and 0.019-0.100 g/100 g de for bark and leaves, respectively. The highest quantity of chlorogenic acid in bark and leaves was obtained by maceration with 60% ethanol. Vanillic acid content was in interval of 0.003 to 0.486 g/100 g de in bark and 0.0002 to 0.017 g/100 g de in leaves. The highest amount of vanillic acid in bark was obtained by maceration with 70% ethanol for 48 hours, and in leaves by maceration with 60% ethanol during 72 h of extraction. The amount of epicatechin was in interval of 0.0006-0.699 g/100 g de and 0.0004-0.087 g/100 g de for bark and leaves, respectively. The highest quantity of epicatechin in bark was obtained by 50% ethanol and in leaves 40% ethanol is found to be most effective extraction solvent. The highest content of rutin in both, bark and leaves, was found in 60% ethanolic extract obtained after 48 hours of maceration. Quercetin was obtained in highest amount in both, bark and leaves, by maceration with 70% ethanol for 48 hours. The amount of naringenin in bark was in interval of 0.050 to 0.157 g/100 g de, which is similar to results obtained for Salix caprea wood and knots (0.5–1.5 mg/g) published earlier.²⁰ Even higher amounts of naringenin were found in leaves extracts (0.091-0.330 g/100 g de). P-hydroxybenzoic acid was detected in bark only (0.0009-0.542 g/100 g de), with the highest amount in 70% ethanolic extract obtained after 48 hours of maceration. Ferulic acid was found in leaves only (0.07-0.100 g/100 g de), with the highest amount in 40% ethanolic extract. Trans-cinnamic acid (0.0008-0.09 g/100 g de) and p-coumaric acid (0.0008-0.020 g/100 g de) were found in low amounts in leaves only. Salicin was detected in bark extracts only. Its content ranged from 0.250 to 0.789 g/100 g de. The highest amount of salicin was obtained in 40% ethanolic extract after 30 min of maceration, while in 30% ethanolic extracts it was not detected at all. Salicin content in our study is higher compared to the amount of salicin obtained in a similar research, where Salix caprea bark and leaves were extracted with methanol.²⁵ However, in the mentioned study, salicin was detected also in leaves extracts, which was not the case in our research. These quantitative variations within

the same species could reflect the influence of environmental and also genetic factors.

Correlation between antioxidant activity and the determined compounds in *Salix caprea* leaves and bark extracts was tested. There is statistically no significant correlation between antioxidant activity and any of the determined compounds in leaves extracts. In case of bark, statistically significant moderate negative correlation between antioxidant activity and rutin (R = -0.485, level of significance p < 0.05), naringenin (R = -0.474, level of significance p < 0.05) and salicin (R = -0.541, level of significance p < 0.05) was observed, suggesting that these compounds might contribute to the antioxidant activity of *Salix caprea* bark extracts.

3. 3. Molecular Docking

Molecular docking, as effective tool used to investigate the active site of a protein and to elucidate the interactions between ligands and the biological molecule, was applied in our research. One of the most important compound of willow bark, salicin, was selected to study its binding affinity and interactions to COX-1 and COX-2 enzymes. Binding energies and inhibition constants for the studied ligand and control inhibitor acetylsalicylic acid are listed in Table 7.

The results presented in Table 7 showed salicin to have similar affinity toward COX-1 and COX-2 enzymes. Also, in comparison with acetylsalicylic acid, salicin showed similar affinity toward COX-2, but lower toward COX-1. Acetylsalicylic acid, also known as aspirin is currently one of the most widely used drugs worldwide owing to its analgesic, antipyretic, anti-inflammatory and cardioprotective effects.³⁶ Aspirin irreversibly inhibits both isozymes of COX, but with a greater potency for COX-1,³⁶ which was demonstrated by our docking study as well. COX-1 is constitutively expressed in blood platelets and most tissues, particularly gastric mucosal cells, whereas COX-2 is an inducible form expressed during inflammation. Therapeutic effects of acetylsalicylic acid are achieved by COX-2 inhibition, while inhibition of COX-1 is responsible for the side effects. ³⁶ The risk of adverse effects, especially gastrointestinal mucosa damage, limits the benefit of aspirin use.³⁷ Lower affinity of salicin toward COX-1 might partially explain why willow bark extract does not damage the gastrointestinal mucosa in contrast to aspirin.38 Interactions of salicin with amino acid residues at

Table 7. Binding energies and inhibition constants

Compound	CO: Binding		COX-2 Binding energy [
-	[kcal/mol]	$K_i[\mu M]$	kcal/mol]	$K_i[\mu M]$	
Salicin	-5.70	66.54	-5.86	50.95	
Acetylsalicylic acid	-6.25	26.1	-5.69	67.66	

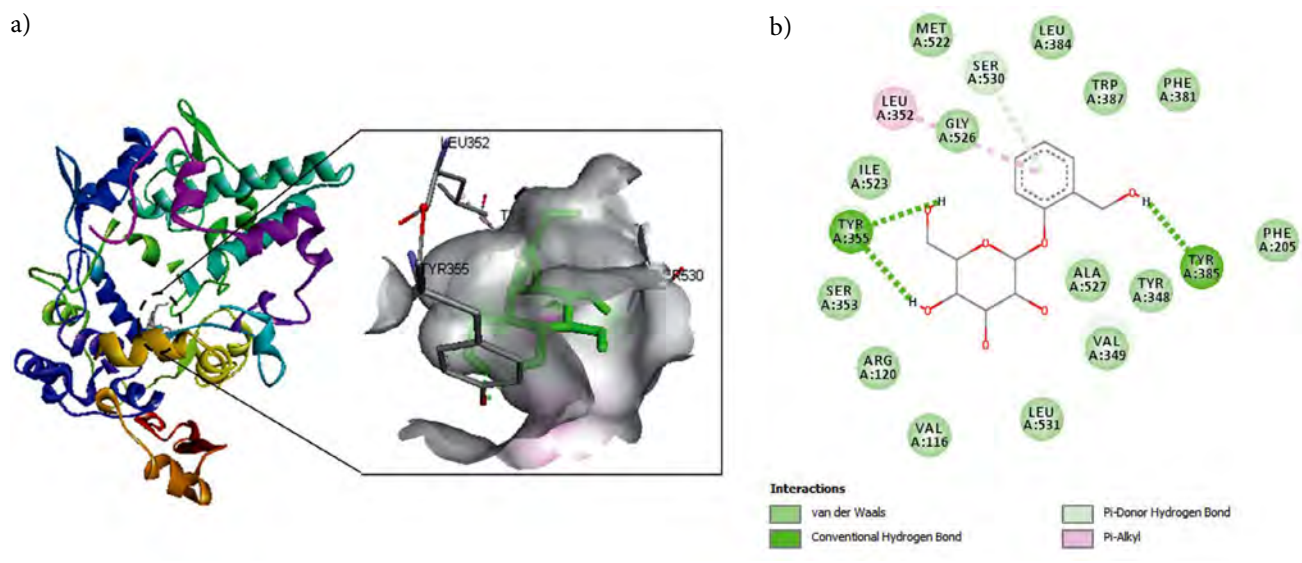


Figure 1. Active site of the COX-1 enzyme with salicin (A) 3D view; B) 2D view)

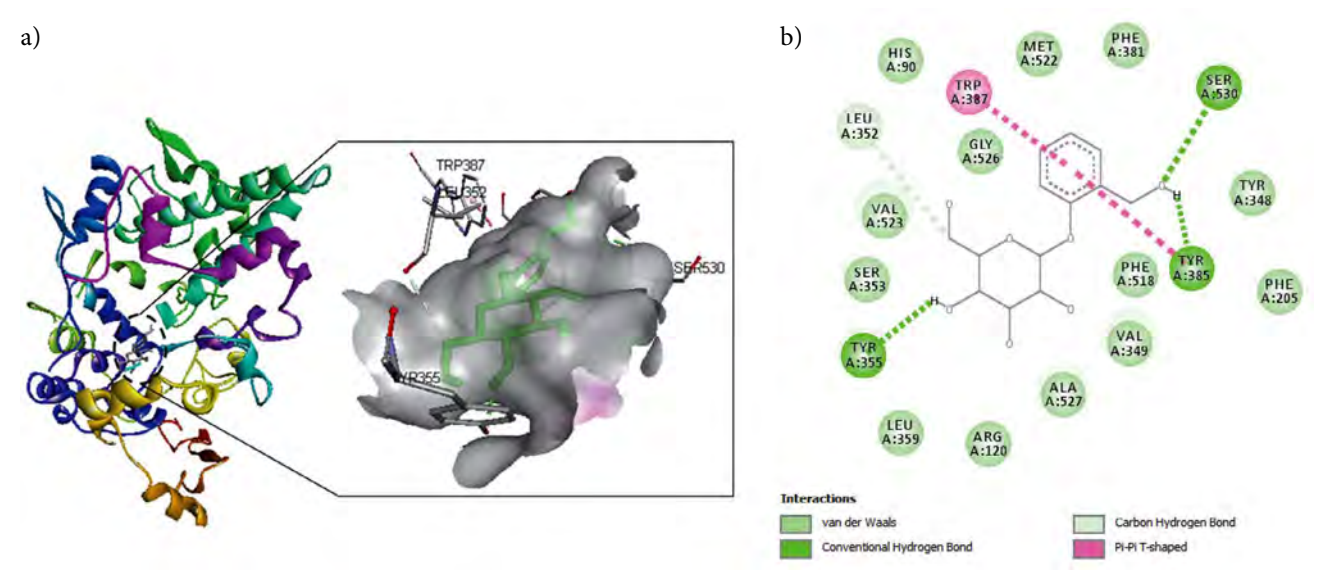


Figure 2. Active site of the COX-2 enzyme with salicin (A) 3D view; B) 2D view)

the active site of COX-1 and COX-2 are shown in Figures 1 and 2.

Salicin was involved in hydrogen bonding with amino acid residues of the active site of COX-1 Tyr 355, Tyr 385 and Ser 530. Other important active site amino acid residues Arg 120, Val 349, Ser 353, Leu 384, Trp 387, Met 522, Ile 523, Gly 526 and Ala 527 form van der Waals interactions with salicin. These amino acid residues have also been reported for curcumin analogues having strong interactions with COX-1.³⁹ Salicin showed hydrogen bonding with Leu 352, Tyr 355, Tyr 385 and Ser 530, which are relevant amino acid residues of the active site of COX-2. Previous studies revealed that Ser-530 and Tyr-385 are important for the inhibition of COX-2.³ Salicin exhibited hydrophobic interactions with important amino acid resi-

dues of the active site, namely Arg 120, Tyr 348, Val 349, Leu 352, Ser 353, Leu359, Trp 387, Phe 518, Met 522, Val 523, Gly 526 and Ala 527. Interactions with most of these residues have also been reported for compounds showing strong inhibition of COX-2 and correspond to the active binding site of non-steroidal anti-inflammatory drugs.³⁹⁻⁴¹

4. Conclusion

Extraction technique showed great impact on yield, antioxidant activity and the amount of active compounds of *Salix caprea* bark and leaves. 70% ethanolic extracts exhibited highest antioxidant activity. Although willow extracts have been traditionally used as anti-inflammatory agents for their salicin content, *Salix caprea* bark and leaves contain significant amounts of other phenolic com-

pounds, especially epicatechin, rutin, quercetin, chlorogenic acid and gallic acid, which act as potent antioxidants, and therefore can contribute to the therapeutic effects of this species. Also, the results obtained in our study showed that *Salix caprea* leaves, as well as bark could be used as a rich natural source of bioactive components and have potential in the pharmaceutical industry for extraction of phenolic antioxidants. Salicin was found in bark extracts only and molecular docking study was applied for evaluation of interactions and binding affinity between salicin and the enzymes COX-1 and COX-2. The results showed that salicin exhibited a number of strong hydrogen bonds and hydrophobic interactions with significant amino acid residues of active sites of COX-2 which could explain major anti-inflammatory potency of this compound.

5. Abbreviations

Ala, alanine; Arg, arginine; COX, cyclooxygenase; d.e., dried extract; DPPH*, 2,2-diphenyl-1-picrylhydrazyl radical; GAE, gallic acid equivalents; Gly, glycine; Ile, isoleucine; Leu, leucine; Met, methionine; *OH, hydroxyl radical; Phe, phenylalanine; Ser, serine; Trp, tryptophan; Tyr, tyrosine; QE, quercetin equivalents.

6. Acknowledgement

This study was supported by the Ministry of Education, Science and Technological Development of the Republic of Serbia, projects no. 172021 and III 46009.

7. References

- B. Schmidt, I. Kötter, L. Heide, Eur. J. Clin. Pharmacol. 2001, 57, 387–391. DOI:10.1007/s002280100325
- L. Poblocka-Olech, A. M. van Nederkassel, Y. Vander Heyden, M. Krauze-Baranowska, D. Głód, T. Bascek, J. Sep. Sci. 2007, 30, 2958–2966. DOI:10.1002/jssc.200700137
- 3. M. Shara, S. J. Stohs, *Phytother. Res.* **2015**, *29*, 1112–1116. **DOI**:10.1002/ptr.5377
- S. Agnolet, S. Wiese, R. Verpoorte, D. Staerk, *J. Chromatogr. A.* 2012, *1262*, 130–137. DOI:10.1016/j.chroma.2012.09.013
- A. Durak, U. Gawlik-Dziki, D. Sugier, J. Funct. Foods, 2015, 18, 1106–1116. DOI:10.1016/j.jff.2014.06.012
- L. Pobłocka-Olech, M. Krauze-Baranowska, D. Głód, A. Kawiak, E. Łojkowska, *Phytochem. Anal.* 2010, 21, 463–469.
 DOI:10.1002/pca.1220
- A. Nahrstedt, M. Schmidt, R. Jaggi, J. Metz, M. T. Khayyal, Wochenschr. 2007, 157, 348–351.
 - **DOI:**10.1007/s10354-007-0437-3
- B. Uehleke, J. Müller, R. Stange, O. Kelber, J. Melzer, *Phytomedicine*, 2013, 20, 980–984.
 - DOI:10.1016/j.phymed.2013.03.023

- Lj. Babincev, Lj. Rajaković, M. Budimir, A. Perić-Grujić, D. Sejmanović, *Chem. Ind.* 2011, 65, 397–401.
 DOI:10.2298/HEMIND110222025B
- A. Ahmed, W. A. Shah, S. Akbar, M. Younis, D. Kumar, Int. J. Res. Phytochem. Pharmacol. 2011, 1, 17–20.
- 11. S. Sultana, M. Saleem, *Ethnopharmacol.* **2004**, *91*, 267–276. **DOI:**10.1016/j.jep.2003.12.028
- 12. M. Anđelković, A. Milenković-Anđelković, B. Radovanović, A. Radovanović, *Acta Chim. Slov.* **2014**, *61*, 858–865.
- S. Grujić, A. Džamić, V. Mitić, V. Stankov-Jovanović, P. Marin,
 G. Stojanović, *Chem. Ind.* **2017**, *71*, 361–370.
 DOI:10.2298/HEMIND160518047G
- B. Teofilović, N. Grujić-Letić, S. Kovačević, S, Podunavac-Kuzmanović, S. Gadžurić, *Chem. Ind. Chem. Eng. Q.* 2017, DOI:10.2298/CICEQ170217035T
- B. Teofilović, N. Grujić-Letić, S. Goločorbin-Kon, S. Stojanović, Gyongyi Vastag, S. Gadžurić, *Ind. Crops. Prod.* 2017, 100, 176–182. DOI:10.1016/j.indcrop.2017.02.039
- N. Grujić-Letić, Ž. Lepojević, B. Srđenović, J. Vladić, J. Suđi, Molecules, 2012, 17, 2518–2528.
 - DOI:10.3390/molecules17032518
- A. Bucić-Kojić, M. Planinić, S. Tomas, S. Jokić, I. Mujić, M. Bilić, *Polish J. Food Nutr. Sci.* **2011**, *61*, 195–199.
 DOI:10.2478/v10222-011-0021-9
- M. Alothman, R. Bhat, A.A. Karim, Food Chem. 2009, 115, 785–788. DOI:10.1016/j.foodchem.2008.12.005
- M. P. Kähkönen, A. I. Hopia, H. J. Vuorela, J. P. Rauha, K. Pihlaja, T. S. Kujala, *J. Agric. Food Chem.* 1999, 47, 3954–3962.
 DOI:10.1021/jf9901461
- S. P. Pohjamo, J. E. Hemming, S. M. Willför, M. H. T. Reunanen, B. R. Holmbom, *Phytochemistry*, **2003**, *63*, 165–169.
 DOI:10.1016/S0031-9422(03)00050-5
- M. Amaravani, N. Prasad, V. Ramakrishna, Springerplus, 2012, 1, 58. DOI:10.1186/2193-1801-1-58
- 22. P. Srivastava, V. Singh, B. Singh, G. Srivastava, B. Misra, V. Tripathi, *J. Proteomics Bioinform.* **2013**, *6*, 109–124.
- 23. EMA/HMPC. http://www.ema.europa.eu/ema/index.jsp?curl=pages/home/Home_Page.jsp&mid=
- A. Ziakova, E. Bransteterova, J. Liq. Chromatogr. Relat. Technol. 2003, 26, 443–453. DOI:10.1081/JLC-120017181
- A. Guvenc, O. Arihan, M. L. Altun, E. Dinc, D. Baleanu, D, Rev. Chim, 2007, 58, 8–12.
- A. Cvetanović, J. Švarc-Gajić, P. Mašković, S. Savić, Lj. Nikolić, *Ind. Crop Prod.* 2015, 65, 582–591.
 DOI:10.1016/j.indcrop.2014.09.044
- M. S. Stankovic, M. Topuzovic, S. Solujic, V. Mihailovic, J. Med. Plant Res. 2010, 4, 2092–2098.
- A. Djeridane, M. Yousfi, B. Nadjemi, D. Boutassouna, P. Stocker, N. Vidal, *Food Chem.* 2006, 97, 654–660.
 DOI:10.1016/j.foodchem.2005.04.028
- D. Picot, P. J. Loll, R. M. Garavito, *Nature*, 1994, 367, 243–249.
 DOI:10.1038/367243a0
- R. G. Kurumbail, A. M. Stevens, J. K. Gierse, J. J. McDonald,
 R. A. Stegeman, J. Y. Pak, *Nature*, 1996, 384, 644–648.
 DOI:10.1038/384644a0
- 31. G. M. Morris, R. Huey, W. Lindstrom, M. F. Sanner, R. K.

- Belew, D. S. Goodsell, *J. Comput. Chem.* **2009**, *30*, 2785–2791. **DOI**:10.1002/jcc.21256
- M. Naczk, F. Shahidi, J. Pharm. Biomed. Anal. 2006, 41, 1523– 1542. DOI:10.1016/j.jpba.2006.04.002
- 33. S. Enayat, S. Banerjee, *Food Chem.* **2009**, *116*, 23–28. **DOI**:10.1016/j.foodchem.2009.01.092
- G. Jürgenliemk, F. Petereit, A. Nahrstedt, *Pharmazie*, 2007, 62, 231–234.
- 35. T. Nyman, R. Julkunen-Tiitto, Phytochemistry, **2005**, *66*, 2836–2843. **DOI:**10.1016/j.phytochem.2005.09.040
- 36. M. N. Marjan, M. T. Hamzek, E. Rahman, V. Sadeq, *Comput. Biol. Chem.*, **2014**, *51*, 57–62.
 - DOI:10.1016/j.compbiolchem.2014.05.002

- A. Negovan, M. Iancu, V. Moldovan, S. Voidazan, S. Bataga, M. Pantea, K. Sarkany, C. Tatar, S. Mocan, C. Banescu, Gastroenterol. Res. Pract., 2016, 2016, 7230626.
 DOI:10.1155/2016/7230626
- J. Vlachojannis, F. Magora, S. Chrubasik, *Phytother. Res.* 2011, 25, 1102–1104. DOI:10.1002/ptr.3386
- C. Selvam, S. M. Jachak, R. Thilagavathi, A. K. Chakraborti, Bioorg. Med. Chem. Lett. 2005, 15, 1793–1797.
 DOI:10.1016/j.bmcl.2005.02.039
- K. C. Duggan, M. J. Walters, J. Musee, J. M. Harp, J. R. Kiefer, J. A. Oates, *J. Biol. Chem.* 2010, 285, 34950–34959.
 DOI:10.1074/jbc.M110.162982
- K. E. Furse, D. A. Pratt, C. Schneider, A. R. Brash, N. A. Porter, T. P. Lybrand, *Biochemistry*, 2006, 45, 3206-3218.
 DOI:10.1021/bi052338h

Povzetek

Vsebino dvanajstih izbranih bioaktivnih snovi in antioksidativni potencial ekstraktov *Salix caprea* L. smo primerjali v dveh vegetativnih organih (lubje in listi) ter glede na različne mešanice etanol/voda, ki se uporabljajo za ekstrakcijo (30–70 % vodni, etanol) in ekstrakcijski čas (30 min; 24, 48 in 72 h). Ekstrakte smo opredelili s tekočinsko kromatografijo pod visokim pritiskom (HPLC), skupni fenoli in flavonoidi pa so bili določeni spektrofotometrično. Vsi sekundarni presnovki, ki so bili opredeljeni v ekstraktih *Salix caprea* L. (galna, klorogena in vanilinska kislina, epikatehin, rutin, kvercetin in naringenin), so se nabrali v lubju. Salicin in *p*-hidroksibenzojska kislina sta bila odkrita le v lubju in ferulinski, *trans*-cimetni in *p*-kumarni kislini le v ekstraktih listov. Rutin je bil najbolj obilna bioaktivna spojina tako v lubju (1,71 g / 100 g de), kot tudi v listih ekstrakta (0,434 g / 100 g de). Ekstrakt lubja z najvišjo vsebnostjo bioaktivnih snovi je bil pridobljen s 70 % vodnega etanola kot najprimernejše topilo v času ekstrakcije 48 h. Molekularno povezovanje je pokazalo, da ima salicin podobne afinitete do COX-2 kot acetilsalicilna kislina, proti COX-1 pa nižje.





Scientific paper

Two Acylated Isoscutellarein Glucosides with Anti-Inflammatory and Antioxidant Activities Isolated from Endemic Stachys Subnuda Montbret & Aucher ex Benth

Ali Sen,1,* Fatih Goger, 2 Ahmet Dogan3 and Leyla Bitis1

¹ Department of Pharmacognosy, Faculty of Pharmacy, Marmara University, Istanbul, Turkey,

² Department of Pharmacognosy, Faculty of Pharmacy, Anadolu University, Eskisehir, Turkey

³ Department of Pharmaceutical Botany, Faculty of Pharmacy, Marmara University, Istanbul, Turkey

* Corresponding author: E-mail: ali.sen@marmara.edu.tr; alisenfb@hotmail.com Phone: +90 535 938 78 94; Fax: +90 216 345 29 52; e-mail

Received: 12-27-2018

Abstract

In this study, we report anti-inflammatory and antioxidant activities of two acylated isoscutellarein glucosides isolated from ethyl acetate extract of *Stachys subnuda* aerial part. 4'-O-methylisoscutellarein-7-O-2"-O-(6"'-O-acetyl- β -D-allopyranosyl)- β -D-glucopyranoside (SS1) and isoscutellarein-7-O-2"-O-(6"'-O-acetyl- β -D-allopyranosyl)- β -D-glucopyranoside (SS2) were isolated as major compounds from ethyl acetate extract (SSEA). Also, 2 hydroxycinnamic acid derivatives, and 5 isoscutellarein glucoside derivatives in the SSEA were identified using LC-MS/MS. SS1 with IC₅₀ values of 2.35 and 1.98 µg/mL and SS2 with IC₅₀ values 13.94 and 12.76 µg/mL showed fairly strong antioxidant activity against DPPH (1,1-diphenyl-2-picrylhydrazyl) and ABTS (2,2'-azino-bis-3-ethylbenzthiazoline-6-sulphonic acid) radicals, respectively. SS1 and SS2 inhibited 5-lipoxygenase (5-LOX) activity with IC₅₀ values of 47.23 and 41.60 µg/mL, respectively. The results demonstrated that SS1 and SS2 have significant anti-inflammatory and antioxidant potential. Acylated flavonoid glycosides have been first reported for *Stachys subnuda*. Also, the activities of SS1 and SS2 have been investigated for the first time in this study.

Keywords: Stachys subnuda; acylated flavonoids; anti-inflammatory activity; antioxidant activity; LC-MS/MS

1. Introduction

The *Stachys* genus is one of the largest species of the Lamiaceae family and is represented by about 300 species worldwide.¹ Also, Turkey is one of the richest countries in terms of variety of *Stachys* species and this genus is represented by 91 species with an endemism rate of 48%. *Stachys* species known as "Deli sage" or "Mountain tea" in Anatolia are used in the skin diseases, ulcers, cancer, respiratory diseases and kidney diseases by the people because of their antibacterial, anti-inflammatory, antipyretic, antioxidant and cytotoxic effects.² In many countries, especially in the Mediterranean regions, *Stachys* species are consumed as herbal tea (Mountain Tea), food and herbal remedies.³

There is only one report on the chemical composition and biological activity of the essential oil of *Stachys*

subnuda in the literature.4 However, no study on isolation of flavonoids from this species and their biological activities have yet been reported. In the studies on other Stachys species, it has revealed that secondary metabolites are generally iridoids, flavone glycosides, diterpenes and essential oils.^{2,5-7} Also, it has been reported that various extracts of Stachys species have antioxidant, anti-proliferative, anti-inflammatory, antiulcer, antinociceptive, antimicrobial activities.8-10 There is no scientific information on chemical composition of Stachys subnuda ethyl acetate extract and anti-inflammatory and antioxidant activities of its active major compounds. Therefore, the aim of this study was to test anti-inflammatory and antioxidant activities of major compounds isolated from ethyl acetate extract of aerial parts of endemic Stachys subnuda Montbret & Aucher Ex Benth.

2. Experimental

2. 1. Plant Material

Aerial parts of plant were collected in the flowering period from the Tunceli province of Turkey in 2015 and identified by Dr. Ahmet Dogan, a botanist of the Faculty of Pharmacy, University of Marmara. Voucher specimens were deposited in the Herbarium of the Faculty of Pharmacy, Marmara University (MARE No: 17720).

2. 2. Extraction

Dried and ground aerial parts of *Stachys subnuda* (10 g) for activities were extracted with CH $_3$ OH (3 × 100 mL), using an ultrasonic bath. After filtration and evaporation, the residue (SSM) was dissolved in 50 mL 50% aqueous methanol, and subjected to solvent-solvent partition between n-hexane (3 × 50 mL), chloroform (3 × 50 mL) and ethyl acetate (3 × 50 mL). The n-hexane, chloroform, ethyl acetate and aqueous methanol extracts were coded as SSH, SSC, SSEA and SSAM, respectively. Also, about 140 g of the plant was weighed for isolation and similar extraction procedures described above were carried out. All extracts were stored under refrigeration for further analysis.

2. 3. In vitro Anti-Inflammatory Activity

The anti-inflammatory activity was evaluated according to the method described by Phosrithong et al. 11 An aliquot of 500 μL at different concentrations of isolated compounds was added to 250 μL of 0.1 M borate buffer pH 9.0, followed by addition of 250 μL of type V soybean lipoxygenase solution in buffer (20.000 U/mL). After the mixture was incubated at 25 °C for 5 min, 1000 μL of 0.6 mM linoleic acid solution was added, mixed well and the change in absorbance at 234 nm was recorded for 6 min. Indomethacin was used as a reference standard. The percent inhibition was calculated from the following equation:

% inhibition=
$$[(A_{control}-A_{sample}) / Ac_{ontrol}] \times 100$$
 (1)

A dose-response curve was plotted to determine the IC_{50} values. IC_{50} is defined as the concentration sufficient to obtain 50% of a maximum anti-inflammatory activity. All tests and analyses were performed in triplicates.

2. 4. DPPH Radical Scavenging Activity

Free radical scavenging capacity of isolated compounds and extracts were evaluated according to the previously reported procedure using the stable DPPH. 12 Briefly, 10 μL of sample in DMSO at different concentrations (125–0.24 $\mu g/mL$) were added to 190 μL methanol solution of DPPH (0.1 mM) in a well of 96-well plate. The mixture was shaken vigorously and allowed to stand in the dark at room temperature for 30 min. Absorbance read-

ings were taken at 517 nm. The percent radical scavenging activity of extracts and standard against DPPH were calculated according to the following:

DPPH radical-scavenging activity (%) =
=
$$[(A_0-A_1)/A_0] \times 100$$
 (2)

where A_0 is the absorbance of the control (containing all reagents except the test extracts or compounds), and A_1 is the absorbance of the extracts/standard. Extracts or compounds concentration providing 50% inhibition (IC₅₀) was calculated from the graph plotting inhibition percentage against extracts concentration. Tests were carried out in triplicate. BHA, Ascorbic acid and Trolox were used as positive control.

2. 5. ABTS Radical-Scavenging Activity

Free radical scavenging capacity of isolated compounds and extracts was evaluated according to the previously reported procedure. ABTS radical cations were prepared by mixing equal volume of ABTS (7 mM in $\rm H_2O$) and potassium persulfate (4,9 mM in $\rm H_2O$), allowing them to react for 12–16 h at room temperature in the dark. Then, ABTS radical solution was diluted with 96% ethanol to an absorbance of about 0.7 at 734 nm. 10 μL of sample in DMSO at different concentrations (125–0.24 $\mu g/mL$) were added to 190 μL of ABTS radical solution in a well of 96-well plate. The mixture was shaken vigorously and allowed to stand in the dark at room temperature for 30 min. Absorbance readings were taken at 734 nm. The percent radical scavenging activity of extracts and standards against ABTS were calculated according to the following:

ABTS radical-scavenging activity (%) =
=
$$[(A_0-A_1)/A_0] \times 100$$
 (3)

where A_0 is the absorbance of the control (containing all reagents except the test extracts or compounds), and A_1 is the absorbance of the extracts/standards. Extracts or compounds concentration providing 50% inhibition (IC₅₀) was calculated from the graph plotting inhibition percentage against extracts concentration. Tests were carried out in triplicate. BHA, ascorbic acid and trolox were used as positive control.

2. 6. Quantitative Determination of the Total Phenolic Contents of *Stachys Subnuda* Extracts

Total phenolic compound content of extracts was determined according to Gao et al. 13 The assay was adapted to the 96 well microplate format. 10 μL of extracts in various concentrations were mixed with 20 μL Folin-Ciocalteu reagent (Sigma), 200 μL of H_2O , and 100 μL of 15% Na_2CO_3 and the absorbance was measured at 765 nm after 2 h incu-

bation at room temperature. Gallic acid was used as a standard and the total phenolic contents of extracts were expressed as mg/g gallic acid equivalents (GAE)

2. 7. Quantitative Determination of the Total Flavonoid Contents of *Stachys Subnuda* Extracts

Total flavonoid compound content of extracts was determined according to Zhang et al. ¹⁴ The assay was adapted to the 96 well microplate format. 25 μ L of extracts in various concentrations were mixed with 125 μ L of H₂O, and 7.5 μ L of 5% NaNO₂. After 6 min, 15 μ L of 10% AlCl₃ solution was added and incubated for 5 min, followed by the addition of 50 μ L of 1 M NaOH solution. Distilled water was added to bring the total volume to 250 μ L, and the absorbance was immediately measured at 510 nm using a Shimadzu UV-1800 spectrometer. Catechin was used as a standard and total flavonoid content was expressed as mg/g catechin equivalents (CE)

2. 8. Isolation of Active Compounds

In antioxidant activity experiments, ethyl acetate extract showed the best antioxidant activity among all extracts. Therefore, ethyl acetate extract was chosen for isolation. The ethyl acetate extract (2.02 g) was fractionated by CC on silica gel, using a gradient system of CHCl₃/EtOAc/ CH₃OH to yield twenty five fractions. Fractions showing similar TLC profiles were combined to give six sub-fractions (F7-F8: 1.00 g, F9-F10: 0.46 g, F11-F13: 0.20 g, F14-F18: 0.15 g, F19-F22: 0.06 g, F23-F25: 0,04 g). DPPH activity test was performed on these fractions. It has been continued the isolation with F7-F8, having the highest DPPH radical scavenging activity and the most intense compound content on TLC among all fractions [DPPH radical inhibition rate at concentration of 10 µg/mL: 47% (F7-F8), 22% (F9-F10), 16% (F11-F13), 44% (F14-F18), 32% (F19-F22), 31% (F23-F25)]. F7-F8 (1,0 g) was repeatedly chromatographed on a Sephadex LH-20 column, eluted with CH₃OH and then combined sub-fractions was re-chromatographed by preparative TLC with CHCl₃: CH₃OH:H₂O (4:1:2 drops) to give SS1 (32 mg) and SS2 (43.6 mg) (Figure 1, Detailed spectral data is included in supporting information).

2. 9. LC-MS/MS Analysis

LC-MS/MS analysis was carried out using an Absciex 3200 Q trap MS/MS dedector. Experiments were performed with a Shimadzu 20A HPLC system coupled to an Applied Biosystems 3200 Q-Trap LC- MS/MS instrument equipped with an ESI source operating in negative ion mode. For the chromatographic separation, ODS 150 × 4.6 mm, i.d., 3 μm particle size, octadecyl silica gel analytical column operating at 40 °C has been used. The solvent flow rate was maintained at 0.5 mL/min. Detection was carried out with PDA detector. The elution gradient consisted of mobile phases (A) acetonitrile:water:formic acid (10:89:1, v/v/v) and (B) acetonitrile:water:formic acid (89:10:1, v/v/v). The composition of B was increased from 10% to 100% in 40 min. LC-ESI-MS/MS data were collected and processed by Analyst 1.6 software. For enhanced mass scan (EMS), the MS was operated at mass range of 100-1000 amu. Enhanced product ion spectra were measured from m/z 100 up to m/z 1000. Nitrogen was used as the collision gas, and the collision energy was set at 30. The parameters were as follows: Collusion Energy Spread (CES)-0, Declustiring Potential (DP)-20, Enterance Potential (EP)-10, Curtain gas (CUR)-20, Gas Source 1 (GS1)-50, Gas Source 2 (GS2)-50, CAD- medium, Ihe- on and Temperature (TEM)-600. For the IDA experiment, the criteria were arranged for ions greater than 100.000 m/z and smaller than 1000 m/z, and excluded former target ions after 3.0 occurrence(s) for 3.000 seconds.

2. 10. Statistical Analysis

The data were given as means±standard deviations and analysed by one-way analysis of variance (ANOVA) followed by the Tukey's multiple comparison tests using GraphPad Prism 5. Differences between means at p<0.05 levels were considered significant.

3. Results and Discussion

In the present study, it was evaluated anti-inflammatory and antioxidant activities of major compounds isolated from ethyl acetate extract of aerial parts of endemic *Stachys subnuda*. Two acylated flavone glycosides, SS1 and

Figure 1. Chemical structures of major compounds isolated from S. subnuda

SS2, were isolated as major compounds from active F7-F8 sub-fraction of ethyl acetate extract (SSEA) of *S. subnuda* aerial part (Figure 1). All isolated compounds were analyzed by spectroscopic methods (¹H NMR and ¹³C NMR-APT) and their data were compared with those reported in the literature. ^{15,16} To the best of our knowledge, there is no study on flavonoids of *S. subnuda*. However, these compounds have been previously isolated from *Stachys recta*. ¹⁷ In previous studies, it has been reported that different acetylated flavonoids have been isolated from other *Stachys* species. ^{5,6,9,17-19}

Seven phenolic compounds including quinic acid (SS3), 5-caffeoylquinic acid (SS4), isoscutellarein 7-O-allosyl(1–2)glucoside (SS5), isoscutellarein 7-O-[6'''-O-acetyl] allosyl(1+2)glucoside (SS2), 4'-O-methylisoscutellarein 7-O-allosyl(1+2)glucoside (SS6), 4'-O-methylisoscutellarein 7-O-allosyl(1+2)-[6'''-O-acetyl]-glucoside (SS1), 4'-O-methylisoscutellarein 7-O-[6'''-O-acetyl]-allosyl(1-2)-[6'''-O-acetyl]-glucoside (SS7)", were detected by LC/MS-MS (Figure 2) (Table 1).

The results of this analysis showed that the main phenolic compounds of the S. subnuda ethyl acetate extract are SS1 and SS2. Also, these two compounds were isolated from the ethyl acetate extract of *S. subnuda* in the present study. SS3 showed a pseudo molecular ion peak at m/z 191 that fragmented to several ions at m/z 173 and m/z 127. This fragmentation pattern is characteristic for quinic acid. 23 SS4 presented the molecular ion peak at m/z 353 $[M-H]^-$ which fragmented to m/z 191 (base peak) m/z 179, m/z 161 and m/z 135. According to Clifford and colleagues, this compound must be caffeoylquinic acids. Moreover, less amount of ion at m/z 179 indicates that the caffeic acid and quinic acid are linked at 3 positions. So, SS4 was identified as 3-caffeoylquinic acid.²³ SS5 and SS2 presented pseudo molecular ion peaks at m/z 609 and m/z 651, respectively. Both compounds showed the same aglycon ion at m/z 285. Luteolin, kaempferol, isoscutellarein etc. show the same molecular ion peak at m/z 285 [M-H]⁻. Several studies published previously about Stachys species, indicate that isoscutellarein is dominant flavonoid aglycon for Stachys

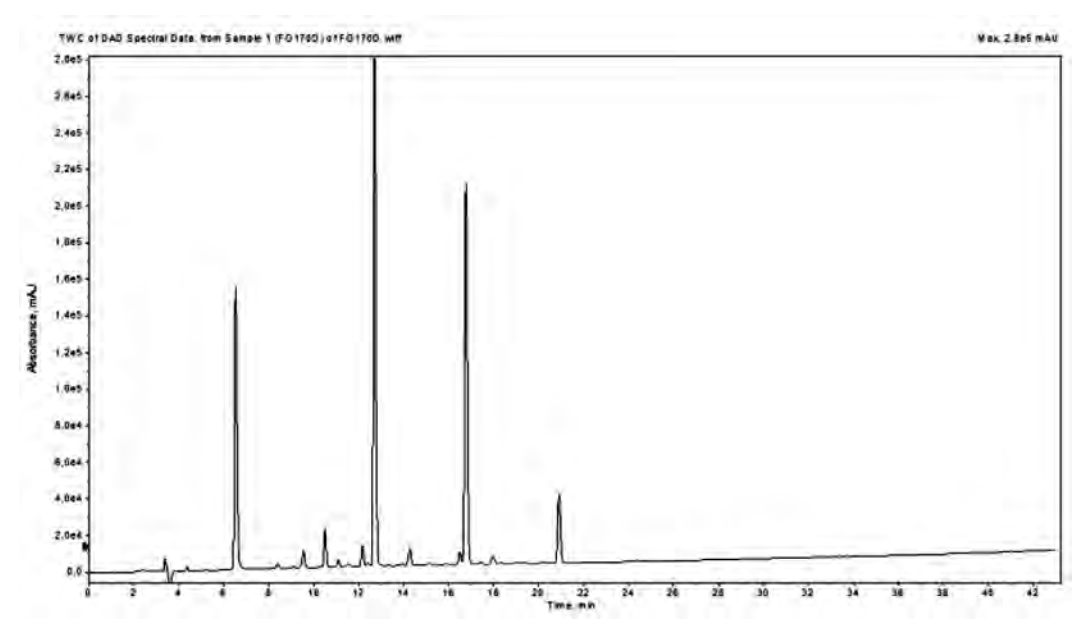


Figure 2. LC-MS/MS chromatogram of ethyl acetate extract of S. subnuda

Table 1. Characterization of phenolic compounds in the ethyl acetate extract of *S. subnuda*

No	Rt min	$[M-H]^-m/z$	MS ²	Identified as	References
SS3	3.3	191	173, 127	Quinic acid	[20]
SS4	6.7	353	191, 179, 161, 135	5-Caffeoylquinic acid	[21]
SS5	10.7	609	429, 285	Isoscutellarein 7-O-allosyl(1–2)glucoside	[21]
SS2	12.9	651	609, 591, 447, 429, 285	Isoscutellarein 7-O-[6'''-O-acetyl]allosyl(1→2)glucoside	
				(Main compound)	[20]
SS6	14.5	623	461, 299, 284	4'-O-methylisoscutellarein 7-O-allosyl(1→2)glucoside	[20]
SS1	17.0	665	299,284	4'-O-methylisoscutellarein 7-O-allosyl(1→2)-[6'''-O-acetyl]	
				-glucoside	[20,22]
SS7	21.2	707	665, 647, 503, 485,	4'-O-Methylisoscutellarein 7-O-[6'''-O-acetyl]-allosyl	
			443, 351, 299, 284	(1-2)-[6"-O-acetyl]-glucoside	[20]

genus. 24,25 Therefore, isoscutellarein was determined as the aglycon of SS5 and SS2. (NMR spectra also supported that the isoscutellarein is an aglycon of this plant material). 324 amu difference between molecular ion peak and aglycon was indicated that isoscutellareain are linked with two-sugar unit. Moreover, the ion at m/z 429 ([M-H]⁻-180) indicates that glycosylation position of the sugars is $1 \rightarrow 2$. ^{22,25} So, according to literature data and MS spectrums, these compounds were identified as Isoscutellarein 7-O-allosyl (1-2) glucoside (SS5) and Isoscutellarein 7-O-[6"'-O-acetyl] allosyl $(1\rightarrow 2)$ glucoside (SS2). According to Petreska et al., there are two substances with the same molecular weight with SS2 which presents similar fragmentation characteristics. The difference between these two compounds is that the acetylation positions of the sugar are different from each other.²² NMR spectrum showed that sugar united acetylated at 6" position for SS2 which was also isolated from the plant material. SS6, SS1 and SS7 showed a molecular ion peak at m/z 623 [M-H]⁻, 665 [M-H]⁻ and 707 [M-H]-, respectively. These compounds presented the same base peak. Ion at m/z 299 that fragmented at m/z 284 is due to the loss of a methyl unit. Methylisoscutellerain is a flavonoid, which is found in many Stachys species.²⁴ Loss of 324 amu between SS6 and its aglycone indicates that SS6 is dihexoside of methylisoscutellerain. Loss of 366 amu (dihexose+acetyl) from molecular ion peak indicates that SS1 is acetyldihexose of methyl isoscutellerain. The difference 408 amu between SS7 and its aglycon indicates that SS7 is diacetyldihexose of methyl isoscutellerain. According to this findings and literature data survey, SS6, SS1 and SS7 identified as 4'-O-methylisoscutellarein 7-O-allosyl $(1\rightarrow 2)$ glucoside, 4'-O-methylisoscutellarein 7-O-allosyl (1→2)-[6"'-O-acetyl]-glucoside and 4'-O-Methylisoscutellarein 7-O-[6" -O-acetyl]-allosyl (1-2)-[6"-O-acetyl]-glucoside, respectively.

All of the extracts except for the SSH extract were found to have a significant antioxidant activity. SSEA extract showed the highest antioxidant activity in DPPH and ABTS assays with IC $_{50}$ values of 3.7 and 5.3 μ g/mL, respectively. Also, the highest total phenol and total flavonoid

content were found in the SSEA (219.4 and 78.3 mg/g, respectively) (Table 2). There are no reports on antioxidant activity of extracts and isolated flavonoids from Stachys subnuda but a large number of studies are available on different Stachys species in the literature. In these studies, Stachys species have been reported to exhibit a significant antioxidant activity. In one of these studies, Erdemoglu et al.²⁶ reported that water extract of Stachys byzantine was active against the DPPH radical with an IC50 value of 640 μg/mL. In another study, the radical scavenging activity of Stachys glutinosa ethanol extract was found to be 280 µg/ mL and 320 μg/mL of IC₅₀ values in DPPH and ABTS experiments, respectively.8 Ghasemi et al.27 reported that methanol extract of Stachys lavandulifolia against DPPH and ABTS radicals had antioxidant activity with the IC₅₀ values of 2320 and 3770 µg/mL, respectively. In the same study, it had been suggested that total phenolic and flavonoid contents of this species were 99 mg/g and 9.05 mg/g, respectively. Also, Šliumpaitė et al.²⁸ reported that total phenol content of methanol extracts of Stachys officinalis was 61.2 mg/g, expressed as gallic acid equivalent. When compared these results with our current study, it can be seen that Stachys subnuda has a better antioxidant activity and a higher total phenolic and flavonoid content. Phenolic compounds present in plants are known to be powerful antioxidants.29 Therefore, these compounds may be responsible for the antioxidant activity of the plant.

Isolated two acylated flavone glycosides were tested for their DPPH and ABTS radical scavenging activity. SS1 showed the highest antioxidant activity in DPPH and ABTS assays with IC50 values of 2.35 and 1.98 µg/mL, followed by SS2 (13.94 and 12.76 µg/mL), respectively. Also, SS1 showed better antioxidant activity compared to standards (Table 3). Delazar et al. 18 investigated antioxidant activity of two flavonoid glycosides, chrysoeriol 7-O-[6-O-acetyl- β -D-allopyranosyl]-(1'2)- β -D-glucopyranoside and apigenin 7-O- β -D-(6-p-coumaroyl)-glucopyranoside, isolated from *Stachys bombycina* and these compounds have been demonstrated to possess strong antioxidant activity with of IC50 values of 12.5 and 0.77 µg/

 Table 2. Antioxidant activities, total phenolic and flavonoid contents of various extracts from aerial parts S. subnuda

Extracts*	DPPH activity	ABTS	activity	TPC****	TFC****
	$IC_{50} (\mu gmL^{-1})^{**}$	$IC_{50}\left(\mu gmL^{-1}\right)$	mM TE/g extract***	(mg GAE/g extract) ^c	(mg CE/g extract) ^d
SSH	180.1 ± 0.26 ^e	97.0 ± 1.37 ^c	5.1 ± 0.79^{a}	33.6 ± 1.54^{a}	10.0 ± 0.82^{a}
SSC	13.4 ± 0.00^{b}	8.2 ± 0.35^{a}	62.4 ± 0.92^{d}	112.3 ± 3.29^{c}	41.5 ± 1.92^{b}
SSEA	3.7 ± 1.00^{a}	5.3 ± 0.20^{a}	99.2 ± 2.02^{e}	219.4 ± 2.18^{d}	78.3 ± 3.13^{d}
SSM	24.4 ± 0.45^{b}	16.0 ± 0.46^{b}	31.2 ± 0.19^{c}	112.6 ± 1.69^{c}	$57.4 \pm 1.63^{\circ}$
SSAM	39.5 ± 1.03^{d}	21.8 ± 1.21^{b}	20.9 ± 1.65^{b}	90.36 ± 2.83^{b}	$63.5 \pm 1.42^{\circ}$

^{*}The methanol, n-hexane, chloroform, ethyl acetate and aqueous methanol extracts were coded as SSM, SSH, SSC, SSEA and SSAM, respectively.

^{**}Values corresponding to the amount of extract required to scavenge 50% of radicals present in the reaction mixture.

^{***}ABTS radical scavenging activity were expressed as trolox equivalent (TE)

^{****}Total phenolic content (TPC) was expressed as gallic acid equivalent (GAE).

^{*****}Total flavonoid content (TFC) was expressed as catechin equivalent (CE). Each value in the table is represented as mean \pm SD (n = 3). Different letter superscripts in the same column indicate significant differences (p < 0.05).

Compounds/ Standards	DPPH activity	ABTS activity	Anti-inflammatory activity
		IC ₅₀ (μgmL ⁻¹)	
SS1	2.35 ± 0.00^{a}	1.98 ± 0.01^{a}	47.23 ± 1.95^{b}
SS2	$13.94 \pm 1,65^{b}$	12.76 ± 0.00^{b}	41.60 ± 2.09^{b}
Ascorbic acid	17.60 ± 0.37^{b}	14.50 ± 0.32^{b}	
Trolox	14.54 ± 0.18^{b}	13.00 ± 0.21^{b}	
Butylated hydroxyanisole	57.15 ± 0.09^{c}	17.06 ± 0.58^{b}	
Indomethacin			22.39 ± 0.26^{a}

Table 3. Antioxidant and anti-inflammatory activities of compounds isolated from Stachys subnuda and standards

Each value in the table is represented as mean \pm SD (n = 3). Different letter superscripts in the same column indicate significant differences (p < 0.05).

mL, respectively. Similarly, two active acylated flavone glycosides isolated in present study, especially SS1, showed strong antioxidant activity. It has also been found that the SS1 has very good antioxidant activity when compared to the standards. When the results of the antioxidant activity of the ethyl acetate extract are compared with the isolated compounds, it might be considered that these compounds are responsible for the activity of the ethyl acetate extract. Also, flavonoids are generally known to be compounds with antioxidant activity. For this reason, it can be assumed that these groups of compounds are responsible for the activity of the extract.

Each value in the table is represented as mean \pm SD (n = 3). Different letter superscripts in the same column indicate significant differences (p < 0.05).

SS1 and SS2 displayed 5-lipoxygenase (5-LOX) inhibitory activity with IC $_{50}$ values of 47.23 and 41.60 µg/mL (Table 3). As far as we know, there is no report on anti-inflammatory activity of these compounds. However, in a previous study, Alcaraz et al. 31 reported that isoscutellarein, a flavonoid aglycone, inhibited 15-lipoxygenase (15-LOX) activity. Also, Yoshimoto et al. 32 have shown that flavonoids are potent inhibitors of 5-lipoxygenase. Similarly, SS1 and SS2, the flavonoids isolated from ethyl acetate extract of *S. subnuda* aerial part in our current study, showed good anti-lipoxygenase activity and these results are compatible with previous findings.

4. Conclusion

These results indicate that SS1 and SS2 with other compounds present in ethyl acetate extract of *Stachys subnuda* may be responsible for the anti-inflammatory and antioxidant activity of the extract. Also, these results show that SS1 and SS2 isolated from *Stachys subnuda* have strong antioxidant and good anti-inflammatory activity. These isolated compounds can be used as a natural antioxidant source in food, pharmaceutical and cosmetic industries. However, further studies, such as *in vivo* tests, are needed to clarify the antioxidant and anti-inflammatory effects of these compounds.

Conflicts of interest

The authors declare no conflict of interest.

Acknowledgements

This work was supported by a grant from the Scientific and Technological Research Council of Turkey (TUBITAK), under the project 1919B011603877 (Code: 2209-A).

Appendix A. Supplementary Data

Spectral data of compounds isolated from ethyl acetate extract of aerial parts of Endemic *Stachys subnuda* can be found in Appendix.

List of Abbreviations

5-LOX: 5-lipoxygenase

ABTS: 2,2'-azino-bis-3-ethylbenzthiazoline-6-sulphonic

acid

BHA: Butylated hydroxyanisole

CE: Catechin equivalent

DMSO: Dimethyl Sulfoxide

DPPH: 1,1-diphenyl-2-picrylhydrazyl

EtOAc: Ethyl acetate

F7-F8: Fraction 7- Fraction 8

F9-F10: Fraction 9- Fraction 10

F11-F13: Fraction 11- Fraction 13

F14-F18: Fraction 14- Fraction 18

F19-F22: Fraction 19- Fraction 22

F23-F25: Fraction 23- Fraction 25

GAE: Gallic acid equivalent

HPLC: High Performance Liquid Chromatography

IC₅₀: The concentration of extract that sweeps 50% of the radical or inhibits the activity of the enzyme by 50%

LC-MS/MS: Liquid chromatography linked to tandem mass spectrometry

MARE: Herbarium of the Faculty of Pharmacy, Marmara University

ODS: Octadecyl-silica

SS1: 4'-*O*-methylisoscutellarein-7-*O*-2"-*O*-(6"'-*O*-acetyl- β -D-allopyranosyl)- β -D glucopyranoside

- SS2: İsoscutellarein-7-*O*-2"-*O*-(6"'-*O*-acetyl-β-D-allopyranosyl)-β-D-glucopyranoside
- SS3: Quinic acid
- SS4: 5-Caffeoylquinic acid
- SS5: Isoscutellarein 7-O-allosyl(1 -2)glucoside
- SS6: 4'-O-methylisoscutellarein 7-O-allosyl(1→2) glucoside
- SS7: 4'-O-Methylisoscutellarein 7-O-[6'''-O-acetyl]-allosyl(1-2)-[6''-O-acetyl]-glucoside
- SSM: Methanol extract of Stachys subnuda
- SSH: Hexane fraction of methanol extract of *Stachys* subnuda
- SSC: Chloroform fraction of methanol extract of *Stachys* subnuda
- SSEA: Ethyl acetate fraction of methanol extract of *Stachys subnuda*
- SSAM: Aqueous methanol fraction of methanol extract of *Stachys subnuda*
- TE: Trolox equivalent
- TFC: Total flavonoid content
- TLC: Thin layer chromatography
- TPC: Total phenolic content

5. References

- 1. V. B. Vundac, H. W. Pfeifhofer, A. H. Brantner, Z. Males, M. Plazibat, *Biochem Syst Ecol* **2006**, *34*, 875–881.
 - DOI:10.1016/j.bse.2006.04.010
- 2. G. İscan, Y. B. Kose, B. Demirci, *Anadolu Univ J Sci Technol-C Life Sci Biotechnol* **2015**, *4*, 41–47.
- 3. A. C. Gören, Rec Nat Prod 2014, 8, 71-82.
- 4. A. Sen, M. Kurkcuoglu, L. Bitis, A. Dogan, K. H. C. Baser, *J Essent Oil Res*, **2019**, *31*, 326–334.
 - **DOI:**10.1080/10412905.2019.1567399
- A. Venditti, A. Bianco, M. Nicoletti, L. Quassinti, M. Bramucci, G. Lupidi, LA. Vitali, F. Papa, S. Vittori, D. Petrelli, L. Maleci Bini, C. Giuliani, F. Maggi, *Chem Biodivers* 2014, 11, 245–261. DOI:10.1002/cbdv.201300253
- A. Venditti, A. Bianco, L. Quassinti, M. Bramucci, G. Lupidi, S. Damiano, F. Papa, S. Vittori, L. Maleci Bini, C. Giuliani, D. Lucarini, F. Maggi, *Chem Biodivers* 2015, 12, 1172–1183. DOI:10.1002/cbdv.201400275
- Ael-H Mohamed, NS. Mohamed, Nat Prod Res 2014, 28, 30–34. DOI:10.1080/14786419.2013.830217
- L. Leporini, L. Menghini, M. Foddai, G. L. Petretto, M. Chessa, B. Tirillini, G. Pintore, *Nat Prod Res* 2015, 29, 899–907.
 DOI:10.1080/14786419.2014.955490
- S. Laggoune, A. Zeghib, A. Kabouche, Z. Kabouche, Y. A. Maklad, F. Leon, I. Brouard, J. Bermejo, C. A. Calliste, J. L. Duroux, *Arabian J Chem* 2016, 9, S191–S197.
 DOI:10.1016/j.arabjc.2011.03.005
- A. H. Ebrahimabadi, E. H. Ebrahimabadi, Z. Djafari-Bidgoli,
 F. J. Kashi, A. Mazoochi, H. Batooli, Food Chem 2010, 119,
 452–458. DOI:10.1016/j.foodchem.2009.06.037

- N. Phosrithong, N. Nuchtavorn, Eur J Integr Med 2016, 8, 281–285. DOI:10.1016/j.eujim.2015.10.002
- 12. Y. Zou, S.K. Chang, Y. Gu, S. Y. Qian, *J Agric Food Chem*, **2011**, 59, 2268–2276. **DOI**:10.1021/jf104640k
- X. Gao, M. Ohlander, N. Jeppsson, L. Björk, V. Trajkovski, *J Agric Food Chem* **2000**, *48*, 1485–1490.
 DOI:10.1021/jf991072g
- 14. R. Zhang, Q. Zeng, Y. Deng, M. Zhang, Z. Wei, Y. Zhan, X. Tang, Food Chem 2013, 136, 1169–1176.
 - DOI:10.1016/j.foodchem.2012.09.085
- D. C. Albach, R. J. Grayer, S. R. Jensen, F. Ozgokce, N. C. Veitch, *Phytochemistry*, **2003**, *64*, 1295–1301.
 DOI:10.1016/j.phytochem.2003.08.012
- I. Saracoglu, Ş. Harput, Y. Ogihara, Turk J Chem 2004, 28, 751–759.
- 17. A. Lenherr, M. F. Lahloub, O. Sticher, *Phytochemistry*, **1984**, **23**, 2343–2345. **DOI**:10.1016/S0031-9422(00)80548-8
- A. Delazar, S. Celik, R. S. Göktürk, O. Unal, L. Nahar, S. D. Sarker, *Pharmazie* 2005, 60, 878–880.
- 19. B. Tepe, S. Degerli, S. Arslan, E. Malatyali, C. Sarikurkcu, *Fitoterapia* **2011**, *82*, 237–246. **DOI:**10.1016/j.fitote.2010.10.006
- J. Petreska Stanoeva, D. Bagashovska, M. Stefova, Maced J Chem Chem En 2012, 31, 229–243.
- 21. J. Petreska, M. Stefova, F. Ferreres, D. A. Moreno, F. A. Tomás-Barberán, G. Stefkov, S. Kulevanova, A. Gil-Izquierdo, *Food Chem* **2011**, *125*, 13–20.
 - DOI:10.1016/j.foodchem.2010.08.019
- J. Petreska, G. Stefkov, S. Kulevanova, K. Alipieva, V. Bankova, M. Stefova, *Nat Prod Commun* 2011, 6, 21–30.
 DOI:10.1177/1934578X1100600107
- M. N. Clifford, K. L. Johnston, S. Knight, N. Kuhnert, *J Agric Food Chem* 2003, 51, 2900–2911. DOI:10.1021/jf026187q
- 24. A. Ulubelen, G. Topcu, U. Kolak, in: R. Atta ur (Ed.): Labiatae flavonoids and their bioactivity, Studies in Natural Products Chemistry, Elsevier. **2005**, pp. 233–302.
 - **DOI:**10.1016/S1572-5995(05)80035-3
- O. R. Pereira, M. R. Domingues, A. M. Silva, S. M. Cardoso, Food Res Inter 2012, 48, 330–335.
 DOI:10.1016/j.foodres.2012.04.009
- N. Erdemoglu, N. N. Turan, I. Cakici, B. Sener, A. Aydin, *Phytother Res* 2006, 20, 9–13. DOI:10.1002/ptr.1816
- A. Ghasemi Pirbalouti, A. Siahpoosh, M. Setayesh, L. Craker, *Med Food* 2014, 17, 1151–1157. DOI:10.1089/jmf.2013.0057
- I. Šliumpaitė, P.R. Venskutonis, M. Murkovic, O. Ragažinskienė, *Ind Crops Prod* 2013, 50, 715–722.
 DOI:10.1016/j.indcrop.2013.08.024
- 29. P. Kapewangolo, J. J. Omolo, R. Bruwer, P. Fonteh, and D. Meyer, *J Inflam* **2015**, *12*, 1–13. **DOI:**10.1186/s12950-015-0049-4
- 30. K. E. Heim, A. R. Tagliaferro, D.J. Bobilya, *J Nutr Biochem* **2002**, *13*, 572–584. **DOI:**10.1016/S0955-2863(02)00208-5
- 31. M. J. Alcaraz, J. R. Hoult, *Arch Int Pharmacodyn Ther*, **1985**, 278, 4–12.
- 32. T. Yoshimoto, M. Furukawa, S. Yamamoto, T. Horie, S. Watanabe-Kohno, *Biochem Biophys Res Commun* **1983**, *116*, 612–618. **DOI**:10.1016/0006-291X(83)90568-5

Povzetek

V tej študiji, smo poročali o protivnetni in antioksidativni dejavnosti dveh aciliranih izoscutelarinskih glukozidov, izoliranih iz etil acetatnega ekstrakta Stachys subnuda it dela zraka. 4 '-o-metilisoscutelaren-7-O-2 ',-O-(6 '''-O-acetil-β-D-alopiranosil)-β-D-glucopiranosid (1) in izooscutelaren-7-O-2"-O-(6 '''-O-acetil-β-D-alopiranosil)-β-D-glucopiranoside (2) so bile izolirane kot glavne spojine iz etil acetatnega izvleček (EAE). Tudi 2 derivata hidroksicinične kisline, in 5 isoscutelaren glukozidni derivati v EAE so bili najdeni z uporabo LC-MS/MS. Spojina 1 z IC50 vrednostjo 2,35 ve 1,98 μg/mL in spojina 2, z IC50 vrednosti 13,94 ve 12,76 μg/mL, je pokazala dokaj močno antioksidantno aktivnost proti radikalom DPPH in ABTS. Spojini 1 in 2 sta inhibirali 5-lipooksigenazno (5-LOX) aktivnost z IC50 vrednostmi približno 47,23 in 41,60 μg/mL. Rezultati so pokazali, da imajo izolirane spojine pomembno protivnetno in antioksidativno zmožnost. Acetilirane flavonoidni glikozidi so bili prvič poročani za Stachys subnuda. Tudi njihove dejavnosti so bile prvič preiskane v tej študiji.



Except when otherwise noted, articles in this journal are published under the terms and conditions of the Creative Commons Attribution 4.0 International License

Scientific paper

Fabrication and Application of a New Modified Electrochemical Sensor Using Newly Synthesized Calixarene-Grafted MWCNTs for Simultaneous Determination of Cu(II) and Pb(II)

Semahat Kucukkolbasi,1,* Serkan Sayin2 and Mustafa Yilmaz1

¹ Selcuk University, Faculty of Science, Department of Chemistry, 42075 Konya, Turkey

² Department of Environmental Engineering, Faculty of Engineering, Giresun University, Giresun-28200, Turkey

* Corresponding author: E-mail: ksemahat@gmail.com Tel:+ 903322233857

Received: 12-18-2018

Abstract

A rapid, simple, selective and highly sensitive simultaneous determination of Cu(II) and Pb(II) via newly fashioned 5,11,17,23-tetra-*tert*-butyl-25,27-dihydrazinamidecarbonylmethoxy-26,28-dihydroxycalix[4]arene-grafted multi-walled carbon nanotubes-modified carbon paste electrode (CNT-Calix/CPE) by differential pulse anodic stripping voltammetry (DPASV) has been introduced. It was observed that CNT-Calix/CPE exhibits higher selectivity and stability for Cu(II) and Pb(II). Different operational parameters such as pH, deposition potential/time, pulse amplitude (5, -1.0 V vs. Ag/AgCl, 300 s, 2 s, 0.05 V) were also optimized for calculation and statistical evaluation of linear range, detection limit and limit of quantification. Interference study shows that the electrode is highly selective for the simultaneous determination of Cu(II) and Pb(II). Standard addition method was used to apply CNT-Calix/CPE in waste water, plant leaves and soft drinks and it was found that the concentration of Cu(II) and Pb(II) were corresponding to standardized values.

Keywords: Calixarene; MWCNT; modified carbon paste electrode; sensor

1. Introduction

In recent years, attention has been paid by scientists to the heavy metal ion discharge into the environment because of their highly toxic effects for the living organisms even at trace concentrations. Lexposure to the lead, which is known as one of the most toxic elements, may result in bioaccumulation processes in the hematopoietic, hepatic, renal, and gastrointestinal systems of humans; therefore, it can cause serious toxic effects on human health. Anthropogenic activities are the main source of lead along with industrial emissions. Particularly water and food samples are highly affected by lead contamination near sources. Copper is an essential element in the nutrition of plants and animals, but higher concentrations of copper can cause symptoms of gastroenteritis with nausea, hypercupremia, vomiting, myalgia, and hemolysis.

Because heavy metal ions are toxic even at trace concentrations, they should be present in limited values in environmental and biological materials. Therefore, rapid, simple, and accurate analytical methods with low detection limits are necessary for the determination of trace level of Pb(II) and Cu(II) in the environment, food, and drinks. A number of qualitative and quantitative methods have been utilized such as atomic absorption spectrometry (AAS), inductively coupled plasma mass spectrometry (ICP MS), inductively coupled plasma optical emission spectrometry (ICP OES) and UV-Vis spectrometry.^{6,7} But these methods require some time-consuming manipulation steps, expensive instruments and special training.^{8,9}

Calixarenes comprising of phenol and formaldehyde via the poly-condensation reaction display immense fundamental role as receptors of a large variety of molecular and ionic guest systems and have the fascinating framework. ^{10–12} In the past few years, various calixarene derivatives, which were functionalized with cationic, anionic, and organic/bimolecular-binding groups, have shown outstanding vehicle properties for the extraction

or recognition of cations, anions, and organic/biomolecules. 13-15

Electrochemical methods, especially anodic stripping voltammetry, provide great advantages compared to other techniques due to their high sensitivity and selectivity, good response with saline matrices, high-speed analysis, multi-elemental analysis, and low-cost. ¹⁶ During the simultaneous voltammetric determination of heavy metals, the hanging mercury drop electrode (HDME) and mercury film electrode (MFE) were used as traditional working electrodes. However, the toxicity of mercury leads to the development of alternative working electrodes. Therefore, mercury-free electrodes such as bismuth film electrode, gold microwire electrode, carbon paste electrodes, carbon nanotube electrodes, and silver electrodes have been developed to determine metal ions. ^{17,18}

To improve the electrochemical performance of electrodes, chemical or physical modification is carried out by altering their surfaces. Because carbon paste electrodes (CPEs) can be easily modified, renewed, and prepared, they have been widely used as matrices for the preparation of the modified electrodes. Moreover, CPEs provide broad potential usages compared to other modified electrodes, ¹⁹ and also show relative residual currents 10 times lower than the solid graphite electrode.²⁰ Functionalization of CNTs with molecules having an affinity toward heavy metals is a good strategy to accumulate higher amounts of metal ions on the surface and to achieve lower detection limits while using lower accumulation times.²¹ Nowadays, carbon nanotubes (CNTs) have also been used in carbon paste electrodes.^{22,23} CNTs have very interesting physicochemical properties, such as ordered structure with high aspect ratio, ultra-light weight, high mechanical strength, high electrical conductivity, high thermal conductivity, metallic or semi-metallic behavior, and high surface area.²⁴

In this work, a new chemically modified carbon paste electrode with calixarene-grafted multi walled carbon nanotubes (MWCNT) has been prepared for the simultaneous determination of trace amounts of Cu(II) and Pb(II) by differential pulse anodic stripping voltammetry (DPASV). Such properties caused observing low detection limits in the voltammetric determinations with modified CPEs as a working electrode. It was successfully applied as a selective agent for the voltammetric determination of copper and lead at a carbon paste electrode. The created selectivity in this method makes the electrode very suitable for the detection of trace amounts of these metal ions in various real samples.

2. Materials and Methods

2. 1. General

All starting materials and reagents used were of standard analytical grade from Merck or Aldrich and used without further purification. All commercial grade solvents were distilled, and then stored over molecular sieves. Dry THF

was distilled from the ketyl prepared from sodium and benzophenone. CH2Cl2 was distilled from CaCl2, while MeOH was distilled over Mg and stored over molecular sieves. All reactions, unless otherwise noted, were conducted under a nitrogen atmosphere. TLC was performed on DC Alufolien-Kieselgel 60 F₂₅₄ (Merck). ¹H NMR was recorded on a Varian 400 MHz spectrometer. IR spectra were acquired on a Perkin–Elmer 1605 FTIR spectrometer through KBr pellets. All aqueous solutions were prepared with deionized water that was obtained via a Millipore Milli-Q Plus water purification system and 100/ATR Sampling Accessory. Thermal gravimetric analysis (TGA) was carried out with Seteram thermogravimetric analyzer. The sample mass was 15-17 mg. Analysis was performed from room temperature to 900 °C at a heating rate of 10 °C/min under argon atmosphere with a gas flow rate of 20 mL/min. Elemental analyses were performed using a Leco CHNS-932 analyzer. Melting points were determined on a Gallenkamp apparatus in a sealed capillary glass tube and are uncorrected. Scanning electron microscopy (SEM-JSM 5600) coupled with Energy dispersive analysis of X-ray (EDX) were used for surface morphology and identification of elemental composition of samples.

Differential pulse anodic stripping voltammeter (DP-ASV) by CHI 600 D was used with conventional three-electrode measuring cells: carbon paste electrode (BAS MF 2010) as working electrode, an Ag/AgCI (3 M NaCI) electrode (BAS MF 2052), and a platinum wire (BAS MW 1034) as reference and auxiliary electrode, respectively, for the simultaneous determination of Pb(II) and Cu(II). 0.2 M PBS (Na₂HPO₄-NaH₂PO₄) electrolyte showed best voltammetric signals for these metals using carbon paste working electrode. To avoid accidental contamination, voltammetric cell was rinsed every day before the measurements with supra pure concentrated HNO3. All measurements were made at room temperature in solutions deoxygenated with N2 for 300 s and kept under a nitrogen atmosphere during the measurement. Teflon-coated magnetic stirring bar was used for stirring the sample solutions in electrolysis step. pH was measured by Orion 410A + pH meter. CEM-MDS 2000 closed vessel microwave system was used in this study to prepare real and certified samples.

2. 2. Synthesis

The syntheses of compounds 1–3 were carried out according to the procedures in literature.^{25–27} Carbon nanotubes (CNTs) were oxidized to afford carboxylic acid functionalized CNTs (CNT-COOH) according to the literature procedure.²⁸ Calixarene-adorned CNT (CNT-Calix) is herein reported for the first time.

2. 2. 1. Synthesis of p-tert-butylcalix[4] arene-diester (2)

Yield: 14 g (63.4 %); mp: 202–207 °C. FTIR (KBr): 1750 cm $^{-1}$ (C=O). 1 H-NMR (CDCl $_{3}$): δ 0.97 (s, 18H, Bu t),

1.24 (s, 18H, Bu^t), 3.35 (d, 4H, J = 12.6 Hz, Ar-CH₂-Ar), 3.85 (s, 6H, -OCH₃), 4.45 (d, 4H, J = 12.6, Ar-CH₂-Ar), 4.78 (s, 4H, -OCH₂CO), 6.85 (s, 4H, ArH), 7.05 (s, 4H, ArH), 7.10 (s, 2H, OH).

2. 2. 2. Synthesis of 5,11,17,23-tetra-tert-butyl-25,27-dihydrazinamidecarbonylmethoxy-26,28-dihydroxy-calix[4]arene (3)

Yield: 1.6 g (53.3 %); mp: 330–333 °C. FTIR (KBr): $1687 \text{ cm}^{-1} \text{ (N-C=O)}. \, ^{1}\text{H-NMR} \text{ (400 MHz, CDCl}_{3}): δ 1.02 (s, 18H, But), 1.26 (s, 18H, But), 2.15 (d, 4H, <math>J = 1.6 \text{ Hz}, \text{NH}_{2})$, 3.42 (d, 4H, J = 13.3 Hz, Ar-CH₂-Ar), 4.11 (d, 4H, J = 13.2 Hz, Ar-CH₂-Ar), 4.63 (s, 4H, -OCH₂), 6.92 (s, 4H, ArH), 7.10 (s, 4H, ArH), 7.70 (s, 2H, -OH), 9.61 (brs, 2H, NH).

2. 2. 3. Preparation of CNT-Calix

A mixture of CNT-COOH (0.4 g), DCC (0.25 g, 1.21 mmol) and HOBt (0.16 g, 1.21 mmol) in 15 mL of DMF was stirred at room temparature for 15 min. Then, dihydrazine amide derivative of calix[4]arene 3 (0.4 g, 0.50 mmol) was added to the mixture and allowed to stir for further 3 days. The mixture was filtered and washed with $\mathrm{CH_2Cl_2}$ to remove unbound calixarene derivative 3, and washed with water to adjust pH 7.0, and the residual solid was then vacuum-dried to yield 0.51 g of CNT-Calix.

2. 2. 2. Preparation of Unmodified Carbon Paste Electrode (CPE) and Carbon Paste Modified by CNT-Calix/CPE

The unmodified CPE was prepared by mixing fine graphite powder with appropriate amount of paraffin oil and thorough hand mixing in a mortar and pestle (79:21, w/w). The modified CNT-Calix/CPE was prepared by hand-mixing graphite powder 72.5% (w/w) with the CNT-Calix 5.0% (w/w) and then paraffin oil 22.5% (w/w) was mixed thoroughly for approximately 20 min to form the homogeneous modified carbon paste electrodes. Afterwards, the paste was positioned into the bottom of the working electrode body (BAS MP 5023) and the electrode surface was polished with a weight paper to have a smooth surface. Calibration curves were plotted for each electrode and the optimum composition was obtained by comparing their sensitivities and working ranges. The electrodes were washed with distillated water and working buffer between measurements. Electrodes were stored in refrigerator at +4 °C when not in use.

2. 3. Analytical Procedure

A certain amount of standard or sample solution and 6.0 mL of PBS (pH 5.0) were transferred into the

electrochemical cell and degassed with highly pure nitrogen gas for at least 5 min. The electrochemical behavior of CNT-Calix was investigated by cyclic voltammetry (CV) in K₃Fe(CN)₆/K₄Fe(CN)₆ solution. The analysis of Cu(II) and Pb(II) using DPASV was carried out in the following steps: (a) deposition step: electrode was held at starting potential of 1.5 V vs. Ag/AgCl in stirred solution for 60 s by applying chronoamperometric method before each measurement to confirm dissolution of the residual deposits on the surface of the modified electrode; (b) the deposition step proceeded at -1.0 V vs. Ag/AgCl in stirred solution for 300 s; at the end of the deposition time, stirring was stopped and a 2 s resting time was allowed for the solution to become quiescent; (c) the differential pulse anodic stripping voltammograms were recorded when swept from -0.8 V to 0.3 V vs. Ag/AgCl. The peak currents at about 0.11 and -0.42 V vs. Ag/AgCl for Cu(II) and Pb(II) were measured, respectively. All measurements were carried out at room temperature. Calibration curve was obtained between net anodic peak currents vs. Cu(II) and Pb(II) concentrations. % recovery was calculated by carrying out the recovery studies with a synthetic sample solution with a wide range of concentration. Synthetic binary mixtures sample solutions were prepared from standard solutions and obtained by adding varying amounts of Pb(II) in a linear concentration range to Cu(II). Various known amounts of Cu(II) and Pb(II) were subsequently analyzed by the proposed elec-

2. 4. Preparation of Real Samples

For the validation, applicability, and reliability of the method, several real samples, including waste water, dried horse chestnut leaf, apple juice, and turnip juice were prepared and analyzed by the proposed method. Waste water samples were taken from KOSKI (Konya Water and Sewerage Administration) without pretreatment before determination. Apple juice, turnip juice were purchased from a local market in Konya, Turkey. The pH of the samples was adjusted before Cu(II) and Pb(II) content determination as described in Section 3.4.

For the determination of Cu(II) and Pb(II) in horse chestnut leaves samples, dried leaf samples were homogenized in a blender and one gram of homogenate was digested by microwave digestion system. CEM-MDS 2000 closed vessel microwave system (maximum pressure 800 psi, maximum temperature 220 °C) was used. Digestion conditions for microwave system for the samples were applied as 2 min for 250 W, 2 min for 0 W, 6 min for 250 W, 5 min for 400 W, 8 min for 550 W and ventilation for 8 min. After digestion, the residues were diluted to 25 mL with deionized water.

The measurements were evaluated according to Apple Leaves standards 1515 which were provided by the High-Purity Standards, NIST.

3. Results and Discussion

3. 1. Preparation of Calixarene-Grafted MWCNT

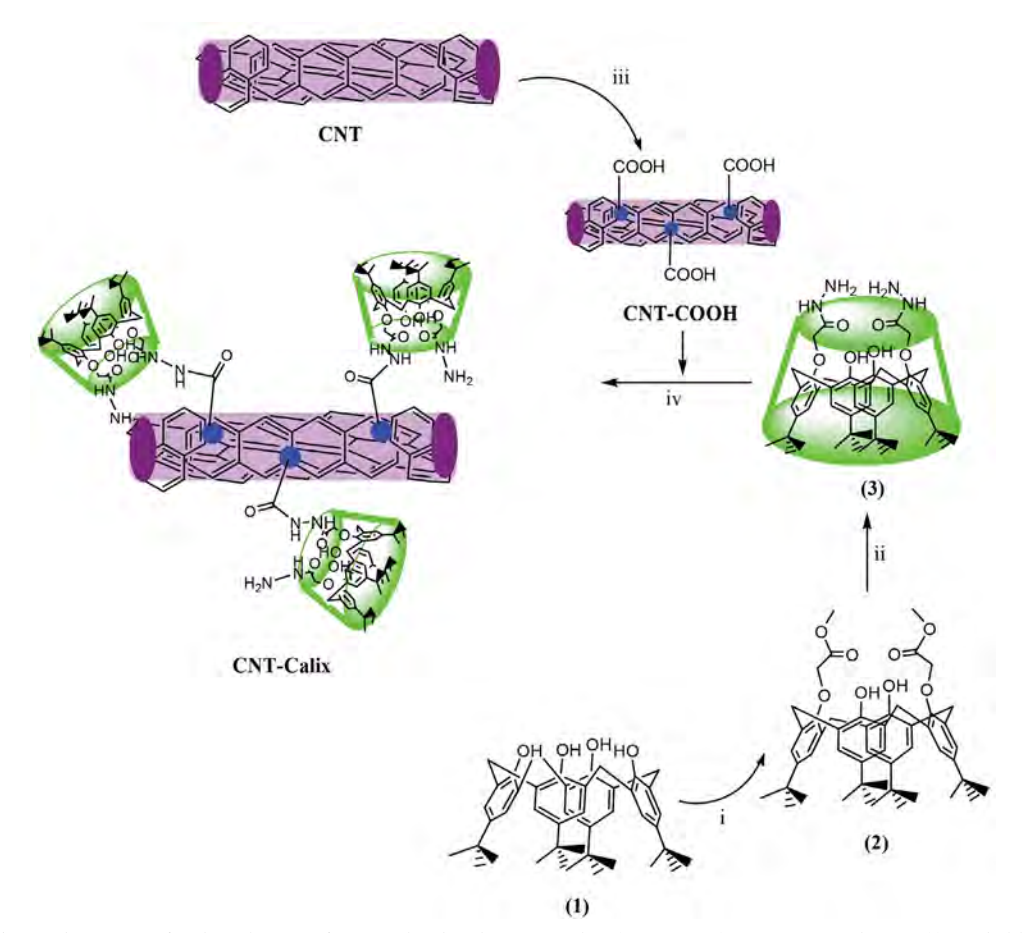
In this study, p-tert-butylcalix[4]arene 1 has been used as the starting compound, which was synthesized according to the literature.²⁴ p-tert-Butylcalix[4]arene 1 was functionalized with methylbromoacetate in the presence of K₂CO₃ to afford di-ester derivative 2.²⁶ Di-ester derivative 2 was then treated with hydrazine under suitable reaction conditions following the literature to obtain dihydrazine amide derivative of calix[4] arene 3 with free primary amine groups.²⁷ Synthesized dihydrazine amide derivative 3 was grafted onto carbon nanotubes containing COOH groups, which oxidized with HNO₃/H₂SO₄ according to the literature²⁸ in order to investigate binding efficiencies of CNT-Calix towards Cu(II) and Pb(II), which is reported for the first time in this article (Scheme 1). Characterization of CNT-Calix was assessed by a combination of FTIR, SEM, TGA and elemental analysis techniques.

FTIR spectroscopy was used to elaborate on the structure of CNT-Calix. Carbon nanotubes with COOH (CNT-COOH) have a characteristic peak at $1700~\rm{cm^{-1}}$ as-

sociated with the carboxylic groups and also provide the absorbance at around 1100 cm⁻¹ corresponding to the other side-groups. On the CNT-Calix curve, the introduction of dihydrazine amide derivative of calix[4]arene 3 is assigned to three different carbonyl peaks which appeared at 1718 cm⁻¹ indicating unbinding COOH unit with calix[4] arene derivative 3, 1628 and 1592 cm⁻¹ associated with the transformation of the carboxylic group to an amide group. In addition, the peaks at 1456 and 1382 cm⁻¹ are attributed to the bending vibration of the aromatic C-C bonds of the calix[4]arene derivative (**Fig. 1**).

The thermogravimetric analysis (TGA) was used to estimate the amount of dihydrazine amide derivative of calix[4]arene 3 onto CNT-COOH. As depicted in Fig. 2, the TGA curve of CNT-Calix reveals that the weight loss of 28.4% mass was due to decomposition of dihydrazine amide derivative of calix[4]arene 3 and unbound CNT-COOH[27] at the range of 200–750 °C.

To obtain more direct information about the amount of loaded dihydrazine amide derivative of calix[4] arene 3 on CNT-COOH, the elemental analysis was evaluated. The results show that CNT-Calix contains 3.59% nitrogen corresponding to 10.27 mmol of Calix/g of CNT (Table 1).



Scheme 1. The synthetic route for the calixarene-functionalized carbon nanotubes (CNT-Calix). Reaction conditions: (i) Methyl bromoacetate, K_2CO_3 , CH_3CN (ii) Hydrazine, CH_2Cl_2/CH_3OH ; (iii) HNO₃, H_2SO_4 ; (iv) DCC, HOBt, DMF.

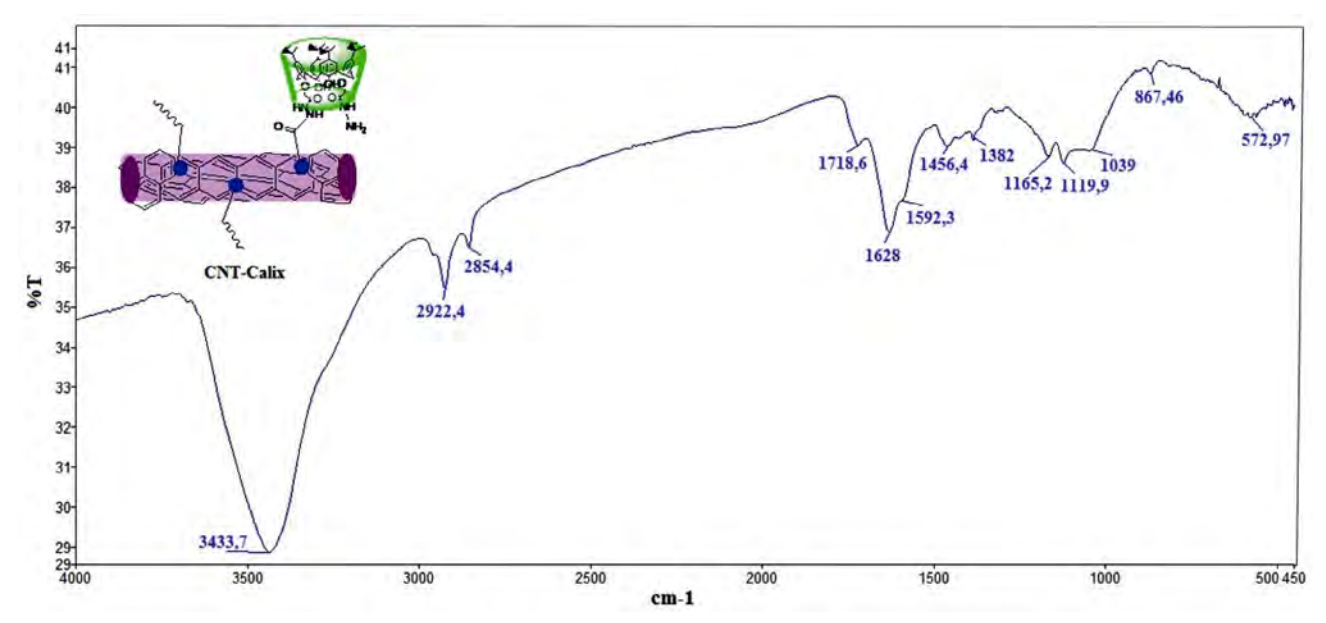


Fig. 1. FTIR spectra of CNT-Calix

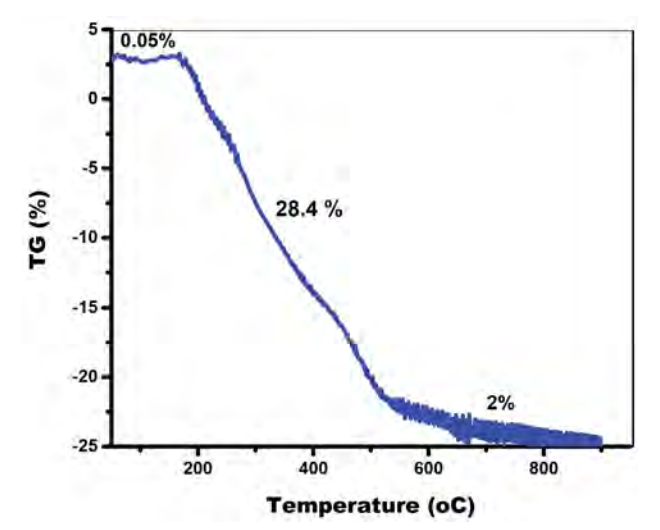


Fig. 2. TGA curve of CNT-Calix

Table 1. Elemental analysis results of CNT-Calix

	C(%)	H(%)	N(%)	Bound amount (mmol/g) ^a
CNT-Calix	75.18	3.84	3.59	10.27

^a Calculated according to the nitrogen content.

3. 2. Characterization of Carbon Paste Electrode

SEM

Scanning electron microscopy (SEM) was used to characterize the morphology of the bare carbon paste electrode and carbon paste electrode modified with CNT-Calix. Fig. 3A represents the SEM morphology of the prepared electrode. Fig. 3A shows the SEM images of the bare carbon

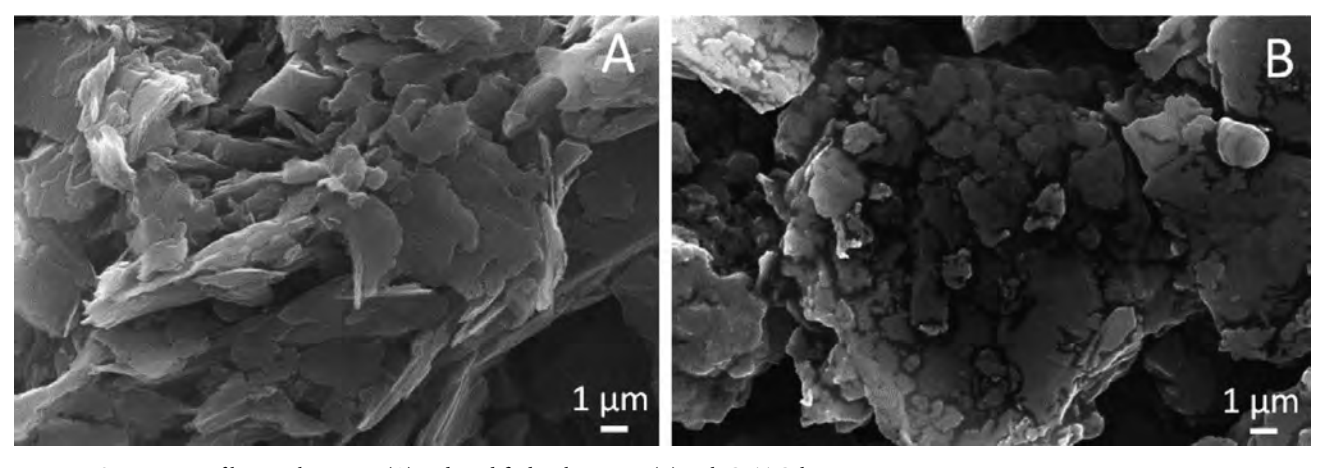


Fig. 3. SEM images of bare carbon paste (A) and modified carbon paste (B) with CNT-Calix

paste electrode and carbon paste electrode modified with CNT-Calix. The SEM image of the bare carbon paste electrode displayed a microstructure with a discontinuous grain growth with a large unclear crystal structure and graphite particles covered by a very thin film of paraffin wax, while at the surface of CPE, the layer of irregular flakes of graphite powder was present and isolated with each other.

Fig. 3B shows that the surface of the carbon paste electrode was modified with CNT-Calix. By addition of CNT-Calix to the carbon paste, most of the MWCNTs were in the form of small bundles or single tubes. It can be seen that MWCNTs were distributed on the surface of the electrode with special three-dimensional structures.²⁹

Cyclic Voltammetry

0.20 mol L⁻¹ PBS solution containing 0.05 M $K_3Fe(CN)_6+0.05$ M $K_4Fe(CN)_6$ was selected as a probe to evaluate the performance of the bare CPE and CNT-Calix/CPE electrodes. **Fig.4** shows cyclic voltammetry obtained with the bare CPE (dotted line) and Calixarene-grafted Multi-Walled Carbon Nanotubes CPE (solid line) electrodes. The CNT-Calix-CPE electrode exhibits the highest activity towards $K_4[Fe(CN)_6]$ / $K_3[Fe(CN)_6]$ redox reactions as promising electrocatalytic materials. It was observed that the peak current of CNT-Calix/CPE greatly increased together with an obvious decrease of ΔEp , behaving as a quasi-reversible electrode, the peak currents are significantly increased compared to the bare carbon paste systems. So we can say

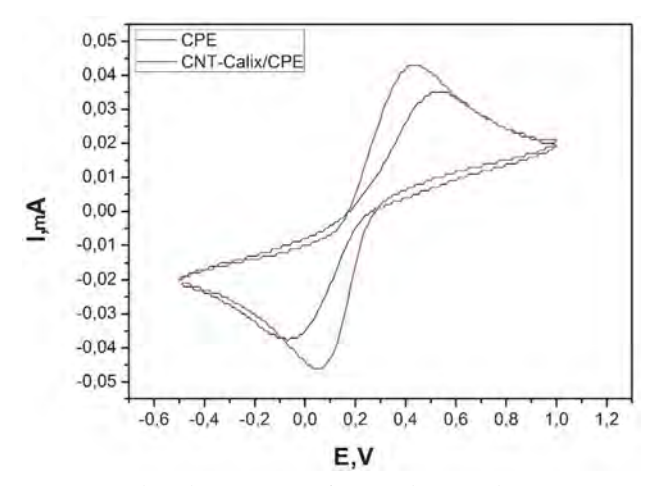


Fig. 4. Cyclic voltammograms of CPE and CNT-Calix at 100 mV s⁻¹, in 0.20 mol L⁻¹ PBS solution containing 0.05 M $K_3Fe(CN)_6/K_4Fe(CN)_6$ (1:1, pH = 5.0) solution.

that the CNT-Calix/CPE electrode can accelerate electron transfer for $0.05~M~K_3[Fe(CN)_6]$ redox probe as compared to CPE electrode. In other words, the prepared electrode has the advantages of high electrical conductivity and high resistance to interferences compared to unmodified CPE.

3. 3. Electrochemical Behaviors of Pb(II) and Cu(II) on the Modified Electrode

The performance of the newly modified carbon paste electrode is based on the deposition of Cu(II) and Pb(II) from aqueous solution onto the surface of the modified electrode by forming complexes with the modifier. The electrochemical performance of the metal ion on the carbon paste electrode modified with CNT-Calix was explored with respect to the effect on the stripping parameter. Lastly, a calibration curve was plotted and under optimized parameters the recovery of lead and copper ions using the modified carbon paste electrode evaluated.

The possible steps are expained below with the optimized experimental values, the likely phases are clarified ("aqueous" or "surface" subscript means the compound is in aqueous solution or on the electrode surface, respectively):

Deposition of M(II)³⁰

$$M^{2+}_{(aqueous)} + (CNT-Calix)_{(surface)} \rightarrow$$

$$[M^{2+} - (CNT-Calix)]_{(surface)}$$
Reduction of accumulated M(II) in PBS
$$[M^{2+} - (CNT-Calix)]_{(surface)} + 2e^{-} \rightarrow$$

$$[M^{0-} - (CNT-Calix)]_{(surface)} (at -1,0 V)$$
Stripping of reduced M(II) in PBS

 $+ (CNT-Calix)_{(surface)} + 2e^{-}(scan from -1.0 to +0.0 V)$

3. 4. Effect of Parameters

Different parameters such as supporting electrolyte, pH, deposition potential, deposition time, stirring rate, and the amount of modifier for a 1.0×10^{-6} mol L⁻¹ Cu(II) and 5.0×10^{-6} mol L⁻¹ Pb(II) solution were studied in order to obtain the optimum experimental conditions. Trials to set up the optimum conditions for the simultaneous determination of the two elements were as follows.

 $[M^0-(CNT-Calix)]_{(surface)} \rightarrow M^{2+}_{(aqueous)}$

3. 4. 1. Effect of Supporting Electrolyte and pH

The influences of different types of supporting electrolytes including phosphate buffer (PBS), Britton–Robinson (BR) buffer, KNO₃, HCl, and acetate buffer were investigated. Higher anodic peak currents, better defined peak shapes and the best sensitivity were observed utilizing 0.20 mol L⁻¹ PBS. The lowest background current, the highest and well-shaped voltammetric peaks were obtained in PBS during the recording of voltammetric peaks in different electrolytes **Fig. 5** shows the voltammetric behavior of modified carbon paste electrode at different pH values. Higher current values were obtained at pH 5.0 for both Pb(II) and Cu(II) ions. It is obvious that the two peaks are distinct and far enough to serve as the basis for quantitative analysis of Pb(II) and Cu(II). When the pH value was below 5.0, the ligand can strictly be protonated, and slowly

dissolve in acidic solution because of the free amine group of calixarene 3 with CNT-COOH, and lose its complexability towards Pb(II) and Cu(II) ions. At pH higher than 5.0, the decrease in the anodic peak current may be due to the hydrolysis of cations.³¹

3. 4. 2. Effect of Electrode Composition

The use of CNT-Calix as a modifier can greatly improve the sensitivity and selectivity of determinations. The effect of the amount of CNT-Calix within carbon paste electrode on the DPASV in PBS of pH 5.0 and deposition time of 300 s was investigated. As **Fig. 6** showed that the

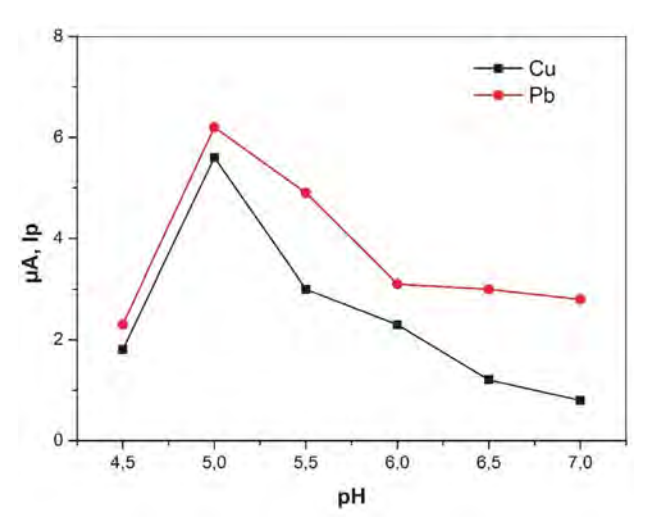


Fig. 5. Effect of pH on the stripping peak current for a solution containing 0.20 mol L^{-1} PBS, 1.0×10^{-6} mol L^{-1} Cu(II) and 5.0×10^{-6} mol L^{-1} Pb(II); deposition potential: -1.0 V vs. Ag/AgCl, deposition time: 300 s, resting time: 2 s, stirring rate: 300 rpm, scan rate: 0.10 V s $^{-1}$.

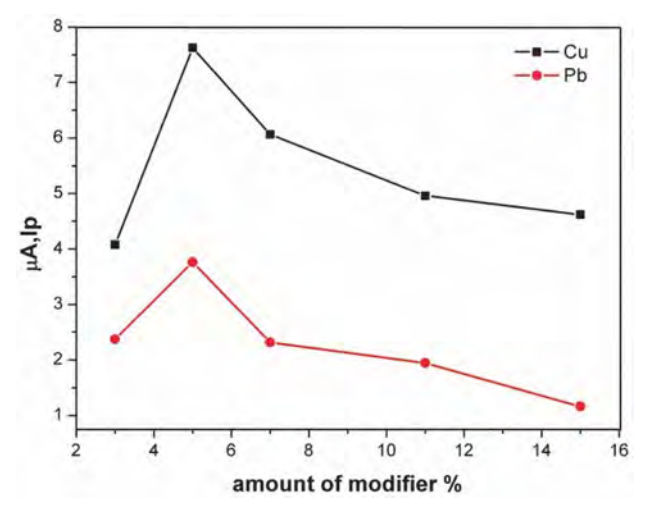


Fig. 6. Effect of amount of modifier on the stripping peak current for a solution containing 0.20 mol L^{-1} PBS (pH = 5), 1.0×10^{-6} mol L^{-1} Cu(II) and 1.0×10^{-6} mol L^{-1} Pb(II); deposition potential: -1.0 V vs. Ag/AgCl, deposition time: 300 s, resting time: 2 s, stirring rate: 300 rpm, scan rate: 0.1 V s^{-1} .

stripping peak current intensities of the two metal ions were increased by increasing the amount of modifier. At 5.0% (w/w) of the modifier, the largest peak current was obtained and decreased at higher amounts. When the amount of CNT-Calix was more than 5.0% (w/w), the peak currents decreased dramatically since excessive modifier may result in a decrease in the conductivity of the electrode. Therefore the best carbon paste composition of 5.0% (w/w) CNT-Calix, 72.5% (w/w) graphite powder and 22.5% (w/w) paraffin oil was used for all experiments.

3. 4. 3. Effect of Deposition Potential, Deposition Time and Stirring Rate

The effects of deposition potential and time on the peak currents were examined to optimize the sensitivity and selectivity. **Fig. 7** shows variation of peak current with the deposition potential between -1.3 to -0.50 V with an increment of 0.10 V, recorded as DPASV voltammogram. In the range of -1.30 to -1.20 V the peak currents for Pb(II) and Cu(II) are low and sudden increase in range of -1.20 V to -1.00 V and -1.00 V deposition potential was selected as optimum deposition potential.

Pb(II) and Cu(II) determination can be actually affected by deposition time. An increase in deposition time in the range of 0–15 min resulted in an increase in stripping peak current with an increase in the amount of reduced Pb(II) and Cu(II) on the surface of the modified electrode. With further increases in deposition time, the peak current flattened out, as the active points on the surface of the modified electrode were completely covered by reduced Pb(II) and Cu(II). Taking into account both sensitivity and efficiency, deposition time was set at 5 min in the following experiments.

3. 5. Analytical Characteristics

The differential pulse anodic stripping voltammograms at different concentrations of Pb(II) and Cu(II) under optimum conditions are shown in **Fig. 8.** The peak currents increase linearly with Pb(II) and Cu(II) concentration over the range of $0.1-1.6~\mu g L^{-1}$. The characteristics of the calibration graphs are given in **Table 2**. The limits of detection (LOD) and quantification (LOQ) under the present optimized conditions were calculated by Equation (A.1) and Equation. (A.2), respectively, where δ is the standard deviation (8 replicate determinations of the blank signals) of blank and s is the slope of calibration curve. ³¹

$$LOD = \frac{3.38}{s} \tag{1}$$

$$LOQ = \frac{10\delta}{s}$$
 (2)

The lowest qualitative and quantitative concentrations (LOD and LOQ) of the tested range of linearity were

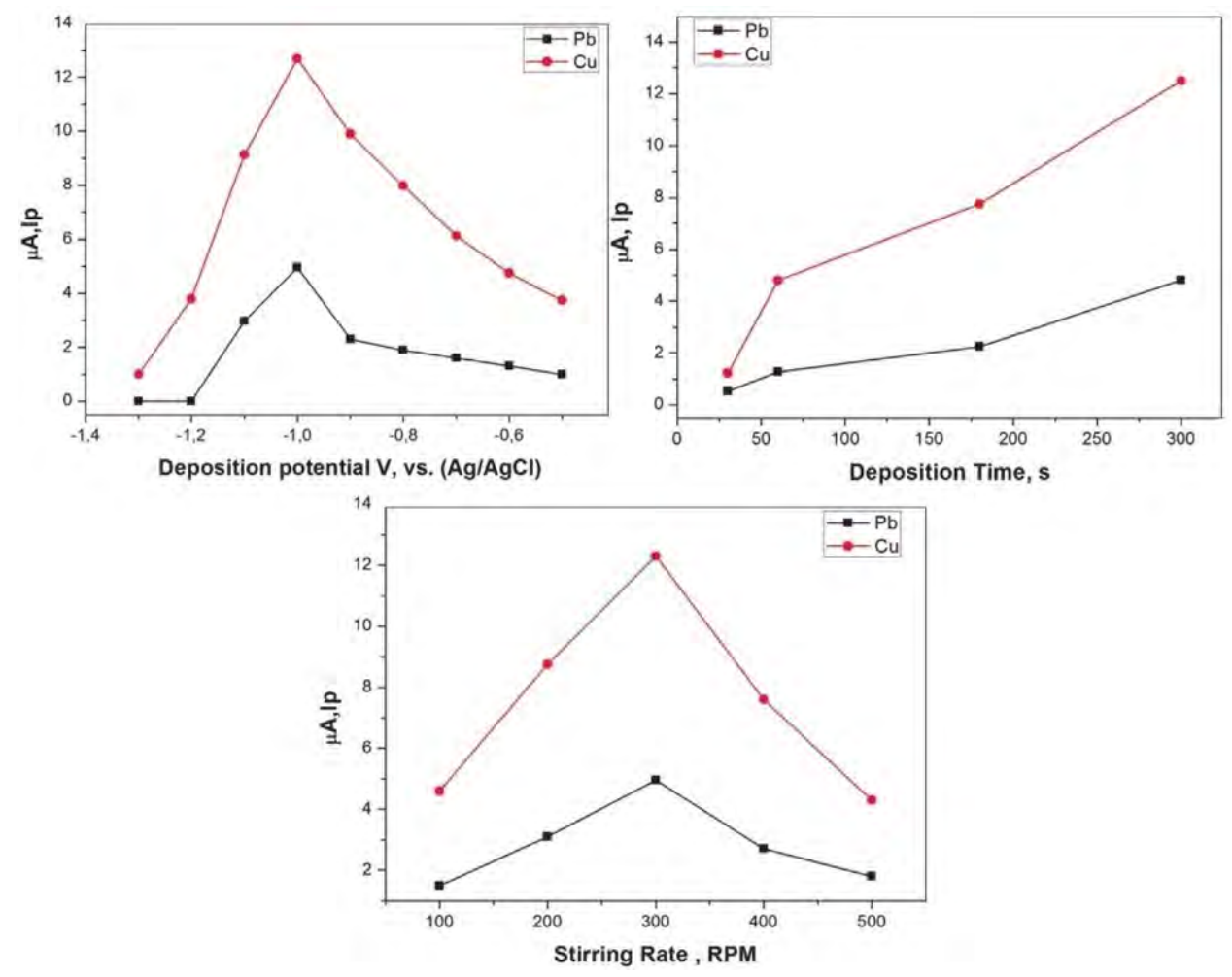


Fig. 7. Effect of deposition potential, deposition time, and stirring rate on the stripping peak current for a solution containing 0.20 mol L^{-1} PBS (pH = 5), 1.0×10^{-6} mol L^{-1} Cu(II) and 1.0×10^{-6} mol L^{-1} Pb(II); scan rate: 0.1 V s⁻¹.

calculated for Pb(II): 0.061 and 0.18 μ g L⁻¹, and for Cu(II): 0.096 and 0.29 μ g L⁻¹, respectively.

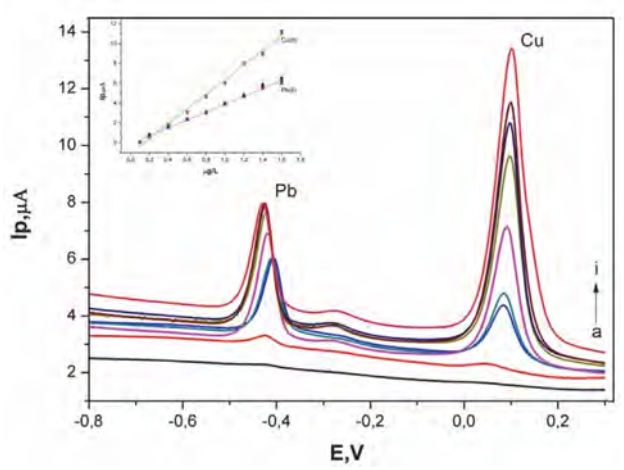


Fig. 8. DPSAV curves of different concentrations of Pb(II) and Cu(II) (a-i, 0.1, 0.2, 0.4, 0.6, 0.8, 1.0, 1.2, 1.4, 1.6 μ g L⁻¹) at CNT-Calix/CPE in 0.20 M PBS pH 5.0 buffer solution. deposition potential: -1.0 V; deposition time: 300 s; pulse amplitude: 0.05 V; pulse width: 0.2 s; scan rate: 0.1 V s⁻¹.

Table 2. Analytical parameters for calibration curves of Cu(II) and Pb(II) obtained with DPASV method. The values of the slopes and intercepts were calculated with a confidence interval of 95%. Number of points in the calibration curves was 9.

Parameter	Cu(II)	Pb(II)	
Linear range (μg L ⁻¹)	0.1-1.6	0.1-1.6	
Equation	y = a + bx	y = a + bx	
Slope (μA L μg ⁻¹)	7.41 ± 0.22	4.00 ± 0.08	
Intercept point (µA)	-1.05 ± 0.21	-0.11 ± 0.07	
Regression coefficient (R ²)	0.99265	0.99697	
LOD (μg L ⁻¹)	0.096	0.061	
$LOQ (\mu g L^{-1})$	0.29	0.18	
Repeatibility (t*s $\sqrt{2}$)	0,17	0,28	

^{*}t shows the experimental student t values ($t_{6,0.05} = 2.45$)

3. 6. Accuracy and Precision

Accuracy and precision of the described DPASV method for simultaneous determination of Pb(II) and Cu(II) at the modified carbon paste electrode (CNT-Calix/CPE) were calculated as recoveries (R%) and standard de-

viation (SD%) by analyzing laboratory-made mixtures prepared with reference standard solutions of each of the investigated metal ions for four replicate times. Synthetically prepared mixtures were prepared as follows: Two different series of stock solutions were prepared from standard solutions. In one of the prepared series, Cu(II) is added in a constant amount of Pb(II) in a linear concentration range. In the other series prepared, synthetic binary mixtures were obtained by adding Pb(II) in a linear concentration range in varying amounts to Cu(II). Mean percentage recoveries of lead and copper from different synthetic samples and standard deviations were obtained by applying standard addition methods and are given in Table 3 and Table 4. Recoveries (%) are constantly increased for Pb concentration in Table 3 and Cu concentration, in Table 4. This is the consequence of added (increased concentration of) Cu and Pb, respectively. These increases are acceptable in the confidence limit of 95%.

Table 3. Results of Pb recoveries obtained with DPASV method in laboratory-made synthetic samples

Sample	Taken (ng/L)	Pb Found (ng/L)	Recovery (%)	Cu Added (ng/L)
1	600	586	97,6	150
2	600	587	97,8	300
3	600	592	98,7	450
4	600	602	100,5	600
		MEAN: SD:	98,6 1.2	

Table 4. Results of Cu recoveries obtained with DPASV method in laboratory-made synthetic samples

Taken (ng/L)	Cu Found (ng/L)	Recovery (%)	Pb Added (ng/L)
600	598	99.7	150
600	602	100.3	300
600	604	100.7	450
600	610	101.7	600
	MEAN:	100.6	
	(ng/L) 600 600 600	Taken (ng/L) Found (ng/L) 600 598 600 602 600 604 600 610	Taken (ng/L) Found (ng/L) Recovery (%) 600 598 99.7 600 602 100.3 600 604 100.7 600 610 101.7 MEAN: 100.6

3. 7. Application to Real Samples

The applicability efficiency of the DPASV method combined with CNT-Calix/CPE for the analysis of real samples with different matrices was assessed by its application to the simultaneous determination of Pb(II) and Cu(II) ions in various real samples including wastewater, dried horse chestnut leaves, apple juice, and turnip juice samples. The standard addition method was used for the

analysis of prepared samples. An example voltammogram for chestnut leaves sample are shown in **Fig. 9**. The results listed in **Table 5** indicate that no matrix effect was observed.

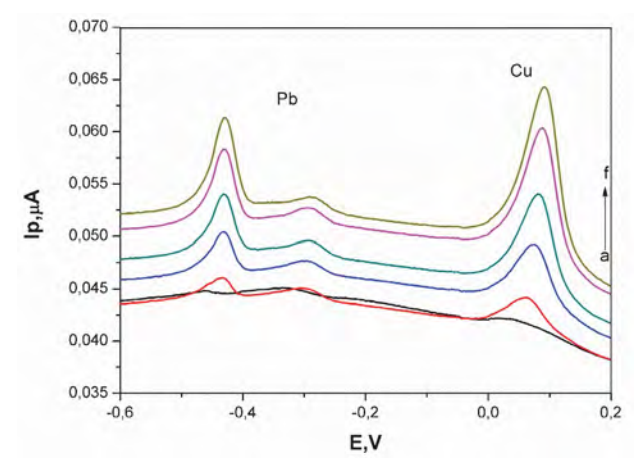


Fig. 9. DPSAV curves of blank solution (a), real sample without addition of Pb(II) and Cu(II) (b) and after additition of different concentrations of Pb(II) and Cu(II) (c-f) at CNT-Calix/CPE in 0.20 M PBS pH 5.0 buffer solution. Deposition potential: -1.0 V; deposition time: 300 s; pulse amplitude: 0.05 V; pulse width: 0.2 s; scan rate: 0.1 V s⁻¹.

Table 5. Simultaneous determination of metal ions in several real samples by the proposed method (n = 5).

Analyte	Found (μ g/L) \pm SD ^a
Cu ²⁺	0.37 ± 0.04
Pb^{2+}	0.24 ± 0.04
Cu^{2+}	0.66 ± 0.07
Pb ²⁺	0.32 ± 0.03
Analyte	Found (μg/g) ± SD ^a
Cu ²⁺	19.82 ± 0.40
Pb^{2+}	2.10 ± 0.06
	Cu^{2+} Pb^{2+} Cu^{2+} Pb^{2+} $Analyte$ Cu^{2+}

^a Average of 5 determinations

3. 8. Applications to the SRM

The accuracy of the proposed method was verified with the analysis of the NIST SRM Apple Leaves standards 1515 after microwave digestion. The reference leave sample was analyzed according to the recommended procedure after the appropriate dilution. The Pb(II) and Cu(II) concentrations in this leave sample were $0.469\pm0.022~\mu g~g^{-1}$ and $5.85\pm0.20~\mu g~g^{-1}$ with the developed method, respectively. F test was applied for comparison in which calculated F values were compared with F critic value. F values for Pb and Cu (0.012 and 1.2) are less than the critical F value (6.39) where $n_1=4$ and $n_2=4$ at 95% confidence level. Furthermore, t-test was carried out and the t values found were smaller than the theoretical t value (2.78) in the confidence limit of 95%. A good agreement with the certified values was achieved (**Table 6**).

Table 6. Analytical results of Pb(II) and Cu(II) determination in Certified Reference Material of Spiked Natural Leave Samples with the proposed method (n = 4)

NIST SRM 1515 Apple leaves ($\mu g g^{-1}$)				
Leave Sample	Certified value	Our Value ^a	t _{exp} ^b	
Cu(μg g ⁻¹) Pb(μg g ⁻¹)	5.64±0.24 0.47±0.02	5.85±0.20 0.47±0.02	0.42 0.01	

^a Average of 4 determinations.

4. Conclusion

In the present study, we synthesized p-tert-butylcalix[4]arene dihydrazine amide derivative and grafted onto COOH groups-modified carbon nanotube. The structure of all synthesized compounds was characterized using FTIR, NMR, TGA, and elemental analysis techniques. The calixarene-grafted carbon nanotube was used as a new material in the preparation of carbon paste-modified electrode. The surface morphology of the modified electrode was assessed by the Scanning Electron Microscopy (SEM) technique. The novel carbon paste modified electrode was employed as an efficient vehicle to determine selectively Pb(II) and Cu(II) ions in both synthetic and real samples. It was found that the modified electrode showed an excellent selectivity and stability for these metals determinations and for accelerated electron transfer between the electrode and the analyte. Regarding high sensitivity and selectivity, and very low detection limits together with the ease of preparation and surface regeneration of the modified electrode makes the proposed modified electrode a good alternative method.

The results reveal that the selectivity and sensitivity of the modified carbon paste electrode with calix-arene-grafted MWCNT towards Cu(II) and Pb(II) were high. These findings clearly address that the calixarene, which is grafted on CNT by means of chemical bonding, is capable of the selectivity and sensitivity in the determination of these metal ions due to well-known complexability of calixarenes including host-guest, self-assembly, and coordination-complementary properties, which depends upon the modified unit over the calixarene such as free amine, carboxylic acid, amide, etc. The obtained results agree well with those of SRM. These made the system promising to be used in routine analytical applications.

Conflicts of interest

There are no conflicts to declare.

Acknowledgement

The authors are grateful for kind financial support provided by Selcuk University Coordination Scientific Research Projects SU-BAP and 13401121.

5. References

- 1. B. B. Rodriguez, J. A. Bolbot and I. E. Tothill, *Biosensors and Bioelectronics* **2004**, *19*, 1157–1167.
 - DOI:10.1016/j.bios.2003.11.002
- C. Zhao, H. Liu and L. Wang, Analytical Methods 2012, 4, 3586–3592. DOI:10.1039/c2ay25525a
- 3. A. Afkhami, M. Saber-Tehrani and H. Bagheri, *Journal of Hazardous Materials* **2010**, *181*, 836–844.
 - DOI:10.1016/j.jhazmat.2010.05.089
- 4. A. M. Beltagi, E. M. Ghoneim and M. M. Ghoneim, *International Journal of Environmental Analytical Chemistry* **2011**, 91, 17–32. **DOI:**10.1080/03067310902962577
- K. Leopold, M. Foulkes and P. J. Worsfold, Trac-Trends in Analytical Chemistry 2009, 28, 426–435.
 - DOI:10.1016/j.trac.2009.02.004
- P. Bermejo-Barrera, M. A. Nancy, D. L. Cristina and B. B. Adela, Microchimica Acta 2003, 142, 101–108.
- L. Ebdon, Evans, E. H., Fisherondo, A., Hill, S. F., An Introduction to Analytical Atomic Spectrometry, Wiley, Chechester, U.K, 1998.
- 8. T. Oymak, Ş. Tokalıoğlu, V. Yılmaz, Ş. Kartal and D. Aydın, *Food Chemistry* **2009**, *113*, 1314–1317.
 - DOI:10.1016/j.foodchem.2008.08.064
- A. Afkhami, F. Soltani-Felehgari, T. Madrakian, H. Ghaedi and M. Rezaeivala, *Analytica Chimica Acta* 2013, 771, 21–30. DOI:10.1016/j.aca.2013.02.031
- E. Macerata, F. Castiglione, W. Panzeri, M. Mariani, F. Sansone, A. Casnati and A. Mele, *New Journal of Chemistry* 2010, 34, 2552–2557. DOI:10.1039/c0nj00269k
- 11. C. D. Gutsche, Book Calixarenes Revitised, Cambridge, 1998.
- 12. R. Joseph and C. P. Rao, *Chemical Reviews* **2011**, *111*, 4658–4702. **DOI**:10.1021/cr1004524
- 13. S. Sayin, M. Yilmaz and M. Tavasli, *Tetrahedron* **2011**, *67*, 3743–3753. **DOI:**10.1016/j.tet.2011.03.012
- 14. S. Sayin and M. Yilmaz, *Journal of Chemical & Engineering Data* **2011**, *56*, 2020–2029. **DOI**:10.1021/je1010328
- E. Akceylan and M. Yilmaz, *Tetrahedron* 2011, 67, 6240–6245.
 DOI:10.1016/j.tet.2011.06.050
- J. Barek, A. G. Fogg, A. Muck and J. Zima, Critical Reviews in Analytical Chemistry 2001, 31, 291–309.
 - **DOI:**10.1080/20014091076776
- 17. A. Afkhami, T. Madrakian, H. Ghaedi and H. Khanmohammadi, *Electrochimica Acta* **2012**, *66*, 255–264.
 - **DOI:**10.1016/j.electacta.2012.01.089
- S. Vasanthi, M. Devendiran and S. S. Narayanan, Applied Surface Science 2017, 422, 138–146.
 - DOI:10.1016/j.apsusc.2017.05.153
- A. Afkhami, T. Madrakian, S. J. Sabounchei, M. Rezaei, S. Samiee and M. Pourshahbaz, Sensors and Actuators B: Chemical 2012, 161, 542–548.
 - DOI:10.1016/j.snb.2011.10.073
- M. H. Mashhadizadeh and M. Akbarian, *Talanta* 2009, 78, 1440–1445. DOI:10.1016/j.talanta.2009.02.040
- G. Aragay and A. Merkoçi, *Electrochimica Acta* 2012, 84, 49–61. DOI:10.1016/j.electacta.2012.04.044

^b t_{exp} shows the experimental student t values (t $_{6,0.05}$ = 2.78).

- B. Rezaei and S. Damiri, *IEEE Sensors Journal* 2008, 8, 1523–1529. DOI:10.1109/JSEN.2008.923585
- 23. M. Siswana, K. Ozoemena and T. Nyokong, *Sensors* **2008**, 8, 5096. **DOI**:10.3390/s8085096
- P. M. Ajayan, Chemical Reviews 1999, 99, 1787–1800.
 DOI:10.1021/cr970102g
- C. D. Gutsche and K. C. Nam, Journal of the American Chemical Society 1988, 110, 6153–6162. DOI:10.1021/ja00226a034
- E. M. Collins, M. A. McKervey, E. Madigan, M. B. Moran, M. Owens, G. Ferguson and S. J. Harris, *Journal of the Chemical Society, Perkin Transactions* 1 1991, 3137–3142.
 DOI:10.1039/p19910003137
- 27. E. A. Alekseeva, V. A. Bacherikov and A. I. Gren, *Russian Journal of General Chemistry* **2000**, *70*, 490–491.
- T. Zhang, M. Xu, L. He, K. Xi, M. Gu and Z. Jiang, Carbon 2008, 46, 1782–1791. DOI:10.1016/j.carbon.2008.07.033
- A. Afkhami, H. Ghaedi, T. Madrakian and M. Rezaeivala, *Electrochimica Acta* 2013, 89, 377–386.
 DOI:10.1016/j.electacta.2012.11.050
- S. Kucukkolbasi, Z. O. Erdogan, J. Barek, M. Sahin and N. Kocak, *International Journal of Electrochemical Science* 2013, 8, 2164–2181.
- 31. N. Kocak, M. Sahin, S. Kücükkolbasi and Z. O. Erdogan, *International Journal of Biological Macromolecules* **2012**, *51*, 1159–1166. **DOI:**10.1016/j.ijbiomac.2012.09.003

Povzetek

Predstavljamo hitro, preprosto, selektivno in visoko občutljivo hkratno določitev Cu(II) in Pb(II) z novo narejeno elektrodo iz ogljikove paste, modificirane z 5,11,17,23-tetra-*terc*-butil-25,27-dihidrazinamidkarbonilmetoksi-26,28-dihidroksikaliks[4]arenom na večstenskih ogljikovih nanocevkah (CNT-Calix/CPE) ob uporabi diferencialne pulzne anodne inverzne voltametrije (DPASV). CNT-Calix/CPE kaže večjo selektivnost in stabilnost za Cu(II) in Pb(II). Optimizirali smo različne delovne pogoje, kot so pH, potencial in čas depozicije, amplituda pulza (5, –1,0 V vs. Ag/AgCl, 300 s, 2 s, 0,05 V) ter izračunali in statistično ovrednotili linearno območje, meje zaznave in kvantifikacije. Interferenčna študija kaže, da je elektroda visoko selektivna za hkratno določitev Cu(II) in Pb(II). S pomočjo metode standardnega dodatka smo CNT-Calix/CPE uporabili za odpadno vodo, rastlinske liste in brezalkoholne pijače ter določili koncentracije Cu(II) in Pb(II), ki se skladajo s standardnimi vrednostmi.



Except when otherwise noted, articles in this journal are published under the terms and conditions of the Creative Commons Attribution 4.0 International License

@creative

Scientific paper

Kinetic, Equilibrium and Phytotoxicity Studies for Dyes Removal by Low Cost Natural Activated Plant-Based Carbon

Emilia Neag,^{1,*} Ana Moldovan,^{1,2} Vanda Băbălău-Fuss,^{1,3} Anamaria Török,¹ Oana Cadar¹ and Cecilia Roman¹

¹ INCDO-INOE 2000, Research Institute for Analytical Instrumentation, 67 Donath Street, 400293 Cluj-Napoca, Romania

² Technical University, Faculty of Materials and Environmental Engineering, 103-105 Muncii Boulevard, 400641 Cluj-Napoca, Romania

³ Faculty of Science and Technology Food, University of Agricultural Sciences and Veterinary Medicine, 3-5 Manastur Street, 400372 Cluj-Napoca, Romania

> * Corresponding author: E-mail: emilia.neag@icia.ro Tel: +40 264 420590, Fax: +40 264 420667

> > Received: 12-09-2018

Abstract

The capacity of commercial natural activated plant-based carbon (CNAC) to remove different dyes such as methylene blue (MB), eosin yellow (EY) and rhodamine B (RB) was studied. Also, the germination index (GI) was calculated in order to examine the dyes toxicity on various plant seeds by recording and measuring the number of germinated seeds and root length, respectively. Generally, the results showed that high concentrations of dyes inhibit the seed germination by changing their colors and affecting their growth. The inhibition of corn seeds germination in RB was very low in the studied range of concentration. The adsorption behavior of dyes onto CNAC surface was investigated through isotherm and kinetics modeling. The parameters predicted from the Langmuir and Freundlich isotherms suggested a favorable adsorption of the considered dyes onto CNAC surface. The kinetic studies showed that the adsorption followed pseudo-second-order kinetic model for MB and RB removal, but was not adequate for EY removal.

Keywords: Activated carbon; dyes removal; isotherm models; kinetic models

1. Introduction

The water pollution caused by textile industries discharges has a negative impact on environment and human health due to their synthetic origin and complex molecular structure, which makes them more stable and difficult to be biodegraded. 1,2

Dyes, such as methylene blue (MB), eosin yellow (EY) and rhodamine B (RB) are used in various areas, including textile, plastics, rubber, leather, cosmetics, food and paper industries, chemistry, biology and medical science. ^{1,3-6} Thus, a suitable treatment method of industrial wastewaters before being released into the water is desirable. ¹ Moreover, the phytotoxicity effect of the textile dyes on environment can be evaluated using simple, rapid, reliable and reproducible techniques such as seed germination and root shoot ratio tests. ⁷

Many cheap, easily available low cost adsorbents, such as rice hull ash, sawdust, pine needle and cone powder, soya bean waste, prawn and coconut shell activated carbon, mango seed kernel powder, *Ficus carica* bast activated carbon and walnut carbon have been used as feed-stock for the production of activated carbon for textile dye effluents treatment. 4,6,8–11

Numerous techniques including physical, chemical and biological treatments have been undertaken for dyes removal from wastewater.¹² Among other methods, adsorption has gained attention due to its efficiency, low energy consumption and cost, high selectivity, and easy operation.^{1,13}

In a previous work, we have successfully identified the optimum adsorption conditions for MB removal on commercial natural activated plant-based carbon (CNAC) using Taguchi experimental design, a simple and fast method.¹⁴ In this work, an important progress was achieved through the application of several models in order to obtain more information related to the adsorption process involved in dyes removal such as MB, EY and RB.

The objectives of this study were: (1) to investigate the capacity of CNAC for MB, EY and RB removal from synthetic aqueous solution; (2) to evaluate the potential application of CNAC for dyes removal; (3) to obtain more information related to the adsorption process through equilibrium and kinetic studies, and (4) to determine the phytotoxic effect of MB, EY and RB on different seeds growth (mustard, chickpea and corn).

2. Materials and Methods

2. 1. Materials

The CNAC was purchased from Romanian market and ground using a mortar and pestle and then sieved through a 0.5 mm sieve. Its physical characteristics, including determination of pH, point zero charge (pH_{pzc}), apparent density, volatile matter, moisture and ash content, were presented in a previous study.¹⁴

2. 2. Chemicals

All used chemicals (Merck, Germany) were of analytical purity and used as received, without any further purification. MB, EY and RB were purchased in powder form. The chemical structures of the considered dyes are presented in Fig. 1. 15,6,5 The stock solutions were prepared by dissolving 1.00 g dye in 1 L of double distilled water. The calibration standards (2–10 mg/L) and a series of solutions (100–300 mg/L) were prepared by appropriate dilution of stock dye solutions of MB, EY and RB.

After 300 min, the dye solutions were separated from the CNAC by centrifugation at 4500 rpm for 5 min. The concentration of MB, EY and RB in solution was determined at previously established time intervals using a Lambda 25 Perkin-Elmer UV/VIS spectrophotometer at 665 nm, 515 nm and 554 nm, respectively.

The amount retained of MB, EY and RB in the adsorbent phase was calculated using equation (1), while dyes removal efficiency was calculated by equation (2):

$$q_{e} = \frac{(C_0 \cdot C_e)}{m} \cdot \frac{V}{1000} \tag{1}$$

$$E(\%) = \frac{(C_0 - C_e)}{C_0} \cdot 100 \tag{2}$$

where q_e is the amount of dye adsorbed per gram of adsorbent, at equilibrium (mg/g), V is the volume (mL), m is the weight of the adsorbent (g), E is the removal efficiency (%), C_o and C_e are the initial and equilibrium concentrations of MB, EY and RB solutions (mg/L).¹⁶

2. 4. Phytotoxicity Study

The phytotoxicity effect of MB, EY and RB dyes was studied on corn, chickpea and mustard seeds. 10 seeds were placed in Petri-dishes and 5 mL dye solution of different initial concentrations (100, 200 and 300 mg/L) were added. The samples were kept in a dark chamber for 5 days at 25 °C. The number of seeds and root growth were recorded every day, up to 5 days. The germination index (*GI*) was calculated using the equations 3, 4 and 5:⁷

$$GI = \frac{RSG \times RG}{100} \tag{3}$$

$$RSG = \frac{N_d}{N_c} \times 100 \tag{4}$$

Fig. 1. Chemical structures of dyes: (a) MB; (b) RB; (c) EY.

2. 3. Adsorption

The experiments were performed in batch conditions, contacting different quantities of CNAC (0.5–1.5 g) with 50 mL dye aqueous solutions at different initial concentrations (100–300 mg/L), room temperature (25 \pm 2 °C) and 75 rpm for 300 min.

$$RG = \frac{M_d}{M_c} \times 100 \tag{5}$$

where RSG is the relative seed germination (%), RG is the root growth (%), N_d is the number of seeds germinated in dye solution, N_c is the number of seeds germinated in con-

trol sample, M_d is the mean root length in dye solution (cm), M_c is the mean root length in control sample cm).⁷

3. Experimental Data Modeling

3. 1. Equilibrium Modeling

In order to investigate the MB, EY and RB removal, the experimental results were analyzed by the Langmuir, Freundlich and Dubinin-Radushkevich isotherms.

The Langmuir isotherm can be used to describe a monolayer adsorption onto a surface¹⁷ and its linear form is as follow:

$$\frac{1}{q_s} = \frac{1}{q_{max} K_L C_s} + \frac{1}{q_{max}} \tag{6}$$

where K_L is the Langmuir adsorption constant (L/mg) and q_{max} is the maximum amount of dye adsorbed per gram of adsorbent (mg/g).^{1,18}

The Langmuir parameters, q_{max} and K_L , are calculated from the slope and intercept of the plot $1/q_e$ vs. $1/C_e$. The Langmuir isotherm can be expressed by a dimensionless constant known as the separation factor or equilibrium parameter (R_L) :¹⁹

$$R_L = \frac{1}{1 + K_L C_0} \tag{7}$$

where C_0 is the initial dye concentration (mg/L).

The R_L value indicates the adsorption nature and may be unfavorable ($R_L > 1$), linear ($R_L = 1$), favorable ($0 < R_L < 1$) or irreversible ($R_L = 0$).²⁰

The Freundlich isotherm is applicable to describe heterogeneous systems.²¹ Its linear form is given as follows:

$$\log q_e = \log K_F + \frac{1}{n} \log C_e \tag{8}$$

where K_F is the adsorption capacity (L/g) and 1/n is the adsorption intensity.^{1,20}

The Freundlich parameters, K_F and n, are obtained from the $\log q_e \, vs. \, \log C_e$ linear plot. The n value between 1 < n < 10 indicates a favorable adsorption.²²

The Dubinin-Radushkevich model is applied to express the nature of adsorption process (physical or chemical)^{23,24} and the related equations are given below:

$$ln q = ln q_{max} - \beta \varepsilon^2$$
(9)

$$\varepsilon = RT \ln(1 + \frac{1}{C_s}) \tag{10}$$

$$E_L = \frac{1}{\sqrt{-2\beta}} \tag{11}$$

where β is the Dubinin-Radushkevich constant (mol²/kJ²), R is the gas constant (8.314 J/mol K), T is the absolute temperature (K), ε is the Polanyi potential and E_L is the mean adsorption energy (kJ/mol).²⁰

Dubinin-Radushkevich parameters, q_{max} and β , are obtained by plotting $\ln q_e \ vs. \ \varepsilon^2$. If $E_L < 8 \ kJ/mol$, the adsorption process is physisorption, while if E_L ranges between 8 and 16 kJ/mol, the process is chemisorption.²⁴

3. 2. Kinetics Modeling

Four kinetics models (pseudo-first-order, pseudo-second-order, intraparticle diffusion and external diffusion) were applied for the considered dyes removal in order to fit the experimental data.

The linearized form of pseudo-first-order equation is expressed as follows:²⁵

$$\ln(q_e - q_t) = \ln q_e - k_1 \iota \tag{12}$$

where q_t is the amount of adsorbed at time t (mg/g), k_1 first-order rate constant (1/min).²⁵

The pseudo-first-order parameters q_e and k_1 are calculated from the slope and intercept of the plot $\ln (q_e-q_t)$ vs. $t^{.25}$

The linearized form of pseudo-second-order equation is expressed as:²⁶

$$\frac{t}{q_t} = \frac{1}{k_2 \, q_e^2} + \frac{1}{q_e} t \tag{13}$$

where k_2 is the pseudo-second-order rate constant (g/mg · min).²⁶

The pseudo-second-order parameters q_e and k_2 are obtained from the slope and intercept of the plot of t/q_t vs. t^{26}

The intraparticle diffusion model is applied to investigate if the diffusion of the solute molecules into the pores is the rate determining step²⁷ and is given as:

$$q_t = k_{ip} \cdot t^{1/2} + b$$
 (14)

where k_{ip} is the intraparticle diffusion rate constant (mg/g·min^{1/2}), b is the intraparticle diffusion constant (mg/g) and t is time (min).

The b value provides information about the thickness of boundary layer and external mass transfer resistance.¹¹

If a plot of q_t vs. $t^{1/2}$ give a straight line, the adsorption process is controlled only by intraparticle diffusion and the rate constant k_{ip} is determined from the slope of the regression line. ¹¹

The linearized form of Elovich model is used to describe the chemisorption kinetics and its equation is given below:³

$$q_t = \frac{1}{C} \ln \alpha C + \frac{1}{C} \ln t \tag{15}$$

where α is the initial rate (mg/g·min) and C is the activation energy for chemisorption (g /mg).³

The Elovich parameters (α, β) are obtained from the slope and intercept of the plot q_t $vs. \ln t.^3$

Bangham model is used to identify if the intraparticle diffusion is the rate-controlling step and is given as follows:³

$$\log\left(\log\frac{C_{\theta}}{C_{\theta} - q_{r}m}\right) = \log\left(\frac{K_{\theta}m}{2.303V}\right) + p\log t \tag{16}$$

where p and K_0 are the Bangham constants.³

The kinetic parameters are obtained from the slope and the intercept of the plot $\log (\log C_o/(C_o - q_t m) vs. \log t.^3)$

Dumwald-Wagner model, which is an intraparticle diffusion model, is applied to determine the rate-controlling step and is given below:²⁸

$$\log \left[1 - \left(\frac{q_t}{q_e}\right)^2\right] = \frac{k}{2.303}t\tag{17}$$

where k is the rate constant of adsorption.²⁸

The kinetic parameters are obtained from the slope and the intercept of the plot $\log \left[1 - (q_t/q_e)^2\right] vs. t.^{28}$

4. Results and Discussion

4.1 Effect of Adsorbent Dose

The effect of adsorbent dose for MB, EY and RB adsorption onto CNAC, was studied by taking different quantities of CNAC (0.5–1.5 g) with 50 mL dye solutions of 100 mg/L at room temperature (25 \pm 2 °C) for 300 min.

The results obtained for MB, EY and RB adsorption onto CNAC surface are presented in Fig. 2. The removal efficiency slowly increased as the adsorbent dosage increase. An increasing trend was observed for MB (46–78 %), EY (51–70 %) and RB (52–60 %) removal by varying the adsorbent doses due to the availability of a larger number of active sites for dyes species in solution.²⁹

After a certain dosage, the increase in removal efficiency is insignificant due to the fast superficial adsorption onto the adsorbent surface. Consequently, with increasing the adsorbent dose, the amount of dye adsorbed per unit mass of adsorbent at equilibrium is reduced thus smaller q_e values were obtained by increasing the adsorbent dose of CNAC. The maximum amounts of adsorbed MB, EY and RB on the surface of 0.5 g CNAC were 4.64, 5.65 and 4.37 mg/g, respectively.

Huang et al. 2011 studied the removal of anionic dye EY from aqueous solution using ethylenediamine modified chitosan. They reported that larger particle size lead to lower amount of dye adsorbed, due to the higher surface

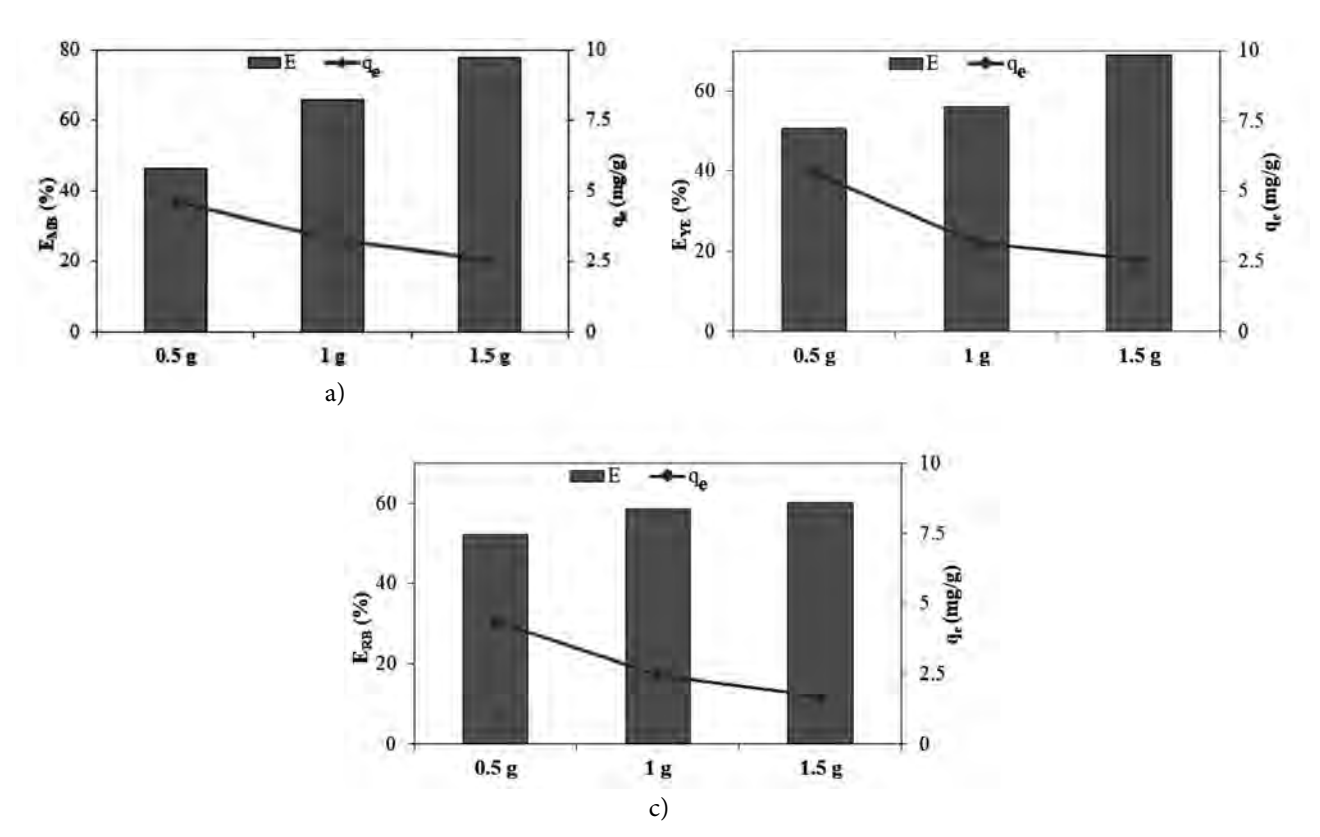


Fig. 2. Removal efficiency of MB (a), EY (b) and RB (c) adsorption onto CNAC surface at different adsorbent doses ($C_o = 100 \text{ mg/L}$, m = 0.5 - 1.5 g, particle size = <0.5 mm, stirring rate = 75 rpm, V = 50 mL; time = 300 min)

area of smaller particles compared to larger particles of the same mass. 31

4. 2. Effect of Initial Dye Concentration

The experiments were carried out using a fixed adsorbent dose (1.5 g) and stirring rate (75 rpm), but varying the initial dyes concentration (100–300 mg/L) (Fig. 3).

The dyes adsorption was rapid in the initial stages (100 min), increases gradually and finally becomes almost constant after reaching equilibrium. The rapid uptake of Astrazone Blue adsorption onto dried biomass of Baker's yeast suggested that the removal process could be ionic in nature due to the fact that the negatively charged organic

functional groups from the adsorbent surface may speed up the adsorption of dyes molecule.³²

The removal efficiency of MB, EY and RB decreases with the increase of initial dye concentration. By increasing the initial dye concentration from 100 to 300 mg/L, the dye amount in the adsorbent phase at equilibrium (q_e) increased from 2.59 to 4.68 mg/g for MB, from 2.56 to 3.36 mg/g for EY, and from 1.65 to 4.34 mg/g for RB removal, respectively and the higher mass transfer is driving force of the process.³⁰

4. 3. Isotherm Modeling

The equilibrium data for RB, MB and EY removal onto CNAC surface were modeled using the Lan-

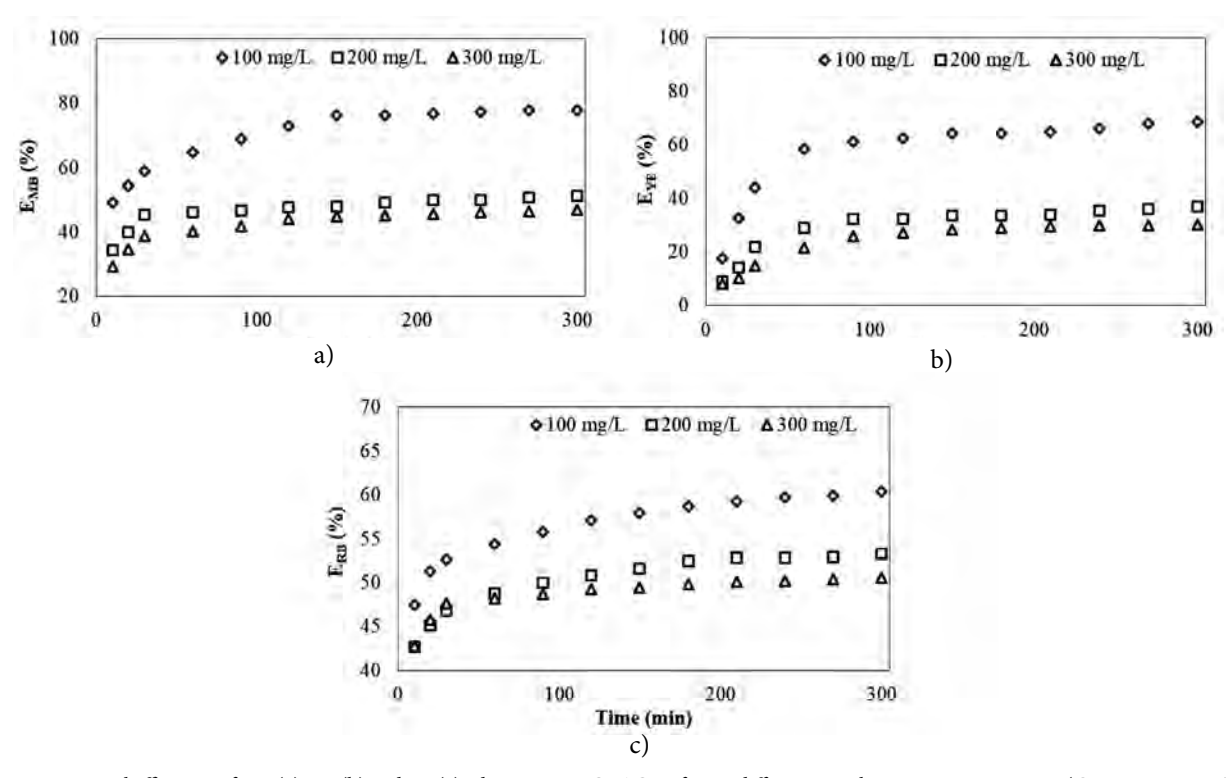


Fig. 3. Removal efficiency of MB (a), EY (b) and RB (c) adsorption on CNAC surface at different initial concentrations in time ($C_o = 100-300 \text{ mg/L}$, m = 1.5 g, particle size = <0.5 mm, stirring rate = 75 rpm, V = 50 mL, time = 300 min)

Table 1. Langmuir, Freundlich and Dubinin-Radushkevich isotherm parameters for dyes removal on CNAC surface.

Isotherm model	Parameters	MB	EY	RB
Langmuir	q _{max/} (mg/g)	4.54	3.09	9.45
	$K_L/$ (L/mg)	0.06	0.13	0.006
	R^2	0.860	0.407	0.999
Freundlich	n	3.64	8.43	1.41
	$K_F/(L/mg)$	1.08	1.63	7.14
	\mathbb{R}^2	0.901	0.569	0.999
Dubinin-Radushkevich	$\beta/(\text{mol}^2/\text{kJ}^2)$	3×10^{-9}	1×10^{-9}	7×10^{-9}
	$E_I/(kJ/mol)$	12.91	22.36	8.45
	$R^{\frac{1}{2}}$	0.887	0.545	1

gmuir, Freundlich and Dubinin-Radushkevich isotherms.

The Langmuir parameters, q_{max} and K_L , for the considered dyes are presented in Table 1. The calculated R_L values for the removal of MB (0.05), EY (0.02) and RB (0.4) indicated a favorable adsorption. Similar results were reported by Hameed et al., 2017 for the adsorption of chromotrope dye onto activated carbons obtained from the seeds of various plants.¹²

The Freundlich parameters, K_F and n are given in Table 1. The n values obtained for MB, EY and RB removal were found to be greater than 1, indicating a favorable adsorption of dyes onto CNAC.

The correlation coefficient (R^2) indicated that Freundlich model fitted better the experimental results for MB and RB removal suggesting a heterogeneous coverage of dye molecules on the CNAC surface. In contrast, for EY removal, the R^2 values were low, suggesting that the monolayer and the heterogeneous coverage of dye molecules on the CNAC surface didn't take place.

The Dubinin-Radushkevich parameters, q_{max} and β , are given in Table 1. The mean free energy value indicated a chemically process involved for MB and RB removal.

4. 4. Kinetics Modeling

In order to describe the adsorption kinetics the pseudo-first-, pseudo-second-order, intraparticle, Elovich, Bangham and Dumwald-Wagner kinetics models were used.

The pseudo-first-order equation parameters are presented in Table 2. The calculated q_e values are different from the experimental values for the considered dyes. Also, the obtained R^2 values are low for MB and RB removal suggesting that pseudo-first-order equation cannot be used to describe the kinetics of MB, EY and RB.

The pseudo-second-order parameters are listed in Table 2. Based on the obtained results, some differences

are observed between the calculated and experimental q_e values for EY removal. On the contrary, the values of these parameters for MB and RB removal are similar.

The values of R^2 are higher than those obtained from the pseudo-first-order model suggesting that the pseudo-second-order kinetics model is adequate to describe the MB and RB removal as chemisorption process. However, the process involved in EY removal cannot be described by the pseudo-second-order kinetic model. Similar results were reported for the adsorption kinetics of RB and MB onto waste of seeds of *Aleurites Moluccanav*, a low cost adsorbent.¹

Elovich kinetics model was employed to confirm the results obtained from Dubinin-Radushkevich isotherm and pseudo-second-order kinetic model. The R^2 values indicated that experimental data fitted well on Elovich equation (Table 2). The obtained results are in agreement with the results obtained from Dubinin-Radushkevich isotherm and pseudo-second-order kinetic model in case of MB and RB.

The intraparticle diffusion model was used to investigate the mechanism of mass transport and to determine the rate controlling step during dyes adsorption on the surface of adsorbent.³ The obtained values (Table 3) indicated that intraparticle diffusion is not the only rate determining step for the considered dyes because the intercept values are higher than 0 and another model is required to follow the experimental data.

Further, Bangham and Dumwald-Wagner kinetic models were taken into consideration. The kinetic parameters obtained for Bangham and Dumwald-Wagner models are presented in Table 3. The experimental data do not give a good fit to the Bangham and Dumwald-Wagner model (low R^2 obtained) for the considered dyes. The results obtained using these kinetic models confirmed that intraparticle diffusion is not the rate-controlling step.

Table 2. Pseudo-first-order, pseudo-second-order reaction and Elovich kinetics constants for dyes removal on CNAC surface at different initial concentrations.

Kinetics Model	Parameters		MB			EY			RB	
Pseudo-first-order	$C_o/(\text{mg/L})$	100	200	300	100	200	300	100	200	300
	$k_1 \cdot 10^{-2} / (1/\text{min})$	2.3	1.2	1.3	1.4	1.2	1.7	1.3	0.8	1.4
	$q_{e (calc)}/(mg/g)$	1.98	1.13	1.96	1.64	1.73	2.83	2.15	1.24	1.28
	R ²	0.888	0.868	0.939	0.915	0.926	0.991	0.860	0.735	0.813
Pseudo-second-	$C_o/(\text{mg/L})$	100	200	300	100	200	300	100	200	300
order	$k_1 \cdot 10^{-2} / (g/\text{mg min})$	3.1	3.9	2.2	1.2	1.0	0.7	9.4	5.1	7.7
	$q_{e (calc)}/(mg/g)$	2.69	3.45	4.78	2.82	2.85	3.81	1.67	3.01	4.36
	\mathbb{R}^2	0.998	0.999	0.999	0.991	0.992	0.997	0.998	0.998	0.999
	$q_{e (exp)}/(mg/g)$	2.59	3.42	4.68	2.56	2.60	3.36	1.65	3.03	4.34
Elovich	$C_o/(\text{mg/L})$	100	200	300	100	200	300	100	200	300
	α	0.65	1.65	1.22	1.15	0.59	0.04	2.66	2.30	3.20
	θ	0.30	0.28	0.48	0.56	0.58	0.80	0.07	0.17	0.13
	R^2	0.981	0.910	0.967	0.912	0.925	0.968	0.907	0.947	0.966

Kinetics Model	Parameters		MB			EY			RB	
Intraparticle	$C_o/(\text{mg/L})$	100	200	300	100	200	300	100	200	300
diffusion	k_{ip} (mg/g min ^{1/2})	0.067	0.061	0.106	0.119	0.125	0.175	0.017	0.038	0.030
	b^{T}	1.565	2.438	3.039	0.762	0.643	0.704	1.354	2.349	3.852
	R^2	0.926	0.800	0.868	0.753	0.808	0.879	0.941	0.911	0.913
Bangham	$C_o/(\text{mg/L})$	100	200	300	100	200	300	100	200	300
· ·	K_0	0.63	0.64	0.65	0.69	0.71	0.72	0.631	0.639	0.632
	p/(dm/g)	0.14	0.10	0.12	0.41	0.40	0.40	0.05	0.06	0.03
	R^2	0.981	0.883	0.943	0.786	0.859	0.936	0.859	0.946	0.963
Dumwald-Wagner	$C_o/(\text{mg/L})$	100	200	300	100	200	300	100	200	300
· ·	k/(1/min)	0.023	0.010	0.012	0.012	0.009	0.015	0.011	0.004	0.011
	C	1.024	0.820	0.617	0.076	0.063	0.059	0.433	0.47	0.06
	R^2	0.858	0.945	0.984	0.919	0.943	0.994	0.935	0.937	0.944

Table 3. Intraparticle diffusion, Bangham and Dumwald-Wagner rate coefficients for dyes removal on CNAC surface at different initial concentrations

4. 5. The Effect of Dyes on Seeds Growth

The effect of MB, EY and RB on germination of chickpea, mustard and corn seeds was studied. Different initial dye concentrations in the range of 100–300 mg/L were used along with control samples. After 5 days, the number of seeds and root growth were recorded. The GI decreases with an increase of dyes concentration from 100 to 300 mg/L (Fig. 4).

At 300 mg/L initial concentration, in case of MB for corn and chickpea seeds, the *GI* was around 63 and 65%, respectively while for mustard seed only 53% suggesting that the inhibition increases with an increase of MB concentration. The same pattern was observed for EY where the GI was lower than in case of MB for mustard and corn seeds.

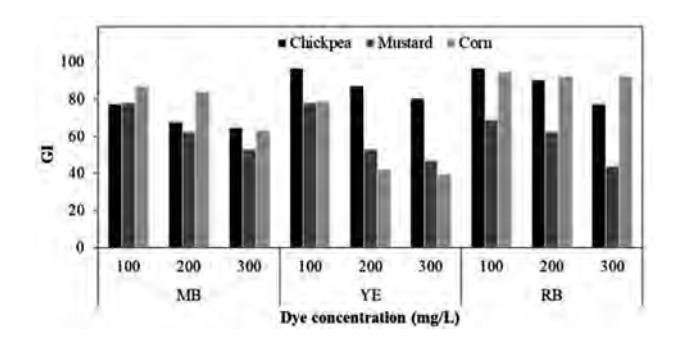


Fig. 4. Germination indices for chickpea, mustard and corn plant seeds after 5 days.

In case of RB, the GI for corn seeds were very high in the studied range of concentration (92–95%), suggesting that the inhibition didn't take place. For mustard seed, the GI values were much lower (44% at 300 mg/L RB), indicating that inhibition was high.

Generally, the seed roots were long in the control sample (chickpea 3.1 cm, mustard 3.2 cm and corn 3.8

cm), while in the dye solution were smaller and became colorful. Rápó et al. also reported that the inhibition increases with an increase of dye concentration for seedling growth for lettuce and mustard seeds.³³

5. Conclusions

The adsorption behaviour of MB, YE and RB removal onto CNAC surface was examined by studying the effect of adsorbent dosage and initial dyes concentration. The adsorption process of MB, YE and RB molecules onto CNAC surface was described by Freundlich model as suggested by regresion analysis. The Dubinin-Radushkevich isotherm indicated a chemisorption process involved in the MB and RB removal process. These results were confirmed by pseudo-second-order reaction model and Elovich kinetics model. Elovich model suggested that the exchange of electrons between adsorbent and adsorbate takes place also for EY removal but pseudo-second-order kinetic model did not confirm this result. The low correlation coefficients values obtained from Bangham and Dumwald-Wagner kinetics models confirmed that intraparticle diffusion was not the only rate-controlling step. Further studies are therefore necessary to determine the rate controlling step for MB, YE and RB removal onto CNAC surface. The effect of dyes on chickpea, mustard and corn seeds through seed GI was carried out. The results showed that the percentage of seed germination decreased as the dyes concentration increased, affecting their germination and growth.

Acknowledgements

The work has been funded by the Competitiveness Operational Programme of the Ministry of European Funds through the Contract No. 7/01.09.2016 and was supported in part by Sectorial Operational Program

"Increase of Economic Competitiveness" Priority Axis II, Project Number 1887, INOVA-OPTIMA, code SMIS-CSNR 49164, by PN18-28 02 01 and 19PFE/17.10.2018.

6. References

- 1. D. L. Postai, C. A. Demarchi, F. Zanatta, D. C. Cipriani Melo, C. A. Rodrigues *Alexandria Engineering Journal*, **2016**, *55*, 1713–1723. **DOI:**10.1016/j.aej.2016.03.017
- A. Ebrahimian Pirbazari, E. Saberikhah, M. Badrouh, M. S. Emami, *Water Resources and Industry* 2014, 6, 64–80 DOI:10.1016/j.wri.2014.07.003
- 3. M. S. Thabet, A. M. Ismaiel, *JEAS*, **2016**, *6*, 70–90. **DOI**:10.4236/jeas.2016.63007
- D. Pathania, S. Sharma, P. Singh, Arab. J. Chem., 2017, 10, S1445–S1451. DOI:10.1016/j.arabjc.2013.04.021
- 5. R. Ansari, Z. Mosayebzadeh, *Iran. Polym. J.*, **2010**, *19*(7), 541–551.
- K. Shen, M. A. Gondal, J. Saudi. Chem. Soc. 2017, 21, S120–S127. DOI:10.1016/j.jscs.2013.11.005
- 7. U. Jadhav Umesh., N. Dhawale Rhushikesh., V. Dawkar Vishal., D. Chougale Ashok, V. Padul Manohar, *TBR* **2016**, 5(2), 1–6.
- A. M. Aljeboree, A. N. Alshirifi, A. F. Alkaim, *Arab. J. Chem.* 2017, 10, S3381–S3393. DOI:10.1016/j.arabjc.2014.01.020
- 9. M. T. Yagub, T. K. Sen, M. Ang., Environ. Earth. Sci. 2014, 71(4), 1507–1519. DOI:10.1007/s12665-013-2555-0
- 10. M. R. R. Kooh, M. K. Dahri, L. B. L. Lim, O. A. Malik, *Environ. Earth. Sci.* **2016**, *75*, 783.
- 11. S. Hajati, M. Ghaedi, H. Mazaheri, *Desalin. Water Treat.* **2016**, *57*(7), 3179–3193. **DOI**:10.1080/19443994.2014.981217
- 12. K. S. Hameed, P. Muthirulan, M. M. Sundaram, *Arab. J. Chem.*, **2017**, *10*, S2225–S2233.
 - **DOI:**10.1016/j.arabjc.2013.07.058
- M. Rafi, B. Samiey, C.-H. Chen, *Materials*, 2018, 11(4), 1–24.
 DOI:10.3390/ma11040496
- A. Moldovan, E. Neag, V. Babalau-Fuss, O. Cadar, V. Micle, C. Roman, *Anal. Lett.* 2019, 52(1), 150–162.
 DOI:10.1080/00032719.2017.1418879
- Y.-Y. Lau, Y.-S. Wong, T.-T. Teng, N. Morad, M. Rafatullaha, S.-A. Ong RSC Adv. 2015, 5, 34206.
 - DOI:10.1039/C5RA01346A

- B. Mudyawabikwa, H. H. Mungondori, L. Tichagwa, D. M. Katwire, *Water. Sci. Technol.* 2017, 75(10), 2390–2402.
 DOI:10.2166/wst.2017.041
- I. Langmuir, J. Am. Chem. Soc. 1916, 38, 2221–2295.
 DOI:10.1021/ja02268a002
- 18. M. Ghaedi, Sh. Heidarpour, S. N. Kokhdan, R. Sahraie, A. Daneshfar, B. Brazesh, *Powder Technol.* **2012**, *228*, 18–25. **DOI:**10.1016/j.powtec.2012.04.030
- F. Kallel, F. Chaari, F. Bouaziz, F. Bettaieb, R. Ghorbel, S. Ellouz Chaabouni *J. Mol. Liq.* 2016, *219*, 279–288.
 DOI:10.1016/j.molliq.2016.03.024
- N. Ayawei, A. N. Ebelegi, D. Wankasi, J. Chem. 2017, Article ID 3039817 DOI:10.1155/2017/3039817
- 21. H. M. F Freundlich, J. Phys. Chem. 1906, 57, 385-471.
- 22. F. Deniz, R. A. Kepekci, *Int. J. Phytoremediat.* **2016**, *19*(6), 579–586. **DOI:**10.1080/15226514.2016.1267707
- 23. M. M. Dubinin, L. V. Radushkevich, *Proc. Acad. Sci. Phys. Chem. Sect. USSR* **1947**, *55*, 331–333.
- F. Deniz, Scientific World. J. 2014, Article ID 138986, 1–10.
 DOI:10.1155/2014/138986
- S. Lagergren, Kungliga Svenska Vetenskapsakademiens. Handlingar, Band, 1898, 24(4):1–39.
- Y. S. Ho, G. McKay, Water. Res. 2000, 34, 735–742.
 DOI:10.1016/S0043-1354(99)00232-8
- 27. W. J. Jr. Weber, R. R. Rummer, *Water Resour. Res.* **1965**, *1*(3), 361–365. **DOI**:10.1029/WR001i003p00361
- 28. H. Qiu, L. Lv, B.-C. Pan, Q.-J. Zhang, W.-M. Zhang, Q.-X. Zhang, *J. Zhejiang Univ. Sci. A*, **2009**, *10*(5), 716–724. **DOI:**10.1631/jzus.A0820524
- S. Banerjee; M. C. Chattopadhyaya; Uma; Y. C. Sharma, Journal Of Hazardous, Toxic, And Radioactive Waste 2014, 18, 56–63. DOI:10.1061/(ASCE)HZ.2153-5515.0000191
- 30. K. S. Bharathi, S. T. Ramesh, *Appl. Water. Sci.*, **2013**, *3*, 773–790. **DOI:**10.1007/s13201-013-0117-y
- 31. X.-Y. Huang, J.-P. Bin, H.-T. Bu, G.-B. Jiang, M.-H. Zeng, Carbohydr. Polym. 2011, 84 1350–1356. DOI:10.1016/j.carbpol.2011.01.033
- 32. J. Y. Farah, N. Sh. El-Gendy, L. A. Farahat, *J. Hazard. Mater.* **2007**, *148*, 402–408.
 - **DOI:**10.1016/j.jhazmat.2007.02.053
- 33. E. Rápó, R. Szép, Á. Keresztesi, M. Suciu, S. Tonk, *Acta Chim. Slov.* **2018**, *65*, 709–717.

DOI:10.17344/acsi.2018.4401

Povzetek

Preučevali smo sposobnost tržnega naravno aktiviranega rastlinskega oglja (ang. kratica CNAC) za odstranjevanje različnih barvil kot so metilensko modro (MB), eosin rumeno (EY) in rodamin B (RB). Na različnih rastlinah smo preko indeksa kaljenja (GI) določili toksičnost barvila, tako da smo merili število vzklitih semen in dolžino korenin. V splošnem se je izkazalo, da visoke koncentracije barvila zavirajo kaljenje, povzročijo spremembo barve in vplivajo na rast. RB pa je imel pri vseh določanih koncentracijah le minimalen vpliv na kaljenje koruznih semen. Adsorpcijo barvil na CNAC smo preučevali preko adsorpcijskih izoterm in modeliranja kinetike. Ugodno adsorpcijo sta pokazala tako Langmuirjev kot tudi Freundlich-ov model. Kinetične študije so pokazale, da lahko hitrost adsorpcije MB in RB opišemo s kinetiko pseudo-drugega-reda, ne pa tudi hitrost adsorpcije EY.



Except when otherwise noted, articles in this journal are published under the terms and conditions of the Creative Commons Attribution 4.0 International License

Scientific paper

Isocratic High Performance Liquid Chromatography Assay for Quantification of Ceftiofur Hydrochloride in Bubaline Plasma

Muhammad Adil,^{1,2} Muhammad Ovais Omer,^{2,*} Aqeel Javeed,² Aamir Ghafoor,³ Muhammad Ashraf² and Abdul Muqeet Khan⁴

¹ Pharmacology and Toxicology Section, University of Veterinary and Animal Sciences (UVAS), Lahore-Jhang Campus, Pakistan.

² Department of Pharmacology and Toxicology, University of Veterinary and Animal Sciences (UVAS), Lahore, Pakistan.

³ University Diagnostic Laboratory (UDL), University of Veterinary and Animal Sciences (UVAS), Lahore, Pakistan.

⁴ Quality Operations Laboratory (QOL), University of Veterinary and Animal Sciences (UVAS), Lahore, Pakistan.

* Corresponding author: E-mail: drovaisomer@uvas.edu.pk Contact no. +923334244780

Received: 01-03-2019

Abstract

We optimized and validated an isocratic high-performance liquid chromatography (HPLC) assay for quantification of ceftiofur hydrochloride in bubaline plasma. Ceftiofur, its metabolic products and protein-bound residues were cleaved, derivatized into desfuroylceftiofur acetamide and injected into HPLC system. The mobile phase comprising of sodium dihydrogen phosphate (0.025 M, pH 7) and acetonitrile (34:66, v/v), was driven at a flow rate of 1 mL/min, and separation was achieved using C18 column. Isocratic elution was performed with an injection volume of 45 μ L and analyte was scanned at 310 nm. The linearity range, limit of detection and limit of quantification were 0.1–10 μ g/mL, 0.03 μ g/mL and 0.11 μ g/mL respectively. Moreover, the accuracy, precision and recovery remained within the acceptable limits. The assay was effectively applied for determining the concentration of ceftiofur in plasma samples collected from ceftiofur-treated buffalo calves.

Keywords: Ceftiofur hydrochloride; bubaline plasma; isocratic; HPLC

1. Introduction

Ceftiofur represents a broad-spectrum, bactericidal, third generation cephalosporin antibiotic specifically developed for use in veterinary medicine. It is available as ceftiofur hydrochloride, ceftiofur sodium and ceftiofur crystalline-free acid suspension. The chemical formula of ceftiofur hydrochloride is $C_{19}H_{17}N_5O_7S_3\cdot HCl$ with a molecular weight of 560.2 grams. The chemical structure of ceftiofur hydrochloride has been illustrated in Figure 1.2 Many gram-positive, gram negative and anaerobic bacterial pathogens of domestic animals are susceptible to ceftiofur. The ready-to-use, parenteral formulation of ceftiofur hydrochloride is predominantly used against the bacterial respiratory disease affecting cattle and pigs. Additionally, it is also approved for the treatment of acute foot rot and postpartum metritis in cattle. Desfuroylceftiofur consti-

tutes the primary metabolite of ceftiofur with proven antimicrobial activity.6 The most primitive analytical assay for estimation of ceftiofur in biological fluids involved the derivatization of parent drug and resultant metabolites followed by a time-consuming, solid-phase extraction process.^{7,8} Furthermore, the suggested alternative method was only applicable for quantification of parent drug without determining the concentration of microbiologically active metabolic compounds.9 Subsequent modification of the conventional analytical method led to simplified assays involving the direct HPLC injection of derivatized sample without solid-phase extraction clean-up. 10,11 Nevertheless, there is scarcity of literature regarding the isocratic, HPLCbased analysis of ceftiofur in water buffalo plasma. Consequently, an isocratic, HPLC assay was optimized and validated for the quantitative assessment of ceftiofur hydrochloride in bubaline plasma.

Figure 1. Chemical structure of ceftiofur hydrochloride (modified from Palur $et\ al^2$)

2. Experimental

2. 1. Reference Standard and Chemicals

The analytical reference standard and injectable formulation of ceftiofur hydrochloride were generously provided by M/S International Pharma Labs, Lahore, Pakistan and M/S Nawan Laboratories (PVT) LTD., Karachi, Pakistan respectively. Dithioerythritol and iodoacetamide were supplied by Sigma-Aldrich (St. Louis, MO, USA). Acetonitrile, disodium tetraborate, sodium dihydrogen phosphate and sodium phosphate dibasic heptahydrate were procured from Merck Millipore, Germany.

2. 2. Preparation of Standard Solutions, Buffers and Reagents

The stock solution of ceftiofur hydrochloride (1 mg/ mL) was prepared in distilled water and diluted further to obtain the quality control (QC) samples and calibration standards. The QC samples of low, medium and high concentrations were prepared in distilled water at concentrations of 0.75, 2.5 and 12.5 µg/mL respectively. Whereas, the calibration standards of ceftiofur hydrochloride were prepared at concentrations of 0.1, 0.15, 0.2, 0.25, 0.5, 1, 5 and 10 µg/mL in buffalo plasma. Borate buffer (0.05 M, pH 7) was prepared by dissolving 1.9 grams of disodium tetraborate in 100 mL of distilled water. Moreover, 0.14 grams of sodium dihydrogen phosphate and 0.38 grams of sodium phosphate dibasic heptahydrate were dissolved in 100 mL of distilled water for the preparation of phosphate buffer (0.025 M, pH 7). The working solutions of iodoacetamide (0.54 M) and dithioerythritol (0.66 M) were obtained by separately dissolving 1 gram each of iodoacetamide and dithioerythritol in 10 mL of phosphate buffer and borate buffer respectively.

2. 3. Synthesis and Derivatization of Desfuroylceftiofur

All plasma samples, calibration standards and QC samples were processed for the synthesis of desfuroylceft-

iofur and subsequent derivatization into desfuroylceftiofur acetamide. In brief, each sample was transferred into a 2 mL microcentrifuge tube and 200 μL of methanol was added. The samples were vortexed for 30 seconds and centrifuged at 13000 rpm for 10 min. The supernatants were collected in separate 2 mL microcentrifuge tubes, mixed with 100 μL of dithioerythritol solution (0.66 M) and kept in water bath at 50 °C for 15 min. Subsequently the tubes were allowed to attain room temperature and covered with aluminum foil after adding 100 µL of iodoacetamide solution (0.54 M). The contents of each tube were centrifuged at 350 rpm for 45 min and mixed with 25 µL of formic acid. Stirring was carried out at 22 °C and the tubes were placed in vortex mixer for 30 seconds. Final centrifugation was performed at 13000 rpm for 10 min and 45 μL of each supernatant was injected into the HPLC system.

2. 4. HPLC System and Chromatographic Conditions

The HPLC system comprised of an auto-sampler (SIL-10AC), system control module (CBM-20A), pump (Schimadzu LC-20AT), column oven (CTO-20AC), degasser (DGU-20A), ultraviolet-visible (UV-VIS) detector (SPD-M20A) and low pressure-gradient flow control valve (FCV-10AL). The chromatograms of QC and calibration samples obtained through C18 and PLRP-S columns were compared for the selection of appropriate analytical column. Several types of mobile phase having varying combinations of 0.1% trifluoroacetic acid and sodium dihydrogen phosphate (0.025 M, pH 7) with acetonitrile were tested after filtration through 0.45 µm nylon filter (Sartorius, Gottingen, Germany) and sonication for 30 min. Assessment of various flow rates (0.5-1.5 mL/min) and wave lengths (254, 265, 266 and 310 nm) was also performed. Isocratic elution was carried out with an injection volume of 45 µL and the column oven was set at 37 °C. Liquid Chromatography (LC) Solutions' software (SSI, Kyoto, Japan) was employed for instrument control and analysis of data.

2. 5. Validation of HPLC Method

The proposed assay was validated for linearity, sensitivity, precision, accuracy, recovery and freeze-thaw stability, in compliance with the recommendations of International Conference on Harmonization (ICH).¹²

2. 6. Linearity

The representative concentrations of ceftiofur (0.1 to 10 μ g/mL) were plotted against corresponding peak areas and resultant calibration curve was used to evaluate the linearity of HPLC method.¹³ The correlation co-efficient, slope and intercept of standard curve were calculated.

2. 7. Sensitivity

The sensitivity of HPLC method was established as the limit of detection (LOD) and limit of quantification (LOQ). The standard deviation of y-intercept of regression line and slope of calibration curve were used to calculate the LOD and LOQ by means of equations 1 and 2 respectively.¹⁴

$$LOD = 3.3 (\sigma/S) \tag{1}$$

$$LOQ = 10 (\sigma/S)$$
 (2)

where " σ " represents the standard deviation of y-intercept of regression line and "S" denotes the slope of regression line.

2. 8. Accuracy and Precision

The intra-day and interday precision, and accuracy were estimated in terms of percent relative standard deviation (RSD %) and percent bias (bias %) respectively.¹⁵

2. 9. Absolute Recovery (Extraction Efficiency)

Peak areas of extracted ceftiofur-containing plasma samples and un-extracted samples of equal concentrations prepared in mobile phase were compared for the calculation of absolute recovery.¹⁶

2. 10. Freeze-Thaw Stability

Six replicates of each low and high QC samples were analyzed over two freeze-thaw cycles within three days for freeze-thaw stability assessment. The samples frozen at -20 °C for 24 h were subjected to unassisted thawing at room temperature. Three replicates of each QC sample were evaluated, while the remaining samples underwent refreezing at -20 °C for 24 h. Freeze-thaw stability was estimated by comparing the relative concentrations of freshly prepared samples and QC samples following the 1st and 2nd freeze-thaw cycles.

2. 11. Application of Assay for Quantification of Ceftiofur Hydrochloride in Buffalo Plasma

The analytical method was applied for estimation of ceftiofur in plasma samples, collected at 10 min after the intramuscular and subcutaneous administration of ceftiofur hydrochloride (Cefur® RTU injection; Nawan Laboratories (PVT) LTD., Karachi, Pakistan) in buffalo calves following a dose rate of 2.2 mg/Kg body weight. The procedures for care and handling of experimental animals were approved by the Institutional Ethical Committee,

University of Veterinary and Animal Sciences, Lahore, Pakistan (Letter No. DR/214, dated 30-03-2017).

3. Results and Discussion

3. 1. Derivatization and Extraction of Desfuroylceftiofur

Desfuroylceftiofur was cleaved and stabilized to yield desfuroylceftiofur acetamide by mixing 0.2 mL of each sample with 0.1 mL each of dithioerythritol and iodoacetamide respectively. Hence, the cleavage and derivatization were carried out following the previously documented procedure^{10,11} with slight modification. Moreover, the final clean-up was successfully accomplished without solid-phase extraction, as described by earlier studies. ^{10,11} Whereas, typical analytical assays suggested either single, double or triple steps of solid-phase extraction for final clean-up.^{7,8,19}

3. 2. Chromatographic Conditions

The μ -Bondapack C18 column (250mm \times 4.6 mm; internal diameter, 5 µm; Supelco, Bellefonte, PA, USA) was chosen for analytical assay on the basis of retention time and peak symmetry. Beckoni-Barkar et al. 19 and Jacobson et al.10 also employed C18 column, whereas, De Baere et al.8 and Altan et al.11 used PLRP-S column. In current study, the combination of sodium dihydrogen phosphate (0.025 M, pH 7) and acetonitrile (34:66, v/v) provided most suitable results, while, earlier studies primarily used the mobile phase consisting of 0.1% trifluoroacetic acid and acetonitrile or water. 8,10,19 Under the prescribed HPLC conditions of isocratic elution, the retention time was 6.8 min with a total run time of 10 min. In contrast, virtually all the previous methods were based on gradient elution, characterized by relatively longer retention times.^{7,10,11,19} The selected flow rate of 1 mL/min provided optimum resolution thus reinforcing the findings of earlier studies. 7,10,19 Whereas, De Baere et al.8 and Altan et al. 11 reported comparatively lower flow rates of 0.4 mL/min and 0.3 mL/min respectively. The UV-VIS detector and column oven were set at 310 nm and 37 °C respectively. Conversely, relatively shorter wave lengths i.e., 254 nm⁷, 265 nm¹⁰ and 266 nm^{8,11,19} were previously used for peak detection.

3. 3. Validation of HPLC Assay

The calibration curve of ceftiofur was linear over the range of 0.1 to 10 $\mu g/mL$ with $r^2=0.999$ (Table 1). The LOD and LOQ of current analytical method were 0.03 $\mu g/mL$ and 0.11 $\mu g/mL$ respectively. Former studies have reported either comparable 11,19 or relatively lower 8,10 sensitivities.

Table 1. Linearity data of analytical assay

Regression parameter	Value
r^2	0.999
Slope	55886
Intercept	6245.2
Concentration range	0.1 – $10 \mu g/mL$

Table 2 indicates the estimated accuracy and precision of HPLC assay. The within-day and between-day accuracy ranged from -0.08 to -4.00% and -0.24 to -1.33% respectively. The precision levels of proposed assay were 0.08 to 4.05% and 0.16 to 1.35% on intra-day and interday basis respectively. In all conditions, the accuracy and precision remained within the acceptable ranges of $\pm 15\%$ and

Table 2. Within-day and between-day accuracy and precision of analytical assay

Spiked concentration	Parameter	w	Between-day		
(µg/mL)	1 arameter	Day 1	ithin-day (n = Day 2	Day 3	(n = 18)
	Mean nominal concentration				
	(μg/mL)				
0.75		0.74	0.72	0.73	0.74
2.5		2.46	2.48	2.49	2.48
12.5		12.48	12.46	12.49	12.47
	Standard deviation				
0.75		0.03	0.02	0.02	0.01
2.5		0.02	0.02	0.01	0.01
12.5		0.01	0.03	0.01	0.02
	Accuracy (% Bias)				
0.75	, ,	-1.33	-4.00	-2.66	-1.33
2.5		-1.60	-0.80	-0.40	-0.80
12.5		-0.16	-0.32	-0.08	-0.24
	Precision (**RSD %)				
0.75	,	4.05	2.77	2.73	1.35
2.5		0.81	0.80	0.40	0.40
12.5		0.08	0.24	0.08	0.16

Table 3. Absolute recovery of HPLC method

Spiked concentration (µg/mL)	Mean peak area of plasma samples after extraction	Mean peak area of QC samples without extraction	% Recovery	Standard deviation	RSD %
0.75	49018	53397	92.1	0.25	0.28
2.5	147221	157237	93.2	0.29	0.31
12.5	696076	731958	94.9	0.31	0.33

Table 4. Freeze-thaw stability of quality control samples

Storage condition	Quality control level	Parameters					
	• •	Spiked concentration (μg/mL)	Mean nominal concentration (μg/mL)	Standard deviation	% Stability		
Fresh samples							
	Low concentration	0.75	0.75	0.003	100		
	High concentration	12.5	12.5	0.126	100		
Freeze thaw cycle 1	· ·						
•	Low concentration	0.75	0.73	0.012	97.3		
	High concentration	12.5	12.25	0.130	98.0		
Freeze thaw cycle 2	· ·						
·	Low concentration	0.75	0.71	0.016	94.6		
	High concentration	12.5	11.92	0.096	95.3		

< 15% respectively.²⁰ These values are in agreement with the findings of Jacobson *et al.*¹⁰

The values of extraction recovery were calculated as 92.1%, 93.2% and 94.9% for low, medium and high QC samples respectively (Table 3). Hence the recovery of analyte was rather equivalent to that documented by Jacobson $et\ al.^{10}$ but higher than the findings of Jaglan $et\ al.^{7}$ and De Baere $et\ al.^{8}$

Furthermore, the proposed assay exhibited efficient quantification of ceftiofur in QC samples exposed to freeze-thaw cycles. The stability of low QC samples following the 1st and 2nd post-thaw cycles were estimated as 97.3% and 94.6% respectively. Likewise, the high QC samples remained 98% and 95.3% stable after the 1st and 2nd post-thaw cycles respectively (Table 4).

3. 3. Analysis of Buffalo Plasma Samples

Representative chromatograms of blank plasma sample, plasma spiked with 10 μ g/mL of ceftiofur, and samples collected at 10 min after the intramuscular and subcutaneous injections of ceftiofur hydrochloride in buffalo calves at 2.2 mg/kg body weight have been presented in Figure 2.

4. Conclusion

Ceftiofur, its metabolic derivatives and protein-bound residues were converted into desfuroylceftio-

fur, derivatized and directly estimated as desfuroylceftiofur acetamide using an isocratic HPLC assay. Under the recommended chromatographic conditions, the linearity, accuracy, precision, sensitivity and recovery of proposed method remained within the acceptable limits. The suggested assay can be effectively used in pharmacokinetic studies for quantitative determination of ceftiofur hydrochloride in buffalo plasma.

5. Acknowledgement

The authors are thankful to Director, Quality Operations Laboratory, University of Veterinary and Animal Sciences (UVAS), Lahore for providing necessary facilities to carry out the research work. The authors also acknowledge M/S International Pharma Labs, Lahore, Pakistan and M/S Nawan Laboratories (PVT) LTD., Karachi, Pakistan, for the provision of reference standard and injectable formulation of ceftiofur hydrochloride respectively.

Conflict of Interest

The authors declare no conflict of interests regarding the publication of this article.

6. References

- R. E. Hornish, S. F. Kotarski, Curr. Top. Med. Chem. 2002, 2, 717. DOI:10.2174/1568026023393679
- 2. K. Palur, S. C. Archakam, N. Lingasani, R. Diviti, R. K. Kuma-

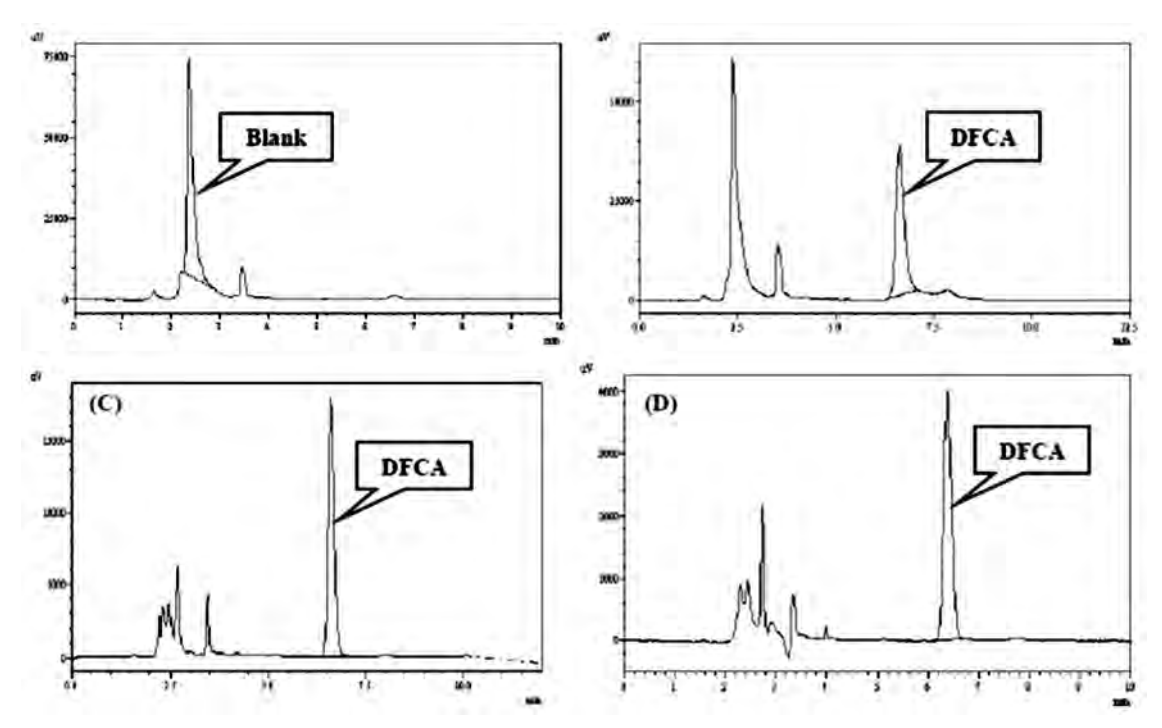


Figure 2. Representative chromatograms of blank buffalo plasma (A); buffalo plasma spiked with $10 \mu g/mL$ of ceftiofur hydrochloride (B); buffalo plasma sample collected at 10 min after intramuscular injection of ceftiofur hydrochloride (C); and buffalo plasma sample obtained at 10 min following the subcutaneous administration of ceftiofur hydrochloride (D). DFCA: Desfuroylceftiofur acetamide.

- rachari, S. Velusamy, *J. Pharm. Res.* **2013**, 7, 246. **DOI:**10.1016/j.jopr.2013.02.027
- 3. W. T. Collard, S. R. Cox, S. P. Lesman, G. S. Grover, J. F. Boucher, J. W. Hallberg, J. A. Robinson, S. A. Brown, *J. Vet. Pharmacol. Ther.* **2011**, 34, 476.

DOI:10.1111/j.1365-2885.2011.01266.x

- 4. F. M. Kausche, E. J. Robb, Vet. Ther. 2003, 4, 83.
- 5. M. G. Papich, Saunders Handbook of Veterinary Drugs. Small and Large Animal, 4th ed., Elsevier Saunders, St. Louis (MO), **2016**, pp. 139–140.

DOI:10.1016/B978-0-323-24485-5.00147-9

- S. A. Salmon, J. L. Watts, R. J. Yancey, J. Vet. Diagn. Invest. 1996, 8, 332. DOI:10.1177/104063879600800309
- P. S. Jaglan, B. L. Cox, T. S. Arnold, J. Assoc. Off. Anal. Chem. 1990, 73, 26.
- S. De Baere, F. Pille, S. Croubels, L. Ceelen, P. De Backer, *Anal. Chim. Acta.* 2004, 512, 75. DOI:10.1016/j.aca.2004.02.017
- C. B. Navarre, L. Zhang, G. Sunkara, S. H. Duran, U. B. Kompella, *J. Vet.* Pharmacol. *Ther.* 1999, 22, 13.
 DOI:10.1046/j.1365-2885.1999.00186.x
- G. A. Jacobson, S. Martinod, C. P. Cunningham, J. Pharm. Biomed. Anal. 2006, 40, 1249.

DOI:10.1016/j.jpba.2005.09.010

11. F. Altan, K. Uney, E. R. Ayse, G. Cetin, B. Dik, E. Yazar, M. Elmas, *J. Vet. Med. Sci.* **2017**, 79, 1245.

DOI:10.1292/jvms.16-0641

- 12. ICH, Q2 (R1); Validation of analytical procedures: text and methodology, International Conference on Harmonization. Geneva, **2005**, pp.11–12.
- S. S. Panda, B. V. Kumar, G. Mohanta, *Braz. J. Pharm. Sci.* 2013, 49, 475. DOI:10.1590/S1984-82502013000300009
- M. N. Irakli, V. F. Samanidou, C. G. Biliaderis, I. N. Papadoyannis, Food chem. 2012, 134, 1624.

DOI:10.1016/j.foodchem.2012.03.046

 J. W. Wu, L. C. Lin, S. C. Hung, C. W. Chi, T. H. Tsai, J. Pharm. Biomed. Anal. 2007, 45, 635.

DOI:10.1016/j.jpba.2007.06.026

- R. Gannu, S. Bandari, S. G. Sudke, Y. M. Rao, B. P. Shankar, Acta Chromatogr. 2007, 19, 149.
- M. Aqil, A. Ali, A. Ahad, Y. Sultana, A. K. Najmi, N. Saha, 2007. Acta Chromatogr. 2007, 19, 130.
- H. Nie, X. Feng, J. Peng, L. Liang, C. Lu, R. V. Tiwari, S. Tang, J. He, Am. J. Vet. Res. 2016, 77, 646.
 DOI:10.2460/ajvr.77.6.646
- M. G. Beconi-Barker, R. D. Roof, L. Millerioux, F. M. Kausche, T. H. Vidmar, E. B. Smith, J. K. Callahan, V. L. Hubbard, G. A. Smith, T. J. Gilbertson, J. Chromatogr. B Biomed. Sci. Appl. 1995, 673, 231.

DOI:10.1016/0378-4347(95)00258-1

K. Uney, F. Altan, M. Elmas, Antimicrob. Agents Chemother.
 2011, 55, 854. DOI:10.1128/AAC.01126-10

Povzetek

Optimizirali in validirali smo izokratsko metodo na osnovi tekočinske kromatografije visoke ločljivosti (HPLC) za kvantitativno določanje ceftiofur hidroklorida v plazmi bivolov. Ceftiofur, njegove metabolne produkte in na beljakovine vezane ostanke smo derivatizirali v desfuroilceftiofur acetamid in injicirali v HPLC-sistem. Ločba je potekala v koloni C18 z uporabo mobilne faze sestavljene iz natrijevega dihidrogenfosfata (0,025 M, pH 7) in acetonitrila (34:66, v/v). Pretok je bil 1 mL/min, volumen injiciranja pa 45 μ L. Detekcijo smo izvedli pri 310 nm. Območje linearnosti je bilo 0,1–10 μ g/mL, meja zaznave 0,03 μ g/mL, meja določitve pa 0,11 μ g/mL. Točnost, natančnost, izkoristek so ustrezali kriterijem. Metodo smo uporabili za določanje koncentracije ceftiofurja v vzorcih plazme bivoljih telet zdravljenih s ceftiofurjem.



Except when otherwise noted, articles in this journal are published under the terms and conditions of the Creative Commons Attribution 4.0 International License

Scientific paper

Separation of Ni (II) from Industrial Wastewater by Kombucha Scoby as a Colony Consisted from Bacteria and Yeast: Kinetic and Equilibrium Studies

Seyyed Mojtaba Mousavi,^{1,2} Seyyed Alireza Hashemi,^{1,2} Aziz Babapoor,³ Amir Savardashtaki,⁴ Hossein Esmaeili,⁵ Yaghoub Rahnema,^{1,2} Fatemeh Mojoudi,⁶ Sonia Bahrani,^{1,2} Sara Jahandideh⁷ and Marziyeh Asadi⁴

¹ Department of Medical Nanotechnology, School of Adanced Medical Sciences and Technologies, Shiraz University of Medical Sciences, Shiraz, Iran.

² Pharmaceutical Sciences Research Center, Shiraz University of Medical Sciences, Shiraz, Iran.71348-14336

³ Department of Chemical Engineering, University of Mohaghegh Ardabili, Ardabil, Iran.

⁴ Department of Medical Biotechnology, School of Advanced Medical Sciences and Technologies, Shiraz University of Medical Sciences, Shiraz, Iran.

⁵ Department of Chemical Engineering, Islamic Azad University of Bushehr, Bushehr, Iran.

⁶ Department of Environment, Faculty of Natural Resources, College of Agriculture & Natural Resources, University of Tehran, Karaj, Iran.

⁷ Department of Chemical and Polymer Engineering, Faculty of Engineering, Yazd University, Yazd, P.O. Box: 891581-8411, Iran.enia

* Corresponding author: E-mail: mousavi.nano@gmail.com Tel: +98-939-926-8875

Received: 01-22-2019

Abstract

Kombucha Scoby is a colony consisted from bacteria, yeast and cellulosic pellicle which has unique outcomes and performances in variety of fields. Along with antimicrobial and anti-toxicity of kombucha, it can be adapted to develop reactors for removal of heavy metals from waste water. The main objective of this study is to investigate the removal of Ni (II) ions from wastewater by Kombucha as a microorganism by considering the pH, time, temperature, the electrolyte solution, the buffer volume and type. The adsorption experiments indicated that the maximum adsorption capacity of Ni (II) occurred at the pH of 7, contact time of 15 min and temperature of 25 °C. In the optimal conditions, 94.5% of Ni (II) ions was removed from the solution, which clarify the significant effectiveness of Kombucha Scoby in matter of heavy metal removal. Besides, equilibrium experiments fitted well with the Langmuir isotherm model and the maximum Kombucha Scoby adsorption capacity at 25 °C was determined to be a very high adsorption capacity of 454.54 mg/g. Additionall, adsorption kinetic behaviour of Ni (II) on to the Kombucha Scoby can be described using the pseudo-second order model.

Keywords: Separation; kombucha; bacteria; adsorption kinetics; Ni (II)

1. Introduction

Heavy metal contamination of water is a common phenomenon which can cause variety of problems in different applications. The discharge of heavy metals into an aquatic ecosystem has become a matter of concern over the last decades. Among these serious pollutants, some contamination such as lead, chromium, mercury, uranium, selenium, zinc, arsenic, cadmium, gold, copper and nickel have significant impacts on the ecosystem.¹ The

presence of heavy metals in the environment is a major concern due to their extreme toxicity and tendency for bioaccumulation in the food chain even in relatively low concentrations.² Researchers have put a great effort to overcome the toxicity of materials within the environment,^{3,4} but removal of heavy metals along with deterioration of their toxicity remains a big concern. Moreover, Nickel is a toxic heavy metal that widely used in silver refineries, electroplating, zinc base casting and storage battery industries. 5,6 Furthermore, the chronic toxicity of nickel to humans and the environment have been well documented, for example, high concentration of nickel (II) within the environment can cause lung, nose and bone cancers. Therefore, it is essential to remove Ni (II) from industrial wastewater before being discharged. For this matter, it is generally used as the advanced treatment processes such as chemical reduction, ion exchange, reverse osmosis, electro-dialysis and activated carbon adsorption. In addition, usage of agricultural residues and their biological activities have received a considerable attention.^{7,8} In recent years, a number of agricultural materials such as moss peat,^{5,9} coconut husk,^{10,11} chitosan,¹² coir pith,⁹ eggshell, ^{13,14} and almond husk⁹ were examined in order to remove heavy metal contaminants. 15On the other hand, adsorption technique is an attractive approach for water treatment, especially if the adsorbent being costly efficient, convenient to separate and easy to regenerate. 16 If the amount of heavy elements in different environments goes beyond a certain dosage, then they would be considered as contaminant sources. Moreover, great deals of heavy metals enter the environments by atmospheric subsidence, mining and agriculture. 17 Besides, one of the most important sources for an increase in the concentration of heavy metals in aqueous environments is the discharge of wastewater.¹⁸ Furthermore, materials that have been widely used for removal of adsorption, not only have a high level of adsorption but also they are not soluble in water. 17 Up to now, some materials such as banana peels, 19,20 oranges, 21 paddy rice,²² groundnuts,²³ activated charcoal²⁴ and other unimportant agricultural wastes have been used to remove heavy metals. In case of removing metals, usage of the adsorption method, extraction of metals ions with solids like bio-solid, modified silica, aluminum, activated charcoal and resin can be mentioned.25-28

Kombucha is a fermentation of sweetened tea, which provide symbiosis of acetic acid bacteria and yeast species. Kombucha Scoby (floating solid part in the liquid media) which so called "tea fungus" (i.e. symbiotic colony of bacteria and yeast)²⁹ is consisted from symbiosis of acetic acid bacteria, various kinds of yeasts and cellulosic pellicle.^{30,31} Kombucha Scoby can generate acetic acid, small quantities of ethanol and CO₂. In the primary stages of fermentation, acetic acid bacteria of kombucha cannot use sucrose directly. In this matter, the yeast will degrade sucrose into the fructose and glucose which can furtherly lead to production of ethanol.³² Acetic acid bacteria and osmophilic

yeasts are the dominant species during the kombucha fermentation. These species developing a cellulosic pellicle (a biofilm) floating on the fermented liquid, which can be thence transferred to another chamber for further use. Kombucha as a beneficial sweetened tea and has some therapeutic benefits (e.g. carcinogenic, anti-diabetic and detoxifying potentials and defined to be highly effective for weight loss and treatment of Cancer, AIDS, gastric ulcers and high blood cholesterol)^{33–35} and provide strong antimicrobial activity against wide range of bacteria.^{35–37}

Additionally, the yeast, ferment the added sugar in the tea medium to ethanol, which will be oxidized by the acetic acid bacteria to generate acetic acid. The outcome of this process lead to low pH, while the presence of antimicrobial metabolites reduces the total composition of other bacteria, filamentous fungi and yeast. Moreover, analyses of fermented liquid media revealed the presence of gluconic, acetic and lactic acids as main chemical compounds in the resulting media. ^{34,38} In fact, gluconic acid is the main therapeutic source in the kombucha and its function in the liver as a detoxification agent. ^{34,39} Furthermore, the presence of usinic acid in the cultured kombucha can act as another source of antibacterial agent, ⁴⁰ while some other researcher suggested that acetic acid is the major antibacterial agent within the Kombucha culture. ³⁶

Symbiosis of bacteria and yeasts within the kombucha lead to its remarkable benefits and outcomes. Different kombucha Scoby provided from diverse sources present different outcomes, bacteria and yeast. Among frequently bacteria within the kombucha we can refer to strains of Acetobacteria (xylinum (cellulose-producing), aceti and pasteurianus), Lactobacillus and Gluconobacter. On other hand, various kinds of yeast were identified within the kombucha among we can refer to the Brettanomyces, Brettanomyces bruxellensis, Brettanomyces intermedius/Dekkera, Candida, Candida famata, Mycoderma, Mycotorula, Pichia, Pichia membranaefaciens, Saccharomyces, Saccharomyces cerevisiae, Schizosaccharomyces, Torula, Zygosaccharomyce, Zygosaccharomyces bailii and Zygosaccharomyces rouzii, Torulospora and Kloeckera. 34,35,41-43

The aim of this research is to evaluate the separation of Ni (II) from aqueous solution using Kombucha Scoby in a batch reactor. The effect of various parameters such as namely contact time, adsorbent dose, pH, and the initial concentration on the removal of Ni (II) was also investigated. Usage of this kind of materials has several advantages such as high treated water quality, low sludge production, small footprint, robustness and flexibility for future expansion. They are particularly attractive for treatment of recalcitrant wastewater, where long sludge retention times (SRT), applied for facilitating the efficient removal of slowly biodegradable pollutants. The fungus known as Kombucha is a waste produced during black fermentation. The objective of this study was to examine the main aspect of a possible strategy for the removal of arsenates by tea fungal bio reactor.

2. Materials and Method

Kombucha Scoby was procured from the Caucasus Mountains. The spectrophotometric measurements were carried out with a UV-Vis spectrophotometer model Cintra 101 (GBC Scientific Equipment, Australia) at a wavelength of 546 nm. Besides, for different stages of this study, some instruments such as pH-meter (632Metrohm, Herisau, Switzerland), digital optical microscope (Rohs, model U1000X) and super magnet (1.2 T, $10 \text{ cm} \times 5 \text{ cm} \times 2 \text{ cm}$) were used.

2. 1. Cultivation of Kombucha Scoby

The Kombucha tea medium was prepared via a multi-stage process. Firstly, 1 L distilled water boiled and thence 100 g white sugar along with 5.4 g black tea leaves added to the suspension, stirred for 5 min and thence the suspension was allowed to steep for 15 min. Tea leaves were removed from sweetened tea and the resulting suspension was transferred to a sterile glass vessel. Once the suspension cooled to the room temperature (25 °C), it was inoculated with a small piece of kombucha Scoby. The suspension was then fed with 40% wt sugar each week till the completion of Kombucha Scoby and creation of a baby Scoby after 21 days. Thereafter, four generated Scobies were cut and transferred to the aerobic reactor to start the experimental evaluation.

2. 2. Experimental Setup and Reactor Operation

The schematic of experimental setup shown in Figure 1. The aerobic reactor made of polypropylene (PP) (38 cm in diameter, 63 cm in height, with an operating level of 58 cm) was coupled to a sub-merged cross-flow ultrafiltration (UF) flat sheet membrane module (Microdyn-Nadir GmbH, Germany) with a total effective filtration area of 0.39 m. This reactor consisted from 3 main parts, in the first part, the unfiltered suspension was poured into a chamber. In the second part, the suspension was passed from 4 layers of Kombucha Scoby and after that entered the third chamber. In the third chamber, suspension pumped and returned to the first chamber and this step was continued continuously for a specific period of time, a view of this bioreactor can be seen in Figure 1. Moreover, not only the biological degradation of organic pollutants is carried out in the bioreactor by adapted microorganisms, but also the separation Ni (II) from the treated wastewater is performed by a membrane module. In addition, the Kombucha Scoby constitute a physical barrier for all suspended solids and therefore enable not only recycling of the activated sludge to the bioreactor but also the production of permeate free of suspended matter, bacteria and viruses. Besides, usage of Kombucha Scoby to separate Ni (II) ions from the treated wastewater is the main difference

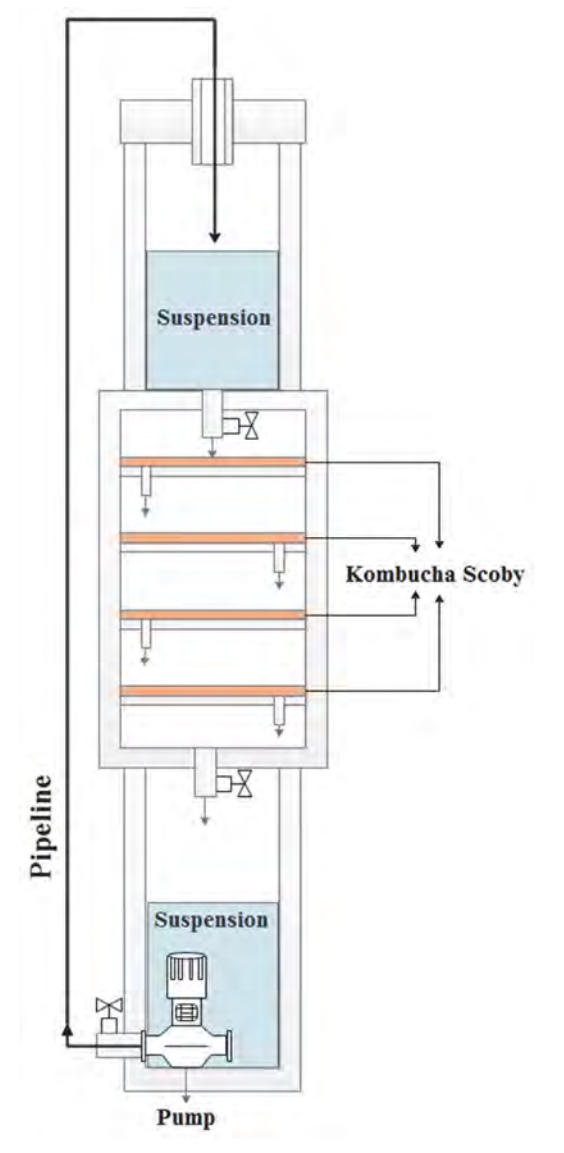


Figure 1. Schematic of experimental setup for reactor operation.

between Kombucha Scoby and traditional treatment plants for which the efficiency of the final clarification step depends mainly on the settling properties of the activated sludge.

In addition, the final ingredients vary with the bacteria and yeast in the mat, as well as the extent to which fermentation has taken place. Analyses have identified small amounts of alcohol (usually pf about 2.5%), substantial acetic acid (vinegar), ethyl acetate, glucuronic acid and lactic acid. Besides, there is some residual sugar, depending on how long it has been fermenting. Caffeine is still present and may be responsible for some of the energy claims. Moreover, it has claimed to contain B vitamins too. Besides, the results show that usage of this kind of bacteria can lead to the removal rate of 90% after 4 purification cycles in a certain period of time. Moreover, in Figure 2, microscope images of Kombucha Scoby layer can be seen.

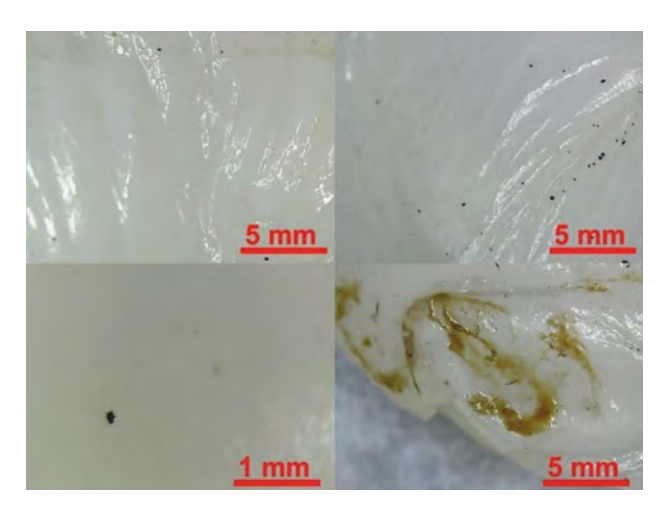


Figure 2. Optical microscopic images of Kombucha Scoby layer in different scales.

2. 3. Experimental Evaluation of Kombucha Adsorption Properties

The adsorption experiments were performed by the batch method. Besides, pH value of the solutions was adjusted by using diluted solutions of NaOH and HCl. Furthermore, completion of the reactor process, the resulting suspension was stirred for a defined time (5 min). Then, the suspension was allowed to settle by a magnet and the supernatant was analyzed for measuring the remaining Ni. Moreover, adsorption percent of Ni, i.e. the Ni removal efficiency, was determined using the following expressions:

(Ni) Removal Efficiency (%)=
$$\frac{c_0 \cdot c_f}{c_0} \times 100$$
 (1)

The amount of Ni ions adsorbed by the adsorbent was given by Eq. (2):

$$q_e = \frac{(c_0 \cdot c_f)^{\vee}}{m} \tag{2}$$

Where where q_e is the amount of equilibrium adsorbed Ni⁺ ion adsorbed by the adsorbent (mg g⁻¹), C_0 and C_f represent the initial and final ion concentrations, respectively. Besides, specimens containing Ni solution were analyzed using a UV–Vis spectrophotometer at $\lambda_{max} = 577$ nm and all of measurements were conducted triplicate. In Figure 3, the adsorption rate of Ni nanoparticles can be seen.

2. 4. Adsorption Isotherms

Batch adsorption applications were analyzed using Freundlich and Langmuir isotherm models. Freundlich model assumes that the uptake of adsorbate occurs on a heterogeneous surface of the adsorbent (see Figure 3). The

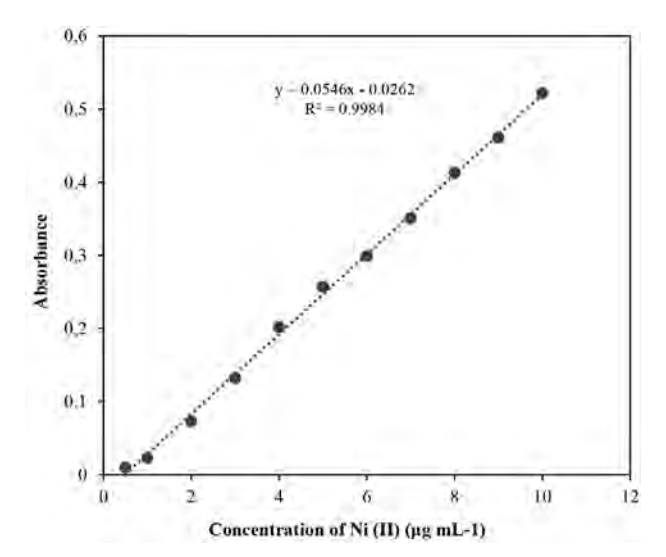


Figure 3. Ni (II) nanoparticles adsorption range.

Langmuir model describes the monolayer sorption process onto the adsorbent surface with specific binding sites. The linearized form the model equation is given as Freundlich model (Eq. 3) and linear plot of the Freundlich model is shown in Figure 4 [44].

$$\ln q_e = \frac{1}{n} \ln C_e + \ln K_f \tag{3}$$

In addition, Langmuir model is as follow [45]:

$$C_e/q_e = 1/K_L q_m + C_e/q_m$$
 (4)

In Eq. (3), K_f (Log⁻¹) and n (dimensionless) are Freundlich isotherm constants and indicative of extended adsorbent and the degree of nonlinearity between solution concentration (C) and adsorption (q), respectively. Moreover, the plot of $\ln q_e$ versus $\ln C_e$ for the adsorption was employed to generate K_f and n from the intercept and the slope values, respectively. Furthermore, in Eq. (4), q_m is the monolayer adsorption capacity of the adsorption (mol $\cdot g^{-1}$); and K_L is the Langmuir constant ($L \mod^{-1}$), and is related to the free energy of adsorption. Besides, the plot of $1/q_e$ versus $1/C_e$ for the adsorption of Ni onto modified biomass shows a straight line of slope, $1/q_m$ K_L , and intercept, $1/q_m$. In order to determine the variability of adsorption, a dimensionless constant called as separation parameter (R_L) was used that is defined as follow:

$$R_L = \frac{1}{1 + k_I C_0} \tag{5}$$

Where C_o is the highest initial Ni concentration (mol.L⁻¹). The value of separation parameter indicates the shape of isotherm to be either favorable (0 < R_L < 1), unfavorable (R_L > 1), linear (R_L = 1) or irreversible (R_L = 0) [46]. Furthermore, the linear plot of the Freundlich model can be seen in Figure 4.

2. 5. Adsorption Kinetics

Batch adsorption kinetics of Ni (II) uptake was examined by using the pseudo-first-order kinetic model of Lagergren and the pseudo-second-order kinetic model intra-particle diffusion model at different temperatures. The adsorption capacity $(q_t, mg/g)$ at any time using was calculated based on the following equation

$$q_t = \frac{(C_0 - C_f)V}{m} \tag{6}$$

where C_0 and Ct (mg L^{-1}) are the concentrations of Ni ion at initial and any time t, respectively. V (L) is the solution volume and m (g) represents the mass of adsorbent.

The equation (7) shows Lagergren pseudo-first-order kinetic model and linearized pseudo-first order plots of Langmuir are illustrated in Figure 5.³²

$$\log(q_e - q_t) = \log q_e - \frac{k_1 t}{2.303} \tag{7}$$

In addition, the equation (8) shows Lagergren pseudo-second-order kinetic model and linearized pseudo-second order plots of Langmuir, an illustration of this plot can be seen in Figure 3.³⁵

$$\frac{1}{at} \frac{1}{k_2 q_e^2 + t/q_e}$$
 (8)

In Eq. (7), q_e and q_t are the adsorption capacities of adsorbent material at equilibrium, and time t (mg g⁻¹), respectively. Besides, k_1 is the rate constant for pseudo-first-order adsorption (min⁻¹). In Eq. (8), (mg g⁻¹) and k_2 (g mg⁻¹ min⁻¹) are the maximum adsorption capacity and the equilibrium rate constant for the pseudo-second-order adsorption, respectively.

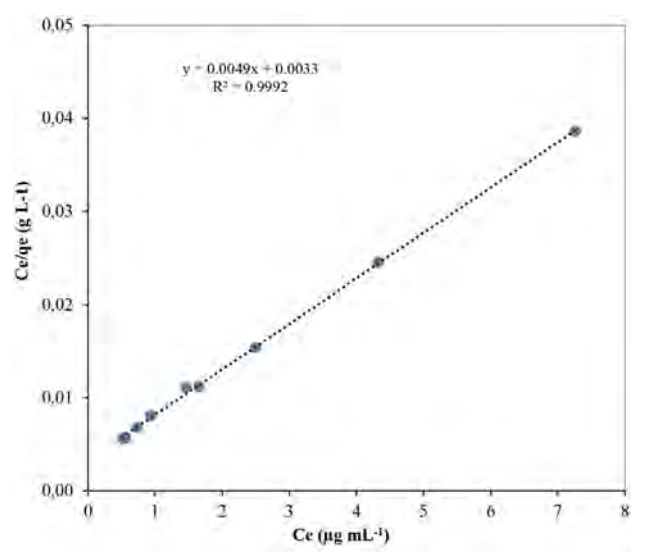


Figure 5. Linear plot of the Langmuir model.

3. Results and Discussion

3. 1. FTIR Investigation

The FTIR spectra of kombucha achieved in the range of $400\text{--}4000~\text{cm}^{-1}$ which providing information about its molecular structure and respective physical-chemical properties. As shown in Figure 6, the broad adsorption band in the wavelengths interval $3000\text{--}3500~\text{cm}^{-1}$ is characteristic to -OH stretching vibration involved in inter and intramolecular hydrogen bonds, while peaks at N-H group appear at around $3400~\text{cm}^{-1}$. The adsorption bands between $1636~\text{cm}^{-1}$ corresponds to C = O stretch bands. A significant increase of the absorption band at around $1400~\text{cm}^{-1}$ assigned to the C-N stretching and the absorption band at $1362~\text{cm}^{-1}$ specific for C-H deformation.

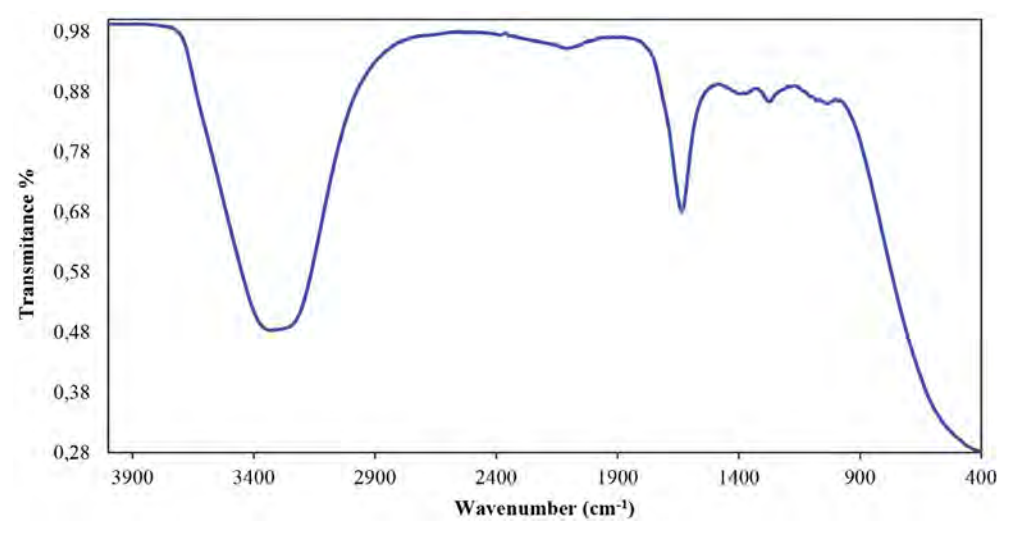


Figure 6. FT-IR study of kombucha.

3. 2. The Effect Solution pH

pH is an important parameter in the adsorption of metal ions from aqueous solutions. The effect of pH was conducted by mixing bio reactor of the adsorbent with 50 ml Ni (II) solution (20 mg/L). HCl or NaOH was utilized in order to keep the pH in the range of 3-9 throughout the experiments. At lower pH values, Ni (II) ion removal was inhibited, because at lower pH's, the medium contains a high concentration of hydrogen ions, therefore competition between H⁺ and Ni²⁺ ions for the available adsorption sites could be possible. The effect of pH on the removal rate of Ni²⁺ from aqueous solution that calculated by equation 1, is presented in the Figure 7. As can be seen, the removal of nickel (II) ion increased with increase in the pH and reached a maximum at pH equals 7. Besides the percentage of Ni removal rate was observed to be changed sharply between pH 3 and pH 9 (from the percentage removal of 93.6 % to 66.38 %). Furthermore, at pH's greater than 7, the adsorption of Ni (II) ions decreases due to the precipitation of nickel hydroxide, resulting from Ni (II) ions reacting with hydroxide ions. Moreover, the suspension was shaken for 5 min at the temperature of 25 °C and the optimum condition was found to be at the pH equals 7. In further works, the pH of the solutions was adjusted by using citrate buffer volume (ml). In addition, effect solution pH on Ni (II) ions removal rate can be seen in Figure 7.

In fact, there is a competition between nickel ions and hydrogen cation in order to occupy active sites within the absorbent. If these sites become occupied with hydrogen cation, there would be no active sites for nickel ions which can reduce the recovery of adsorption. At high pH values (pH > 7), hydrogen cation content is low, while the hydroxyl (-OH) content inside the solution is high. In this matter, there would be no competition between hydrogen cations and nickel ions, thereby the active sites become occupy with nickel ions which can improve the removal rate.

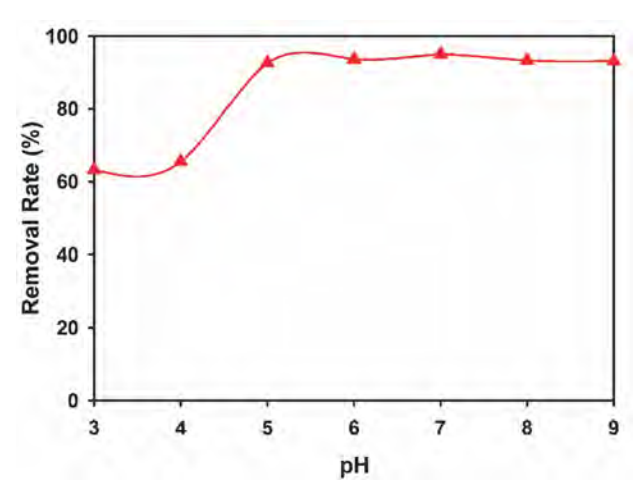


Figure 7. Effect of initial solution pH of Ni (II) ions on removal efficiency.

Moreover, at higher pH values, a majority of hydroxide anions create a complex with nickel ions and thence these ions deposit and accumulate in the solution.

3. 3. The Effect of Contact Time

The effect of contact time on the performance of Kombucha Scobies in matter of Ni (II) adsorption was investigated separately. The solution pH and Kombucha Scoby dosage were fixed at their obtained optimum values. Figure 8 shows removal efficiencies for Ni (II) as a function of bioreactor time (in the range of 1 and 20 min). According to these results, the optimum stirring time for removal by Kombucha Scoby is 15 min. The contact time between adsorbent and adsorbent is the most important design parameter that affects the performance of adsorption processes. These data indicate that adsorption started immediately upon adding the Kombucha Scoby to the dye solution. The removal efficiency of Ni (II) was rapidly increased from 56.81 % in the first minute of contact to 93.88 %, when the stirring time was increased to 15 min and the equilibrium condition reached.

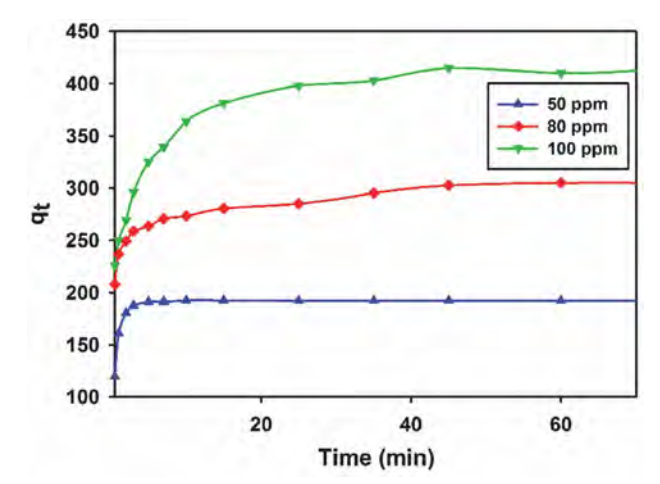


Figure 8. The effect of contact time on the bioreactor performance.

3. 4. The Effect of Electrolyte on Removal Rate

The effect of electrolyte concentration (adjusted by KCl) on the adsorption rate of Ni (II) was studied. As can be seen in Figure 9, the adsorption efficiency of Ni (II) decreased within the concentration range of 0.0–1 mol \cdot L⁻¹ of NaCl in the test solution. At higher concentration, nickel removal efficiency was decreased. Besides, concentration rate of 0.0 mol.L⁻¹ (91.98 % removal) was used for further evaluations.

3. 5. The Effect of Solution Temperature on Removal Rate

The effect of temperature on the adsorption rate of Ni (II) was examined within the temperature range of (5 to

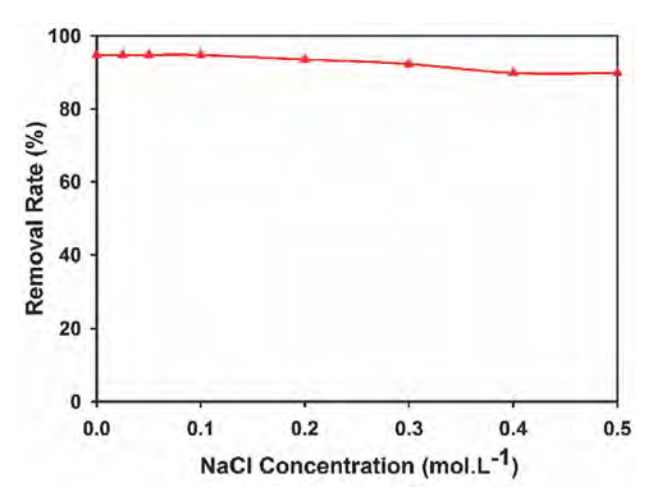


Figure 9. The effect of electrolyte on the bioreactor performance.

60) °C. Achieved results indicated that the adsorption rate of Ni (II) in a 50 ml solution by usage of Kombucha at the pH of 7 is constant versus variation of temperature. Besides, at higher temperatures, the dye removal efficiency was decreased. Furthermore, the temperature value of 25 °C (94.5% removal) was used for further works. In addition, the effect of contact time on the nickel (II) removal rate and final adsorbent on Kombucha Scoby can be seen in Figure 10.

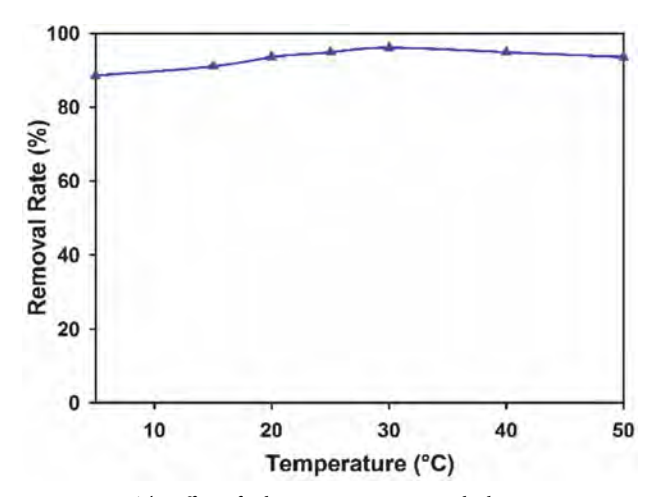


Figure 10. The effect of solution temperature on the bioreactor performance.

3. 6. Isothermal Adsorption Modeling

The capacities of Kombucha Scoby for adsorption of Ni (II) ions were examined by measuring the initial and final concentration of Ni (II) at the pH and temperature values of 7 and 25 °C in a batch bioreactor system, respectively. Both Langmuir and Freundlich adsorption isotherms were used to normalize the adsorption data. The correlation of ion adsorption data with the Langmuir isotherm model was higher (with R^2 values of 0.9992) than the Freundlich model ($R^2 = 0.9522$). This implies mono-

layer absorption of nickel ions onto active sites of biosorbent.

Besides, the maximum predictable adsorption capacity of Ni (II) ions is defined to be 454.54, a view of isothermal adsorption modelling results can be seen in Figure 11.

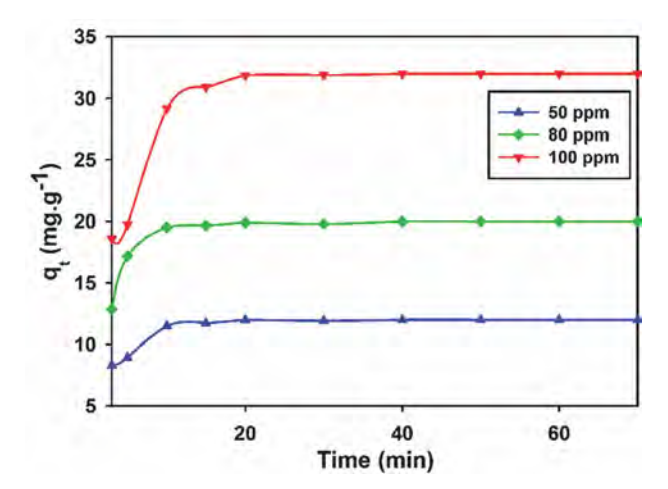


Figure 11. Isothermal adsorption modeling results.

3. 7. Kinetic Modelling of Adsorption

To describe the adsorption rate and performance of Kombucha Scoby, the data obtained from adsorption kinetic experiments were evaluated using pseudo first and second-order reaction rate models that give a summary of these models and constants along with the determination coefficients for the linear regression plot of the testing ion. As shown in Figure 12 and 13, higher values of \mathbb{R}^2 were obtained for pseudo second-order adsorption rate model, indicating that the adsorption rate of Ni (II) on to the Kombucha Scoby can be described better, by using of the pseudo-second order than the first order. This indicates the mechanism of chemical adsorption.

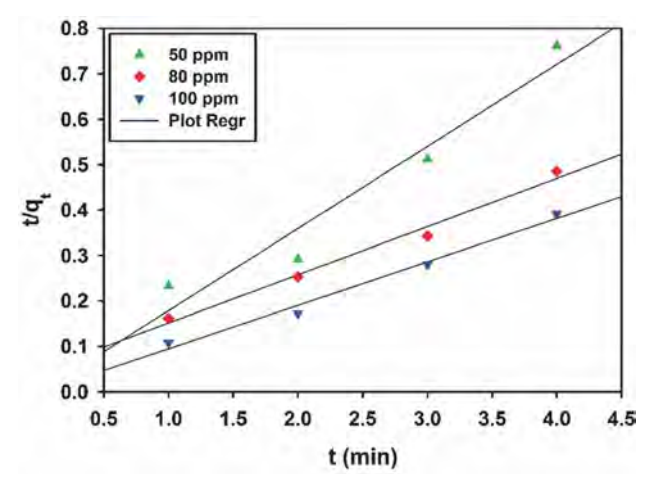


Figure 12. Results of the pseudo first-order reaction rate model.

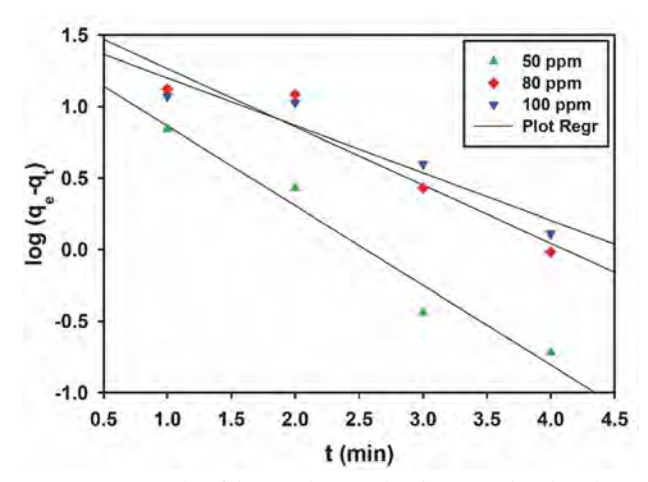


Figure 13. Results of the pseudo second-order rate rather than the first-order model.

3. 8. Adsorption Mechanism

Based on the results of isotherm and kinetic models analysis, the mechanism of adsorption for the removal of Ni ions can be suggested. The Freundlich isotherm model shows a deviation from straight line indicating that intra-particle diffusion is not the rate-limiting step of the adsorption mechanism. Meanwhile, the kinetic modelling results suggest the chemical sorption mechanism is dominated in the adsorption process.

Since kombucha is a complex biological material, it operates variety of mechanisms under given conditions. The presence of materials with diverse structures in kambucha presented many functional groups (carboxyl, hydroxyl, amino, etc.) embedded on the surface which be able to interact with nickel ions and responsible for binding metal ions onto kambucha. In this regard, different mechanisms may be involved including ion-exchange, surface complexation, electrostatic interactions, etc. however, many parameters including pH and temperature can alter the adsorption mechanism of ions onto the surface.

4. Conclusions

In this study, Kombucha Scoby was used as an applicatory adsorbent for the removal of Nickel (II) particles. The effects of pH, adsorbent dosage, temperature and time on the adsorption rate were studied. Besides, high adsorption capacity was obtained at low pH values. Furthermore, the adsorption kinetics and equilibrium data fit well with the pseudo second-order model and Langmuir model respectively. Moreover, usage of Kombucha Scoby in a bioreactor with 4 adsorption cycles and at pH = 7, indicated that this bacteria is very effective for removal of Ni (II) ions from aqueous solution. By comparison of this method with the conventional activated sludge system, the Kombucha Scoby system requires smaller bacteria area and produces a better quality treated water reusable

in the industry. With the obvious advantages of the bioreactor technology, it shall gradually replace the conventional activated sludge system in large industrial plants. Besides, by usage of this bacteria, not only the Ni particles can be removed from the suspension but also some products such as alcohol (usually under 2.5%), substantial acetic acid (vinegar), ethyl acetate, glucuronic acid and lactic acid can be added to the suspension. In fact, further evaluations showed that low cost Kombucha system can remove the Nickel (II) of about 94.5%, while along with antimicrobial performance of kombucha system, this proposed method can be adapted for waste water purification and restoration of polluted environment via cost affordable method.

5. References

- P. Aikpokpodion, R. Ipinmoroti, S. Omotoso, Aejts. 2010, 2, 72–82.
- F. S. Khoo, H. Esmaeili, J. Serb. Chem. Soc. 2018, 83, 237–249
 DOI:10.2298/JSC170704098S.
- S. M., Mousavi, S. A. Hashemi, A. M. Amani, H. Saed, S. Jahandideh, F. Mojoudi, *Polymers from Renewable Resources*. 2017, 8, 177–196. DOI:10.1177/204124791700800403
- 4. N. Goudarzian, Z. Sadeghi, S. M. Mousavi, S. A. Hashemi, N. Banaei, *Ijser.* **2017**, *8*, 1275–1279
- K. Kadirvelu, K. Thamaraiselvi, C. Namasivayam, Sep. Purif. Technol. 2001, 24, 497–505.

DOI:10.1016/S1383-5866(01)00149-6

- S. M. Mousavi, S. A. Hashemi, A. M. Amani, H. Esmaeili, Y. Ghasemi, A. Babapoor, O. Arjomand, PCR. 2018, 6, 759–771.
- T. W. Tee, A. R. M. Khan, Environ. Technol. 1988, 9, 1223– 1232. DOI:10.1080/09593338809384685
- S. M. Mousavi, S.A. Hashemi, O. Arjmand, A. Babapoor, A. M. Amani, F. Mojoudi, H. Esmaeili, S. Jahandideh, *Acta Chim. Slov.* 2018, 65, 882–894. DOI:10.17344/acsi.2018.4537
- H. Hasar, J. Hazard. Mater. 2003, 97, 49–57.
 DOI:10.1016/S0304-3894(02)00237-6
- W. Tan, S. Ooi, C. Lee, Environ. Technol. 1993, 14, 277–282.
 DOI:10.1080/09593339309385290
- K. Low, C. Lee, S. Wong, Environ. Technol. 1995, 16, 877–883.
 DOI:10.1080/09593331608616326
- I. Saucedo, E. Guibal, Ch. Roulph, P. Le Cloirec, Environ. Technol. 1992, 13, 1101–1115.
 DOI:10.1080/09593339209385250
- 13. B. S. Zadeh, H. Esmaeili, R. Foroutan, *Indonesian Journal of Chemistry*. **2018**, 18. **DOI:**10.22146/ijc.28789
- S. M. Mousavi, H. Esmaeili, O. Arjmand, Sh. Karimi, S. A. Hashemi, *Journal of Materials*. 2015, 2015, 1–6.
 DOI:10.1155/2015/131957
- S. M. Mousavi, S. A. Hashemi, H. Esmaeili, A. M. Amani, F. Mojoudi, *Acta Chim. Slov.* 2018, 65, 750–756.
 DOI:10.17344/acsi.2018.4536
- R. Foroutan, H. Esmaeili, M. Abbasi, M. Rezakazemi, M. Mesbah, Environ. Technol. 2018, 39, 2792–2800.

- 17. A. Agrawal, K. Sahu, B. Pandey, Colloids Surf. A. 2004, 237, 133-140. **DOI:**10.1016/j.colsurfa.2004.01.034
- 18. H. Esmaeili, R. Foroutan, Ijbpas. 2015, 4, 611-619.
- 19. M. R. Mehrasbi, Z. Farahmandkia, B. Taghibeigloo, A. Taromi, Water Air Soil Pollut. 2009, 199, 343-351. **DOI:**10.1007/s11270-008-9883-9
- 20. R. S. D. Castro, L. Caetano, G. Ferreira, P. M. Padilha, M. J. Saeki, L.F. Zara, M. A. U. Martines, G. Castro, R.Ind. Eng. Chem. Res. 2011, 50, 3446v3451. DOI:10.1021/ie101499e
- 21. X. Li, Y. Tang, X. Cao, D. Lu, F. Luo, W. Shao, Colloids Surf. A. 2008, 317, 512-521. DOI:10.1016/j.colsurfa.2007.11.031
- 22. H. Z. Shahmohammadi, Removal of low concentrations of cadmium from water using improved rice husk. 2008.
- 23. F. D. Oliveira, A. C. Soares, O. M. Freitas, S. A. Figueiredo, Global Nest J. 2010, 12, 206-214.
- 24. I. Maiz, M.V. Esnaola, E. Millan, Sci Total Environ. 1997, 206, 107-115. **DOI:**10.1016/S0048-9697(97)80002-2
- 25. L. Norton, K. Baskaran, T. McKenzie, Adv. Environ. Res. **2004**, 8, 629–635. **DOI:**10.1016/S1093-0191(03)00035-2
- 26. M. Ghaedi, E. Asadpour, A. Vafaie, Bull. Chem. Soc. Jpn. 2006, 79, 432-436. DOI:10.1246/bcsj.79.432
- 27. M. Ghaedi, F. Ahmadi, Z. Tavakoli, M. Montazerozohori, A. Khanmohammadi, M. Soylak, J. Hazard. Mater. 2008, 152, 1248-1255. DOI:10.1016/j.jhazmat.2007.07.108
- 28. X. Huang, X. Chang, Q. He, Y. Cui, Y. Zhai. N. Jiang, J. Hazard. Mater. 2008, 157, 154-160. DOI:10.1016/j.jhazmat.2007.12.113
- 29. G. Sreeramulu, Y. Zhu, W. Knol, J. Agric. Food Chem. 2000, 48, 2589–2594. **DOI:**10.1021/jf991333m
- 30. T. Kappel, R. Anken, Mycologist. 1993, 7, 12-13. **DOI:**10.1016/S0269-915X(09)80616-2
- 31. K. H. Steinkraus, Food Control. 1997, 8, 311–317. DOI:10.1016/S0956-7135(97)00050-9
- 32. M. Sievers, C. Lanini, A. Weber, U. Schuler-Schmid, M. Teuber, Syst. Appl. Microbiol. 1995, 18, 590-594. DOI:10.1016/S0723-2020(11)80420-0

- 33. C. Dufresne, E. Farnworth, Food. Res. Int. 2000, 33, 409-421. DOI:10.1016/S0963-9969(00)00067-3
- 34. G. W. Frank, A. Tyndale, Kombucha: Healthy Beverage and Natural Remedy from the Far East, Its Correct Preparation and Use. Publishing House W. Ennsthaler, 1995.
- 35. C. Greenwalt, K. Steinkraus, R. Ledford, J. Food Prot. 2000, 63, 976-981. **DOI:**10.4315/0362-028X-63.7.976
- 36. C. Greenwalt, R. Ledford, K. Steinkraus, LWT-Food Science and Technology. 1998, 31, 291-296. DOI:10.1006/fstl.1997.0354
- 37. G. Sreeramulu, Y. Zhu, W. Knol, Acta Biotechnol. 2001, 21, 49-56. **DOI:**10.1002/1521-3846(200102)21:1<49::AID-ABIO 49>3.0.CO;2-G
- 38. C. Hobbs, Kombucha, Tea Mushroom: The Essential Guide. Botanical Press, 1995.
- 39. E. S. Lončar, S. E. Petrovič, R. V. Malbača, R. M. Verac, Mol. Nutr. Food. Res. 2000, 44, 138-139. DOI:10.1002/(SICI)1521-3803(20000301)44:2<138::AID-FOOD138>3.0.CO;2-#
- 40. H. Tietze, Kombucha: The miracle fungus. Harald Tietze Publishing, 1996.
- 41. I. Jankovic, M. Stojanovic, Mikrobiologija (Yugoslavia), 1994.
- 42. P. Mayser, S. Fromme, G. Leitzmann, K. Gründer, MYCOSES. 1995, 38, 289-295. DOI:10.1111/j.1439-0507.1995.tb00410.x
- 43. C. H. Liu, W. H. Hsu, F. L. Lee, C. C. Liao, Food Microbiol. 1996, 13, 407-415. DOI:10.1006/fmic.1996.0047
- 44. F. S. Sarvestani, H. Esmaeili, and B. Ramavandi, 3 Biotech. **2016**, 6, 251.
- 45. R. Foroutan, H. Esmaeili, Hossein; S. M. D. Rishehri, F. Sadeghzadeh, S. R. Mirahmadi, M. Kosarifard, B. Ramayandi, Data brief. 2017, 12, 485-492. DOI:10.1016/j.dib.2017.04.031
- 46. A. Teimouri, H. Esmaeili, R. Foroutan, B. Ramavandi, Korean *J Chem Eng.* **2018**, *35*, 479–488.

DOI:10.1007/s11814-017-0311-y

Povzetek

Kombuča (ang. Kombucha Scoby) imenujemo združbo sestavljeno iz bakterij in kvasovk na nosilcu iz celuloznih vlaken, ki ima edinstvene lastnosti uporabne na mnogih področjih. Poleg antimikrobnih in antitoksičnih lastnosti kombuče, jo lahko uporabimo v reaktorjih za odstranjevanje težkih kovin iz onesnaženih voda. Cilj študije je bil preučiti možnost odstranjevanja Ni (II) ionov iz odpadnih vod s pomočjo kombuče pri različnih pH vrednostih, času, temperature, raztopni elektrolitov, volumnu pufra in vrsti. Eksperimenti adsorpcije so pokazali, da je maksimalna kapaciteta vezave Ni (II) ionov dosežena pri pH vrednosti 7, kontaktnem času 15 min in temperaturi 25 °C. Pod optimalnimi pogoji se adsorbira 94.5 % Ni (II) ionov, kar kaže na znaten potencial kombuče pri odstranjevanju težkih kovin. Ravnotežne rezultate lahko učinkovito opišemo z Langmuirjevo izotermo na osnovi česar je bila določena maksimalna kapaciteta vezave, ki znaša 454.54 mg/g pri 25 °C. Kinetiko adsorpcije Ni (II) ionov na kombučo smo uspešno opisali z modelom pseudo-drugega reda.



Except when otherwise noted, articles in this journal are published under the terms and conditions of the Creative Commons Attribution 4.0 International License

@creative

Scientific paper

Synthesis, Antifungal Evaluation and Molecular Docking Studies of Some Tetrazole Derivatives

Mohammad Hosein Afsarian,¹ Mojtaba Farjam,^{2,3,*} Elham Zarenezhad,^{2,*} Somayeh Behrouz⁴ and Mohammad Navid Soltani Rad⁴

 1 Department of Medical Mycology & Parasitology, School of Medicine, Fasa University of Medical Sciences, Fasa, Iran

² Noncommunicable Diseases Research Center, School of Medicine, Fasa University of Medical Sciences, Fasa, Iran

³ Department of Medical pharmacology, school of medicine, Fasa University of medical sciences, Fasa, Iran

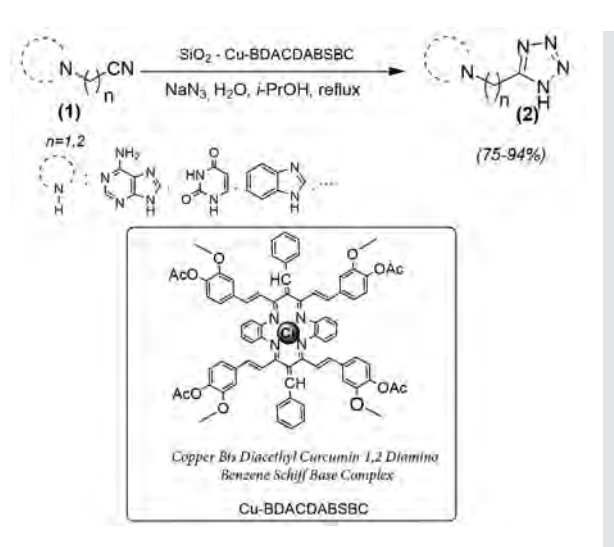
⁴ Medicinal Chemistry Research Laboratory, Department of Chemistry, Shiraz University of Technology, Shiraz, Iran

* Corresponding author: E-mail: El.Zarenezhad@gmail.com farjam.md@gmail.com; mfarjam@fums.ac.ir

Received: 01-25-2019

Abstract

A facile and simple protocol for the [3+2] cycloaddition of alkyl nitriles (RCN) with sodium azide (NaN₃) in the presence of copper bis(diacetylcurcumin) 1,2-diaminobenzene Schiff base complex, SiO₂-[Cu-BDACDABSBC] as a heterogeneous catalyst in the presence of ascorbic acid and a solution of water/i-PrOH (50:50, V/V) media at reflux condition is described. The supported catalyst was prepared by immobilization of a copper bis(diacetylcurcumin) 1,2-diaminobenzene Schiff base complex [Cu-BDACDABSBC] on silica gel. The complex has high selectivity, catalytic activity, and recyclability. The significant features of this procedure are high yields, broad substrate scope and simple and efficient work-up procedure. According to this synthetic methodology, excellent yields of 5-substituted 1H-tetrazoles having bioactive N-heterocyclic cores were synthesized. The in vitro antifungal activities of title compounds were screened against various pathogenic fungal strains, such as Candida species



involving *C. albicans, C. glabrata, C. krusei, C. parapsilosis* as well as filamentous fungi like *Aspergillus* species consisting of *A. fumigatus* and *A. flavus*. The molecular docking analysis is discussed for one most potent compound against fungi. The docking study determined a remarkable interaction between the most potent compounds and the active site of *Mycobacterium* P450DM.

Keywords: 'Click' cycloaddition; tetrazoles; heterogeneous catalyst; antifungal activity; docking studies.

1. Introduction

Tetrazole and its derivatives have attracted considerable interest in recent years because of their unique structure and wide range of applications.¹ Heterocyclic com-

pounds exhibiting tetrazole structures are known as bioactive compounds, encompassing a broad spectrum of biological activities such as antihypertensive,² antibacterial,^{3,4} antifungal,⁵ anticonvulsant,⁶ analgesics,⁷ anti-inflammatory,⁸ antitubercular,⁹ anticancer,¹⁰ antineoplastic,¹¹ antial-



Figure 1. Structure of some of known tetrazol derivatives

lergic, ¹² antiviral, ¹³ and especially anti-HIV activities. ¹⁴ They play important roles in coordination chemistry as ligands, ¹⁵ in medicinal chemistry as lipophilic spacers and metabolically stable surrogates for the carboxylic acid group and *cis*-amide bond, ¹⁶ also in the photographic industry, ¹⁷ in agriculture as plant growth regulators. ¹⁸ This synthetic heterocyclic nitrogen-rich compounds are also useful synthons in synthetic organic chemistry. ¹⁹ In addition, the syntheses of tetrazole moieties are very essential in modern medicinal chemistry, since they can behave as bioisosters for carboxylate moieties. Angiotensin (II) blockers often contain tetrazole cores, as losartan and candesartan. ²⁰ 3-(4,5-Dimethylthiazol-2-yl)-2,5-diphenyltetrazolium bromid (MTT) is a well-known tetrazole useful for evaluating cell metabolic activity (Figure 1). ^{21,22}

The different preparative methods for synthesis of tetrazoles are well documented. The traditional synthesis of 5-substituted 1H-tetrazoles is conducted via [3+2] cycloaddition of azides to the corresponding nitriles, as developed by Sharpless and coworkers.²³ However, several synthetic approaches have been determined so far that mostly proceed through the non-concerted types of mechanisms.²⁴ Many homogeneous and heterogeneous catalysts were developed for the synthesis of tetrazoles such as Cu₂O,²⁵ AlCl₃,²⁶ BF₃·OEt₂,²⁷ Pd(PPh₃)₄,²⁸ Yb(OTf)₃,²⁹ Zn(OTf)₃,³⁰ CuSO₄,³¹ and boron azides,³² also several heterogeneous catalyst systems, such as silica-supported FeCl₃,³³ ZnS nanospheres,³⁴ zinc hydroxyapatite,³⁵ Cu–Zn alloy nanopowder,³⁶ Zn/Al hydrotalcite,³⁷ Sb₂O₃,³⁸ metal tungstates, ³⁹ CdCl₂, ⁴⁰ γ-Fe₂O₃, ⁴¹ and natural natrolite zeolite⁴² were reported.

The copper-based complexes have undeniable roles in 'Click' chemistry; so far various solid compounds were used to support the copper species containing alumina, charcoal, silica gel and zeolites. Recently, the improvement of complexes supported on silica gel has received a great attention, ⁴³ because silica gel as an inorganic support has a high surface area (5–800 m² kg⁻¹) compared with other inorganic supports and silica gel consequently ranks at the top of the list of solids with high-surface areas. ^{44–46} The

development of complexes supported on silica gel has received considerable attention, because industry seeks more eco-friendly chemical manufacturing processes.^{47–49}

Immobilization of organometallic complexes or homogenous catalysts on inorganic supports seems to be an appropriate approach to improve their stability, reactivity and selectivity. This method obtained the remarkable attention due to the ability of both, to facilitate the catalyst separation and its recycling. ^{50–56}

The chemical structure of curcumin was discovered by Milobedzka and coworkers. Curcumin as a tautomeric form is diarylheptanoic compound, which represents natural phenols responsible for turmeric's yellow color. The presence of the aromatic ring systems, which are phenols, and connected by two α,β -unsaturated carbonyl groups allows the possibility of grafting with many biomolecules, organic and inorganic materials. Curcumin possesses very interesting pharmacological and biological properties exhibiting a variety of biological activities. The heterocyclic N,O-donor Schiff base ligands display a great role in the development of coordination chemistry because they easily form complexes with most of the transition metal ions. $^{60-61}$

The incidence of opportunistic fungal infections has remarkably increased in recent years by normal flora fungi or acquired from the environment, especially *Candida* and *Aspergillus* species in immunocompromised or immunosuppressed patients. 62-64 Increasing of opportunistic pathogenic fungal infections in these patients has become one of the most essential challenges for medicine. To date, it was observed that some of these fungi have become resistant to the established drugs, despite the introduction of new antifungal agents. 65-66 Numerous antifungal drugs are available, such as: azoles (fluconazole, voriconazole and itraconazole) which are considered as the first-line therapy in current clinical use. 67-69 However, the discovery of new antifungal drugs particularly for the treatment of opportunistic pathogenic fungal infections is critically essential.

Since the considerable therapeutic activities of N-heterocyclic compounds⁷⁰ were demonstrated and also

in continuation of our interest in discovering copper(II) Schiff base complexes $^{71-72}$ and the new N-heterocyclic bioactive compounds, $^{73-79}$ herein we report the application of a suitable and reusable Cu(II)-curcumin complex supported on silica gel and ascorbic acid as the reducing agent. This heterogeneous catalyst system exhibits a potent catalytic activity for the synthesis of some 5-substituated-1H-tetrazole derivatives tethered to bioactive N-heterocyclic cores.

2. Experimental

2. 1. General

All preliminary chemicals and solvents were purchased from Fluka or Merck. The catalyst was prepared according to the reported procedure.80 Reactions were monitored by TLC using SILG/UV 254 silica-gel plates. Column chromatography was performed on silica gel 60 (0.063-0.200 mm, 70-230 mesh; ASTM). IR spectra were measured using a Shimadzu FT-IR-8300 spectrophotometer. ¹H and ¹³C NMR spectra were obtained on Bruker Avance-DPX-250/400 spectrometer operating at 250/62.5 and/or 400/100 MHz, respectively. Chemical shifts are given in δ relative to tetramethylsilane (TMS) as the internal standard, coupling constants J are given in Hz. Abbreviations used for ¹H NMR signals are: s = singlet, d = doublet, t = triplet, q = quartet, m = multiplet, br = broad. Elemental analyses were performed on a Perkin-Elmer 240-B micro-analyzer.

2. 2. General Procedure for Immobilization of [Cu-BDACDABSBC] on Silica Gel

To a solution of [Cu-BDACDABSBC] (1.28 g, 1 mmol) in anhydrous dimethyl sulfoxide (55 mL), it was added a fresh and active silica gel (0.6 g, 10 mmol) in 0.063–0.200 mm or 70–230 mesh size, then the mixture was sonicated for 1 h and stirred at room temperature for 48 h. Afterward, the resulting precipitate was filtered off and the solid residue (catalyst) was washed with dimethyl sulfoxide (2 × 50 mL), methanol (3 × 50 mL) and ether (2 × 50 mL), dried in vacuum oven at 60 °C for 4 h and stored in a refrigerator.

2. 3. General Procedure for the Preparation of Alkyl Nitriles 1a-0

To a round bottom flask (100 mL), equipped with a condenser, was added N-heterocyclic compound (0.01 mol), 3-chloroacetonitrile or 2-chloropropanenitrile (0.013 mol), K_2CO_3 (0.01 mol), Et_3N (0.01 mol), and a catalytic amount of TBAI (0.1 g) in anhydrous MeCN (40 mL). The reaction mixture was refluxed until TLC monitoring indicated no further progress in the conversion. The solvent was evaporated *in vacuo* to remove the solvent. To

continue, the remaining foam was dissolved in CHCl $_3$ (100 mL) and subsequently washed with water (2 × 100 mL). The organic layer was dried (Na $_2$ SO $_4$) and evaporated. The crude product was purified by column chromatography on silica gel. The catalyst was filtered off, washed with THF/H $_2$ O (5 × 10 mL) and the filtrate was evaporated under vacuum to remove the solvent. The remaining foam was dissolved in CHCl $_3$ (100 mL) and subsequently washed with water (2 × 100 mL). The organic layer was dried (Na $_2$ SO $_4$) and evaporated. The crude product was purified by column chromatography on silica gel and eluted with proper solvents.

2. 4. General Procedure for the Catalytic Test

In a double-necked round bottom flask (100 mL) equipped with a condenser was added a mixture consisting of alkyl nitrile (0.01 mol), NaN₃ (0.015 mol), and SiO₂-[Cu-BDACDABSBC] (0.05 mol %) in H₂O/i-PrOH (1:1 V/V, 50 mL). The mixture was heated at reflux until TLC monitoring indicated no further improvement in the conversion (Table 4). The reaction mixture was then cooled to room temperature, vacuum-filtered and the residue was washed with ethyl acetate (2×20 mL). To achieve pH 3, the filtrate was treated with 5 N HCl and stirred at room temperature for 30 minutes. Subsequently, the organic layer was separated, dried over anhydrous Na2SO4 and evaporated in vacuo. The crude product was purified by column chromatography on silica gel eluted with proper solvents and/or recrystallization was applied. Characterization data of all synthesized compounds are described below.

((1H-Tetrazol-5-yl)methyl)-2-methyl-1H-benzo[d]imidazole (2a)

Recrystallization (EtOAc) afforded a creamy solid; yield: 1.71 g (80%); mp >300 °C (dec.); R_f = 0.25 (EtOAc–MeOH, 1:1); IR (KBr): 3384, 3100, 2982, 1619, 1580, 1480 cm⁻¹; ¹H NMR (250 MHz, DMSO- d_6): δ 7.57–7.46 (m, 2H, aryl), 7.16–7.08 (m, 2H, aryl), 5.46 (s, 2H, NCH₂), 4.55 (s, 1H, exchangeable with D₂O, NH, tetrazole), 2.67 (s, 3H, CH₃); ¹³C NMR (250 MHz, DMSO- d_6): δ 17.90, 49.18, 115.53, 116.64, 121.56, 123.05, 134.72, 140.35, 151.27, 158.41; MS (EI): m/z (%) 214 (11.4) [M⁺]. Anal. Calcd for $C_{10}H_{10}N_6$: C, 56.07; H, 4.71; N, 39.23. Found: C, 56.19; H, 4.62; N, 39.35.

((1*H*-Tetrazol-5-yl)methyl)-1*H*-benzo[*d*]imidazole (2b)

Recrystallization (EtOAc) afforded a yellow solid; yield: 1.80 g (90%); mp 235–240 °C (dec.); R_f = 0.25 (EtO-Ac–MeOH, 1:1); IR (KBr): 3385, 3100, 2968, 2800, 1616, 1462, 1410 cm⁻¹; ¹H NMR (250 MHz, DMSO- d_6): δ 8.28 (s, 1H, C(2)-H, benzimidazole), 7.64–7.61 (m, 2H, aryl), 7.22–7.13 (m, 2H, aryl), 5.55 (s, 2H, NCH₂), 2.51 (s, 1H, exchangeable with D₂O, NH, tetrazole); ¹³C NMR (250 MHz, DMSO- d_6): δ 51.70, 116.65, 117.85, 122.22, 123.25,

133.61, 137.50, 145.60, 155.69; MS (EI): m/z (%) 200 (14.5) [M⁺]. Anal. Calcd for C₉H₈N₆: C, 53.99; H, 4.03; N, 41.98. Found: C, 54.06; H, 4.15; N, 41.92.

((2-Methyl-4-nitro-1*H*-imidazol-1-yl)methyl)-1*H*-tetrazole (2c)

Column chromatography (silica gel, EtOAc–MeOH, 1:1) afforded a brown solid; yield: 1.56 g (75%); mp 208–212 °C (dec.); $R_f = 0.31$ (EtOAc–MeOH, 1:1); IR (KBr): 3350, 3128, 2900, 1645, 1500, 1456, 1300 cm⁻¹; ¹H NMR (250 MHz, DMSO- d_6): δ 8.30 (s, 1H, C(5)-H, imidazole), 5.40 (s, 2H, NCH₂), 4.40 (s, 1H, exchangeable with D₂O, NH, tetrazole), 2.43 (s, 3H, CH₃); ¹³C NMR (250 MHz, DMSO- d_6): δ 15.74, 48.22, 121.10, 147.82, 153.09, 160.97; MS (EI): m/z (%) 209 (8.1) [M⁺]. Anal. Calcd for $C_6H_7N_7O_2$: C, 34.45; H, 3.37; N, 46.88. Found: C, 34.38; H, 3.42; N, 46.94.

((2-Phenyl-1*H*-imidazol-1-yl)methyl)-1*H*-tetrazole (2d)

Recrystallization (EtOAc) afforded a bright brown solid; yield: 1.92 g (85%); mp 216–220 °C (dec.); R_f = 0.33 (EtOAc–MeOH, 1:1); IR (KBr): 3280, 3150, 2937, 2850, 1653, 1476 cm⁻¹; ¹H NMR (250 MHz, DMSO- d_6): δ 7.94–7.91 (m, 2H, aryl), 7.58–7.46 (m, 3H, aryl), 7.20 (s, 1H, C(4)-H, imidazole), 6.95 (s, 1H, C(5)-H, imidazole), 5.28 (s, 2H, NCH₂), 2.50 (s, 1H, exchangeable with D₂O, NH, tetrazole); ¹³C NMR (250 MHz, DMSO- d_6): δ 49.07, 121.03, 125.54, 127.07, 127.46, 129.68, 131.07, 152.18, 160.14; MS (EI): m/z (%) 226 (17.3) [M⁺]. Anal. Calcd for C₁₁H₁₀N₆: C, 58.40; H, 4.46; N, 37.15. Found: C, 58.31; H, 4.58; N, 37.02.

((1*H*-Tetrazol-5-yl)methyl)-1,3-dimethyl-1*H*-purine-2,6(3*H*,7*H*)-dione (2e)

Recrystallization (EtOAc–MeOH) afforded a brown solid; yield: 2.46 g (94%); mp >300 °C (dec.); $R_f = 0.27$ (EtOAc–MeOH, 1:1); IR (KBr): 3391, 2996, 1720, 1705, 1690, 1650, 1375 cm⁻¹; ¹H NMR (250 MHz, DMSO- d_6): δ 8.38 (s, 1H, exchangeable with D₂O, NH, tetrazole), 7.39 (s, 1H, C(8)-H, theophylline), 5.04 (s, 2H, NCH₂), 2.59 (s, 3H, N(1)-CH₃), 2.31(s, 3H, N(3)-CH₃); ¹³C NMR (250 MHz, DMSO- d_6): δ 27.30, 31.18, 47.34, 104.91, 144.41, 149.32, 151.57, 154.19, 159.10; MS (EI): m/z (%) 263 (10.7) [M⁺]. Anal. Calcd for $C_9H_{10}N_8O_2$: C, 41.22; H, 3.84; N, 42.73. Found: C, 41.28; H, 3.80; N, 42.81.

((1*H*-Tetrazol-5-yl)methyl)pyrimidine-2,4(1*H*,3*H*)-dione (2f)

Recrystallization (EtOAc) afforded a creamy solid; yield: 1.55 g (80%); mp 285–290 °C; $R_f = 0.09$ (EtOAc–MeOH, 1:1); IR (KBr): 3365, 3129, 2876, 1723, 1706, 1650, 1458 cm⁻¹; ¹H NMR (250 MHz, DMSO- d_6): δ 11.37 (s, 1H, exchangeable with D₂O, NH, uracil), 7.67 (d, 1H, J = 7.5 Hz, C(6)-H, uracil), 5.70 (d, 1H, J = 7.5 Hz, C(5)-H, uracil), 5.07 (s, 2H, NCH₂), 4.07 (s, 1H, exchangeable with D₂O, NH, tetrazole); ¹³C NMR (250 MHz,

DMSO- d_6): δ 47.32, 103.40, 142.15, 151.57, 156.46, 161.72; MS (EI): m/z (%) 194 (10.8) [M⁺]. Anal. Calcd for $C_6H_6N_6O_2$: C, 37.12; H, 3.11; N, 43.29. Found: C, 37.24; H, 3.26; N, 43.24.

((1H-Tetrazol-5-yl)methyl)-9H-purin-6-amine (2g)

Recrystallization (EtOAc) afforded a creamy solid; yield: 1.71 g (79%); mp >300 °C (dec.); R_f = 0.25 (EtOAc–MeOH, 1:1); IR (KBr): 3328, 3100, 2853, 1676, 1520, 1471 cm⁻¹; ¹H NMR (250 MHz, DMSO- d_6): δ 8.12 (s, 1H, C(8)-H, adenine), 8.05 (s, 1H, C(2)-H, adenine), 7.17 (s, 2H, exchangeable with D₂O, NH₂), 5.42 (s, 2H, NCH₂), 4.80 (s, 1H, exchangeable with D₂O, NH, tetrazole); ¹³C NMR (250 MHz, DMSO- d_6): δ 54.31, 118.43, 139.90, 147.78, 151.57, 155.69, 162.84; MS (EI): m/z (%) 217 (9.5) [M⁺]. Anal. Calcd for C₇H₇N₉: C, 38.71; H, 3.25; N, 58.04. Found: C, 38.63; H, 3.18; N, 58.12.

((1*H*-Tetrazol-5-yl)methyl)isoindoline-1,3-dione (2h)

Recrystallization (EtOAc) afforded a creamy solid; yield: 2.08 g (91%); mp 245–249 °C; R $_f$ = 0.47 (EtOAc–MeOH, 1:1); IR (KBr): 3370, 3068, 2981, 1766, 1700, 1660, 1495 cm $^{-1}$; ¹H NMR (250 MHz, DMSO- d_6): δ 7.90–7.85 (m, 4H, aryl), 4.87 (s, 2H, NCH $_2$), 4.04 (s, 1H, exchangeable with D $_2$ O, NH, tetrazole); ¹³C NMR (250 MHz, DMSO- d_6): δ 42.20, 127.27, 131.49, 133.48, 157.10, 167.81; MS (EI): m/z (%) 229 (15.9) [M $^+$]. Anal. Calcd for C $_{10}$ H $_7$ N $_5$ O $_2$: C, 52.40; H, 3.08; N, 30.56. Found: C, 52.48; H, 3.01; N, 30.69.

((1H-Tetrazol-5-yl)methyl)benzo[d] isothiazol-3(2H)-one 1,1-dioxide (2i)

Recrystallization (EtOAc) afforded a pale-yellow solid; yield: 2.12 g (80%); mp 225–229 °C (dec.); $R_f=0.18$ (EtOAc–MeOH, 1:1); IR (KBr): 3324, 3050, 2976, 1715, 1600, 1460, 1321, 761 cm⁻¹; ¹H NMR (250 MHz, DMSO-d₆): δ 7.84–7.45 (m, 4H, aryl), 4.44 (s, 2H, NCH₂), 2.51 (s, 1H, exchangeable with D₂O, NH, tetrazole); ¹³C NMR (250 MHz, DMSO-d₆): δ 39.52, 126.32, 126.88, 127.33, 131.63, 132.06, 139.30, 156.66, 169.10. MS (EI): m/z (%) 265 (19.7) [M⁺]. Anal. Calcd for C₁₀H₈N₄O₃S: C, 45.45; H, 3.05; N, 21.20; S, 12.13. Found: C, 45.56; H, 3.11; N, 21.14; S, 12.25.

(2-(2-Methyl-4-nitro-1*H*-imidazol-1-yl)ethyl)-1*H*-tetrazole (2j)

Column chromatography (silica gel, EtOAc–MeOH, 1:1) afforded a creamy solid; yield: 1.74 g (78%); mp 210–215 °C; $R_f = 0.23$ (EtOAc–MeOH, 1:1); IR (KBr): 3358, 3100, 2965, 1653, 1525, 1460, 1345 cm⁻¹; ¹H NMR (250 MHz, DMSO- d_6): δ 8.26 (s, 1H, C(5)-H, imidazole), 4.27 (t, 2H, J = 7.2 Hz, NCH₂), 3.61 (s, 1H, exchangeable with D₂O, NH, tetrazole), 3.12 (t, 2H, J = 7.2 Hz, NCH₂CH₂), 2.21 (s, 3H, CH₃); ¹³C NMR (250 MHz, DMSO- d_6): δ 15.99, 27.43, 52.03, 121.49, 148.55, 153.83, 163.97; MS (EI): m/z (%) 223 (10.6) [M⁺]. Anal. Calcd for

C₉H₁₁N₅O₂: C, 48.86; H, 5.01; N, 31.66. Found: C, 48.94; H, 5.13; N, 31.59.

5-(2-(2-Phenyl-1*H*-imidazol-1-yl)ethyl)-1*H*-tetrazole (2k)

Recrystallization (EtOAc) afforded a creamy solid; yield: 1.92 g (80%); mp 250–255°C (dec.); $R_f = 0.38$ (EtOAc–MeOH, 1:1); IR (KBr): 3300, 3050, 2960, 1650, 1485 cm⁻¹; ¹H NMR (250 MHz, DMSO- d_6): δ 7.58–7.44 (m, 5H, aryl), 7.32 (s, 1H, C(4)-H), 6.95 (s, 1H, C(5)-H), 4.29 (t, 2H, J = 7.5 Hz, NCH₂), 3.07 (t, 2H, J = 7.5 Hz, NCH₂CH₂), 1.98 (s, 1H, exchangeable with D₂O, NH, tetrazole); ¹³C NMR (250 MHz, DMSO- d_6): δ 30.01, 54.59, 120.83, 125.87, 126.30, 127.05, 127.27, 130.29, 149.77, 155.14; MS (EI): m/z (%) 240 (15.8) [M⁺]. Anal. Calcd for C₁₂H₁₂N₆: C, 59.99; H, 5.03; N, 34.98. Found: C, 60.07; H, 5.16; N, 34.87.

(2-(1*H*-Tetrazol-5-yl)ethyl)-1*H*-benzo[*d*]imidazole (2l)

Recrystallization (EtOAc) afforded a brown solid; yield: 1.79 g (84%); mp 300–304 °C (dec.); $R_f=0.70$ (EtOAc–MeOH, 1:1); IR (KBr): 3326, 3100, 2926, 1653, 1501, 1470 cm⁻¹; ¹H NMR (250 MHz, DMSO- d_6): δ 8.10 (s, 1H, C(2)-H, benzimidazole), 7.62–7.55 (m, 2H, aryl), 7.24–7.14 (m, 2H, aryl), 4.55 (t, 2H, J=6.5 Hz, NCH₂), 3.17 (t, 2H, J=6.5 Hz, NCH₂CH₂), 2.51 (s, 1H, exchangeable with D₂O, NH, tetrazole); ¹³C NMR (250 MHz, DMSO- d_6): δ 31.15, 60.59, 116.19, 117.33, 124.12, 125.22, 134.64, 138.76, 149.31, 161.72; MS (EI): m/z (%) 214 (12.7) [M⁺]. Anal. Calcd for C₁₀H₁₀N₆: C, 55.94; H, 4.63; N, 39.14. Found: C, 55.83; H, 4.75; N, 39.28.

2-(2-(1H-Tetrazol-5-yl)ethyl)isoindoline-1,3-dione (2m)

Recrystallization (EtOAc) afforded a creamy solid; yield: 2.11 g (87%); mp >300 °C (dec.); R_f = 0.70 (EtOAc–MeOH, 1:1); IR (KBr): 3374, 3063, 2950, 1772, 1620, 1510, 1458 cm⁻¹; ¹H NMR (250 MHz, DMSO- d_6): δ 7.28–7.09 (m, 4H, aryl), 4.34 (t, 2H, J = 7.2 Hz, NCH₂), 3.46 (s, 1H, exchangeable with D₂O, NH, tetrazole), 3.08 (t, 2H, J = 7.2 Hz, NCH₂CH₂); ¹³C NMR (250 MHz, DMSO- d_6): δ 27.64, 42.69, 126.35, 131.64, 134.28, 159.48, 167.02; MS (EI): m/z (%) 243 (13.9) [M⁺]. Anal. Calcd for C₁₁H-9N₅O₂: C, 54.32; H, 3.73; N, 28.79. Found: C, 54.43; H, 3.82; N, 28.86.

1-(2-(1*H*-Tetrazol-5-yl)ethyl)-4-phenylpiperazine (2n)

Column chromatography (silica gel, EtOAc–n-hexane, 1:1) afforded a bright brown solid; yield: 2.35 g (91%); mp >300 °C (dec.); $R_f = 0.23$ (EtOAc–MeOH, 1:1); IR (KBr): 3340, 3100, 2992, 1659, 1653, 1476 cm⁻¹; ¹H NMR (250 MHz, DMSO- d_6): δ 7.26–7.20 (m, 2H, aryl), 6.91–6.81 (m, 3H, aryl), 4.96 (s, 1H, exchangeable with D₂O, NH, tetrazole), 3.83 (t, 2H, J = 6.5 Hz, CH₂), 3.09 (t, 2H, J = 7.2 Hz, CH₂), 2.72–2.65 (m, 8H, 4 CH₂); ¹³C NMR (250 MHz, DMSO- d_6): δ 28.22, 49.15, 52.27, 56.11, 114.32, 119.58, 130.51, 150.05, 160.23; MS (EI): m/z (%) 258 (19.7)

[M⁺]. Anal. Calcd for $C_{13}H_{18}N_6$: C, 60.44; H, 7.02; N, 32.53. Found: C, 60.31; H, 7.08; N, 32.61.

7-(2-(1*H*-Tetrazol-5-yl)ethyl)-1,3-dimethyl-1*H*-purine-2,6(3*H*,7*H*)-dione (20)

Column chromate-graphy (silica gel, MeOH) afforded a brown foam; yield: 2.34 g (85%); R_f = 0.15 (EtOAc–MeOH, 1:1); IR (KBr): 3300, 2985, 1716, 1702, 1693, 1658, 1379 cm⁻¹; ¹H NMR (250 MHz, DMSO– I_6): δ 7.86 (s, 1H, C(8)-H, theophylline), 4.55 (t, 2H, I_6 = 5.7 Hz, NCH₂), 3.41 (t, 2H, I_6 = 5.7 Hz, NCH₂CH₂), 3.27 (s, 3H, N(1)-CH₃), 3.09 (s, 3H, N(3)-CH₃), 2.54 (s, 1H, exchangeable with D₂O, NH, tetrazole); ¹³C NMR (250 MHz, DMSO– I_6): δ 20.17, 31.08, 32.38, 34.54, 106.39, 136.89, 145.91, 147.79, 154.58, 159.86; MS (EI): I_6

3. Results and Discussion

3. 1. Chemistry of Synthesized Compound

Initially, we prepared an active catalyst according to the procedure reported in the literature⁸⁰ as shown in Scheme 1. First, curcumin (3) and acetic anhydride (4) were stirred in dry pyridine, the yellow crude product was collected and recrystallized from EtOAc/n-hexane (60/40) to give diacetylcurcumin (DAC (5)) in 95% yield. Then, DAC (452 mg, 1 mmol) and benzaldehyde (108 mg, 1 mmol) were dissolved in alcoholic media in the presence of a catalytic amount of piperidine and which readily afforded Ben-acetyl-curcumin ligand (6) in a good yield (76%). Afterwards, for preparation of Cu^(II) complex 7, in a conical flask, copper(II) chloride (1 mmol) and orthophenylenediamine (109 mL, 1 mmol) was refluxed in methanol for about 3 h. To the above solution, benzilidene-acetyl curcumin (574 mg, 1 mmol) (6) in methanol was added and the contents were stirred for 24 hour. The microcrystalline product formed, after filtering, the crude was washed with methanol and dried in vacuo. After synthesis and supporting the catalyst on silica gel, we applied this heterogeneous catalyst in synthesis of some 1,2,3-triazolyl carbocyclic nucleoside de-

In this methodology, the diverse N-heterocycles including imides, xanthines, azoles, purine and pyrimidine nucleobases react with 3-chloropropanenitrile or 2-chloroacetonitrile, in the presence of an equimolar mixture of triethylamine and potassium carbonate (TEA)- K_2CO_3 as the base, and catalytic amount of tetrabutylammonium iodide (TBAI) in acetonitrile at reflux conditions to afford nitriles 1. In continuation, these nitriles were able to perform the [3+2] cycloaddition reaction with sodium azide using SiO_2 -[Cu-BDACDABSBC] as the catalyst, and ascorbic acid as the reducing agent, in water-isopropanol media at reflux condition to yield tetrazoles 2. In most cas-

 $\textbf{Scheme 1.} \ \text{Preparation of SiO}_2\text{-}[\text{Cu-BDACDABSBC}].$

es, the *N*-alkylation reactions were completed after refluxing for 48 h (Scheme 2).

The first step of this synthetic approach was represented by optimization of the reaction conditions. At first, we carried out the cycloaddition reaction of 2-(2-methyl-1H-benzo[d]imidazol-1-yl) acetonitrile ($\mathbf{1a}$) and sodium azide as the model reaction to afford the 1-((1H-tetrazol-5-yl)methyl)-2-methyl-1H-benzo[d]imidazole ($\mathbf{2a}$) (Table 1). The 1,3-dipolar cycloaddition of the model reaction was carried out in the presence of ascorbic acid (1

mmol) and SiO_2 -Cu-BDACDABSBC (0.05 mol %) in H_2O at different temperatures, which afforded $\bf 2a$ in 51% yield (as the best result) after refluxing for 5 h (Table 1, entry 6).

To study the influence of temperature and $\rm H_2O$, the model reaction was carried out at different temperatures (Table 1, entries 2–6). Due to Table 1, an increase in the temperature resulted in the promotion of cycloaddition reaction. The best result was obtained when the cycloaddition reaction was conducted at 100 °C for 5 h (Table 1, entry 6).

Scheme 2. Synthesis of 5-substituated-1*H*-tetrazole derivatives tethered to bioactive *N*-heterocyclic cores using SiO₂-[Cu-BDACDABSBC] and ascorbic acid.

Table 1. Effect of H_2O and temperature on [3+2] cycloaddition reaction of azide-nitrile using Cu-BDACDABSBC and ascorbic acid to afford ${\bf 2a}^a$.

1a C:N SiO₂-Cu-BDACDABSBC
Ascorbic acid , solvent,
$$\Delta$$
2a N
N-N

Entry	Solvent	T °C	Time (h)	Yield ^b (%)
1	H ₂ O	R.T.	24	10
2	H_2O	50	10	20
3	H_2O	60	8	39
4	H_2O	70	8	38
5	H_2O	80	6	49
6	H_2O	Reflux	5	51

^a Reaction conditions: nitrile (0.01 mol), NaN₃ (0.015 mol), catalyst (0.05 mol %), ascorbic acid (1 mmol), H₂O(50 mL). ^b Isolated yield.

To further optimize the reaction conditions, the influence of various organic solvents/ H_2O (V/V) was examined in the presence of SiO_2 -Cu-BDACDABSBC (0.05 mol %) and ascorbic acid at various temperature (Table 2).

From Table 2 it is well demonstrated that the solvent has a significant role in the progress of the reaction. Among the examined solvents, a mixture of *i*-PrOH and water (Table 2, entry 1) afforded the best result, compared to pure water (Table 1, entry 6), The best ratio of *i*-PrOH to water for the progress of the reaction was observed to be 1 : 1 (Table 2, entry 2); however other ratios also yielded the product, albeit in lower amounts (Table 2, entries 3, 4). Employing the other mixtures of solvents afforded a moderate yield of the product over longer periods of time

Table 2. Effect of solvent type and temperature on [3+2] cycloaddition reaction of azide-nitrile using Cu-BDACDABSBC and ascorbic acid to afford **2a**^a.

Entry	Solvent	T °C	Time (h)	Yield ^b (%)
1	H ₂ O/i-PrOH ^c	R.T.	24	60
2	H ₂ O/i-PrOH ^c	Reflux	4	94
3	H ₂ O/i-PrOH ^d	Reflux	6	83
4	H ₂ O/i-PrOH ^e	Reflux	4	65
5	H ₂ O/Me ₂ CO ^c	Reflux	4	36
6	H ₂ O/DMF ^c	Reflux	7	40
7	H ₂ O/DMSO ^c	Reflux	8	42
8	H ₂ O/THF ^c	Reflux	8	60
9	H ₂ O/HMPA ^c	Reflux	6	40
10	H ₂ O/NMP ^c	Reflux	5	52
11	H ₂ O/Toluene ^{c, f}	Reflux	24	45
12	DMSO	120	24	56
13	DMF	120	24	58
14	THF	Reflux	11	50
15	i-PrOH	Reflux	7	52
16	EtOH	Reflux	5	45

 $^{^{\}rm a}$ Reaction conditions: nitrile (0.01 mol), NaN $_3$ (0.015 mol), SiO $_2$ -Cu-BDACDABSBC (0.05 mol %), solvent (50 mL). $^{\rm b}$ Isolated yield. $^{\rm c}$ 50:50 (V/V). $^{\rm d}$ 70:30 (V/V). $^{\rm e}$ 30:70 (V/V). $^{\rm f}$ In the presence of a catalytic amount (0.16 g, 0.0005 mol) of tetrabutylammonium bromide (TBAB)

(Table 2, entries 5–11). Additionally, when pure aprotic solvents such as DMSO, DMF, THF (Table 2, entries 12–14) and i-PrOH and EtOH as protic solvents were used

alone, moderate yields were obtained (Table 2, entries 15–16).

To investigate the catalytic potency of heterogeneous ${\rm SiO_2}$ -Cu-BDACDABSBC catalyst and other reported copper catalysts in cycloaddition reactions of azide-nitrile, the comparative results are summarized in Table 3. As shown in Table 3, when the reaction was carried out in the absence of a catalyst, this resulted in only marginal yield as indicated by GC analysis (<%7), even if the reaction time was prolonged (Table 3, entry 1).

Table 3. Comparing the catalytic potency of SiO₂-Cu-BDACDABSBC with various catalysts.^a

$$\begin{array}{c|c} & & \\ & &$$

Entry	Catalyst	Time (h)	Yield b (%)	Ref.
1	_	72	<8	_
2	Cu_2O	10	64	[25]
3	AlCl ₃	10	76	[26]
4	FeCl ₃ -SiO ₂	24	75	[33]
5	This catalyst	4	94	_

^a Reaction conditions: nitrile (0.01 mol), NaN₃ (0.015 mol), catalyst, H_2O/i -PrOH (50 mL). ^b Isolated yield. ^c 0.05 mol %.

The potency of different reported heterogeneous or homogeneous catalysts in tetrazole synthesis was assessed (Table 3, entries 2–4). As shown in Table 3, higher yield of **2a** were obtained and shorter reaction times were necessary when using heterogeneous SiO₂-Cu-BDACDABSBC catalyst (Table 3, entry 5).

To illustrate the scope of this method, we extended the optimized reaction condition to the cycloaddition reaction of nitrile 1a with sodium azide (Table 4). As the results in Table 4 indicate, heterogeneous SiO_2 -Cu-BDAC-DABSBC catalyst proved to be useful catalyst for Huisgen cycloaddition between the structurally diverse β -azido alcohols and alkynes. All synthesized compounds 2a-o were fully characterized, and their structures were confirmed by 1 H and 13 C NMR spectroscopy, elemental analysis, mass spectrometry and IR spectroscopy methods.

The reusability and recoverability of the SiO₂-Cu-BDACDABSBC catalyst on the sample reaction was studied during the synthesis of **2a** (Table 5). In this connection, prior to the use and also final testing of the catalyst for indicating its activity in many subsequent runs, the catalyst was recycled from the reaction mixture through a sintered glass funnel (vacuum-filtering). The catalyst was washed successively with THF or acetone (10 mL) and dried in a vacuum oven at 80 °C for 30 min.

The catalyst was tested for five consecutive runs and through each run, no fresh catalyst was added. Furthermore, the ICP analysis has confirmed the reusability of

Table 5. The reusability of SiO_2 -Cu-BDACDABSBC in successive runs for the synthesis of 2a.^a

Run no. ^b	Time (h)	Yield ^c (%)
1	4	94
2	4	92
3	4.5	91
4	4.5	91
5	5	88

 $^{^{\}rm a}$ Reaction conditions: nitrile (0.01 mol), NaN $_{\rm 3}$ (0.015 mol), recovered SiO $_{\rm 2}$ -Cu-BDACDABSBC, $~H_{\rm 2}O/i$ -PrOH (50 mL). $^{\rm b}$ The entry number corresponds to the trial number. $^{\rm c}$ Isolated yield.

the SiO₂-Cu-BDACDABSBC without significant desorption of Cu species from the silica matrix. As it is well indicated, the amount of leached Cu from SiO₂-Cu-BDACDABSBC is extremely negligible (0.06% after five consecutive runs).

As the results in Table 5 indicate, the catalyst can be reused for many consecutive runs without considerable decrease in its catalytic reactivity.

3. 2. Antifungal Studies

The antifungal activities of 5-substituted-1*H*-tetrazole derivatives against yeasts and filamentous fungi were evaluated in vitro. The minimal inhibitory concentrations (MICs) of the tested compounds were determined by the micro broth dilution method in 96-well microplates according to the CLSI-M27-A3 and M27-S4 methods for yeasts⁸¹⁻⁸² and CLSI-M38-A2 for filamentous fungi.⁸³ Antifungal agents as quality controls including amphotericin B (AMB) (Bristol-Myers-Squib, Woerden, The Netherlands), itraconazole (ITZ) (Janssen Research Foundation, Beerse, Belgium), voriconazole (VRZ) (Sigma), posaconazole (PSZ) (Sigma) and fluconazole (FLZ) (Pfizer, Groton, CT, USA) were obtained as reagent-grade powders from the respective manufacturers for the preparation of CLSI microdilution trays. The standard isolates as quality controls were obtained from collections of ATCC (American Type Culture Collection); its yeasts consist of: Candida species [C. albicans (ATCC 10231), C. glabrata (ATCC 2001), C. krusei (ATCC 6258), C. parapsilosis (ATCC 22019)] and filamentous fungi consist of Aspergillus species [A. fumigatus (ATCC MYA-2636), A. flavus (ATCC 204304)]. Some tetrazol compounds were dissolved in DMSO and serially diluted in the standard RPMI-1640 medium (Sigma Chemical Co.) and buffered to pH 7.0 with 0.165 M-morpholinepropanesulfonic acid (MOPS) buffer (Sigma) and L-glutamine without bicarbonate (maximum concentration was considered 512 µg/mL for

Table 4. The synthesized new 1*H*-tetrazoles using SiO₂-Cu-BDACDABSBC $^{\rm a}$

Entry	Nitrile	Product ^b	Time (h)	Yield ^c (%)
1	OH ₅ N CH ₅ Ta CN	CH ₂ N-N 2a HN-N	4	94
2	1b CN	CH ₀ CH ₀	6	90
3	O ₂ N 1c	O ₂ N 2c HN N N	6	75
4	N Ph1d	HN N N	3	80
5	H ₃ C _N -CN	HICK THE THE THE THE THE THE THE THE THE THE	4	95
6	N N N	HN H H	3	82
7	NH2 N N 1g CN	NATH N N	6	80
8	CN CN	NAN N	4	91
9	C S CN	O HANNA	3	79
10	O ₅ N O ₅ N O ₇ CN	O ₂ N N N N N	8	79
11	N CN	N N N N N N N N N N N N N N N N N N N	7	82
12	CTN CN	HN N N	6	85
13	CHN-CN Im	1 N N N N N N N N N N N N N N N N N N N	5	85
14	In In	CN H-N-N-N-N-N-N-N-N-N-N-N-N-N-N-N-N-N-N-	6	93
15	HAC N IN CH.	HC W NH	5	90

 $^{^{\}rm a}$ Reaction conditions: nitrile (0.01 mol), NaN $_3$ (0.015 mol), SiO $_2$ -Cu-BDACDABSBC (0.05 mol %), water/i-PrOH (50 mL). $^{\rm b}$ All products were characterized by $^{\rm 1}$ H and $^{\rm 13}$ C NMR, IR, CHN, and MS analysis. $^{\rm c}$ Isolated yield.

all compounds). Briefly, the inoculum suspension was added to each well and incubated at 35 °C. MIC was defined as the minimum inhibitory concentration of the tested compound which resulted in total inhibition of the fungal growth. All susceptibility testing was performed in duplicate.

Table 6 summarizes the MIC values of 6 standard isolates of yeasts and filamentous fungi of five antifungal drugs and 15 tetrazol compounds. The *in vitro* susceptibility results obtained for FLZ, ITZ, VRZ, PSZ and AMB against the standard isolates were within the ranges that are considered normal for these strains.⁸⁴

The results of MIC of 15 tetrazol derivatives have shown that the lowest MIC with 64 µg/mL was obtained for five compounds (2g, 2k, 2l, 2m and 2n) against Aspergillus fumigatus (ATCC MYA-2636), and the highest MIC with 512 and >512 μg/mL was measured for all compounds against Candida glabrata (ATCC 2001). In addition, the lowest MIC values against all standard isolates were measured for three tetrazols (2g, 2l, and 2n), and the highest MIC values against all standard isolates for 2e. So, Table 6 shows MIC₅₀ and MIC₉₀ values expressed in µg/mL for all tetrazole derivatives. The lowest MIC₅₀ (128 µg/mL) was obtained for 2g, 2h, 2i, 2k, 2l, 2m and 2n and the highest MIC_{50} (512 µg/mL) for **2e**, thus the lowest MIC_{90} (128 µg/ mL) was measured for 2g, 2l and 2n and the highest MIC₉₀ (>512 μ g/mL) for **2e** and MIC₉₀ (512 μ g/mL) for **2j** and **2o** (Table 6).

3. 3. Molecular Docking Study

Molecular docking study is a procedure which predicts the interactions of the novel synthetic compound as a drug candidate with the target enzyme and/or receptor binding sites to form a stable complex. Since 2n was specified as the most potent antifungal agent, thus the binding mode of 2n in the active site of cytochrome P450-dependent 14 α -lanosterol demethylase was investigated carrying out a molecular docking study.

In the case of docking method, every ligand was optimized with different minimization structures, they were thereafter converted to PDBQT using MGL tools 1.5.6.86 Co-crystal ligand molecules were excluded from the structures and the PDBs were corrected in terms of missing atom types by modeler 9.12.87 A house application (MOD-ELFACE) was used for the generation of python script and running modeller software. Consequently, the enzymes were transformed to PDBQT and Gasteiger partial charges were added using MGLTOOLS1.5.6. The docking simulations were achieved by means of an in-house batch script (DOCK-FACE) for automatic running of Auto Dock 4.2,88 in a parallel mode, using all system resources.

In all experiments genetic algorithm search technique was applied to find the best pose of each ligand in the active site of the target enzyme. Random orientations of the conformations were obtained after translating the center of the ligand to a specified position within the re-

Table 6. In vitro susceptibility testing of 6 standard isolates of yeasts and filamentous fungi to four antifungal agents and 15 novel compounds, and MIC_{50} and MIC_{90} values expressed in $\mu g/ml$ for 5-substituted-1*H*-tetrazole derivatives^a

Compound	MIC ^b (μg/mL)							
	Candida albicans	Candida glabrata	Candida krusei	Candida parapsilosis	Aspergillus fumigatus	Aspergillus flavus	MIC ₅₀	MIC ₉₀
2a	256	512	256	512	128	256	256	256
2b	256	512	256	256	128	256	256	256
2c	256	512	256	256	128	>512	256	256
2d	256	512	256	256	128	>512	256	256
2e	512	>512	512	512	>512	>512	512	>512
2f	256	512	256	256	128	256	256	256
2g	128	256	128	128	64	128	128	128
2h	128	256	128	128	128	256	128	256
2i	256	512	128	256	128	256	128	256
2j	256	512	256	256	256	>512	256	512
2k	128	256	128	128	64	256	128	256
21	128	256	128	128	64	128	128	128
2m	128	512	256	128	64	256	128	256
2n	128	256	128	128	64	128	128	128
2o	256	512	256	256	>512	256	256	512
Fluconazole ^c	0.25	32	64	0.125	2	2	_	_
Itraconazole c	0.25	0.25	0.25	0.063	1	0.5	_	_
Voriconazole ^c	0.125	0.25	0.125	0.031	0. 5	0. 5	_	_
Posaconazole ^c	0.125	0.25	0.125	0.031	0.5	0.25	_	_
Amphotricin B ^c	0.5	0.5	0.5	0.063	1	1	_	_

^a Examined fungi: Candida albicans (ATCC 10231), C. krusei (ATCC 6258), C. glabrata (ATCC 2001), C. parapsilosis (ATCC 22019), Aspergillus fumigatus (ATCC MYA-2636) and A. flavus (ATCC 204304) ^b Minimal inhibitory concentration ^c Reference drugs for fungal species

ceptor active site, and making a series of rotamers. This process was recursively repeated until the desired number of low energy orientations was obtained. Cluster analysis was performed on the docked results using a root mean square deviation (RMSD) tolerance of 1.8 Å. For the internal validation phase, ligand inside the pdb file of aromatase (1ea1) was extracted using a viewer and treated the same as other ligands in this study.

It is well known that the azoles as antifungal agents are able to inhibit CYP51 through the binding to N-atoms in azoles with the iron core inside the haem. To accredit the docking protocol, fluconazole was redocked in the active site of *Mycobacterium* P450DM (Figure 2). As can be seen, the substrate-binding pocket of *Mycobacterium*

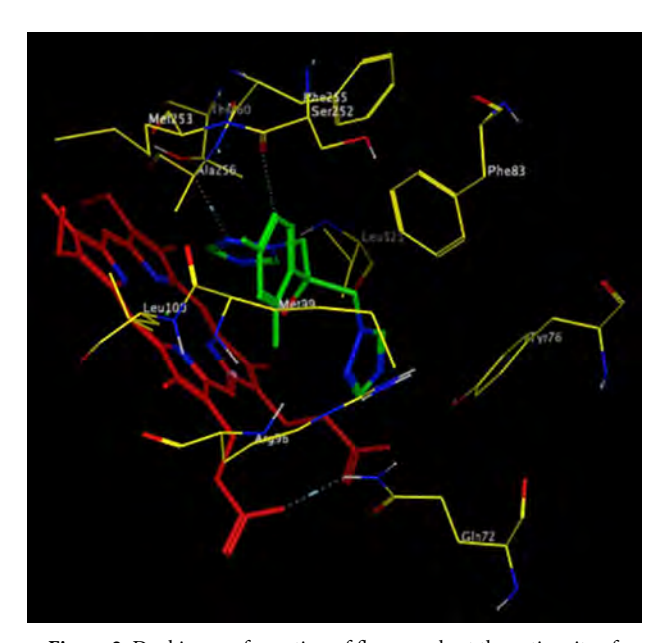


Figure 2. Docking conformation of fluconazole at the active site of *Mycobacterium* P450DM

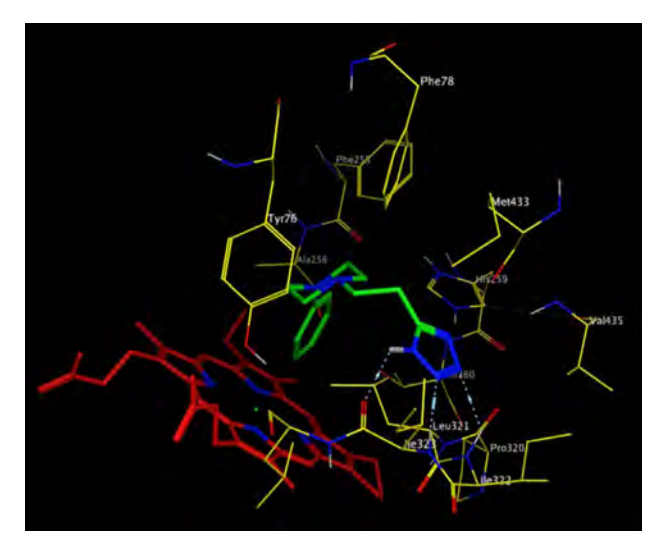


Figure 3. Docking conformation of **2n** at the active site of *Mycobacterium* P450DM

P450DM is above the porphyrin ring with the ceiling lipophilic amino acid residues (Phe78, Met79, Phe83, and Phe255). Moreover, access to the pyrrole rings is restricted by Thr260, Ala256, and Leu321, respectively.⁸⁹ Just as it was found with fluconazole, compound **2n** is accommodated at the same binding site and showed a strong interaction with *Mycobacterium* P450DM enzyme (Figure 3).

Interestingly, similarly to fluconazole, 2n is incorporated in the same binding site and showed a strong interaction with the enzyme active site. The calculated bonding energy values for fluconazole and 2n are -8.10 and -9.22 kcal/mol, respectively, indicating there is an energy gap of about 1.12 kcal/mol. To this energy gap the stronger binding of 2n at the active site of the enzyme can be attributed. As can be seen in Figure 2, which clearly shows the hydrogen bondings of N^1 –H tetrazol with oxygen in Leu324, this hydrogen bonding plays an important role in the higher affinity of 2n to the active site of the *Mycobacterium* P450DM enzyme. The aliphatic side chain tethered to the tetrazol ring is bound in the hydrophobic pocket above the haem group with residues including Ile323 and Ile 322.

4. Conclusions

In conclusion, we have explained a recyclable heterogeneous catalysts that was used in synthesis of some 5-substituted 1*H*-tetrazoles bearing bioactive *N*-heterocyclic cores. The main advantages of this methodology are its simplicity of the reaction procedure, mild reaction condition, and good to excellent yields. Furthermore, copper(II) catalyst can be recovered and recycled by simple filtration of the reaction mixture and reused for at least five consecutive trials without significant loss of its activity. The antifungal tests have shown antifungal activity against all groups of fungal for some compounds. The docking analysis has demonstrated the appropriate fitting of **2n** in active site of *Mycobacterium* P450DM enzyme.

5. Acknowledgement

We are grateful to Fasa University of Medical Sciences for their financial support.

6. References

- 1. R. N. Butler, in: A. R. Katritzky, C. W. Rees, E. F. V. Scriven (Ed.): *Comprehensive Heterocyclic Chemistry*, Pergamon, Oxford, **1996**, *4*, pp. 1–126.
- H. Bräuner-Osborne, J. Egebjerg, E. Ø. Nielsen, U. Madsen, P. Krogsgaard-Larsen, J. Med. Chem. 2000, 43, 2609–2645.
 DOI:10.1021/jm000007r
- 3. J. M. Essery, *J. Med. Chem.* **1996**, *12*, 703–705. **DOI:**10.1021/jm00304a039

- A. Andrus, B. Partridge, J. V. Heck. B. G. Christensen, *Tetrahedron Lett.* 1984, 25, 911–1917.
 DOI:10.1016/S0040-4039(01)80060-5
- V. Dhayanithhi, S. S. Syed, K. Kumaran, K. R. J. Sankar, R. V. Ragavan, P. S. K. Goud, N. S. Kumari, H. N. Pati, *J. Serb. Chem. Soc.* 2011, 76, 165–175. DOI:10.2298/JSC090421001D
- R. S. Upadhayaya, S. Jain, N. Sinha, N. Kishore, R. Chandra, S. K. E. Arora, *Eur. J. Med. Chem.* 2004, 39, 579–592.
 DOI:10.1016/j.ejmech.2004.03.004
- A. Rajasekaran, N. Sankar, A. Murugesh, A. R. Kalasalingam, *Arch. Pharm. Res.* 2006, 29, 535–540.
 DOI:10.1007/BF02969261
- P. B. Mohite, R. B. Pandhare, S. G. Khanage, V. H. Bhaskar, *Adv. Pharm. Bull.* 2012, 2, 31–36.
- J. Adamec, K. Waisser, J. Kunes, J. Kaustova, J. Arch. Pharm.
 2005, 338, 385–389. DOI:10.1002/ardp.200400967
- A. O. De Souza, M. T. Pedrosa, J. B. Alderete, A. F. Cruz, M. A. Prado, R. B. Alves, C. L. Silva, *Pharmazie* 2005, 60, 396–397.
- H. Akimoto, K. Ootsu, F. Itoh, Eur. Patent EP 530537; Chem. Abstr. 1993, 119, 226417.
- 12. G. P. Ellis, D. Shaw, *J. Med. Chem.* **1972**, *15*, 865–867. **DOI:**10.1021/jm00278a027
- E. Vieira, S. Huwyler, S. Jolidon, F. Knoflach, V. Mutel, J. Wichmann, *J. Bioorg. Med. Chem. Lett.* **2005**, *15*, 4628–4631.
 DOI:10.1016/j.bmcl.2005.05.135
- A. Gagnon, S. Landry, R. Coulombe, A. Jakalian, I. Guse. B. Thavonekham, P. R. Bonneau, C. Yoakim, B. Simoneau, *Bioorg. Med. Chem. Lett.* 2009, 19, 1199–1205.
 DOI:10.1016/j.bmcl.2008.12.074
- P. N. Gaponik, S. V. Voitekhovich, O. A. Ivashkevich, *Russ. J. Chem. Rev.* 2006, *75*, 507–539.
 DOI:10.1070/RC2006v075n06ABEH003601
- 16. R. J. Herr, *Bioorg. Med. Chem.* **2002**, *10*, 3379–3393. **DOI:**10.1016/S0968-0896(02)00239-0
- G. I. Koldobskii, V. A. Ostrovskii, *Usp. Khim.* **1994**, *63*, 847–865. **DOI:**10.1070/RC1994v063n10ABEH000119
- 18. J. M. McManus, R. M. Herbst, *J. Org. Chem.* **1959**, *24*, 1464–1467. **DOI**:10.1021/jo01092a021
- 19. V. Rama, K. Kanagaraj, K. Pitchumani, *J. Org. Chem.* **2011**, *76*, 9090–9095. **DOI:**10.1021/jo201261w
- V. A. Ostrovskii, R. E. Trifonov, E. A. Popova, Russ. Chem. Bull. 2012, 61, 768–780. DOI:10.1007/s11172-012-0108-4
- 21. B. Dahlof, R. B. Deveruex, S. E. Kjeldsen, *Lancet* **2002**, *359*, 995–1003. **DOI:**10.1016/S0140-6736(02)08089-3
- 22. T. Mosmann, *J. Immunol. Methods* **1983**, *65*, 55–63. **DOI:**10.1016/0022-1759(83)90303-4
- Z. P. Demko, K. B. Sharpless, Org. Lett. 2001, 3, 4091–4094.
 DOI:10.1021/ol010220x
- 24. A. R. Katritzky, C. Cai, N. K. Meher, *Synthesis* **2007**, *8*, 1204–1208. **DOI**:10.1055/s-2007-966001
- 25. T. Jin, F. Kitahara, S. Kamjio, Y. Yamamoto, *Tetrahedron Lett.* **2008**, *49*, 2824–2827. **DOI:**10.1016/j.tetlet.2008.02.115
- D. P. Matthews, J. E. Green, A. J. Shuker, *J. Comb. Chem.* 2000, 2, 19–23. DOI:10.1021/cc990035z
- A. Kumar, R. Narayanan, H. Shechter, *J. Org. Chem.* 1996, 61, 4462–4465. DOI:10.1021/jo952269k

- Y. S. Gyoung, J. G. Shim, Y. Yamamoto, Tetrahedron Lett.
 2000, 41, 4193–4196. DOI:10.1016/S0040-4039(00)00563-3
- W. K. Su, Z. Hong, W. G. Shan, X. X. Zhang, Eur. J. Org. Chem.
 2006, 12, 2723–2726. DOI:10.1002/ejoc.200600007
- 30. S. Hajra, D. Sinha, M. Bhowmick, *J. Org. Chem.* **2007**, *72*, 1852–1855. **DOI:**10.1021/jo062432j
- 31. B. Akhlaghinia, S. Rezazadeh, *J. Braz. Chem. Soc.* 2012, *23*, 2197–2203. **DOI:**10.1590/S0103-50532013005000005
- 32. Y. Yao, Y. Zhou, B. Lin, C. Yao, *Tetrahedron Lett.* **2013**, *54*, 6779–6781. **DOI:**10.1016/j.tetlet.2013.10.019
- M. Nasrollahzadeh, Y. Bayat, D. Habibi, S. Moshaee, *Tetrahedron Lett.* 2009, 50, 4435–4438.
 DOI:10.1016/j.tetlet.2009.05.048
- 34. L. Lang, B. Li, W. Liu, L. Jiang, Z. Xu, G. Yin, *Chem. Commun.* **2010**, *46*, 448–450. **DOI:**10.1039/B912284B
- M. Lakshim Kantam, V. Balasubramanyam, K. B. Shiva Kumar, *Synth. Commun.* 2006, *36*, 1809–1814.
 DOI:10.1080/00397910600619630
- 36. G. Aridoss, K. K. Laali, Eur. J. Org. Chem. 2011, 52, 6343-6355. DOI:10.1002/ejoc.201100957
- M. Lakshmi Kantam, K. B. Shiva Kumar, K. Phani Raja, *J. Mol. Catal. A* 2006, 247, 186–188.
 DOI:10.1016/j.molcata.2005.11.046
- G. Venkateshwarlu, K. C. Rajanna, P. K. Saiprakash, *Synth. Commun.* 2009, 39, 426–432.
 DOI:10.1080/00397910802378381
- J. He, B. Li, F. Chen, Z. Xu, G. Yin, J. Mol. Catal. A 2009, 304, 135–138. DOI:10.1016/j.molcata.2009.01.037
- G. Venkateshwarlu, A. Premalatha, K. C. Rajanna, P. K. Saiprakash, Synth. Commun. 2009, 39, 4479–4485.
 DOI:10.1080/00397910902917682
- 41. G. Qi, Y. Dai, *Chin. Chem. Lett.* **2010**, *21*, 1029–1032. **DOI**:10.1016/j.cclet.2010.05.003
- M. Nasrollahzadeh, D. Habibi, Z. Shahkarami, Y. Bayat, *Tetrahedron* 2009, 65, 10715–10719.
 DOI:10.1016/j.tet.2009.10.029
- M. N. Soltani Rad, S. Behrouz, M. Doroodmand, A. Movahedian, *Tetrahedron* 2012, 68, 7812–7821.
 DOI:10.1016/j.tet.2012.07.032
- 44. A. Corma, H. Garcia, Adv. Synth. Catal. 2006, 348, 1391– 1412. DOI:10.1002/adsc.200606192
- S. Minakata, M. Komatsu, Chem. Rev. 2009, 109, 711–724.
 DOI:10.1021/cr8003955
- 46. C. A. McNamara, M. J. Dixon, M. Bradley, *Chem. Rev.* **2002**, *102*, 3275–3300. **DOI:**10.1021/cr0103571
- H. Hirai, N. Ohtsuka, T. Shimazawa, React. Funct. Polym.
 1998, 37, 199–212. DOI:10.1016/S1381-5148(97)00170-3
- 48. T. Toupance, M. Kermarec, C. Louis, *J. Phys. Chem. B* **2000**, *104*, 965–972. **DOI**:10.1021/jp993399q
- N. L. Dias Filho, Y. Gushikem, D. W. Franco, M. S. Schultz,
 L. C. G. Vasconcellos, *Colloids Surf.*, A 1998, 141, 181–187.
 DOI:10.1016/S0927-7757(98)00333-1
- F. Cozzi, Adv. Synth. Catal. 2006, 348, 1367–1390.
 DOI:10.1002/adsc.200606096
- K. Binnemans, Chem. Rev. 2009, 109, 4283–4374.
 DOI:10.1021/cr8003983

- C. Baleizão, H. Garcia, Chem. Rev. 2006, 106, 3987–4043.
 DOI:10.1021/cr050973n
- 53. A. F. Trindade, P. M. P. Gois, C. A. M. Afonso, *Chem. Rev.* **2009**, *109*, 418–514. **DOI**:10.1021/cr800200t
- J. M. Fraile, J. I. García, J. A. Mayoral, Chem. Rev. 2009, 109, 360–417. DOI:10.1021/cr800363y
- A. P. Wight, M. E. Davis, Chem. Rev. 2002, 102, 3589–3614.
 DOI:10.1021/cr020068s
- L. Yin, J. Liebscher, Chem. Rev. 2007, 107, 133–173.
 DOI:10.1021/cr0505674
- J. Miłobędzka, S. von Kostanecki, V. Lampe, Ber. Dtsch. Chem. Ges. 1910, 43, 2163–2170. DOI:10.1002/cber.191004302168
- R. Waranyoupalin, S. Wongnawa, M. Wongnawa, C. Pakawatchai, P. Panichayupakaranant, P. Sherdshoopongse, Cent. Eur. J. Chem. 2009, 7, 388–394.

DOI:10.2478/s11532-009-0037-8

- A. Goel, A. B. Kunnumakkara, B. B. Aggarwal, *Biochem. Pharmacol.* 2009, 75,787–809.
 DOI:10.1016/j.bcp.2007.08.016
- T. Ueno, M. Ohashi, M. Kono, K. Kondo, A. Suzuki, T. Yamane, Y. Watanabe, *Inorg. Chem.* 2004, 43, 2852–2858.
 DOI:10.1021/ic0498539
- S. Pal, A. K. Barik, S. Gupta, A. Hazra, S. K. Kar, S. M. Peng, G. H. Lee, R. J. Butcher, M. S. E. I. Fallah, J. Ribas, *Inorg. Chem.* 2005, 44, 3880–3889. DOI:10.1021/ic0501420
- 62. M. Babazadeh-Qazijahani, H. Badali, H. Irannejad, M. H. Afsarian, S. Emami, *Eur. J. Med. Chem.* **2014**, *76*, 264–273. **DOI:**10.1016/j.ejmech.2014.02.019
- 63. S. M. H. Afsarian, H. Badali, T. Shokohi, S. Najafipour, *Iran. J. Public Health* **2015**, *44*, 1262.
- M. H. Afsarian, H. Badali, T. Boekhout, T. Shokohi, F. Katiraee, *J. Med. Microbiol.* 2015, 64, 248–253.
 DOI:10.1099/jmm.0.000015
- S. M. Hashemi, H. Badali, M. A. Faramarzi, N. Samadi, M. H. Afsarian, *Mol. Divers.* 2015, 19, 15–27.
 DOI:10.1007/s11030-014-9548-0
- 66. M. A. Pfaller, *Am. J. Med.* **2012**, 125, 3–13. **DOI:**10.1016/j.amjmed.2011.11.001
- K. Chai, J. Zhang, Y. Cao, Y. Zou, Q. Wu, D. Zhang, Eur. J. Med. Chem. 2012, 46, 3142–3148.
 DOI:10.1016/j.ejmech.2011.02.042
- 68. Y. Y. Zhang, J. L. Mi, C. H. Zhou, X. D. Zhou, *Eur. J. Med. Chem.* **2011**, *46*, 4391–402. **DOI:**10.1016/j.ejmech.2011.07.010
- T. Shokohi, H. Badali, N. Amirrajab, M. R. Ataollahi, S. A. Kouhpayeh, M. H. Afsarian, *Iran. Curr. Med. Mycol.* 2016, 2, 34–39. DOI:10.18869/acadpub.cmm.2.2.8
- 70. M. A. Asif, J. Bioorg. Chem. 2017, 2, 146-152.
- S. Esmaielzadeh, E. Zarenezhad, Acta Chim. Slov. 2018, 65, 416–428. DOI:10.17344/acsi.2018.4159
- E. Zarenezhad, M. N. Soltani Rad, S. Behrouz, S. Esmaielzadeh, M. Farjam, *J. Iran. Chem. Soc.* 2017, 14, 509–519.
 DOI:10.1007/s13738-016-0999-3

- S. Behrouz, M. N. Soltani Rad, S. Rostami, M. Behrouz, E. Zarehnezhad, A. Zarehnezhad, *Mol. Divers.* 2014, 18, 797–808.
 DOI:10.1007/s11030-014-9539-1
- M. N. Soltani Rad, S. Behrouz, M. Behrouz, A.Sami, M. Mardkhoshnood, A. Zarenezhad, E. Zarenezhad, *Mol. Divers*.
 2016, 20, 705–718. DOI:10.1007/s11030-016-9678-7
- M. N. Soltani Rad, S. Behrouz, E. Zarenezhad, M. H. Moslemin, A. Zarenezhad, M. Mardkhoshnood, M. Behrouz, S. Rostami, *Med. Chem. Res.* 2014, 23, 3810–3822.
 DOI:10.1007/s00044-014-0967-3
- M. N. Soltani Rad, S. Behrouz, E. Zarenezhad, N. Kaviani, J. Iran. Chem. Soc. 2015, 12, 1603–1612.
 DOI:10.1007/s13738-015-0633-9
- Zarenezhad, M. N. Soltani Rad, M. H. Mosslemin, M. Tabatabaee, S. Behrouz, *J. Chem. Res.* 2014, 38, 607–610.
 DOI:10.3184/174751914X14115772243815
- M. H. Mosslemin, E. Zarenezhad, N. Shams, M. N. Soltani Rad, J. Chem. Res. 2014, 38, 169–171.
 DOI:10.3184/174751914X13917105358323
- M. N. Soltani Rad, S. Behrouz, V. Sadeghi Dehchenari, S. J. Hoseini, *J. Heterocycl. Chem.* 2017, 54, 355–365.
 DOI:10.1002/jhet.2777
- J. Rajesh, A. Gubendran, G. Rajagopal, P. Athappan, J. Mol. Struct. 2012, 1010, 169–178.
 DOI:10.1016/j.molstruc.2011.12.002
- P. A. Wayne: Reference method for broth dilution antifungal susceptibility testing of yeasts, approved standard. CLSI document M27-A2, 2002.
- P. Wayne: Clinical and laboratory standards institute. Implementation Guide of POCT for health care providers, 2006, 1–37.
- 83. Clinical Institute LS. Reference Method for Broth Dilution Antifungal Susceptibility Testing of Filamentous Fungi: Approved Standard. *CLSI document M38-A2*, **2008**.
- A. L. Barry, M. A. Pfaller, S. D. Brown, A. Espinel-Ingroff, M. A. Ghannoum, C. Knapp, R. P. Rennie, J. H. Rex, M. G. Rinaldi, J. Clin. Microbiol. 2000, 38, 3457–3459.
- 85. T. Lengauer, M. Rarey, Curr. Opin. Struct. Biol. 1996, 6, 402–406. DOI:10.1016/S0959-440X(96)80061-3
- 86. G. M. Morris, R. Huey, A. J. Olson: Using autodock for ligand-receptor docking. *Current Protocols in Bioinformatics*. 2008, 24, 8–14. DOI:10.1002/0471250953.bi0814s24
- 87. N. Eswar, B. Webb, M. A. Marti-Renom, M. S. Madhusudhan, D. Eramian, M. Y. Shen, U. Pieper, A. Sali, Comparative protein structure modeling using Modeller. *Current Protocols in Bioinformatics.* **2006**, *15*, 5–6.

DOI:10.1002/0471250953.bi0506s15

- 88. A. Sakhteman: PreAuposSOM, https://www.biomedicale.univ-paris5.fr/aupossom/.
- L. M. Podust, T. L. Poulos, M. R. Waterman, *Proc. Natl. Acad. Sci. U. S. A.* 2001, 98, 3068–3073.
 DOI:10.1073/pnas.061562898



Except when otherwise noted, articles in this journal are published under the terms and conditions of the Creative Commons Attribution 4.0 International License

Povzetek

V članku opisujemo enostavno sintezno pot, ki temelji na [3+2] cikloadiciji alkil nitrilov (RCN) z natrijevim azidom (NaN₃) v prisotnosti bakrovega kompleksa z bis(diacetilkurkumin) 1,2-diaminobenzensko Schiffovo bazo, ki je imobiliziran na silikagelu: SiO₂-[Cu-BDACDABSBC], ter igra vlogo heterogenega katalizatorja, in askorbinske kisline v zmesi topil vode in *i*-PrOH (50:50, V/V) pod pogoji refluksa. Katalizator na nosilcu smo pripravili z imobilizacijo bakrovega kompleksa bis(diacetilkurkumin) 1,2-diaminobenzenske Schiffove baze [Cu-BDACDABSBC] na silikagel. Ta kompleks se je izkazal kot visokoselektiven katalizator z veliko aktivnostjo in z dobro možnostjo recikliranja. Glavne odlike opisane sinteze so visoki izkoristki, široka paleta možnih izhodnih spojin ter enostavna in učinkovita izolacija, kar je omogočilo pripravo 5-substituiranih 1*H*-tetrazolov, ki so vključevali *N*-heterociklične bioaktivne sisteme, z odličnimi izkoristki. Za pripravljene spojine smo *in vitro* določili protiglivično učinkovanje na nekatere vrste patogenih gliv iz rodu *Candida* (*C. albicans*, *C. glabrata*, *C. krusei* in *C. parapsilosis*) ter na nekatere filamentne glive iz rodu *Aspergillus* (*A. fumigatus* in *A. flavus*). Študije molekulskega sidranja smo izvedli za najbolj učinkovito izmed pripravljenih spojin, kar nam je omogočilo, da smo razvoljali izjemno interakcijo med to spojino in aktivnim mestom *Mycobacterium* P450DM.



Scientific paper

Sulfate Ion Removal from Water Using Activated Carbon Powder Prepared by Ziziphus Spina-Christi Lotus Leaf

Morteza Rahmati, 1 Golan Yeganeh 2 and Hossein Esmaeili 3,*

 1 Department of Chemical Engineering, Datshtestan Branch, Islamic Azad University, Dashtestan, Iran

² Young Researchers and Elite Club, Bushehr Branch, Islamic Azad University, Bushehr, Iran

³ Department of Chemical Engineering, Bushehr Branch, Islamic Azad University, Bushehr, Iran

* Corresponding author: E-mail: esmaeili.hossein@gmail.com & esmaeili.hossein@iaubushehr.ac.ir

Received: 02-28-2019

Abstract

In this paper, the adsorption potential of activated carbon prepared by *Ziziphus spina-christi* lotus leaf for the removal of sulfate from aqueous solution was investigated. To this end, the effect of different parameters such as pH, contact time, temperature, adsorbent concentration, and initial sulfate ion concentration was investigated. The results indicated that the highest adsorption efficiency (84.5%) was obtained at pH 6, adsorbent concentration of 5 g/L, sulfate ion concentration of 20 ppm, 65 min and temperature of 45 °C. Also, the adsorption equilibrium study showed that the adsorption process follows the Langmuir isotherm model with the maximum adsorption capacity of 9.3 mg/g. In addition, the thermodynamic study showed that the adsorption process on the activated carbon surface was spontaneous. Moreover, the adsorption process was exothermic accompanied by a decrease in irregularity. Furthermore, the adsorption kinetic study indicated that the adsorption process follows the pseudo-second-order kinetic model.

Keywords: Adsorption; lotus leaf; sulfate ion; water purification

1. Introduction

Industrial and urban effluents are one of the main pollutants which can cause environmental pollution. Among the pollutants, sulfate is one of the significant inorganic pollutants found in urban effluents and with different amounts in industrial wastewaters; its concentration in lakes and seas is increasing quickly due to the urban and industrial effluents drainage. ²

When too much sulfate gets into the human stomach, it endangers health. Sulfate along other minerals cause pipe corrosion. Also, it may cause undesirable taste in water, diarrhea in human and young livestock. The taste threshold varies between 250 mg/L sodium sulfate and 1000 mg/L calcium sulfate. The undesirable taste of water usually gets reduced at values below 250 mg/L. Also, the maximum desirable amount of sulfate in drinking water is 250 mg/L and its maximum permitted is 400 mg/L.³

Several methods such as distillation, reverse osmosis, ion exchange, and adsorption are available for sulfate removal from water.⁴ Physicochemical treatment systems such as ion exchange, reverse osmosis and electrodialysis are

costly and produce sludge, which is difficult to dispose.⁵ Adsorbents are widely used among many technologies for the removal of anions from water. Also, the adsorption method is economically feasible, frequent, diverse, effective, simple and eco-friendly.⁶⁻⁹ In recent years, many researchers have been attracted to cheap adsorbents.⁸⁻¹⁵ The use of activated carbon has been introduced as a widely used method for sulfate removal due to its efficiency and easy usage.⁶

Any carbon material can be used to produce activated carbon. Up to now, several studies have been conducted using activated carbon derived from agricultural wastes such as peanut crust, nuts shell, tamarind shell, peanut shell, ¹⁶ rice bran, rice hulls, banana peel, orange peel, apple peel, hazelnut, walnut shell, tree's leaf and bark, oak essence, cane bagasse, corn, wheat bran, sawdust, sunflower stem, grape stem, modified algae, alfalfa and mustard^{13–15,17–27} for the removal of pollutants from wastewater.

In this work, the activated carbon powder obtained from lotus leaf was used to remove sulfate ion from aqueous solution and the effect of different parameters such as temperature, contact time, pH, adsorbent concentration and sulfate ion concentration in aqueous solution were investigated and also, the optimum operational conditions for getting maximum adsorption was obtained. Lotus or Cedar is a plant from jujube family which grows wildly in Saudi Arabia, North Africa and Southern Iran which is used in this work.²⁸ Therefore, this plant is economically preferred a lot. Also, the adsorbent surface properties were studied via different analyses such as SEM, EDAX, FTIR, BET, and XRD. Eventually, the kinetic, equilibrium and thermodynamic studies of adsorption process were carried out and the adsorption process characteristics were investigated.

2. Materials and Method

2. 1. Chemical

In this work, sodium sulfate decahydrate with a purity of 99% was purchased from Merck Co., Germany. The HCl and NaOH made by Merck Co. (Germany) were also used to adjust the pH of the samples.

2. 2. Stock Solution

In order to prepare a stock solution containing sulfate ion, a certain amount of sodium sulfate decahydrate was poured into a 250 ml Erlenmeyer and double-distilled water was added to it to reach a volume of 100 ml. Standard solutions with low sulfate concentrations were prepared through diluting a certain volume of this stock solution using double-distilled water.

2. 3. Preparation of Lotus Leaf Powder

In order to prepare activated carbon adsorbent from lotus leaf, first, the leaves were washed with a lot of distilled water to remove dust. Then, they were placed in an oven at 100 °C for 60 minutes to completely dry. The dried leaves were placed in a furnace under 700 °C for 2 hours until they turned to charcoal. After carbonization, the leaves turned to powder by milling and graded through sieve No.25 then stored inside anti-moisture plastic bottles.

2. 4. Adsorbent Analysis

BET, SEM, FT-IR, EDAX, and XRD analyses were used to determine structural and morphological properties of activated carbon produced from Lotus leaves. In order to determine the functional groups in the adsorbent, the FT-IR Perkin device was used; surface structure and adsorption morphology was determined by SEM (Philips-x130), the XRD device made by GNR Npd3000 company was used to determine the adsorbent crystalline phases, the EDAX device (Philips-x130) was used to determine the adsorbent elements and the adsorbent specific surface area was determined through BET device (Philips model, USA).

2. 5. Adsorption Experiments

Adsorption experiments were conducted in a batch manner. To do this, the effect of sulfate ion concentration (20, 40, 60, 80, 100 and 120 mg/L), contact time (5 to 80 minutes), adsorbent dose (1–10 g/L), pH (4 to 10) and temperature (25, 35, 45, 55, 65 and 75 °C) on the sulfate ion adsorption from aqueous solution was investigated. In all experiments, the mixing speed was considered 200 rpm. The residual sulfate ion in the solution was obtained by spectrophotometer (DR 5000 Hach, USA). To this end, 10 mL sample volume containing sulfate ion was added to the device to measure the remaining sulfate at a wavelength of 450 nm.

First, in order to get the optimum pH, 7 samples of 100 ml aqueous solution containing 100 ppm sulfate ion were prepared. Then, the pH of the solutions was adjusted by NaOH (I M) and HCl (1 M) at the pH values from 4 to 10. After that, 5 g/L of activated carbon adsorbent was added to each sample containing sulfate ions and stirred by a magnetic stirrer with a mixing rate of 200 rpm at room temperature for 60 min. Then, the solution was filtered by Whatman filter paper, the adsorbent was removed and the amount of residual sulfate ion was obtained within the solution. The sulfate adsorption percentage by the adsorbent (%A) is calculated for each sample using equation (1), so the best pH value for maximum removal efficiency was achieved.

$$\%A = = \left(\frac{Ci - Co}{Ci}\right) \times 100 \tag{1}$$

where C_i and C_o (mg/L) are the initial concentration and the equilibrium concentration of the metal ion.

In order to investigate the adsorbent concentration effect in aqueous solutions, the effect of different concentrations of 1 to 10 g/L were considered. After that, 5 g/L of adsorbent was added to each aqueous solution with different concentrations at optimum pH; the solutions were stirred by magnetic stirrer with a mixing rate of 200 rpm at 25 °C for 60 min. After a specific time, the process was stopped and the solution was filtered by Whatman filter paper (No. 42) and the adsorbent was separated from the solution. Then, the residual sulfate ion in the solution was obtained and the best adsorbent concentration that is most adsorbed was determined. In order to determine the effect of other parameters, the same actions were performed. At each stage, in order to examine each parameter, other parameters considered as constant and the optimum values in the previous stage were used.

3. Results and Discussion

3. 1. Characteristics of the Adsorbent

BET analysis determines the specific surface area of the adsorbent (cavities identification and surface roughness). Working with this device is based on measuring the amount of neutral gas adsorption, such as nitrogen, at a

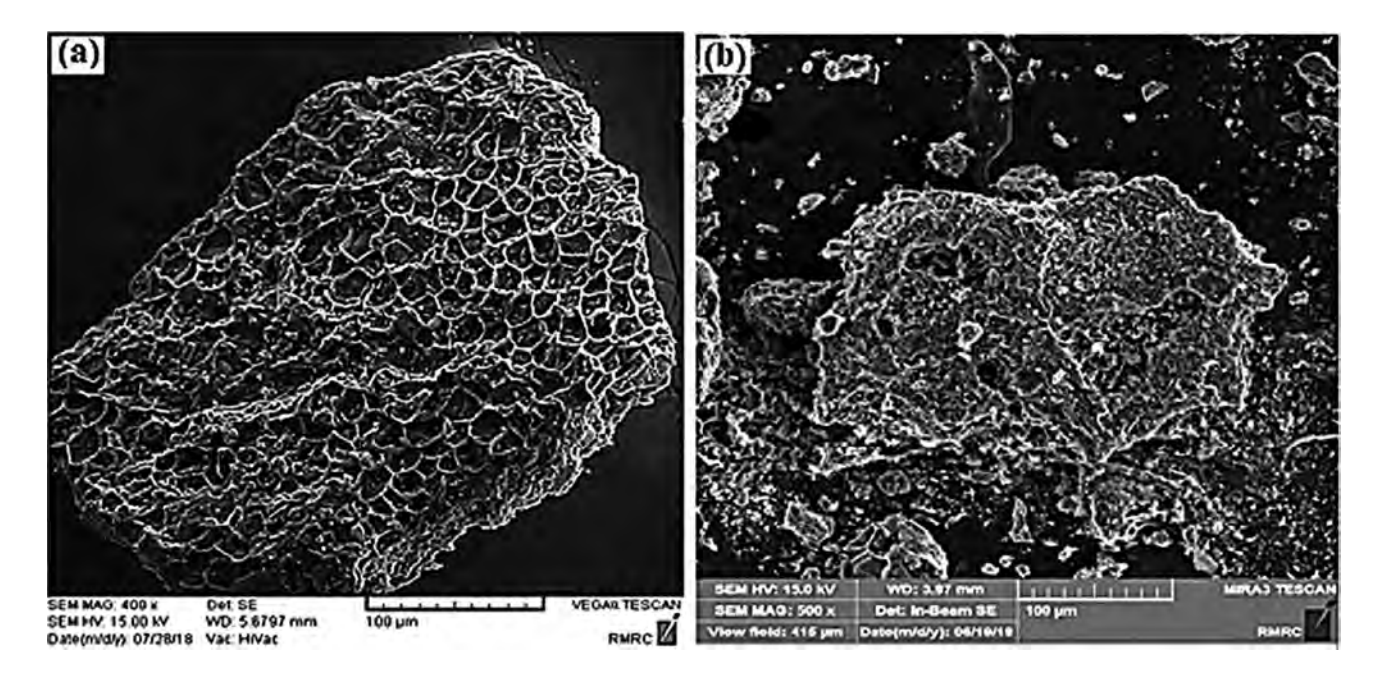


Figure 1. SEM analysis of adsorbent before (a) and after adsorption (b)

constant temperature on the adsorbent surface. The results showed that the adsorbent surface area of the lotus leaf is 51.024 m²/g. Also, the average pore diameter (ADP) and the total pore volume (TPV) of Lotus leaf adsorbent are obtained 196.573 A and 0286800 cm³/g.

SEM device was used to identify the adsorbent structure and morphology before and after the sulfate ion adsorption process. SEM images of the Lotus leaf adsorbent before and after adsorption are shown in Fig.1. As known, there are many roughness and cavities on the adsorbent surface which leads to adsorbent surface area increase representing different sites for sulfate ion adsorption. These cavities are coated after sulfate ion adsorption process which is clearly shown in the figure.

Fig. 2 shows the XRD pattern of the lotus leaf adsorbent. The spectra in 2 29 and 40° are related to Calci-

um Carbonate and the spectra in 2θ 28 and 34° are related to Potassium Chloride. According to Debye-Scherrer equation, the average diameters of Lotus leaf adsorbent crystals were determined 25.12 nm. Also, the spectra in 2θ 0.499 and 0.998 are related to empty cavities in the adsorbent.

Also, in the XRD analysis after adsorption, spectra in 20 29 and 40° are related to Calcium Carbonate and the spectra in 20 28 and 34° are related to Potassium Chloride. According to Debye-Scherrer equation, the average diameters of Lotus leaf adsorbent were determined 29.88 nm. Also, the spectra in 20 0.499 and 0.998 are related to empty cavities in the adsorbent sample. By comparing the graphs before and after adsorption, it can be seen that both graphs have very similar peaks which shows that the adsorbent structure has not changed much after adsorption.

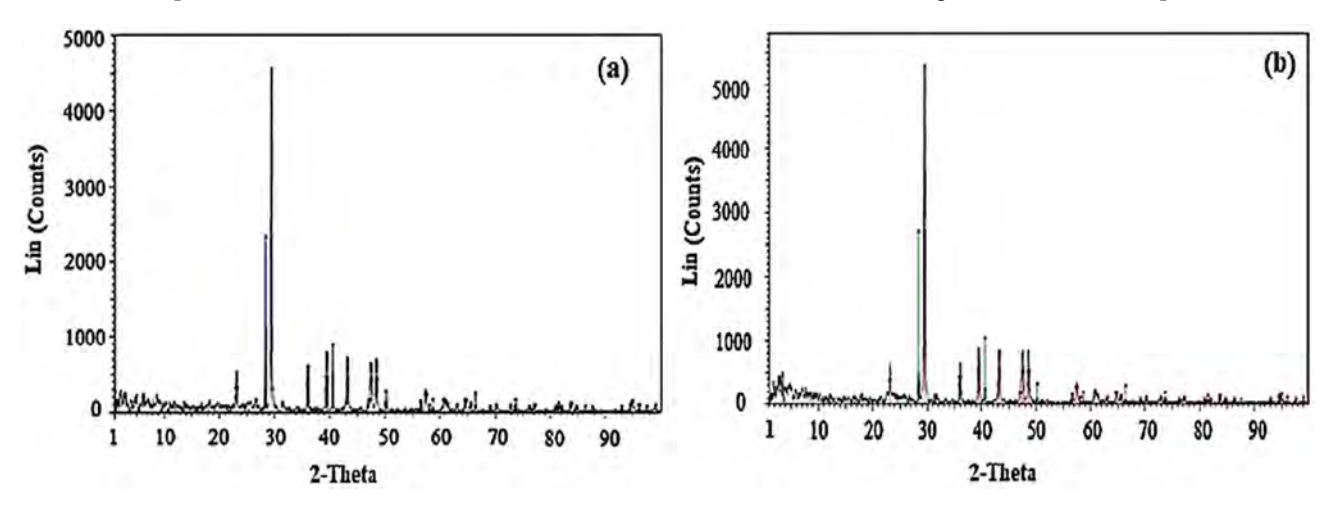


Figure 2. XRD analysis of activated carbon adsorbent before (a) and after adsorption (b)

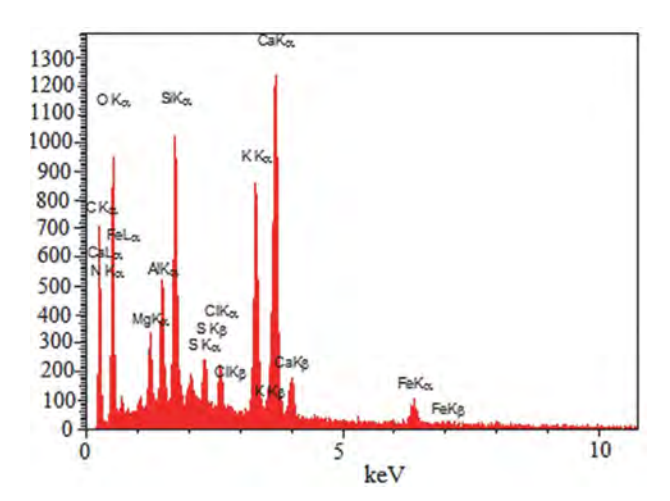


Figure 3. EDAX analysis of activated carbon adsorbent

Also, the EDAX analysis on the Lotus leaves for the adsorbent elements determination is shown in Fig. 3 and Table 1. As is evident in the Fig, there are various elements such as Fe, Ca, K, Cl, S, Si, Al, Mg, O, C, N in the Lotus leaf sample which their weight percentage are 2.39, 11.96, 6.81, 1.15, 1.22%, 4.40, 2.11, 1.39, 38.89, 25.80 and 3.86%, respectively. So, the most important components in its structure were oxygen and carbon.

Table 1. Elemental analysis of the adsorbent by EDX apparatus

Elements	Weight (%)	Atomic (%)
C	25.80	37.47
N	3.86	4.81
O	38.89	42.40
Mg	1.39	1.00
Al	2.11	1.37
Si	4.40	2.73
S	1.22	0.66
Cl	1.15	0.57
K	6.81	3.04
Ca	11.96	5.20
Fe	2.39	0.75
Total	100.00	100.00

Also, the FTIR analysis results for functional groups determination in the 400–4000 cm⁻¹ range are shown in Fig. 4. The results show that the spectrum of 798.795 cm⁻¹ is related to the aromatic tensile bond of –C–H, 1016.45 cm⁻¹ frequency shows the C–O group (carboxylic acid), 1315.19 cm⁻¹ frequency shows the C-F functional group, 2158.81 cm⁻¹ frequency shows the functional group of C \equiv C, 3101.21 cm⁻¹ frequency shows the H–O (alcohol) functional group and the frequency of 3451.37 cm⁻¹ shows the N–H functional group (amide).

3. 2. The pH Effect on Adsorption

The initial pH of the solution containing sulfate ions affects the changes in surface charge of the adsorbent and

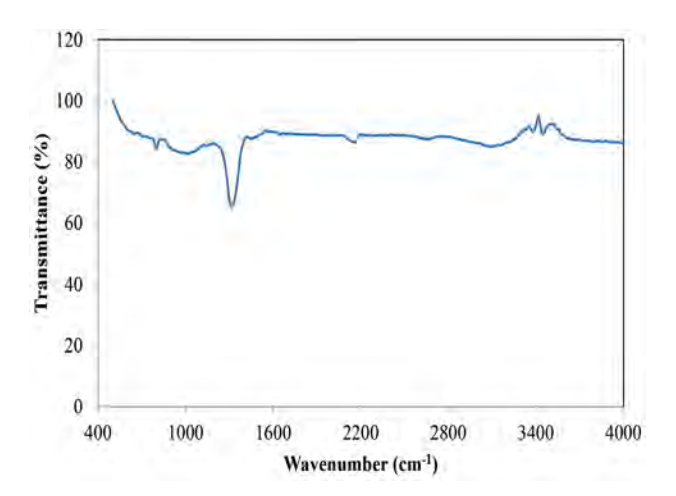


Figure 4. FT-IR analysis of activated carbon adsorbent

the adsorption mechanism of sulfate ions in the adsorption process. 29 Also, the initial pH of the solution is considered as one of the important parameters during the adsorption process. 30 Because the existing hydrogen ions (H⁺) in the aqueous solution compete with other ions to sit on the adsorbent surface. Also, the initial pH of the solution affects the variations of adsorbent surface charge and ionization degree of the adsorbed material (sulfate) during the adsorption process. The pH effect on the SO_4^{2-} ion adsorption on the activated carbon surface derived from lotus leaf is shown in Fig. 5.

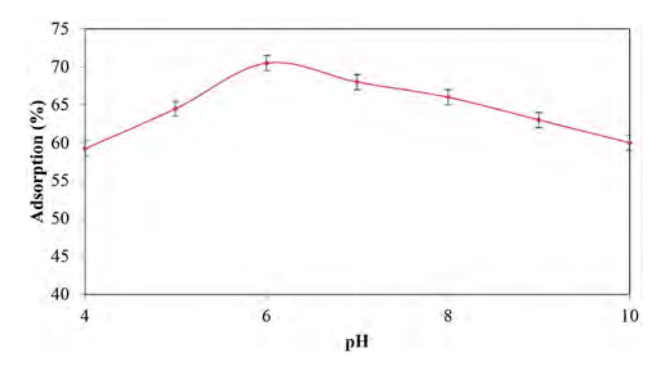


Figure 5. The pH effect on the SO_4^{2-} ion adsorption using the activated carbon derived from lotus leaf (Other conditions: T = 298 K, m = 0.5 g, Tc = 60 min, $SO_4 = 100 \text{ mg/l}$)

As shown in the figure, the sulfate ion adsorption efficiency increases by raising pH from 4 to 6. Since the ambient is acidic at low pH, so, the Hydrogen ions concentration in the aqueous solution is high and since the hydrogen ion is placed on the adsorbent surface, the adsorbent load gets positive; therefore, the electrostatic force makes adsorption between the adsorbent positive load and Sulfate anion negative load. The maximum percentage of sulfate ion adsorption happens at pH = 6. Sulfate anion is better adsorbed at low pHs. After that, sulfate adsorption decreases. The maximum adsorption of sulfate ion

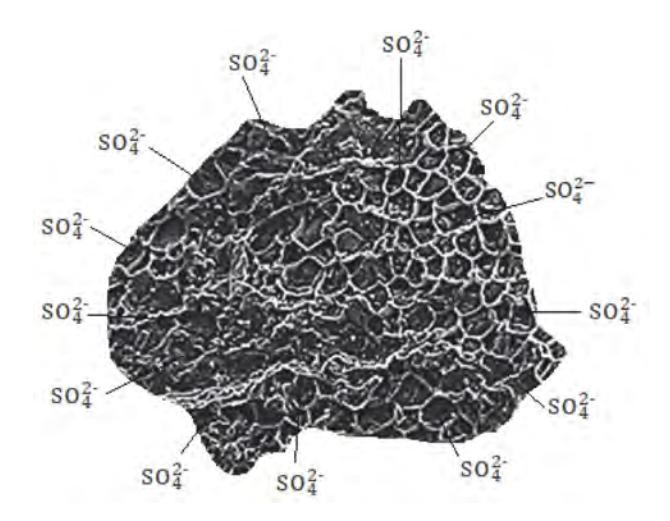


Figure 6. The adsorption mechanism of sulfate ions on the active sites of the activated carbon

through Lotus leaf was obtained 70.5%. The adsorption efficiency decreased after pH = 6 and by changing the pH from 6 to 10, sulfate ion adsorption percentage decreased from 70.5 to 60%. At this point, the hydroxide ion concentration increases inside the solution which leads to $SO_4(OH^-)$ hydrolysis, complex formation and sulfate ion sedimentation is as $SO_4(OH_2)$ Due to the sediment and complex formation, sulfate ions decreased in the aqueous solution, subsequently reduced the adsorption efficiency. Fig. 6 shows the adsorption mechanism of sulfate ions for sitting on the active sites of the adsorbent.

3. 3. The Effect of Adsorbent Dose

Adsorption dose is one of the important parameters on the adsorption process because it represents the maximum adsorption rate.³¹ The effect of adsorption dose on the sulfate ion adsorption efficiency is shown in Fig. 7. According to the graph, increasing the adsorbent concentration from 1 to 5 g/L caused significant changes in adsorption. By increasing the adsorbent dose from 1 to 5 g/L, sulfate ion adsorption percentage increases from 45 to

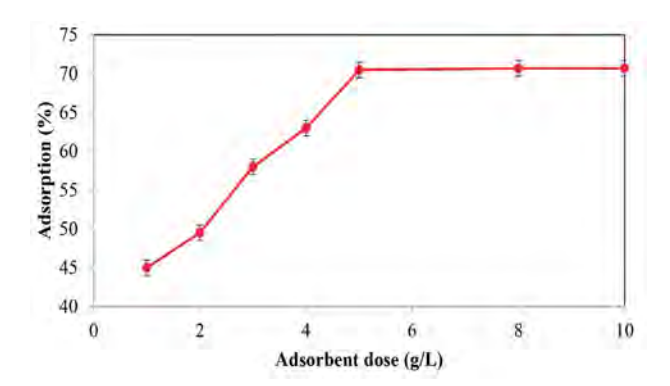


Figure 7. The effect of the adsorbent dose on the adsorption of sulfate ion (T = 298 K, pH = 6, Tc = 60 min, $SO_4 = 100$ mg/L)

70.5%. Also, at concentration more than 5 g/L, no change in adsorption was observed. The increase in slope at the beginning of the graph is mainly due to the increase of adsorbent surface area and a large number of active sites for sulfate ion adsorption.

3. 4. The Contact Time Effect on the Adsorption Amount

The effect of contact time on the adsorption of sulfate ion from aqueous media using activated carbon prepared by lotus leaf is shown in Fig. 8.

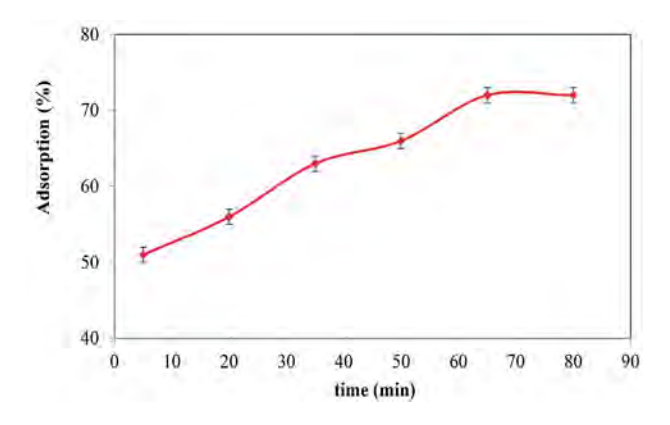


Figure 8. The effect of contact time on the adsorption of sulfate ion (T = 298 K, m = 0.5 g, pH = 6, sulfate ion concentration = 100 mg/L)

According to the figure, the optimum time for SO_4^{2-} ion adsorption on the active carbon surface is 65 minutes. For sulfate ion adsorption as shown in the graph, the graph's slope gets sharper by increasing the contact time, the slope steepness means that adsorption has occurred at high rate, because many active sites on the adsorbent surface are empty at the beginning of the sulfate ion adsorption process through Lotus leaf adsorbent and sulfate is placed on the sites. Therefore, the removal percentage has been increased by increasing the contact time; the graph's slope remained constant after 65 minutes and sulfate removal percentage got balanced. After 65 min, the sulfate removal efficiency remained constant due to the saturation of adsorbent active sites. Therefore, the contact time of 65 min was considered as the optimum time for sulfate ion adsorption.

3. 5. Temperature Effect

Another important parameter in the adsorption process is temperature. This parameter indicates that the adsorption process is exothermic or endothermic. The temperature effect on SO_4^{2-} ion adsorption on the active carbon surface is shown in Figure 9.

According to the figure, when temperature increases from 298 to 348 K, the sulfate removal percentage by the

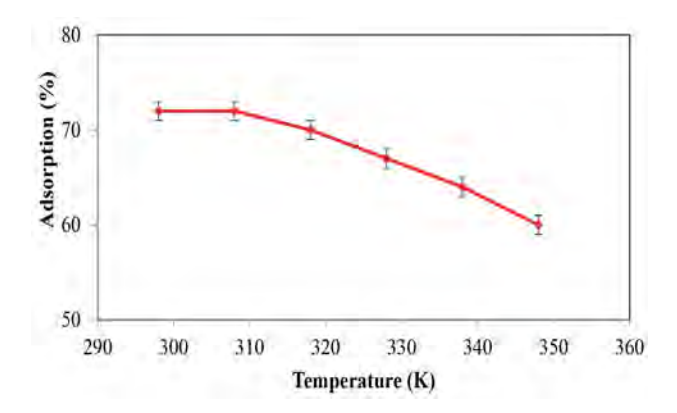


Figure 9. Temperature effect over SO_4^{2-} ion adsorption on the activated carbon derived from lotus leaf (Other terms: Tc = 65 min, m = 0.5 g, pH = 6, $SO_4 = 100 \text{ mg/L}$)

adsorbent decreases. This percentage decrease is due to the molecular movement reduction. The adsorption reaction rate decreases by the molecular movement reduction. On the other hand, according to le Chatelier principle, adsorption level decreases when the temperature rises. This is somehow associated with irregularities reduction. The adsorption capacity reduction by temperature increase represents an exothermic reaction. Therefore, the optimum adsorption temperature for SO₄²⁻ ion is 298 K.

3. 6. The Initial Concentration of SO₄²⁻ Ion

In the adsorption process, the initial concentration of metal ions in aqueous solution plays an important role as the mass transfer force between the solution and solid phase (adsorbent). The sulfate ion concentration effect on the removal from aqueous solution is shown in Fig. 10. At initial concentrations, the ratio of active sites to the initial concentration of sulfate in aqueous solution raises, so, the

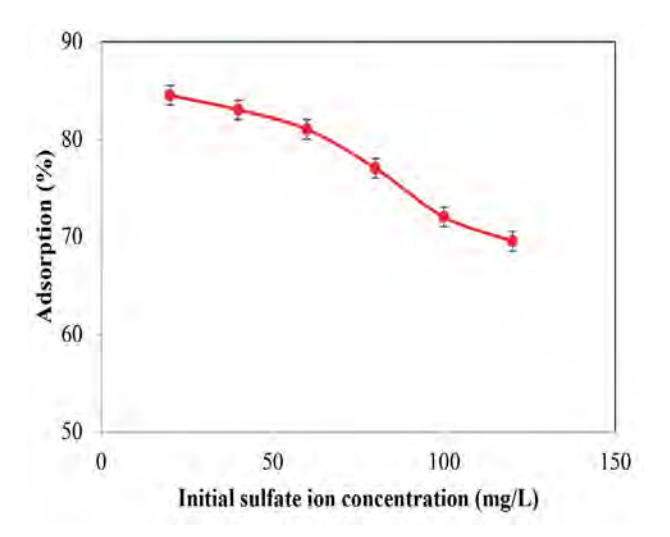


Figure 10. The investigation of SO_4^{2-} ion's initial concentration on the adsorption over the carbon surface derived from Lotus leaf (Other conditions: T = 298 K, m = 0.5 g, pH = 6, Tc = 65 min)

interaction between adsorbent and sulfate ion increases and anion gets removed from aqueous solution. The adsorption efficiency of sulfate ion decreased by increasing the initial sulfate ion concentration which is ascribed to the competition of sulfate ion to sit on active sites of the adsorbent. Also, the ions in the aqueous solution can be able to be interacted with prepared adsorbent and be removed from the aqueous solution.¹⁷ Therefore, the initial ion concentration of 20 mg/L with an adsorption efficiency of 84.5 was considered as an optimum value.

3. 7. Adsorption Isotherm Study

The adsorption isotherm study presents information about the effective interaction between adsorbent and the absorbed. In order to evaluate the equilibrium adsorption, the Langmuir, Freundlich, Temkin and Dubinin-Radushkevich isotherm models were studied. The Langmuir adsorption isotherm is used for monolayer adsorption on surfaces with limited identical adsorption positions. The linear form of this model is described as follows:^{29,32}

$$\frac{1}{q_{x}} = \frac{1}{K_{t}q_{m}} (\frac{1}{C_{x}}) + \frac{1}{q_{m}}$$
 (2)

For determining the K_L and $q_{\rm m}$, the slope and intercept of $1/q_{\rm e}$ based on $1/C_{\rm e}$ can be used. One of the based uses of Langmuir's constant is to determine the separation factor (R_L) according to Equation (3). If $R_L > 1$, $R_L = 0$ or $0 < R_L < 1$, the process will be undesirable, irreversible, linear and desirable, respectively.³³

$$R_L = \frac{1}{1 + K_f C_r} \tag{3}$$

Also, the Freundlich isotherm describes the adsorption on inhomogeneous surfaces with uniform energy sites. The linear form of Freundlich isotherm follows from Equation $4.^{33}$

$$log q_e = log K_f + \frac{1}{n} log C_e \tag{4}$$

In this equation, if 1/n is between zero and one, it shows that the adsorption process intensity is non-uniform at all levels. If 1/n is less than one, it shows that the adsorption process has been chemical and when 1/n value is more than 1, the adsorption process will be physical.

In these equations, q_e is the amount of adsorbed pollutant (mg/g) at the equilibrium time, q_m is the maximum adsorption capacity by adsorbent (mg/g), C_e is the equilibrium concentration of absorbed component (mg/L) and K_L is the equilibrium constant (L/mg) which depends on the degree of absorbed component tendency towards adsorbent; K_F and n are Freundlich isotherm constants which represent the capacity and intensity of adsorption, respectively.

In the Langmuir model, K_L and q_m are obtained from the slope and intercept of $1/q_e$ based on $1/C_e$. Also, in the

Freundlich model, K_F and n are calculated from the slope and intercept of log q_e versus log C_e .

Temkin model is another isothermal model. In this double-parameter model, it is assumed that the adsorption is monolayer and heterogeneous. The linear form of this model is as follows:

$$q_e = B_T L n A_T + B_T L n C_e \tag{5}$$

 A_T is the Temkin constant based on (L mg⁻¹) and it is compatible with adsorbent-absorbed adhesion.

The B_T constant is defined as H_0 $^{\frac{HP}{K_*}}$. K_T is the Temkin constant based on (J mol⁻¹) which is proportionate with adsorption heat. The A_T and B_T amounts are calculated from the slope and intercept of q_e based on $\ln C_e$.

The Dubinin-Radushkevich (D-R) isotherm model which is a semi-experimental relation. It assumes that the adsorption process is monolayer, so, it can be both chemical and physical. This model assumes that the surface is uneven, it has a linear form as follows:

$$Lnq_e = Lnq_d - K_D \varepsilon^2 \tag{6}$$

Here, q_d is the D-R isotherm constant which is proportionate with saturation capacity expressed by mg g⁻¹. K_D is another constant based on (mol J⁻¹)² expressed by $E = -0.7 \ K_D^{-0.5}$. More negative free energy means the adsorption is more chemical. Finally, ε represents the Polanyi potential (J/mol) defined by the $\varepsilon^{-RDD(0,\frac{1}{C_c})}$ equation. This is calculated by drawing $Ln\ q_e$ graph based on

 ε^2 , and q_d and K_D are measured by its slope and intercept.³⁴

The isothermal results are shown in Tables 2 and 3 and Figure 11. According to these results, the correlation coefficient (R²) in Langmuir isotherm model is higher than other models and also closer to 1; showing that Langmuir isotherm model has more capability for describing the isothermal behavior of adsorption process which also indicates the monolayer adsorption nature of sulfate ion

Table 2. The results of various isotherms of SO_4^{2-} ion adsorption on the activated carbon surface derived from Lotus leaf (Other terms: T = 298 K, m = 0.5 g, pH = 6, Tc = 65 min)

Isotherm	Parameter	value	
Langmuir	q _m (mg/g)	9.3	
	$K_{\rm L}$ (L/mg)	0.2	
	\mathbb{R}^2	0.9742	
	n	0.61	
Freundlich	$K_{\rm F}({ m mg})^{1-{ m n}}~{ m L^{ m n}}~{ m g}^{-1}$	2.0	
	\mathbb{R}^2	0.8719	
	$A_{\rm T}$ (L mg ⁻¹)	1.1	
Temkin	$B_{ m T}$	10.576	
	\mathbb{R}^2	0.6071	
	$q_{\rm d}$ (mg/g)	15.6	
D-R	$K_D \times 10^{-6} (\text{mol/J})^2$	6.0	
	E (kJ/mol)	-903.7	
	\mathbb{R}^2	0.7801	

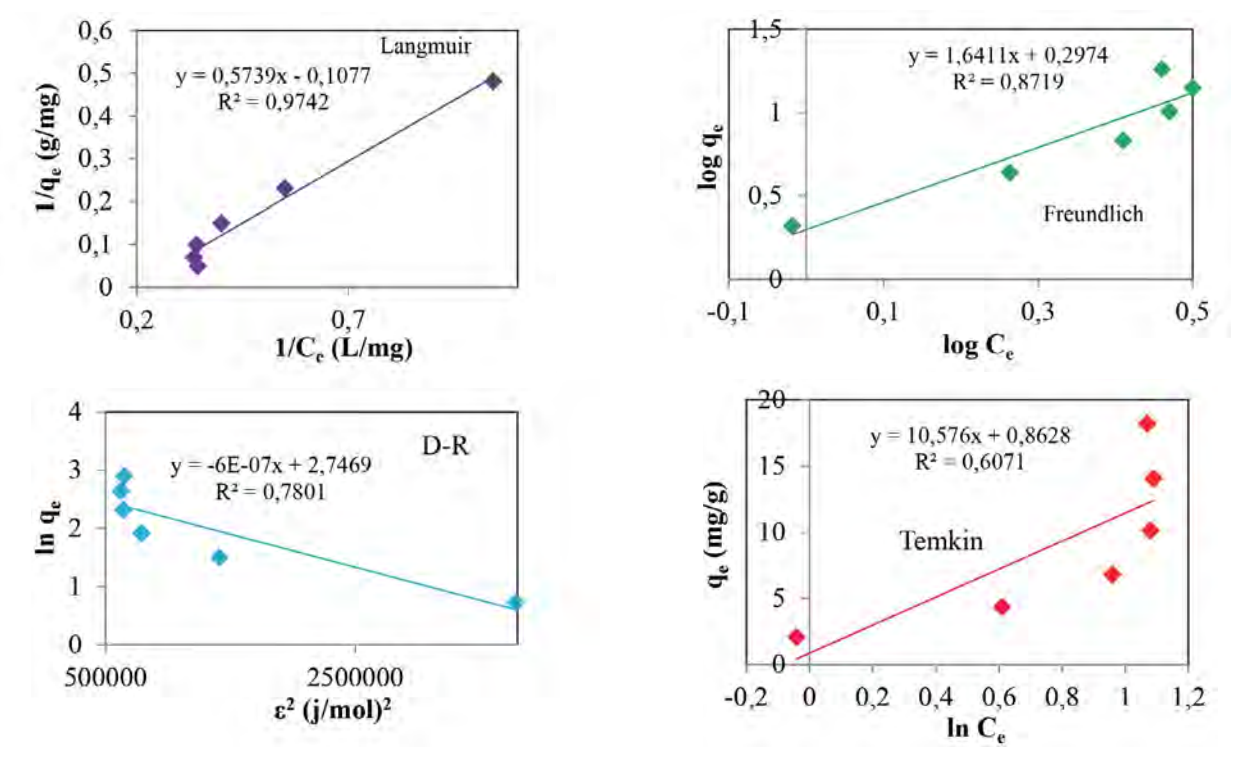


Figure 11. Adsorption isotherms of SO_4^{2-} ion on the activated carbon surface including Langmuir, Freundlich, Temkin, and Dubinin-Radushkevich isotherms

Table 3. The amount of adsorption separation factor of various SO_4^{2-} ion concentrations on the activated carbon surface derived from Lotus leaf, regarding the R_L

Initial ion concentration (mg/L)	20	40	60	80	100	120
$R_{ m L}$	0.71	0.6	0.5	0.4	0.33	0.3

on the adsorbent's heterogeneous surface. Also, Temkin and D-R isotherm models are not suitable due to their data dispersion and low correlation coefficient. Furthermore, in the Freundlich model, the n value was determined 0.61 for sulfate ion adsorption which indicates that sulfate ion adsorption mechanism through Lotus leaf adsorbent is physical. The $\rm R_L$ values at sulfate ion concentrations between 20 and 120 mg/L were obtained between 0 and 1. The $\rm R_L$ values show that the adsorption process is desirable and reversible.

3. 8. Thermodynamic Study

Thermodynamic parameters include enthalpy changes (ΔH_{ads}), entropy (ΔS_{ads}) and Gibbs free energy (ΔG_{ads}); they have special importance for describing adsorption process and achieving a reaction equilibrium. Whenever there is an adsorption equilibrium constant, then, the thermodynamic functions can be evaluated through equations 7 to 9.^{32–33}

$$K = \frac{C_{AS}}{C_A} = \frac{q_e}{C_e} \tag{7}$$

$$\Delta G_{ads} = -RTLnK \tag{8}$$

Also, (ΔH_{ads}) and (ΔS_{ads}) can be calculated through equation 9 from the slope and interface of LnK against 1/T plot.

$$LnK = \frac{\Delta S_{ads}}{R} - \frac{\Delta H_{ads}}{RT}$$
 (9)

The equilibrium constant is calculated at any temperature using equation 7.

The thermodynamic data graph of sulfate ion adsorption process by activated carbon is shown in Fig. 12. Also, the extracted data from this graph is presented in Table 4. According to the data presented in Table 4, ΔH_{ads} ,

 ΔS_{ads} and ΔG_{ads} values are negative. Therefore, sulfate ion adsorption process by activated carbon is spontaneous. Given being negative, its adsorption percentage decreases with increasing temperature. Considering the enthalpy changes in anion's adsorption on the activated carbon surface, it can be said that the adsorption process is physical; because $\Delta H < 40$ Kj/mol. Since the adsorption process is exothermal, according to le Chatelier principle, it decreases with increasing temperature which is somehow accompanied by irregularities reduction. Moreover, Gibbs free energy for sulfate ions decreased by increasing temperature which indicated that when temperature increases, the amount of spontaneous adsorption process for anion decreases.

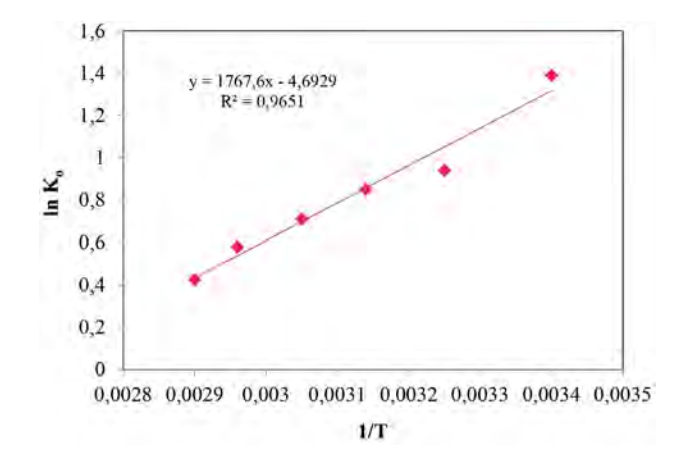


Figure 12. The $\ln K_0$ diagram versus 1/T for thermodynamic parameters estimation of sulfate ion adsorption from aqueous solution by activated carbon

3. 9. Kinetic Study of the Adsorption Process

The adsorption kinetic study is highly important because it provides valuable information on the reaction

Table 4. Thermodynamic functions of 100 mg/L SO_4^{2-} ion on the activated carbon surface derived from Lotus leaf (Other terms: m = 0.5 g, pH = 6, Tc = 65min)

T(K)	K	ΔG_{ads} (kJ/mol)	ΔH_{ads} (kJ/mol)	ΔS_{ads} (kJ/mol)
298	4.15	-3.44		
308	2.6	-2.4		
318	2.33	-2.31	15.10	10.00
328	2.03	-1.94	-15.12	-40.09
338	1.87	-1.63		
348	1.5	-1.16		

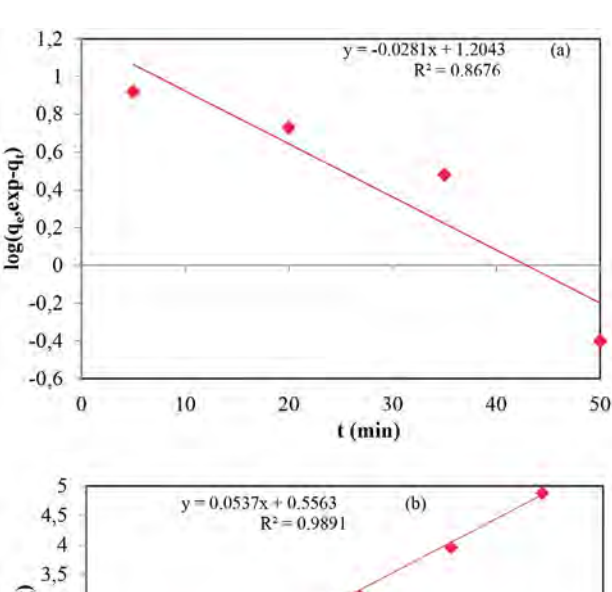
pathway and the control mechanism of the adsorption process.²³ In this study, first and second-order pseudo kinetic models were used for kinetic evaluation of sulfate ion on the activated carbon adsorbent. The linear form of the first and second-order kinetic models are presented in terms of equations 10 and 11, respectively:^{35–37}

$$\log(q_{e/exp} - q_t) = \log q_{e/cal} - \frac{\kappa_1}{2.303}t \tag{10}$$

$$\frac{t}{q_t} = \frac{1}{K_2 q_{e/cal}^2} + \frac{t}{q_{e/cal}} \tag{11}$$

Here, K_1 pseudo-first-order reaction rate constant, K_2 pseudo-second-order reaction rate constant, $q_{e/cal}$ computational equilibrium adsorption capacity (mg/g), $q_{e/exp}$ empirical equilibrium adsorption capacity (mg/g), q_t adsorption capacity at the time t (mg/g) and t is the time (minute). In order to determine the reaction rate constant of K_1 and $q_{e/cal}$, the log($q_{e,exp}$ – qt) graph was drawn based on t and in order to determine the reaction rate constant of K_2 and $q_{e/cal}$, in the second-order kinetic equation, the t/qt graph based on t was used.

The kinetic study results are shown in Table 5 and Fig. 13. By comparing the kinetic models' correlation coefficient (\mathbb{R}^2), we can say that the kinetics of sulfate ion ad-



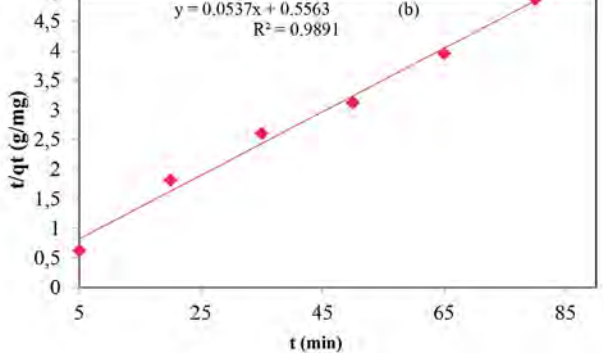


Figure 13. First-order kinetic (a) and second-order kinetic models (b) of SO_4^{2-} ion adsorption on the activated carbon surface derived from Lotus leaf

sorption on the activated carbon derived from lotus leaves has the most conformity with the second-order pseudo model. Also, the K_1 value in the first-order pseudo model is less than K_2 second-order pseudo model. Therefore, sulfate ions adsorption through lotus leaves adsorbent follows the second-order kinetic model.

Table 5. Results of kinetic adsorption models of $100 \text{ mg/L SO}_4^{2-}$ ion on the activated carbon surface derived from Lotus leaf (Other terms: T = 328 k, m = 0.5 g, pH = 6, Tc = 65min)

Kinetic models	Parameter	value
Pseudo second-order	q _{e'cal} (mg/g)	16
	$K_1 (\text{min}^{-1})$	0.065
	\mathbb{R}^2	0.8676
Pseudo second-order	$q_{\rm e,cal}$ (mg/g)	18.62
	K_2 (g/mg min)	5.2
	R^2	0.9891

4. Conclusion

In this study, sulfate ion adsorption from aqueous solutions through activated carbon adsorbent in the Lotus leaf was studied. Initially, activated carbon adsorbent was prepared and SEM, FTIR, BET, XRD, EDAX analyses were used to determine its surface properties. Then, the effect of various parameters such as pH, temperature, contact time, initial sulfate ion concentration and adsorbent dose on the sulfate ion removal from aqueous solutions through adsorbent was investigated. The results showed that the highest sulfate ion removal efficiency occurs at pH = 6, Tc = 65 min, temperature = 25 °C, initial concentration of 20 mg/L and the adsorbent dose of 5 g/L. After determining the optimum terms, the isotherm, kinetics and thermodynamic behavior of the adsorption process was studied. Langmuir, Freundlich, Temkin and Dubinin-Radushkevich isotherm models were considered to study the adsorption process behavior. The results showed that the Langmuir isotherm model can better describe the equilibrium behavior of the adsorption process due to a higher correlation coefficient. Also, it was determined that sulfate ion adsorption process through lotus leaf adsorbent is physical. During the kinetic models examination, the first and second- order pseudo kinetics models were investigated. The kinetic analysis of the adsorption process was performed using laboratory data at different contact times. The results showed that the second-order pseudo kinetics model has a higher correlation coefficient. The thermodynamic adsorption behavior of sulfate ion through adsorbent was also studied. According to the results, Gibbs free energy for sulfate ions was obtained negative which represents that the adsorption process is possible and spontaneous. Also, the negative amount of enthalpy showed that the adsorption process

was exothermal. Since the adsorption process is exothermal, according to le Chatelier principle, it decreases when temperature raises which is somehow accompanied by a decrease in irregularity. In addition, the amount of entropy was negative showing that the adsorption process is spontaneous.

Conflict of Interests Statement

The authors declare that there is no conflict of interests.

5. References

- F. Ahmadi, H. Esmaeili. Desalin. Water Treat. 2018, 110, 154– 167. DOI:10.5004/dwt.2018.22228
- R. Mahini, H. Esmaeili, R. Foroutan. *Turk. J. Biochem.* 2018, 43, 623–631. DOI:10.1515/tjb-2017-0333
- 3. L. W. H. Pol, P. N. L. Lens, A. J. M. Stams, G. Lettinga. *Biodeg-radation* **1998**, 9, 213–222.

DOI:10.1023/A:1008307929134

- A. Teimouri, H. Esmaeili, R. Foroutan, B. Ramavandi. *Korean J. Chem. Eng.* 2018, 35, 479–488.
 DOI:10.1007/s11814-017-0311-y
- J. Y. park, Y. J. Yoo. Appl. Microbiol. Biotechnol. 2009, 82, 415–429. DOI:10.1007/s00253-008-1799-1
- H. Demiral, G. Gunduzogla. Bioresour. Technol. 2010, 101, 1675–1680. DOI:10.1016/j.biortech.2009.09.087
- A. Goshadrou, A. Mohed. *Desalination*. 2010, 269, 170–176.
 DOI:10.1016/j.desal.2010.10.058
- X. Wang, L. Chen, L. Wang, Q. Fan, D. Pan, J. Li, F. Chi, Y. Xie,
 S. Yu, C. Xiao, F. Luo, J. Wang, X. Wang, C. Chen, W. Wu, W.
 Shi, S. Wang, X. Wang. Sci. China Chem. 2019, 62, 933–967.
 DOI:10.1007/s11426-019-9492-4
- X. Liu, R. Ma, X. Wang, Y. Ma, Y. Yang, L. Zhuang, S. Zhang,
 R. Jehan, J. Chen, X. Wang. *Environ. Pollut.* 2019.
 DOI:10.1016/j.envpol.2019.05.050
- S. M. Mousavi, S. A. Hashemi, A. M. Amani, H. Esmaeili,
 Y. Ghasemi, A. Babapoor, F. Mojoudi, O. Arjomand. *Phys. Chem. Res.* 2018, 6, 759–771.
- Y. Wu, H. Pang, Y. Liu, X. Wang, S. Yu, D. Fu, J. Chen, X. Wang. *Environ. pollution.* 2019, 246, 608–620.
 DOI:10.1016/j.envpol.2018.12.076
- 12. Q. Huang, S. Song, Z. Chen, B. Hu, J. Chen, X. Wang. *Biochar*. **2019**, *1*, 45–73. **DOI**:10.1007/s42773-019-00006-5
- M. J. Akhtar, S. Ullah, I. Ahmad, A. Rauf, S. M. Nadeem, M. Y. Khan, S. Hussain, L. Bulgariu. *Chemosphere*. **2018**, *190*, 234–242. **DOI**:10.1016/j.chemosphere.2017.09.136
- G. Nacu, D. Bulgariu, M. Cristina Popescu, M. Harja, D. Toader Juravle, L. Bulgariu. *Desalin. Water Treat.* **2016**, *57*, 21904–21915. **DOI:**10.1080/19443994.2015.1128366
- V. K. Gupta, I. Ali. J. Colloid Interface Sci. 2004, 271, 321–331.
 DOI:10.1016/j.jcis.2003.11.007
- Z. Khademi, B. Ramavandi, M. T. Ghaneian. *J. Environ. Chem. Eng.* 2015, 3, 2057–2067. DOI:10.1016/j.jece.2015.07.012

- S. M. Mousavi, S. A. Hashemi, H. Esmaeili, A. M. Amani, F. Mojoudi. *Acta Chim. Slov.* 2018, 65, 750–756.
 DOI:10.17344/acsi.2018.4536
- L. A. Rodrigues, M. L. C. P. da Silva, M. O. Alvarez-Mendes, Ad. R. Coutinho, G. P. Thim. *Chem. Eng. J.* 2011, *174*, 49–57. DOI:10.1016/j.cej.2011.08.027
- 19. K. K. Singh, R. Rastogi, S. H. Hasan. *J. Colloid Interface Sci.* **2005**, 290, 61–68. **DOI**:10.1016/j.jcis.2005.04.011
- 20. S. H. Min, J. S. Han, E. W. Shin, J. K. Park. *Water Res.* **2004**, *38*, 1289–1296. **DOI**:10.1016/j.watres.2003.11.016
- M. Martinez, N. Miralles, S. Hidalgo, N. Fiol, I. Villaescusa, J. Poch. *J. Hazard. Mater.* 2006, *133*, 203–211.
 DOI:10.1016/j.jhazmat.2005.10.030
- V. K. Gupta, C. K. Jain, I. Ali, M. Sharma, V. K. Saini. Water Res. 2003, 37, 4038–4047.
 DOI:10.1016/S0043-1354(03)00292-6
- J. Anwar, U. Shafique, M. Salman, A. Dar, S. Anwar. *Bioresour. Technol.* 2010, 101, 1752–1762.
 DOI:10.1016/j.biortech.2009.10.021
- E. I. El-Shafey. J. Hazard. Mater. 2007, 147, 546–556
 DOI:10.1016/j.jhazmat.2007.01.051
- 25. A. O. Zer, C. Pirinc. *J. Hazard. Mater.* **2006**, *137*, 849–858 **DOI**:10.1016/j.jhazmat.2006.03.009
- R. A. K. Rao, M. A. Khan, F. Rehman. Chem. Eng. J. 2010, 156, 106–113. DOI:10.1016/j.cej.2009.10.005
- M. Harja, G. Buema, L. Bulgariu, D. Bulgariu, D. M. Sutiman,
 G. Ciobanu. *Korean J. Chem. Eng.* 2015, 32, 1804–1811.
 DOI:10.1007/s11814-015-0016-z
- M. Shams, I. Nabipour, S. Dobaradaran, B. Ramavandi, M. Qasemi, M. Afsharnia. Fresen. Environ. Bull. 2013, 22, 723–727.
- S. Tamjidi, H. Esmaeili, Chem. Eng. Technol. 2019, 42, 607–616. DOI:10.1002/ceat.201800488
- 30. L. S. Panchakarla, A. Govindaraj, C. N. R. Rao. *Inorg. Chim. Acta.* **2010**, *363*, 4163–4174. **DOI:**10.1016/j.ica.2010.07.057
- 31. V. J. Larson, H. H. Schierup. *J. Environ. Qual.* **1981**, *10*, 188–193. **DOI:**10.2134/jeq1981.00472425001000020013x
- 32. I. Volf, N. G. Rakoto, L. Bulgariu. Sep. Sci. Technol. 2015, 50, 1577–1586. DOI:10.1080/01496395.2014.978018
- D. Bulgariu, L. Bulgariu. *Bioresour. Technol.* 2012, 103, 489–493. DOI:10.1016/j.biortech.2011.10.016
- H. Esmaeili, R. Foroutan. J. Dispers. Sci. Technol. 2018.
 DOI:10.1080/01932691.2018.1489828
- L. Bulgariu, D. Bulgariu, M. Macoveanu. Sep. Sci. Technol.
 2011, 46, 1023–1033. DOI:10.1080/01496395.2010.536192
- R. Foroutan, H. Esmaeili, S. M. D. Rishehri, F. Sadeghzadeh,
 R. Mirahmadi, M. Kosarifard, B. Ramavandi. *Data Brief*.
 2017, 12, 485–492. DOI:10.1016/j.dib.2017.04.031
- G. Nacu, L. N. Nemes, L. Bulgariu. Rev. Roum. Chim. 2017, 62, 439–447.

Povzetek

V članku so preučevali potencial aktivnega oglja pridobljenega iz listov lotusa *Ziziphus spina-christi* za odstranjevanje sulfatnih ionov iz vodnih raztopin. S tem namenom so preučili vpliv različnih parametrov kot so pH vrednost, kontaktni čas, temperatura, koncentracija adsorbenta in začetna koncentracija sulfatnih ionov. Rezultati so pokazali, da je bila največja adsorpcijska učinkovitost (84.5 %) dosežena pri pH vrednosti 6, koncentraciji adsorbenta 5 g/L, koncentraciji sulfatnih ionov 20 ppm, *času 65 min in temperaturi* 45 °C. Študija adsorpcijskega ravnotežja je pokazala, da lahko proces opišemo z Langmuirjevo adsorpcijsko izotermo z maksimalno kapaciteto vezave 9.3 mg/g. Termodinamska študija je pokazala, da je proces adsorpcije na površino aktivnega oglja spontan in eksotermen, kinetiko adsorpcije pa lahko opišemo z modelom psevdo-drugega reda.



Except when otherwise noted, articles in this journal are published under the terms and conditions of the Creative Commons Attribution 4.0 International License

© creative

Scientific paper

New Fluorescent, Thermally Stable and Film Forming Polyimines Containing Naphthyl Rings

Farah Qureshi,* Muhammad Yar Khuhawar and Taj Muhammad Jahangir

Institute of Advanced Research Studies in Chemical Sciences, University of Sindh, Jamshoro, Sindh-Pakistan

* Corresponding author: E-mail: farahqureshi94@yahoo.com Tel: +92-229213213, +92-3313534844

Received: 03-01-2019

Abstract

Three new aliphatic-aromatic polymers having naphthyl rings were prepared by the polycondenstion of dialdehydes or diketone monomers with 1,5-naphthalenediamine or 1,4-phenylenediamine. The monomers were prepared by the reaction of aromatic aldehyde or ketone with 1,6-dibromohexane. The molecular mass of the monomers was confirmed through E.I mass spectroscopy. The structures of monomers and polymers were characterized by ¹HNMR, FT-IR, UV-Vis Spectroscopy, SEM and TG/DTA. Fluorescence emissions of monomers and polymers were recorded and their quantum yields were calculated, all the compounds showed fluorescence property and indicated violet, blue-green, orange and red light emissions. The quantum yields of the polymers were obtained within the range of 0.04 to 24.3%. The semicrystalline and amorphous nature of the polymers was analyzed through powdered X-ray diffraction. Antimicrobial activities of the polymers were examined against different bacterial and fungal species. Thin film forming ability of the synthesized polymers was evaluated by making their blends with PVC (poly vinyl chloride) in different w/w% ratios.

Keywords: Polyimines; fluorescence; thermal stability; thin films; morphology

1. Introduction

Schiff base polymers also called polyimines or polyazomethines (CH=N) have been the subject of interest from last several decades and prepared by the polycondensation reaction of carbonyl compounds (dialdehydes or diketones) with aliphatic or aromatic diamines. 1-3 The researchers are attracted towards the synthesis of new polyimines because of their advantageous properties such as liquid-crystalline,⁴ fluorescence,^{5,6} optical and electronic properties,^{7,8} high thermal stability,^{9,10} fiber forming,^{11,12} thin film forming, 13-15 coordination abilities with metal ions¹⁶ and antimicrobial activities.^{17,18} These properties make them important candidate for application in solar cells, 19,20 optoelectronic sensors, 21 photo-luminescent devices,²² aerospace,²³ packaging materials and antifouling paints.²⁴ The redox activity of the Schiff base polymers was also reported, therefore they can be employed as redox indicators.²⁵ The polymer blends are also seeking attention in technological fields during last two decades because of their mechanical properties, which can be altered according to desired application. ²⁶ The polymer blends comprise about 30% of the total industrial plastic products.²⁷ However aromatic polyimines are difficult to process due to

their low solubility and high melting points which limits their applications.²⁸ To overcome these difficulties researchers have made different attempts which are introduction of ester, ether, alkyl or alkoxy groups and chains of methylene spacers between the aromatic rings.^{29,30} Mondal and Das reported the effect of chain flexibility on the morphology of polyamides, they have observed decrease in thermal stability with the inclusion of aliphatic chains.³¹ In the present work three new polyimines were prepared by the polycondensation reaction of dialdehydes or diketone monomers with diamines. The obtained polymers contained flexible aliphatic spacers of n-hexane and ether linkages between the aromatic rings. One of the polymers (PoHOAND) contained alkyl group attached with the imine bond. These structural variations have effected on the solubility and other properties (thermal stability, fluorescence and thin film forming ability) of polyimines.

2. Experimental

2. 1. Materials

3-hydroxybenzaldehyde (Sigma-Aldrich Corp. St. Louis, MO USA) (purity 99%), 2-hydroxyacetophenone

(Fluka, Switzerland), 2-hydroxynaphthaldehyde (Sigma-Aldrich Corp. St. Louis, MO USA), 1,6-dibromohexane (Sigma Aldrich, St. Louis USA) (purity 96%), 1,4-phenylenediamine (Alfa-Aesar, UK) (purity 97%), 1,5-naphthalenediamine (Toshima, Kita-ka, Tokyo, Japan), N,N-dimethylformamide (AnalaR BDH, England) (purity 98%), dimethylsulfoxide (AnalaR BDH, England), anhydrous sodium carbonate (Sigma-Aldrich, Germany), p-toluenesulfonic acid monohydrate (Daejung Chemicals & Metals Co. Ltd. Korea) (purity 99%), ethanol (E. Merck, Germany), potassium hydroxide (E. Merck, Gerrmany), chloroform (Merck, KGaA, Darmstadt, Germany), tetrahydrofuran (THF) (E. Merck, Germany), acetone (Sigma-Aldrich Chemie GmbH, Steinheim, Germany) (purity 99.5%), quinine sulfate (Alfa-Aesar, UK) (98% purity) and poly vinyl chloride (Sigma-Aldrich Corp. St. Louis, MO USA) were used without further purification and double distilled water obtained from glass assemblies.

2. 2. Characterization

The melting point of the monomers and polymers were recorded on Gallenkamp Melting point apparatus (made in England) equipped with thermometer. The E.I mass spectra of the monomers were recorded on JEOL JMS-600 (Japan) mass spectrometer at HEJ Research Institute of Chemistry, University of Karachi, Sindh-Pakistan. The Proton NMR (¹HNMR) spectra of the monomers and polymers were recorded on BRUKER AVANCE-NMR 400 MHz spectrometer at HEJ Research Institute of Chemistry, University of Karachi, Sindh-Pakistan, using TMS as internal standard and deuterated dimethylsulfoxide (DM- $SO-d_6$) as solvent. The FT-IR spectra of the monomers and polymers were recorded on Thermo Scientific™ Nicolet iS10 FT-IR Spectrometer with Attenuated total reflectance (ATR) accessory equipped with OMNIC™ Software. The UV-Visible spectra of monomers and polymers were recorded within 200-700 nm spectral range on a double beam spectrophotometer Shimadzu UV-1800 with UV Probe software at Mehran University of Engineering & Technology, Jamshoro, Sindh-Pakistan, using 1 cm quartz cuvettes and DMSO as solvent. The Fluorescence emission spectra of monomers and polymers were recorded on Spectrofluorophotometer RF-5301PC Series (Shimadzu, Kyoto, Japan) using 1cm quartz cuvette and DMSO as solvent. The morphologies of the compounds were observed through SEM images recorded on Scanning Electron Microscope IEOL ISM-6490 LV at Center for Pure and Applied Geology, University of Sindh, Jamshoro, Sindh-Pakistan or on JEOL JSM 5910 at Centralized Resource Laboratory (CRL), University of Peshawar, Peshawar-Pakistan, using 15 kV accelerating voltage. The powder X-ray diffraction (XRD) of the polymers was recorded on X-ray Diffractometer JDX 3532 (JEOL, Japan) equipped with Cu Kα radiation (wavelength: 1.54056 Å) at Centralized Resource Laboratory, University of Peshawar, Peshawar- Pakistan. The TG/DTA graphs of monomers and polymers were recorded at Centralized Resource Laboratory, University of Peshawar, Peshawar- Pakistan on Pyris Diamond Series TG/DTA (Perkin Elmer, USA) thermal analyzer in nitrogen atmosphere with flow rate of 20 ml/ min and heating rate of 20 °C/min, the sample (5-10 mg) was placed on ceramic pan and heated from 50 °C to 800 °C using alumina as reference material. Thin film forming ability of the polymers were tested by making their blends with PVC (poly vinyl chloride) in different w/w ratios (10-50%). The polymers were dissolved separately in DMSO while PVC was dissolved in THF and their mixtures (10-50%) w/w were transferred in glass Petri dishes of 2 inch diameter, the petri dishes were placed in an oven at 60 °C for evaporating the solvent. After drying the resulting thin films were removed from the glass surface of petri dishes with the help of spatula and the film forming ability of the polymers was confirmed as thin layers were easily separated from the glass surface without breaking. Antibacterial activities of the polymers were examined by microplate alamar blue assay using 96 well plate method. The antibacterial activities of the polymers were tested against different strains of bacteria which included Staphylococcus aureus, Salmonella typhi, Pseudomonas aeruginosa, Bacillus subtilis and Escherichia coli using Ofloxacin as standard drug. The polymer (2 to 4 mg) was dissolved in DMSO to make concentration 50 or 200 µg/ml. The growth of bacteria was carried out in Mueller-Hinton Agar medium and the incubation period was 18 to 20 hrs. The % inhibition of bacterial species by the polymers was calculated by using reported method and formula given as equation 1.32

% inhibition =
$$\frac{(\varepsilon_{ox})\lambda_2 A \lambda_1 - (\varepsilon_{ox})\lambda_1 A \lambda_2}{(\varepsilon_{red})\lambda_1 A' \lambda_2 - (\varepsilon_{red})\lambda_2 A' \lambda_1} \times 100 \quad (1)$$

Where ε_{ox} and ε_{red} are the molar extinction coefficient of Alamar blue dye in the oxidized (blue) and reduced (pink) form respectively, $\lambda_1 = 570$ nm, $\lambda_2 = 600$ nm, A and A' are the absorbance reading of the test and negative control well respectively. The antifungal activities of the polymers were tested by agar tube dilution method against different fungal strains which were Candida albicans, Canadida glabrata, Aspergillus niger, Fusarium lini, Trichphyton rubrum and Microsporum canis using standard drug Amphotericin B for Aspergillus niger and Miconazole for other species. SDA (Sabouraud dextrose agar) media was used for fungal growth where 12 mg of polymer was dissolved in DMSO to make concentration 200 µg/ml. The incubation period was 7 days and the temperature was 27 °C. The % inhibition of fungal strains by the polymers was calculated using the formula given as equation 2.

% inhibition = (2)

$$100 - \frac{linear\ growth\ in\ test\ (mm)}{linear\ growth\ in\ control\ (mm)} \times 100$$

2. 3. Synthesis of Monomers

Three new monomers (two dialdehydes and one diketone) were prepared by following a reported procedure.33-35 0.2 mol of aromatic aldehyde [3-hydydroxybenzaldehyde (24.42 g), 2-hydroxynaphthaldehyde (34.43 g) or 2-hydroxyacetophenone (27.23 g)] dissolved in 50 ml of DMF was added into 250 ml round bottom flask equipped with a condenser and magnetic stirrer, 0.25 mol (25 g) anhydrous sodium carbonate and 0.1 mol of 1,6-dibromohexane (15.38 ml) were also added to the reaction flask. The contents were refluxed for 5 h at 150 °C with continuous stirring, the resulting product was poured into 500 ml cold water and allowed to form precipitates. The precipitates were filtered and washed once with 0.1 M potassium hydroxide and then three times with distilled water, dried and recrystallized from ethanol. The structures and the reactions for the syntheses of monomers are given in **Figure 1**.

2. 3. 1. 3,3'-hexamethylenebis(oxybenzaldehyde) (m-HOB)

Yield = 78%, Mp. 60 °C, $C_{20}H_{22}O_4$, FT-IR cm⁻¹ (relative intensity) 3066(w), 2944(w), 2912(w), 2866(w), 2808(w), 2719(w), 1717(m), 1694(s), 1592(m), 1486(m), 1472(m), 1450(m), 1384(m), 1323(m), 1294(w), 1258(s), 1169(s), 1148(m), 1082(w), 1021(s), 990(w), 931(w), 876(w), 864(w), 785(s), 755(s), 730(w), 682(s). ¹HNMR (DMSO- d_6), δ ppm 1.489(q), 1.762(t), 4.050(t), 7.258(m), 7.405(d), 7.486(m), 9.959. UV (DMSO), λ-max, nm (ε, L. mole⁻¹ cm⁻¹) 314(6976). E.I mass spectrum m/z (relative intensity %) M+ 326(33.2), 297(1.3), 221(1.5), 205(8.1), 177(5.0), 163(2.5), 149(3.0), 135(10.9), 121(31.6), 105(19.4), 83(65.5), 55(100).

2. 3. 2. 2,2'-hexamethylenebis(oxynaphthaldehyde) (o-HON)

Yield = 85%, Mp. 180 °C, $C_{28}H_{26}O_4$, FT-IR cm⁻¹ (relative intensity) 2939(w), 2878(w), 1990(w), 1661(s), 1620(w), 1590(m), 1511(m), 1459(w), 1434(m), 1368(w), 1343(m), 1268(m), 1246(s), 1150(s), 1058(s), 1022(m), 942(w), 900(w), 866(w), 804(s), 758(s), 708(m), 645(s). ¹HNMR (DMSO- d_6), δ ppm 1.361, 1.455(d), 1.575, 1.871, 4.324(t), 7.446(t), 7.589(m), 7.925(d), 8.257(q), 9.083(d), 10.794. UV (DMSO), λ-max, nm (ε, L. mole⁻¹ cm⁻¹) 320(3043), 340(2199). E.I mass spectrum m/z (relative intensity %) M⁺ 426(52.2), 398(89.9), 397(28.3), 271(3.5), 255(19.3), 241(1.0), 227(8.2), 213(4.4), 199(3.2), 185(21.8), 171(100), 155(7.7), 83(30.6), 55(57.2).

2. 3. 3. 2,2'-hexamethylenebis(oxyacetophenone) (o-HOA)

Yield = 81%, Mp. 80 °C, $C_{22}H_{26}O_4$, FT-IR cm⁻¹ (relative intensity) 2951(w), 2870(w), 1661(s), 1593(s), 1575(w), 1485(m), 1469(w), 1449(m), 1411(w), 1395(w), 1361(m), 1293(s), 1232(s), 1162(m), 1129(m), 1043(m), 1014(m), 865(m), 828(w), 763(s). ¹HNMR (DMSO- d_6), δ ppm 1.530(t), 1.815(t), 2.534(d), 4.099(t), 6.989(t), 7.136(d), 7.500(m), 7.557(m). UV, λ-max, nm (ε, L. mole⁻¹ cm⁻¹) 306(7076), 444(233.7). E.I mass spectrum m/z (relative intensity %) M⁺ 354(2.3), 339(19.5), 235(13.5), 219(20), 191(3.0), 177(1.5), 163(1.7), 149(23.9), 135(2.9), 119(13.9), 83(69.4), 55(100), 43(37.3).

2. 4. Synthesis of Polymers

2,2'-hexamethylenebis(oxyacetophenone)(o-HOA)

Three new polymers were synthesized by following reported method^{33–35} with slight modification in the proce-

Figure 1. Synthetic reactions for the dialdehydes or diketone monomers

Figure 2: Synthetic reactions for the polyimines

dure as under: the monomer (5 mmol) [*m*-HOB (1.63 g), *o*-HON (2.13 g) or *o*-HOA (1.77 g)] dissolved in 25 ml DMF and 5 mmol of diamine [1,5-naphthalenediamine (0.79 g) or 1,4-phenylenediamine (0.54 g)] dissolved in 25 ml DMF were transferred in a 250 ml round bottom flask equipped with condenser and magnetic stirrer bar and 0.01 g of *p*-toluenesulfonic acid was also added into the flask as catalyst. The contents were refluxed for 6 to 7 hours with continuous stirring in nitrogen atmosphere. The resulting product was poured into 250 or 500 ml distilled water and allowed to settle precipitates. The product was filtered and finally dried at room temperature. The synthetic reactions for the polymers with their structures are given in **Figure 2**.

2. 4. 1. Poly-3,3'-hexamethylenebis(oxybenzldehyde)-1,5-naphthalenediimine (PmHOBND)

Yield = 76%, Mp. 210 °C (decomposed), $(C_{30}H_{28}N_{2}O_{2})_{n}$, FT-IR, cm⁻¹ (rel. intensity), 2939(w), 2863(w), 1694(w), 1620(m), 1578(s), 1503(w),1485(w), 1447(m), 1404(w), 1360(w), 1360(w), 1318(w), 1248(s), 1206(s), 1174(w), 1150(m), 1024(m), 992(w), 974(w), 862(w), 778(s), 684(m). ¹HNMR (DMSO- d_{6}), δ ppm 1.496, 1.764, 2.721, 2.880, 4.052(m), 7.942, 9.980. UV (DMSO), λ-max nm (1% absorptivity) 287(145), 321(236.5).

2. 4. 2. Poly-2,2'-hexamethylenebis(oxynaphthaldehye)-1,4-phenylenediimine (PoHONPD)

Yield = 78%, Mp. 185–210 °C, $(C_{34}H_{30}N_2O_2)_n$, FT-IR, cm⁻¹ (rel. intensity) 3367(w), 2936(w), 2857(w), 1683(w), 1618(w), 1592(s), 1505(w), 1487(w), 1456(m), 1387(w),

1285(m), 1243(s), 1188(w), 1143(s), 1101(s), 1073(w), 1005(w), 887(w), 826(m), 754(s), 722(m). 1 HNMR (DMSO- d_6), δ ppm 2.722, 2.881, 7.942. UV (DMSO), λ-max nm (1% absorptivity) 265(1120), 318(940).

2. 4. 3. Poly-2,2'-hexamethylenebis(oxyacetophenone) -1,5-naphthalenediimine (PoHOAND)

Yield = 74%, Mp. 250 °C (decomposed), $(C_{32}H_{32}N_2O_2)_n$, FT-IR, cm⁻¹ (rel. intensity) 3339(w), 2938(w), 1594(s), 1517(w), 1485(w), 1450(s), 1407(w), 1358(w), 1293(m), 1237(m), 1164(w), 1122(w), 1033(w), 1010(w), 754(s), 681(m). ¹HNMR (DMSO- d_6), δ ppm 1.223, 1.417(m), 1.666, 1.775(t), 2.275, 4.078(t), 6.594(t), 6.736(d), 6.986(t), 7.039, 7.114(m), 7.197(m), 7.308(t), 7.509(m). UV (DMSO), λ-max nm (1% absorptivity) 307(1580), 477(500).

3. Results and Discussion

3. 1. Synthesis

Three new monomers (dialdehydes or diketone) *m*-HOB, *o*-HON and *o*-HOA were prepared by condensation of 3-hydroxybenzaldehyde, 2-hydroxynaphthaldehyde or 2-hydroxyacetophenone with 1,6-dibromohexane. The monomers were obtained in good yield (78–85%). In the present work new meta oriented dialdehyde *m*-HOB was prepared while its ortho and para oriented isomers were reported in our earlier work.^{34,35} Three new polyimines (*Pm*HOBND, *Po*HONPD and *Po*HOAND) were prepared by the polycondensation of dialdehydes or diketone monomers (*m*-HOB, *o*-HON or *o*-HOA) with di-

amines (1,5-naphthalenediamine or 1,4-phenylenediamine). The polymers have ether linkages, azomethine or imine bonds and spacers of n-hexane between the aromatic rings and the polymer derived from diketone monomer (*o*-HOA) contains methyl group attached with the imine (C=N) group. The polymers were also obtained in good yield (74–78%). The synthesized polymers can also be called as polyethers because all the three polymers contain ether linkages in their main chain.

3. 2. Solubility

The solubility of the monomers and polymers was tested in various solvents and the results are given in **Table 1**. The monomers were soluble in organic solvents and in-

soluble in water. The polymer PmHOBND was soluble in chloroform and THF without heating while in DMSO and DMF on heating, the polymer PoHONPD was soluble in DMF and DMSO on heating and the polymer PoHOAND indicated highest solubility in all the tested solvents except water, it is soluble in chloroform, acetone, THF, DMF and DMSO without heating while in ethanol with heating. The increased solubility of the polymer PoHOAND may be due to presence of methyl side group attached with the imine bond.

3. 3. E.I Mass Spectra of Monomers

The mass spectrum of the dialdehyde m-HOB indicated M^+ at m/z 326 and other fragment ion peaks ap-

Table 1. Solubility of monomers and polymers in different solvents at the concentration of 5mg/5ml

S. No	Compound			Solub	oility in different so	lvents		
	•	H_2O	Ethanol	Acetone	Chloroform	THF	DMF	DMSO
1	mHOB	IS	S	S	S	S	S	S
2	oHON	IS	$PS(\Delta)$	$S(\Delta)$	S	S	S	S
3	oHOA	IS	S	S	S	S	S	S
4	PmHOBND	IS	IS	SS	S	S	$S(\Delta)$	$S(\Delta)$
5	PoHONPD	IS	$SS(\Delta)$	$PS(\Delta)$	PS	PS	$S(\Delta)$	$S(\Delta)$
6	PoHOAND	IS	$S(\Delta)$	S	S	S	S	S

S=Soluble, $S(\Delta)$ =Soluble on heating, PS=Partially Soluble, PS(Δ)=Partially Soluble on heating, SS=Slightly Soluble, SS(Δ)=Slightly soluble on heating, IS=Insoluble

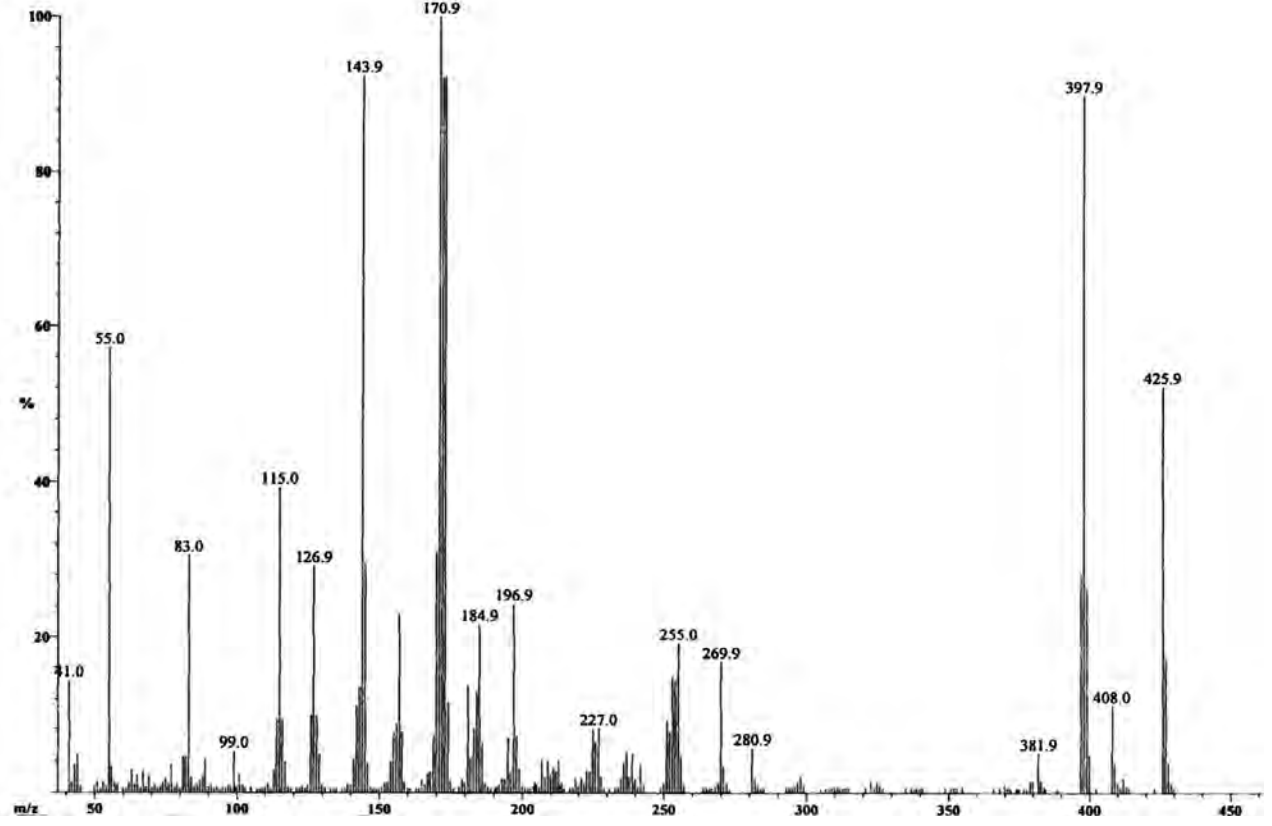


Figure 3. E.I mass spectrum of the monomer o-HON

peared at m/z 297, 221, 205, 177, 163, 149, 135, 121 and 105 corresponding to $[M-(CHO)]^+$, $[M-(C_6H_4.CHO)]^+$, $[M-(O.C_6H_4.CHO)]^+$, $[CHO.C_6H_4.O.(CH_2)_4]^+$, $[CHO.C_6H_4.O.(CH_2)_2]^+$, $[CHO.C_6H_4.O.(CH_2)_2]^+$, $[CHO.C_6H_4.O.(CH_2)_2]^+$, $[CHO.C_6H_4.O.CH_2]^+$, $[CHO.C_6H_4.O.CH_2]^+$ and $[CHO.C_6H_4]^+$ respectively while the peaks at 83(65.5%) and 55(100%) corresponded to C_6H_{11} and C_4H_7 (supplementary Fig. S1).

The mass spectrum of the dialdehyde o-HON indicated M⁺ at m/z 426 and the other fragment ion peaks appeared at m/z 398, 397, 271, 255, 241, 227, 213, 199, 185, 171(100%) and 155 corresponding to [M-(CHO)+1]⁺, [M-(CHO)]⁺, [M-C₁₀H₆.CHO]⁺, [CHO.C₁₀H₆.O.(CH₂)₆]⁺, [CHO.C₁₀H₆.O.(CH₂)₃]⁺, [CHO.C₁₀H₆.O.(CH₂)₂]⁺, [CHO.C₁₀H₆.O.(CH₂)₂]⁺, [CHO.C₁₀H₆.O.(CH₂)₂]⁺, [CHO.C₁₀H₆.O.(CH₂)₂]⁺, respectively while the peaks at 83(30%) and 55(57.2%) were of C₆H₁₁ and C₄H₇(**Figure 3**).

The mass spectrum of diketone o-HOA indicate M^+ at m/z 354 and the other fragment ion peaks appeared at m/z 339, 235, 219, 191, 177, 163, 149, 135 and 119 were corresponding to $[M-(CH_3)]^+$, $[M-(C_6H_4\cdot CO.CH_3)]^+$, $[M-(C_6H_4\cdot CO.CH_3)]^+$, $[CH_3\cdot CO.C_6H_4\cdot O.(CH_2)_4]^+$, $[CH_3\cdot CO.C_6H_4\cdot O.(CH_2)_2]^+$, $[CH_3\cdot CO.C_6H_4\cdot O.(CH_2)_2]^+$, $[CH_3\cdot CO.C_6H_4\cdot O.(CH_2)_2]^+$, $[CH_3\cdot CO.C_6H_4\cdot O]^+$ and $[CH_3\cdot CO.C_6H_4]^+$ respectively while the peaks at 83(69.4), 55(100) and 43(37.3) were of C_6H_{11} , C_4H_7 and $CH_3\cdot CO$ respectively (**supplementary Fig. S2**).

3. 4. FT-IR Spectroscopy of Monomers and Polymers

The FT-IR spectra of dialdehydes and diketone monomers indicated two or five weak bands within 2951–2719 cm⁻¹ due to υ C-H aliphatic corresponding to n-hexane and CHO (of dialdehydes) groups. A strong band was indicated within 1694–1661 cm⁻¹ due to υ C=O of aldehyde or ketone group. The band within 1595–1590 cm⁻¹ was assigned for υ C=C aromatic rings and the band within 1233–1257 cm⁻¹ for υ C-O-C of etheric bond (**supplementary Fig. S3-S5**), similar assignments have been reported in the literature for dicarbonyl monomers. ^{36,37}

The polymers PmHOBND and PoHONPD showed weak band at 1694 and 1683 cm⁻¹ respectively for υ C=O contributed from end on group, this band was present as a strong band in their corresponding monomers which showed that carbonyl group was converted into imine group. All the three polymers (PmHOBND, PoHONPD and PoHOAND) showed strong to medium intensity band within 1594-1620 cm⁻¹ for υ C=N and the band within 1592-1518 cm⁻¹ due to aromatic rings of the polymers. Two bands were observed within 1237-1248 cm⁻¹ and 1024-1005 cm⁻¹ due to v C-O-C asymmetric and symmetric vibrations and number of bands within 973-681 cm⁻¹ were for C-H in plane and out of plane vibrations of aromatic rings (Figure 4) (supplementary Fig. S6 and S7). Similar assignments indicated for related polymines.36,38

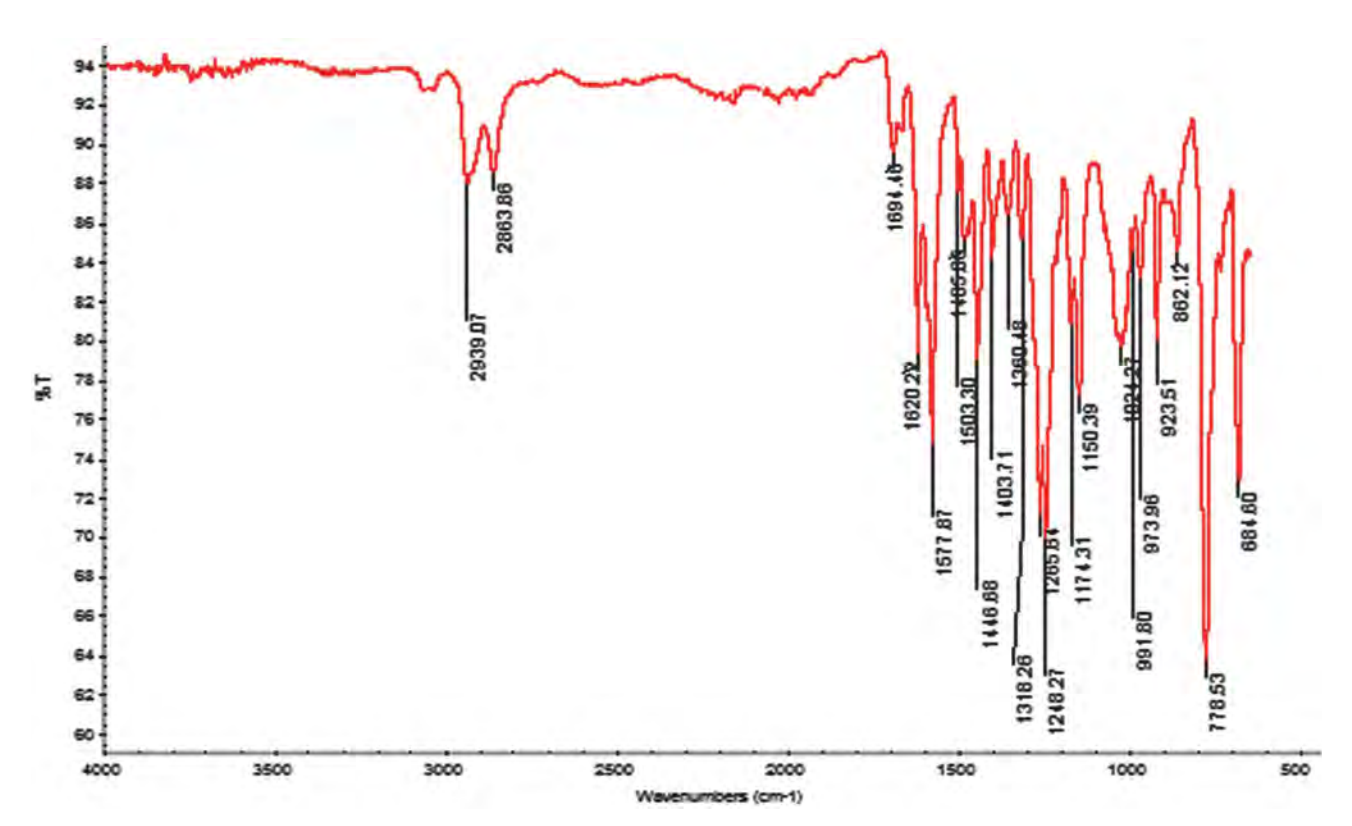


Figure 4. FT-IR spectrum of polymer PmHOBND

3. 5. ¹HNMR Spectroscopy of Monomers and Polymers

The ¹HNMR spectra of all the synthesized compounds (monomers and polymers) were recorded in DM- $SO-d_6$ solvent. The dialdehyde monomers m-HOB and o-HON indicated CHO group signal at δ ppm 9.959 and 10.794 respectively, all the three monomers (m-HOB, o-HON and o-HOA showed signals within the range of δ ppm 6.989-8.257 due to protons of the aromatic rings (benzene or naphthalene), one triplet within δ ppm 4.050– 4.324 due to etheric group (O-CH₂) protons and CH₂ aliphatic protons signals within δ ppm range of 1.361–1.871 due to n-hexane while diketone o-HOA also showed signal at δ ppm 2.534 due to CH₃ protons of acetophenone group (**supplementary Fig. S8-S10**). The polymers PmHOBND and PoHONPD showed singlet at δ ppm 7.942 for azomethine group proton (CH=N) while the polymer PoHO-AND did not showed any proton signal at this position because it contains imine bond (C=N) instead of azomethine group. The polymer PoHOAND showed CH aromatic proton signals within δ ppm range of 6.594–7.509 while aromatic CH signals were missing in PmHOBND and Po-HONPD because of their lower solubility in DMSO- d_6 , the polymers PmHOBND and PoHOAND indicated triplet at δ ppm 4.052 and 4.078 due to OCH₂ group, all the three polymers showed signals within the range of δ ppm 1.417– 2.880 due to CH₂ group protons of n-hexnane and PoHO-

AND showed singlet at δ ppm 2.275 due to CH₃ group protons (**Figure 5**). Similar ¹HNMR assignment have been reported for related monomers and polymers.^{38,39}

3. 6. UV-Vis Spectroscopy of Monomers and Polymers

UV-visible spectra of monomers and polymers were recorded using DMSO solvent and the results including molar absorptivity (L.mole⁻¹ · cm⁻¹) of monomers and 1% absorptivity of polymers (because molecular weight of polymers was unknown) are provided in **Table 2**. The meta oriented monomer *m*-HOB showed only one band at 314 nm for π - π * transition within aromatic ring while the ortho oriented monomers o-HON and o-HOA showed two bands each, the first bands at 320 nm and 306 nm respectively were attributed to π - π * transition within aromatic ring and second at 340 nm and 444 nm respectively was for π – π * within conjugated aromatic ring and carbonyl (C=O) group. The appearance of second peak in ortho oriented monomers may be due to greater influence of lone pairs of oxygen on conjugation as compared to meta oriented monomer (supplementary Fig. S11-S13). All the three polymers showed two bands, the first band appeared due to π - π * transition within aromatic ring and the second band was due to π - π * transition involving aromatic ring (phenyl or naphthyl) and conjugated azomethine

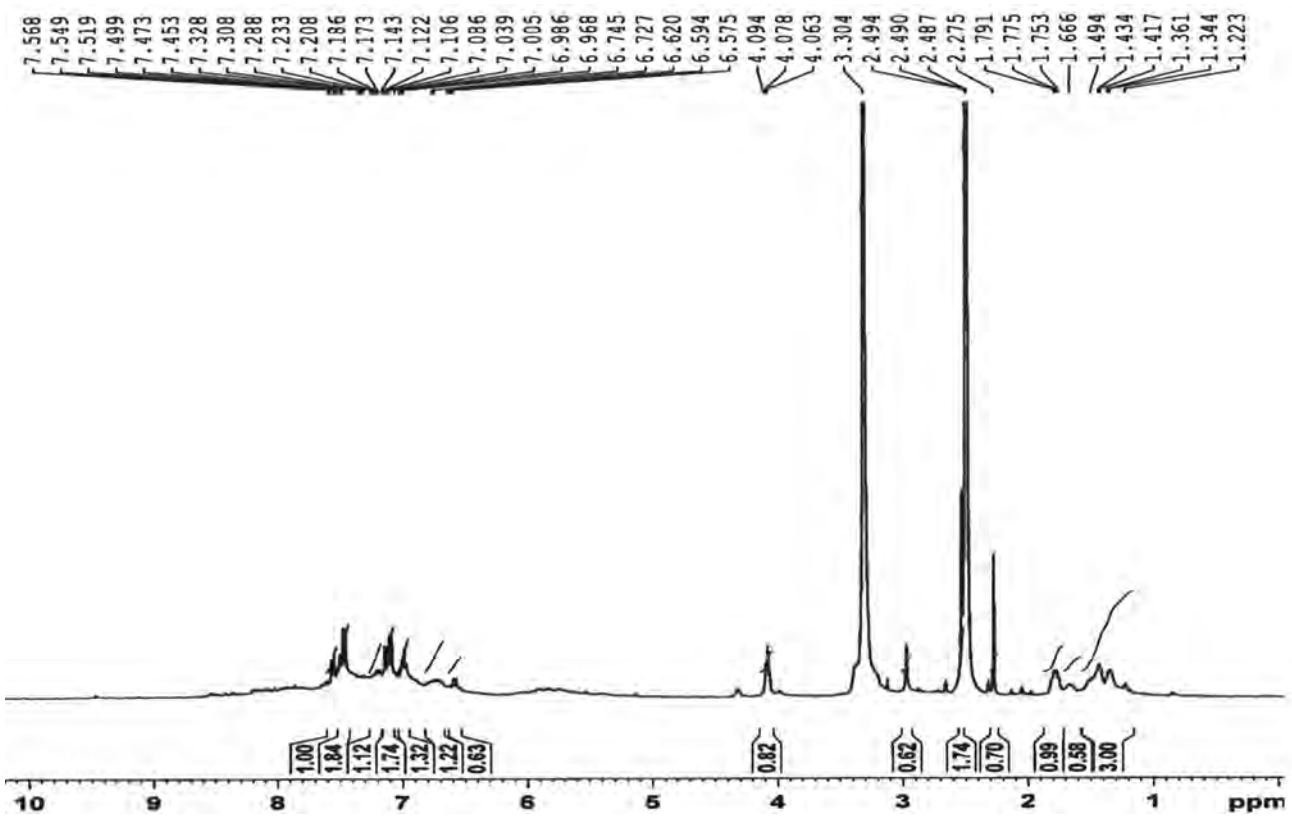


Figure 5. ¹HNMR spectrum of polymer PoHOAND

S. No	Compound	λ nm (ε 1%)	Possible transition
1	тНОВ	314 (6976)	π– $π$ * transition within benzaldehyde ring system
2	P <i>m</i> HOBND	287 (145) 321 (236.5)	π – π * transition within aromatic ring system π – π * transition involving naphthyl ring and conjugated C=C-N=C π -electron system
3	οHON	320 (3043) 340 (2199)	π – π^* transition within naphthaldehyde ring system π – π^* transition involving naphthyl ring with conjugated O=C-C=C-O π -electron system and lone pair of etheric oxygen.
4	P₀HONPD	265 (1120) 318 (940)	$\pi-\pi^*$ transition within aromatic ring system $\pi-\pi^*$ transition involving phenyl ring and conjugated C=C-N=C π -electron system
5	oHOA	306 (7076) 444 (233.7)	π – π^* transition within acetophenone ring system π – π^* transition involving naphthyl ring with conjugated O=C-C=C-O π -electron system and lone pair of etheric oxygen
6	PoHOAND	307 (1580) 477 (500)	π - π^* transition within aromatic ring system π - π^* transition involving phenyl ring and conjugated C=C-N=C π -electron system

Table 2. Results of spectrophotometric studies of monomers and polymers in DMSO Solvent

(C=C-N=C) group (**Figure 6**) (**supplementary Fig. S14-S15**). Similar UV-Vis assignment for related monomers and polymers were reported.^{40,41}

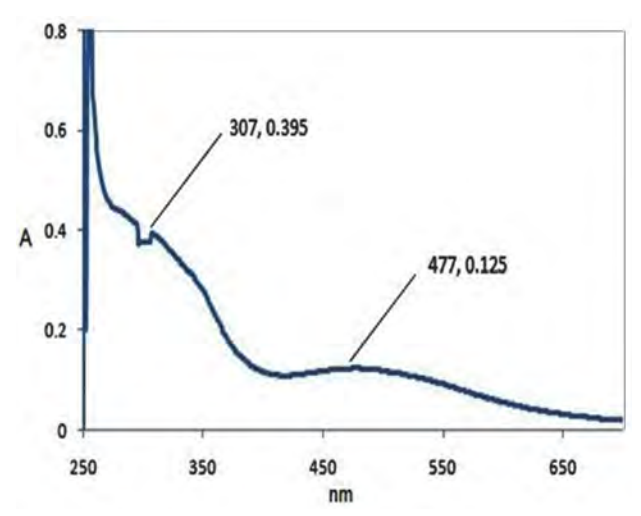


Figure 6. UV/Vis Spectrum of polymer (PoHOAND)

3. 7. Fluorescence Spectroscopy of Monomers and Polymers

All the synthesized monomers and polymers indicated fluorescence emission due to the presence of conjugated chromophoric groups in their structure (supplementary Fig. S16-S20). The fluorescence quantum yields of the synthesized compounds were calculated at different excitation wavelengths through reported comparative method. Quinine sulphate was dissolved in $0.1 \mathrm{M} \; \mathrm{H_2SO_4}$ and used as standard for all the measurements while the solutions of monomers and polymers were prepared in DMSO. The excitation and emission spectra of both the compound (monomers and polymers) and standard (qui-

nine sulphate) were recorded at solutions concentration 0.025 mg/ml because maximum emission intensities of the synthesized compounds were observed at this concentration. The excitation and emission slit width was adjusted at 5 nm for both the compound (monomers and polymers) and standard (quinine sulphate). The quantum yields of monomers and polymers were calculated using the following equation 3

$$Q_{MX} = Q_{YS} \left[\frac{A_x}{A_s} \right] \times \left[\frac{f_s}{f_x} \right] \times \left[\frac{n_x}{n_s} \right]$$
 (3)

Where Q_{MX} is the quantum yield of compound whose quantum yield want to be calculated, Q_{ys} is the quantum yield of quinine sulphate standard (0.54), Ax is the area under the emission peak of the compound whose quantum yield want to be calculated, As is area under the emission peak of quinine sulphate standard (190059), f_s (1-10^{-D}, D: absorbance value (0.20) of the quinine sulphate standard measured in UV-Vis at excitation wavelength), f_x (1–10^{-D}, D: absorbance value of the compound measured in UV-Vis at excitation wavelength), n_x is the refractive index of DMSO (1.479), n_x is the refractive index of 0.1M H₂SO₄ (1.33). All the monomers and polymers showed different color emissions at different excitation wavelengths, the results of spectrofluorometric measurements of all the monomers and polymers with their calculated quantum yields are summarized in Table 3. The monomers mHOB and oHON showed red and violet light emissions while the monomer oHOA showed violet, orange and red light emissions, the calculated quantum yields of monomers were obtained within the range of 0.04 to 3.35%. The polymer PmHOBND showed red and violet light emissions, PoHONPD showed violet light emission and PoHOAND indicated violet, bluegreen and orange light emission, the calculated quantum

Table 3. Spectrofluorometric determination of monomers and polymers in DMSO solvent

S. No	Compound	Excitation wavelength (nm)	Emission wavelength (nm)	Emission color	Relative intensity of emission	% Q _{MX}
			348	_	274	3.1
1	mHOB	314	631	red	16.9	0.04
			691	red	24.3	0.33
			398	violet	1016	24.3
2	PmHOBND	321	645	red	22.2	0.04
			742	red	400	6.27
			357	_	79.4	2.50
		320	642	red	39.6	0.20
3	oHON		706	red	5.2	0.15
		2.40	378	violet	89.9	0.56
		340	681	red	36.11	0.36
	D HOMBD	265	356	_	403	7.38
4	PoHONPD	318	374	violet	345.4	4.92
			380	violet	217.5	3.35
5	oHOA	306	614	orange	21.36	0.04
			688	red	14.6	0.22
		205	391	violet	442	4.81
6	PoHOAND	307	616	orange	47.3	0.06
		477	513	blue-green	50.2	0.2

[%] Q_{MX} (calculated % quantum yield of monomers and polymers)

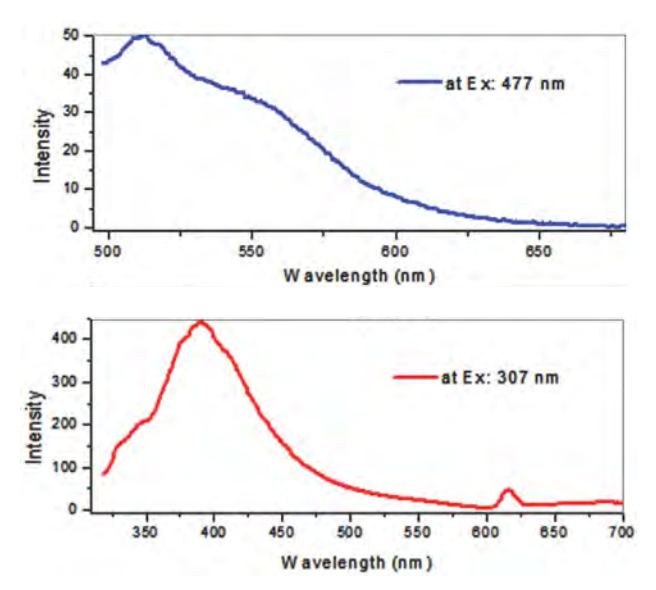


Figure 7. Fluorescence emission spectra of polymer PoHOAND at different excitation wavelengths

yields of polymers were obtained within the range of 0.04 to 24.3%. The fluorescence quantum yields of all the polymers were higher than their corresponding monomers while the polymer PmHOBND indicated highest quantum efficiency among all the synthesized compounds which is 24.3% for violet light emission (398 nm) at excitation 321 nm.

3. 8. Scanning Electron Microscopy of Monomers and Polymers

The SEM images of monomers and polymers were recorded at micron marker scale length range of 500 µm to 1 μm at different magnifications. The dialdehyde m-HOB showed crystalline morphology and looked like iron blocks while its corresponding polymer PmHOBND had sponge like morphology. The monomer o-HON had clay rock like morphology and showed non-homogeneous surface, while its corresponding polymer PoHONPD showed smooth and porous surface (supplementary Fig. S21 and S22). The surface morphology of diketone monomer o-HOA was fibrous and looked like cotton wool while morphology of its corresponding polymer PoHOAND looked like cheese pieces with clearly visible pores of different sizes (Figure 8). The surface morphology of all the three polymers was different from their corresponding monomers which support their formation.

3. 9. Powdered X-ray Diffraction (XRD) of Polymers

The X-ray diffraction patterns of the polymers were acquired over 2θ range of 5° – 80° (**Figure 9**). The meta-oriented polymer P*m*HOBND showed intense peaks within $2\theta = 5^{\circ}$ – 30° which indicates its semicrystalline nature which may be attributed to the presence of polar CH=N

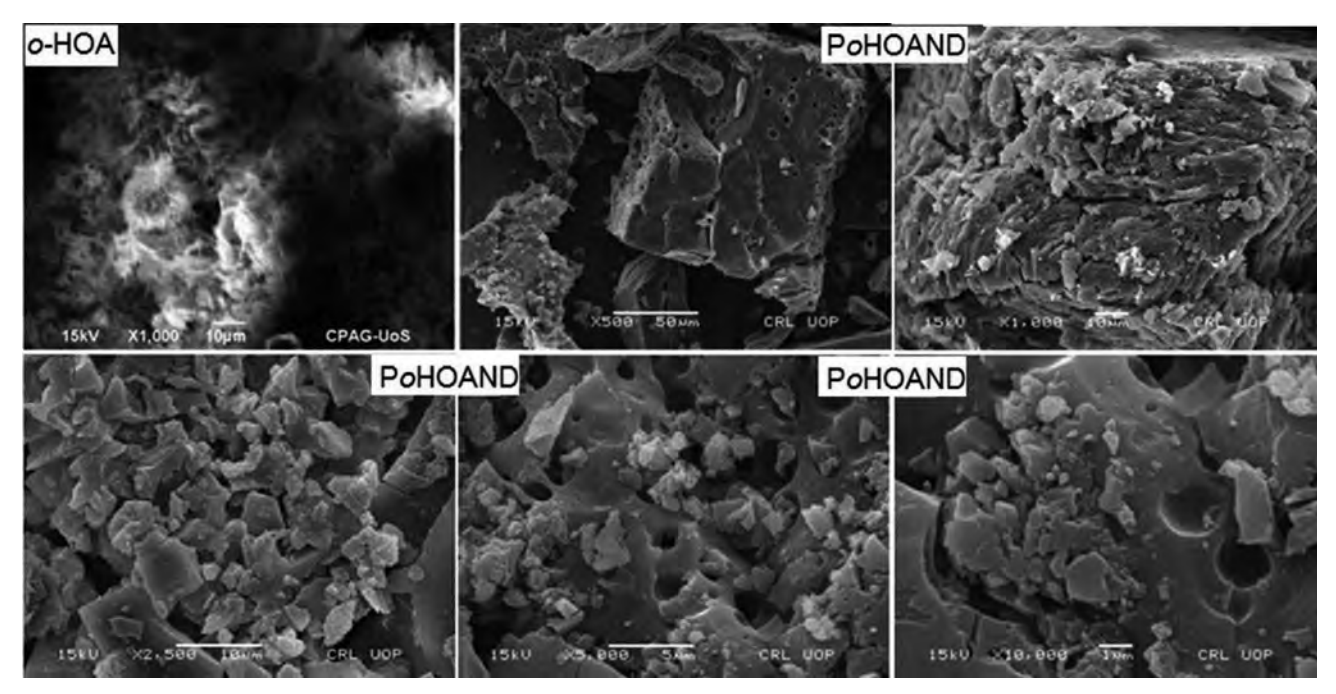


Figure 8. SEM images of monomer o-HOA and its derived polymer PoHOAND at different micron-marker scale lengths (50 μm to 1 μm)

groups and C=C bonds of aromatic rings in its structure.⁴³ The polymers PoHONPD and PoHOAND showed one broad diffraction hump centered at $2\theta = 20.6^{\circ}$ and $2\theta = 22.5^{\circ}$ respectively, which indicated their amorphous na-

1,2- linkages and flexible aliphatic (CH₂)₆ groups in their structures.⁴⁵
3. 10. Thermal Analysis of Monomers and Polymers

ture.44 The amorphous nature of ortho oriented polymers

(PoHONPD and PoHOAND) was due to the presence of

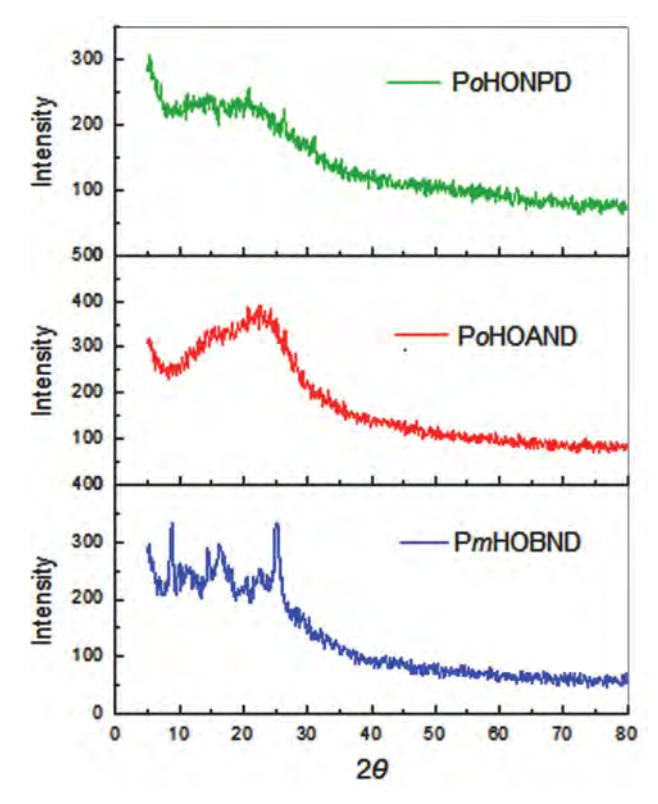


Figure 9: XRD patterns of polymers PmHOBND, PoHOAND and PoHONPD

Thermal properties of monomers and polymers were evaluated by thermogravimetric (TG) and differential thermal analysis (DTA) and the results are summarized in Table 4. Thermal stability of the compounds was estimated from the T_{max} value (temperature indicating maximum rate of weight loss) in TG graph. TG of dialdehyde m-HOB indicated weight loss in single step of 93% within 265 °C-590 °C and T_{max} value at 394 °C, DTA showed two endotherms first at 82 °C due to melting and second at 324 °C for vaporization/decomposition followed by four exotherms due to decomposition at 263, 393, 479 and 558 °C. TG of o-HON showed three steps of weight loss, 54% weight loss within 294-413 °C, 14% loss within 414-514 °C and 19% loss within 515-611 °C, its T_{max} was observed at 354 °C, DTA indicated one endotherm at 193 °C due to melting followed by two exotherms at 362 °C and 545 °C due to decomposition. TG of diketone monomer o-HOA showed three steps of weight loss, 71% loss within 209- 377 °C, 12% loss within 378-490 °C and 9% loss indicated within 491–550 °C, its T_{max} was observed at 342 °C, DTA showed melting endotherm at 97 °C, vaporization/decomposition exotherm at 371 °C and large decomposition exotherm at 545 °C. The dialdehyde m-HOB indicated highest thermal stability among the

Table 4. Thermal analysis (TG/DTA) data of monomers and polymers

			TG			
		Weight loss stages	3	Maximum rate		
Compound	I	II	III	of wt. loss		DTA
	Wt. loss	% (temperature r	ange °C)	$(T_{max} {}^{\circ}C)$	Endo °C	Exo °C
т-НОВ	93 (265–590)	_	_	394	82, 324	263, 393, 479, 558
o-HON	54 (294-413)	14 (414-514)	19 (515-611)	354	193	362, 545
o-HOA	71 (209-377)	12 (378-490)	9 (491-550)	342	97	371, 545
PmHOBD	8 (194-415)	36 (416-503)	50 (504-651)	577	_	456, 639
PoHONPD	44 (324-468)	6 (469-557)	39 (558-678)	396	_	54, 365, 448, 624
PoHOAND	98 (42-727)	_	-	385	_	676

monomers (supplementary Fig. S23-S25). TG of polymer PmHOBND indicated weight loss in three steps 8% loss was observed within 194-415 °C, 36% weight loss within 416-503 °C and 50% loss within 504-651 °C with T_{max} at 577 °C. DTA showed two exothermic curves, vaporization/decomposition exotherm at 456 °C and decomposition exotherm at 639 °C (Figure 10a). TG of Po-HONPD showed three steps of weight loss, 44% weight loss was observed within 324-468 °C, 6% weight loss within 469-557 °C and 39% weight loss within 558-678 °C, T_{max} showed at 396 °C, DTA showed two volatilization/ decomposition exotherms at 365 °C and 448 °C and large decomposition exotherm at 624 °C (Figure 10b). TG of PoHOAND indicated 98% weight loss within 42-727 °C in one step with T_{max} at 385 °C, DTA showed one exotherm at 676 °C due to decomposition (Figure 10c). Thermal stability of the polymers was higher than their corresponding monomers and the polymer PmHOBND showed higher T_{max} value (577 °C) among all the synthesized compounds.

3. 11. Biological Activities of Polymers

The antimicrobial activities of the polymers were examined against different species of bacteria and fungi but the polymers showed non-significant antimicrobial activities. The polymer PmHOBND showed 10% antibacterial activity against Staphylococcus aureus and Bacillus subtilis while only 2% inhibition against Salmonella typhi. Po-HOBND showed 11% inhibition against Staphylococcus aureus, 8% inhibition against Bacillus subtilis and 7.4% inhibition against Salmonella typhi. PoHOAND indicated no inhibition against Staphylococcus aureus, only 1% inhibition against Bacillus subtilis and 15.4% inhibition against Salmonella typhi. All the three polymers not showed any activity against Escherichia coli and Pseudomonas aeruginosa. The polymers PmHOBND and PoHOBND showed 12.5% antifungal activity against Candida albicans while PoHOAND showed 10% activity against the same strain. All the three polymers did not show any activity against Canadida glabrata, Aspergillus niger, Fusarium lini, Trichphyton rubrum and Microsporum canis.

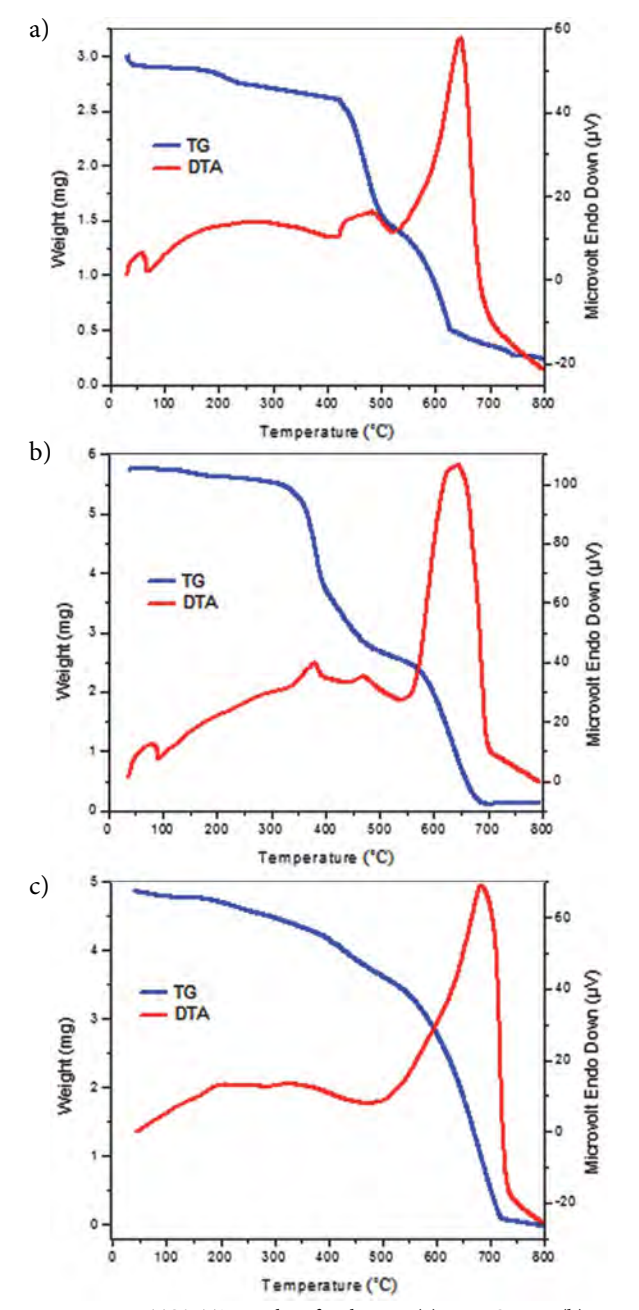


Figure 10. TG/DTA graphs of polymers (a) PmHOBND (b) PoHONPD (c) PoHOAND

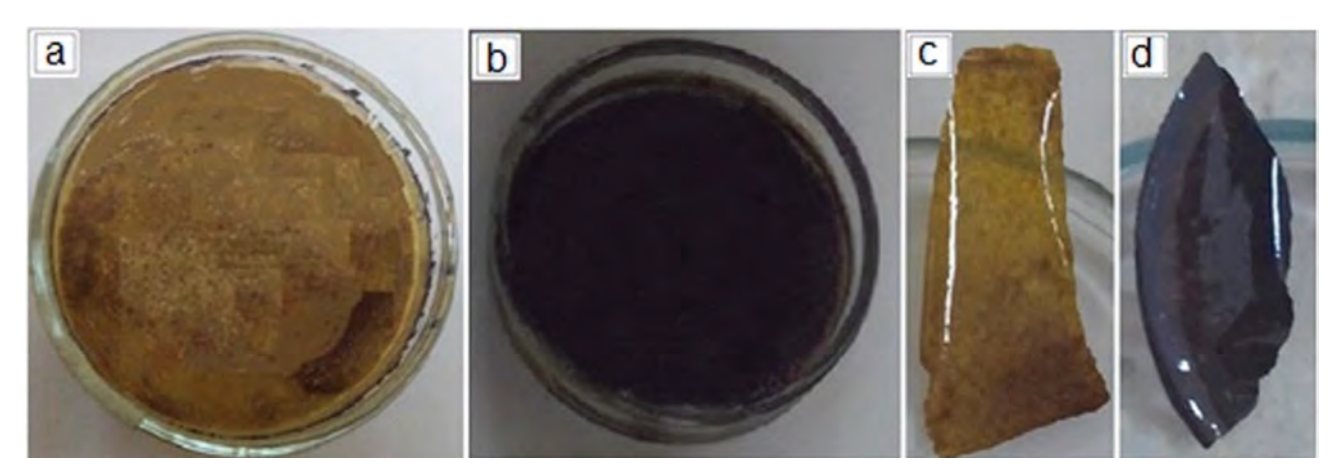


Figure 11.Images of dried homogenized polymer-PVC blends (50–50%) w/w and their resulting thin films (a) PoHONPD-PVC blend (b) Po-HOAND-PVC blend (c) thin film of PoHONPD-PVC and (d) thin film of PoHOAND-PVC.

3. 11. Thin Films of Polymer-PVC Blends

The polymers PmHOBND, PoHONPD and PoHO-AND were tested for their thin film forming ability, the synthesized polymers could not form thin films alone therefore polymer-PVC blends in different w/w% ratios (10:90, 20:80, 30:70, 40:60 and 50:50) were prepared, among them only 50:50 w/w% blends of ortho-oriented polymers PoHONPD and PoHOAND were transformed into thin layers having shiny finishing (**Figure 11**).

4. Conclusion

Three new aliphatic-aromatic polyimines containing naphthyl rings in their main chain were prepared by the polycondensation reaction of newly synthesized dialdehydes and diketone monomers with diamines. The solubility of the polymers were improved significantly due to solubility enhancing arrangements made in their structures which include their aliphatic-aromatic nature, introduction of ether linkages between the aliphatic and aromatic groups and non-linear orientation (ortho and meta) of the groups attached with the aromatic ring. In addition to these structural modifications the polymer PoHOAND contain methyl side group attached at ortho position of the aromatic ring and this polymer indicates highest solubility among the synthesized polymer, it was soluble in all the organic solvent tested which include acetone, chloroform, THF, DMF and DMSO. All the synthesized compounds (monomers and polymers) were fluorescent, the polymer PmHOBND showed violet and red light emission, PoHONPD showed violet light emission while PoHOAND showed multi-color emissions which include violet, blue-green and orange. The highest quantum yield (24.3%) was indicated by the meta-oriented polymer PmHOBND for violet light emission (398 nm) at excitation 321 nm. The polymers were thermally stable up to 400 °C, therefore they can be applied as fluorescent and heat-resistant materials. The 50:50 w/w% polymer-PVC blends of PoHONPD and PoHOAND were transformed into thin films with shiny finishing.

5. References

- K. Suematsu, K. Nakamura, and J. Takeda, Colloid Polym. Sci. 1983, 261, 493–501. DOI:10.1007/BF01419833
- S. Banerjee and C. Saxena, J Polym Sci A Polym Chem. 1996, 34, 3565–3572.
 - **DOI**:10.1002/(SICI)1099-0518(199612)34:17<3565::AID-POLA11>3.0.CO;2-C
- 3. P. Kumar Gutch, S. Banerjee, D. Gupta, and D. Jaiswal, *J Polym Sci A Polym Chem.* **2001**, *39*, 383–388.
 - **DOI:**10.1002/1099-0518(20010201)39:3<383::AID-PO-LA1005>3.0.CO;2-3
- M. A. Hussein, M. A. Abdel-Rahman, A. M. Asiri, K. A. Alamry, and K. I. Aly, *Des. Monomers Polym.* 2012, *15*, 431–463.
 DOI:10.1080/1385772X.2012.688325
- 5. N. Khalid, A. Bibi, K. Akhtar, K. Mustafa, M. Khan, and N. Saeed, *Polym Plast Technol Eng.* **2019**, *15*, 419-426.
 - DOI:10.1080/03602559.2018.1471719
- E. Hamciuc, M. Homocianu, C. Hamciuc, and I.-D. Carja, *High Perform Polym.* 2018, 30, 339–346.
 DOI:10.1177/0954008317697367
- M. Palewicz, A. Iwan, A. Sikora, J. Doskocz, W. Strek, D. Sek, and B. Mazurek, *Acta Phys. Pol. A.* 2012, *121*, 439–444.
 DOI:10.12693/APhysPolA.121.439
- 8. S. Dineshkumar, A. Muthusamy, P. Chitra, and S. Anand, *J ADHES SCI TECHNOL.* **2015**, 29, 2605–2621.
 - **DOI:**10.1080/01694243.2015.1079455
- 9. İ. Kaya, A. Avcı, F. Kolcu, and S. Çulhaoğlu, *Des. Monomers Polym.* **2014**, *17*, 481–490.
 - **DOI:**10.1080/15685551.2013.867581
- H. Niu, Y. Huang, X. Bai, X. Li, and G. Zhang, *Mater Chem Phys.* 2004, 86, 33–37.
 - DOI:10.1016/j.matchemphys.2004.01.023

- P. W. Wojtkowski, Macromolecules. 1987, 20, 740–748.
 DOI:10.1021/ma00170a0077
- T. Borukaev, A. K. Shaov, A. Kharaev, R. C. Bazheva, L. Pashtova, A. K. Malamatov, and V. Shogenov, Fibre Chemistry.
 2018, 49, 425–427. DOI:10.1007/s10692-018-9913-3
- M. Palewicz, A. Iwan, J. Doskocz, W. Strek, D. Sek, B. Kaczmarczyk, and B. Mazurek, *Polym. Bull.* 2011, 66, 65-76.
 DOI:10.1007/s00289-010-0308-8
- B. Jarząbek, B. Kaczmarczyk, J. Jurusik, M. Siwy, and J. Weszka, *J. Non-Cryst. Solids.* **2013**, *375*, 13–18.
 DOI:10.1016/j.jnoncrysol.2013.05.013
- M. Rusu, A. Airinei, G. G. Rusu, L. Marin, V. Cozan, P. RÂmbu, I. Caplanus, and G. I. Rusu, *J MACROMOL SCI B.* 2011, 50, 1285–1297. DOI:10.1080/00222348.2010.507444
- M-F. Zaltariov, M. Cazacu, A. Vlad, L. Sacarescu, and S. Shova, *High Perform. Polym.* 2015, 27, 607–615.
 DOI:10.1177/0954008315584176
- 17. N. Nishat, S. Parveen, S. Dhyani, and Asma, *J. Coord. Chem.* **2009**, *62*, 1091–1099. **DOI**:10.1080/00958970802416020
- N. Nishat, S. A. Khan, S. Parveen, and R. Rasool, *J. Coord. Chem.* 2010, 63, 3944–3955.
 DOI:10.1080/00958972.2010.526207
- A. Iwan, B. Boharewicz, I. Tazbir, M. Malinowski, M. Filapek, T. Kłąb, B. Luszczynska, I. Glowacki, K. P. Korona, and M. Kaminska, SOL ENERGY. 2015, 117, 246–259.
 DOI:10.1016/j.solener.2015.03.051
- K. Gawlinska, A. Iwan, Z. Starowicz, G. Kulesza-Matlak, K. Stan-Glowinska, M. Janusz, M. Lipinski, B. Boharewicz, I. Tazbir, and A. Sikora, *OPTO-ELECTRON REV.* 2017, 25, 274–284. DOI:10.1016/j.opelre.2017.07.004 4
- C. Mallet, M. Le Borgne, M. Starck, and W. Skene, *Polym. Chem.* 2013, 4, 250–254. DOI:10.1039/C2PY20703F
- M. Kamacı and İ. Kaya, J FLUORESC. 2015, 25, 1339–1349.
 DOI:10.1007/s10895-015-1624-z
- 23. A. Iwan and D. Sek, *Prog. Polym. Sci.* **2008**, *33*, 289–345. **DOI:**10.1016/j.progpolymsci.2007.09.005
- 24. N. Nishat, R. Rasool, S. Parveen, and S. A. Khan, *J. Appl. Polym. Sci.* **2011**, *122*, 2756–2764. **DOI:**10.1002/app.34100
- A. Vlad, M. Cazacu, G. Munteanu, A. Airinei, and P. Budrugeac, *Eur. Polym. J.* 2008, 44, 2668–2677.
 DOI:10.1016/j.eurpolymj.2008.05.014
- L. Ravi Kumar, V. Sengodan, M. Balaji Prasad, K. Gopalakrishnan, and K. Sethupathi, *Int J Polym Mater.* 2007, 56, 197–206. DOI:10.1080/00914030600773628
- 27. J. Runt and J. Huang, in: S. Z. D. Cheng (Ed.): Chapter 8 Polymer blends and copolymer, Applications to polymers and plastics, Handbook of Thermal Analysis and Calorimetry. vol. 3, Elsevier Science B.V., 2002, pp. 273–294.
 DOI:10.1016/S1573-4374(02)80011-5

- Z. Youming, D. Xinrong, W. Liangcheng, and W. Taibao, *J Incl Phenom Macrocycl Chem.* 2008, 60, 313–319.
 DOI:10.1007/s10847-007-9379-z
- D. Nepal, S. Samal, and K. E. Geckeler, Macromolecules.
 2003, 36, pp. 3800–3802. DOI:10.1021/ma0258410
- 30. S. B. Park, H. Kim, W. C. Zin, and J. C. Jung, Macromolecules. **1993**, *26*, 1627–1632. **DOI**:10.1021/ma00059a021
- 31. S. Mondal, and N. Das. *RSC Advances*. **2014**, *4*, 61383–61393. **DOI:**10.1039/C4RA10476E
- R. K. Pettit, C. A. Weber, M. J. Kean, H. Hoffmann, G. R. Pettit, R. Tan, K. S. Franks, and M. L. Horton, *ANTIMICROB AGENTS CH.* 2005, 49, pp. 2612–2617.
 DOI:10.1128/AAC.49.7.2612-2617.2005
- O. Catanescu, M. Grigoras, G. Colotin, A. Dobreanu, N. Hurduc, and C. I. Simionescu, *Eur. Polym. J.* 2001, *37*, 2213–2216.
 DOI:10.1016/S0014-3057(01)00119-7
- F. Qureshi, M. Y. Khuhawar, T. M. Jahangir, and A. H. Channar, *Acta Chim Slov.* 2016, 63, 113–120.
 DOI:10.17344/acsi.2015.1994
- F. Qureshi, M. Y. Khuhawar, and T. M. Jahangir, Acta Chim Slov. 2018, 65, 718–729. DOI:10.17344/acsi.2018.4419
- 36. S. Çulhaoğlu and İ. Kaya, *₹८१७*. **2015**, *39*, pp. 225–234. **DOI:**10.7317/pk.2015.39.2.225
- S. Ankushrao, Y. Patil, V. Ubale, N. Maldar, and A. Ghanwat, *J MACROMOL SCI A.* 2017, 54, 411–417.
 DOI:10.1080/10601325.2017.1313155
- D. Sek, B. Jarzabek, E. Grabiec, B. Kaczmarczyk, H. Janeczek, A. Sikora, A. Hreniak, M. Palewicz, M. Lapkowski, and K. Karon, Synth. Met. 2010, 160, 2065–2076.
 DOI:10.1016/j.synthmet.2010.07.026
- 39. İ. Kaya, A. Avcı, and K. Temizkan, *Macromol res.* **2017**, *25*, 45–53. **DOI**:10.1007/s13233-017-5002-3
- 40. P. Dutta, P. Jain, P. Sen, R. Trivedi, P. Sen, and J. Dutta, *Eur. Polym. J.* **2003**, *39*, 1007–1011.

DOI:10.1016/S0014-3057(02)00328-2

- A. Hafeez, Z. Akhter, J. F. Gallagher, and H. M. Siddiqui, *DES MONOMERS POLYM.* 2017, 20, 74–88.
 DOI:10.1080/15685551.2016.1231042
- 42. İ. Kaya B. Ayten, and D. Şenol, *Opt. Mater.* **2018**, *78*, 421-431. **DOI:**10.1016/j.optmat.2018.02.057
- 43. N.Y. Baran, M. Karakışla, H.Ö. Demir, and M. Saçak, *J. Mol. Struct.* **2016**, *1123*, 153–161. **DOI:**10.1016/j.molstruc.2016.06.028
- 44. F. Deng, W. He, A. S. Luyt, and Y. Y. Jiang. *Chin. Chem. Lett.* **2011**, *22*, 109–113. **DOI:**10.1016/j.cclet.2010.09.019
- 45. S. Banerjee, C. Saxena, P. K. Gutch, and D. C. Gupta. *Eur. Polym. J.* **1996**, *32*, 661–664.

DOI:10.1016/0014-3057(95)00178-6

Povzetek

Tri nove alifatsko-aromatske polimere z naftilnimi obroči smo pripravili s polikondenzijo dialdehidov ali diketonskih monomerov z 1,5-naftalendiaminom ali 1,4-fenilendiaminom. Monomere smo pripravili z reakcijo aromatskega aldehida ali ketona z 1,6-dibromoheksanom. Molekulsko maso monomerov smo določili z masno spektrometrijo z elektronsko ionizacijo (EI-MS). Monomere in polimere smo karakterizirali z NMR spektroskopijo (¹H NMR), infrardečo spektroskopijo (FT-IR), UV-VIS spektroskopijo, vrstično elektronsko mikroskopijo (SEM) in termogravimetrično analizo (TG / DTA). S fluorescenčno spektroskopijo monomerov in polimerov smo določili kvantne izkoristke spojin. Pri vseh preučevanih spojinah smo zaznali fluorescenco, ki se je kazala v vijoličnih, modro-zelenih, oranžnih in rdečih emisijah. Kvantni izkoristek polimerov so bili v razponu od 0,04 % do 24,3 %. Semikristalinično in amorfno naravo polimerov smo analizirali s pomočjo rentgenske praškovne difrakcije. Proučevali smo protimikrobne aktivnosti polimerov napram različnimi vrstam bakterij in gliv. Sposobnost tvorbe sintetiziranih polimerov s tankim filmom smo ocenili tako, da smo pripravili njihove mešanice s PVC (polivinilklorid) v različnih masnih razmerjih.



Except when otherwise noted, articles in this journal are published under the terms and conditions of the Creative Commons Attribution 4.0 International License

6

Scientific paper

A Novel Application of EIS for Quantitative Coating Quality Assessment During Neutral Salt Spray Testing of High-Durability Coatings

Marina Mrđa Lalić^{1,2*} and Sanja Martinez¹

¹ University of Zagreb, Faculty of Chemical Engineering and Technology, Department of Electrochemistry, Savska cesta 16/I, 10000 Zagreb, Croatia

> ² Koncar Power Transformers Ltd, A Joint Venture of Siemens and Koncar d.d., Josipa Mokrovica 12, 10000 Zagreb, Croatia

* Corresponding author: E-mail: marina.mrda@siemens.com Phone: +385 99 2951 416

Received: 03-07-2019

Abstract

The aim of the study was to exemplify the benefits of using electrochemical impedance spectroscopy (EIS) for quantification of coating quality during accelerated corrosion testing before the appearance of visual changes on the surface of the coating. The study included an innovative application of the commercial flexible gel electrodes in a two-electrode setup for following the impedance of the two high-durability offshore coating systems exposed to 1440 h of neutral salt spray (NSS) according to EN ISO 9227. The results were compared to those of the EIS measurements during 8000 h long exposure to a liquid electrolyte in a press-on cell according to the established EN ISO 16773 method. Complementary methods of differential scanning calorimetry, Fourier transform infrared spectroscopy and thermogravimetric analysis have been used for surface, interface and depth profiling of coating characteristics that were commented with respect to the EIS results.

The technique was applied on high-durability coatings Zn(R) + EP + EP or PUR intended for the protection in the coastal and offshore areas corresponding to C5- (H) and CX corrosivity categories in accordance with EN ISO 12944. EIS has been found to give sound quantitative results for coating impedance and a good estimation of long term coating behaviour within the first 100 h of accelerated exposure. It can be considered a promising tool for the early detection of coating damage during weathering tests.

Keywords: Durability of coatings; EIS; salt spray chamber; organic coatings degradation

1. Introduction

At present, epoxy and polyurethane coatings are the predominant types of coatings used in the offshore industry. Since offshore construction coatings face outdoor exposure continuously throughout their service life, which includes high relative humidity, rain, a saline corrosive atmosphere and high UV radiation, their lifetime is shortened. The expected lifetime for an offshore construction is 20 years or more and high-performance coatings are required for this application to avoid excessive and expensive maintenance operations and the loss of revenue. An anticorrosive coating system usually consists of multiple layers of different coatings with different properties and purpose. A typical anticorrosive system for highly corrosive marine environments usually consists of a primer, one or several intermediate coats, and a top coat. The function

of the primer is to protect the substrate from corrosion and to ensure good adhesion to the substrate. The function of the intermediate coat is to build up the thickness of the coating system and impede the transport of aggressive species to the substrate surface. The topcoat is exposed to the external environment and must provide the surface with the required colour and gloss.

The overall system is characterized by high electrical resistance and low capacitance which may quickly and easily be quantitatively measured, especially, after the development of advanced EIS instruments having: pA current measurement range, high input impedance up to 1 $T\Omega$, variable gain amplifiers, variable filters input front-ends and a floating ground. 2,3 Over the last few decades, electrochemical methods have found widespread use for characterization of anticorrosive coatings and have been commonly employed to assess the performance and durability

of anticorrosive coatings in the laboratory.4 By making periodic EIS measurements during the exposure to the corrosive environment, the level of coating damage can be estimated. EIS is a non-destructive measurement that may be used to track the condition of a coated metal sample as it changes.⁵ Equivalent circuit models using passive electrical engineering and physics circuit elements have commonly been used to help interpret EIS studies of coating systems. Data analysis procedures need to use non-linear, complex least squares fitting algorithm program of these equivalent electrical circuits (EEC) models to the EIS data.6 EEC is commonly used to interpret EIS studies of coating systems, but in some cases, calculated data from EEC models are not completely comparable with experimental data, moreover finding an exact matched model is quite difficult. The performance of the coating is evaluated according to the magnitude of the parameters in the equivalent circuit and their changes with exposure time.⁷⁻¹⁰ Other approaches such as minimum phase angle and its frequency, frequency breakpoint, the impedance at low frequency, the changing rate of impedance and phase angle at high frequencies have been used by some researchers to avoid these problems. 11 It is accepted among researchers that the initial step in the degradation process is the loss of dielectric properties of the polymer resulting from water ingress into the coating film. The relation between the initial and final coating capacitance may be an appropriate parameter by which to rank coating lifetime. 12 Also, low frequency coating resistance is taken as an indicator of coating quality.⁷⁻⁹ Excellent coatings have resistance values $10^{8} - 10^{12} \Omega \text{cm}^{2}$ and poor corrosion protection properties are exhibited when resistance intensity drops below $10^5 \,\Omega \text{cm}^2$. The appearance of coating defects is observed when coating impedance value falls below $10^6 \,\Omega \text{cm}^{2.14} \,\text{Im}$ pedance greater or equal to $10^9 \Omega$ corresponds to excellent protecting properties of coatings which provide almost purely capacitive behaviour over long exposure periods.¹⁵ The described EIS model may be applied to various industrial coating types and thicknesses providing a universal tool for coating quality and protective ability compari son^{1-18} .

The coatings industry regularly applies spectroscopic^{16–21} and thermal analysis^{18,22,23} methods that allow the assessment of coating characteristics before and after their exposure to a wide variety of service conditions. These methods are complementary to EIS because unlike EIS, they do not generate quantitative data that relates to barrier properties of a coating on a metal substrate but rather data related to the coating surface chemistry and bulk polymer thermal behaviour.

Nowadays, the most commonly employed method to assess offshore (CX corrosivity class) coating systems quality relies on long-term cyclic exposure in a climatic chamber until visible signs of coating degradation appear. Moreover, the 2017 edition of EN ISO 12944-6 standard redefines coating durability classes and suggests the appli-

cation of cyclic accelerated corrosion tests for C4 of high and very high durability and C5 coating systems of high and very high durability. Due to the long duration of 4200 h and a high cost of such tests, the change could incur significant expense to coating manufacturers. The advantage of EIS is that it can indicate changes in the coating long before any visible damage commences,^{5,24} hence it is of great technical importance to investigate quantification of the coating quality by EIS with the prospects of early detection of coating degradation during accelerated testing as well as during exposure to service conditions.

In the present study, two coating systems consisting of zinc epoxy primer and two epoxy coats one with, and the other without the polyurethane topcoat, have been investigated. The focus of the investigation was on early detection of coating degradation during exposure to neutral salt spray (NSS) done according to the EN ISO 9227 standard and corresponding to the requirement for C5 and CX categories as defined by ISO 12944-6. EIS has been measured periodically during the NSS test by shortly stopping the exposure to salt mist and performing measurements with the flexible gel electrodes which enabled capturing of the momentary coating state. ^{2,3,25-27} For comparison, measurements have also been done by EIS according to EN ISO 16773 standard and by FTIR, DSC and TGA methods.

2. Experimental

2. 1. Material and Preparation

Carbon steel sheets with dimensions of $(100 \times 150 \times$ 10 mm) were used as a metallic substrate. The samples were sand-blasted to Sa 2.5 (according to EN ISO 8501-1) and the surface was cleaned from visible oil and dirt. Two coating system denoted as System A and System B have been applied to the carbon steel panels by the air spraying technique. The application has been done according to the instructions of the manufacturer, and therefore it may be assumed that the application process has no consequences on the observed behaviour of the coatings. Specifications of the selected two-component coating systems are shown in Table 1. The main component in basecoat is zinc dust (50-75%) in addition bisphenol A epoxy resin, xylene, solvent naphtha. The intermediate coat is high solids epoxy polyamide adduct cured contain bisphenol A epoxy resin (10-25%). Topcoat cured with aliphatic isocyanate and contains zinc phosphate. The minimum number of layers and the nominal film thickness of each coating is determined according to the type of coating materials, the corrosivity category and the required durability. System A corresponded to the System No. C5.7, for corrosivity category C5, with a lifetime of 15 to 25 years and a nominal dry film thickness (NDFT) > 260 µm according to ISO 12944-5. System B corresponded to the System No. C5.8, for the extreme corrosivity category CX (Offshore) with a lifetime of range more than 25 years and an NDFT > 320 μm. The

Table 1. Specifications for the investigated commercial coating systems

Coating system	Number of layers	Coating type	Cumulative thickness (µm)	Base polymer	VOC (g/L)	Solvents by weight (%)
System A	2	Basecoat	270	Zinc rich epoxy	307	44
		Intermediate coat		Epoxy (polyamide)	216	50
System B	3	Basecoat	460	Zinc rich epoxy	307	44
•		Intermediate coat		Epoxy (polyamide)	216	50
		Topcoat		Acrylic polyurethane	336	36

coatings consisted of two components, a resin and a hardener component.

2. 2. Instrumentation

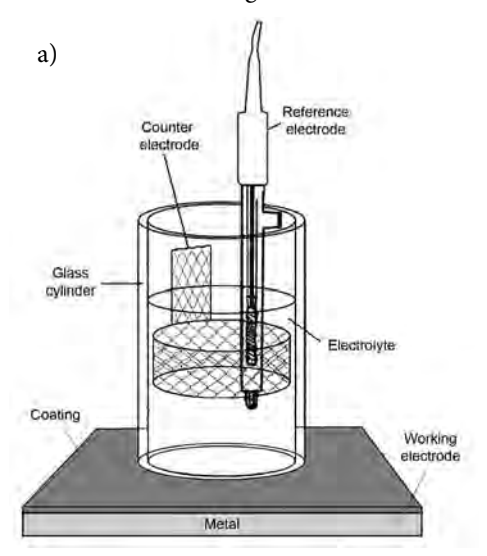
2. 2. 1. Electrochemical Impedance Spectroscopy (EIS) Measurements

EIS measurements started two months after the application of the coating which allowed for proper drying. EIS measurements were carried out at the open circuit potential (OCP) with a DC potential amplitude of 10 mV in the frequency range of 10^4 Hz to 10^{-2} Hz. The coated steel panels were put into a Faraday cage which eliminated external electromagnetic noise during the EIS testing. The three-electrode cell constructed according to EN ISO 16773 consists of an inert cylinder, which is attached to the coating surface and filled with electrolyte. A stainless-steel mesh serves as the counter electrode (CE) and the metal substrate is the working electrode (WE). The counter electrode has a circular hole in the middle where the calomel reference electrode (SCE) is protruding.²⁸ A two gel-electrode system consists of a pair low-cost, commercial polymeric gel electrodes placed in parallel at the surface of the metal.²⁹⁻³¹ One electrode is connected to the working electrode input of the potentiostat and the other to the reference and counter electrode input. Schematic setup of the measurement cells is shown in Figure 1. Details of the Recorr CQC customized instrumental setup that has been developed in our laboratory were presented previously.³² Calibration of the setup has been done according to EN ISO 16773-3, on a high-impedance dummy cell mimicking the coating. The EIS data is analysed based on the low frequency impedance at 0.1 Hz and the shape of the Bode plot curves. The performance of the coating is evaluated according to the magnitude of impedance and its change with the exposure time.^{33,8–9}

For the three-electrode system the exposed coated sample area was $28,27~\rm cm^2$ and for the two-electrode system, the area was $32~\rm cm^2$. Coating degradation was induced in two ways: by exposure to liquid 3.5% sodium chloride (NaCl) at room temperature (21 °C) for 8000 h in a test conducted according to EN ISO 16772 and by exposure to NSS of 5% NaCl at 35 °C according to EN ISO 9227 for $1440~\rm h$. In both cases measurements were carried out in time intervals that enabled capturing of the significant changes in the extent of coating degradation.

2. 2. 2. Fourier Transform-Infrared Spectroscopy (FTIR) Measurements

Chemical changes were measured with Fourier Transform Infrared (ATR-FTIR)³⁴ spectroscopy method before and after exposure of the samples to external conditions. *PerkinElmer spectrometer Spectrum One*, USA con-



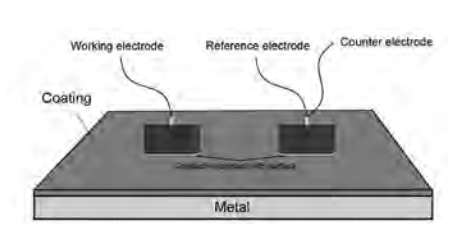


Figure 1. a) a three-electrode cell constructed according to EN ISO 16733 and b) a two-electrode setup.³²

b)

nected to a computer program interface for capturing the sample spectrum has been used. Each spectrum was an average of ten scans recorded with a resolution of 4 cm⁻¹. Attenuated Total Reflection (ATR-FTIR) method applied directly on coated samples has a limitation of the measurement range from 4000 to 650 cm⁻¹ and part of the spectrum between 650 and 200 cm⁻¹ is lost. Therefore, FTIR was also measured in transmission mode in a spectral range from 4000 to 450 cm⁻¹. This required preparation of samples in the form of pellets in accordance with the standard ASTM E1252:200735. 3 mg of scraped powder from the surface of each coated sample was mixed into 350 mg of spectroscopically pure KBr. The mixture was milled in agate mortar until we obtained a fine and very homogeneous mixture. Samples with KBr were then hydraulically pressed into a 13 mm stainless steel die and resulting pellets further subjected to FTIR measurement.

2. 2. 3. Thermogravimetric Analysis (TGA) Measurements

Thermal stability of each coating system was investigated using Q500 (TA instruments) with auto sampler controlled by TA Universal Analysis software. The epoxy (polyamide) and acrylic polyurethane films were applied on a plastic foil with an applicator in range 0.16–0.25 mm and dried at room temperature for 72 h. The experiments were performed in nitrogen atmosphere (flow of 40–60 ml min⁻¹) at a heating rate of 10 °C min⁻¹ over the temperature range of 1000 °C.

2. 2. 4. Differential Scanning Calorimetry (DSC)

DSC is a thermal analysis technique commonly used to determine parameters such as glass transition temperatures (Tg), melting points (mg) and heat capacities of materials. 9 Tg of samples was measured by DSC before and after exposure to the salt spray chamber. The measurements were carried out on Mettler Toledo DSC 823 controller at a scan rate of 20 °C min $^{-1}$ over the temperature range from 0 to 90°C in two heating cycles under a nitrogen atmosphere with a constant flow of 60 mL min $^{-1}$. All samples (10 mg \pm 3 mg) were weighed and sealed in a hermetic aluminium pan with lids. The measurement was conducted according to the EN ISO 11357.

3. Results and Discussion

3. 1. EIS Results

Measurements of impedance obtained by the two flexible electrodes setup are shown in Figure 2 for systems A and B. Bode plots of the intact coating show its excellent protective action, i.e. the low-frequency impedance greater than $1.0 \times 10^{11} \, \Omega$. Measurements of impedance obtained by the three electrodes setup in a cell filled with

3.5% NaCl are shown in Figure 3. The initial measurements were done after 2.5 h of exposure and the measured Bode curves show the low-frequency impedance value is already below $1.0 \times 10^{10} \Omega$, which is significantly lower than the impedance of the intact coating.

Low-frequency impedance read at 0.1 Hz and normalized by the electrode area is shown as a function of exposure time for coating systems A and B in Figure 3, for the NSS and 3.5% NaCl tests. It is evident that the low-frequency impedance value in all cases drops sharply during the first 100 h of exposure. For system A, in both tests, the final impedance falls to the values around $10^7 \Omega \text{ cm}^2$, although initially being by almost an order of magnitude lower for the NSS test. This would imply that more severe corrosive conditions are attained during the NSS test than during immersion in 3.5% NaCl when it comes to epoxy coating. Deflorian et al. compared the results obtained by EIS and salt spray, have visually observed that the samples were nearly intact after more than three months of immersion but had many blisters on the coating after only a few weeks of salt spray exposure.³⁶

System A is made up of zinc rich basecoat and an epoxy topcoat applied at a thickness of 270 μ m. Hence, the drop in low-frequency impedance is larger for system A than for the System B that has an extra layer of polyure-thane and a total thickness of 460 μ m.

For system B, in both tests, the final impedance falls to values around $10^{10}~\Omega~cm^2$, although initially being by about half an order of magnitude higher for the NSS test. This would imply that more severe corrosive conditions are attained during the 3.5 % NaCl immersion test than during the NSS test when it comes to polyurethane coating. This is in concordance with the well-known, superior performance of epoxy coatings over the polyurethane coatings under immersion conditions. 14

The oscillatory behaviour of impedance during the EIS tests has been observed previously and might be explained by pore blockage by corrosion products and the random formation of macroscopic perforations in the coating.³⁷ Although the authors refer to the observed oscillations as a drawback of the EIS method and its failure to give reproducible results, it should be noted that the result in fact shows the ability of EIS to authentically reflect the true state of the coating. The oscillatory effect is more pronounced for the lower quality coating and for the NSS exposure. Nevertheless, the average impedance of each system can readily be deduced from the plots and rating of the coating quality can be done with reasonable confidence. According to the literature criteria based on the impedance at 0.1 Hz,³⁸ system B may be rated as excellent and system A as fair.

Besides the quantitative rating of the coating quality, much can also be deduced from the shape of the Bode plots.³⁹ To simplify conclusions and explicate the potential for widespread use of the suggested method, the shape of the Bode curves is explained.

It is widely accepted that the EIS spectrum of an efficient protective coating can be presented by a simple model of capacitance in a parallel to a resistance. 40 High-frequency impedance response for the intact coating is a straight line with the unit negative slope and the phase angle close to -90°, as seen from Figure 2 a) and Figure 3 a). Such a dependency is characteristic of almost pure capacitive behaviour. It is well known that, during exposure to an electrolyte, the coating first shows deviation from the capacitive behaviour. 41 An increase of the phase angle slope from -1 to higher values in the high-frequency region signifies frequency dispersion that requires the substitution of pure capacitance for the CPE element in the coating equivalent circuit. CPE probably reflects water ingress within the polymer matrix causing a variety of RC combinations in parallel forming a distributed equivalent circuit.⁴²

Corrosion initiation at the substrate causes a second time constant appearance at frequencies below 1 Hz. ⁴⁰ The low frequency response depends on the rate of the charge transfer reaction at the base of polymer defects and below the delaminated coating. The nested low-frequency equivalent circuit is comprised of a double layer capacitance and a polarization resistance. When diffusion effects in the coating pores are present, the Warburg element is added in series with the charge transfer resistance.

In the case of System A, the two time constants are clearly visible even for the 100 h of exposure to NSS. In the case of system B, a mild indication of the low-frequency time constant that almost completely overlaps with the high-frequency one is observed. Narrowing of the capacitive region, depression of the phase angle and deflection of the impedance slope from -1 are more pronounced for the system A.

For the 3.5% NaCl immersion tests, system A shows poorly resolved low-frequency time constant only for the longest time of exposure confirming the previously mentioned good protective properties of the epoxy coating under immersion conditions. System B again shows overlapping time constants but retains higher phase angle values than in the NSS experiment.

Photographs of both systems prior to exposure and after the NSS and 3.5% NaCl tests are shown in Figure 5. No apparent coating defects are visible. System B shows mild browning of the surface colour after the NSS test that may indicate substrate corrosion and corresponds to the pronounced low-frequency time constant observed for this coating. A conclusion about the comparable protective ability of the coatings might be drawn from the visual assessment of the coated specimen after the NSS and 3.5% NaCl tests. It is now obvious why the coating tests for high

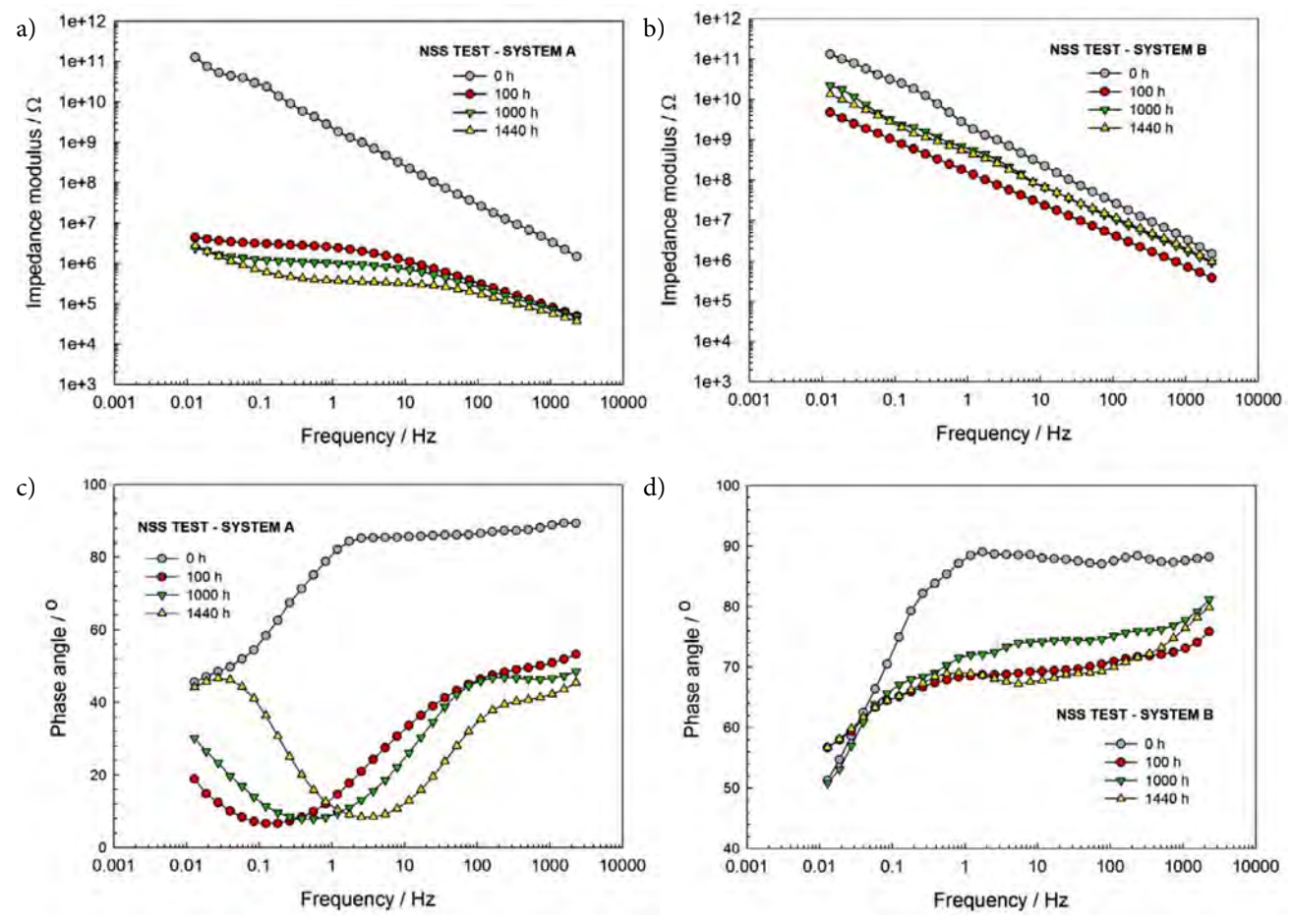


Figure 2. Bode plots of a) and c) system A samples and b) and d) of system B samples exposed to NSS.

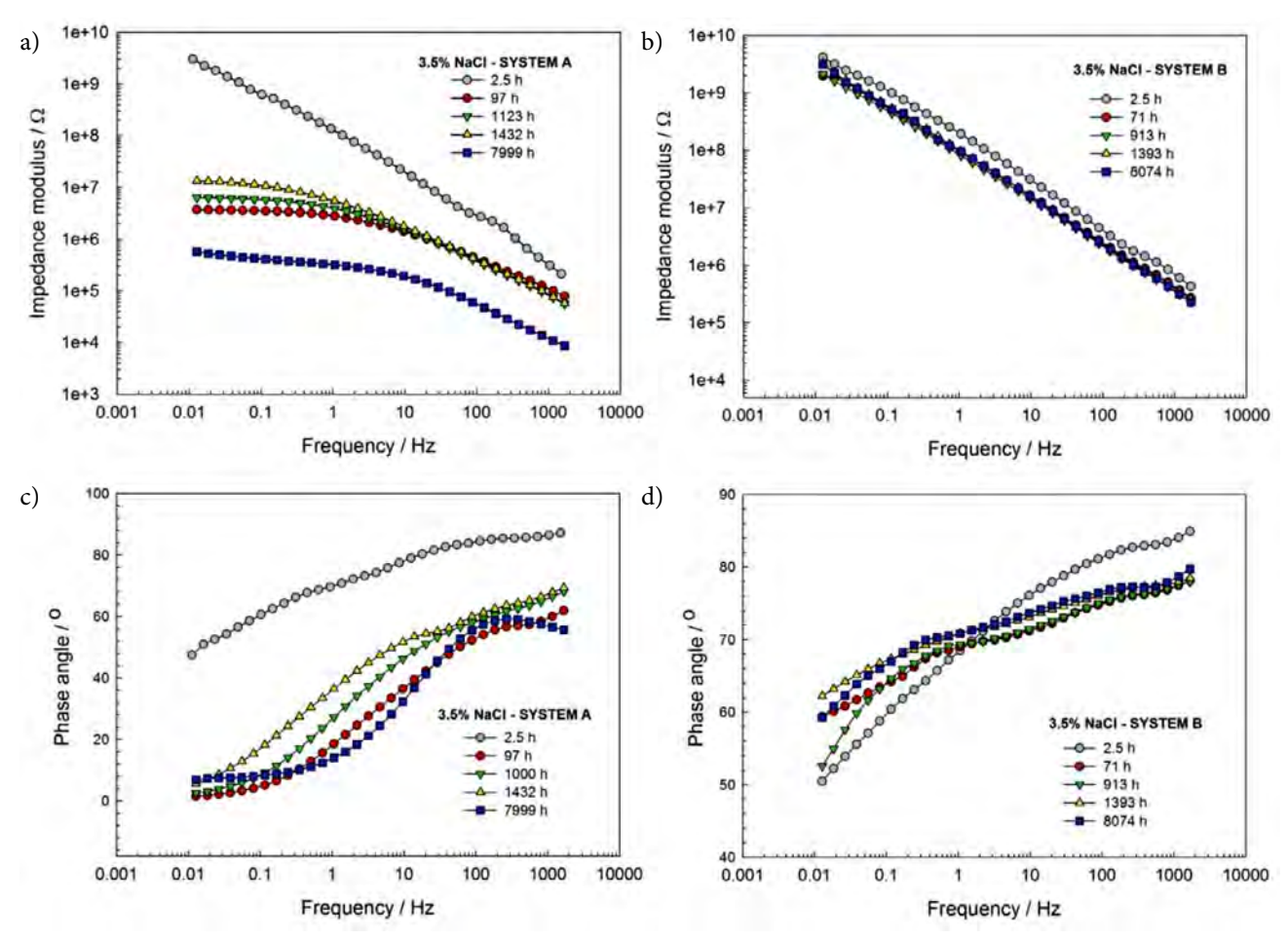


Figure 3. Bode plots of a) and c) system A samples and b) and d) of system B samples exposed to 3.5 % NaCl.

and very high durability coating systems given in the new edition of the EN ISO 12944-6 standard suggest gradual transfer from the NSS test to the considerably longer and more expensive cyclic exposure tests that would probably inflict visible difference among the coating systems intended for heavy-duty service conditions.

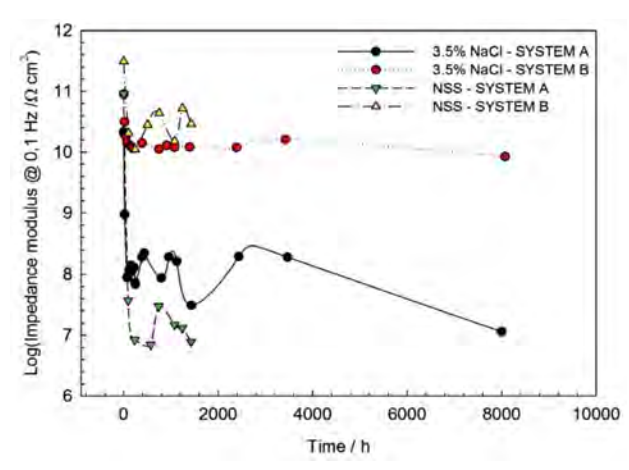


Figure 4. Low-frequency impedance read at 0.1 Hz as a function of exposure time for coating systems A and B during exposure to 3.5 % NaCl and NSS.

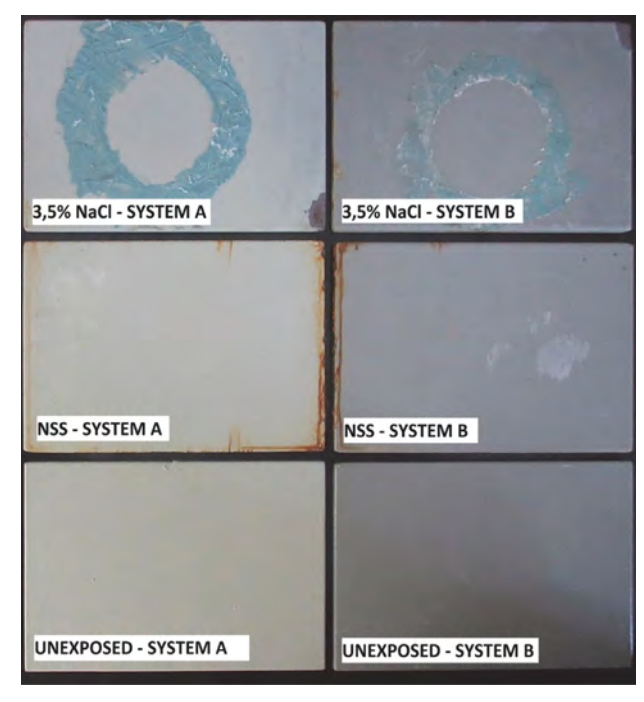


Figure 5. Photographs of specimens coating systems A and B before exposure, after exposure NSS and after exposure 3.5 wt% NaCl solution

3. 2. Characterization of Coating System by FTIR

Figures 6 and 7 show the spectra for systems A and B, respectively, before and after exposure to NSS and 3.5% NaCl tests. Spectra were obtained in two ways, by the ATR FTIR method and from KBr pellets containing scraped powder form the sample surface. It can be concluded that all the spectra shown in Figure 6 show characteristic bands of epoxy resin bisphenol A around 827 cm⁻¹; 1245 cm⁻¹; 1509 cm⁻¹.⁴³ The spectra in Figure 7 correspond to acrylic polyurethane resin.⁴⁴

tigated organic coatings do not change significantly after exposure which demonstrates a lack of degradation. No bands corresponding to corrosion products are observed. New absorption bands did not appear, except in the case of the system B exposed to 3.5% NaCl which shows a new band at 2345 cm $^{-1}$ corresponding to $\mathrm{CO}_2.^{45}$

It has been observed that when chemical bonds in the polyurethane coating are fractured under UV irradiation free radicals are generated, releasing $\mathrm{CO_2}$. Since the sample has not been exposed to UV irradiation, the appearance of $\mathrm{CO_2}$ is probably due to the reaction of unreacted isocyanate with the water from the salt cabinet. The

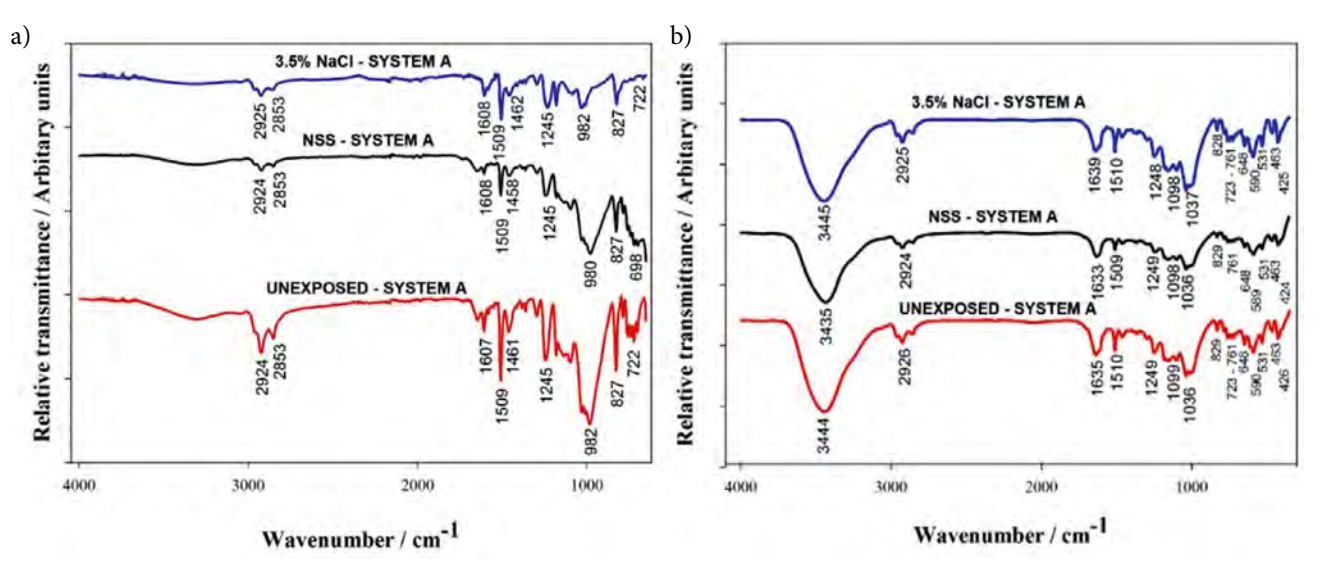


Figure 6. Spectra for system A before and after exposure to NSS and 3.5% NaCl tests obtained a) by the ATR FTIR method and b) from KBr pellets containing the scraped powder form the sample surface.

No clear conclusion about the difference in the state of the coatings before and after exposure can be deduced from the fingerprint region in Figures 6 and 7. The locations, the width and the intensity of the bands of the invesfact that CO₂ is observed only in the scraped powder indicates its residence within the polymer matrix.

S. Rashtchi et al. state that the spectral region between 3400 cm⁻¹ and 3700 cm⁻¹ is the best indicator of the

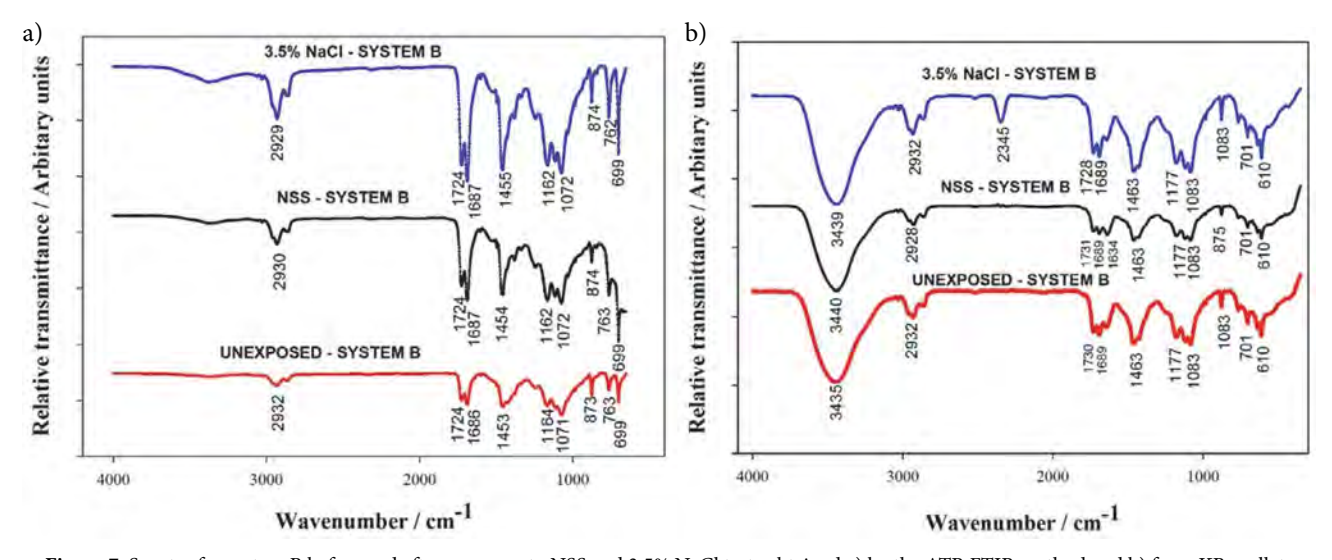


Figure 7. Spectra for system B before and after exposure to NSS and 3.5% NaCl tests obtained a) by the ATR FTIR method and b) from KBr pellets containing the scraped powder form the sample surface.

moisture presence.⁴⁶ It should be noted that after the NSS and 3.5% NaCl experiments the painted samples were left for 3 months at room temperature and humidity, which allowed them to dry.⁴⁷ This could account for the almost complete lack of bands ascribed to water in ATR spectra.

Conversely, KBr pellets' show a well resolved band at $3440~\rm cm^{-1}$ as well as the less resolved bands between $1634~\rm and~1639~\rm cm^{-1}$ for both coating systems. These bands denote the presence of water and indicate (–OH) stretching and scissors vibrations of the bonded water molecules, respectively. This water is probably due to the improper drying of KBr pellets.

3. 3. Characterization of Coating System by DSC and TGA

Glass transition temperature for coating systems A and B before and after exposure to NSS in test and to 3.5 % NaCl test is presented in Figure 8. Two glass transition temperatures denoted as T_{ghi} and T_{glo} have been measured for all the coatings indicating a biphasic system that could be related to the homogeneity of water distribution in the polymer.⁴⁸

For both systems decrease in T_{ghi} values after exposure to NSS is \leq 4 °C and may be considered insignificant as it barely exceeds the measurements uncertainty of DSC that is taken as equal to 3 °C. T_{ghi} values after exposure to 3.5% NaCl, as well as all the T_{glo} values, are increased by up to 12 °C.

 $T_{\rm g}$ decrease for both systems is probably related to the water residing in the polymer free volume. The increase in $T_{\rm g}$ values may be explained by the water ingress into the polymer network and secondary cross-linking through the formation of multiple hydrogen bonds between water and polymer. DSC experiments were done on the same samples as FTIR. Apparently, after the 3

months drying period, the final state of the samples indicates irreversible changes in the form of multiple hydrogen bonded water residing in highly cross-linked zones of the polymer. 50

According to Del Grosso the water in the intact coating can be detected with TGA at 110 °C. ⁵¹ TGA curves of the intact epoxy and polyurethane coatings are shown in Figure 8 b. Weight losses of 1.62% for epoxy (polyamide) and 1.30%, for acrylic polyurethane, corresponding to the water content were recorded when the temperature reached 110 °C.

Full degradation occurred beyond 900 °C leaving the residues of various weight loss percentages at the end of the TGA curve presented in Table 2. These are in good agreement with the declared percentage of solids by weight for the two coatings. TGA experiments showed two stages of weight loss for epoxy (polyamide) and three stages for acrylic polyurethane. An abrupt weight loss in coating systems was observed at high temperatures from approximately 300 to 500 °C.

Table 2. Residual weight loss percentage of coating systems by thermogravimetric analysis

Coating system	Residue at 900 °C (% by weight)
epoxy (polyamide)	50,11
acrylic polyurethane	34,29

4. Conclusions

It has been demonstrated by this investigation that the EIS method gives a possibility of quantification of coating degradation and estimation of its long-term performance from the first 100 h of exposure to NSS in the EN

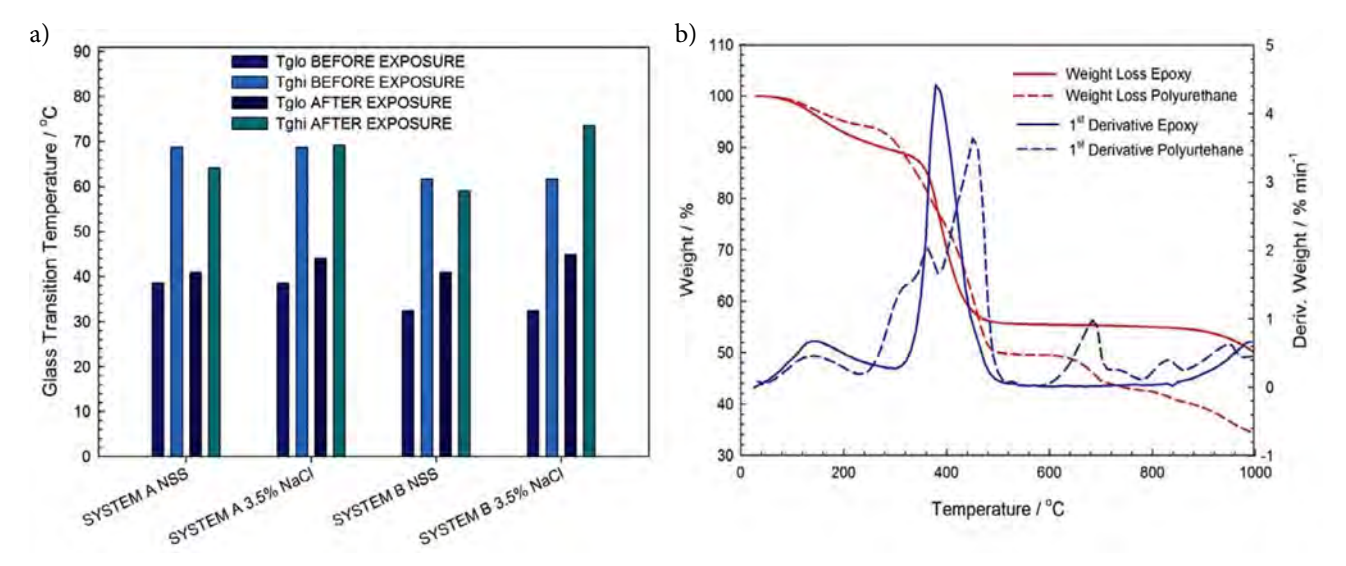


Figure 8. a) glass transition temperatures for coating systems A and B before and after exposure to NSS and to 3.5% NaCl and b) TGA curves of intact epoxy (polyamide) epoxy and acrylic polyurethane coatings.

ISO 9227 test and to the 3.5% NaCl in EN ISO 16773 test. Contrarily, prolongation of the tests to 1440 h in the case of NSS exposure and to 8000 h in the case of 3.5% NaCl exposure has produced no visible degradation signs on the coatings.

FTIR, DSC and TGA results preferentially gave information about the water absorbed within the coating that resides within the polymer free volume and within the polymer network. DSC method indicates irreversible changes related to the water ingress into the polymer network. Besides the water ingress, further irreversible changes related to the degradation of barrier properties of the coatings due to the corrosion at the bottom of the coating pores and under delaminated coating are DSC method indicates irreversible changes related to the water ingress into the polymer network. Besides the water ingress, further irreversible changes related to the degradation of barrier properties of the coatings due to the corrosion at the bottom of the coating pores and under delaminated coating are detectible by EIS.

Finally, both, quantitation of the coating behaviour during long-term accelerated weathering exposures by the impedance modulus at 0.1 Hz and the analysis of the shape of the Bode plots can give early information about the coating quality. Widespread use of this method could reveal patterns common to the frequently used high-performance coatings, strengthen the conclusions of this study and considerably shorten the time and cost of coating quality assurance.

Acknowledgements

The authors would like to thank professor dr. sc. Mirela Leskovac from the Department of Surface Engineering of Polymer Materials, Faculty of Chemical Engineering and Technology to helped in handling of the instruments for DSC and TGA methods and Ivana Šoić for help with FTIR method.

5. References

- 1. H. L. Dedeurwearder, Protecting Offshore Wind Farm Towers, *JPCL*, **2015**, https://www.paintsquare.com (assessed: March 04, 2019)
- S. Grassini, S. Corbellini, M. Parvis, E. Angelini, F. Zucchi, J. Int. Meas. Confed., 2018, 114, 508–514.
 DOI:10.1016/j.measurement.2016.07.014
- 3. B. Ramirez Barat, E. Cano, *Chem. Electro. Chem.*, **2018**, 5, 2698–2716. **DOI**:10.1002/celc.201800844
- P. A. Sørensen, S. Kiil, K. Dam-Johansen, C. E. Weinell, J. Coat. Technol. Res., 2009, 6,135–176.
 DOI:10.1007/s11998-008-9144-2
- D. Loveday, P. Peterson, B. Rodgers, Evaluation of Organic Coatings with Electrochemical Impedance Spectroscopy Part
 Application of EIS to Coatings, http://www.consultrsr.net/ files/jct/JCT200502.pdf (assessed: February 28, 2019)

- B. R. Hinderliter, S. G. Croll, D. E. Tallman, Q. Su, G. P. Bierwagen, Electrochem. Acta, 2006, 51, 4505–4515.
 DOI:10.1016/j.electacta.2005.12.047
- A. A. Hashem, J. A. Carew, A. Hasan, Surf. Coat. Int., 1999, 82, 26–30. DOI:10.1007/BF02693014
- C. H. Tsai, F. Mansfeld, Corros. Sci., 1993, 49, 726–737.
 DOI:10.5006/1.3316106
- 9. C. Kong, *Material Mind.*, **2015**, 9, 27–28. **DOI**:10.1038/scientificamericanmind1116-28
- S. Skale, V. Doleček, M. Slemnik, *Prog. Org. Coat.*, **2008**, *62*, 387–392. **DOI**:10.1016/j.porgcoat.2008.02.003
- E. Akbarinezhad, M. Bahremandi, H. R. Faridi, F. Razaei, *Corros. Sci.*, 2009, 51, 356–364.
 DOI:10.1016/j.corsci.2008.10.029
- L. De Rosa, T. Monetta, D. B. Mitton, F. Bellucci, J. Electrochem. Soc., 1998, 145, 3830–3838. DOI:10.1149/1.1838881
- J. Neshati, M. Faradi, Surf. Eng., 2009, 20, 299–303.
 DOI:10.1179/026708404225016418
- S, Shreepathi, A. K. Gui, S. M. Naik, M. R. Vattipalli, *Jour. Coat. Techn. & Rese.*, 2011, 8, 191–200.
 DOI:10.1007/s11998-010-9299-5
- B. J. Merten, A. Skaja, D. Tordonato, D. Little, Re- evaluating Electrochemical Impedance Spectroscopy (EIS) for the Field Inspector's Tolbox: A Frst Approach https://www.usbr.gov/ research/projects/researcher.cfm?id=2334 (assessed: February.28, 2019)
- J. T. Zhang, J. M. Hu, J. Q. Zhang, C. N. Cao, *Prog. Org. Coat.*,
 2004, 51, 145–151. DOI:10.1016/j.porgcoat.2004.08.001
- X. F. Yang, C. Vang, D. E. Tallman, G. P. Bierwagen, S. G. Croll, S. Rohlik, *Polym. Degra. Stab.*, **2001**, *74*, 341–351.
 DOI:10.1016/S0141-3910(01)00166-5
- F. Deflorian, L. Fedrizzi, S. Rossi, Corros. Sci., 1998, 54, 98–605. DOI:10.5006/1.3287635
- E. Almeida, M. Balmayore, T. Santos, *Prog. Org. Coat.*, 2002, 44, 233–242. DOI:10.1016/S0300-9440(02)00056-5
- 20. M. R. Costa, M. T. Santos, T C. Diamantino, *Corros. Prot. Mater.*, **2011**, *30*, 57–64.
- 21. J. Li, L. Ecco, Fedel, Ermini, G. Delmas, J. Pan, *Prog. Org. Coat.*, **2015**, *87*, 179–188. **DOI**:10.1016/j.porgcoat.2015.06.003
- 22. J. Li, C. S. Jeffcoate, G. P. Bierwagen, D. J. Mills, D. E. Tallma, *Corros. Sci.*, **1998**, *54*, 763–771. **DOI**:10.5006/1.3284797
- 23. M. F. M. Nazeri, M. S. M. Suan, M. N. Masri, N. Alias, M. W. A. Rashid, Y. Alias, A. A. Mohamad, *Int. J. Electrochem.*, 2012, 7, 9633–9642.
- 24. J. Mlntyre, H. Pham, Prg. Org. Coat., 1996, 27, 201–207. DOI:10.1016/S0022-4375(96)90001-8
- S. Grassini, Corros. Conser. Cult. Her Met. Art., 2013, 347–367. DOI:10.1533/9781782421573.4.347
- E. Anglini, S. Grassini, M. Parvis, F. Zucchi, Surf. Interface Anal., 2012, 44, 942–946. DOI:10.1002/sia.3842
- 27. S. Corbellini, M. Parvis, S. Grassini, *IEEE Transac. Instr. & Meas.*, **2012**, *61*,1193–1200. **DOI**:10.1109/TIM.2011.2175816
- 28. T. Bos, "Prediction of coating durability Early detection using electrochemical methods, *Delft University*, *The Netherlands*, PhD *Thesis*, **2008**.
- 29. S. Jamali, Y. Zhao, Z. Gao, H. Li, A. C. Hee, J. Int. Eng. Chem.,

- **2016**, 43, 36–43. **DOI:**10.1016/j.jiec.2016.07.045
- 30. B. Ramirez Barat, E. Cano, P. Letardi, Sens. Actuators B., **2016**, 43, 36–43. **DOI:**10.1016/j.snb.2018.01.180
- 31. Y. Kuo, Y. Lee, Y. L. Lee, *Jour. Inter. Measu. Confe.*, **2018**, *124*, 303–308. **DOI**:10.1016/j.measurement.2018.04.041
- 32. S. Martinez, Conference Corrosion and Surface Treatment in Industry, Viglas, Slovakia, 2019.
- A. A. Hashem, J. A. Carew, A. Hasan, Surf. Coat. Int., 1999, 82, 26–30. DOI:10.1007/BF02693014
- J. Coates, Encyclopedia of Analytial Chemistry: Application, Theory and Instrumentation. Interpretation of Infrared Spectra A Practical Approach, Newtown, USA, 2006.
 DOI:10.1002/9780470027318.a5606
- "ASTM Standard E1252: General Techniques for Obtaining Infrared Spectra for Qualitative Analysis, ASTM International, 2007.
- F. Deflorian, S. Rossi, L. Fedrizzi, J. Coat. Technol., 2000, 72, 81–87. DOI:10.1007/BF02698001
- M. Del Grosso Destreri, J. Vogelsang, L. Fedrizzi, F. Deflorian, *Prog. Org. Coat.*, **1999**, *37*, 69–81.
 DOI:10.1016/S0300-9440(99)00056-9
- 38. L. Gray, B. Drader, M. O'Donoghue, R.Garret, J. Garret, R. Graham, V. Datta, *Corrosion NACE*, **2003**, 03382.
- A. Alizadeh Razin, B. Ramezanzadeh, H. Yari, *Prog. Org. Coat.*,
 2016, 92, 95–109. DOI:10.1016/j.porgcoat.2015.11.023
- F. Mansfeld, J. Appl. Electrochem., 1994, 25, 187–202.
 DOI:10.1007/BF00262955

- 41. M. Kendig, J. Scully, *Corrosion*, **1990**, *46*, 22–29. **DOI:**10.5006/1.3585061
- 42. G. M. Ferra, E. M. P. van Westing, J. H. W. de Wit, *Corrosion Sci.*, **1994**, *36*, 957–977. **DOI:**10.1016/0010-938X(94)90197-X
- 43. N. Tudorachi, F. Mustata, *Arab. J. Chem.*, **2017**. In Press, **DOI**:10.1016/j.arabjc.2017.07.008
- 44. F. Lu, B. Song, P. He, Z. Wang, J. Wang, RSC Adv., 2017, 7, 13742–13748. DOI:10.1039/C6RA26341K
- 45. Y. Zhang, A spectroscopic study of the degradation of polyurethane coil coatings, *PhD Thesis*, *Queen Mary University of London*, **2012**.
- S. Rashtchi, P. D. Ruiz, R. Wildman, I. Ashcroft, SPIE Solar Energy and Technology, San Diego, California, United States, 2012. DOI:10.1117/12.928959
- 47. S. G. Croll, *Prog. Org. Coat.*, **2018**, *124*, 41–48. **DOI:**10.1016/j.porgcoat.2018.07.027
- 48. M. Y. M. Chiang, M. Fernandez-Garcia, *J. Appl. Polym. Sci.*, **2003**, *89*, 1436–1444. **DOI:**10.1002/app.11576
- 49. N. Fredj, S. Cohendoz, X. Feaugas, S. Touzain, *Prog. Org. Coat.*, **2010**, *69*, 82–91. **DOI:**10.1016/j.porgcoat.2010.05.009
- F. Deflorian, L. Fedrizzi, S. Rossi, P.L. Bonora, Electrochim. Acta, 1999, 44, 4243–4249.
 DOI:10.1016/S0013-4686(99)00139-5
- M. Del Grosso Destreri, J. Vogelsang, L. Fedrizzi, F. Deflorian, *Prog. Org. Coat.*, **1999**, *37*, 57–67.
 DOI:10.1016/S0300-9440(99)00056-9

Povzetek

Namen študije je bil prikazati prednosti uporabe elektrokemijske impedančne spektroskopije (EIS) za kvantifikacijo kakovosti premaza pri pospešenem korozijskem testiranju pred pojavom vizualnih sprememb na površini premaza. Študija je vključevala inovativno uporabo komercialnih fleksibilnih elektrod na osnovi gela za spremljanje impedance dveh visoko obstojnih premaznih sistemov, ki se uporabljajo v morski vodi. Vzorce smo 1440 ur testirali v slani komori v skladu z EN ISO 9227 (NSS test). Rezultate smo primerjali z meritvami EIS med 8000-urno izpostavljenostjo tekočemu elektrolitu v preskusni celici po uveljavljeni metodi EN ISO 16773. Za površinsko, vmesno in globinsko profiliranje premaznih lastnosti materiala smo poleg EIS uporabili še dodatne metode: diferenčno dinamično kalorimetrija (DSC), infrardečo spektroskopijo (FT-IR) in termogravimetrično analizo (TGA).

Metodo smo preučevali na visoko obstojnih premazih Zn(R) + EP + EP ali PUR, namenjenih za zaščito na obalnih in morskih območjih, ki ustrezajo kategorijam C5- (H) in CX korozivnosti v skladu z EN ISO 12944. Z EIS lahko dobimo dobre kvantitativne rezultate in tudi dobro oceno dolgoročnega obnašanja premaza v prvih 100 urah pospešene izpostavljenosti. Metoda EIS bi bila lahko primerna za zgodnje odkrivanje poškodb premazov.



Except when otherwise noted, articles in this journal are published under the terms and conditions of the Creative Commons Attribution 4.0 International License

Scientific paper

Interactions between Ibuprofen and Silicified-MCC: Characterization, **Drug Release and Modeling Approaches**

Rudra Narayan Sahoo, ¹ Ashirbad Nanda, ¹ Arunima Pramanik, ¹ Souvik Nandi, ¹ Rakesh Swain, 1 Sukanta Kumar Pradhan 2 and Subrata Mallick 1,*

> ¹ School of Pharmaceutical Sciences, Siksha 'O' Anusandhan (Deemed to be University), Kalinganagar, Bhubaneswar-751003, Odisha, India.

² Department of Bioinformatics, Orissa University of Agriculture and Technology, Bhubaneswar, Odisha, India.

* Corresponding author: E-mail: profsmallick@gmail.com Fax: +91-674-2350642; Tel: +91-674-2350635

Received: 03-06-2019

Running Title: Docking analysis of ibuprofen with SMCC

Abstract

Analysis of the binding interactions of ibuprofen and silicified-microcrystalline cellulose (SMCC) has been undertaken. Co-processing of ibuprofen with SMCC was carried out by solid state ball milling, and aqueous state equilibration followed by freeze drying to investigate the effect of silicified-microcrystalline cellulose on ligand. Molecular docking study revealed that ibuprofen formed complex through hydrogen bond with microcrystalline cellulose (MCC) and silicon dioxide (SiO₂); the binding energy between MCC and SiO₂, and ibuprofen and SMCC were found as -1.11 and -1.73 kcal/mol respectively. The hydrogen bond lengths were varying from 2.028 to 2.056 Å. Interaction of Si atom of SMCC molecule with Pi-Orbital of ibuprofen has shown the bond length of 4.263 Å. Significant improvement in dissolution of ibuprofen has been observed as a result of interaction. Binary and ternary interactions revealed more stabilizing interactions with ibuprofen and SMCC compared to SMCC formation.

Keywords: Co-processing; silicified microcrystalline cellulose; molecular docking analysis; binary interaction; ternary interaction.

1. Introduction

Molecular docking experiment was used to predict the binding mode interactions between the molecules.¹ The program uses Lamarckian genetic algorithm, semi empirical free energy force field, grid box based method to allow rapid evaluation of the binding energy and pre-calculating the interaction between every atom type pair at every distance and result clustering procedures. The force field is based on a comprehensive thermodynamic model that allows incorporation of intramolecular energies into the predicted free energy of the binding.²

Rheumatoid arthritis, a systemic inflammatory disease causes pain, stiffness, and swelling of joints and, over the time, the disease has a severe, chronic and invalid progression with loss of mobility.^{3,4} Ibuprofen could be considered as the drug of choice in the management and therapy of inflammation in rheumatoid arthritis. 5 Oral bioavailability of ibuprofen is very poor due to its poor water solubility.⁶ Low oral bioavailability limits therapeutic efficacy of the drug.⁷ Dissolution rate of ibuprofen (BCS class II) in gastrointestinal fluid is the rate limiting step in its oral absorption and often results in low and erratic oral bioavailability.^{8,9} Many techniques have been reported to improve the bioavailability of poorly water-soluble drugs. 10,11 Solid state amorphization can achieve improved solubility.¹²

Microcrystalline cellulose is used in many solid oral dosage formulations in the pharmaceutical industry. Microcrystalline cellulose has outstanding compressibility properties and is commonly used in tablets. After silicification microcrystalline cellulose can improve binding capability and drug release as a material in tablet formulations by direct compression, wet granulation, dry granulation, and extrusion/spheronization processes. ^{13–15} The present work was undertaken to analyze the binding interactions between ibuprofen and silicified-microcrystalline cellulose. Chemical structure of ibuprofen, silicon dioxide and microcrystalline cellulose is shown in Figure 1. Solid state ball milling, and aqueous state equilibration and freeze drying were the co-processing techniques applied to investigate the effect of silicified-microcrystalline cellulose on ligand. Interactions were monitored by FTIR, DSC and SEM followed by *in vitro* drug release studies. Molecular docking analysis of binary and ternary interactions would reveal stabilizing interactions of silicone dioxide-MCC (formation of SMCC) and ibuprofen-SMCC, which has not been found in extensive literature survey.

Infrared spectroscopy, a commanding technique gives a quantitative estimation of infrared intensity of absorption which is proportional to the magnitude of the change in the dipole moment of a bond during vibration. Drug-excipient interaction study in the solid state has been reported very recently without any co-processing (physical mixture) using infrared spectroscopy and DSC studies. Infrared spectroscopy results have been supported by differential scanning calorimetry (DSC) and scanning electron microscopy (SEM) in a report of drug excipient interaction study.

AutoDock 4 programme was used to predict the binding mode interactions between ibuprofen as a ligand against MCC and silicon dioxide complex (SMCC). Docking calculations was performed with the grid box of the same size $[(40 \times 40 \times 40)]$ with different grid centre to find out the potential binding conformations between ibuprofen, MCC and silicon dioxide. The least binding energy scored conformations were considered as the best conformation. The detailed procedure of molecular docking (using AutoDock) was adopted from a recent study. 19

2. Experimental

2. 1. Materials

Ibuprofen, Colloidal Silicone Dioxide (Aerosil 200vv) was taken from Aristro Pharma as a gift sample, silicified

microcrystalline cellulose were taken from Caplin Point, Chennai. All other chemical were used as analytical grade.

2. 2. Co-processing of Ibuprofen and Silicified Microcrystalline Cellulose

Ibuprofen and silicified microcrystalline cellulose were mixed for 10 minutes by blending process using mortar and spatula at laboratory ambient condition (~30 °C and 60 % RH). Physical mixture of ibuprofen and silicified microcrystalline cellulose at weight ratio of 1:1 was co-processed by ball-milling in the dry state, and aqueous state kneading and freeze drying and tabulated presented in Table 1.

Table 1. Formulation of co-processing of ibuprofen with silicified microcrystalline cellulose

Formulation code	Ibu : SMCC (by weight)	Co-processing
I_1S_1P	1:1	Physical mixture
I_1S_1B	1:1	Dry- state ball milling
I_1S_1F	1:1	Aqueous state kneading and freeze drying

(Ibuprofen = Ibu; Silicified microcrystalline cellulose = SMCC)

2. 3. Ball Milling

The physical mixture of ibuprofen and silicified microcrystalline cellulose in the solid state was placed into the cylindrical vessel of ball mill (Swastik Electro and Scientific Work, India) and 1 h period of constant milling was done at lab ambient condition at 100 rpm (Figure 2). The ball volume to the milling vessel volume was about 30 % and milling was carried out using balls of 4, 8, 14 and 20 mm in diameter. The milling experiments with constant set-up of ball-to-physical mixture mass ratio of 25:1 was used.²⁰

2. 4. Freeze – Drying

Sufficient amount of distilled water was added in the physical powder mixture of ibuprofen and silicified microcrystalline cellulose to make slurry and kneaded well for a

$$CH_3$$
 CH_3
 CH_3
 CH_3
 $O=Si=O$
 $O+O$
 $O+O$
 $O+O$
 $O+O$
 $O+O$
 $O+O$
 $O+O$
 $O+O$
 $O+O$
 $O+O$
 $O+O$
 $O+O$
 $O+O$
 $O+O$
 $O+O$
 $O+O$
 $O+O$
 $O+O$
 $O+O$
 $O+O$
 $O+O$
 $O+O$
 $O+O$
 $O+O$
 $O+O$
 $O+O$
 $O+O$
 $O+O$
 $O+O$
 $O+O$
 $O+O$
 $O+O$
 $O+O$
 $O+O$
 $O+O$
 $O+O$
 $O+O$
 $O+O$
 $O+O$
 $O+O$
 $O+O$
 $O+O$
 $O+O$
 $O+O$
 $O+O$
 $O+O$
 $O+O$
 $O+O$
 $O+O$
 $O+O$
 $O+O$
 $O+O$
 $O+O$
 $O+O$
 $O+O$
 $O+O$
 $O+O$
 $O+O$
 $O+O$
 $O+O$
 $O+O$
 $O+O$
 $O+O$
 $O+O$
 $O+O$
 $O+O$
 $O+O$
 $O+O$
 $O+O$
 $O+O$
 $O+O$
 $O+O$
 $O+O$
 $O+O$
 $O+O$
 $O+O$
 $O+O$
 $O+O$
 $O+O$
 $O+O$
 $O+O$
 $O+O$
 $O+O$
 $O+O$
 $O+O$
 $O+O$
 $O+O$
 $O+O$
 $O+O$
 $O+O$
 $O+O$
 $O+O$
 $O+O$
 $O+O$
 $O+O$
 $O+O$
 $O+O$
 $O+O$
 $O+O$
 $O+O$
 $O+O$
 $O+O$
 $O+O$
 $O+O$
 $O+O$
 $O+O$
 $O+O$
 $O+O$
 $O+O$
 $O+O$
 $O+O$
 $O+O$
 $O+O$
 $O+O$
 $O+O$
 $O+O$
 $O+O$
 $O+O$
 $O+O$
 $O+O$
 $O+O$
 $O+O$
 $O+O$
 $O+O$
 $O+O$
 $O+O$
 $O+O$
 $O+O$
 $O+O$
 $O+O$
 $O+O$
 $O+O$
 $O+O$
 $O+O$
 $O+O$
 $O+O$
 $O+O$
 $O+O$
 $O+O$
 $O+O$
 $O+O$
 $O+O$
 $O+O$
 $O+O$
 $O+O$
 $O+O$
 $O+O$
 $O+O$
 $O+O$
 $O+O$
 $O+O$
 $O+O$
 $O+O$
 $O+O$
 $O+O$
 $O+O$
 $O+O$
 $O+O$
 $O+O$
 $O+O$
 $O+O$
 $O+O$
 $O+O$
 $O+O$
 $O+O$
 $O+O$
 $O+O$
 $O+O$
 $O+O$
 $O+O$
 $O+O$
 $O+O$
 $O+O$
 $O+O$
 $O+O$
 $O+O$
 $O+O$
 $O+O$
 $O+O$
 $O+O$
 $O+O$
 $O+O$
 $O+O$
 $O+O$
 $O+O$
 $O+O$
 $O+O$
 $O+O$
 $O+O$
 $O+O$
 $O+O$
 $O+O$
 $O+O$
 $O+O$
 $O+O$
 $O+O$
 $O+O$
 $O+O$
 $O+O$
 $O+O$
 $O+O$
 $O+O$
 $O+O$
 $O+O$
 $O+O$
 $O+O$
 $O+O$
 $O+O$
 $O+O$
 $O+O$
 $O+O$
 $O+O$
 $O+O$
 $O+O$
 $O+O$
 $O+O$
 $O+O$
 $O+O$
 $O+O$
 $O+O$
 $O+O$
 $O+O$
 $O+O$
 $O+O$
 $O+O$
 $O+O$
 $O+O$
 $O+O$
 $O+O$
 $O+O$
 $O+O$
 $O+O$
 $O+O$
 $O+O$
 $O+O$
 $O+O$
 $O+O$
 $O+O$
 $O+O$
 $O+O$
 $O+O$
 $O+O$
 $O+O$
 $O+O$
 $O+O$
 $O+O$
 $O+O$
 $O+O$
 $O+O$
 $O+O$
 $O+O$
 $O+O$
 $O+O$
 $O+O$
 $O+O$
 $O+O$
 $O+O$
 $O+O$
 $O+O$
 $O+O$
 $O+O$
 $O+O$
 $O+O$
 $O+O$
 $O+O$
 $O+O$
 $O+O$
 $O+O$
 $O+O$
 $O+O$
 $O+O$
 $O+O$
 $O+O$
 $O+O$
 $O+O$
 $O+O$
 $O+O$
 $O+O$
 $O+O$
 $O+O$
 $O+O$
 $O+O$
 $O+O$
 $O+O$
 $O+O$
 $O+O$
 $O+O$
 $O+O$
 $O+O$
 $O+O$
 $O+O$
 $O+O$
 $O+O$
 $O+O$
 $O+O$
 $O+O$
 $O+O$
 $O+O$
 $O+O$
 $O+O$
 $O+O$
 $O+O$
 $O+O$
 $O+O$
 $O+O$
 $O+O$
 $O+O$
 $O+O$
 $O+O$
 $O+O$
 $O+O$
 $O+O$
 $O+O$
 $O+O$
 $O+O$
 $O+O$
 $O+O$
 $O+O$
 $O+O$
 $O+O$
 $O+O$
 $O+O$
 $O+O$
 $O+O$
 $O+O$
 $O+O$
 $O+O$
 $O+O$
 $O+O$
 $O+O$
 $O+O$
 $O+O$
 $O+O$
 $O+O$
 $O+O$

Fig. 1. Chemical structure of (a) ibuprofen, (b) silicon dioxide, and (c) microcrystalline cellulose.

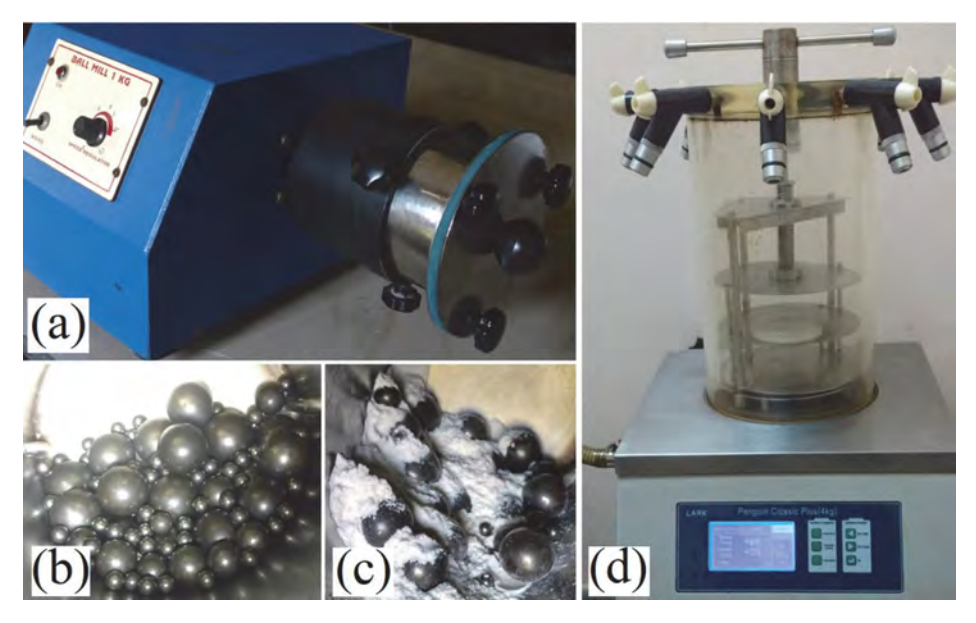


Fig. 2. Co-processing of ibuprofen with SMCC: (a) Laboratory Ball mill (1 kg) used for solid-state milling; (b) The balls charged for milling process; (c) Ibuprofen -SMCC physical mixture just after loading for the milling process; (d) Freeze dryer used for drying the physical mixer after aqueous state equilibration.

period of 30 min. The slurry then placed in the dark for a period of about 12 h at room ambient condition for equilibration. The kneaded samples were freeze dried for 12 hours for effective drying using a laboratory vacuum freeze dryer (4 kg, 220 V) with attached vacuum (220 V, 2.7 A, 370W, 1400 rpm, 50 Hz) (Lark, Penguin Classic Plus, India). Temperature maintained at -40 °C (approx.) and pressure during freeze-drying was adjusted to 15-20 Pa. The freeze dried samples were preserved in the desiccators till further analysis. The ball milled and freeze dried samples were placed at ambient condition for few hours and dried in an incubator (Labotech, India) at 50 °C. The dried powder were passed through mesh 44 (opening ~350 µm) and assayed for drug content determination from the absorbance measured at 222 nm (λ_{max}) in the UV visible spectrophotometer (Jasco-V630 UV spectrophotometer).

2. 5. FTIR Study

The FTIR spectra of pure ibuprofen and co-processed powder samples were performed for a comparative study between co-milling and co-freeze drying interaction. All the samples were thoroughly mixed with potassium bromide in the ratio 1:100. KBr discs were prepared by compressing the powders at a pressure of 6 tons for the 10 min in a hydraulic pellet press (Technosearch Instruments, Maharashtra, India). FTIR spectrometer (FTIR-4100 type A, Jasco, Tokyo, Japan) was used for collecting all scans from 4000–400 cm⁻¹ of 80 accumulations at a resolution of 4 cm⁻¹ and scanning of 2 mm/s. Spectra manager for windows software (Jasco, Tokyo, Japan) was used for data acquisition and holding.

2. 6. Surface Morphology and Thermal Analysis of the Particle

The surface morphology and crystalline nature of the particle samples were investigated by using Scanning Electron Microscope (Instrument: JSM-6390, Jeol, Tokyo, Japan). The dried samples were coated with gold and scanned at room temperature using voltage 10 kV (Wd 19 and spot size 48). Downloaded Imagej software (https://imagej.nih.gov/ij/download.html) was used for determining particle size distribution of the powder samples. Thermal behavior of powder samples were characterized by using Differential Scanning Calorimeter (DSC, Universal V4.2E TA Instrument). Powder samples approximately 2–4 mg were weighed accurately and put into crimped aluminum pans with a pin hole in the lid. All samples were heated at a heating rate of 10 °C/min in a nitrogen atmospheric condition up to 300 °C.

2. 7. In-vitro Dissolution Release

Powdered samples containing 10 mg equivalent of ibuprofen were dispersed in 900 ml of distilled water and drug release was carried out using USP XXIV type II dissolution apparatus (Electrolab dissolution tester USP) at a temperature of 37 \pm 0.2 °C at an rpm of 100. Ibuprofen concentration was determined by UV absorbance at 222 nm. Samples were withdrawn at appropriate time intervals of 5, 10, 15, 30, 60, 90 and 120 min, and replaced with a fresh dissolution medium. After proper rinsing of the cuvette and filtration of the sample through a 0.45 μ m membrane filter, absorbance was recorded using the UV visible spectrophotometer. Standard calibration curve was used

for calculating the respective concentration and the data were reported as the mean of not less than three determinations.

2. 8. Molecular Docking Analysis

The molecular visualizations and interaction analysis was performed using Discovery studio visualizer (Acceleris Inc.). The 3-D Structure file of ibuprofen was downloaded from Drug Bank (ID: DB01050) as PDB format. The 3-D structures of silicon dioxide and MCC were drawn by using marvin sketch^{19,21} and saved as PDB extension files. The non-bonded H-atoms were merged, Kollman united atom type charges and solvation parameters were added. The PDBQT files of ibuprofen, MCC and silicon dioxide were prepared with the help of Auto Dock tools programme.²² The ibuprofen non-steroidal anti-inflammatory drug was taken as a ligand to identify its binding affinity against the MCC and silicon dioxide complex (SMCC). In order to understand the interaction between MCC (receptor) with the ligand silicon dioxide another molecular docking experiment was carried out using these molecules. The docking complex stability was measured on the basis of binding constant and interaction energy.

3. Results and Discussion

The dry-state co-milling and aqueous state co-processing could be analogous to the commonly followed process in the tablet granulation department of pharmaceutical industries. Ball milling studies in different literature has shown different duration and speed of rotation. Median particle diameter has not been changed significantly upon milling of alfa-lactose monohydrate at a milling time of 60 and 300 min (ball-to-powder mass ratio of 25:1 and

13:1), and highest degree of amorphization was resulted at the ratio of 25:1.20 In another milling study increasing powder loading decreased milling efficiency at a given rotation speed of 50, 100, and 153 rpm.²³ Hence, 1 h milling time and 100 rpm of milling speed could be justifiable or closely resembling to the dosage form processing. These processes are simple, effective and scalable for interaction study. Due to presence of varying amount of bound moisture in the native silicified microcrystalline cellulose the milled material became moisty in nature and needed drying. Instant character of freeze dried sample is to absorb moisture like a sponge when left at ambient condition of -60 % RH and 30 °C for few hours and drying in an incubator at 50 °C becomes necessary. The co-processed dried and equilibrated powder materials were passed through mesh of opening ~350 µm and assayed for actual drug content determination. Ibuprofen-silicified microcrystalline cellulose interaction study has been characterized by FTIR and the usefulness of this powerful technique has been supported by scanning electron microscopy and differential scanning calorimetry as described below. Drug release from the formulated dosage form is important and ultimately related to the bioavailability of the drug. Dissolution of ibuprofen from the co-processed material has also been described below.

3. 1. FTIR Analysis

Spectral figure and data of FTIR band assignments of ibuprofen and co-processed samples are tabulated presented in Table 2 and Figure 3 respectively. FTIR spectrum of ibuprofen has shown medium to very strong band at 3094, 2958 and 2901 cm $^{-1}$ assigned to CH $_2$ asymmetric stretching, CH $_3$ asymmetric stretching and CH $_2$ · CH symmetric stretching respectively. Strong peaks in the region of 2800–3000 cm $^{-1}$ of ibuprofen are still present when co-milled in

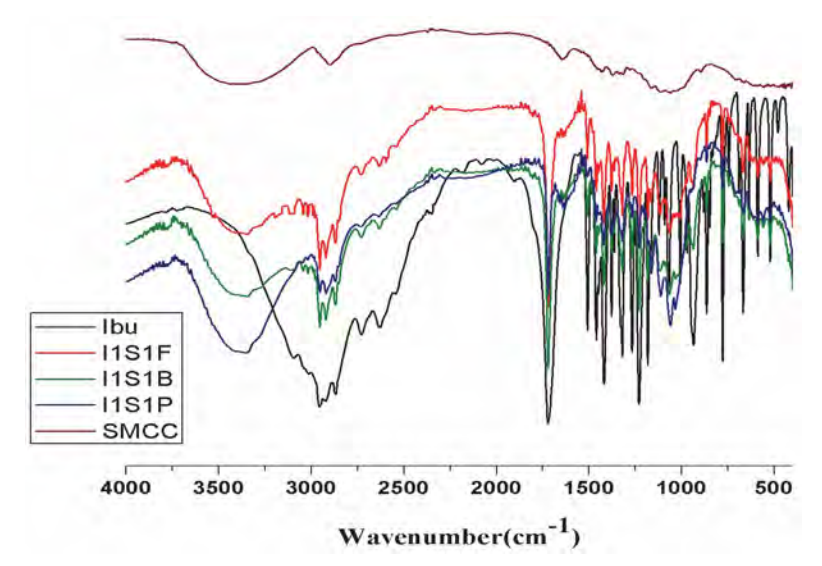


Fig. 3. FTIR Spectra of Ibuprofen co-processed with SMCC

Table 2. Spectral data of FTIR band assignments of ibuprofen and co-processed samples.

			V	Vave number (cm	-1)	
Band	Tentative assignment	Ibuprofen	SMCC	I_1S_1B	I_1S_1F	I_1S_1P
1	OH stretching	Absent	3200-3550 bb	3200-3550 bb	3200-3550 bb	3200-3550 bb
2	CH ₂ asym str	3094 m	-	absent	absent	absent
3	CH ₃ asym str	2958 vs	-	2955 vs	2954 vs	2955 vs
4	CH ₂ CH sym str	2901 s	2901 s	2901 s	2901 s	2901 s
5	CH ₂ sym str	2868 m	-	2868 m	2869 m	2868 m
6	O-HO valance str combination	2729 m	-	2730 m	2730 m	2728 m
7	O-HO valance str combination	2630 m	_	2629 m	2629 m	2629 m
8	C=O str	1722 vs	_	1721 vs	1720 vs	1722 vs
9	conjugated C=O stretching mode	Absent	1645 s	1645 m	1645 m	1645 m
10	aromatic C=C str	1507 s	_	1508 s	1510 s	1507 s
11	CH ₃ asym deformation, CH ₂ scissoring	1462 s	_	1461 s	1461 s	1461 s
12	CH-CO deformation	1420 s	_	1420 s	1422 s	1420 s
13	CH3 sym str	1380 s	_	1379 s	1378 s	1379 s
14	OH in plane deformation	1321 s	_	1321 s	1321 s	1321 s
15	=C-H in plane deformation	1268 s	_	1267 s	1267 s	1268 s
16	CC str	1230 vs	_	1231 vs	1231 vs	1231 vs
17	C-O str	1183 s	_	1183 s	1183 s	1183 s
18	Si-O-Si asym str	Absent	1059 bb	1066 bb	1059 bb	1075 bb
19	C-O-C str	970 m	_	_	_	Absent
20	C-H out of plane vibration	866 s	_	865 s	866 s	866 s
21	CH ₂ rocking	779 s	_	780 s	780 s	779 s
22	CH ₂ in plane rocking	522 m	_	521 m	521 m	521 m
23	O-Si-O bending	Absent	451 bb	461 bb	461 bb	451 bb

(s- strong; bb- broad band; mbb- medium broad band; w- weak; sym-symmetrical; asym-asymmetrical; str-stretching; m- medium; vs- very strong; vw – very weak; vvw – very weak; aa- almost absent.)

the dry-state as well as co-freeze-dried after aqueous state kneading and equilibration with silicified microcrystalline cellulose assigned to the characteristic symmetric and asymmetric stretching vibrations of alkyl chain. High intensity carbonyl peak at 1722 cm⁻¹ of ibuprofen became very weak after co-processing in the solid-state as well as wet-state with silicified microcrystalline cellulose.²⁴ The band at 1645 cm⁻¹ of silicified microcrystalline cellulose designated to conjugated C=O in the aldehyde on the terminal anhydro-glucose unit is also present in co-processed samples. A strong CH₂ rocking vibration band is noticed at 779 cm⁻¹ in ibuprofen and the intensity observed to be weaker and weaker after co-processing. CH2 in plane rocking vibration (522 cm⁻¹) is identified in pure ibuprofen and became weaker when co-milled and freeze dried after co-kneading. C-O stretching at 1183, CH2 scissoring vibration at 1462 and CH-CO deformation at 1420 cm⁻¹ contributed their occurrence strongly in ibuprofen alone and weakly in the co-processed sample. A big broad band between 3200 to 3550 cm⁻¹ attributed to the presence of the O-H stretching frequency of silanol group bonded to the inorganic structure of containing SiO₂ (SMCC), and also hydrogen bonds between adsorbed water and silanol.²⁵ This bulky broad band is not present in ibuprofen pure drug but consistently maintained in all the co-processed formulations might be due to intermolecular hydrogen bonding. The band related to the Si-O-Si (silanol)

asymmetric stretching was found at 1059 cm⁻¹ with elevated intensity in SMCC and also in the co-processed materials. Another peak at 451 cm⁻¹ due to O-Si-O bending notably observed in the formulations. The small changes in the band orientation, band intensity and overlapping indicated only Vander Waals or dipole-dipole interactions between ibuprofen and silicified microcrystalline cellulose molecules.

3. 2. SEM and DSC

Scanning electron microscopy is a commanding tool for examining the inhibition of crystal growth morphology. Figure 4 shows distinctive plate like geometric layers of the initial samples of pure ibuprofen indicating crystalline nature. Slightly damaged morphology of the crystal geometry of ibuprofen is seen in the physical mixture of 1:1 ratio of I_1S_1P in presence of fine particles of SMCC. Crystal geometry of ibuprofen has been damaged appreciably after co-milling in the solid-state and cofreeze-drying after aqueous state kneading and equilibration with silicified microcrystalline cellulose. The Feret diameter and its distribution of the powder sample were evaluated opening the SEM image (Figure 5). Feret diameter is an estimate of a particle size along a specified direction and can be defined as the distance between the two parallel planes restricting the particle perpendicular to

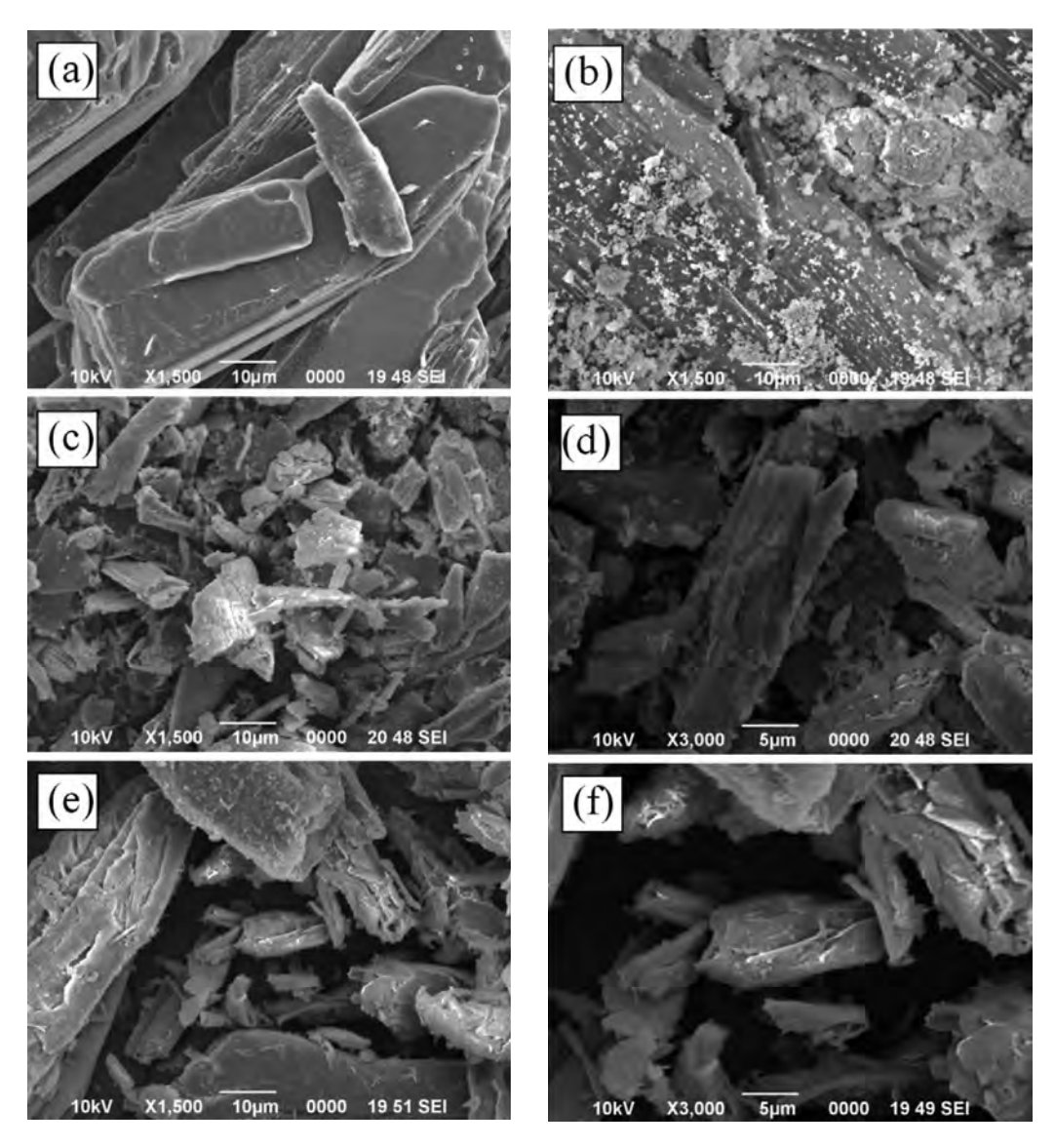
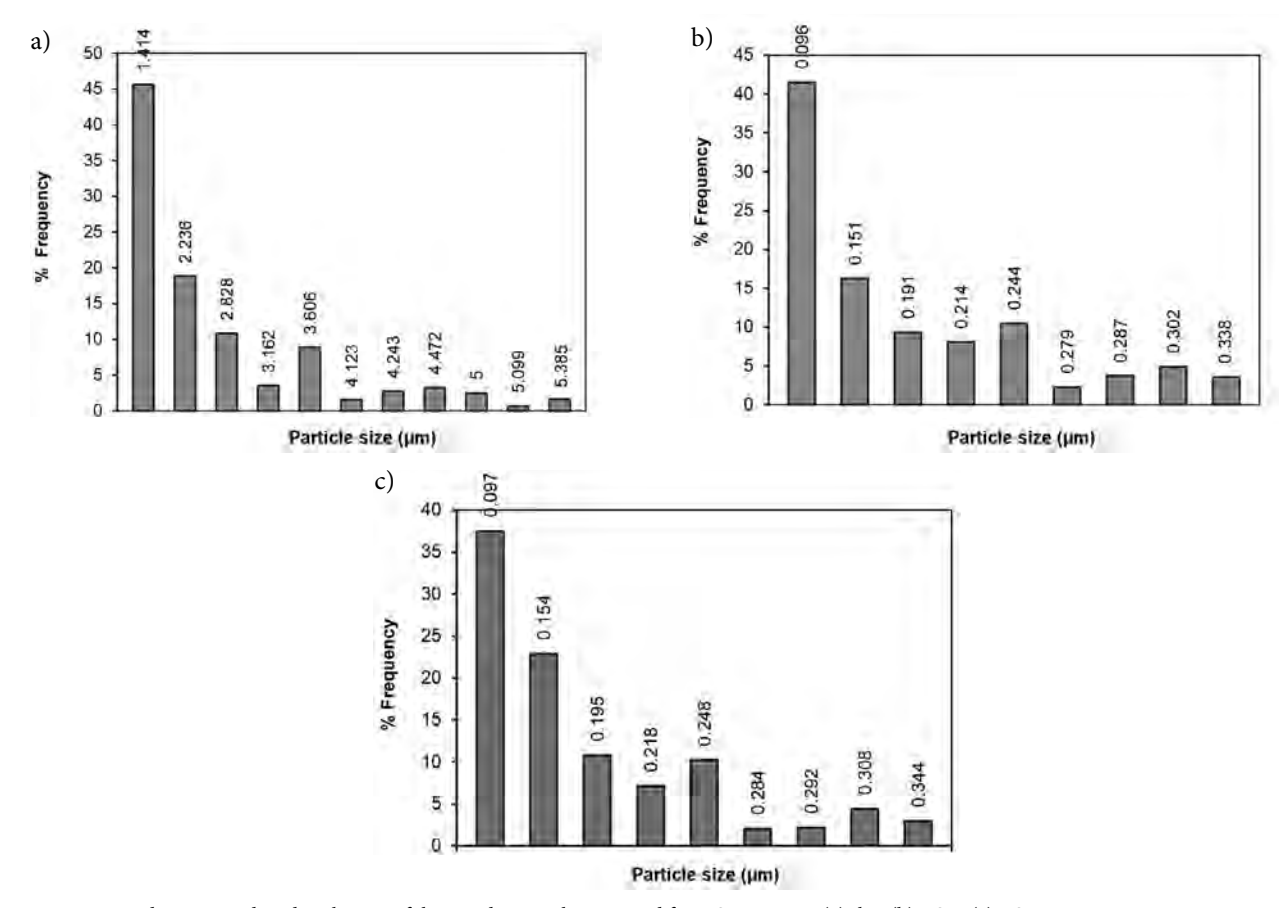


Fig. 4. SEM Images (a) Ibu; (b) I_1S_1P ; (c) and (d) I_1S_1B ; (e) and (f) I_1S_1F .

that direction. In both cases $(I_1S_1B \text{ and } I_1S_1F)$ particle size has been significantly reduced. Irregular particles in agglomerated and discrete forms are prominently seen after co-processing. These noticeable changes in morphology may be due to amorphization of ibuprofen to the large extent.

Differential scanning calorimetry is frequently used in pharmaceutical research as an analytical tool for the identification and interaction study of active drug after co-processing with other pharmaceutical compounds. It can explain the miscibility/incompatibility with its effects on thermal stability, yielding results promptly and efficiently. Thermograms after differential scanning calorimetry of pure ibuprofen and co-processed powder samples are depicted in Figure 6. Pure ibuprofen has shown the melting endotherm at 76.66 °C which is approximately similar to the literature value. The peak, onset and

endset of melting of ibuprofen in the formulated powder samples have not been changed significantly (Table 3) but the enthalpy of melting (normalized, J/g) of ibuprofen (-322.55) decreased drastically after co-processing and that is the indication of amorphous transformation of ibuprofen in the co-processed formulations. Solid-state ball-milling sample exhibited lesser enthalpy content (-42.93) compared to freeze-dried material (-63.40). This result suggested that the extent of amorphization of ibuprofen is more in I₁S₁B rather than I₁S₁F material (relative crystallinity 13.31 and 19.66 % respectively with reference to pure drug ibuprofen). The physical mixture has shown only 22.49 %. The zero crystallinity corresponds to a totally amorphous particle. In our present work relative crystallinity (%) has been shown with reference to the pure drug ibuprofen which is highly crystalline (reference).



 $\textbf{Fig. 5.} \ \ \textbf{Feret diameter and its distribution of the powder sample estimated from SEM image: (a) Ibu, (b) I_1S_1F, (c) I_1S_1B.$

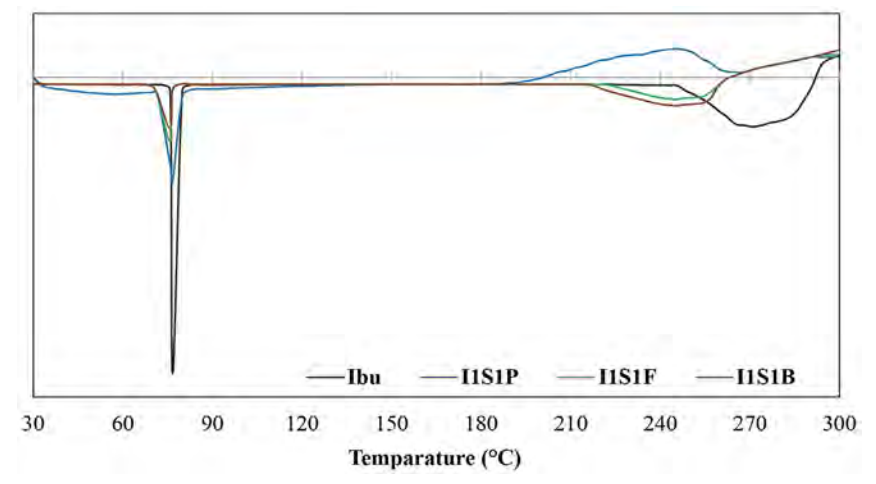


Fig. 6. DSC Thermogram of ibuprofen co-processed with SMCC.

Table 3. Thermal analysis after co-processing of ibuprofen with microcrystalline cellulose

Formulation	Peak melting (°C)	Onset melting (°C)	End set melting (°C)	Normalized (J/g)	Relative crystallinity (%)
Ibu	76.66	75.78	79.93	-322.55	Reference
I_1S_1P	76.56	73.03	80.43	-72.53	22.49
I_1S_1B	74.71	73.04	76.34	-42.93	13.31
I_1S_1F	75.66	73.03	77.99	-63.40	19.66

3. 3. In-vitro Drug Release

Many research reports used distilled water²⁸⁻³⁰ as media to determine the solubility of drug substance. Ibuprofen drug release from microemulsion was studied also in distilled water by Hu et al.³¹ Ibuprofen release profiles were similar for three kinds of microspheres in distilled water and with solution of low pH of 1.2 because of poor solubility of the drug.³² Like ibuprofen many other non-steroidal anti-inflammatory drugs tend to self-associate by forming mixed-charged micelles or micelle-like structures and the solubility-pH profiles cannot be described properly with the Henderson-Hasselbalch eq. 33,34 However, release of ibuprofen in distilled water will give an idea about its overall improvement in dissolution. Figure 7 shows cumulative percentage release of ibuprofen in distilled water of the co-processed material up to 120 min. The powder materials have shown significantly improved dissolution of drug after co-processing. Comparison of two dissolution profiles is based on the determination of a model independent statistical method, the difference factor f_1 and the similarity factor f_2 . Similarity or equivalence between two dissolution profiles is based on $f_1 \le 15$ and f_2 ≥ 50.³⁵⁻³⁷ Significantly improved drug dissolution of solid state milling, and aqueous state kneading and freeze drying has been understood by using f_1 and f_2 values when pair wise formulation vs pure drug was compared $(f_1:$ 32.75, & f_2 : 13.29 and f_1 : 15.05, & f_2 : 28.93 respectively). Crystalline ibuprofen exhibited only 52.89 % dissolution whereas, dry-state co-milling and freeze dried co-processed material has improved dissolution to a great extent (85.84 and 81.35 % respectively). Silicified microcrystalline cellulose has shown more impact in solid state milling compared to aqueous state kneading and equilibration and brought about more amorphization of ibuprofen. As a result more improved dissolution has been achieved in ball milled product.38

Drug release mechanism has been predicted to develop a rational formulation utilizing mathematical models. The drug release data was analyzed by applying different kinetic models as First order, Higuchi, Korsmeyer–Peppas kinetics^{39,40} using Origin Pro 8.0 (Originlab Corporation, US) software by non-linear regression analysis. These models are represented as follows:

First order model: $Q = 100 - \exp((-K_F * t) + 4.605)$ (1)

Higuchi model:
$$Q = K_H \times \sqrt{t}$$
 (2)

Korsmeyer-Peppas model:
$$Q = K_p \times t^n$$
 (3)

Q =Cumulative percent drug release at time t

 K_F = First order release rate constant

 K_H = Higuchi release rate constant,

 K_P = Parameter reflecting the structural and geometric characteristics of the delivery device, or Peppas release rate constant,

n = Power law exponent, or release exponent.

This n value indicates drug release controlled by Fick's laws and also confirmed by the Higuchi model. Matrix controlled release has been followed (Figure 8). The kinetic parameters as per model are presented in the Table 4. As per Peppas model, n value 0.5 is referred to Fickian release pattern. The n value of I_1S_1P , I_1S_1F and I_1S_1B was found to be 0.400, 0.408 and 0.143 respectively (less than 0.5) which indicated the diffusion controlled release mechanism. The diffusion controlled release mechanism has also been supported by the fitting of Higuchi model (R^2 is 0.354–0.973).

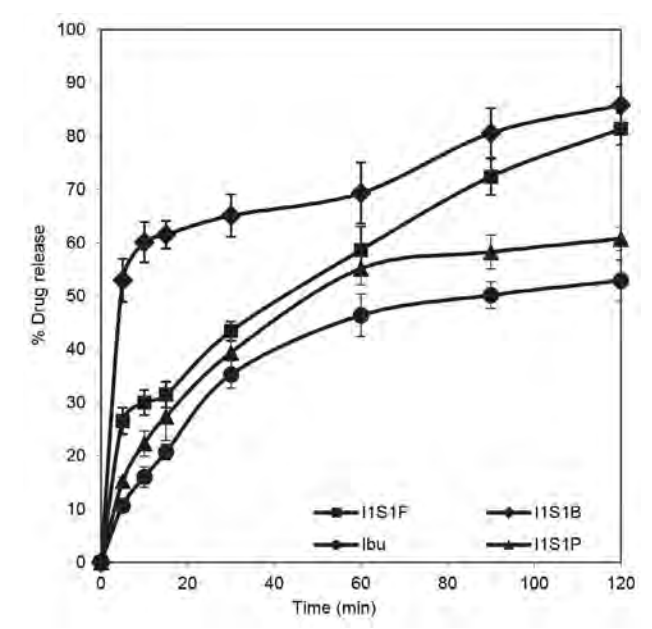


Fig. 7. Cumulative percentage release profiles of ibuprofen co-processed with SMCC.

Table 4. Model fitting and kinetic parameters of drug dissolution of ibuprofen co-processed material.

Formulation	f_1	f_2	First o	order		Hig	uchi		Kors	meyer-P	eppas	
			K_F (min^{-1})	<i>r</i> ²	RSS	K_H (%.min ^{-1/2}	r ²	RSS	n	K_{p}	r ²	RSS
$\overline{I_1S_1P}$	6.25	48.96	0.011	0.789	727	6.27	0.956	150	0.400	9.544	0.976	69
I_1S_1F	15.04	28.93	0.017	0.854	729	7.71	0.973	133	0.408	11.363	0.990	40
I_1S_1B	32.75	13.28	0.07	0.466	2590	9.52	0.354	3131	0.143	41.497	0.986	54

RSS = Sum of $(Q_{exp} - Q_{calc})^2$

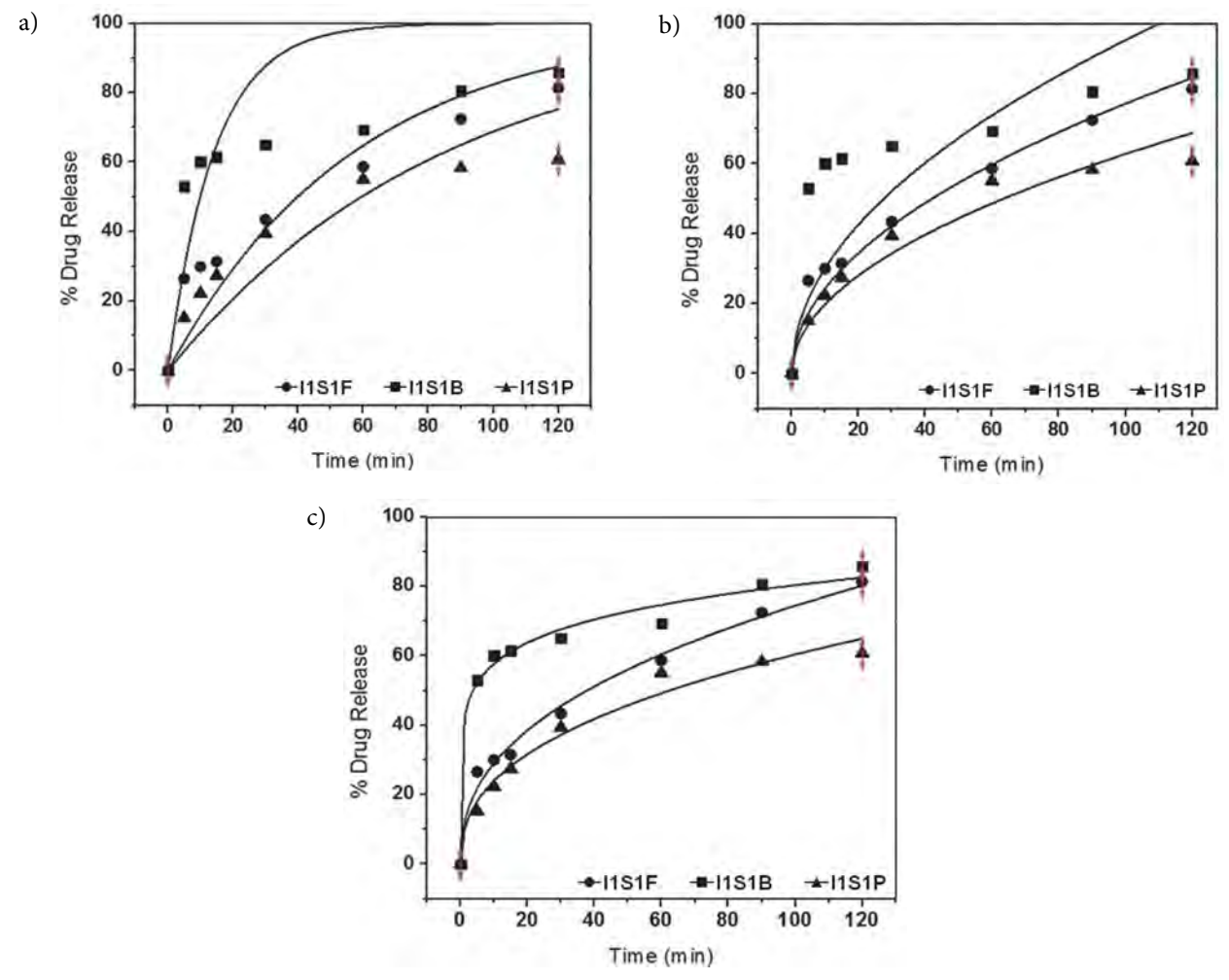


Fig. 8. Kinetics of drug release applying kinetic models to plot both the experimental data (symbols) and the models (curves): (a) First order (b) Higuchi (c) Korsmeyer–Peppas.

3. 4. Molecular Docking Analysis of the Complexes

The predicted co-ordinates of ibuprofen and silicone dioxide complex were monitored by molecular docking method Table 5 and Figure 9 respectively. The interaction between MCC-SiO $_2$ would be obtained from inter molecular hydrogen bonding between OH group of MCC and H atom of SiO $_2$. The hydrogen bond lengths are varying from

2.028 to 2.056 Å. The binding energy value was found –1.11kcal/mol. Hydrogen bonding plays a vital role in H-bonded network systems. Hydrogen bond length between ibuprofen and SMCC are ranging from 2.028 to 2.930 Å and the most interesting other probable interaction of Si atom of SMCC molecule with Pi-Orbital of ibuprofen showing bond length of 4.263 Å. The binding energy was found to be –1.73 kcal/mol. The higher negative binding energy values indicate stable interactions than

Table 5. Molecular docking and binding parameter interactions in the co-processing of ibuprofen with silicified microcrystalline cellulose

Binding Molecules	Binding energy (Kcal/mol)	Binding atoms	Bond name	Bond length (Å)
MCC – SiO ₂	-1.11	OH O	Hydrogen Bond	2.028
(SMCC)		H O	Hydrogen Bond	2.056
SMCC - Ibuprofen	-1.73	OH O	Hydrogen Bond	2.028
•		OH O	Hydrogen Bond	2.930
		Н О	Hydrogen Bond	2.056
		Si Pi-orbital	Pi-Sulfur Bond	4.263

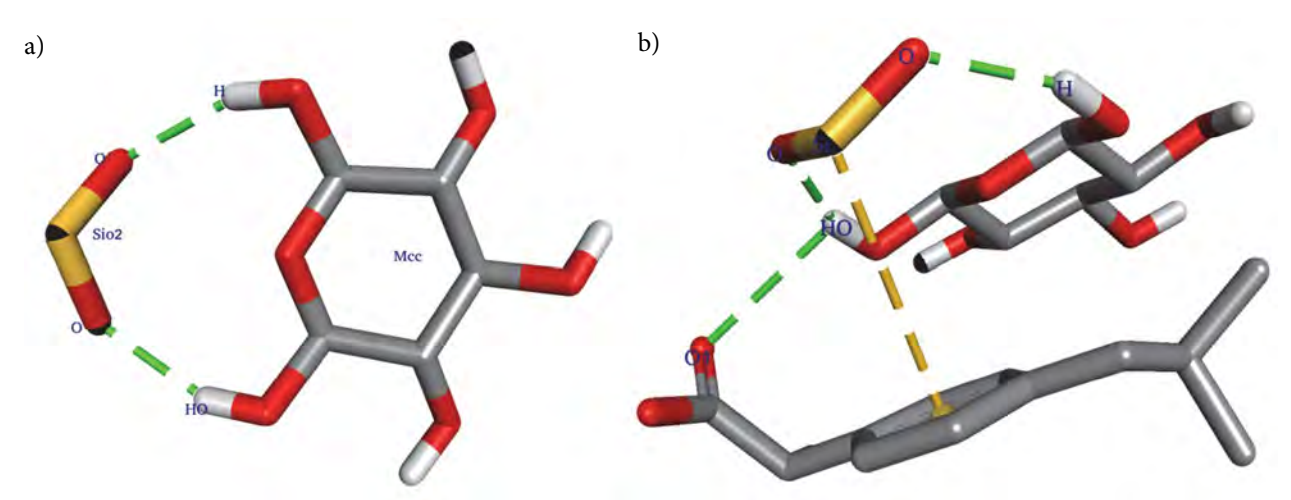


Fig. 9. Molecular docking study of (a) SMCC (binary); and (b) ibuprofen-microcrystalline cellulose -silicon dioxide (ternary).

that of lower negative values, which indicate destabilizing interactions. 21,41

4. Conclusions

Binding interactions of ibuprofen and silicified-microcrystalline cellulose (SMCC) has been analysed. The drystate and aqueous state co-processing of ibuprofen was performed by co-milling and co-freeze-drying after aqueous state kneading and equilibration with silicified microcrystalline cellulose in at laboratory scale to investigate the effect of silicified-microcrystalline cellulose on ligand. The changes in the band intensity, band orientation, and overlapping of FTIR indicated only the H-bond, Van der Waals and/or dipole-dipole interactions between ibuprofen and silicified microcrystalline cellulose molecules. SEM study revealed that the ibuprofen crystal morphology has been damaged appreciably after co-processing in the solid-state and wetstate with SMCC. Thermal analysis has shown significantly decreased enthalpy of melting of ibuprofen after co-processing with SMCC. Silicified microcrystalline cellulose has transformed more amorphization of ibuprofen by solid state milling compared to aqueous state kneading and freeze drying and brought about more improved dissolution of ibuprofen of ball milled product rather than freeze dried product. Matrix controlled release mechanism has been predicted utilizing mathematical kinetic models. Molecular docking study revealed the formation of ibuprofen complex through hydrogen bonding with MCC and silicon dioxide. The binding energy between MCC and SiO2, and ibuprofen and SMCC were found as -1.11 and -1.73 kcal/mol respectively.

5. Acknowledgements

The authors are acknowledging gratefulness to the Department of Science & Technology, Ministry of Science & Technology, New Delhi, India, for providing INSPIRE fel-

lowship to Rudra Narayan Sahoo (IF 150987). The authors are also very much grateful to Prof. Manoj Ranjan Nayak, President, Siksha O Anusandhan (Deemed to be University) for providing other facilities and encouragement.

Conflicts of interest

The authors declare that there is no conflict of interest.

6. References

- W. P. Sohtun, A. Kannan, K. Hari Krishna, D. Saravanan, M. S. Kumar, M. Velusamy, *Acta Chim. Slov.* **2018**, *65*, 621–629. **DOI**:10.17344/acsi.2018.4275
- G. M Morris, R. Huey, W. Lindstrom, M. F. Sanner, R. K. Belew, D. S. Goodsell, A. J. Olson, J. Comput. Chem. 2009, 16, 2785–2791. DOI:10.1002/jcc.21256
- P. O. Carvalho, Q. B. Cass, S. A. Calafatti, F. J. Contesini, R. Bizaco, *Braz. J. Chem. Eng.* 2006, 23(03), 291–300.
 DOI:10.1590/S0104-66322006000300003
- T. Chaban, V. V. Ogurtsov, V. S. Matiychuk, G. Chaban, L. Demchuk, A. Nektegayev, *Acta Chim. Slov.* 2019, 66, 103–111. DOI:10.17344/acsi.2018.4570
- Q. Wei, H. Yuanzhi, G. Zhen, L. Zhang, W. Li, Y. Xianzhen,
 S. Shakya, A. Maharjan, T. Yan, Z. Weifeng, Z. Jiwen, *Asian J. Pharm. Sci.* 2018, 4, 1–9.
- 6. M. Mombeini, G. Saki, L. Khorsandi, N. Bavarsad, *Medicina*, **2018**, *54*(1), 1–9. **DOI**:10.3390/medicina54010001
- 7. R. Lobenberg, G. L Amidon, *Eur. J. Pharm. Biopharm.* **2000**, *50*(1), 3–12.
- 8. R. P. Swain, B. B. Subudhi, *Drug. Dev. Ind. Pharm.* **2019**, (Published online: 16 Feb 2019).

DOI:10.1080/03639045.2019.1572183

- 9. S. Mallick, S. Pattnaik, K. Swain, P. K. De, *Drug Dev. Ind. Pharm.* **2007**, *33*, 535–541. **DOI**:10.1080/03639040601050130
- S. Mallick, S. Pattnaik, K. Swain, P. K De, A. Saha, G. Ghoshal,
 A. Mondal, *Drug Dev. Ind. Pharm.* 2008, 34, 726–734.
 DOI:10.1080/03639040801901868

- 11. S. Mallick, A. Sahu, K. Pal, Acta Pol. Pharm. 2004, 61, 21-30.
- 12. R. H. Dave, Overview of Pharmaceutical Excipients used in tablets and capsules, https://www.drugtopics.com/hospital-health-system-pharmacy/overview-pharmaceutical-excipients-used-tablets-and-capsules, (assessed: March 13, 2019).
- S. Lijun, L. Liping, S. Xiaoying, C. Honglang, Z. Shumin, C. Wenfeng, Z. Ruoxia, Z. Wenchang, *Asian J. Pharm. Sci.* 2018, 19(13), 1–10.
- R. Vasluianu, D. A. Forna, M. Zaltariov, A. Murariu, Rev. Chim. (Bucharest). 2016, 67(12), 2475–2478.
- M. S. Bhandari, S. M. Wairkar, U. S. Patil, N. R. Jadhav, *Acta Chim. Slov.* 2018, 65, 492–501. DOI:10.17344/acsi.2017.3822
- F. Dragan, I. Kacso, S. Dreve, F. Martin, G. Borodi, I. Bratu, K. Earar, Rev. Chim. (Bucharest). 2015, 66(2), 191–195.
- 17. B. Tita, G. Furau, E. Marian, D. Tita, C. Furau, *Rev. Chim.* (Bucharest). **2016**, *67*(4), 706–710.
- E. Marian, T. Jurca, B. Tita, P. Sfirloaga, D. Tita, N. Duteanu, *Rev. Chim.* (Bucharest). 2015, 66(4), 477–481.
- J. Maharana, M. C. Patra, B. C. De, B. R. Sahoo, B. K. Behera,
 S. De, S. K Pradhan, J. Mol. Recog. 2014, 27(5), 260–275.
 DOI:10.1002/jmr.2357
- S. Pazesha, J. Grasjo, J. Berggren, G. Alderborn, *Int. J. Pharm.* 2017, 528, 215–227.
 DOI:10.1016/j.ijpharm.2017.05.043
- R. Mohapatra, S. Mallick, A. Nanda, R. N. Sahoo, A. Pramanik, A. Bose, D. Das, L. Pattnaik, RSC Adv. 2016, 6, 31976–31987. DOI:10.1039/C6RA03604J
- G. M. Morris, D. S. Goodsell, R. S. Halliday, R. Huey, W. E. Hart, R. K. Belew, A. J. Olson, *J. Comput. Chem.* 1998, 19(14), 1639–1662. DOI:10.1002/(SICI)1096-987X(19981115)19:14 <1639::AID-ICC10>3.0.CO:2-B
- H. Shin, S. Lee, H. S. Jung, J. Kim, Ceram. Int. 2013, 39(8), 8963–8968. DOI:10.1016/j.ceramint.2013.04.093
- S. Mallick, S. K. Pradhan, R. Mohapatra, *Int. J. Biol. Macro-mol.* 2013, 60, 148–155. DOI:10.1016/j.ijbiomac.2013.05.021
- A. L. Balieiro, R. A. Santos, M. M. Pereira, R. T. Figueiredo, L. S. Freitas, O. L. S. de Alsina, A. S. Lima, C. M. F. Soares, *Braz. J. Chem. Eng.* 2016, 33(2), 361–372.

DOI:10.1590/0104-6632.20160332s20140089

- B. Panda, A. S. Parihar, S. Mallick, *Int. J. Biol. Macromol.* 2014, 67, 295–302. DOI:10.1016/j.ijbiomac.2014.03.033
- S. Mallick, S. K. Pradhan, M. Chandran, M. Acharya, T. Digdarsini, R. Mohapatra, *Results Pharm. Sci.* 2011, 1(1), 1–10.
 DOI:10.1016/j.rinphs.2011.05.003
- 28. P. Arya, K. Pathak. *Int J Pharm.* **201**4, 460(1–2), 1–12. **DOI:**10.1016/j.ijpharm.2013.10.045
- F. L. Mota, A. P. Carneiro, A. J. Queimada, S. P. Pinho, E. A. Macedo. *Eur J Pharm Sci.* 2009, 37(3-4), 499-507.
 DOI:10.1016/j.ejps.2009.04.009
- F. A. Maulvi, S. J. Dalwadi, V. T. Thakkar, T. G. Soni, M. C. Gohel, T. R. Gandhi. *Powder Technol.* 2011, 207(1–3), 47–54.
 DOI:10.1016/j.powtec.2010.10.009
- L. Hu, J. Yang, W. Liu, L. Li, Drug Deliv. 2011, 18(1), 90-95,
 DOI:10.3109/10717544.2010.522613
- 32. Q. Wei, *Asian J. Pharm. Sci.* **2019**, *14*, 174–182. **DOI:**10.1016/j.ajps.2018.05.003
- 33. A. Avdeef, *ADMET DMPK*. **2014**, *2*(1), 33–42. **DOI:**10.5599/admet.2.1.30
- 34. A. Fini, *Int. J. Pharm.* **1995**, *126*(*1*–*2*), 95–102. **DOI:**10.1016/0378-5173(95)04102-8
- 35. P. Costa, J. Manuel, S. Lobo, *Eur. J. Pharm. Sci.* **2001**, *13*, 123–133. **DOI**:10.1016/S0928-0987(01)00095-1
- A. Pramanik, R. N. Sahoo, A. Nanda, R. Mohapatra, R. Singh,
 S. Mallick, *Curr. Eye Res.* 2018, 43(6), 828–838.
 DOI:10.1080/02713683.2018.1446534
- D. Vetchy, M. Vetcha1, M. R. Artina, E. Gryczova, L. Bartošikova, *Medicina*, 2007, 43(4), 326–330.
 DOI:10.3390/medicina43040040
- S. Mallick, S. Pattnaik, K. Swain, P. K. De, *Drug Dev. Ind. Pharm.* 2007, 33(8), 865–873.
 DOI:10.1080/03639040701429333
- 39. S. Mallick, K. Roy, A. Saha, *Acta Pol. Pharm.* **2002**,*59*(3), 193–
- 40. S. Mallick, B. K. Gupta, S. K. Ghoshal, *J. Sci. Ind. Res.* **1999**, 58, 1010–1016.
- 41. A. Nanda, R. N. Sahoo, A. Pramanik, R. Mohapatra, S. K. Pradhan, A. Thirumurugan, D. Das, S. Mallick, *Colloids Surf. B Biointerfaces.* 2018, 172, 555–564.
 DOI:10.1016/j.colsurfb.2018.09.011

Povzetek

Opravili smo analizo veznih interakcij med ibuprofenom in silicificirano mikrokristalno celulozo (SMCC). Procesiranje ibuprofena s SMCC je bilo izvedeno z mletjem kroglic v trdnem stanju in ravnotežjem v vodni fazi, čemur je sledilo sušenje z zamrzovanjem. Želeli smo raziskati vpliv silificirane mikrokristalne celuloze na ligand. Z metodo molekulskega sidranja (»molecular docking«) smo pokazali, da ibuprofen tvori kompleks preko vodikove vezi z mikrokristalno celulozo (MCC) in silicijevim dioksidom (SiO₂); izračunana energija vezave med MCC in SiO₂ ter ibuprofenom in SMCC je bila kot –1,11 kcal/mol oziroma –1,73 kcal/mol. Dolžine vodikovih vezi so se gibale od 2,028 Å do 2,056 Å. Interakcije atoma Si SMCC molekule s π -orbitalmi ibuprofena smo zaznali na razdalji 4,263 Å. Kot rezultat interakcij smo opazili pomembno izboljšanje raztapljanja ibuprofena. Binarne in ternarne interakcije so pokazale bolj stabilne interakcije z ibuprofenom in SMCC v primerjavi s samo silificirano mikrokristalno celulozo (SMCC).



Except when otherwise noted, articles in this journal are published under the terms and conditions of the Creative Commons Attribution 4.0 International License

@creative

Scientific paper

Comparison of the NMR and the Acid Value Determination Methods for Quality Control of Input Polysorbates

Ema Valentina Brovč,^{1,2} Stane Pajk,¹ Roman Šink² and Janez Mravljak^{1,*}

¹ The Chair of Pharmaceutical Chemistry, University of Ljubljana, Faculty of Pharmacy, Aškerčeva 7, SI-1000 Ljubljana, Slovenia

² Drug Product Development Biosimilars, Formulation Development, Lek d.d., Kolodvorska 27, SI-1234 Mengeš, Slovenia

* Corresponding author: E-mail: janez.mravljak@ffa.uni-lj.si phone.: +386 1 4769500; fax: +386 1 4258031

Received: 03-19-2019

Abstract

Polysorbates (PS) are the most common non-ionic surfactants used in protein formulations. Their degradation has been studied intensively in recent years. Ester bond hydrolysis is one of many pathways of PS degradation that can lead to accumulation of free fatty acids (FFAs) and particle formation. The distribution and quantity of FFAs in PSs impacts directly on product quality. Characterization of input PS is highly relevant, because the initial content of FFAs differs greatly between manufacturers. The purpose of this study was to set up a quick and simple analytical method for the quantitative evaluation of FFAs in PS. The content of FFAs was measured for selected PS 20 and 80, using two methods, 1 H nuclear magnetic resonance spectroscopy (1 H NMR) and the European pharmacopoeia method for determining acid value (I_A). These methods have been evaluated using the method of standard addition and, based on the results, they are interchangeable. It was concluded that 1 H NMR is a useful tool for quality control of input PS and a rapid method for indicating the rate of PS degradation by hydrolysis and oxidation. Further, a newly discovered impurity in PS raw material, the long chain ketone 12-tricosanone, can be identified using 1 H NMR.

Keywords: Nuclear magnetic resonance; acid number; fatty acids; polysorbates; degradation.

1. Introduction

One of the aspects that are important during the development of a biopharmaceutical is its physical and chemical stability. The most common way to stabilize protein formulations is by the use of surfactants.^{1,2,3} PS are the most widely used non-ionic surfactants, but they are prone to degradation by hydrolysis and/or oxidation pathways. Degradation of PS not only reduces its concentration but can also lead to formation of various degradation products. Some of them are poorly soluble in water, including free fatty acids (FFAs), which could precipitate and form particles under long-term or accelerated storage conditions. Thus, one of the quality evaluation parameters that is an important indicator of PS degradation, is FFA content.^{4,5,6,7} Acid formation can be measured by varying the pH of the solution or by determining the total content of FFAs. Among the methods

prescribed by the pharmacopoeia acid value (I_A) is the only method that can detect higher FFAs content.

The characterization of PS is very important because they are in contact with the active pharmaceutical ingredient and other excipients. In the current study of Torosantucci et al., the binding of phenol to a model fusion protein as well as to PS 20 was investigated and successfully quantified via diffusion ordered ¹H nuclear magnetic resonance spectroscopy (1H NMR).8 For the pharmaceutical industry, it is of key importance that the analytical methods used are comprehensive, rapid and simple. The main benefits of ¹H NMR spectroscopy are its high sensitivity with a minimal amount of the sample required compared to I_A. Sample preparation is very easy and rapid and does not require prior separation of PS constituents. Change in shift and/or the integration area of the proton signals can provide information about degradation mechanism, especially ester hydrolysis of PS. 9,10,11,12 Verbrugghe et al. used diffusion ordered ¹H NMR to quantify non-esterified ethoxylates in PS surfactants. This is important since these do not contribute to stabilisation of therapeutic proteins. However, we focused on FFAs that contribute to the formation of particles.¹³

Determination of I_A is a quantitative method used to determine the presence of acids in the sample under examined. According to the European pharmacopoeia (Ph. Eur.), I_A is the number that expresses in milligrams the quantity of potassium hydroxide required to neutralise free acids present in 1 g of the substance. Ph. Eur. specifies a limit of I_A for a PS 80 maximum of 2.0, while the Chinese Pharmacopoeia has the stricter requirements that the I_A should be limited to not more than 1.0. In order to ensure high sensitivity of I_A method both pharmacopoeias prescribe a large quantity of the tested PS sample (10.00 g) (Ph. Eur. 9.0, 0426 (01 / 2018), Ph. Eur. 9.0, 0428 (01 / 2011)).

The main manufacturers offer PS samples of two different grades for pharmaceutical applications. Multicompendial grade PS 80 meets the specifications from some particular pharmacopoeias: United States, Ph. Eur., British and Japanese. The Chinese Pharmacopoeia recently established a set of stricter requirements for PS 80 intended for injections. A new generation of superior grade PSs has been introduced to the market. This grade is sometimes referred to as "super-refined" or "ultra-pure", depending on the vendor. "Super-refined" is usually claimed to contain low peroxide, low endotoxin, and low impurity levels, while "ultra-pure" in the case of PS 80 refers to an oleic acid (OA) component comprising 98% pure OA. Moreover, depending on manufacturer and supplier's lot, acid values vary greatly. 9,14,15

2. Experimental

2. 1. Solvents and Reagents

Lauric acid (LA) and OA were purchased from Sig-

Table 1. Analysed fresh PS samples.

Sample	Data	Declared acid value	
PS 20	Tween® 20 Manufacturer: Sigma-Aldrich (USA) Material number: P2287 Lot number: MKCD6838	no data available	
PS 80	Tween® 80 Manufacturer: Sigma-Aldrich (USA) Material number: P4780 Lot number: BCBV4473	no data available	
PS 80 (HX2)	Tween® 80 Manufacturer: NOF Corporation (Japan) Material number: no available data Lot number: 612357Z2	0.1	

Table 2. Analysed PS samples with elapsed shelf life.

Sample	Data	Declared acid value
1	Tween® 20 Manufacturer: Sigma-Aldrich (USA) Material number: P1378 Lot number: SZBC2010V	1.1
2	Tween® 20 Manufacturer: Merck KGaA (Germany) Material number: 817072 Lot number: K47210572	1.6
3	Tween® 20 Manufacturer: Merck KGaA (Germany) Material number: 817072 Lot number: K46977172	1.6
4	Tween® 20 Manufacturer: Merck KGaA (Germany) Material number: 817072 Lot number: K47210572	1.6
5	Tween® 20 Manufacturer: J.T.Baker (USA) Material number: 4116-04 Lot number: 0000140208	1.3
6	Tween® 80 Manufacturer: Sigma-Aldrich (USA) Material number: P4780 Lot number: BCBG4950V	no data available
7	Tween® 80 Manufacturer: Merck KGaA (Germany) Material number: 817061 Lot number: K46921061	1.4

ma-Aldrich (USA) and Lauron (12-tricosanone) from Sigma-Aldrich (USA). Deuterated solvents: CD_3OD , $CDCl_3 + 0.03\%$ TMS and DMSO- $d_6 + 0.03\%$ TMS were purchased from Euriso-Top (France). All the information about the PS samples analysed is listed in Tables 1 and 2. Until the analysis all samples were stored at 2-8 °C in the refrigerator.

2. 2. ¹H NMR

Three parallel samples of fresh PS 20 and of PS 80 spiked (0-5%) samples were weighed (\sim 150 mg), dissolved in CD₃OD, CDCl₃ or DMSO- d_6 (450 μ L), and transferred to 5 mm NMR tubes. Another parallel of expired samples was prepared in CD₃OD.

All ¹H-NMR spectra were recorded using a Bruker AVANCE III 400 MHz NMR spectrometer. Acquisition parameters were set according to Zhang et al.; spectral width was set to 20.55 ppm, acquisition time to 4.3 s, relaxation delay to 20 s and number of scans to 16.¹² In order to cover 99% of the peak area, the integration region covers approximately 20 times the line width in

each direction. In cases where signal overlap was too severe to allow appropriate integration regions, peak deconvolution was used.

2. 3. Lauric/Oleic Acid and Lauron Spiking

In order to investigate the correlation between I_A and NMR integrals of FFA using linear regression, samples of PS20 and PS80 were spiked with LA and OA, respectively. Two parallels of fresh PS 20 and PS 80 samples with different FFA contents were prepared – 1%, 2%, 3%, 4% and 5% (w/w) (Figures S1 and S2). The samples were sealed under argon atmosphere and tightly closed with parafilm, stirred on a magnetic stirrer for approximately 6 hours at 300 rpm to give a homogeneous mixture. During mixing, the first parallel of the LA spiked samples was also heated in a sand bath, at 50 °C because of the LA melting temperature, which is approximately 45 °C in the solid state. Additionally, PS 20 samples were spiked with 5% (w/w) lauron in order to evaluate the presence of lauron in the raw PSs material.

2. 4. Determination of I_A

IA was determined according to the procedure for

testing PS 20 and PS 80, and prescribed in the Ph. Eur. 9.0. Approximately 10.0 g of sample was weighed into a 100 mL flask. 50 mL of a 1:1 (v/v) mixture of 96% ethanol and petroleum ether was added and mixed well. 0.5 mL of *phenolphthalein solution* R1 indicator was added to the sample solutions. The sample solutions were titrated with a 0.1 M NaOH solution until the pink colour persisted for at least 15 s.

3. Results and Discussion

3. 1. ¹H NMR

In order to establish the correlation between $^1\mathrm{H}$ NMR and I_A , a spiking study was carried out. Lauric and oleic acids were chosen because they form the main FA moiety of PS 20 and PS 80, respectively. The established method was tested on a series of PS 20 and PS 80 elapsed shelf life samples. The resulting values of the measured I_A were compared with those of I_A listed in the specifications of the individual PS sample.

The individual functional groups of PS 80 that correspond to the signals in the ¹H NMR spectra are shown in Figure 1. The main PS 80 peaks had already been charac-

HO 12 0 W-1 O 12 1 OH
$$X-1$$
 O 12 1 OH $X-1$ O

-O-CH₂-CH₂-O-C
H₂O

-CH₂-CH₂-O-C
CH₃

-CH₂-O-C-CH₂
CH₃OH

HO-C-CH₂-CH₂
O-C-CH₂-CH₂
O-C-CH₂-CH₂-

Fig 2. ¹H NMR spectrum of the fresh PS 20 sample recorded in CD₃OD.

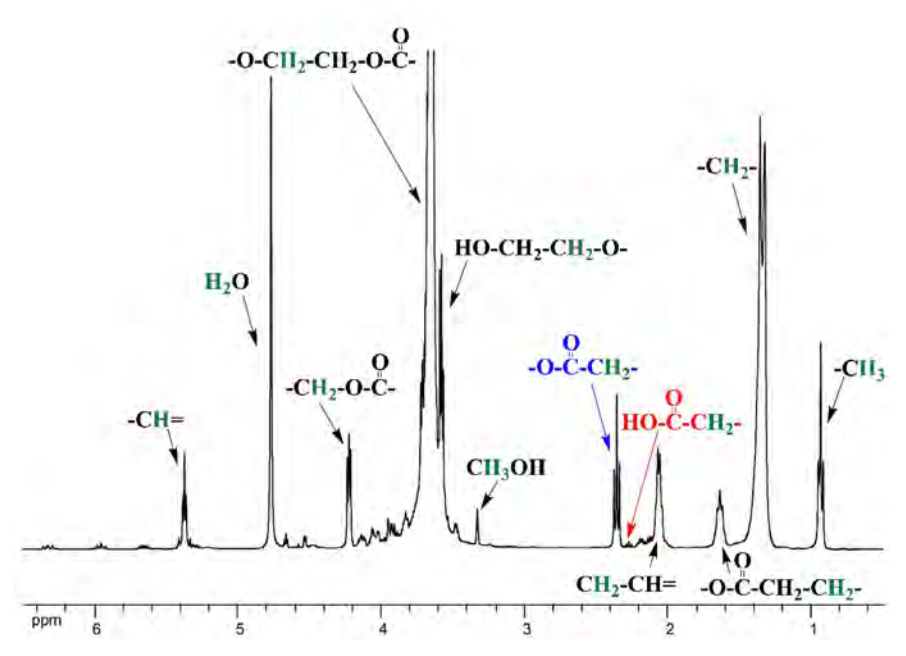


Fig 3. ¹H NMR spectrum of the fresh PS 80 sample recorded in CD₃OD.

terized. 12 Only spectra recorded in $\mathrm{CD_3OD}$ were used for comparison and evaluation of the obtained results; explanation of solvent selection is discussed below. The spectra were normalized by integrating the $\mathrm{CH_2}$ group at 2.36 ppm. The α -methylene groups of FFAs present in PS exhibit a distinctive chemical shift at 2.26 ppm (marked with red in Figures 2 and 3) clearly separable from those of esterified FAs (marked with blue in Figures 2 and 3).

The molar ratio between FFAs and esterified FA was determined by comparing their respective ¹H NMR signals for α-methylene groups (Figure 4). The signals for FFAs (2.26 ppm) and esterified FAs (2.36 ppm) are clearly separated and, most importantly, could be integrated separately. The values of integrals for esterified FA were set to 1, while those for FFA integrals are reported relative to the first ones. The ratios between integrals were then compared. On the other hand, signals in ¹H NMR spectrum corresponding to sorbitan polyoxyethylene (POE) of degraded and nondegraded PS 20 are practically indistinguishable as reported by Khossravi et al. and cannot be used to determine the ratio between nonesterified and esterified sorbitan POE.16 Quantification of nonesterified and esterified sorbitan POE is important, since nonesterified sorbitan POE may be present as impurity arising from PS synthesis without elevated levels of FFAs. 13 Perhaps the ratio between integrals of esterified FAs and sorbitan POE could indicate the presence of nonesterified sorbitan POE, however this is beyond the scope of this article.

In the ¹H NMR spectra, the most signals for PS constituents are well separated when recorded in CDCl₃, however the signals for FAs and FFAs are partly overlapping (Figures S5 and S6). Additionally, the chemical shift of the

signal for the α -methylene group of FFAs depends on the percentage of added FA. However, for the samples of PS 20 recorded in DMSO- d_6 , the signals are sufficiently apart, although there is overlapping of α -methylene peaks with other signals in the spectra of PS 80 (Figures S3 and S4). Signals for esterified FAs and FFAs are sufficiently separated in samples recorded in CD₃OD to allow accurate integration. Only spectra recorded in CD₃OD were used for comparison and evaluation of obtained results.

The results of the 1 H NMR method are given below as the molar percentage (n/n) of FFA molecules relative to that of all FA molecules (esterified and free) in the samples. The molar percentages of FFA were calculated (Equation S1) from the corresponding integrals of the signals belonging to FFA α -methylene and esterified FA (Figure 5).

3. 2. Determination of I_A

Values of I_A were calculated by considering the mass of weighed samples and the consumption of NaOH solution (Equation S2). Unlike the results obtained using the 1H NMR method, the values of I_A represent the content of all FAs in the sample, including formic acid, acetic acid and other organic acids (Figure 5).

3. 3. Method Correlation and Comparison of ¹H NMR and I_A Results

Using linear regression, the square of the correlation coefficient (R^2) was calculated for both PS 20 and PS 80 samples examined by the 1H NMR and I_A methods. It shows the percentage of the total variance of the variable y

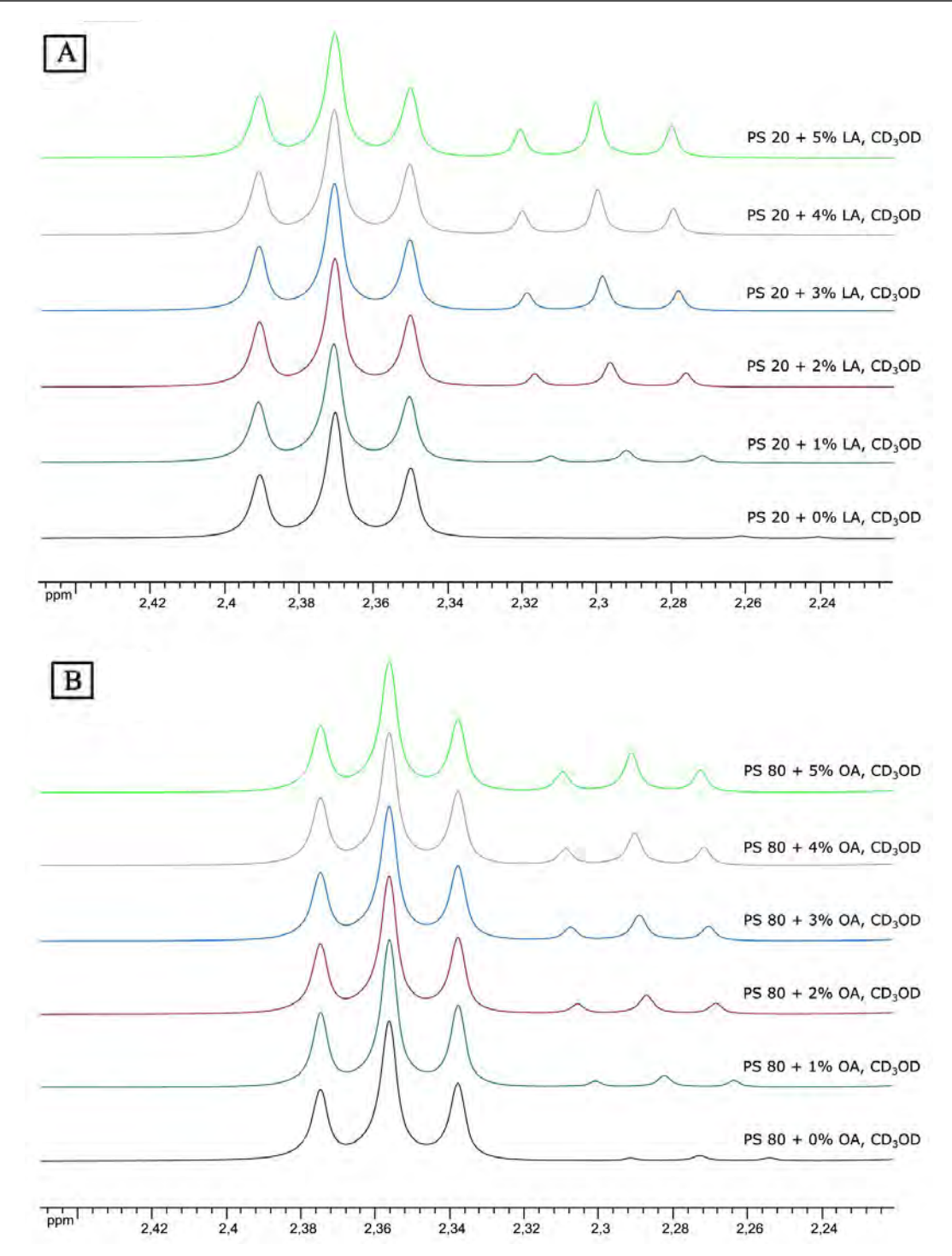


Fig 4. Comparison of spectra for PS 20 (A) and PS 80 (B) in CD₃OD after spiking with LA or OA.

(% FFAs and values of I_A) with respect to the variable x (% spiked FA). For evaluation of the methods, correlation R^2 values were rooted. The Pearson correlation coefficient (R) values obtained are very close to 1, which indicates that the calculated values of % FFAs and of the I_A are highly dependent on % spiked FA in PS samples, which is expected (Figure 6). The values obtained vary only slightly and depend strongly on each other. It can be concluded that there

is a good correlation between the two methods and that the methods are comparable to each other.

From the results of 1H NMR (Tables S1 and S2) and I_A (Tables S3 and S4) determination it is seen that the values of FFA and I_A in the PS 20 samples increase more rapidly with increasing the % LA than those in the corresponding PS 80 samples with increasing the % OA. The reason for the difference lies in the molecular weight of

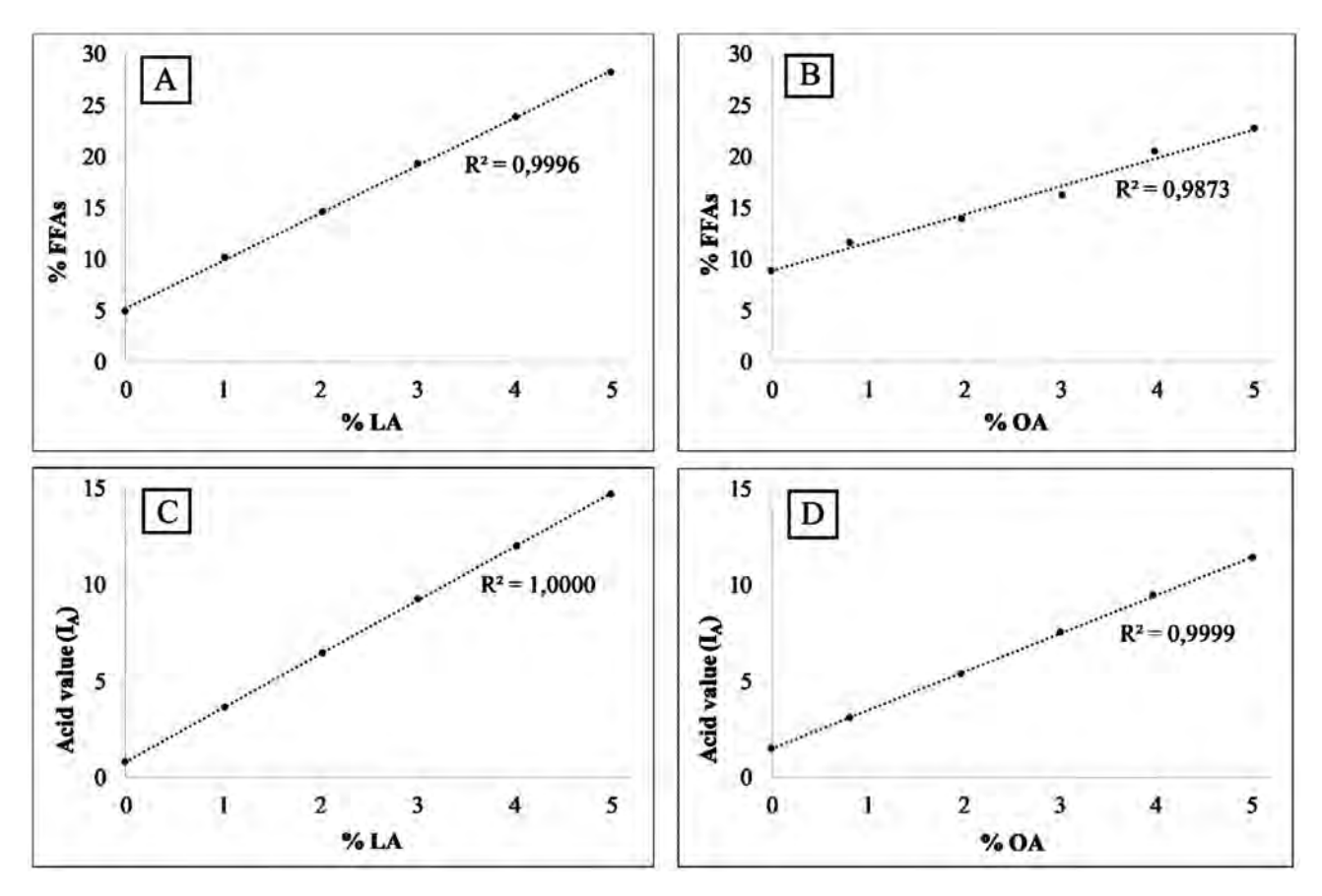


Fig 5. Values of % FFAs (n/n %) relative to % LA (w/w) in PS 20 (A), values of % FFAs (n/n) relative to % OA (w/w) in PS 80 (B), I_A values relative to % LA (w/w) in PS 20 (C) and I_A values relative to % OA (w/w) in PS 80 (D).

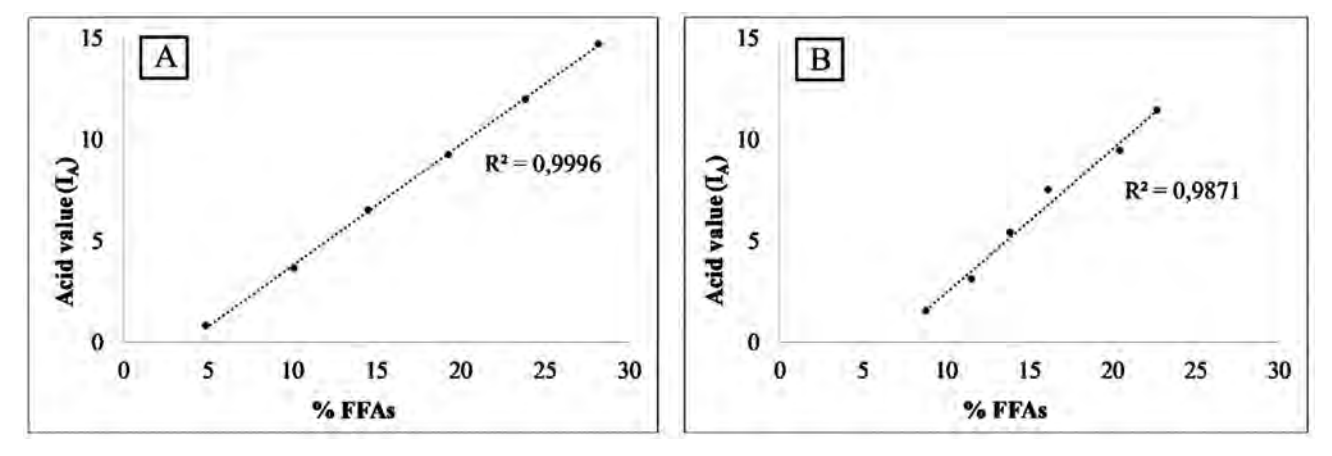


Fig 6. $I_{\rm A}$ values in correlation to % FFAs (w/w) in PS 20 (A) and PS 80 (B) samples.

added FA; the same added mass of FA corresponds to more moles in the case of LA.

3. 4. Benefits of ¹H NMR Method

¹H NMR enables comprehensive PS structural information in terms of quality control of input PS and differentiation between PS 20 and PS 80 of different quality grades.

Long-chain ketone lauron (12-tricosanone) is a newly identified impurity present already in specific PS raw material lots and is not a degradation product. It is poorly soluble in water and therefore forms visible particles in protein formulations. ¹⁷ In spiked PS 20 samples, the lauron signal is well separated from the α -methylene group signal for esterified FA and FFAs. Using the ¹H NMR method, lauron can be easily identified (Figure 7).

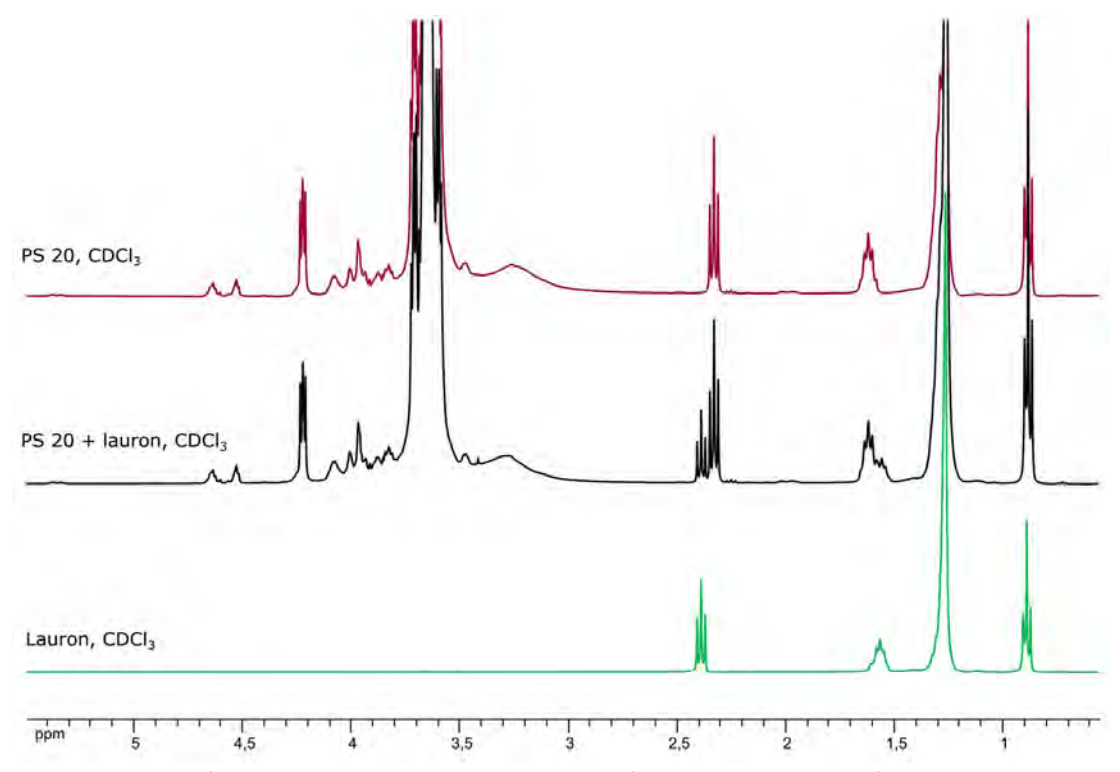


Fig 7. Comparison of raw PS 20 ¹H NMR spectra, lauron spiked (10% w/w) PS 20 ¹H NMR spectra and lauron ¹H NMR spectra.

¹H NMR can also be used as a stability indicating method for PS degradation. One big difference between PS 20 and PS 80 ¹H NMR spectra is that signals belonging to the OA double bond, which is found only in PS 80, are seen as -CH= and -CH₂-CH= groups. The first one is visi-

ble at a chemical shift of about 5.4 ppm and is a signal for the CH groups at the double bond in the FA chain, marked by the number 8 in Figure 1. The second is visible at a chemical shift of about 2.0 ppm and constitutes a signal for the following double bond adjacent to the CH_2 group in

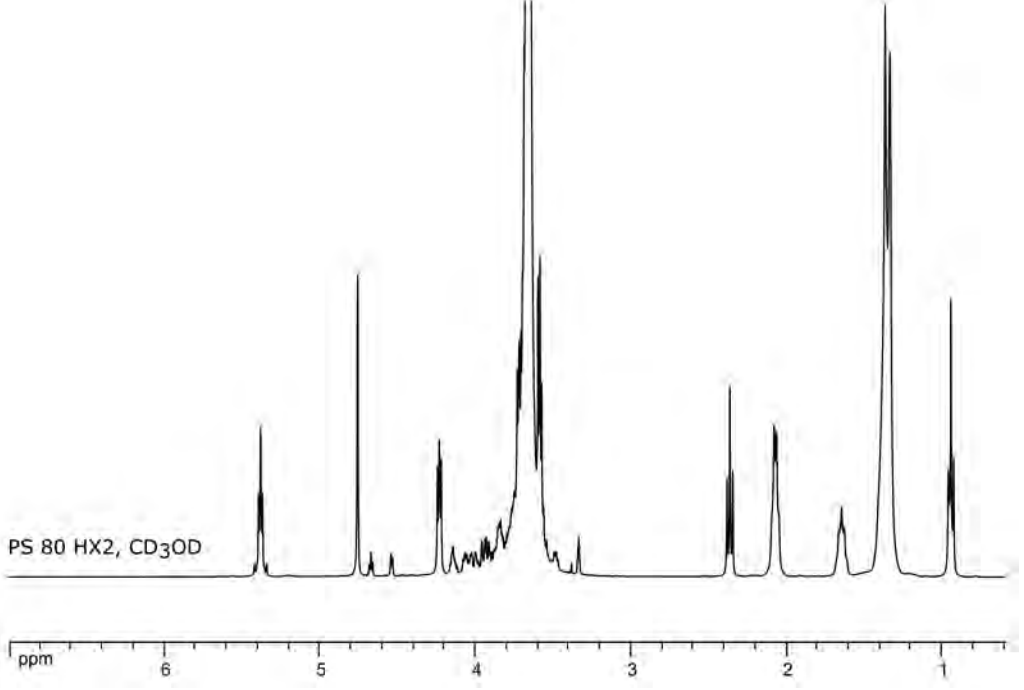


Fig 8. ¹H NMR spectrum, recorded in CD₃OD, of the fresh "ultra-pure" PS 80 sample. In comparison to the spectrum of "multicompendial-grade" PS 80 (Figure 3) the triplet at 2.3 ppm belonging to FFA is absent, indicating that there is no FFA in the sample.

the FA chain, marked by a number 9 in Figure 1. The proportion of OA in the FA fraction can be estimated from the ratio of the double bond integral at 5.4 ppm to that at 0.9 ppm of the terminal CH_3 group protons.

During their study of the thermal oxidation of PS 80, using ¹H NMR, Hvattum et al. discovered that about 9% of all FAs present contained a *ZE* or *EZ* conjugated double bond. ¹⁸ We can also confirm the presence of conjugated (9*Z*,11*E*)-linoleic acid, which has multiple double bonds seen as an additional 4 signals ranging from 5 to 6 ppm. The described signals were seen only in multicompendial grade PS 80 in Figure 2, not in the "ultra-pure" one in Figure 8. Conjugated double bond FAs are more susceptible to auto-oxidation than FAs with isolated double bound, so their characterization already in raw PS samples is very important.

3. 5. Comparison of the Results of the Use of ¹H NMR and I_A for Elapsed Shelf Life Samples

The content of FFAs in the samples with elapsed shelf life was determined relative to the total content of FA. Seven randomly selected elapsed shelf life PS samples were analyzed in order to confirm the correlation of $^1\mathrm{H}$ NMR and I_A methods (Table 3). From the results for elapsed shelf life PS samples, maximum values of % FFA and I_A were found in sample 6, which is expected since it is the oldest sample according to the date of production (October 2011). The value determined exceeded the maximum allowable value of I_A for PS 80, 2.0, as prescribed by Ph. Eur. 9.0. The same trend was observed in sample 1 which, according to the date of production (July 2012), is the second oldest sample in the analysed PSs. In all other samples, the I_A values were still within Ph. Eur. specifications, despite their expiry date.

Comparing samples 1, 2 and 4, the values of % FFAs are seen to be practically the same (around 7%), while

Table 3. The integral values of signals relating to FFA $\alpha\text{-methylene}$ groups and their measured I_A values.

Sample	% FFAs	I_A
1	7.41	2.3
2	7.06	1.8
3	4.76	1.7
4	7.06	1.8
5	4.40	1.3
6	10.63	2.7
7	7.49	1.5

those of I_A vary greatly between sample 1 and samples 2 and 4 (Figure 9). The fact that I_A values give an indication of all the acids present in the sample must be considered, while the 1H NMR values exclude the content of formic, acetic and other organic acids. If there was autoxidation along the ethylene oxide portion of the PS during storage, short-chain fatty acids, such as formic and acetic acid, would result in increased I_A values. An increase in I_A in sample 1 can therefore be interpreted as a consequence of oxidation processes.

4. Conclusions

The content of FFAs is an important indicator of PS degradation, especially ester hydrolysis, and therefore a useful parameter from the standpoint of PS stability testing. The source of FFAs present in PS could be either degradation processes or synthesis. The distribution and quantity of FFAs in PSs impact on the product quality. Accumulated FFAs, which are insoluble in water, could ultimately precipitate to form visible particles. In this study, the ¹H NMR method and the pharmacopoeia method for determination of I_A were compared. In the case of FFAs, the results obtained by the two methods

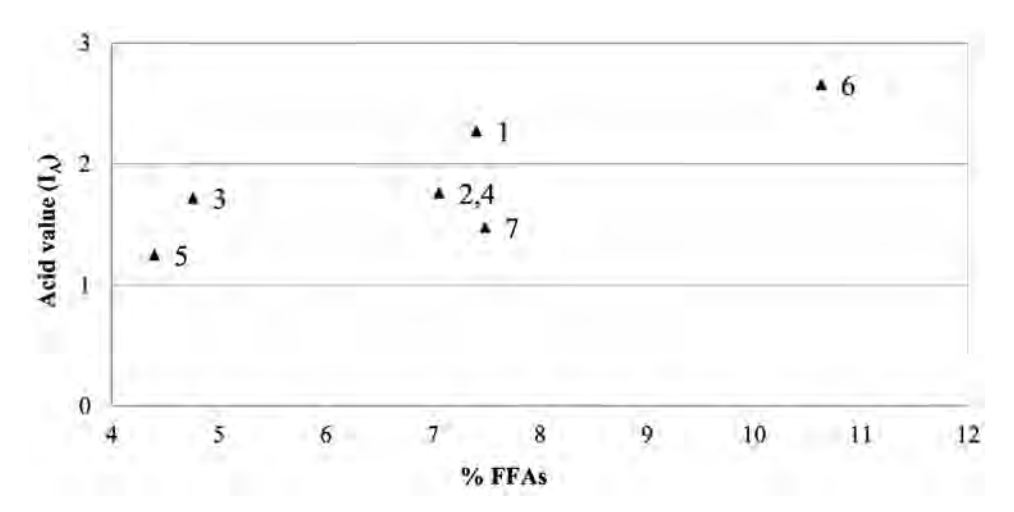


Fig 9. I_A values correlated to the % FFAs (w/w) in PS 20 (1-5) and PS 80 samples (6,7).

correlate strongly with each other. However, the pharmacopoeia I_A method is non-specific and measures the total amount of acidic components whereas, with ¹H NMR, the amount of FFAs could be measured specifically. Additional benefits of ¹H NMR method are, especially, the much simpler and faster sample preparation and the lower amounts of sample needed when comparing with the I_A determination method. The ¹H NMR method gives comprehensive PS structural information, information of PS degradation and the impurity profile. It could be definitively used as alternative method for monitoring PS degradation, instead of decrease in PS POE part, is much easier to monitor increase in FFAs signals as we have shown in our manuscript. Moreover, a newly discovered impurity in PS raw material, the long chain ketone lauron (12-tricosanone), can be identified using ¹H NMR.

Abbreviations

FA Fatty acidFFAs Free fatty acidsIA Acid valueLA Lauric acid

NMR Nuclear magnetic resonance spectroscopy

OA Oleic acid POE Polyoxyethylene PS Polysorbate

R² Square of the correlation coefficient

RSD Relative standard deviation

5. References

- H.-C. Mahler, F. Senner, K. Maeder, R. Mueller, *J. Pharm. Sci.* 2009, 98, 4525–33. DOI:10.1002/jps.21776
- 2. S. Kiese, A. Papppenberger, W. Friess, H.C. Mahler, *J. Pharm. Sci.* 2008, *97*, 4347–66. **DOI:**10.1002/jps.21328
- P. Garidel, C. Hoffmann, A. Blume, *Biophys. Chem.* 2009, 143, 70–8. DOI:10.1016/j.bpc.2009.04.004
- R. S. K. Kishore, S. Kiese, S. Fischer, A. Pappenberger, U. Grauschopf, H.C. Mahler, *Pharm. Res.* 2011, 28, 1194–210. DOI:10.1007/s11095-011-0385-x
- X. Cao, R.M. Fesinmeyer, C. J. Pierini, C. C. Siska, J. R. Litowski, S. Brych et al., *J. Pharm. Sci.* 2015, 104, 433–46.
 DOI:10.1002/jps.24126
- A. W. Ralston, C. W. Hoerr, J. Org. Chem. 1942, 7, 546–55.
 DOI:10.1021/jo01200a013
- 7. N. Doshi, B. Demeule, S. Yadav, *Mol. Pharm.* 2015, *12*, 3792–804. **DOI**:10.1021/acs.molpharmaceut.5b00310
- R. Torosantucci, B. Furtmann, B. Elshorst, S. Pfeiffer-Marek, T. Hartleb, N. Andres et al., *J. Pharm. Sci.* 2018, *107*, 2531–7. DOI:10.1016/j.xphs.2018.05.021
- A. Martos, W. Koch, W. Jiskoot, K. Wuchner, G. Winter, W. Friess et al., *J. Pharm. Sci.* 2017, *106*, 1722–35.
 DOI:10.1016/j.xphs.2017.03.001

- H. Vu Dang, A. I. Gray, D. Watson, C. D. Bates, P. Scholes, G. M. Eccleston, *J. Pharm. Biomed. Anal.* 2006, 40, 1155–65.
 DOI:10.1016/j.jpba.2005.10.007
- Z. Wu, Q. Zhang, N. Li, Y. Pu, B. Wang, T. Zhang, J. Sep. Sci. 2017, 40, 288–98. DOI:10.1002/jssc.201600707
- Q. Zhang, A. Wang, Y. Meng, T. Ning, H. Yang, L. Ding et al., *Anal. Chem.* 2015, 87, 9810–6.
 - DOI:10.1021/acs.analchem.5b02096
- 13. M. Verbrugghe, E. Cocquyt, P. Saveyn, P. Sabatino, D. Sinnaeve, J. C. Martins et al., *J. Pharm. Biomed. Anal.* 2010, *51*, 583–9. **DOI**:10.1016/j.jpba.2009.09.025
- S. R. Singh, J. Zhang, C. O'Dell, M.-C. Hsieh, J. Goldstein, J. Liu et al., AAPS PharmSciTech. 2012, 13, 422–30.
 DOI:10.1208/s12249-012-9759-6
- A. C. McShan, P. Kei, J. A. Ji, D. C. Kim, Y. J. Wang, PDA J. Pharm. Sci. Technol. 2016, 70, 332–45.
 DOI:10.5731/pdajpst.2015.005942
- M. Khossravi, Y.-H. Kao, R. J. Mrsny, T. D. Sweeney, *Pharm. Res.* 2002, *19*, 634–9. **DOI**:10.1023/A:1015306112979
- V. Hampl, X. Guo, C. Ehrenstrasser, M. Viertler, L. Rayner, G. Campanelli et al., *J. Pharm. Sci.* 2018, *107*, 1552–61.
 DOI:10.1016/j.xphs.2018.02.017
- 18. E. Hvattum, W. L. Yip, D. Grace, K. Dyrstad, *J. Pharm. Biomed. Anal.* 2012, *62*, 7–16. **DOI:**10.1016/j.jpba.2011.12.009

Povzetek

Polisorbati (PS) so najpogosteje uporabljene neionske površinsko aktivne snovi v formulacijah s proteini. Njihovo razgradnjo so v zadnjih letih intenzivno proučevali. Hidroliza estrske vezi je ena od številnih razgradnih poti polisorbatov, ki lahko vodi v kopičenje prostih maščobnih kislin (FFAs) in v tvorbo delcev. Razporeditev in količina FFAs v PS neposredno vplivata na kakovost končnega izdelka. Karakterizacija vhodnega PS je izredno pomembna, saj se začetna vsebnost FFAs med različnimi proizvajalci zelo razlikuje. Namen naše študije je bil razviti hitro in enostavno metodo za kvantifikacijo FFAs v PS. Vsebnost FFAs smo izmerili izbranim vzorcem PS 20 in 80 z uporabo dveh metod, z metodo protonske jedrske magnetne resonančne spektroskopije (¹H NMR) in s farmakopejsko metodo določanja kislinskega števila (I_A). Metodi smo ovrednotili z uporabo metode standardnega dodatka in na podlagi dobljenih rezultatov ugotovili, da sta metodi zamenljivi. Zaključili smo, da je ¹H NMR uporabna metoda za kontrolo kakovosti vhodnih PS in hitra metoda za spremljanje razgradnje PS s hidrolizo in oksidacijo. Tudi novo odkrito nečistoto v vhodnem PS, dolgoverižni keton 12-trikozanon, lahko identificiramo z uporabo ¹H NMR.



Except when otherwise noted, articles in this journal are published under the terms and conditions of the Creative Commons Attribution 4.0 International License



Scientific paper

DNA Interaction, *in vitro* Antibacterial and Cytotoxic Activities of Ru(III) Heterochelates

Parag S. Karia, Pankaj A. Vekariya, Anshul P. Patidar, Darshana N. Kanthecha, Bhupesh S. Bhatt and Mohan N. Patel*

Department of Chemistry, Sardar Patel University, Vallabh Vidyanagar-388 120, Gujarat, India

* Corresponding author: E-mail: jeenen@gmail.com, bhupeshbhatt31@gmail.com Phone number: (+912692) 226856*218

Received: 04-10-2019

Abstract

Ruthenium(III) complexes $[Ru(bphtpy)(PPh_3)Cl_3]$ (bphfpy = diphenylfuranylpyridine derivatives) were synthesized and characterized by LCMS, IR spectroscopy, elemental analysis and magnetic measurements. All the complexes were screened for their antibacterial activity in terms of minimum inhibitory concentration against two Gram-positive and three Gram-negative bacterial species. DNA binding study by absorption titration and viscosity measurement shows that complexes bind in an intercalating mode, which is also confirmed by molecular docking. All the complexes were also screened for the DNA nuclease property of pUC19 plasmid DNA. The cytotoxicity study of the synthesized complexes was performed to elucidate the LC_{50} values to find out the toxicity profile of the complexes.

Keywords: N,O-donor ligand; Ruthenium(III)complexes; DNA interaction; Cytotoxicity

1. Introduction

A great history of transition metal complexes is associated with their effectiveness in the numerous diseases cure, 1-3 including the major application in the field of novel anticancer drug discovery. The interaction of coordination compounds with various biomolecules is facilitated due to varying oxidation states of central metal ion, which can eventually result in surprising pharmacological and exceptional curative properties. 4-8 Metals can alter the physiological condition and the intrinsic toxicity of metal ions can be reduced by their coordination with ligands. The biological properties of ligands can increase with metal chelation and can cause a synergistic effect on both ligand and metal ion. 10 Recently large interest has been drawn on the ruthenium based coordination compounds in anticancer drug development. 11-13

Ruthenium can be seen as a promising metal after platinum due to its kinetics and timescales comparison to cellular division processes similar to platinum.¹⁴ Ruthenium complexes with N,N-donor ligand have found significant application as metallo-intercalators.^{15,16} Changing substituent groups in the ligand can create electron density distribution and space configuration differences of complexes, resulting in diverse spectral properties and biolog-

ical activities.^{17,18} The N,O-donor ligand has been selected owing to its antifungal activity exhibited due to furan ring,¹⁹ and the role of bulky co-ligand is to stabilize the complex which prevents quick dissociation of the complex. hence the compound can reach the pharmacological target such as DNA.²⁰

Keeping these aspects in mind, we synthesized of ruthenium(III) complexes with PPh₃ and N,O-donor ligand, and studied the antimicrobial activity, DNA interaction study and cytotoxic activity.

2. Experimental

Material and reagents: The analytical grade chemicals purchased were used as such without further purification. RuCl₃·3H₂O, 4-chlorobenzaldehyde, 2-acetylfuran, 4-fluorobenzaldehyde, 4-bromobenzaldehyde, 3-chlorobenzaldehye, 3-fluorobenzaldehyde, 3-bromobenzaldehyde and HS-DNA were purchased from Sigma Chemical Co., India. Bromophenol blue, ethidium bromide (EB), Luria Broth and agarose were purchased from Himedia, India. Perkin–Elmer 240 Elemental Analyzer was used to collect microanalytical data. Room temperature magnetic susceptibility was measured by Gouy's method. FT-IR

data were collected by FT–IR ABB Bomen MB 3000 spectrophotometer. The ¹H NMR and ¹³C NMR were recorded on a Bruker Avance (400 MHz). UV–Vis spectra of the complexes were recorded on UV-160A UV–Vis spectrophotometer, Shimadzu (Japan). Cleavage of pUC19 DNA was quantified by AlphaDigiDocTM RT. Version V.4.0.0. The thermogram of complexes were recorded with a Mettler Toledo TGA/DSC 1 thermogravimetric analyser.

Synthesis of ligands: The ligands (L¹–L⁶) were synthesized according to the reported method using modified Krohnke pyridine synthesis method.²¹ The synthesis and characterization of ligands are provided in the supplementary material.

Synthesis of Ru(III) complexes (1–6): [RuCl₃(PPh₃)₃] was prepared by refluxing methanolic solution (50 mL) of RuCl₃·3H₂O (0.01 mol) with PPh₃ (0.03 mol) and conc. HCl (60 mL) for 1 h. The obtained reddish brown precipitates were filtered, dried and recrystallized by using hot methanol.

Synthesis of [$Ru(L^1)(PPh_3)Cl_3$] (1): [$RuCl_3(PPh_3)_3$] (0.1 mmol) in toluene (20 mL) and a methanolic solution (20 mL) of 4-(4-fluorophenyl)-2-(furan-2-yl)-6-p-tolylpyridine (L^1) (0.1 mmol) were combined and refluxed for 4 h. (Scheme 1). The blackish brown product obtained was washed with toluene to remove unreacted precursor and next washed with methanol to remove unreacted ligand and dried under vacuum. Yield: 22 %, m.p.: 287–290 °C, μ_{eff} : 1.89 B.M. Anal. Calc. for: $C_{40}H_{31}Cl_3FNOPRu$ (799.08): Calc. (%): C, 60.12; H, 3.91; N, 1.75; Ru, 12.65. Found (%): C, 60.03; H, 3.93; N, 1.70, $Ru_{(gravimetrically)}$, 12.60. IR (KBr, 4000–400 cm⁻¹): 3030, ν (C–H)ar stretching; 1545, ν (C=C); 1505, ν (C=N); 543, ν (Ru-O); 445, ν (Ru-N); 1454, 1032, 698, ν (PPh₃). UV–Vis. λ_{max} (nm) (DMSO): 560, 420, 260, Mass (m/z%): 800.06 (100) [M^+].

Synthesis of $[Ru(L^2)(PPh_3)Cl_3]$ (2): $[RuCl_3(PPh_3)_3]$ (0.1 mmol) in toluene (20 mL) and a methanolic solution (20 mL) of 4-(4-chlorophenyl)-2-(furan-2-yl)-6-*p*-tolylpyridine (L²) (0.1 mmol) were combined and refluxed for 4 h. (Scheme 1). The blackish brown product obtained was washed with toluene to remove unreacted precursor and next washed with methanol to remove unreacted ligand and dried under vacuum. Yield: 19.9%, m.p.: 274-276 °C, μ_{eff}: 1.81 B.M. Anal. Calc. for: C₄₀H₃₁Cl₄NOPRu (815.54): Calc. (%): C, 58.91; H, 3.83; N, 1.72; Ru, 12.39. Found (%): C, 58.84; H, 3.89; N, 1.78, Ru_(gravimetrically), 12.37. IR (KBr, 4000–400 cm⁻¹): 3038, ν(C–H)ar stretching; 1541, ν(C=C); 1509, ν(C=N); 561, ν(Ru-O); 456, ν(Ru-N); 1458, 1029, 689, ν(PPh₃). UV–Vis. λ_{max} (nm) (In DMSO): 565, 425, 261.

Synthesis of $[Ru(L^3)(PPh_3)Cl_3]$ (3): $[RuCl_3(PPh_3)_3]$ (0.1 mmol) in toluene (20 mL) and a methanolic solution (20 mL) of 4-(4-bromophenyl)-2-(furan-2-yl)-6-*p*-tolylpyridine (L³) (0.1 mmol) were combined and refluxed for 4 h. (Scheme 1). The dark brown product obtained was

washed with toluene to remove unreacted precursor and next washed with methanol to remove unreacted ligand and dried under vacuum. Yield: 20.1%, m.p. >300 °C, μ_{eff}: 1.84 B.M. Anal. Calc. for: C₄₀H₃₁Cl₃BrNOPRu (859.99): Calc. (%): C, 55.86; H, 3.63; N, 1.63; Ru, 11.75. Found (%): C, 55.78; H, 3.64; N, 1.66, Ru_(gravimetrically), 11.79. IR (KBr, 4000–400 cm⁻¹): 3041, υ(C–H)ar stretching; 1541, υ(C=C); 1506, υ(C=N); 554, υ(Ru-O); 449, υ(Ru-N); 1462, 1029, 694, υ(PPh₃). UV–Vis. λ_{max} (nm) (In DMSO): 575, 430, 263.

Synthesis of $[Ru(L^4)(PPh_3)Cl_3]$ (4): $[RuCl_3(PPh_3)_3]$ (0.1 mmol) in toluene (20 mL) and a methanolic solution (20 mL) of 4-(3-fluorophenyl)-2-(furan-2-yl)-6-p-tolylpyridine (L⁴) (0.1 mmol) were combined and refluxed for 4 h. (Scheme 1). The blackish brown product obtained was washed with toluene to remove unreacted precursor and next washed with methanol to remove unreacted ligand and dried under vacuum. Yield: 18.4%, m.p.: 286-290 °C, μ_{eff} : 1.86 B.M. Anal. Calc. for: $C_{40}H_{31}Cl_3FNOPRu$ (799.08): Calc. (%): C, 60.12; H, 3.91; N, 1.75; Ru, 12.65. Found (%): C, 60.13; H, 3.97; N, 1.68, $Ru_{(gravimetrically)}$, 12.72. IR (KBr, 4000–400 cm⁻¹): 3033, ν (C–H)ar stretching; 1549, ν (C=C); 1512, ν (C=N); 549, ν (Ru-O); 453, ν (Ru-N); 1456, 1021, 697, ν (PPh₃). UV–Vis. λ_{max} (nm) (In DMSO): 563, 420, 260.

Synthesis of $[Ru(L^5)(PPh_3)Cl_3]$ (5): $[RuCl_3(PPh_3)_3]$ (0.1 mmol) in toluene (20 mL) and a methanolic solution (20 mL) of 4-(3-chlorophenyl)-2-(furan-2-yl)-6-*p*-tolylpyridine (L⁵) (0.1 mmol) were combined and refluxed for 4 h. (Scheme 1). The blackish brown product obtained was washed with toluene to remove unreacted precursor and next washed with methanol to remove unreacted ligand and dried under vacuum. Yield: 17%, m.p.: 276-278 °C, μ_{eff}: 1.80 B.M. Anal. Calc. for: C₄₀H₃₁Cl₄NOPRu (815.54): Calc. (%): C, 58.91; H, 3.83; N, 1.72; Ru, 12.39. Found (%): C, 58.89; H, 3.79; N, 1.68, Ru_(gravimetrically), 12.39. IR (KBr, 4000–400 cm⁻¹): 3054, υ(C–H)ar stretching; 1543, υ(C=C); 1507, υ(C=N); 563, υ(Ru-O); 446, υ(Ru-N); 1443, 1024, 692, υ(PPh₃). UV–Vis. λ_{max} (nm) (In DMSO): 570, 428, 262.

Synthesis of [$Ru(PPh_3)(L^6)(Cl_3]$ (6): [$RuCl_3(PPh_3)_3$] (0.1 mmol) in toluene (20 mL) and a methanolic solution (20 mL) of 4-(3-bromophenyl)-2-(furan-2-yl)-6-p-tolylpyridine (L^6) (0.1 mmol) were combined and refluxed for 4 h. (Scheme 1). The dark brown product obtained was washed with toluene to remove unreacted precursor and next washed with methanol to remove unreacted ligand and dried under vacuum. Yield: 19%, m.p.: >300 °C, μ_{eff}: 1.89 B.M. Anal. Calc. for: $C_{40}H_{31}Cl_3BrNOPRu$ (859.99): Calc. (%): C_7 , 55.86; C_7 , 1.61, C_7 , C_7 , C_7 , 11.70. IR (KBr, 4000–400 cm $^{-1}$): 3063, C_7 , C_7 (C_7) ar stretching; 1554, C_7 , C_7 (C_7) (C_7) (C_7), 546, C_7 0(C_7), 460, C_7 0(C_7 1, 1443, 1027, 690, C_7 1, C_7 1, C_7 1, 424, 262.

In vitro antibacterial screening: In vitro antibacterial study of all compounds was performed against three

Gram-negative and two Gram-positive bacteria according to the literature method. 22

DNA interaction study: Metal–DNA interactions was probed using electronic absorption titration and viscosity measurement, according to the literature method.^{23,24} The molecular docking study was performed by HEX 8.0 software.²⁵

Cytotoxicity study: The Brine shrimp lethality activity (BSLA) test was carried out referring to the protocol of Mayer *et al.*²²

Gel electrophoresis study: The DNA cleavage study for synthesized complexes was performed using the reported procedure.²⁶

3. Results and Discussion

Synthesis: The N,O-donor ligands (L^1 – L^6) were synthesized by refluxing the mixture of pyridinium salt of 2-acetylfuran and substituted enones in methanol in presence of excess of ammonium acetate for 6 h. The methanolic solution of the ligands and solution of ruthenium precursor [RuCl₃(PPh₃)₃] in toluene were refluxed for 4 h to obtain complexes 1–6. General reaction scheme for the synthesis of complexes is given in Scheme 1.

magnetic moment values were found in the range of 1.80–1.89 BM. The theoretical spin-only value is 1.73 BM, which suggests that the metal ion in complexes possess one unpaired electron and possess $s = \frac{1}{2}$ system.

The thermogravimetric curve of complex 1 (Supplementary material) shows no mass loss up to 180 °C signifying the absence of water molecule or any volatile component. First mass loss (13.34%) during 190–260 °C corresponds to the loss of chlorine atoms. Second mass loss (32.72%) during 360–520 °C corresponds to the loss of PPh₃ moiety. The third mass loss (41.14%) during 610–810 °C corresponds to the loss of neutral bidentate ligand and leaving behind residual metal oxide.

Mass spectrum of complex **1** shows molecular ion peak at m/z = 800.06 (M), 802.06 (M+2), 804.07 (M+4) and 806.06 (M+6) (Supplementary material), due to the presence of covalently bonded three chlorine atoms (with metal ion). The peak observed at m/z = 763.09 corresponds to the one Cl atom loss. Other fragments observed are 728.09, 693.12, 470.91, 435.07, 431.07, 398.97, 364.07, 329.08 and 262.11 m/z, for which proposed fragmentation pattern is shown in supplementary material.

IR spectral data of ligands and complexes were compared (Supplementary material) to investigate the coordination of ligand with ruthenium ion. The ring stretching frequencies of v(C=N) of ligands (1497–1487 cm⁻¹)^{27,28} were shifted to higher frequencies (1505–1512 cm⁻¹) in metal complex, suggests the metal ion coordination with

Scheme 1. Synthesis of ruthenium(III) complexes.

Spectral and analytical characterization: The electronic spectra showed three bands in the 260–575 nm region. The bands at 560–575 nm, 420–430 nm, 260 nm region corresponds to d–d transition, metal-to-ligand charge transfer and intraligand charge transfer, respectively. The magnetic moment of Ru(III) complexes was measured using Gouy's magnetic balance at room temperature. The

the nitrogen atoms of heterocycles.²⁹ The ν (C=C)_{ar} and ν (C-H)_{ar} bands were observed at 1541–1554 cm⁻¹ and 3030–3063 cm⁻¹, respectively. Additional bands in metal complexes were observed at 543–563 cm⁻¹ and 445–460 cm⁻¹ corresponds to ν (Ru–O) and ν (Ru–N), respectively.^{30,31}

In vitro antibacterial activity: The antibiotics resistance among bacteria has become a global problem, which has risen the need of novel antimicrobial agents. The results

(Supplementary material) of antibacterial screening shows higher efficiency of ruthenium complexes than the parent ligands and ruthenium salt against tested bacterial species under identical experimental conditions. However, the synthesized complexes show lower antibacterial potency compared to standard antibiotic like ofloxacin (MIC = 1.24-2.0 µM, for different bacterial species under investigation). The increase in lipophilic nature due to chelation may be the reason for the potentiation of antibacterial activity of complexes. The different molecular targets of antibacterial agents for exerting their mode of action are cell wall synthesis and cytoplasmic membrane. The chelation increases the ability of a complex to cross a cell membrane³² according to the Tweedy's chelation theory,³³ by decreasing the polarity of metal ion through partial sharing of positive charge over chelating atoms.

DNA interaction study: *Absorption titration:* The observed absorbance is plotted against wavelength and shift in absorbance and change in wavelength is calculated to investigate the binding mode. In the absorption spectra of $[Ru(L^1)(PPh_3)Cl_3]$ (Figure 1), it is found that upon increasing the DNA concentration, hypochromism is observed in MLCT (around 420 nm) and intra-ligand charge transfer bands (around 260 nm) with slightly red shift indicative of the intercalative mode of binding. The strength of binding is measured from K_b values obtained using the equation

[DNA]/ $(\varepsilon_a - \varepsilon_f) = [DNA]/(\varepsilon_b - \varepsilon_f) + 1/K_b(\varepsilon_b - \varepsilon_f)$ where ε_a , ε_f , and ε_b correspond to A_{obsd} /[complex], the extinction coefficient of free complex, and complex in the fully bound form, respectively. The K_b values for complexes **1–6** are found 5.18×10^5 , 3.41×10^5 , 1.69×10^5 , 1.66×10^5 , 1.46×10^5 and 1.78×10^5 M⁻¹, respectively. The observed results show that complex **1** has the highest binding propensity with DNA, which can be attributed to the presence of most electronegative F atom as a substituent atom at p-po-

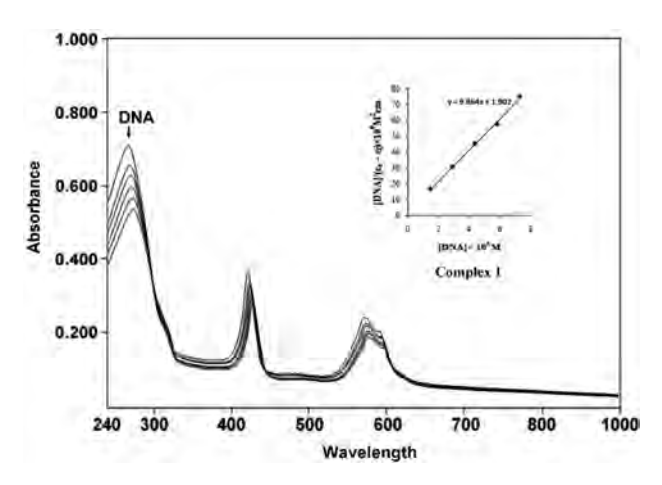


Figure 1. Electronic absorption spectra of complex 1 with increasing concentration of Herring Sperm DNA (HS–DNA) in phosphate buffer Inset: Plots of [DNA]/ $(\epsilon_a - \epsilon_f)$ versus [DNA] for the titration of DNA with ruthenium(III) complex 1.

sition to the ancillary ligand. The trend is also followed for complex **2** and complex **3**, having Cl and Br atom as substituent atom at *p*-position to the ancillary ligand. The other complexes having ligand with halogen substituent at *m*-position have a relatively lower binding propensity. So we can say that the DNA binding affinity of complexes depends upon the electronic properties of ligands. The obtained K_b values of complexes are found higher than $[Ru(NH_3)_4(dip)]^{2+}$ $(1.50\times10^4 M^{-1})$, ³⁴ comparable to $[Ru(phen)_2pzip]^{2+}$ $(9.5\times10^5 M^{-1})^{35}$ and lower than $[Ru(bpy)_2(HBT)]^{2+}$ $(5.71\times10^7 M^{-1})$. The absorption spectral data and plots of $[DNA]/(\varepsilon_a - \varepsilon_f)$ versus [DNA] for the titration of DNA with complexes **1–6** are shown in supplementary material.

Viscosity measurement: The viscosity of HS-DNA was measured by varying the concentration of the complexes, to further explore the interaction between ruthenium(III) complexes and DNA. The relative viscosity of the HS-DNA increases with complex solution addition (Supplementary material), suggesting intercalative mode of binding. The curve of complex 1 resembles very similar to EtBr and is much higher in magnitude than other complexes suggesting a strong interactive binding of complex 1 than other synthesized complexes.

Molecular docking study: To explore the interaction mode and binding affinity, docking studies were performed. The binding interaction of Ru(III) complexes (Figure 2) with duplex DNA sequence d(ACCGACGTCGGT)₂ was performed to explore the DNA binding site and complex-DNA helix orientation. Molecular docking study suggests preferentially intercalative mode of complex to DNA interaction, involving stacking interaction. The docked

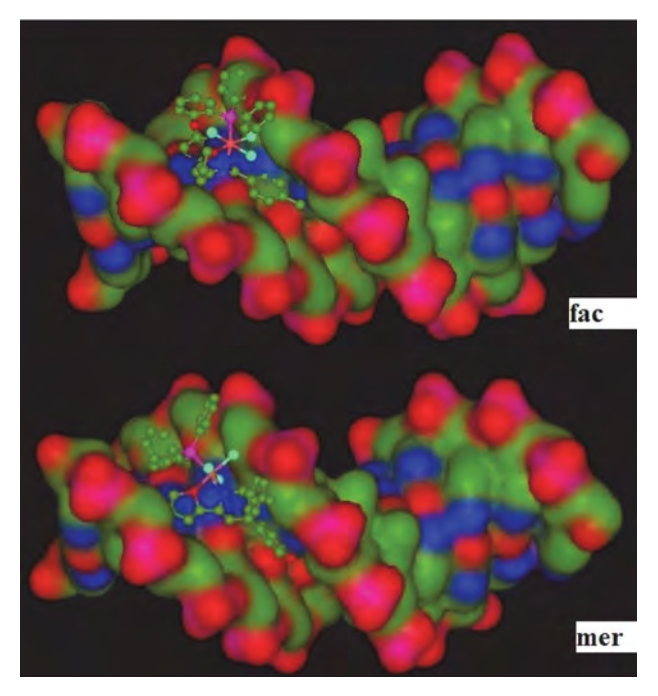


Figure 2. Molecular docking of the complex 1 (*fac* and *mer* isomers) with the DNA duplex.

structure showed the complexes fit well in between the stacks of rich A–T base pair region, which may be stabilized through hydrophobic or van der Waal's interaction. The binding energies of DNA-complexes interactions are –326.15, –326.58, –329.95, –325.63, –333.74, –329.94 kJ mol⁻¹ for *fac*-complexes **1–6**, and –333.27, –338.44, –341.23, –343.46, –348.38, –339.77 kJ mol⁻¹ for *mer*-complexes **1–6**, respectively.

Cytotoxicity: In this assay, the %mortality of brine shrimp nauplii was determined after 24 and 48 h of complexes treatment. The LC₅₀ was evaluated from the plot of log[complex] against %mortality of nauplii. From the result, it is inferred that the complex **1** shows higher toxicity than other synthesized complexes and toxicity value (LC₅₀ = 12.2, 14.1, 13.7, 12.9, 21.2 and 18.5 μ M for complex **1–6**, respectively) of synthesized complexes are comparable to standard anticancer agent *cis*-platin (LC₅₀ < 13.3 μ M).

Gel electrophoresis study: Figure 3 shows the cleavage of DNA by the test compounds. Lane 1 is a control representing DNA cleavage into only two forms, supercoiled (Form I) and open circular (Form III). Lane 2 with the reference compound RuCl₃·2H₂O representing cleavage into only two forms similar to the control. Lane 3–8 contains synthesized ruthenium complexes 1–6 respectively, representing the cleavage of DNA into three forms Form I, Form III and Form II (linear) in between Form I and III generated by the scission of both the strands of DNA. The photographed image is quantified by AlphaDigiDoc software. The relative decrease in the supercoiled form of control after the addition of test compounds is a measure of percent cleavage. The results (Table 1) clearly indicate that



Figure 3. Cleavage of pUC19 plasmid DNA under the influence of ruthenium complexes. Lane 1, DNA control; Lane 2, RuCl₃·3H₂O; Lane 3, $[Ru(L^1)(PPh_3)Cl_3]$; Lane 4, $[Ru(L^2)(PPh_3)Cl_3]$; Lane 5, $[Ru(L^3)(PPh_3)Cl_3]$; Lane 6, $[Ru(L^4)(PPh_3)Cl_3]$; Lane 7, $[Ru(L^5)(PPh_3)Cl_3]$; Lane 8, $[Ru(L^6)(PPh_3)Cl_3]$.

percent cleavage value is highest for the complex-1 indicating its strong binding efficiency to DNA. The DNA cleavage data also follow the similar trend of binding constant value as measured by UV-visible absorption titration of metal complexes with increasing the concentration of DNA. So we can conclude that metal complex having higher DNA binding affinity can effectively cleave the DNA strand.

4. Conclusion

The data of various physicochemical activities like gravimetry, magnetic moment measurement and electronic spectral measurement are in good agreement with the proposed structure of metal complexes. The complexes have a paramagnetic nature. The MIC data suggest a significant increase in antibacterial activity of ligands after complexation with the metal ion. Also, that complexes 1–3 have comparatively higher antibacterial activity than complexes 4-6. The MIC data clearly indicate that electronic properties (metal complexation and presence of F-substituent at p-position of L^1) play a vital role in enhancing the biological activities of complex 1 by increasing its lipophilic nature. Complex 1 binds more efficiently to the DNA via classical intercalation mode. The cytotoxic study displays good potency of the complexes against brine shrimp and 100% mortality is observed after 48 h of incubation. The efficient cleavage of supercoiled pUC19 DNA by all the complexes was observed. The higher efficacy of complex 1 in the various activity performed may be attributed to strong electron withdrawing potency of F-atom at the para position while and chlorine and bromine has less electron withdrawing capacity than bromine. This electron withdrawing capacity of fluorine atom makes the complex more polar and hence easily permeable to lipophilic layers of the target species and onset its action readily.

5. Acknowledgments

We are thankful to the Head, Department of Chemistry, Sardar Patel University; and UGC RFSMS Scheme for providing financial support.

 Table 1. Gel electrophoresis analysis of complexes.

Lanes	Complexes	% OC	% LC	% SC	% Cleavage
1	Control	4.90	_	95.1	_
2	RuCl ₃ ·3H ₂ O	27.2	_	72.8	22.44
3	$[Ru(L^1)(PPh_3)Cl_3]$	68.2	24.0	7.80	91.79
4	$[Ru(L^2)(PPh_3)Cl_3]$	74.3	6.50	19.2	79.81
5	$[Ru(L^3)(PPh_3)Cl_3]$	73.3	9.00	17.7	81.39
6	$[Ru(L^4)(PPh_3)Cl_3]$	73.5	9.30	17.2	81.91
7	$[Ru(L^5)(PPh_3)Cl_3]$	58.7	5.20	36.0	62.14
8	$[Ru(L^6)(PPh_3)Cl_3]$	58.1	4.90	37.0	61.09
	[()(3)3]				

6. References

- 1. N. Farrell, Transition metal complexes as drugs and chemotherapeutic agents, Springer Science & Business Media, 2012.
- U. Ndagi, N. Mhlongo, M. E. Soliman, Drug Des. Devel. Ther. 2017, 11, 599. DOI:10.2147/DDDT.S119488
- S. J. S. Franchi, R. A. de Souza, A. E. Mauro, I. Z. Carlos, L. C. de Abreu Ribeiro, F. V. Rocha, A. V. de Godoy-Netto, *Acta Chim. Slov.* 2018, 65, 547–553. DOI:10.17344/acsi.2017.4112
- 4. R. S., Biotech. Mol. Biol. Rev. 2010, 5, 38.
- N. Vamsikrishna, M. P. Kumar, G. Ramesh, N. Ganji, S. Daravath, *J. Chem. Sci.* 2017, 129, 609–622.
 DOI:10.1007/s12039-017-1273-7
- B. B. Rajaretnam, J. Chellappa, D. A. Solomon, I. P. Subramanian, T. D. M. Selvanayagam, *Acta Chim. Slov.* 2019.
- M. Nišavić, R. Masnikosa, A. Butorac, K. Perica, A. Rilak, L. Korićanac, A. Hozić, M. Petković, M. Cindrić, *J. Inorg. Bio-chem.* 2016, 159, 89–95.

DOI:10.1016/j.jinorgbio.2016.02.034

- P. A. Vekariya, P. S. Karia, B. S. Bhatt, M. N. Patel, *Appl. Biochem. Biotech.* 2019, 187, 556–569.
 - DOI:10.1007/s12010-018-2835-y
- K. P. Thakor, M. V. Lunagariya, B. S. Bhatt, M. N. Patel, *Luminescence* 2019, 34, 113–124. DOI:10.1002/bio.3587
- K. P. Thakor, M. V. Lunagariya, B. S. Bhatt, M. N. Patel, *Appl. Organomet. Chem.* 2018, 32, e4523. DOI:10.1002/aoc.4523
- 11. K. Lin, Z. Zhao, H. Bo, X. Hao, J. Wang, Front. Pharmacol. **2018**, 9, 1323. **DOI:**10.3389/fphar.2018.01323
- 12. T. Lazarević, A. Rilak, Ž. D. Bugarčić, *Eur. J. Med. Chem.* **2017**, *142*, 8–31. **DOI:**10.1016/j.ejmech.2017.04.007
- D. Lazić, A. Arsenijević, R. Puchta, Ž. D. Bugarčić, A. Rilak, *Dalton Trans.* 2016, 45, 4633–4646.
 DOI:10.1039/C5DT04132E
- 14. J. Reedijk, *Platin. Met. Rev.* **2008**, *52*, 2–11. **DOI:**10.1595/147106708X255987
- 15. J. K. Barton, A. Danishefsky, J. Goldberg, *J. Am. Chem. Soc.* **1984**, *106*, 2172–2176. **DOI:**10.1021/ja00319a043
- 16. J. Barton, *Science* **1986**, *233*, 727–734.

DOI:10.1126/science.3016894

17. L.-F. Tan, X.-J. Chen, J.-L. Shen, X.-L. Liang, *J. Chem. Sci.* **2009**, *121*, 397–405. **DOI**:10.1007/s12039-009-0046-3

- P. A. Vekariya, P. S. Karia, B. S. Bhatt, M. N. Patel, J. Inorg. Organomet. Polym. Mater. 2018, 28, 2749–2758.
 DOI:10.1007/s10904-018-0957-x
- J.-Q. Huo, L.-Y. Ma, Z. Zhang, Z.-J. Fan, J.-L. Zhang, T. V. Beryozkina, V. A. Bakulev, *Chin. Chem. Lett.* **2016**, *27*, 1547–1550. **DOI**:10.1016/j.cclet.2016.06.019
- S. Nadeem, M. Bolte, S. Ahmad, T. Fazeelat, S. A. Tirmizi, M. K. Rauf, S. A. Sattar, S. Siddiq, A. Hameed, S. Z. Haider, *Inorg. Chim. Acta* 2010, 363, 3261–3269.

DOI:10.1016/j.ica.2010.06.015

- 21. F. KrÖHnke, *Synthesis* **1976**, *1976*, 1. **DOI:**10.1055/s-1976-23941
- 22. M. N. Patel, B. S. Bhatt, P. A. Dosi, *Inorg. Chem. Commun.* **2013**, *29*, 190–193. **DOI**:10.1016/j.inoche.2012.12.013
- D. Lawrence, V. G. Vaidyanathan, B. U. Nair, *J. Inorg. Biochem.* 2006, 100, 1244–1251. DOI:10.1016/j.jinorgbio.2006.02.003
- 24. M. N. Patel, P. A. Dosi, B. S. Bhatt, Acta Chim. Slov. 2012, 59.
- M.-L. Liu, M. Jiang, K. Zheng, Y.-T. Li, Z.-Y. Wu, C.-W. Yan, J. Coord. Chem. 2014, 67, 630–648.
 DOI:10.1080/00958972.2014.884218
- 26. M. N. Patel, P. A. Dosi, B. S. Bhatt, *Med. Chem. Res.* **2012**, *21*, 2723–2733. **DOI**:10.1007/s00044-011-9799-6
- L.-W. Xue, H.-J. Zhang, P.-P. Wang, Acta Chim. Slov. 2019, 66, 190–195.
- 28. Y.-L. Sang, X.-S. Lin, Acta Chim. Slov. 2019, 66, 168-172.
- P. R. Reddy, A. Shilpa, *Polyhedron* 2011, 30, 565–572.
 DOI:10.1016/j.poly.2010.11.015
- 30. G. G. Mohamed, E. M. Zayed, A. M. Hindy, *Spectrochim. Acta A* **2015**, *145*, 76–84. **DOI:**10.1016/j.saa.2015.01.129
- A. S. Alturiqi, A.-N. Alaghaz, R. A. Ammar, M. E. Zayed, J. Chem. 2018, 2018. DOI:10.1155/2018/5816906
- C. S. Allardyce, P. J. Dyson, D. J. Ellis, P. A. Salter, R. Scopelliti,
 J. Organomet. Chem. 2003, 668, 35–42.
 DOI:10.1016/S0022-328X(02)01926-5
- 33. B. Tweedy, *Phytopathology* **1964**, *55*, 910–914.
- 34. P. Uma Maheswari, M. Palaniandavar, *J. Inorg. Biochem.* **2004**, 98, 219–230. **DOI:**10.1016/j.jinorgbio.2003.09.003
- 35. X.-W. Liu, J.-L. Lu, Y.-D. Chen, L. Li, D.-S. Zhang, *Inorg. Chim. Acta* **2011**, *379*, 1–6.
- D. Lawrence Arockiasamy, S. Radhika, R. Parthasarathi, B. U. Nair, *Eur. J. Med. Chem.* 2009, 44, 2044–2051.
 DOI:10.1016/j.ejmech.2008.10.013

Povzetek

Sintetizirali smo rutenijeve(III) komplekse [Ru(bphtpy)(PPh₃)Cl₃] (bphfpy = derivati difenilfuranilpiridina) in jih okarakterizirali z LCMS, IR spektroskopijo, elementno analizo in magnetnimi meritvami. Vsem kompleksom smo določili antibakterijsko aktivnost z minimalno inhibitorno koncentracijo na dveh Gram pozitivnih in treh Gram negativnih bakterijskih vrstah. Študij vezave na DNA z absorptivno titracijo in viskozimetričnimi meritvami kaže, da se kompleksi vežejo na interkalacijski način, kar smo potrdili tudi z molekulskim dokingom. Vse komplekse smo tudi testirali za DNA nukleazne lastnosti na pUC19 plazmidski DNA. S citostatičnimi testi smo določili LC₅₀ vrednosti z namenom določitve toksičnega profila kompleksov.



Except when otherwise noted, articles in this journal are published under the terms and conditions of the Creative Commons Attribution 4.0 International License

@creative

Scientific paper

Amperometric Glucose Biosensor Based on Homopolymer-Chitosan Double Layered Glucose Oxidase Electrode Modified with Zinc Oxide Nanoparticles

Gul Ozyilmaz,* Ali Tuncay Ozyilmaz, Esiye Irem Bayram and Ragibe Hulya Akyürekoğlu

University of Hatay Mustafa Kemal, Faculty of Arts & Sciences, Department of Chemistry 31040 Hatay/ Turkey

* Corresponding author: E-mail: gozyilmaz@gmail.com Fax: 90-326 2455867

Received: 04-05-2019

Abstract

GOD was immobilized onto polypyrrole (PPy) or poly(o-anisidine) (POA) coated Pt electrode to construct glucose sensitive biosensor. Because polymer film properties and enzyme activity affect the current response, PPy and POA synthesis conditions and also enzyme immobilization parameters were optimized in detail. The optimal monomer concentrations were determined as 25 and 50 mM for PPy and POA, respectively, whereas scan rate was 50 mV/s for both polymer films. In case of immobilization procedure, the optimal Chitosan (Chi), glucose oxidase (GOD) and glutaral-dehyde (GAL) concentrations were determined as 0.5%, 2 mg/ml and 0.05% for PPy and 0.5%, 4 mg/ml and 0.075% for POA, respectively. Zinc oxide nanoparticles (ZnONP) were co-immobilized with GOD enzyme and it was revealed that ZnONP modification enhanced the efficiencies of both electrodes in terms of current responses and stabilities. Nyquist diagrams showed that enzyme electrodes were sensitive to glucose molecule and ZnONP modification improved the sensor efficiency.

Keywords: Amperometric biosensor; polypyrrole; poly(o-anisidine); zinc oxide nanoparticles; glucose oxidase

1. Introduction

Glucose is one of the most analyzed components in biological fluids and foods. Compared to spectrophotometric and colorimetric methods, electrochemical methods have significant advantages in terms of simplicity, cost effective, quick way, excellent sensitivity and easy applicability. 1-3 Enzyme electrodes have been widely applied to construct biosensors for analyte determination.⁴⁻⁹ Fabrication of the enzyme containing biosensor requires immobilization of the enzyme molecule onto/into the electrode surface. There are several strategies for immobilization techniques to obtain GOD biosensor such as crosslinking with glutaraldehyde, 10-11 applying enzyme on an electrode in a gel film, 12-17 entrapment or incorporation in a polymer matrix during electropolymerization, 6,18-20 by covalent attachment²¹⁻²² or adsorbing onto electrode surface.²⁴⁻²⁶ Chitosan (Chi) is a type of natural cationic polymer, which has shown attractive characteristics such as film-forming ability, permeability, and good adhesion. Therefore, chitosan can be used as a gel matrix for enzyme immobilization through glutaraldehyde (GAL) or another reagent.^{27–29} However, the poor electrochemical conductivity of Chi reduces the performance of the enzyme-based biosensor.³⁰ To overcome this problem, several strategies were developed by adding various materials in Chi matrix such as nanoparticles^{15,32,34} ionic liquid,^{29,33} or by modifying interface between electrode surface and Chi layer by nanoparticles,^{7,31} Prussian Blue³⁰ and electropolymers.³¹ Electropolymerization is one of the cheap but powerful methods focusing on selective modification of various types of electrodes with desired matrices.³ Several electropolymers were used to fabricate the glucose biosensor such as PPy^{18,28,32-33} polyaniline (PANI), 34-35 poly(o-anisidine) (POA),^{36–37} poly(N-methyl pyrrole) (PNMP),²⁷ poly(o-phenylenediamine)³⁸ and polythophen³⁹ derivative. Recent studies reveal that the nanostructured metal oxides with reduced size have unique advantages in immobilizing enzymes and have high sensitivity due to high surface area, desirable microenvironment, and direct electron transfer between the enzyme active sites and electrode. ZnO nanomaterials have been widely used for this purpose. 40-43

The present study deals with the fabrication of a glucose biosensor based on redox polymers such as PPy and POA. Construction of biosensor was optimized in terms of PPy and POA synthesis parameters, enzyme immobilization conditions and also the amount of ZnONP by comparing current response in the glucose solution. Enzyme electrodes were characterized by cyclic voltammograms, Nyquist diagrams, kinetic parameters and operational stabilities.

2. Experimental

2. 1. Chemicals

Aspergillus niger origin glucose oxidase (GOD) (EC 1.1.3.4), pyrrole (Py), o-anisidine (OA), Chi, ZnONP (<100 nm), glucose anhydrous, GAL were purchased from Sigma. Py and OA were used after distillation and were stored in the dark until use. All other reagents were of analytical grade and used without further purification. The polymer synthesis baths were prepared using 0.15 M aqueous sodium oxalate solution with Py or OA monomers. Enzyme immobilization solution was obtained by mixing Chi and GOD at appropriate concentration in aqueous media. The concentration range of glucose solutions was between 0.2 and 3.0 mM and solutions were used after 24 h of mutarotation equilibrium.

2. 2. Preparation of Enzyme Electrodes

Enzyme electrodes were prepared in three steps. 27-28 Firstly, homopolymer films were synthesized onto Pt electrode (PPy/Pt or POA/Pt). Secondly, GOD enzyme was immobilized onto polymer coated Pt electrodes by immersing in GOD containing Chi solution for 3 seconds (GOD-Chi/PPy/Pt or GOD-Chi/POA/Pt) and electrodes were dried for 2 hours open to atmosphere. Lastly, GOD-Chi/PPy/Pt or GOD-Chi/POA/Pt electrodes were incubated in GAL solution for 10 seconds for crosslinking between amine groups of the enzyme and Chi to hinder GOD leakage. Modification of the GOD electrode with ZnONP was achieved by adding ZnONP to the Chi solution, and the mixture was homogenized using a sonicator. After the addition of GOD, the final solution was used to make the enzyme electrode as previously described. Electrodes were stored at 4°C when they were not used.

2. 3. Synthesis of Homopolymer Films

Polymer films were achieved in a single compartment cell with three electrode configurations. The reference electrode was an Ag/AgCl (3 M KCl) electrode and the counter electrode was a platinum plate with a surface area of 0.25 cm². CHI 660b model electrochemical analyzer (serial number: A1420) was employed in electrochemical experiments. All potential values were referred to the Ag/AgCl (3 M KCl) electrode. PPy and POA films were synthesized onto Pt electrode with 0.25 cm² surface area

by cyclic voltammetry technique in a monomer solution containing 0.15 M sodium oxalate electrolyte.

Biosensor electrodes were optimized in terms of polymer synthesis conditions (monomer concentration and scan rate) and also enzyme immobilization conditions (Chi, GOD and GAL concentration). Current values of each electrode that was constructed at different parameters were compared using glucose solution.

2. 4. Electrochemical Measurements

Electrochemical experiments were performed in a single compartment cell with three electrode configurations. The reference electrode was an Ag/AgCl (3 M KCl) electrode and the counter electrode was a platinum plate with a surface area of 0.25 cm². CHI 660b model electrochemical analyzer (serial number: A1420) was employed in electrochemical experiments. The biosensor response was monitored by the chronoamperometric technique at 0.60 V as current value that was measured depending on hydrogen peroxide oxidation which was formed by the GOD activity in the glucose solution. The chronoamperometric measurements were performed at room temperature in steady state conditions in potassium phosphate buffer (50 mM, pH 7.0) solution. Each measurement was lasted 120 s.

2. 5. Characterization of Enzyme Electrodes

The electrochemical characterization of enzyme electrodes was investigated by using cyclic voltammetry and also by AC impedance spectroscopy (EIS) techniques in the presence and in the absence of glucose. The cyclic voltammetry technique was applied at a potential range between 0.10 and 1.00 V by 50 mV/s scan rates. Nyquist plots were recorded at 0.60 V potential and in the frequency range from 10^5 to 10^{-3} Hz using the amplitude of 4 mV for electrochemical impedance spectroscopy investigations.

All electrodes were compared according to measured net current response depending on glucose concentration at the constant potential. The net current value, represented as μA , was got by subtracting current value of the glucose-free buffer solution from those of glucose-containing solution.

 I_{max} and K_{M} values were calculated from Lineweaver-Burk Plot using current values depending on glucose concentrations.

Operational stabilities were investigated by 20 successive using of each electrode in 5 mM glucose solution.

3. Results and Discussion

3. 1. Optimization of PPy and POA Synthesis Parameters

In order to obtain the maximum current response, polymer film synthesizing parameters were optimized in

terms of monomer concentration and scan rate. Because the pore size of polymer film is especially important for adsorption of GOD molecule, firstly, monomer concentrations, which were employed to obtain polymer layers on Pt electrode were changed between 10 and 100 mM for PPy and 40 and 80 mM for POA. Concentration ranges of monomers were determined according to preliminary studies. All other parameters such as scan rate, concentrations of GOD, Chi and GAL were kept constant while enzyme electrodes were constructed. Obtained electrodes were used to measure the current values depending on glucose concentrations and results were given as percentage of maximal current value in Fig. 1 and Fig. 2 for PPy and POA, respectively. As seen in Fig. 1, the highest current values and the most linear current curve were obtained for PPy electrode that was constructed using 25 mM pyrrole monomer.

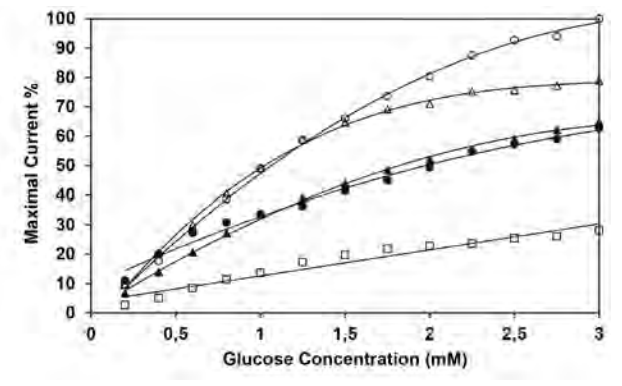


Figure 1. The effect of pyrrole concentration, that was used for PPy based electrode construction, on current values. Pyrrole concentrations: $10 \text{ mM } (\bullet)$; 25 mM (O); $50 \text{ mM } (\triangle)$; $75 \text{ mM } (\blacktriangle)$ and $100\text{mM } (\Box)$.

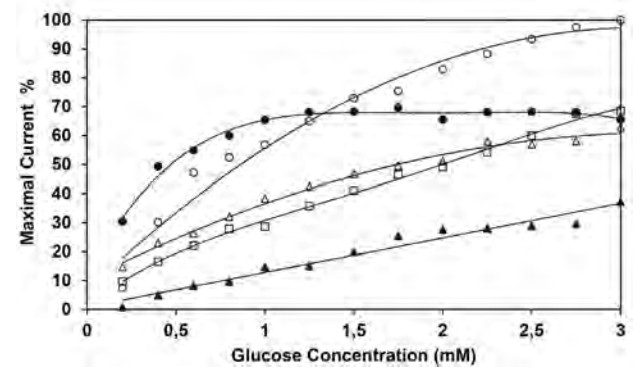


Figure 2. Current values depending on glucose concentration of GOD electrode constructed by POA layer obtaining by different o-anisidine concentrations as 40 mM (\bullet); 50 mM (\bigcirc); 60 mM (\triangle); 70 mM (\square) and 80mM (\blacktriangle).

In case of POA electrode (Fig.2), the optimal o-anisidine concentration was chosen as 50 mM. The change in the current response depending on the monomer concentration used in electrode preparation of enzyme electrodes

can be explained by the effect on the porosity of the polymer films. Polymerization rate is affected from several parameters such as monomer concentration, scan rate, etc. It is expected that, polymerization rate increases by increase in monomer concentration. The polymer structure generally tends to be tight stacking and to have a small pore structure as the rate of polymerization increases. Thus, the pore diameters of the polymer will be large at low monomer concentration and small at high monomer concentration. Polymer synthesis rate was low at the low monomer concentration, so pore sizes may be too high that enzyme molecule can't adsorb onto polymer film. However, polymerization rate was high at high monomer concentrations, and because the polymer film is tightly stacked, pore sizes are too small to allow the enzyme binding. The PPy and POA films formed by 25 mM for pyrrole and 50 mM for o-anisidine exhibited better current response results in the different glucose concentration solution. Therefore, to construct glucose sensitive electrode, PPy and POA were synthesized in 25 mM pyrrole and 50 mM o-anisidine solutions, respectively in the subsequent studies. In our knowledge, the effect of monomer concentration on biosensor efficiency has not been investigated until now.

As the scan rate increases, the irregularity in the formed polymer film increases, yet, when scan rate is low, more regular and tightly stacked polymer film forms. Therefore, since the scan rate affects the structure and conductivity of the polymer, the current response of the biosensor will also be affected by the scanning rate. PPy and POA films were coated on the Pt electrode by applying scan rates of 20, 50 and 100 mV/s. The synthesizing of thin homopolymer films was provided with the help of proper scan number from -0.50 to 1.80 V for PPy and from 0.35 to 1.50 V for POA in 0.150 M NaOX solution with optimal monomer concentration. So, in order to maintain the same polymerization duration, 10 cycles for 20 mV/s, 26 cycles for 50 mV/s and 50 cycles for 100 mV/s were applied for the synthesis of the polymer films. Fig. 3 (PPy) and Fig. 4 (POA) represent the current re-

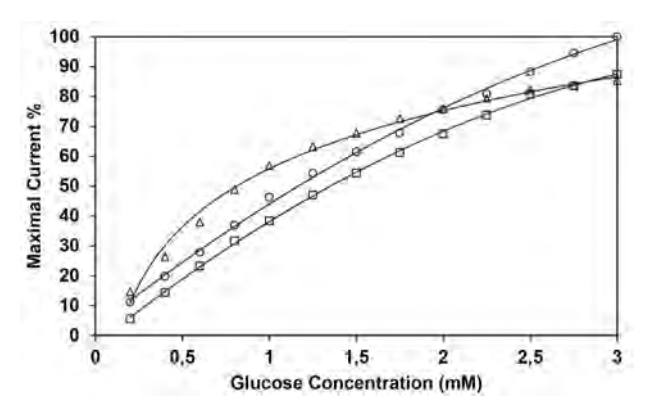


Figure 3. Current response of PPy based electrode prepared applying different scan rates; \triangle : 20 mV/s; O: 50 mV/s; \square : 100 mV/s.

sponse of ezyme electrodes of which polymer layers were obtained applying different scan rate. As shown in the Fig. 3, the current values of the electrode, that was obtained applying 20 mV/s scan rate, were the highest at the lower glucose concentrations. In contrast, the current values of the electrode, that was obtained applying the scan rate of 50 mV/s, were high at the higher glucose concentrations. However, because of the more linear current response depending on glucose concentration was observed, 50 mV/s was selected as optimal scan rate for PPy synthesis.

In case of POA based enzyme electrode, the current values measured with the electrode prepared by applying 50 mV/s scan rate are significantly higher and the current-glucose concentration curve is highly linear. But, net current value did not observe for POA based electrode prepared by applying 20 mV/s scan rate. So, 50 mV/s scan rate was applied in the subsequent studies for both PPy and POA synthesis.

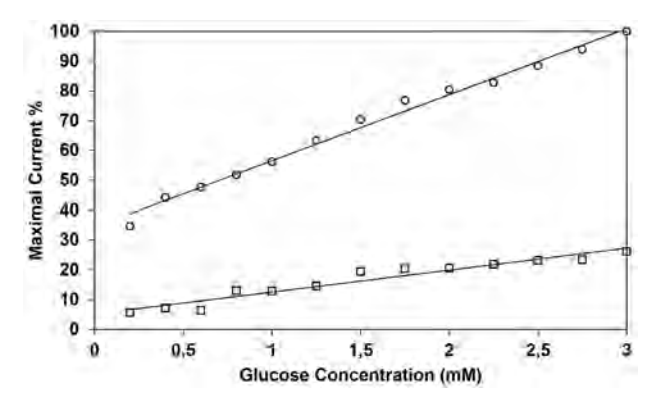
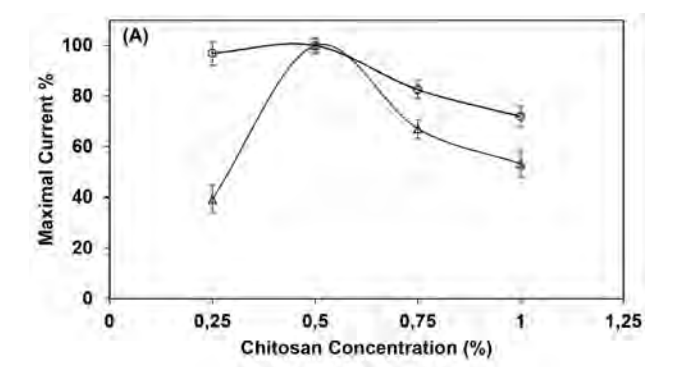


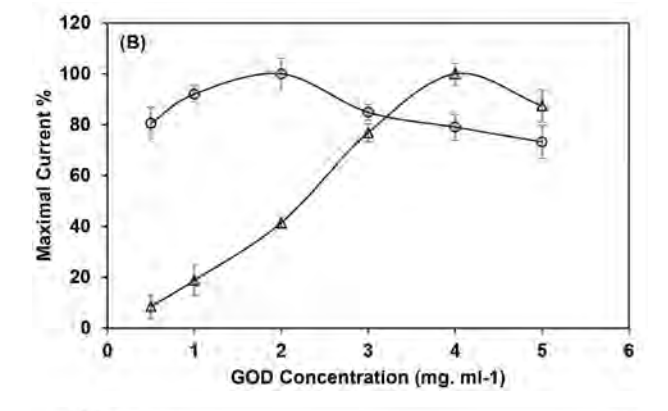
Figure 4. Current response of POA based electrode prepared applying different scan rates; O: 50 mV/s; \square : 100 mV/s.

The effects of enzyme immobilization conditions such as Chi, GOD and GAL concentrations were also investigated and current responses were given for 3 mM glucose solution in the Fig. 5 A, B and C, respectively.

The highest current response for both PPy and POA based electrodes were measured by enzyme electrodes constructed using 0.5% Chi solution (Fig. 5 (A)).

As seen in the Fig. 5 (B) and (C), the maximal current responses were observed when enzyme electrodes were prepared using 0.05% GAL and 2 mg/ml GOD for PPy based electrode whereas 0.075% GAL and 4 mg/ml GOD for POA based electrode. So, enzyme immobilization parameters were chosen as 0.5% Chi, 2 mg/ml GOD and 0.05% GAL for PPy whereas, as 0.5% Chi, 4 mg/ml GOD and 0.75% GAL for POA based electrodes in the subsequent studies. Since the enzyme immobilization conditions will affect the activity of the enzyme, it is expected that it will affect the amount of hydrogen peroxide to be formed and thus the current response to be measured.





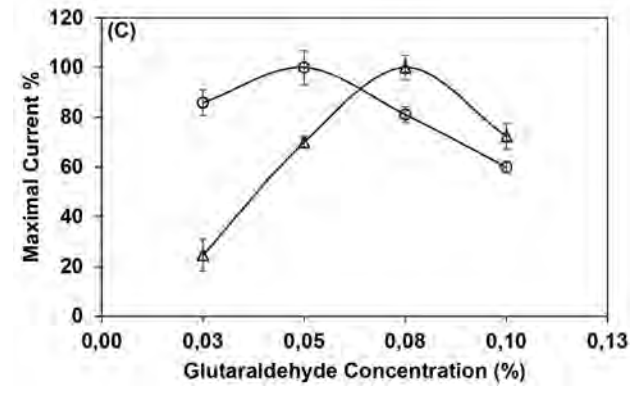


Figure 5. The effect of immobilization conditions as Chi (A), GOD (B) and GAL(C) concentrations on the current response. PPy (o); POA (Δ).

3. 2. The Effect of ZnONP Modification on Current Response

Enzyme electrodes were modified by ZnO nanoparticles using three concentrations as 0.1, 0.5 and 2 mg per ml of Chi solution. As seen in Fig. 6 (A), it can be said that ZnONP modification enhanced the biosensor efficiency. The highest currents were obtained for PPy based electrode when 2 mg ZnONP/ml was added to GOD containing Chi solution. In case of POA based electrode, when 0.1 mg ZnONP/ml was used the efficiency of electrode enhanced, but for higher amounts of nanoparticle, the current values were lower than those of ZnONP free electrode.

Nanoparticles were used to enhance glucose oxidase electrode in the literature. $^{35,43-46}$ German et al $(2015)^{43}$

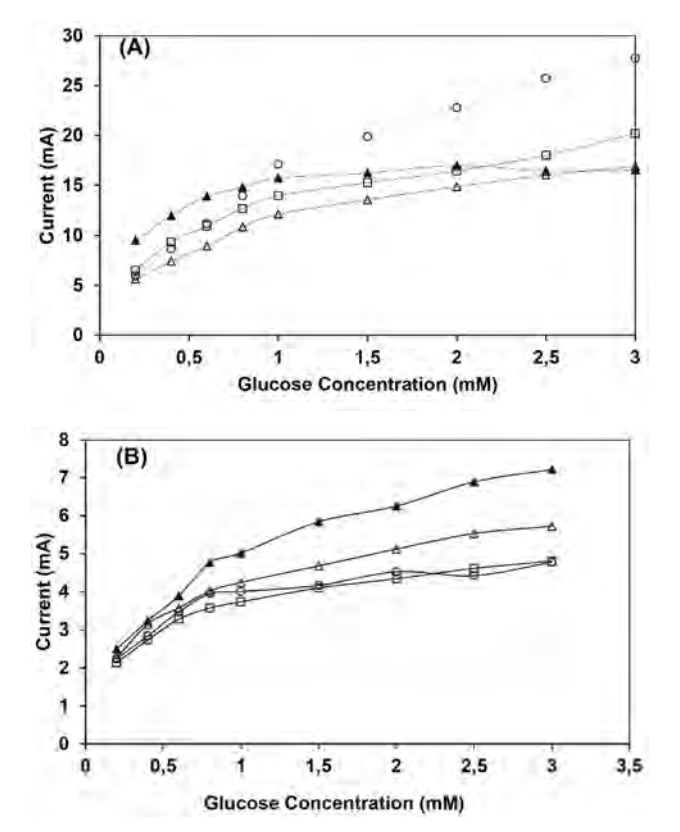


Figure 6. Current response of PPy (A) and POA (B) based biosensors modified with ZnONP. △:ZnONP-free; ▲:0.1; □:0.5 and O: 2 mg ZnONP/ml Chi.

GOD based amperometric biosensor constructed by coating PPy on graphite rod in presence of gold nanoparticle (AuNP), and they reported that, AuNP enhanced the sensor efficieny but, current response decreased by increase in AuNP amount.

3. 3. Electrochemical Characterization of the Enzyme Electrodes

The glucose sensitivities of electrodes were investigated firstly by cyclic voltammetry technique in glucose free and glucose containing buffer solution. In Fig. 7 (A) and (B) shows the first cyclic voltammograms which were recorded for Pt/PPy/Chi-GOD and Pt/POA/Chi-GOD electrodes, respectively, with and without ZnONP. As seen in Fig. 7(A) and 7(B), the current values of Pt/PPy/Chi-GOD and Pt/POA/Chi-GOD electrodes with and without ZnONP remained almost constant in glucose free solution. But, in the glucose solution, current responses started to increase approx. 0.4 V when compared with current responses of glucose free buffer solution. It was clearly seen that, current values were higher in glucose solution than that of glucose free solution for all enzyme electrodes. This shows us, enzyme electrodes are sensitive to glucose molecule. On the other hand, Pt/PPy/Chi-GOD and Pt/POA/ Chi-GOD electrodes with ZnONP exhibited higher current values than those of ZnONP-free electrodes.

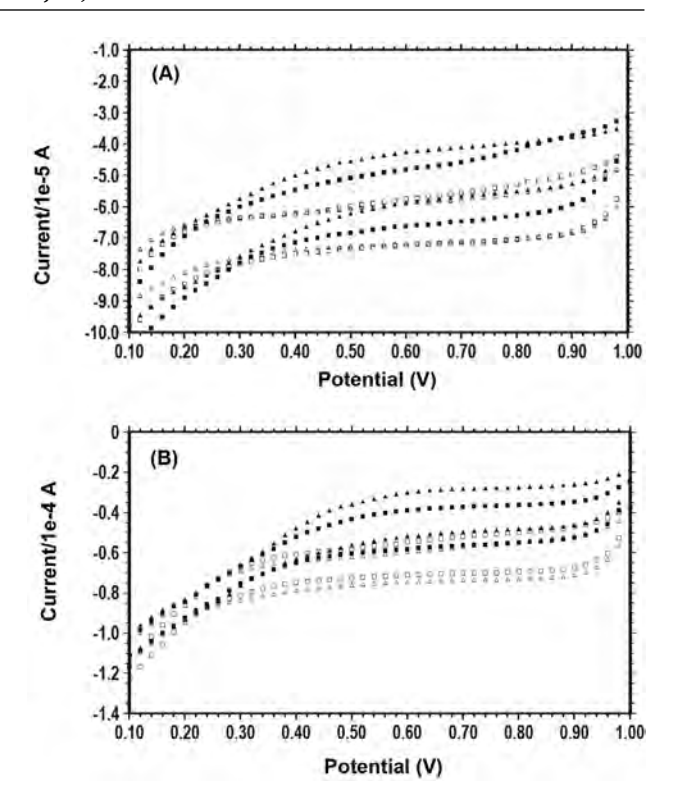


Figure 7. Cyclic voltammograms of nanoparticle free enzyme electrode in the buffer (\square) and in the glucose solution (\blacksquare), cyclic voltammograms of ZnONP containing enzyme electrodes in the buffer (\triangle) and in the glucose solution (\blacktriangle) for PPy (A) and for POA (B) (5 mM glucose solution).

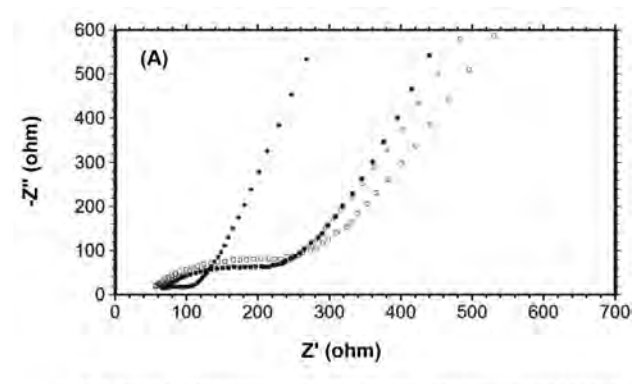
This proved that ZnONP contributed to the electron transfer between metal and enzyme active center.

Pt/PPy/Chi-GOD and Pt/POA/Chi-GOD electrodes with and without ZnONP were characterized by EIS technique and Nyquist diagrams are given in the Figure 8(A) and 8(B), respectively.

In the Nyquist diagrams, the first and second depressed semicircles at high and low frequencies consisted of charge transfer resistance (R_{ct}) corresponding to the anodic reaction of the substrate at the bottom of the pores and the resistances of the oxide layer (R_o) + polymer film (R_f), respectively. The first partial semicircle at the high frequency region is related to R_{ct} for processes occurring at the bottom of the pores of coatings.

The charge transfer reactions are known to take place at the metal/polymer interfaces. Consequently, the high $R_{\rm ct}$ values of coated electrodes can be explained by the build-up of protective layers and the effective barrier behavior of films on the surface.

In Fig 8 (A), the R_{ct} value recorded for Pt/PPy/Chi-GOD-ZnONP electrode in glucose free buffer solution was the highest due to forming a barrier layer such as coating, enzyme and nanoparticle on the Pt surface. However, the feature of same electrode was exactly different in the glucose solution with the lowest R_{ct} value. On the other hand, the magnitude of semicircle observed at high fre-



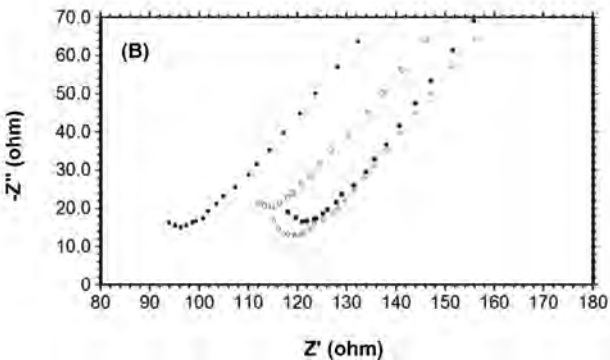


Figure 8. The Nyquist diagrams of Pt/PPY/Chi-GOD/GAL (A) and and Pt/POA/Chi-GOD/GAL (B) electrodes. ZnONP free in the buffer (\square) and in the glucose (\blacksquare), ZnONP containing in the buffer (\bigcirc) and in the glucose (\blacksquare) solution.

quency region recorded for Pt/PPy/Chi-GOD electrode in the glucose solution was significantly higher when compared with that the presence of glucose free solution. The lowest R_{ct} value recorded for Pt/PPy/Chi-GOD-ZnONP electrode in the glucose solution was related to the increase of the charge transfer rate between the metal and the solution. At the same time, the semicircle observed at high frequency region recorded for Pt/POA/Chi-GOD-ZnONP electrode in the glucose solution is incredibly low when compared with other three semicircles in Fig 8 (B). The low R_{ct} values of Pt/PPy/Chi-GOD and Pt/POA/Chi-GOD electrodes which were modified with ZnONP showed that ZnO nanoparticles in glucose solution contributed to the increase in the charge transfer rate at the metal/polymer interfaces. Tang et al. (2015)35 prepared GOD based GCE electrode and modified the electrode with PANI and nanometer sized TiO2. They reported that n-TiO₂ enhanced conductivity and improved the interfacial electron transfer ability.

3. 4. Biochemical Characterization of Enzyme Electrodes

For biochemical characterization, optimal pH values, kinetic parameters and operational stabilities were investigated for each electrode. Firstly, current responses were measured in 3 mM glucose solution at different pH values and results were given in Table 1. The highest current values were observed at pH 6.0 for GOD-Chi/PPy/Pt, ZnONP-GOD-Chi/PPy/Pt and GOD-Chi/POA/Pt whereas at pH 4.0 for ZnONP-GOD-Chi/POA/Pt. Imax and KM values of each electrode were calculated by Lineweaver-Burk plot using current values depending on glucose concentration of which range between 0.1 and 10 mM and results were given in the Table 1. As seen in Table 1, Imax values of GOD-Chi/ PPy/Pt, ZnONP-GOD-Chi/PPy/Pt were considerably higher than those of GOD-Chi/POA/Pt and ZnONP-GOD-Chi/POA/Pt. Besides, I_{max} values of enzyme electrodes prepared with ZnONP were higher than those of their nanoparticle free counterparts. K_M values of enzyme electrodes that were modified by ZnONP were slightly lower.

Metaloxide nanoparticles such as ${\rm TiO_2}^{\bar{35}}$, ${\rm CuGeO_3}^{44}$, ${\rm ZrO_2}^{45}$, ${\rm IrO_2}^{46}$ were used to enhance the GOD based amperometric biosensor in the literature. Yang et al. (2004) modified the Chi-GOD based amperometric glucose biosensor by ${\rm ZrO_2}$ nanoparticles and they found ${\rm I}_{\rm max}$ value as 0.29 $\mu{\rm A}$ whereas ${\rm K}_{\rm M}$ values as 3.14 mM. Jhas et.al (2010)⁴⁵ constructed ${\rm IrO_2}$ -NP containing GOD electrode and ${\rm I}_{\rm max}$ and ${\rm K}_{\rm M}$ values were calculated as 46 mA/m² and 27 mM, respectively.

Operational stabilities of the electrodes were also analyzed by 20 successive using in the 5 mM of glucose solution. Studies were repeated five times and results were very similar and SD were between 3.2 and 8.2%. For all 20 cycles, measured currents as the percentage of initial current were calculated and results were given in the Fig.9. As seen, 92.73 % and 93.13 % of initial currents were observed for GOD-Chi/POA/Pt and ZnONP-GOD-Chi/POA/Pt, respectively at the 20th cycle. However, Initial current activities of GOD-Chi/PPy/Pt kept nearly same (100.25 % at the end of 20th cycle) and there was a very slight increase (102.08%) compared to the first measured current value in the case of ZnONP-GOD-Chi/PPy/Pt. This could occure because of change in microenvironment of GOD and PPy, that enhance enzyme activity and electron transport rate. It can be easily said that, prepared enzyme electrodes are very stable in terms of reuse.

Table 1. Kinetic parameters and optimal pH values of GOD electrodes with and without ZnONP

	pН	PPy I _{max} (μA)	K _M (mM)	рН	POA I _{max} (μA)	K _M
(mM)						
ZnO-NP-Free	6.0	29.8 ± 1.2	1.2 ± 0.1	6.0	5.8 ± 0.2	0.3 ± 0.0
ZnO-NP	6.0	40.7 ± 2.2	1.5 ± 0.1	4.0	8.6 ± 0.3	0.4 ± 0.0

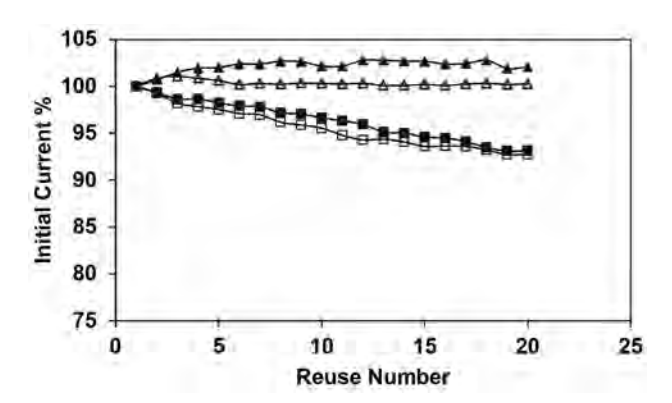


Figure 9. Operational stabilities of enzyme electrodes GOD-Chi/POA/Pt (□), ZnONP-GOD-Chi/POA/Pt (■), GOD-Chi/PPy/Pt (△) and ZnONP- GOD-Chi/PPy/Pt (▲)

4. Conclusion

PPy and POA coated Pt electrodes were easily and successfully used to construct glucose sensitive enzyme electrode. It was found that electrode construction parameters significantly affected the current values depending on glucose concentration. The current values and stabilities were higher for PPy based electrode than those of POA based electrode. Also, it was revealed that, modification of enzyme electrode by ZnONP contributed to the electron transfer between metal and enzyme active center. This study revealed that biosensor design parameters significantly affect the efficiency of biosensors. Glucose biosensors are one of the most widely used sensor systems in the world. So, the development of more stable and sensitive sensor platforms is extremely important.

Acknowledgements

This study was funded by Scientific Research Units of The University of Mustafa Kemal in Turkey, Project nos.9080 and 8681.

5. References

- J. G. Manjunatha, *Heliyon*, **2018**, 4, e00986.
 DOI:10.1016/j.heliyon.2018.e00986
- N. Hareesha, J. G. G.Manjunatha, C. Raril, G. Tigarl, Adv. Pharm. Bull., 2019, 9, 132–137. DOI:10.15171/apb.2019.016
- 3. C. Raril, J. G.Manjunatha, Mod. Chem. & Appl., 2018, 6, 1-8.
- K. Khun, Z.H. Ibupoto, J. Lu, M.S. AlSalhi, M. Atif, A. Ansari, M. Willander, Sens. Actuators, B 2012, 173, 698–703.
 DOI:10.1016/j.snb.2012.07.074
- A. Salimi, A. Noorbakhsh, *Electrochim. Acta*, 2011, 56, 6097–6105. DOI:10.1016/j.electacta.2011.04.073
- Y. M. Uang, T. C. Chou, Biosens. Bioelectron., 2003, 19, 141–147. DOI:10.1016/S0956-5663(03)00168-4
- M. Guo, H. Fang, R. Wang, Z. Yang, X. Xu, J. Mater. Sci.: Mater. Med., 2011, 22, 1958–1992.

- DOI:10.1007/s10856-011-4363-v
- P. E. Erden, Ş. Pekyardımcı, E. Kılıç, *Acta Chim. Slov.* 2012, 59, 824–832.
- 9. J. Kochana, Acta Chim. Slov. 2012, 59, 760-765.
- M. E. Ghica, C. M. A. Brett, J. Electroanal. Chem., 2009, 629, 35–42. DOI:10.1016/j.jelechem.2009.01.019
- L. V. Shkotova, N. Y. Piechniakova, O. L. Kukla, S. V. Dzyadevych, *Food Chem.*, **2016**, *197*, 972–978.
 DOI:10.1016/j.foodchem.2015.11.066
- 12. L. Wang, X. Gao, L. Jin, Q. Wu, Z. Chen, X. Lin, Sens. Actuators B, 2013, 176, 9–14. DOI:10.1016/j.snb.2012.08.077
- Y. Hui, L. Nan, X. Jhing-Zhong, Z. Jun-Jie, Chin. J. Chem., 2005, 23, 275–279. DOI:10.1002/cjoc.200590275
- B. Haighi, L. Nazari, S. M. Sajjadi, Electroanalysis, 2012, 24, 2165–2175. DOI:10.1002/elan.201200277
- 15. S. Huang, Y. Ding, Y. Liu, L. Su, R. Filosa Jr, Y. Lei, *Electroanalysis*, **2011**, 23, 1912–1920. **DOI:**10.1002/elan.201100221
- R. Pauliukaite, A. M. C. Paquim, A. M. O. Brett, C. M. A. Brett, *Electrochim. Acta*, 2006, 52, 1–8.
 DOI:10.1016/j.electacta.2006.03.081
- 17. N. Demirkıran, E. Ekinci, Acta Chim. Slov. 2012, 59, 302-306
- G. Ozyilmaz, A. T. Ozyilmaz, F. Can, Appl. Biochem. Microbiol. 2011, 47, 217–225. DOI:10.1134/S0003683811020153
- 19. E. H. Yu, K. Sundmacher, Trans IChemE, Part B, Process Saf. Environ. Prot., 2005, 85, 489-493.
- A. Eftekhari, *Synth. Met.*, **2004**, *145*, 211–216.
 DOI:10.1016/j.synthmet.2004.05.016
- 21. K. Abu-Rabeah, R. S. Marks, Sens. Actuators B, 2009, 136, 516–522. DOI:10.1016/j.snb.2008.09.020
- F. Ekiz, F. Oğuzkaya, M. Akın, S. Timur, C. Tanyeli, L. Toppare, *J. Mater. Chem.*, 2011, 21, 12337–12343.
 DOI:10.1039/c1jm12048d
- 23. R. K. Shervedani, A. Hatefi-Mehrjardi, *Sens. Actuators B*, **2007**, *126*, 415–423. **DOI**:10.1016/j.snb.2007.03.023
- C. Guadalupe de Jesus, D. Lima, V. Santos, K. Wohnrath, C. A. Pessoa, *Sens. Actuators B*, **2013**, *186*, 44–51.
 DOI:10.1016/j.snb.2013.05.063
- 25. A. Salimi, A. Noorbakhsh, *Electrochim. Acta*, **2011**, *56*, 6097–6105. **DOI:**10.1016/j.electacta.2011.04.073
- Y. Jiang, Q. Zhang, F. Li, L. Niu, Sens. Actuators B, 2012, 161, 728–733. DOI:10.1016/j.snb.2011.11.023
- G. Ozyilmaz, A. T. Ozyilmaz, R. H. Akyürekoğlu, *Nat. Eng. Sci.*, 2017, 2, 123–134. DOI:10.28978/nesciences.354825
- G. Ozyilmaz, A. T. Ozyilmaz, S. Ağçam, *Nat. Eng. Sci.*, 2018,
 1–15. DOI:10.28978/nesciences.379311
- 29. J. Li, R. Yuan, Y. Chai, X. Che, W. Li, *Bioprocess Biosys Eng*, **2012**, *35*, 1089–1095. **DOI:**10.1007/s00449-012-0693-5
- 30. Zhang Y, Liu Y, Chu Z, Shi L, Jin W, Sens. Actuators B, **2013**, 176, 978–984. **DOI:**10.1016/j.snb.2012.09.080
- S. Chen, P. Fu, B. Yin, R. Yuan, Y. Chai, Y. Xiang, *Bioprocess Biosyst Eng*, 2011, 34, 711–719.
 DOI:10.1007/s00449-011-0520-4
- 32. M. Raicopol, A. Prună, C. Damian, L. Pilan, *Nanoscale Res. Letters*, **2013**, *8*, 1–8. **DOI**:10.1186/1556-276X-8-316
- D. Olea, O. Viratelle, C. Faure, *Biosens. Bioelectron.*, 2008, 23, 788–794. DOI:10.1016/j.bios.2007.08.018

- C. Ozdemir, F. Yeni, D. Odaci, S. Timur, Food Chem., 2010, 119, 380–385. DOI:10.1016/j.foodchem.2009.05.087
- 35. W. Tang, L. Li, X. Zeng, *Talanta*, **2015**, *131*, 417–423. **DOI:**10.1016/j.talanta.2014.08.019
- P. A. Savale, M. D. Shirsat, Appl. Biochem. Biotechnol. 2009, 159, 299–309. DOI:10.1007/s12010-008-8135-1
- D. D. Borole, U. R. Kapadi, P. P. Mahulikar, D. G. Hundiwale, J. Mater. Sci., 2007, 42, 4947–4953.
 DOI:10.1007/s10853-006-0164-y
- 38. S. A. Rothwell, S. J. Killoran, R. D. O'Neill, *Sensors*, **2010**, *10*, 6439–6462. **DOI**:10.3390/s100706439
- 39. M. F. Abasiyanik, M. Senel, *J Electroanal Chem*, **2010**, *639*, 21–26. **DOI**:10.1016/j.jelechem.2009.11.001
- S. Jung, S. Lim, Appl Surface Sci, 2013, 265, 24–29.
 DOI:10.1016/j.apsusc.2012.10.069

- 41. Y. T. Wang, L. Yu, J. Wang, L. Lou, W. J. Du, W. Q. Zhu, H. Peng, J. Z. Zhu, *J Electroanal. Chem.*, **2011**, *661*, 8–12. **DOI:**10.1016/j.jelechem.2011.06.024
- X. Q. Hou, X. Ren, F. Q. Tang, D. Chen, Z.P. Wang, Chin. J. Anal. Chem., 2006, 34 303–306.
- N. German, A. Kausaite-Minkstimiene, A. Ramanaviicius, T. Semashko, R. Mikhailova, A. Ramanaviciene, *Electrochim. Acta*, 2015, 169, 326–333.
 DOI:10.1016/j.electacta.2015.04.072
- 44. Y. P. Dong, L. Huang, X. F. Chu, L. Z. Pei, Russian J Electrochem, 2013, 49, 571–576. DOI:10.1134/S1023193513060037
- 45. Y. Yang, H. Yang, M. Yang, Y. Liu, G. Shen, R. Yu, *Anal. Chim. Acta*, **2004**, *525*, 213–220. **DOI:**10.1016/j.aca.2004.07.071
- 46. A. S. Jhas, H. Elzanowska, B. Sebastian, V. Birss, *Electrochim. Acta*, **2010**, *55*, 7683–7689.

DOI:10.1016/j.electacta.2010.03.093

Povzetek

GOD smo imobilizirali na Pt elektrodo, prevlečeno s poliprolom (PPy) ali poly(o-anizidinom) (POA), in tako skonstruirali biosensor, občutljiv na glukozo. Ker lastnosti filma in encimska aktivnost vplivajo na tokovni odziv elektrode, smo natančno optimizirali sintezne pogoje za PPy in POA in tudi parametre za imobilizacijo encima. Optimalna monomerna koncentracija je bila 25 mM za PPy in 50 mM za POA, medtem ko je bila hitrost skeniranja za oba polimerna filma 50 mV/s. V primeru imobilizacijskega postopka so bile optimalne koncentracije kitozana (Chi), glukoza oksidaze (GOD) in glutaraldehida (GAL) enake 0,5 %, 2 mg/ml in 0,05 % za PPY in 0,5 %, 4 mg/ml in 0,075 % za POA. Hkrati smo z encimom GOD imobilizirali tudi nanodelce cinkovega oksida (ZnONP) in pokazalo se je, da modifikacija z ZnONP poveča učinkovitost obeh elektrod s stališča tokovnega odziva in stabilnosti. Nyquistovi diagrami so pokazali, da sta bili obe encimski elektrodi občutljivi na molekule glukoze in da je modifikacija z ZnONP izboljšala učinkovitost senzorja.



Except when otherwise noted, articles in this journal are published under the terms and conditions of the Creative Commons Attribution 4.0 International License

@creative

Scientific paper

Application of Solvatic Model for Prediction of Retention at Gradient Elution in Reversed-Phase Liquid Chromatography

Tina Snoj Ekmečič^{1,2} and Irena Kralj Cigić^{1,*}

¹ Faculty of Chemistry and Chemical Technology, University of Ljubljana, Slovenia.

² Krka d.d., R&D, Novo Mesto, Slovenia.

* Corresponding author: E-mail: irena.kralj-cigic@fkkt.uni-lj.si

Received: 04-11-2019

Abstract

There are several different approaches for LC method development; beside traditional, different software programs for method development and optimization are available. The solvatic retention model of reversed-phase LC was applied for prediction of retention in the gradient elution mode for aripiprazole and its related substances described in European Pharmacopoeia. As some of these compounds have very similar and others quite different chemical structure, their separation is challenge. Prediction was suitable on examined stationary phases (C18, C8 and phenyl-hexyl) with 0.1% phosphoric acid as aqueous mobile phase and acetonitrile or methanol as organic modifier. Predicted retention times take into account structural formulae of compounds and properties of stationary and mobile phases result in average difference of 14–17% compared to experimental ones on phenyl-hexyl stationary phase, where the highest matching was obtained. After utilisation of the retention models with data from one experimental run, the average difference decrease to maximal 7% and after contribution of data from two experimental runs, to maximal 2%. For majority of studied compounds difference between predicted and experimental values on all examined stationary phases is lower than 3%.

Keywords: High-performance liquid chromatography; quantitative structure-retention relationships (QSRRs); solvatic retention model; RP stationary phases; gradient elution; aripiprazole

1. Introduction

As development and optimization of HPLC methods can be very time-consuming, 1,2 for rapid method development a systematic, automated approach is needed.³ This approach includes identification of most suitable initial conditions (column and mobile phase), analysis of multi-component mixture (e. g. active pharmaceutical compound with typical impurities) and evaluation of the results.4 Presumably methods developed using computer-assisted procedures are expected to be more robust than those, developed by the traditional »trial and error« approach.5-7 Three main factors affect analyte partition between the stationary and the mobile phase. Those are the chemical structure of analyte, characteristics of the stationary phase and physico-chemical properties of the mobile phase at the constant temperature.⁸ Several software programs for method development and method optimization are available - ACD/LC simulator®,

ChromSmart®, ChromSword®, DryLab®, Osiris®, Preopt-W® and others. ChromSword® and ACD/LC simulator® contain algorithms for prediction of initial conditions from structural formulae of compounds. In ACD/ LC simulator[®] correlation between logarithm of partition (log P) or logarithm of distribution (log D) and retention in reversed phase liquid chromatography is used. In ChromSword® the solvophobic (solvatic) model or reversed-phase liquid chromatography is applied for predictions. Different kind of quantitative structure-retention relationships (QSRRs) have also been described in literature for prediction of retention. 9-15 Optimization of gradient elution is more complex compared to isocratic one and requires more experiments.^{5,16-18} In the literature successful prediction of isocratic retention parameters is reported.¹⁶ In 2003, Baczek and Kaliszan applied quantitative structure retention relationships (QSRRs) to predict retention in reversed-phase HPLC with linear gradient. 19 Well known is the model based on LSER (linear solvation energy relationships) developed by Abraham and coworkers.²⁰ The most known QSRR approach and generally accepted is the solvophobic theory of reversed-phase liquid chromatography. The solvophobic model of interaction of an analyte with surrounding liquid was proposed by Sinanoglu and Haliloglu and applied by Horvath and coworkers^{21–23} for a retention description in reversed-phase HPLC. Galushko used the solvophobic theory to calculate retention and in his approach a two-layer continuum model of reversed-phase liquid chromatography was applied.^{24–25} It this approach a stationary phase is considered as a quasi-liquid layer that has its own characteristics, which vary with mobile and stationary phase composition. An analyte interacts with the surface layer and retention is determined by the difference in molecule solvation energies in the mobile phase and stationary phase: $\ln k_x = aV_x^{2/3}$, + $b\Delta G_{e.s.x.H_2O}$ + c, where $V_x^{2/3}$ is the partial molecular volume of the analyte in water, which determines the value of energy to create a cavity in the mobile and stationary phases, $\Delta G_{e.s.x.H_2O}$ is the energy of electrostatic interaction of the analyte with water and a, b, c are the parameters, determined by the properties of a reversed-phase column and a mobile phase. Thus, in the Galushko's model the molecular interactions of analytes with the stationary and mobile phase are assumed to be accounted by the partial molar surface, S (S = $V^{2/3}$) that determines the energy to create a cavity in the phases.⁵ The partial molar volume parameter (V) appears to be a reasonably reliable parameter of structurally nonspecific determination of analyte retention. Another molecular parameter ΔG , energy of interaction, reflects differences in the so-called electrostatic intermolecular interactions of analytes with a surrounding mobile phase.5

The main limitation for retention prediction of chemical compounds from their structure is the inadequacy of the translation of structural formulas into sets of numerical descriptors. 19 Kaliszan's approach needs three molecular descriptors and four regression coefficients, Abraham's approach needs five molecular descriptors, constant log k₀ and five regression coefficients and Galushko's approach needs only two molecular parameters and three regression coefficients.^{2,20,24-25} It should be noted that Kaliszan's approach can be used only for prediction on selected stationary phase and only for the same gradient that was used for deriving the model,16 while Galushko's approach enables prediction of retention also for other stationary phases and multistep gradients.⁵ Other practical important point to be considered is that in OSRR modelling retention behaviour is usually performed in one software, and different software is used to calculate the molecular descriptors.²⁶ ChromSword® enables all operations - structures drawing, molecular parameters calculation, chromatogram simulation for different columns and gradients in one software platform. In off-line mode ChromSword® software utilise defined relationships between separation, retention, and chromatographic conditions for the prediction. Chemical structures of analytes are entered and the software model chromatographic retention behaviour consider organic modifier in mobile phase. Additionally, the software uses chromatographic data obtained from at least two initial experiments to predict optimum separation condition for different type of retention models.¹³

In the present work, the solvatic retention model in reversed-phase HPLC for retention prediction in gradient elution mode, using different types of stationary phases (C18, C8 and phenyl-hexyl) was applied for aripiprazole and its related substances described in European Pharmacopoeia. Also, two different organic modifiers (acetonitrile and methanol) were utilised. As some of the compounds have basic properties, effects of organic modifiers are important as methanol is concerned mainly in proton acceptor interactions, while acetonitrile mainly to dipole-dipole interactions.²

2. Experimental

2. 1. Chemicals and Reagents

Acetonitrile and methanol were ultra-gradient HPLC grade and were obtained from J.T.Baker (Avantor Performance Materials, USA). Ultrapure water was obtained with Milli-Q water system (Millipore Merck, Germany). Acetic acid and phosphoric acid (49–51%) were obtained from Sigma-Aldrich, USA.

2. 2. Standards

Standards of aripiprazole, impurity B (European Pharmacopoeia), impurity E (Eur. Ph.) and impurity F (Eur. Ph.) were obtained from USP (USA). Standards of impurity A (Eur.Ph.), impurity C (Eur.Ph.) and impurity D (Eur.Ph.) were obtained from Toronto research Chemicals, Canada. Impurity G (Eur.Ph.) was obtained from Molcan, Canada.

2. 3. Mobile Phases and Dilution Solvent

Mobile phase A was prepared with addition of 2.0 mL of 49–51% phosphoric acid to 1000 mL of Milli Q water. Mobile phase B was either acetonitrile or methanol. Dilution solvent was mixture of acetic acid: methanol: acetonitrile: water = 1:10:30:60 (V/V/V/V).

2. 4. Equipment

HPLC system Agilent 1260 series (Agilent Technologies, USA) equipped with quaternary pump, vacuum degasser, autosampler, temperature-controlled column compartment for five columns and diode array detector was used. The mobile phases were A aqueous solution of phosphoric acid, B acetonitrile and C methanol.

2. 5. Software

ChromSwordAuto® method development chromatography data system (ChromSword, Germany), version 5.0.234.300, was used for HPLC system control, aqusition of chromatographic data and the rapid automatic optimization of gradient methods. ChromSword® software for computer-assisted method development was used for retention prediction from structural formulae, stationary and mobile phase with simulation of gradient elution.

2. 6. HPLC Columns and Chromatographic Conditions

Five HPLC columns with the same dimensions were utilised (Table 1): three Halo columns with identical particle and pore size, the same surface area, but different type of reversed phase (C18, C8 and phenyl-hexyl) and two columns from different vendors, slightly different particle and pore size and the same phases as two Halo columns. Software input parameters concerning stationary phase were: column name, type of stationary phase, column and particle dimensions. Columns temperature was maintained at 30 °C. Flow rate of mobile phase was 1.0 mL/min and injection volume 5 µL. Detection was at 220 nm. Concentration of each compound in standard solution was 0.1 mg/ mL. Gradient profiles for all five columns and both organic modifiers are shown in Table 2. Minimum and maximum percent of organic modifier in gradient was preselected and then software delivers initial gradient conditions: the same for all selected columns (1st run). Gradient was determined independent from chemical structures of analytes. Then software modelled two different gradient conditions (2nd and 3rd run).

3. Results and Discussion

3. 1. Investigated Compounds

Drug aripiprazole and its related substances were studied. All compounds are described and marked with

letters in European Pharmacopoeia (Figure 1). Aripiprazole is chemically 7-[4-[4-(2,3-dichlorophenyl)piperazin-1-yl]butoxy]-3,4-dihydroquinolin-2(1*H*)-one. Chemical structures of aripiprazole and impurities C, D, E, F and G are very similar as 7-hydroxy-3,4-dihydroquinolin-2(1H)-one is part of the structure. Aripiprazole and impurities B, E, F and G have 1-(2,3-dichlorophenyl)piperazine, but impurities C and D have only 1-(2-chlorophenyl)piperazine. These structural parts include basic N atoms, therefore analytes are bases. Piperazine part and dihydroquinolin-2(1H)- one part are linked via butyl in aripiprazole, impurity C, D, E, F and G. Impurity G is chemically the most different from aripiprazole, while impurities C and D have the most similar chemical structures (they are positional isomers).

Separation of analytes, which have very similar chemical structures, and separation of far different chemical structures in one analysis represents a challenge and can require a large number of experiments for separation optimisation, therefore this group of compounds was selected for automatic method optimisation.

3. 2. Method Development

Software ChromSword[®] was used for automatic method optimisation using the rapid method development algorithm, which usually performes 3 gradient runs (1st, 2nd and 3rd) to achieve separation of all analytes.¹³ The optimisation of the method was performed on five different reversed-phase HPLC columns (Table 1) with acetonitrile or methanol as organic modifier.

Retention prediction in the reversed-phase HPLC from chemical structure of analytes (Figure 1) and stationary/mobile phase characteristics can be considered as the zero approximation level and can be used for selection of initial conditions (the "first guess method"). Parameters of the impurity F contains the N-oxide fragment, which is charged and cannot be calculated with the Chromsword® software. Therefore, simulated chromatograms have seven peaks and the experimental one eight peaks. The main

Column	Stationary phase	Column zero time, min	Length, mm	Internal diameter, mm	Particle size, µm	Pore size, nm	Surface area, m ² /g	Carbon load,%	Vendor
Triart C18	Silica/C18	1.5	150	4.6	3.0	12	360	20.0	YMC, USA
Halo C18	Silica/C18	1.5	150	4.6	2.7	9	135	7.7	Advanced materials technology, USA
Halo Phenyl- Hexyl	Silica/Phenyl- Hexyl	1.5	150	4.6	2.7	9	135	7.1	Advanced materials technology, USA
Halo C8	Silica/C8	1.5	150	4.6	2.7	9	135	5.4	Advanced materials technology, USA
Symmetry C8	Silica/C8	1.5	150	4.6	3.5	10	335	11.7	Waters, USA

Table 1. Utilised reversed-phase HPLC columns.

Table 2. Gradient profiles for selected columns with acetonitrile (B) as organic modifier or with methanol (C) as organic modifier.

l st run	Column	2 nd run	3 rd run
	YMC Triart C18	0.0 min = 2% B, 32.6–49.6 min = 50% B	0.0 min = 0% B or C 5.8 min = 19% B, 12.8 min = 28% B, 15.3 min = 29% B, 23.6 min = 36% B, 30.7 min = 40% B 32.9–52.7 min = 47% B
		0.0 min = 1% C, 32.6–50.8 min = 100% C	0.0 min = 2% C, 16.3 min = 56% C, 23.6 min = 74% C, 31.5-64.5 min = 100% C
	Halo C18	0.0 min = 0% B, 32.8-53.4 min = 80% B	0.0 min = 0% B, 8.2 min = 27% B, 1 4.0 min = 34% B, 19.9 min = 39% B, 32.9–51.5 min = 82% B
.0 min = 0% B, 0.0 min =20% B or C		0.0 min = 0% C, 32.8–56.3 min = 97% C	0.0 min = 0% C, 16.9 min = 56% C, 21.0 min = 62% C, 23.2 min = 64% C, 32.9–58.5 min = 96% C
5.0 min = 70% B or C 5.0–60.0 min = 100% B or C	Halo Phenyl-Hexyl	0.0 min = 0% B, 32.8-50.4 min = 82% B	0.0 min = 0% B, 5.5 min = 18% B, 14.7 min = 28% B, 17.5 min = 37% B, 22.6 min = 38% B, 32.4–49.8 min = 70% B
		0.0 min = 0% C, 32.8-54.8 min = 97% C	0.0 min = 0% C, 13.9 min = 46% C, 15.2 min = 49% C, 21.1 min = 68% C, 24.2 min = 69% C, 32.9–55.0 min = 97% C
	Halo C8	0.0 min = 0% B, 32.8–52.6 min = 98% B	0.0 min = 0% B, 2.3 min = 1% B, 10.7 min = 28% B, 13.2 min = 31% B, 32.9–51.8 min = 96% B
		0.0 min = 0% C, 32.5-51.6 min = 100% C	min = 0% C, 0.6 min = 1% C, 30.6-61.7 min = 100% C
	Symmetry C8	0.0 min = 0% B, 32.8-52.7 min = 96% B	0.0 min = 1% B, 7.0 min = 24% B, 12.0 min = 31% B, 32.9-51.9 min = 100% B
		0.0 min = 2% C, 30.9–49.5 min = 100% C	0.0 min = 3% C, 19.7min = 67% C, 21.8 min = 68% C, 31.6–54.0 min = 100% C

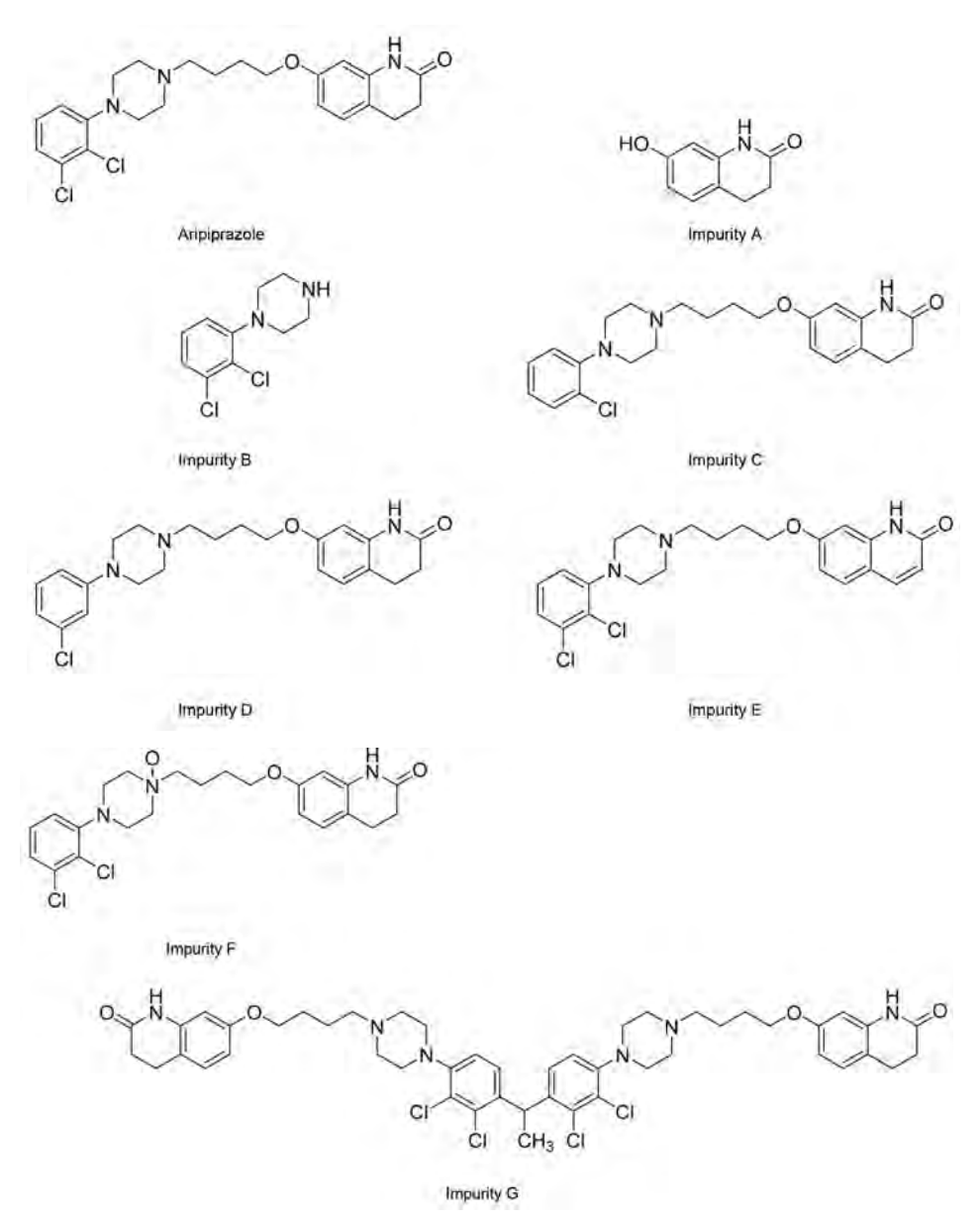


Figure 1. Structure of aripiprazole and its impurities described in European Pharmacopoeia.

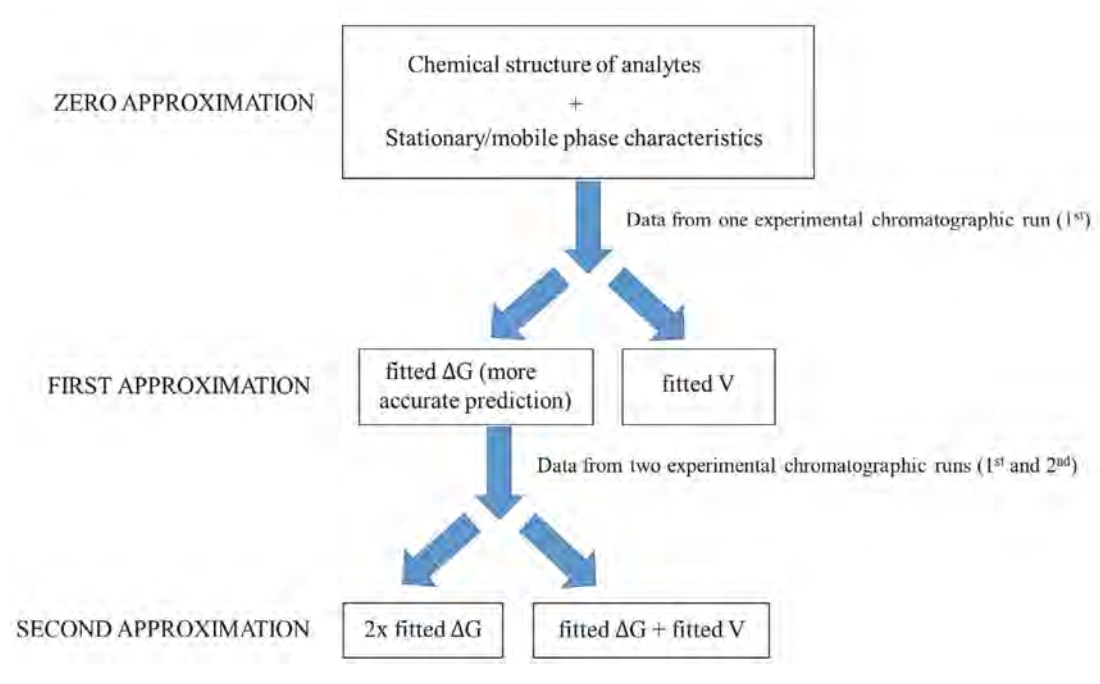
goal of these experiments was to predict conditions that provide as short as possible and practically acceptable retention times. Values for ΔG and V for aripiprazole and its impurities are presented in Table 3. The software ChromSword® does not distinguish between positional isomers for the zero approximation level and the estimated ΔG and V values are therefore the same for impurity C and impurity D.

Input and output data for individual approximation are presented in Sheme 1. For the first approximation the results of one experimental run (1st) are used to correct retention models for analytes which were derived from structual formulae and characteristics of the reversed-phase column and the mobile phase. The second approximation procedure provides fine tuning of the re-

Table 3. Estimated ΔG and V for aripiprazole and its impurities.

Compound	ΔG	\mathbf{V}
Impurity A	-101	120
Impurity B	-93	184
Impurity C	-191	332
Impurity D	-191	332
Impurity E	-184	345
ARIPIPRAZOLE	-189	350
Impurity G	-380	717

tention models using results of two experimental runs (1st and 2nd). The first and the second approximations provide retention prediction much more precisely than the zero



Sheme 1. Input and output data for zero, first and second approximation.

Table 4. Differences of retention times at zero approximation for 1st run of rapid method development (acetonitrile as organic modifier) on all five tested columns.

Column	Difference (%)							
Compound	YMC Triart C18	Halo C18	Halo Phenyl-Hexyl	Halo C8	Symmetry C8			
Impurity A	-26.3	-30.1	-16.5	-33.7	-10.9			
Impurity B	-55.6	-72.7	-32.7	-68.6	-82.1			
Impurity C	-28.6	-38.5	-17.4	-35.2	-43.5			
Impurity D	-27.5	-38.1	-16.3	-34.3	-42.8			
Impurity E	-33.7	-43.7	-18.7	-38.4	-45.7			
ARIPIPRAZOLE	-27.8	-37.8	-15.0	-33.2	-40.8			
Impurity G	-11.4	-19.6	-2.9	-17.1	-23.4			
Average	-30.1	-40.1	-17.1	-37.2	-41.3			

Table 5. Differences of retention times at zero approximation for 1st run of rapid method development (methanol as organic modifier) on all five tested columns.

Column	Difference (%)						
Compound	YMC Triart C18	Halo C18	Halo Phenyl-Hexyl	Halo C8	Symmetry C8		
Impurity A	-5.4	-21.6	-10.5	-26.1	-10.1		
Impurity B	-41.6	-56.5	-31.8	-59.7	-58.8		
Impurity C	-29.3	-34.8	-15.7	-39.4	-39.8		
Impurity D	-28.1	-36.9	-16.4	-41.2	-41.8		
Impurity E	-25.2	-31.0	-13.8	-35.2	-34.4		
ARIPIPRAZOLE	-23.7	-29.1	-10.9	-33.2	-32.6		
Impurity G	-12.5	-14.3	-0.6	-18.5	-19.1		
Average	-23.7	-32.0	-14.3	-36.2	-33.8		

approximation. Using retention data from experimental run, either the energy of electrostatic interaction of the analyte with water ($\Delta G_{e.s.x.H_2O}$) or the partial molecular volume of the analyte in water ($V_x^{2/3}$) can be corrected. The results for zero approximation are presented in Table 4 and

Table 5 and for the first and second approximation in Table 6 and Table 7 respectively.

Results of the zero approximation step enable prediction of approximate elution order and approximate retention times. Table 4 and Table 5 (and additional tables in

Supplementary Material) represent results for zero approximation for all five tested columns. On phenyl-hexyl stationary phase the highest matching for zero approxima-

tion step was obtained with both organic modifiers. The lowest matching for zero approximation step was obtained on C8 stationary phase. Therefore further optimization

Table 6. Difference between experimental and predicted retention times (in%) for the first and the second approximation with acetonitrile as organic modifier on all selected columns.

	First approa		Second approximation for 3 rd consecutive run		
YMC TRIART C18	ΔG fitted	V fitted	2x ΔG fitted	ΔG fitted + V fitted	
Impurity A	-2.2	-3.4	-2.4	-2.5	
Impurity B	no difference	-2.2	-0.7	-0.7	
Impurity C	-0.1	0.4	-2.7	-2.7	
Impurity D	-0.1	0.5	-2.8	-2.8	
Impurity E	0.1	0.8	-1.9	-1.9	
ARIPIPRAZOLE	0.1	0.7	-2.2	-2.2	
Impurity G	0.7	0.9	-0.2	-0.2	
Average	-0.2	-0.3	-1.8	-1.9	
HALO C18	ΔG fitted	V fitted	2x ΔG fitted	ΔG fitted + V fitted	
Impurity A	-3.7	-5.6	-1.3	-1.4	
Impurity B	-1.4	-9.1	-1.3	-1.3	
Impurity C	-0.3	-1.5	no difference	no difference	
Impurity D	-0.1	-1.3	0.2	0.2	
Impurity E	-0.4	-1.5	0.8	0.8	
ARIPIPRAZOLE	-0.4	-1.3	1.2	1.2	
Impurity G	-0.3	-0.5	4.7	4.7	
Average	-0.9	-3.0	0.6	0.6	
HALO Phenyl-Hexyl	ΔG fitted	V fitted	2x ΔG fitted	ΔG fitted + V fitted	
Impurity A	-6.3	-7.5	-1.9	-2.0	
Impurity B	-3.4	-9.4	0.8	0.9	
Impurity C	-0.7	-1.5	-0.7	-0.7	
Impurity D	-0.7	-1.4	-0.7	-0.7	
Impurity E	-0.9	-1.7	-0.4	-0.3	
ARIPIPRAZOLE	-1.1	-1.6	-0.5	-0.5	
Impurity G	-2.5	-2.6	-0.8	-0.6	
Average	-2.2	-3.7	-0.6	-0.6	
Symmetry C8	ΔG fitted	V fitted	2x ΔG fitted	ΔG fitted + V fitted	
Impurity A	-8.5	-9.3	-1.2	-1.4	
Impurity B	-5.1	-17.1	-0.7	-0.7	
Impurity C	-1.3	-4.8	0.2	0.2	
Impurity D	-0.9	-4.4	0.2	0.2	
Impurity E	-1.3	-4.6	1.3	1.4	
ARIPIPRAZOLE	-1.1	-3.8	1.8	1.8	
Impurity G	-0.8	-1.3	0.9	0.9	
Average	-2.7	-6.5	0.3	0.3	
Halo C8	ΔG fitted	V fitted	2x ΔG fitted	ΔG fitted + V fitted	
Impurity A	-2.5	-5.3	0.6	0.7	
Impurity B	-1.0	-9.8	-0.4	-0.5	
Impurity C	-0.2	-2.2	0.1	0.1	
Impurity D	0.2	-1.8	0.1	0.1	
Impurity E	-0.7	-2.6	0.8	0.8	
ARIPIPRAZOLE	-0.8	-2.2	0.7	0.8	
Impurity G	-1.1	-1.4	0.1	0.1	
Average	-0.9	-3.6	0.3	0.3	

ΔG fitted = fitted energy of electrostatic interaction of the analyte with water; V fitted=fitted partial molecular volume of the analyte in water

was done on column Symmetry C8 (first and second approximation) and it is graphically represented in Figure 2 and Figure 3. In practice, the first guess method is used

mainly for retention optimization – retention time should be between 5 and 30 of the column zero time value. Obtained results are reasonable and practically useful to pre-

Table 7. Difference between experimental and predicted retention times (in %) for the first and the second approximation with methanol as organic modifier on all selected columns.

	First approx for 2 nd consec		Second approximation for 3 rd consecutive run		
YMC TRIART C18	ΔG fitted	V fitted	2x ΔG fitted	ΔG fitted + V fitted	
Impurity A	-10.3	-10.9	-0.1	-0.2	
Impurity B	0.4	-3.4	0.2	0.2	
Impurity C	0.2	-0.9	0.5	0.5	
Impurity D	-0.1	-1.1	0.4	0.4	
Impurity E	no difference	-0.9	0.2	0.2	
ARIPIPRAZOLE	no difference	-0.8	0.2	0.2	
Impurity G	-0.5	-0.8	1.0	1.0	
Average	-1.5	-2.7	0.3	0.3	
HALO C18	ΔG fitted	V fitted	2x ΔG fitted	ΔG fitted + V fitted	
Impurity A	-1.2	-3.3	-0.2	-0.2	
Impurity B	1.5	-3.9	-0.1	-0.1	
Impurity C	-0.9	-2.0	-0.3	-0.3	
Impurity D	-0.6	-1.8	-0.2	-0.2	
Impurity E	-0.0 -1.1	-1.8 -2.1	-0.3	-0.2 -0.3	
ARIPIPRAZOLE	-1.1 -1.2	-2.1 -2.1	-0.3 -0.2	-0.3 -0.2	
	-1.2 -1.3	-2.1 -1.6	2.8	2.8	
Impurity G Average	-1.3 -0.7	-1.6 -2.4	0.2	0.2	
	ΔG fitted	V fitted	2x ΔG fitted	Δ G fitted + V fitted	
HALO Phenyl-Hexyl					
Impurity A	-1.6	-2.6	-0.1	-0.1	
Impurity B	-0.5	-2.8	-0.3	-0.4	
Impurity C	-1.6	-2.1	-0.3	-0.3	
Impurity D	no difference	-0.6	-0.4	-0.3	
Impurity E	-0.7	-1.2	-0.3	-0.3	
ARIPIPRAZOLE	-0.7	-1.1	-0.5	-0.5	
Impurity G	-1.3	-1.3	-0.8	-0.8	
Average	-0.9	-1.7	-0.4	-0.4	
Symmetry C8	ΔG fitted	V fitted	$2x \Delta G$ fitted	ΔG fitted + V fitted	
Impurity A	-5.1	-6.3	-0.1	-0.2	
Impurity B	-0.1	-9.4	no difference	no difference	
Impurity C	-0.5	-3.0	0.1	0.1	
Impurity D	-0.2	-2.9	0.2	0.2	
Impurity E	-0.7	-2.7	no difference	no difference	
ARIPIPRAZOLE	-0.7	-2.5	-0.1	-0.1	
Impurity G	-1.0	-1.6	-0.1	-0.1	
Average	-1.2	-4.0	no difference	no difference	
Halo C8	ΔG fitted	V fitted	2x ΔG fitted	ΔG fitted + V fitted	
Impurity A	0.2	-2.3	no difference	no difference	
Impurity B	1.7	-4.5	-0.2	-0.1	
Impurity C	-0.9	-2.4	-0.2	-0.2	
Impurity D	-0.6	-2.1	-0.2	-0.2	
Impurity E	-1.3	-2.5	-0.3	-0.3	
ARIPIPRAZOLE	-1.3	-2.4	-0.3	-0.3	
Impurity G	-1.5 -1.5	-2.4 -1.9	-0.3	-0.3 -0.3	
Average	-0.5	-1.9 -2.6	-0.3 -0.2	-0.3 -0.2	
	-0.3	-2.0	-0.2	-0.2	

 $\Delta G \text{ fitted} = \text{fitted energy of electrostatic interaction of the analyte with water; } V \text{ fitted} = \text{fitted partial molecular volume of the analyte in water}$

dict the first guess gradient just from structural formulae and stationary/mobile phase characteristics. Software ChromSword® utilise for zero approximation combination of eluents water-acetonitrile or water-methanol and stationary phase. Previously published predicted elution order was the same as the experimental one as buffer with pH 6.4 was used, which is similar as pH of water.² In our experiments acidic pH (0.1% H_3PO_4 pH = 2.4) was used. Analytes are bases and have charged structures at acidic conditions to have retention as low as possible. Additionally, predicted retention times are longer than experimental ones. This can be explained as all analytes except impurity A contain N atoms, which are strong bases and are protonated at acidic pH conditions (pH = 2.4), therefore their retention is lower than in the neutral eluent (that was obtained in 1st, 2nd and 3rd run).

Results in Table 6 and Table 7 demonstrate that retention prediction after the first approximation is much more precise: maximal average difference from experimental values is 6.5% with acetonitrile and 4.0% with methanol. At this step a correction of interaction energy of the analyte, ΔG with water is fitted. Difference between predicted and experimental retention is lower if ΔG is fitted compared to partial molecular volume, V. We consider that the reason for this is that partial molecular volume can be calculated from structure more precisely than energy of interaction.

After the second approximation (Table 6 and Table 7) even more precise prediction of experimental retention times on all columns with both organic modifiers was achieved. The average difference between predicted and experimental values is maximal 1.9% with acetonitrile and 0.4% with methanol. For all tested compounds on all five columns, exception is Impurity G, difference between predicted and experimental values is lower than 3% (maximal difference is 2.8% for Impurity D on column YMC Triart C18). Difference between predicted and experimental values is the highest (4.7%) for impurity G on column Halo

C18. Impurity G is dimeric impurity and its chemical structure differ from other compounds and this could be the reason.

For the second approximation step either the interaction energy can be fitted twice (option one) or both the interaction energy and the partial molecular volume (option two) can be fitted. According to the results in Table 6 and Table 7 there is no significant difference between these two options. Results show that second approximation gives much more precise results for predicted retention for 3rd consecutive run. However, both the first and second approximations give satisfactory prediction of elution order and retention time for all selected stationary phases (C18, C8 and phenyl-hexyl).

High correlation between experimental and predicted retention from the structure of examined compounds and data from two experiments (second approximation) on all selected columns in both cases – after use of twice ΔG fitted (Table 8) or after use ΔG fitted + V fitted (Table 9) was obtained. The highest correlation coefficients are obtained with phenyl-hexyl stationary phase and the lowest with C18 stationary phase, where R^2 is 0.9973 and can be also considered as a very good result.

3. 4. Comparison of Experimental and Predicted Chromatograms

Figure 2 and Figure 3 represent chromatograms of aripiprazole (ARI) and its impurities (A to G as are marked in Pharmacopoeia) on column Symmetry C8. On experimental chromatogram presented in Figure 2a peaks for all eight analytes appear. Peaks for impurity C and impurity D are not baseline separated. That is expected, because their chemical structure is very similar (positional isomers) and therefore their separation is challenging. Figure 2b and Figure 2c represent predicted chromatograms – for the first and the second approximations, where only 7 chromatographic peaks are presented (peak for impurity F is

Table 8. Correlation between predicted and experimental retention times from the structure and data of two experiments (second approximation) on all selected columns after use of twice ΔG fitted.

Column Organic modifier	YMC Triart C18	Halo C18	Correlation coefficient (R²) Halo Phenyl-Hexyl	Halo C8	Symmetry C8
Acetonitrile	0.9990	0.9982	0.9998	0.9994	0.9991
Methanol	0.9998	0.9973	1.0000	1.0000	1.0000

Table 9. Correlation between predicted and experimental retention times from the structure and data of two experiments (second approximation) on all selected columns after use of ΔG fitted + V fitted.

Column Organic modifier	YMC Triart C18	Halo C18	Correlation coefficient (R ²) Halo Phenyl-Hexyl	Halo C8	Symmetry C8
Acetonitrile	0.9991	0.9982	0.9997	0.9993	0.9990
Methanol	0.9998	0.9973	1.0000	1.0000	0.9999

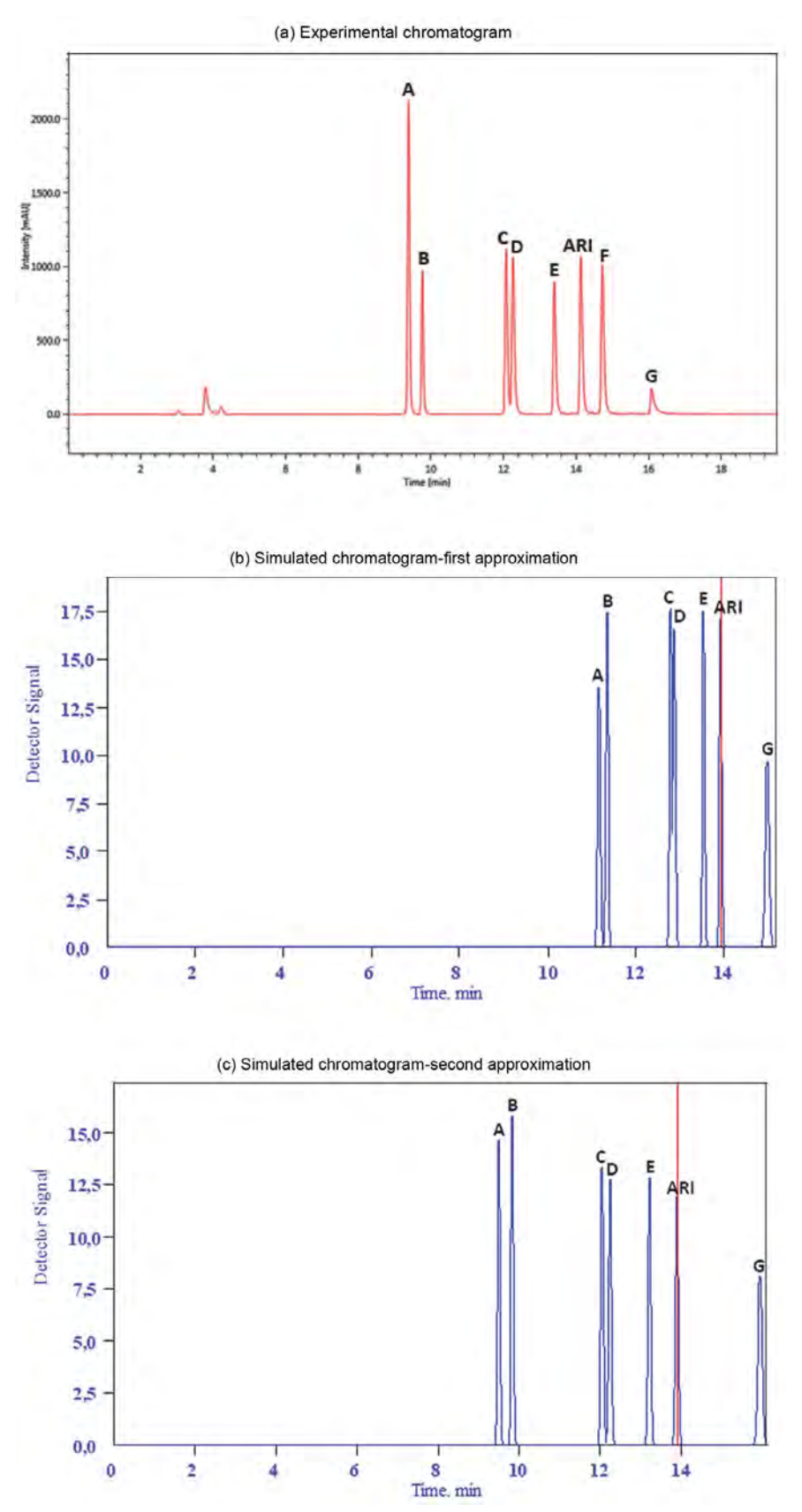


Figure 2. (a) Experimental chromatogram of 3rd run of rapid method development (b) predicted chromatogram – first approximation and (c) predicted chromatogram – second approximation on column Symmetry C8, with acetonitrile as organic modifier. Chromatographic conditions are shown in Table 2.

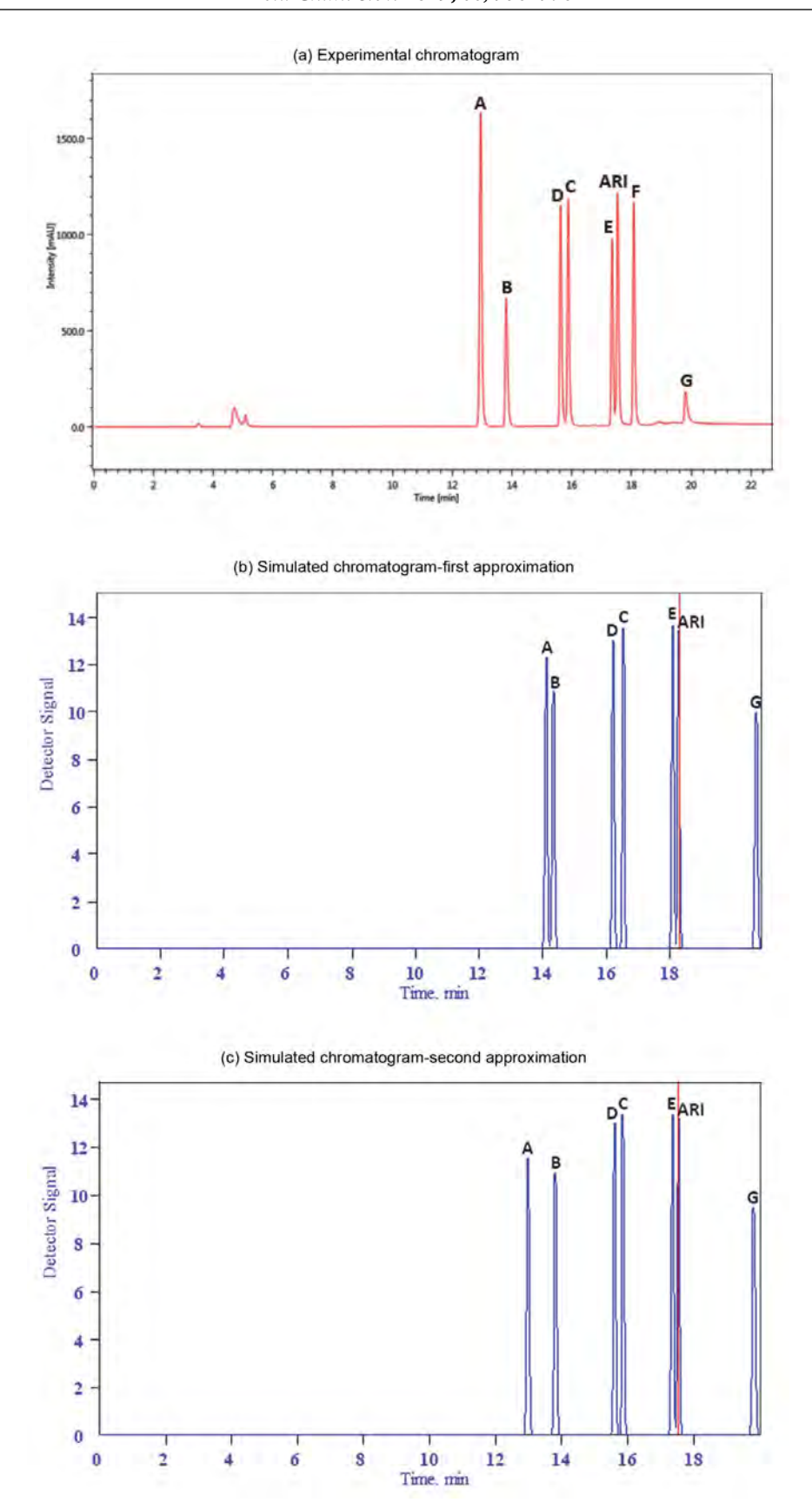


Figure 3. (a) Experimental chromatogram of 3rd run of rapid method development (b) predicted chromatogram – first approximation and (c) predicted chromatogram – second approximation on column Symmetry C8, with methanol as organic modifier. Chromatographic conditions are shown in Table 2.

missing as explained in paragraph 3.2.). After the first approximation there is a low resolution between peaks for impurities A and B, but after the second approximation step separation practically corresponds to the experimental one.

On another experimental chromatogram presented in Figure 3a obtained with methanol as organic modifier on column Symmetry C8 again eight peaks for all analytes are separated. Separation of peaks for impurity C and impurity D (positional isomers) is better with methanol than with acetonitrile as organic modifier but elution order is reversed. Figure 3b and Figure 3c represent predicted chromatograms for the first and the second approximation correspondently. For these conditions (Figure 3b) there is better resolution between impurities A and B than with acetonitrile as an organic modifier (Figure 2b). After the second approximation (Figure 2c and Figure 3c) these two analytes are baseline separated in both cases (with acetonitrile or methanol as organic modifier).

4. Conclusions

The solvatic retention model of reversed-phase high-performance liquid chromatography was applied for prediction of aripiprazole and its impurities retention in multi-step gradient elution mode on C18, C8 and phenyl-hexyl stationary phases with acetonitrile or methanol and 0.1% phosphoric acid mobile phases. In the zero approximation step - only from structural formulae and column/mobile phase characteristics reasonable prediction of retention times was obtained. The average difference between experimental retention and predicted retention is 17.1% with acetonitrile and 14.3% with methanol as the organic modifier on phenyl-hexyl stationary phase, where highest matching was obtained. Retention data from one experimental run (1st) were used to correct the retention models. The first approximation step enables prediction of retention time with maximal average difference from experimental values 6.5% with acetonitrile and 4.0% with methanol. After the second approximation step retention data from two runs (1st and 2nd) were used for further fine-tuning of the retention models. The average difference between predicted and experimental values is maximal 1.9% with acetonitrile and 0.4% with methanol. For all tested compounds on all five columns difference between predicted and experimental values is lower than 3%. Exception is dimeric Impurity G, where on column Halo C18 difference is 4.7%.

Some of investigated compounds, aripiprazole and its related substances described in European Pharmacopoeia, have very similar chemical structure; two of them are even positional isomers. On the other hand, some of the compounds have very different chemical structure. Therefore, appropriate separation of all these compounds in one analysis represent complex problem and the opti-

misation can be time consuming. Using solvatic retention model optimisation was successful; exception is the compound with charged structure, as there is no option for prediction of retention time of such compounds.

In the present research solvatic retention model was investigated for prediction on different reversed stationary phases (C18, C8 and phenyl-hexyl), while in literature generally for reversed phase investigations C18 is used as model phase. In our study best matching between experimental and predicted retention was observed on phenyl-hexyl stationary phase, which was not described so far as model reversed phase and also comparison with C18 and C8 stationary phases was made. Additionally, there are several published investigations using isocratic elution, while few investigations describe results with gradient elution mode. In our research we perform experiments with multi-step gradient and obtained quality results (average difference between predicted and experimental values below 2%) compared to the literature data.

Results of this investigation, where solvatic model was utilised, can serve as support for further usage of this approach for fast development and optimisation of robust analytical methods.

5. Acknowledgment

The authors acknowledge the financial support from the Slovenian Research Agency (research core funding No. P1-0153) and Krka d.d., Novo Mesto.

6. References

- 1. A. Wang, P. W. Carr, *J. Chromatogr. A* **2002**, 965, 3–23. **DOI**:10.1016/S0021-9673(01)01472-8
- S. Vorslova, J. Golushko, S. Galushko, A. Viksna, *Proc. Est. Acad. Sci.* 2016, 65, 37–49. DOI:10.3176/proc.2016.1.03
- K. P. Xiao, Y. Xiong, F. Z. Liu, A. M. Rustum, J. Chromatogr. A 2007, 1163, 145–156. DOI:10.1016/j.chroma.2007.06.027
- 4. E. F. Hewitt, P. Lukulay, S. Galushko, *J. Chromatogr. A* **2006**, *1107*, 79–87. **DOI**:10.1016/j.chroma.2005.12.042
- S. Vorslova, J. Golushko, S. Galushko, A. Viksna, *Chromatographia* 2015, 78, 899–908. DOI:10.1007/s10337-014-2816-4
- A. A. D'Archivio, M. A. Maggi, P. Mazzeo, F. Ruggieri, *Anal. Chim. Acta* 2008, 628, 162–172.
 DOI:10.1016/j.aca.2008.09.018
- A. A. D'Archivio, M.A. Maggi, F. Ruggieri, *Anal. Chim. Acta* 2011, 690, 35–46. DOI:10.1016/j.aca.2011.01.056
- 8. S. Vorslova, J. Golushko, S. Galushko, A. Viksna, *Latvian J. Chem.* **2014**, *52*, 61–70. **DOI:**10.2478/ljc-2013-0007
- 9. www.chromsword.com (accessed: March 3, 2019)
- 10. www. molnar-institute.com (accessed: March 3, 2019)
- 11. www.acdlabs.com (accessed: March 3, 2019)
- 12. S. Fekete, S. Rudaz, J. Fekete, D. Guillarme, *J. Pharm. Biomed. Anal.* **2012**, *70*, 158–168. **DOI:**10.1016/j.jpba.2012.06.021

- S. Kromidas, HPLC made to measure: A Practical Handbook for Optimization, first ed., Wiley-VCH, Weinheim, Germany, 2008. DOI:10.1002/9783527611973
- A. A. D'Archivio, M. A. Maggi, F. Ruggieri, J. Sep. Sci. 2010, 33, 155–166. DOI:10.1002/jssc.200900537
- A. A. D'Archivio, M. A. Maggi., F. Ruggieri, *Anal. Bioanal. Chem.* 2015, 407, 1181–1190.
- T. Baczek, R. Kaliszan, J. Chromatogr. A 2002, 962, 41–55.
 DOI:10.1016/S0021-9673(02)00557-5

DOI:10.1007/s00216-014-8317-3

- M. Szultka-Mlynska, B. Buszewski, J. Chromatogr. A 2016, 1478, 50–59. DOI:10.1016/j.chroma.2016.11.057
- A. A. D'Archivio, M. A. Maggi, C. Marinelli, F. Ruggieri, F. Stecca, *J. Chromatogr. A* 2015, 1423, 149–157.
 DOI:10.1016/j.chroma.2015.10.082

- T. Baczek, R. Kaliszan, J. Chromatogr. A 2003, 987, 29–37.
 DOI:10.1016/S0021-9673(02)01701-6
- T. Baczek, R. Kaliszan, K. Novotna, P. Jandera, *J. Chromatogr. A* 2005, *1075*, 109–115. DOI:10.1016/j.chroma.2005.03.117
- 21. C. Horvath, W. Melander, I. Molnar, *Anal. Chem.* **1977**, *49*, 142–154. **DOI**:10.1021/ac50009a044
- 22. C. Horvath, W. Melander, I. Molnar, *J. Chromatogr. A* **1976**, 125, 129–156. **DOI**:10.1016/S0021-9673(00)93816-0
- 23. I. Molnar, *Chromatographia* **2005**, *62*, 7–17. **DOI:**10.1365/s10337-005-0645-1
- 24. S. V. Galushko, A. A. Kamenchuk, G. L. Pit, J. Chromatogr. A 1994, 660, 47–59. DOI:10.1016/0021-9673(94)85098-4
- S. V. Galushko, Chromatographia 1993, 36, 39–42.
 DOI:10.1007/BF02263833
- H. Du, J. Wang, X. Yao, Z. Hu, J. Chromatogr. Sci. 2009, 47, 396–404. DOI:10.1093/chromsci/47.5.396

Povzetek

Za razvoj kromatografskih metod lahko uporabimo različne pristope; tako poleg tradicionalnega pristopa lahko optimiziramo metode z različno programsko opremo. Za napoved retencijskih časov pri gradientnem načinu za aripiprazol in njegove nečistote, opisane v Evropski farmakopeji, je bil uporabljen solvatni retencijski model za reverznofazno tekočinsko kromatografijo. Nekatere preučevane spojine imajo zelo podobno kemijsko strukturo, druge pa zelo različno, zato njihova separacija predstavlja izziv. Napoved retencije je bila zadovoljiva na vseh preiskovanih stacionarnih fazah (C8, C18 in fenil-heksil) z 0,1 % fosforno kislino kot vodno mobilno fazo in acetonitrilom ali metanolom kot organskim modifikatorjem. Pri napovedanih retencijskih časih, kjer se je upoštevala kemijska struktura spojin ter lastnosti stacionarne in mobilne faze, je bila povprečna razlika med napovedanimi in eksperimentalnimi retencijskimi časi 14–17 % v primeru stacionarne faze fenil-heksil, pri kateri je bilo ujemanje največje. Pri uporabi retencijskega modela skupaj s podatki enega eksperimenta se je povprečna razlika zmanjšala na največ 7 %, pri uporabi podatkov dveh eksperimentov pa se je povprečna razlika zmanjšala na največ 2 %. Za večino preiskovanih spojin je bila razlika med napovedanimi in eksperimentalno dobljenimi retencijskimi časi manjša od 3 % na vseh preiskovanih stacionarnih fazah.





Scientific paper

Synthesis, Spectroscopic Characterization, Crystal Structures and Antibacterial Activity of Vanadium(V) Complexes of Fluoro- and Chloro-Substituted Benzohydrazone Ligands

En-Cheng Liu,1 Wei Li1,* and Xiao-Shan Cheng2

 1 Department of Radiology, The Second Hospital of Dalian Medical University, Dalian 116023, P.R. China

² Department of Chemistry and Chemical Engineering, Liaoning Normal University, Dalian 116029, P. R. China

* Corresponding author: E-mail: liwei dlmu@126.com, youzhonglu@126.com

Received: 04-25-2019

Abstract

A new vanadium(V) complex, [VOL(OMe)(MeOH)]·MeOH (1·MeOH), was prepared by the reaction of VO(acac)₂ with 2-chloro-N-(5-fluoro-2-hydroxybenzylidene)benzohydrazide (H₂L) in methanol. By addition of salicylhydroxamic acid (HSHA) to the methanolic solution of 1, a new salicylhydroxamate-coordinated vanadium(V) complex, [VOL(SHA)]·H₂O (2·H₂O), was obtained. Both complexes were characterized by elemental analysis, infrared spectroscopy, thermal analysis and single crystal X-ray diffraction. Complex 1 crystallizes with methanol molecule as a solvate, and complex 2 as a monohydrate. The V atoms in the complexes are in octahedral coordination. In the crystal structure of 1·MeOH, the vanadium complexes are linked by methanol solvate molecules through intermolecular O-H····N and O-H····O hydrogen bonds to form chains along the c axis. In the crystal structure of 2·H₂O, the vanadium complexes are linked by water molecules through intermolecular O-H····O hydrogen bonds, to form 1D chains along the c axis. The chains are further linked through intermolecular O-H····N and O-H····O hydrogen bonds in the c direction to form 2D layers. The antimicrobial activities of the complexes against c0. c1. c2. c3. c4. c4. c4. c4. c5. c6. c6. c6. c6. c8. c8. c8. c8. c9. c

Keywords: Hydrazone ligand; Salicylhdroxamate ligand; Vanadium complex; Crystal structure; Antibacterial activity.

1. Introduction

In recent years, vanadium complexes have been reported to have interesting biological activities such as normalizing the high blood glucose levels and acting as models of haloperoxidases. Hydrazone compounds derived from the condensation reaction of aldehydes with various hydrazides are much attractive for their structures, coordinate ability to metal atoms and extensive biological applications.² Recently, our research group has reported a few vanadium complexes with hydrazone ligands and their biological activities.³ In general, V atom is readily adopt octahedral coordination. Hydrazone ligands can coordinate to the V atoms through three donor atoms. The remaining three positions of the octahedral coordination are usually occupied by one oxo oxygen and two solvent molecules, one with deprotonated and the other one neutral.^{3a,4} The two solvent ligands are not coordinate so strong to the V atom that they are readily substituted by bidentate ligands, such as benzohydroxamate,⁵ propane-1,3-diol-2-olate or propan-1-ol-3-olate,⁶ 2-hydroxyethanolate,⁷ *etc.* Salicylhydroxamic acid is a bidentate ligand, but very few examples of vanadium(V) complexes with this ligand have been reported. Fluoro- and chloro-substituted compounds are reported to have effective antibacte-

Scheme 1. H_2L

rial activities.⁸ In the present paper, a new methanol and methoxy-coordinated vanadium(V) complex, [VOL(OMe)(MeOH)]·MeOH (1) and a salicylhydroxamate (SHA) coordinated vanadium(V) complex, [VOL(SHA)]·H₂O (2), where $H_2L = 2$ -chloro-N'-(5-fluoro-2-hydroxybenzylidene)benzohydrazide (Scheme 1), are presented and studied on their antibacterial activities.

2. Experimental

2. 1. Materials and Measurements

Commercially available 5-fluorosalicylaldehyde, 2-chlorobenzohydrazide and salicylhyroxamic acid were purchased from Sigma-Aldrich and used without further purification. Other solvents and reagents were made in China and used as received. C, H and N elemental analyses were performed with a Perkin-Elmer elemental analyser. Infrared spectra were recorded on a Nicolet AV-ATAR 360 spectrometer as KBr pellets in the 4000–400 cm⁻¹ region. Thermal stability analysis was performed on a Perkin-Elmer Diamond TG-DTA thermal analyses system. NMR spectra were recorded on a Bruker 500 MHz instrument.

2. 2. Synthesis of H₂L

5-Fluorosalicylaldehyde (1.0 mmol, 0.14 g) and 2-chlorobenzohydrazide (1.0 mmol, 0.17 g) were dissolved in methanol (30 mL) with stirring. The mixture was stirred for about 30 min at room temperature to give a clear solution. The solvent was evaporated to give colorless crystalline products. Yield, 96%. Analysis: Found: C 57.6%, H 3.5%, N 9.5%. Calculated for $C_{14}H_{10}ClFN_2O_2$: C 57.4%, H 3.4%, N 9.6%. IR data (KBr, cm⁻¹): ν 3372 (w, OH), 3232 (w, NH), 1651 (s, C=O), 1619 (s, C=N). UV-Vis (MeOH, nm): λ 225, 289, 305, 330, 405. ¹H NMR (d^6 -DMSO, ppm) δ 12.16 (s, 1H, OH), 10.77 (s, 1H, NH), 8.49 (s, 1H, CH=N), 7.61–7.42 (m, 5H, ArH), 7.17 (d, 1H, ArH), 7.03 (d, 1H, ArH). ¹³C NMR (d^6 -DMSO, ppm) δ 162.85, 156.78, 154.91, 146.62, 135.23, 132.08, 131.24, 130.02, 128.99, 127.60, 120.31, 120.25, 118.82, 114.13.

2. 3. Synthesis of [VOL(OMe)(MeOH)]·MeOH (1)

A methanolic solution (10 mL) of [VO(acac)₂] (0.1 mmol, 26.5 mg) was added to a methanolic solution (10 mL) of H_2L (0.1 mmol, 29.2 mg) with stirring. The mixture was stirred for 30 min at room temperature to give a brown solution. The resulting solution was allowed to stand in air for a few days. Brown block-shaped crystals suitable for X-ray single crystal diffraction were formed at the bottom of the vessel. The isolated products were washed three times with cold ethanol, and dried in air. Yield, 72%. Anal-

ysis: Found: C 44.9%, H 4.4%, N 6.2%. Calculated for $C_{17}H_{19}ClFN_2O_6V$: C 45.1%, H 4.2%, N 6.2%. IR data (KBr, cm⁻¹): ν 3437 (m, OH), 1607 (s, C=N), 981 (V=O). UV-Vis (MeOH, nm): λ 270, 325, 413. ¹H NMR (d^6 -DMSO, ppm) δ 8.88 (s, 1H, CH=N), 7.83 (d, 1H, ArH), 7.61–7.20 (m, 5H, ArH), 6.94 (d, 1H, ArH), 5.26 (s, 3H, CH₃), 3.94 (s, 3H, CH₃). ¹³C NMR (d^6 -DMSO, ppm) δ 171.50, 160.25, 156.55, 154.68, 132.52, 132.25, 131.72, 131.35, 131.12, 127.60, 120.73, 118.19, 117.97, 117.78, 74.54, 49.07. ⁵¹V NMR (d^6 -DMSO, ppm) δ –555.

2. 4. Synthesis of [VOL(SHA)]·H₂O (2)

A methanolic solution (10 mL) of salicylhydroxamic acid (0.1 mmol, 15.3 mg) was added to a methanolic solution (10 mL) of 1 (0.1 mmol, 45.3 mg) with stirring. The mixture was stirred for 30 min at room temperature to give a deep brown solution. The resulting solution was allowed to stand in air for a few days. Brown block-shaped crystals suitable for X-ray single crystal diffraction were formed at the bottom of the vessel. The isolated products were washed three times with cold ethanol, and dried in air. Yield, 51%. Analysis: Found: C 47.7%, H 3.0%, N 7.8%. Calculated for C₂₁H₁₆ClFN₃O₇V: C 47.8%, H 3.1%, N 8.0%. IR data (KBr, cm⁻¹): v 3454 (m, OH), 3278 (w, NH), 1607 (s, C=N), 979 (V=O). UV-Vis (MeOH, nm): λ 266, 327, 408. ¹H NMR (d^6 -DMSO, ppm) δ 12.16 (s, 1H, OH), 12.10 (s, 1H, NH), 9.13 (s, 1H, CH=N), 7.71-7.57 (m, 4H, ArH), 7.48-7.38 (m, 3H, ArH), 7.01-6.87 (m, 4H, ArH). ¹³C NMR (d^6 -DMSO, ppm) δ 163.70, 160.89, 157.36, 156.50, 155.75, 151.79, 134.93, 132.62, 131.20, 130.89, 130.80, 129.88, 128.99, 127.56, 122.89, 119.97, 119.72, 118.82, 118.15, 117.93, 115.35. ⁵¹V NMR (*d*⁶-DMSO, ppm) δ –553.

2. 5. X-ray Crystallography

Diffraction intensities for the complexes were collected at 298(2) K using a Bruker D8 VENTURE PHO-TON diffractometer with MoKa radiation (l = 0.71073 Å). The collected data were reduced using the SAINT program,9 and multi-scan absorption corrections were performed using the SADABS program.¹⁰ The structures were solved by direct method, and refined against F^2 by full-matrix least-squares method using the SHELXTL.¹¹ All of the non-hydrogen atoms were refined anisotropically. The coordinated methanol hydrogen atom in 1-MeOH and the amino hydrogen atom in 2·H₂O were located from difference Fourier maps and refined isotropically, with O-H and N-H distances restrained to 0.85(1) Å and 0.90(1) Å, respectively. All other hydrogen atoms were placed in idealized positions and constrained to ride on their parent atoms. The crystallographic data for the complexes are summarized in Table 1. Selected bond lengths and angles are given in Table 2. Hydrogen bonding information is listed in Table 3.

Table 1. Crystallographic data and refinement parameters for the complexes

Table 2. Selected bond distances (Å) and angles (°) for the complexes

	1 ·MeOH	$2 \cdot H_2O$			1	
Chemical formula	C ₁₇ H ₁₉ ClN ₂ O ₆ V	C ₂₁ H ₁₆ ClF-	V(1)-O(1)	1.849(4)	V(1)-O(2)	1.975(4)
N_3O_7V			V(1)-O(3)	1.580(5)	V(1)-O(4)	1.747(4)
Mr	452.7	527.8	V(1)-N(1)	2.129(5)	V(1)-O(5)	2.289(5)
Crystal color, habit	Brown, block	Brown, block	O(3)-V(1)-O(4)	102.1(2)	O(3)-V(1)-O(1)	100.2(2)
Crystal system	Monoclinic	Monoclinic	O(4)-V(1)-O(1)	103.2(2)	O(3)-V(1)-O(2)	96.6(2)
Space group	Cc	$P2_1/c$	O(4)-V(1)-O(2)	93.5(2)	O(2)-V(1)-O(1)	153.1(2)
Unit cell parameters			O(3)-V(1)-N(1)	94.8(2)	O(4)-V(1)-N(1)	160.2(2)
a (Å)	17.938(1)	7.577(2)	O(1)-V(1)-N(1)	83.6(2)	O(2)-V(1)-N(1)	74.2(2)
b (Å)	12.072(1)	23.119(3)	O(3)-V(1)-O(5)	175.5(2)	O(4)-V(1)-O(5)	82.1(2)
c (Å)	10.250(1)	12.393(2)	O(1)-V(1)-O(5)	80.3(2)	O(2)-V(1)-O(5)	81.4(2)
β(°)	98.617(2)	97.507(2)	N(1)-V(1)-O(5)	80.8(2)	. , , , , , ,	
$V(Å^3)$	2194.5(3)	2152.4(6)		* * *		
Z	4	4			2	
$D_{\text{calc}} (\text{g cm}^{-3})$	1.370	1.629	V(1)-O(1)	1.863(2)	V(1)-O(2)	1.942(2)
Temperature (K)	298(2)	298(2)	V(1)-O(3)	2.185(2)	V(1)-O(4)	1.872(2)
$\mu (\text{mm}^{-1})$	0.614	0.644	V(1)-N(1)	2.081(2)	V(1)-O(6)	1.577(2)
F(000)	928 3579	1072	O(6)-V(1)-O(1)	99.2(1)	O(6)-V(1)-O(4)	95.6(1)
Number of unique data Number of observed data	3579 2756	3800 2667	O(4)-V(1)-O(1)	107.8(1)	O(6)-V(1)-O(2)	102.0(1)
[I > $2\sigma(I)$]	2/30	2007	O(1)-V(1)-O(2)	150.6(1)	O(4)-V(1)-O(2)	90.2(1)
Number of parameters	259	317	O(6)-V(1)-N(1)	95.8(1)	O(1)-V(1)-N(1)	83.3(1)
Number of restraints	3	4	O(4)-V(1)-N(1)	162.5(1)	O(2)-V(1)-N(1)	74.5(1)
R_1 , $wR_2[I > 2\sigma(I)]$	0.0656, 0.1666	0.0410, 0.0808	O(6)-V(1)-O(3)	171.2(1)	O(1)-V(1)-O(3)	81.4(1)
R_1 , wR_2 [1 > 20(1)] R_1 , wR_2 (all data)	0.0890, 0.1833	0.0738, 0.0926	O(4)-V(1)-O(3)	76.0(1)	O(2)-V(1)-O(3)	80.7(1)
K_1 , WK_2 (all data) Goodness of fit on F^2	1.046	1.011	N(1)-V(1)-O(3)	93.0(1)	0(2) ((1) 0(3)	00.7(1)

Table 3. Hydrogen bond distances (Å) and bond angles (°) for the complexes

D–H··· A	$d(D ext{-H})$, Å	$d(H\cdots A)$, Å	$d(D\cdots A)$, Å	Angle (D-H···A), o
1 ⋅MeOH				
$O(5)-H(5)-O(6)^{i}$	0.85(1)	1.79(2)	2.626(7)	166(8)
$O(6)-H(6)\cdots N(2)^{ii}$	0.82	2.19	2.790(7)	131
2 ·H ₂ O				
O(5)-H(5)-O(7)	0.82	1.79	2.607(3)	171
N(3)-H(3)···O(5)	0.90(1)	1.99(3)	2.608(3)	125(3)
N(3)-H(3)···O(4) ⁱⁱⁱ	0.90(1)	2.59(3)	3.310(3)	138(3)
$O(7)-H(7A)\cdots O(1)^{iv}$	0.85(1)	2.04(2)	2.853(3)	160(4)
$O(7)-H(7A)\cdots O(3)^{iv}$	0.85(1)	2.61(3)	3.225(3)	131(3)
O(7)-H(7B)···O(6) ⁱⁱⁱ	0.85(1)	2.23(3)	2.808(3)	125(3)
$O(7)-H(7B)N(2)^{v}$	0.85(1)	2.47(2)	3.183(3)	142(3)

Symmetry codes: i) x, -1 + y, z; ii) x, 1 - y, -1/2 + z; iii) 1 - x, -y, 1 - z; iv) 2 - x, -y, 1 - z; v) x, y, -1 + z.

3. Results and Discussion

Replacement of two acetylacetonate ligands in $[VO(acac)_2]$ by H_2L in methanol resulted in the formation of 1 (Scheme 2). The complex was further reacted with salicylhydroxamic acid to give complex 2 (Scheme 2). The latter complex can also be directly prepared by the reaction of H_2L , salicylhydroxamic acid and $[VO(acac)_2]$ in methanol. The V^{IV} in $[VO(acac)_2]$ was oxidized to V^V by air during the reaction. Both complexes are soluble in

DMF, DMSO, methanol, ethanol, and acetonitrile, insoluble in water, chloroform and dichloromethane. Molar conductance of complexes 1 and 2 at the concentration of 10^{-4} M are 17 and 33 Ω^{-1} cm² mol⁻¹, respectively, indicating they are non-electrolytes.¹²

3. 1. Crystal Structure Description of 1-MeOH

The molecular structure and atom numbering scheme of complex **1** is shown in Figure 1. The V atom in the com-

Scheme 2. The synthesis of the complexes

plex is in octahedral coordination, which is coordinated by one oxo oxygen, one neutral and one deprotonated methanol ligands, and the three donor atoms of the doubly deprotonated hydrazone ligand. The neutral methanol ligand is coordinated trans to the oxo oxygen, which is similar to those observed in the solvent coordinated vanadium complexes.^{3a,4} The vanadium to terminal oxo group (O(3)) bond length for the complex (1.580(5) Å) is within normal range for oxovanadium(V) complexes.¹³ The short V(1)–O(3) distance indicates the presence of a vanadium– oxygen double bond.¹⁴ The angular distortion in the octahedral environment around V comes from the five- and six-membered chelate rings taken by the hydrazone ligand, with angles of 83.6(2)° and 74.2(2)°. Distortion of the octahedral coordination can be observed from the coordinate bond angles, ranging from 74.2(2) to 103.2(2)° for the perpendicular angles, and from 153.1(2) to 175.5(2)° for the diagonal angles. Relative to the equatorial plane defined by O(1), O(2), O(4) and N(1), the vanadium atom is displaced toward the axial oxygen atom O3 by 0.291(1) Å. The dihedral angle between the two benzene rings is 83.6(3)°. The double deprotonated form of the hydrazone ligand is consistent with the observed O2-C8 and N2-C8 bond lengths of 1.292(7) Å and 1.302(7) Å, respectively. This is in agreement with reported vanadium complexes containing the enolate form of hydrazone ligands.^{4,13b}

In the crystal of 1, the vanadium complexes are linked by methanol molecules through intermolecular $O(5)-H(5)\cdots O(6)$ and $O(6)-H(6)\cdots N(2)$ hydrogen bonds, to form chains along the c axis (Figure 2).

3. 2. Crystal Structure Description of 2·H₂O

The molecular structure and atom numbering scheme of complex **2** is shown in Figure 3. The V atom in the com-

plex is in octahedral coordination, which is coordinated by one oxo oxygen, one hydroxyl and one carbonyl oxygen atoms of SHA ligand, and the three donor atoms of the hydrazone ligand. The carbonyl oxygen atom is coordinated trans to the oxo oxygen, with the bond length much longer than the remaining ones. The vanadium to terminal oxo group (O(6)) bond length for the complex (1.577(2) Å) is comparable to that in complex 1, and within normal range for oxovanadium(V) complexes. 13 The short V(1)–O(6) distance indicates the presence of a vanadium-oxygen double bond. 14 The coordinate bond lengths in the complex are comparable to those observed in 1 and the oxovanadium(V) complexes with octahedral coordination.4 The angular distortion in the octahedral environment around V comes from the five- and six-membered chelate rings taken by the hydrazone ligand, with angles of 83.34(9)° and 74.47(8)°. Distortion of the octahedral coordination can be observed from the coordinate bond angles, ranging from 74.5(1) to 107.8(1)° for the perpendicular angles, and from 150.6(1) to 171.2(1)° for the diagonal angles. Relative to the equatorial plane defined by O(1), O(2), O(4) and N(1), the vanadium atom is displaced toward the axial oxygen atom O3 by 0.268(1) Å. The dihedral angle between the substituted benzene rings is 21.0(3)°. The double deprotonated form of the hydrazone ligand is consistent with the observed O2-C8 and N2-C8 bond lengths of 1.302(3) Å and 1.297(3) Å, respectively. This is in agreement with reported vanadium complexes containing the enolate form of hydrazone ligands. 4,13b

In the crystal of **2**, the vanadium complexes are linked by water molecules through intermolecular O(7)– $H(7B)\cdots O(6)$ and O(7)– $H(7A)\cdots O(1)$ hydrogen bonds, to form 1D chains along the *a* axis. The chains are further linked through intermolecular O(5)– $H(5)\cdots O(7)$ and O(7)– $H(7A)\cdots O(3)$ hydrogen bonds in the *c* direction, to form 2D layers (Figure 4).

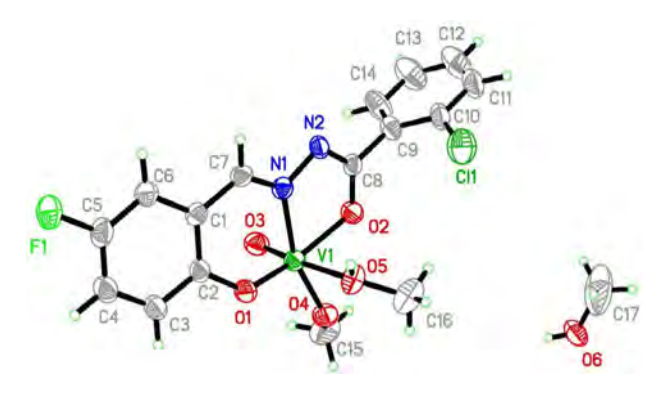


Figure 1. ORTEP plot of the crystal structure of **1.** Displacement ellipsoids of non-hydrogen atoms are drawn at the 30% probability level.

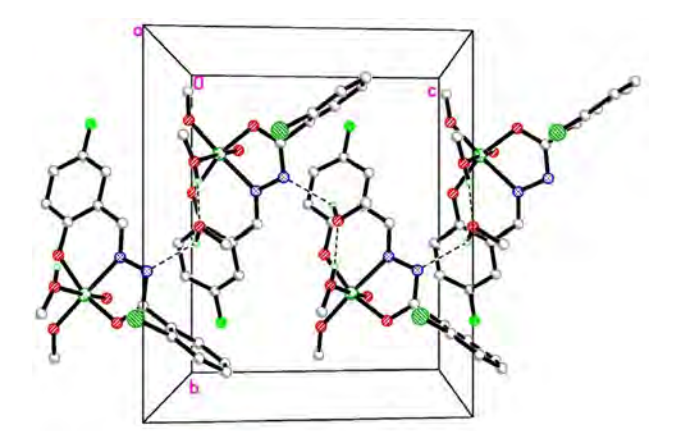


Figure 2. Molecular packing diagram of **1**. Viewed along the *a* axis. Hydrogen atoms not related to hydrogen bonding are omitted. Hydrogen bonds are shown as dashed lines.

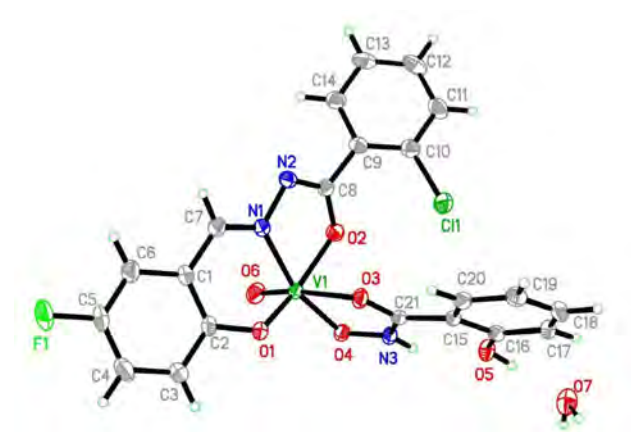


Figure 3. ORTEP plot of the crystal structure of **2.** Displacement ellipsoids of non-hydrogen atoms are drawn at the 30% probability level.

3. 3. IR and Electronic Spectra

The hydrazone ligand showed stretching bands attributed to C=O, C=N, C-OH and NH at about 1651, 1619, 1155 and 1220, and 3232 cm⁻¹, respectively. The complexes exhibit typical bands at about 980 cm⁻¹, as-

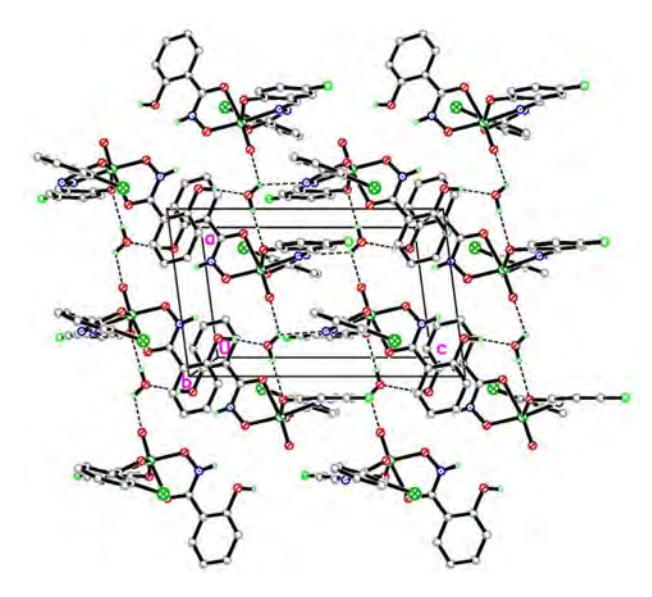


Figure 4. Molecular packing diagram of **2.** Viewed along the *c* axis. Hydrogen atoms not related to hydrogen bonding are omitted. Hydrogen bonds are shown as dashed lines.

signed to the V=O vibration. ¹⁵ In the spectrum of **1**, the bands due to $\nu_{C=O}$ and ν_{NH} were absent, but new C–O stretch appeared at 1253 cm $^{-1}$. This suggests occurrence of $\it keto$ -imine tautomerization of the hydrazone ligand during complexation. The same phenomenon should occur in complex **2**. But the existence of ν_{NH} at 3278 cm $^{-1}$ made an interruption. The $\nu_{C=N}$ absorption observed at 1619 cm $^{-1}$ in the free hydrazone ligand shifted to 1607 cm $^{-1}$ for both complexes upon coordination to the V atoms. ¹⁶ The weak peaks in the low wave numbers in the region 400–650 cm $^{-1}$ may be attributed to V–O and V–N bonds in the complexes.

Methanol solutions of the complexes are brown-yellow in color. These solutions have been used to record the electronic spectra. The hydrazone ligands and their vanadium(V) complexes have bands in the range 205–240 and 300–330 nm, which can be assigned as $\pi \rightarrow \pi^*$ and $n \rightarrow \pi^*$ transitions, respectively. All bands shift to lower energy in complexes indicating the coordination of ligands to the vanadium ions. The shoulder at about 270 nm for the complexes corresponds to LMCT band of V=O which it is observed at 274 nm for [VO(acac)₂].¹⁴

3. 4. Thermal Property

Differential thermal and thermal gravimetric analyses were conducted to examine the stability of the complexes. For 1 (Figure 5), the first step started at 50 °C and ended at 160 °C, with a weight loss of 14.0%, might be caused by the loss of the lattice and coordinated neutral methanol molecules. Then the complex continued to decompose, until 470 °C, corresponding to the loss of the remaining parts of the ligands, and formation of $\rm V_2O_5$. The total weight loss of 78.5% is in agreement with the ideal

value of 79.9%. For **2** (Figure 6), this complex is not very stable in air at room temperature. It might have lost the lattice water molecules before the thermal analysis. The complex started to decompose at 109 °C and completed at 470 °C, corresponding to the loss of the hydrazone and salicylhdroxamate ligands, and formation of V_2O_5 . The total weight loss of 83.7% is in agreement with the ideal value of 85.5%.

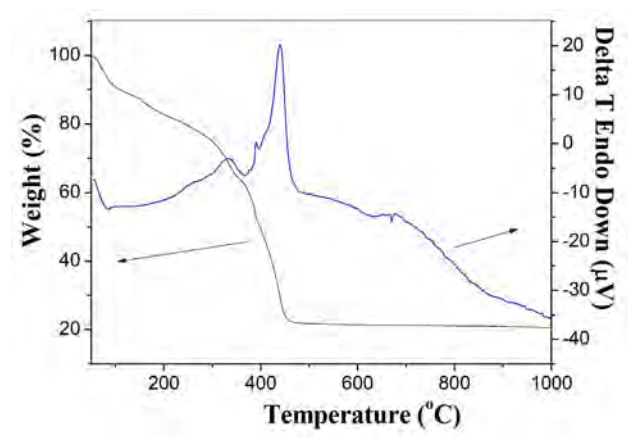


Figure 5. DT-TGA curves of 1.

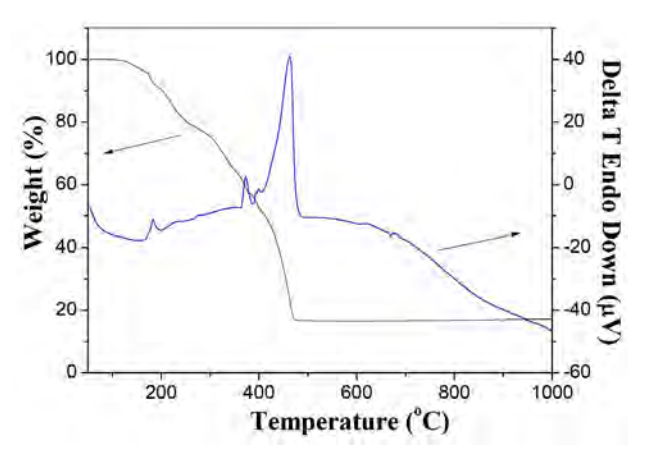


Figure 6. DT-TGA curves of 2.

3. 5. Antibacterial Activity

The free benzohydrazone and the vanadium complexes were assayed for *in vitro* antibacterial activity against *K. pneumoniae*, *S. aureus*, *P. aeroginosa*, *E. coli*, and *B. subtilis* at 50 µg mL⁻¹ using ethanol as solvent and control, and using tetracyclin as the standard drug. The minimum inhibitory concentrations (MIC) were determined

by broth micro-dilution method.¹⁷ The observed MIC values in µg mL⁻¹ are reported in Table 4. The antibacterial activity was evaluated by measuring the zone of inhibition in mm. Ethanol had no antibacterial activity on the bacteria at the concentration studied. The results revealed that the hydrazone compound and the two complexes showed from weak to effective activities against the tested microorganisms. In general, the complexes showed higher activities than the free aroylhydrazones. Such an enhancement in the activity of metal complexes against certain specific microorganisms may be explained on the basis of Overtone's concept and Tweedy's chelation theory. 18 The least MIC with 11 μg mL⁻¹ was observed for complex 1 against S. aureus. The activity on B. subtilis and S. aureus of the free hydrazone is less than N'-(5-chloro-2-hydroxybenzylidene)-4-hydroxybenzohydrazide (H₂L'), but on *E. coli*, the free hydrazone is higher than the above mentioned compound.¹⁹ The activity of the complexes on S. aureus and E. coli is similar to the vanadium complex with L' and 2-hydroxybenzoate ligands, while on B. subtilis, the complexes are much less than the vanadium complex mentioned above. 19 Thus, more work need to be done to find the relationship between the structures and the antibacterial activities.

4. Supplementary Material

CCDC-978393 for 1 and 978394 for 2 contain the supplementary crystallographic data for this paper. These data can be obtained free of charge at http://www.ccdc.cam.ac.uk/const/retrieving.html or from the Cambridge Crystallographic Data Centre (CCDC), 12 Union Road, Cambridge CB2 1EZ, UK; fax: +44(0)1223-336033 or e-mail: deposit@ccdc.cam.ac.uk.

5. References

- (a) G. R. Willsky, A. B. Goldfine, P. J. Kostyniak, J. H. McNeill,
 L. Q. Yang, H. R. Khan, D. C. Crans, J. Inorg. Biochem. 2001,
 85, 33–42; DOI:10.1016/S0162-0134(00)00226-9
 - (b) P. Caravan, L. Gelmini, N. Glover, F. G. Herring, H. L. Li, J. H. McNeill, S. J. Rettig, I. A. Setyawati, E. Shuter, Y. Sun, A. S. Tracey, V. G. Yuen, C. Orvig, *J. Am. Chem. Soc.* **1995**, *117*, 12759–12770; **DOI**:10.1021/ja00156a013
 - (c) A. Messerschmidt, L. Prade, R. Wever, *Biol. Chem.* **1997**, 378, 309–315. **DOI:**10.1515/bchm.1997.378.3-4.309

Table 4. Minimum inhibitory concentrations (MICs, µg mL⁻¹) of the compounds

Compound	K. pneumoniae	S. aureus	P. aeroginosa	E. coli	B. subtilis
H_2L	27	35	> 50	22	36
1	15	11	> 50	17	23
2	17	13	> 50	14	19

- (a) M. D. Altintop, A. Ozdemir, G. Turan-Zitouni, S. Ilgin, O. Atli, G. Iscan, Z. A. Kaplancikli, *Eur. J. Med. Chem.* 2012, 58, 299–307; DOI:10.1016/j.ejmech.2012.10.011
 - (b) X.-L. Wang, Z.-L. You, C. Wang, J. Chem. Crystallogr. **2011**, 41, 621–624; **DOI**:10.1016/j.bmc.2011.04.027
 - (c) M. A. A. El-Sayed, N. I. Abdel-Aziz, A. A. M. Abdel-Aziz, A. S. El-Azab, Y. A. Asiri, K. E. H. El Tahir, *Bioorg. Med. Chem.* **2011**, *19*, 3416–3424.
- 3. (a) L. L. Wang, W. Li, Y. J. Mei, Russ. J. Coord. Chem. **2019**, 45, 154–162; **DOI**:10.1134/S1070328419020118
 - (b) Z.-L. You, D.-H. Shi, J.-C. Zhang, Y.-P. Ma, C. Wang, K. Li, *Inorg. Chim. Acta* **2012**, *384*, 54–61;

DOI:10.1016/j.ica.2011.11.039

(c) S. Y. Li, W. Q. Zhai, Z. W. Li, A. Li, Y. M. Jiang, W. Li, Russ. J. Coord. Chem. **2018**, 44, 701–706;

DOI:10.1134/S1070328418110052

(d) Z.-L. You, Y.-M. Cui, Y.-P. Ma, C. Wang, X.-S. Zhou, K. Li, *Inorg. Chem. Commun.* **2011**, *14*, 636–640.

DOI:10.1016/j.inoche.2011.01.038

- (a) N. A. Lalami, H. H. Monfared, H. Noei, P. Mayer, *Transition Met. Chem.* 2011, 36, 669–677;
 - DOI:10.1007/s11243-011-9517-8
 - (b) T. N. Mandal, S. Roy, A. K. Barik, S. Gupta, R. J. Butcher, S. K. Kar, *Polyhedron* **2008**, *27*, 3267–3274.

DOI:10.1016/j.poly.2008.07.024

- S. Gao, Z.-Q. Weng, S.-X. Liu, Polyhedron 1998, 17, 3595–3606. DOI:10.1016/S0277-5387(98)00154-5
- S. P. Rath, K. K. Rajak, S. Mondal, A. Chakravorty, J. Chem. Soc. Dalton Trans. 1998, 2097–2101. DOI:10.1039/a801355a
- 7. M. Sutradhar, T. R. Barman, G. Mukherjee, M. G. B. Drew, S. Ghosh, *Polyhedron* **2012**, *34*, 92–101.

DOI:10.1016/j.poly.2011.12.022

8. M. Zhang, D.-M. Xian, H.-H. Li, J.-C. Zhang, Z.-L. You, *Aust. J. Chem.* **2012**, *65*, 343–350. **DOI**:10.1071/CH11424

- Bruker, SMART and SAINT, Bruker AXS Inc., Madison, Wiscon sin, USA, 2012.
- G. M. Sheldrick, SADABS Program for Empirical Absorption Correction of Area Detector, University of Göttingen, Germany, 1996.
- 11. G. M. Sheldrick, *Acta Crystallogr.* **2008**, *A64*, 112–122. **DOI:**10.1107/S0108767307043930
- 12. W. J. Geary, *Coord. Chem. Rev.* **1971**, *7*, 81–122. **DOI:**10.1016/S0010-8545(00)80009-0
- 13. (a) M. R. Prathapachandra Kurup, E. B. Seena, M. Kuriakose, *Struct. Chem.* **2010**, *21*, 599–605;

DOI:10.1007/s11224-010-9589-7

(b) Y. Li, L. Xu, M. Duan, J. Wu, Y. Wang, K. Dong, M. Han, Z. You, *Inorg. Chem. Commun.* **2019**, *105*, 212–216.

DOI:10.1016/j.inoche.2019.05.011

- H. H. Monfared, R. Bikas, P. Mayer, *Inorg. Chim. Acta* 2010, 363, 2574–2583. DOI:10.1016/j.ica.2010.04.046
- S. Guo, N. Sun, Y. Ding, A. Li, Y. Jiang, W. Zhai, Z. Li, D. Qu,
 Z. You, Z. Anorg. Allg. Chem. 2018, 644, 1172–1176.
 DOI:10.1002/zaac.201800060
- H. Yu, S. Guo, J.-Y. Cheng, G. Jiang, Z. Li, W. Zhai, A. Li, Y. Jiang, Z. You, J. Coord Chem. 2018, 71, 4164–4179.
 DOI:10.1080/00958972.2018.1533959
- J. H. Jorgensen, J. D. Turnidge, Manual of Clinical Microbiology, Washington (DC, USA): American Society for Microbiology, 2003.
- (a) N. Dharamaraj, P. Viswanathamurthi, K. Natarajan, *Transition Met. Chem.*, **2001**, *26*, 105–109;
 DOI:10.1023/A:1007132408648
 - (b) J. W. Searl, R. C. Smith, S. Wyard, *J. Proc. Phys. Soc.*, **1961**, 78, 1174–1181. **DOI**:10.1088/0370-1328/78/6/311
- C. Li, Y.-L. Dong, X.-F. Meng, X. Zhou, J.-J. Ma, Synth. React. Inorg. Met.-Org. Nano-Met. Chem., 2016, 46, 118–122.
 DOI:10.1080/15533174.2014.900791

Povzetek

Nov vanadijev(V) kompleks, [VOL(OMe)(MeOH)]·MeOH (1·MeOH), smo pripravili z reakcijo VO(acac)₂ z 2-kloro-*N*'-(5-fluoro-2-hidroksibenziliden)benzohidrazidom (H₂L) v metanolu. Z dodatkom salicilhidroksamske kisline (HSHA) k metanolni raztopini 1, smo izolirali nov salicilhidroksamato vanadijev(V) kompleks, [VOL(SHA)]·H₂O (2·H₂O). Oba kompleksa smo okarakterizirali z elementno analizo, infrardečo spektroskopijo, termično analizo in rentgensko monokristalno analizo. Kompleks 1 kristalizira z molekulo metanola kot solvatom in kompleks 2 kot hidrat. V kompleksih so V atomi oktaedrično koordinirani. V kristalni strukturi 1·MeOH so vanadijevi kompleksi povezani z molekulo metanola preko intramolekularnih O–H···N in O–H···O vodikovih vezi v verige vzdolž osi *c*. V kristalni strukturi 2·H₂O so vanadijevi kompleksi povezani z molekulo vode preko intermolekularnih O–H···O vodikovih vezi v verige vzdolž osi *a*. Nadalje so verige povezane v plasti preko intermolekularnih intermolekularnih O–H···N in O–H···O vodikovih vezi vzdolž osi *c*. Določili smo tudi antimikrobno aktivnost obeh kompleksov proti *K. pneumoniae*, *S. aureus*, *P. aeroginosa*, *E. coli* in *B. subtilis*.



Except when otherwise noted, articles in this journal are published under the terms and conditions of the Creative Commons Attribution 4.0 International License

@creative

Scientific paper

Synthesis and Characterization of High-Efficiency Red Phosphorescent Iridium(III) Complexes with 1-(4-(Trifluoromethyl)phenyl)isoquinoline Ligand

Zheng Zhao,¹ Xiao-Han Yang,¹ Zi-Wen Tao,¹ Han-Ru Xu,¹ Kai Liu,¹ Guang-Ying Chen,² Zheng-Rong Mo,² Shui-Xing Wu,¹ Zhi-Gang Niu,^{1,2} and Gao-Nan Li^{1,*}

¹ Key Laboratory of Electrochemical Energy Storage and Energy Conversion of Hainan Province, College of Chemistry and Chemical Engineering, Hainan Normal University, Haikou 571158, China

² Key Laboratory of Tropical Medicinal Plant Chemistry of Ministry of Education, Hainan Normal University, Haikou 571158, China

* Corresponding author: E-mail: ligaonan2008@163.com (G.-N. Li)

Received: 05-05-2019

Abstract

Two new tfmpiq-based bis-cyclometalated iridium(III) complexes, [(tfmpiq)₂Ir(imdzppo)] (**2a**) and [(tfmpiq)₂Ir(idzpo)] (**2b**) (where tfmpiq = 1-(4-(trifluoromethyl)phenyl)isoquinoline, imdzppo = 2-(imidazo[1,2-a]pyridin-2-yl)phenol, idzpo = 2-(2H-indazol-2-yl)phenol), have been synthesized and fully characterized. The single crystal structure of **2b** has been determined. The relationship between the structures and photophysical properties of both complexes are considered, and the DFT calculations have been used to further support the deduction. These Ir(III) complexes emit red light with quantum yields of 39.9–51.9% in degassed CH_2Cl_2 solution at room temperature. Also, their emission originates from a hybrid $^3MLCT/^3LLCT/^3LC$ excited state. All these results show that iridium(III) complexes **2a-2b** are suitable for red-phosphorescent materials in OLEDs.

Keywords: Iridium(III) complex; 1-(4-(Trifluoromethyl)phenyl)isoquinoline; Red phosphorescence; DFT calculation

1. Introduction

Organic light-emitting diodes (OLEDs) have attracted great attention on the development of modern optoelectronic technologies such as full-color displays and solid-state lighting sources. Particularly, cyclometalated iridium(III) complexes ([Ir(C^N)₃] or [(C^N)₂Ir(LX)]) are the most valuable emitting materials in the fabrication of OLEDs, owing to their relatively short excited-state lifetime, high phosphorescence efficiency and excellent color-tuning capability. As compared to other colors, red electrophosphorescent emitting phosphors are difficult to maintain high device efficiency, since their quantum efficiencies tend to decrease as the emission wavelength increases in accordance with the energy gap law. Thus, the design and syntheses of highly efficient red-emitting iridium complexes remain a challenge.

1-Phenylisoquinoline (piq) is one typical ligand framework to construct red iridium complexes. A large number of pig-based Ir(III) complexes have been reported during the past decade. 9-13 Among these examples, iridium complexes of fluorinated phenylisoquinoline show strong electroluminescence brightness and efficiency. This is because the fluorine groups could not only modify the electronic properties but also decrease the rate of nonradioactive deactivation and improve phosphorescence quantum yields.¹⁴ Therefore, in 2006, K.-H. Fang and co-workers first reported Ir(tfmpiq)₂acac (acac = acetylacetonate) complex, which emitted red phosphorescence with a wavelength maximum at 631 nm, and the quantum yield was up to 31%.15 Subsequently, in 2014, S. Zhang et al. developed red Ir(tfmpiq)2tpip complex (tpip = tetraphenylimidodiphosphinate), which achieved emission at 622 nm with quantum efficiency of 15%. 16 In the same year, we employed 2,2-bipyridine as the ancillary ligand to synthesize Ir(tfmpiq)₂bipy complex, which exhibited a maximum emission peak at 594 nm with quantum yield of 14%.¹⁷ Recently, in 2016, S. Aoki group reported tris-cy-clometalated iridium complex, Ir(tfpiq)₃, which displayed red phosphorescence at 600 nm with quantum yield of 25%.¹⁸

However, these conventional ancillary ligands used in tfmpiq-based iridium (III) complexes didn't show significantly red-shift with high quantum efficiencies. Thus, we wanted to attempt other types of ancillary ligands for Ir(tfmpiq)₂(LX) complexes, aiming to increase quantum efficiencies and further reduce the energy gap to reach to longer wavelength region. Our group previously reported four btp-based deep-red phosphorescent iridium(III) complexes with different ancillary ligands. 19 Among them, the Ir(III) complex with the picolinic acid as ancillary ligand could achieve a more red-shift relative to ones with N^N ancillary ligands. The N^O-type ancillary ligand containing -OH group could dramatically raise the highest occupied molecular orbital (HOMO) level and lead to a narrow HOMO-LUMO energy gap. Unfortunately, the quantum yield is very low (12%), as results of the fluorine-free main ligands in [Ir(btq)₂pic] complex.

Herein, we chose fluorinated 1-phenylisoquinoline (tfmpiq) as the cyclometalated ligand and N^O-type ligand (imdzppo/idzpo) as the ancillary ligand to synthesize two iridium(III) complexes (Scheme 1). Their photophysical and electrochemical properties are investigated, and the lowest-energy electronic transitions and the lowest-lying triplet excited state are calculated with density functional theory (DFT) and time-dependent DFT (TD-DFT).

2. Experimental

2. 1. Materials and Instrumentations

 $IrCl_3 \cdot 3H_2O$ was purchased from Energy Chemical and all reagents were used without further purification unless otherwise stated. All solvents were dried using standard procedures. Solvents used for electrochemistry and spectroscopy were spectroscopic grade. The target ligands, 1-(4-(trifluoromethyl)phenyl)isoquinoline (1), 20 2-(imidazo[1,2-a]pyridin-2-yl)phenol (a) 21 and 2-(2H-indazol-2-yl)phenol (b) 22 were prepared according to the literature procedures.

 1 H NMR spectra were recorded on a Bruker AM 400 MHz instrument. Chemical shifts were reported in ppm relative to Me₄Si as internal standard. MALDI-TOF-MS spectra were recorded on a Bruker Autoflex TM TOF/TOF instrument. Elemental analyses were performed on a Vario EL Cube Analyzer system. UV–vis spectra were recorded on a Hitachi U3900/3900H spectrophotometer. Fluorescence spectra were carried out on a Hitachi F-7000 spectrophotometer in deaerated CH_2Cl_2 solutions at 298 K and 77 K.

Cyclic voltammetry (CV) was performed on a CHI 1210B electrochemical workstation, with a glassy carbon electrode as the working electrode, a platinum wire as the counter electrode, an Ag/Ag^+ electrode as the reference electrode, and $0.1~M~n\text{-Bu}_4NClO_4$ as the supporting electrolyte.

2. 2. Synthesis of (tfmpiq)₂Ir(imdzppo) (2a)

A mixture of IrCl₃·3H₂O (295 mg, 0.84 mmol) and the 1-(4-(trifluoromethyl)phenyl)isoquinoline (500 mg,

Scheme 1. Synthetic routes of Ir(III) complexes 2a-2b.

1.82 mmol) in 15 mL of 2-ethoxyethanol and H_2O (v:v = 2:1) was heated at 120 °C under nitrogen for 12 hours. Upon cooling to room temperature, the orange-red precipitate was collected by filtration and washed with cooled ether and MeOH. After drying, the crude product of chloro-bridged dimer complex [(tfmpiq)₂Ir(μ-Cl)]₂ was used directly in next step without further purification. Then a slurry of the crude chloro-bridged dimer (100 mg, 0.065 mmol), 2-(imidazo[1,2-a]pyridin-2-yl)phenol (35 mg, 0.16 mmol) and Na₂CO₃ (55 mg, 0.52 mmol) in 2-ethoxyethanol (10 mL) was heated at 120 °C under nitrogen for 10 hours. After the solvent was removed, the mixture was poured into water and extracted with CH2Cl2 three times, and then evaporated. The residue was purified by flash column chromatography (petroleum ether : dichloromethane = $5:1\sim1:1$) to afford the iridium complex **2a** as a red solid (55 mg, yield: 45%). ¹H NMR (400 MHz, CDCl₃) δ (ppm) 8.95 (d, J = 8.0 Hz, 1H), 8.92 (d, J = 6.4Hz, 1H), 8.78 (d, J = 4.8 Hz, 2H), 8.29 (s, 1H), 8.24 (d, J =8.0 Hz, 1H), 7.81-7.92 (m, 10H), 7.71-7.75 (m, 3H), 7.38-7.40 (m, 2H), 7.18 (d, J = 4.8 Hz, 2H), 7.08–7.10 (m, 2H), 6.61 (d, J = 6.4 Hz, 1H), 6.21 (s, 1H). MALDI-TOF calcdfor C₄₅H₂₇F₆IrN₄O: 946.172 ([M+H]⁺). Found: 946.504. Anal. Calcd. for C₄₅H₂₇F₆IrN₄O: C 57.14, H 2.88, N 5.92. Found: C 57.10, H 2.97, N 5.89.

2. 3. Synthesis of (tfmpiq)₂Ir(idzpo) (2b)

Complex **2b** (52 mg, yield: 46%) was obtained by the method similar to the preparation of **2a** using 2-(2*H*-indazol-2-yl)phenol instead of 2-(imidazo[1,2-a]pyridin-2-yl) phenol. 1 H NMR (400 MHz, CDCl₃) δ (ppm) 9.01 (d, J = 8.4 Hz, 1H), 8.87 (d, J = 6.4 Hz, 1H), 8.84 (d, J = 8.4 Hz, 1H), 8.49-8.51 (m, 2H), 8.25 (d, J = 6.4 Hz, 1H), 8.18 (d, J = 8.4 Hz, 1H), 7.87-8.89 (m, 1H), 7.67-7.83 (m, 5H), 7.61 (d, J = 8.4 Hz, 1H), 7.35 (d, J = 6.4 Hz, 1H), 7.30 (dd, J = 1.6 Hz, 8.4 Hz, 1H), 7.13-7.15 (m, 2H), 7.04-7.09 (m, 2H), 6.85-6.88 (m, 1H), 6.69-6.73 (m, 1H), 6.44-6.48 (m, 1H), 6.32-6.36 (m, 1H), 6.16-6.21 (m, 2H). MALDI-TOF calcd for $C_{45}H_{27}F_6IrN_4O$: 946.172 ([M+H]+). Found: 946.386. Anal. Calcd. for $C_{45}H_{27}F_6IrN_4O$: C 57.14, H 2.88, N 5.92. Found: C 56.97, H 2.81, N 5.99.

2. 4. Crystallographic Studies

X-ray diffraction data were collected with an Agilent Technologies Gemini A Ultra diffractometer equipped with graphite-monochromated Mo-Kα radiation (λ = 0.7107 Å) at room temperature. Data collection and reduction were processed with CrysAlisPro software.²³ The structure was solved and refined using full-matrix least-squares based on F^2 with program SHELXS-97 and SHELXL-97²⁴ within Olex2.²⁵ Crystallographic data (excluding structure factors) for the structural analysis have been deposited with the Cambridge Crystallographic Data Center as supplementary publication No. CCDC

1836887 (**2b**). Copies of the data can be obtained free of charge via www.ccdc.ac.uk/conts/retrieving.html (or from The Director, CCDC, 12 Union Road, Cambridge CB2 1EZ, UK, Fax: +44-1223-336-033. E-mail: deposit@ccdc.cam.ac.uk.).

2. 5. Computational Method

All calculations were carried out with Gaussian 09 software package.²⁶ The density functional theory (DFT) and time-dependent DFT (TD-DFT) were employed with no symmetry constraints to investigate the optimized geometries and electron configurations with the Becke three-parameter Lee-Yang-Parr (B3LYP) hybrid density functional theory.^{27–29} The LANL2DZ basis set was used for the iridium(III), whereas the 6-31G* basis set was adopted for the ligands. Solvent effects were considered within the SCRF (self-consistent reaction field) theory using the polarized continuum model (PCM) approach to model the interaction with the solvent.^{30,31}

3. Results and Discussion

3. 1. Synthesis and Characterization

Scheme 1 outlines the synthetic routes for iridium complexes 2a-2b investigated in this work. The main ligand, 1-(4-(trifluoromethyl)phenyl)isoquinoline (tfmpiq), was prepared from the synthesis of 1-chloroisoquinoline and (4-(trifluoromethyl)phenyl)boronic acid according to the literature procedure. 20 The two constitutional isomer ligands, 2-(imidazo[1,2-a]pyridin-2-yl)phenol (imdzppo) and 2-(2H-indazol-2-yl)phenol (idzpo), were formed by an Ortoleva-King reaction and a PIII/PV = O redox cycling reaction, respectively.^{21,22} Complexes 2a-2b were obtained in moderate yields from the above ligands by a conventional two-step reaction. In the first step, a chloro-bridged dimer was formed by the reaction of iridium trichloride hydrate with an excess of main ligand. Then this dimmer was cleaved via treatment with ancillary ligand in the presence of Na₂CO₃ to produce the heteroleptic iridium complex. The two complexes were structurally characterized by ¹H NMR spectroscopy, mass spectrometry and elemental analysis.

3. 2. Structural Description

The crystal of 2b was obtained by slow evaporation of $CH_2Cl_2/MeOH$ solution and the structure was determined through X-ray diffraction analysis (Fig. 1a). The crystallographic data and structure refinement details are listed in Table 1; selected bond lengths and bond angles are collected in Table 2.

As shown in Fig. 1a, the Ir(III) adopts a distorted octahedral geometry with the C^N ligands in *cis*-C,C' and *trans*-N,N' configurations. The average distance of Ir-C

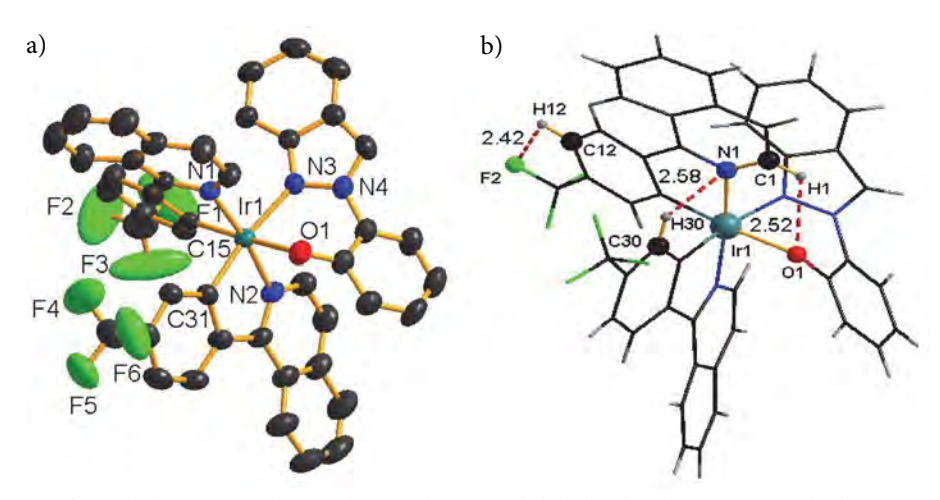


Fig. 1. (a) ORTEP view of 2b with the atom-numbering scheme at the 50% probability level. Hydrogen atoms and solvent molecules are omitted for clarity. (b) Selected non-covalent contacts of the C-H···O, C-H···F and C-H···N types (dashed red lines). Atoms involved in hydrogen bonds are shown as balls of arbitrary radii. All other atoms and covalent bonds are represented as wires or sticks.

bonds (Ir– C_{av} = 1.989 Å) is shorter than that of the Ir–N bonds (Ir– N_{av} = 2.082 Å), as reported in other iridium(III) complexes.^{32,33} Notably, bonds between iridium and the N^O ligand (Ir–N3 = 2.156 Å, Ir–O1 = 2.153 Å) are longer than those between iridium and the C^N ligands (Ir–C15 = 1.985Å, Ir–C31 = 1.993Å, Ir–N1 = 2.040 Å, Ir–N2 = 2.051 Å), resulting from strong *trans* influence of the carbon donors.³⁴ The angles of atoms on the para positions of the octahedron range from 171.61(18)° to 172.59(17)°, which are close to straight lines. For comparison, the two C–Ir–N bite angles of the C^N ligand are 79.23° and 79.47°, while the N–Ir–O bite angle of the ancillary ligand is 82.78°. This may be due to the rigid effect of the five-membered ring at the metal center.³⁵ In addition, the hydrogen-bonding interactions in the crystal structure are

Table 1. Crystallographic data for complex 2b · H₂O.

Empirical formula	$C_{45}H_{29}F_6IrN_4O_2$
M _r (g/mol)	963.92
Crystal system	Monoclinic
Space group	$P2_1/c$
a (Å)	12.5501(5)
b (Å)	18.1261(7)
c (Å)	16.6857(5)
α (°)	90
β (°)	95.252(3)
γ (°)	90
$V(\mathring{A}^3)$	3779.8(2)
Z	4
$D_{\rm calcd}$ (Mg/m ³)	1.694
F(000)	1896
Absorption coefficient (mm ⁻¹)	3.607
$R_{ m int}$	0.0354
$\operatorname{GOF}(F^2)$	1.026
R_1^{a} , wR_2^{b} (I>2 σ (I))	0.0378, 0.0796
R_1^{a} , wR_2^{b} (all data)	0.0592, 0.0909

 $^{{}^{}a}R_{1} = \Sigma ||F_{o}| - |F_{c}||/\Sigma |F_{o}|. \ {}^{b}wR_{2} = [\Sigma w(F_{o}{}^{2} - F_{c}{}^{2})^{2}/\Sigma w(F_{o}{}^{2})]^{1/2}$

Table 2. Selected bond distances (Å) and angles (°) for complex $2b\cdot H_2\mathrm{O}.$

Ir1-N1	2.040(4)	Ir1-N3	2.156(4)
Ir1-O1	2.153(4)	Ir1-C31	1.993(5)
Ir1-N2	2.051(4)	Ir1-C15	1.985(5)
N1-Ir1-O1	93.51(15)	C31-Ir1-N2	79.47(19)
N1-Ir1-N2	172.47(17)	C31-Ir1-N3	171.61(18)
O1-Ir1-N3	82.78(15)	C15-Ir1-O1	172.59(17)
C31-Ir1-O1	90.02(17)	C15-Ir1-N3	98.77(17)
C15-Ir1-N1	79.23(19)	C15-Ir1-C31	88.93(19)

Table 3. Hydrogen bonding arrangements for complex $2\mathbf{b} \cdot H_2O$ (Å, °).

D- H ···A	D -H	H A	D•••A	D -H ···A
C1-H1···O1	0.93	2.52	3.075(6)	118
C12-H12···F2	0.93	2.42	2.732(1)	100
C30-H30···N1	0.93	2.58	3.091(6)	115

presented in Fig. 1b and the details are summarized in Table 3. From Fig. 1b, the three selected non-covalent contacts of the C-H···O, C-H···F and C-H···N types are attributed to intramolecular hydrogen bonds, making three five-membered rings, respectively.

3. 3. Electronic Absorption Spectra

The UV-vis absorption spectra of complexes 2a-2b measured in CH_2Cl_2 solution at room temperature are depicted in Fig. 2, and the data are provided in Table 4. The absorption spectra reveal strong absorption bands below 400 nm, which are assigned to intraligand $\pi-\pi^*$ transitions centered on the C^N main ligand and the N^O ancillary ligand. The weak absorption bands extending from 400 nm to 550 nm are attributed to the metal to ligand $^1MLCT/^3MLCT$ transitions. $^{36-38}$ In comparison

Table 4. Photophysical and electrochemical data of 2a-2b.

Complex	$\begin{array}{ccc} \textbf{Absorption}^a & \textbf{Emission} \\ \lambda_{abs} (\textbf{nm}) & \lambda_{em}^{298 K} (\textbf{nm})^a & \lambda_{em}^{77 K} (\textbf{nm})^b \end{array}$			Φ _{em} ^c (%)	E _{ox} ^a (V)	HOMO ^d (eV)	HOMO ^e (eV)
2a	237, 293, 360, 399, 464	618, 662(sh)	621, 666(sh)	39.9	0.87	-5.67	-4.91
2b	234, 288, 342, 397, 477	628, 670(sh)	630, 680(sh)	51.9	1.05	-5.85	-5.20

^aData were collected from degassed CH_2Cl_2 solutions at 298 K. ^bData were collected from degassed CH_2Cl_2 solutions at 77 K. ^cfac-Ir(ppy)₃ as referenced standard (0.4).⁴¹ ^dHOMO energies are deduced from the equation HOMO = – (E_{ox} + 4.8 eV). ^eObtained from theoretical calculations.

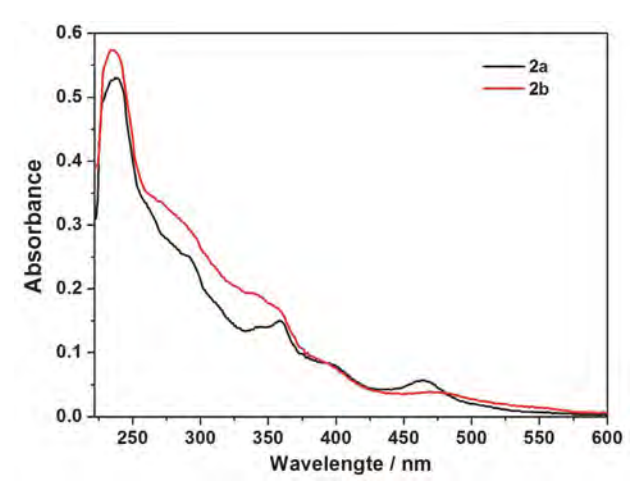


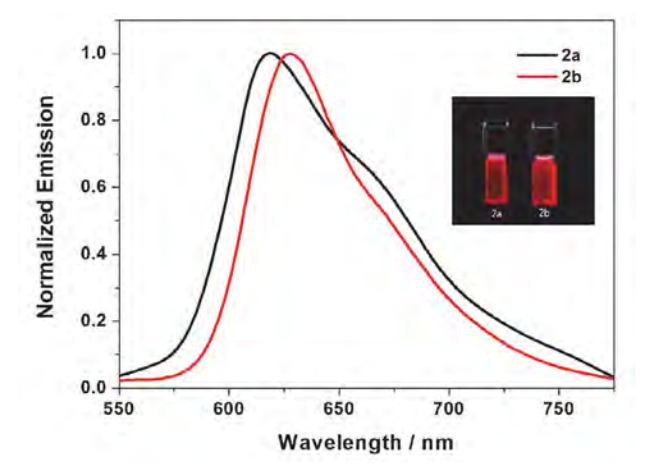
Fig. 2. Electronic absorption spectra of ${\bf 2a{\text -}2b}$ in ${\rm CH_2Cl_2}$ at room temperature.

with **2a**, the lowest lying absorption band for complex **2b** is slightly red-shifted, presumably depending on the different N-heterocycle ancillary ligands. This assumption will be proved by electrochemistry analyses and DFT calculations.

3. 4. Emission Properties

Photoluminescence (PL) emission spectra of complexes 2a-2b in degassed CH₂Cl₂ solution at 298 K and 77 K are displayed in Fig. 3 and the corresponding data are also summarized in Table 4. In both cases, the emission spectra show the broad emission maxima at 618-628 nm together with a shoulder peak at 662-670 nm, which makes them red emitters. For their emission, the excited states are attributed to a mixing of ³MLCT and ³LC state. ^{39,40} As seen, the emission band of 2b is also red-shifted relative to 2a, in good agreement with absorption analyses. When the temperature is decreased to 77 K, the emission maxima of 2a-2b are a slightly bathochromic shift compared to the 298 K spectra, as reported in our earlier literature. 13 Clearly, these complexes exhibit vibronic bands at 77 K, which again demonstrate that their emission states are hybrid states with ³MLCT and ³LC characters.

Phosphorescence relative quantum yields ($\Phi_{\rm em}$) of **2a** and **2b** in dichloromethane solution at room temperature were measured to be 39.9 and 51.9% (Table 4) respectively,



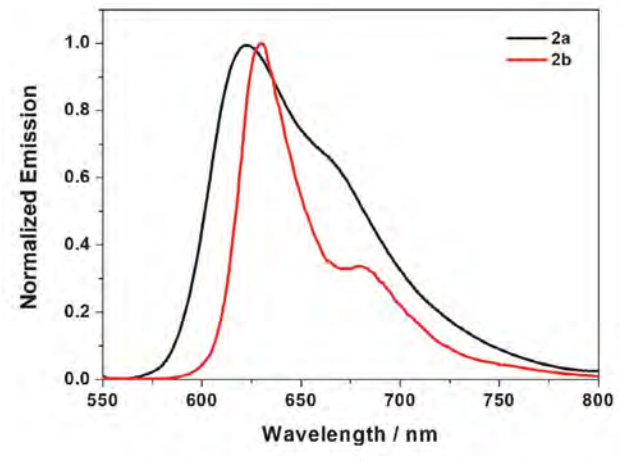


Fig. 3. Normalized emission spectra of 2a-2b in degassed CH_2Cl_2 solution at 298 K (left) and 77 K (right).

using typical phosphorescent fac-Ir(ppy)₃ as a standard $(\Phi_{\rm em}=0.40)$.⁴¹ As expected, complexes ${\bf 2a-2b}$ have relatively high quantum yields, due to the effect of fluorinated backbones.^{42,43} Specially, the quantum efficiency of ${\bf 2b}$ is larger than that of ${\bf 2a}$. The results manifest nitrogen atoms at 1,2-positions are more effective than 2,8-positions.

3. 5. Theoretical Calculations

Density functional theory (DFT) and time-dependent DFT (TDDFT) calculations have been performed for complexes 2a-2b to gain insights into the lowest-energy

electronic transitions. The most representative molecular frontier orbital diagrams for these complexes are presented in Fig. 4. The calculated spin-allowed electronic transitions are provided in Table 5, as well as compared with the experimental absorption spectra data. The electron density distributions are summarized in Table S1.

As shown in Fig. 4, the HOMOs of these complexes are mainly localized on the metal center and the phenyl ring of ancillary ligands, whereas the LUMOs are primarily dominated on the whole C^N ligands. Besides, the HOMO-1 of complex 2a is located on iridium ion, the cyclometalated ligands and a little part of the ancillary ligands. The theory calculations of DFT reveal that the lowest-energy spin-allowed transitions of 2a-2b are derived from HOMO/HOMO-1 \rightarrow LUMO and HOMO \rightarrow LUMO transitions (Table 5), consequently assigned to metal-to-ligand charge transfer transitions and ligand-to-ligand $\pi-\pi^*$ transitions. These calculations support the photophysical properties discussed above.

To gain the origins of emission for complexes 2a-2b, we also employed the DFT calculations to investigate the triplet excited-state characters. The results of the TD-DFT calculations for the triplet states are listed in Table 6. For both the studied complexes, the two lowest lying triplet states (T_1 and T_2) are predominantly from HOMO \rightarrow LU-MO, HOMO-1 \rightarrow LUMO, HOMO-1 \rightarrow LUMO+1, HO-MO-1 \rightarrow LUMO+1 HOMO-2 \rightarrow LUMO and HOMO-3 \rightarrow LU-MO transitions. According to electron density distributions in Table S1, the HOMOs are mainly localized at the ancillary ligands, while LUMOs/LUMO+1s at the C^N ligands. The HOMO-1s/HOMO-2s/HOMO-3s are composed of Ir d-orbital, C^N ligands and ancillary ligands. Thereby, both of the two lowest-lying triplet states (T_1 and T_2) have a mixed 3 MLCT/ 3 LLCT/ 3 LC character for the two

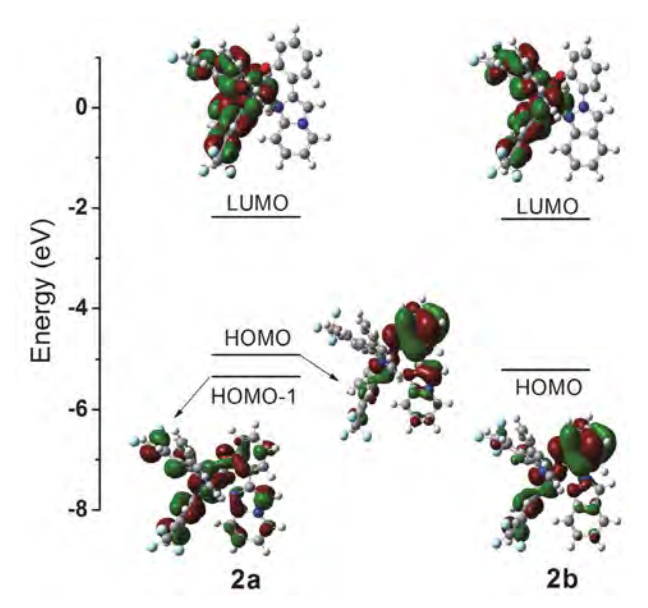


Fig. 4. The frontier molecular orbital diagrams of complexes 2a-2b from DFT calculations.

complexes, except T₂ of **2a** with limited ³MLCT contribution. The lowest-lying triplet states of **2a** have similar transition paths with those of **2b**, indicating that the different positions of N atoms on ancillary ligands have no obvious effect on emissive behavior.

3. 6. Electrochemical Properties

The electrochemical behaviors of both iridium complexes were investigated by cyclic voltammetry and the electrochemical waves are shown in Fig. 5. The respective electrochemical data and estimated HOMO energy levels are also reported in Table 4. Complexes 2a-2b exhibit a

Table 5. Major configuration, transition characters, oscillator strength and calculated/experimental absorption wavelengths for 2a-2b.

Comple	ex	Major Configuration	Transition	Character	Oscillation Strength	Calcd (nm)	Exptl (nm)
2a	S_1	HOMO → LUMO (93%)	LLCT	$\pi_{imdzppo} \Rightarrow \pi^*_{tfmpiq}$	0.0308	576	464
	S_2	HOMO-1 → LUMO (94 %)	MLCT/LC	$d\pi_{Ir}/\pi_{tfmpiq} \rightarrow \pi^{*}_{tfmpiq}$	0.0401	501	
2b	S_1	HOMO → LUMO (91%)	MLCT/LLCT	$d\pi_{Ir}/\pi_{idzpo} \rightarrow \pi^*_{tfmpiq}$	0.0641	526	477

Table 6. Contribution of triplet transitions and transition characters for complexes 2a-2b.

Comple	ex	Major Configuration	Transition	Character
2a	T_1	HOMO → LUMO (57 %) HOMO-1 → LUMO (26 %)	³ LLCT ³ MLCT/ ³ LC	$\begin{array}{c} \pi_{idzpo} \!$
	T_2	HOMO → LUMO+1 (61%) HOMO → LUMO (15%)	³ LLCT	$\pi_{\rm idzpo} \rightarrow \pi^{\circ}_{\rm tfmpiq}$
2b	T_1	HOMO → LUMO (31 %)	³ MLCT/ ³ LLCT	$ \pi_{\text{idzpo}} \rightarrow \pi^{*}_{\text{tfmpiq}} $ $ d\pi_{\text{Ir}}/\pi_{\text{imdzppo}} \rightarrow \pi^{*}_{\text{tfmpiq}} $
	T_2	HOMO-1 → LUMO (30%) HOMO-1 → LUMO+1 (25%) HOMO-2 → LUMO (14%)	³ MLCT/ ³ LLCT/ ³ LC ³ MLCT/ ³ LLCT/ ³ LC ³ MLCT/ ³ LLCT/ ³ LC	$\begin{array}{l} d\pi_{\rm Ir}/\pi_{\rm tfmpiq}/\pi_{\rm imdzppo} \!$
		HOMO-3 → LUMO (12%)	³ MLCT/ ³ LLCT/ ³ LC	$d\pi_{Ir}/\pi_{tfmpiq}/\pi_{imdzppo} \rightarrow \pi^*_{tfmpiq}$

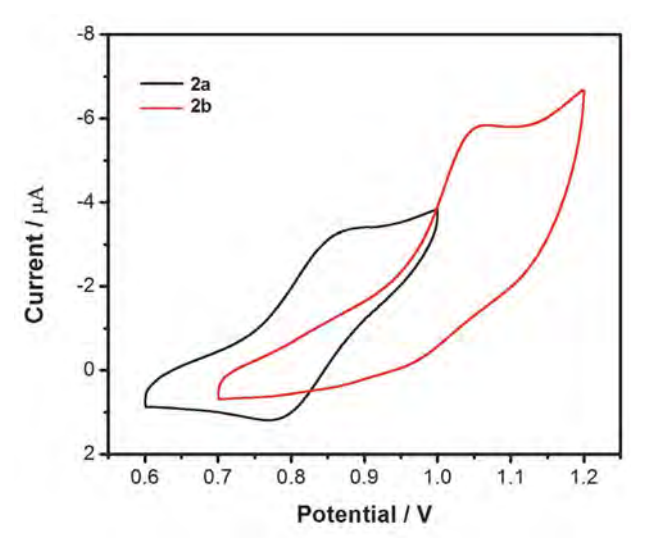


Fig. 5. Cyclic voltammograms for complexes 2a-2b in CH_2Cl_2 solution containing $n-Bu_4NClO_4$ (0.1 M) at a sweep rate of 100 mV/s.

quasi-reversible/irreversible oxidation peak (E_{ox}) at 0.87 and 1.05 V, respectively. As inferred from DFT calculations (Table S1), the HOMOs are mainly localized on the Ir ion (13.88 % for **2a**, 24.74 % for **2b**) and ancillary ligands (75.74 % for **2a**, 58.06 % for **2b**). Therefore, the oxidation is assigned to Ir(III) to Ir(IV) with some contribution from ancillary ligand. On the basis of the potentials of the oxidation, the HOMO energy is deduced by the equation $E_{\rm HOMO} = -(E_{\rm ox} + 4.8 \text{ eV})$, ⁴⁴ and the trend is quite consistent with theoretical calculation values (Table 4). As it can be seen from these results, through changes of nitrogen atoms from 2,8-positions to 1,2-positions, the HOMO level of **2b** is more stable and the oxidation process is more difficult than those of analogue **2a**.

4. Conclusions

In conclusion, two red-emitting iridium(III) complexes (2a-2b) equipped with tfmpiq cyclometalated ligand and imdzppo/idzpo ancillary ligand, have been successfully synthesized and characterized. Their photophysical properties, electrochemical behaviors and theoretical calculations have been systematically studied. The calculated absorptions of the two complexes 2a-2b are in full agreement with the experimental data, which indicate that the lowest lying absorptions are assigned to MLCT/LLCT transitions. Both Ir(III) complexes exhibit red phosphorescence in dichloromethane solution at 298 K and at 77 K, and the lowest lying triplet excited states have a mixed ³MLCT/³LLCT/³LC character. By changing the positions of N atoms in the ancillary ligand, we have confirmed complex 2b had a further red-shift relative to 2a in the emission spectra. These research results will facilitate the design of new piq-based ligands for red-emitting iridium complexes.

5. Acknowledgments

This work was supported by the Natural Science Foundation of Hainan Province (218QN236, 219MS043, 217115), the 2018 National Innovation Experiment Program for University Students and Program for Innovative Research Team in University (IRT-16R19).

References

- Y. S. Li, J. L. Liao, K. T. Lin, W. Y. Hung, S. H. Liu, G. H. Lee, P. T. Chou, Y. Chi, *Inorg. Chem.* 2017, 56, 10054–10060.
 DOI:10.1021/acs.inorgchem.7b01583
- R. D. Costa, E. Orti, H. J. Bolink, F. Monti, G. Accorsi, N. Armaroli, *Angew. Chem. Int. Ed.* 2012, *51*, 8178–8211.
 DOI:10.1002/anie.201201471
- B. W. D'Andrade, S. R. Forrest, Adv. Mater. 2004, 16, 1585–1595. DOI:10.1002/adma.200400684
- 4. C. H. Fan, P. Sun, T. H. Su, C. H. Cheng, *Adv. Mater.* **2011**, *23*, 2981–2985. **DOI:**10.1002/adma.201100610
- C. H. Chen, L. C. Hsu, P. Rajamalli, Y. W. Chang, F. I. Wu, C. Y. Liao, M. J. Chiu, P. Y. Chou, M. J. Huang, L. K. Chu, C. H. Cheng, J. Mater. Chem. C 2014, 2, 6183–6191.
 DOI:10.1039/C4TC00523F
- J. Qiao, L. Duan, L. T. Tang, L. He, L. D. Wang, Y. Qiu, J. Mater. Chem. 2009, 19, 6573–6580. DOI:10.1039/b906675f
- S. C. Lo, E. B. Namdas, P. L. Burn, I. D. W. Samuel, *Macromolecules* 2003, 36, 9721–9730. DOI:10.1021/ma030383w
- 8. C. T. Chen, *Chem. Mater.* **2004**, *16*, 4389–4400. **DOI**:10.1021/cm049679m
- A. Tsuboyama, H. Iwawaki, M. Furugori, T. Mukaide, J. Kamatani, S. Igawa, T. Moriyama, S. Miura, T. Takiguchi, S. Okada, M. Hoshino, K. Ueno, *J. Am. Chem. Soc.* 2003, 125, 12971–12979. DOI:10.1021/ja034732d
- Y. J. Su, H. L. Huang, C. L. Li, C. H. Chien, Y. T. Tao, P. T. Chou, S. Datta, R. S. Liu, *Adv. Mater.* 2003, *15*, 884–888.
 DOI:10.1002/adma.200304630
- C. L. Li, Y. J. Su, Y. T. Tao, P. T. Chou, C. H. Chien, C. C. Cheng, R. S. Liu, *Adv. Funct. Mater.* **2005**, *15*, 387–395.
 DOI:10.1002/adfm.200305100
- S. Huo, J. C. Deaton, M. Rajeswaran, W. C. Lenhart, *Inorg. Chem.* 2006, 45, 3155–3157. DOI:10.1021/ic060089v
- G. N. Li, S. B. Dou, T. Zheng, X. Q. Chen, X. H. Yang, S. Wang,
 W. Sun, G. Y. Chen, Z. R. Mo, Z. G. Niu, *Organometallics* 2018, 37, 78–86. DOI:10.1021/acs.organomet.7b00740
- F. Babudri, G. M. Farinola, F. Naso, R. Ragni, Chem. Commun. 2007, 0, 1003–1022. DOI:10.1039/B611336B
- K. H. Fang, L. L. Wu, Y. T. Huang, C. H. Yang, I. W. Sun, *Inorg. Chim. Acta* 2006, 359, 441–450.
 DOI:10.1016/j.ica.2005.10.003
- S. Zhang, L. S. Xue, C. Wu, Y. X. Zheng, J. L. Zuo, Chin. J. Inorg. Chem. 2014, 30, 134–141.
 DOI: 10.11862/CJIC.2014.073
- Z. G. Niu, D. Liu, J. Zuo, Y. Zou, J. M. Yang, Y. H. Su, Y. D. Yang, G. N. Li, *Inorg. Chem. Commun.* 2014, 43, 146–150.
 DOI:10.1016/j.inoche.2014.02.031

- Y. Tamura, Y. Hisamatsu, S. Kumar, T. Itoh, K. Sato, R. Kuroda, S. Aoki, *Inorg. Chem.* 2017, 56, 812–833.
 DOI:10.1021/acs.inorgchem.6b02270
- G. N. Li, Y. Zou, Y. D. Yang, J. Liang, F. Cui, T. Zheng, H. Xie,
 Z. G. Niu, J. Fluoresc. 2014, 24, 1545–1552.
 DOI:10.1007/s10895-014-1443-7
- H. H. Rhoa, Y. H. Parkb, Y. H. Leeb, N. G. Parkc, Y. Had, Y. S. Kimd, *Mol. Cryst. Liq. Cryst.* 2006, 444, 145–155.
 DOI:10.1080/15421400500365326
- A. J. Stasyuk, M. Banasiewicz, M. K. Cyrański, D. T. Gryko, J. Org. Chem. 2012, 77, 5552–5558. DOI:10.1021/jo300643w
- T. V. Nykaza, T. S. Harrison, A. Ghosh, R. A. Putnik, A. T. Radosevich, *J. Am. Chem. Soc.* 2017, *139*, 6839–6842.
 DOI:10.1021/jacs.7b03260
- CrysAlisPro Version 1.171.36.21; Agilent Technologies Inc., Santa Clara, CA, USA, 2012.
- 24. G. M. Sheldrick, *Acta Cryst. A* **2008**, *64*, 112–122. **DOI:**10.1107/S0108767307043930
- O. V. Dolomanov, L. J. Bourhis, R. J. Gildea, J. A. K. Howard, H. Puschmann, J. Appl. Cryst. 2009, 42, 339–341.
 DOI:10.1107/S0021889808042726
- 26. M. J. Frisch, G. W. Trucks, H. B. Schlegel, G. E. Scuseria, M. A. Robb, J. R. Cheeseman, J. A. Montgomery, T. Vreven, K. N. Kudin, J. C. Burant, J. M. Millam, S. S. Iyengar, J. Tomasi, V. Barone, B. Mennucci, M. Cossi, G. Scalmani, N. Rega, G. A. Petersson, H. Nakatsuji, M. Hada, M. Ehara, K. Toyota, R. Fukuda, J. Hasegawa, M. Ishida, T. Nakajima, Y. Honda, O. Kitao, H. Nakai, M. Klene, X. Li, J. E. Knox, H. P. Hratchian, J. B. Cross, C. Adamo, J. Jaramillo, R. Gomperts, R. E. Stratmann, O. Yazyev, A. J. Austin, R. Cammi, C. Pomelli, J. W. Ochterski, P. Y. Ayala, K. Morokuma, G. A. Voth, P. Salvador, J. J. Dannenberg, V. G. Zakrzewski, S. Dapprich, A. D. Daniels, M. C. Strain, O. Farkas, D. K. Malick, A. D. Rabuck, K. Raghavachari, J. B. Foresman, J. V. Ortiz, Q. Cui, A. G. Baboul, S. Clifford, J. Cioslowski, B. B. Stefanov, G. Liu, A. Liashenko, P. Piskorz, I. Komaromi, R. L. Martin, D. J. Fox, T. Keith, M. A. Al-Laham, C. Y. Peng, A. Nanayakkara, M. Challacombe, P. M. W. Gill, B. Johnson, W. Chen, M. W. Wong, C. Gonzalez, J. A. Pople, Gaussian 09, Revision A.01, Gaussian, Inc. Wallingford, CT, 2009.
- C. Lee, W. Yang, R. G. Parr, *Phys. Rev. B* 1988, *37*, 785–789.
 DOI:10.1103/PhysRevB.37.785
- B. Miehlich, A. Savin, H. Stoll, H. Preuss, Chem. Phys. Lett. 1989, 157, 200–206. DOI:10.1016/0009-2614(89)87234-3

- 29. A. D. Becke, *J. Chem. Phys.* **1993**, 98, 5648–5652. **DOI:**10.1063/1.464913
- M. Cossi, N. Rega, G. Scalmani, V. Barone, *J. Comput. Chem.* 2003, 24, 669–681. DOI:10.1002/jcc.10189
- J. Tomasi, B. Mennucci, R. Cammi, Chem. Rev. 2005, 105, 2999–3093. DOI:10.1021/cr9904009 9
- S. Lamansky, P. Djurovich, D. Murphy, F. Abdel-Razzaq, R. Kwong, I. Tsyba, M. Bortz, B. Mui, R. Bau, *Inorg. Chem.* 2001, 40, 1704–1711. DOI:10.1021/ic0008969
- A. B. Tamayo, B. D. Alleyne, P. I. Djurovich, S. Lamansky, I. Tsyba, N. N. Ho, R. Bau, M. E. Thompson, *J. Am. Chem. Soc.* 2003, 125, 7377–7387. DOI:10.1021/ja034537z
- 34. K. K. W. Lo, C. K. Chung, N. Y. Zhu, *Chem. Eur. J.* **2003**, 9, 475–483. **DOI:**10.1002/chem.200390050
- S. Lamansky, P. Djurovich, D. Murphy, F. Abdel-Razzaq, R. Kwong, I. Tsyba, M. Bortz, B. Mmui, R. Bau, M. E. Thompson, *Inorg. Chem.* 2001, *40*, 1704–1711.
 DOI:10.1021/ic0008969
- C. H. Yang, J. Beltran, V. Lemaur, J. Cornil, D. Hartmann, W. Sarfert, R. Fröhlich, C. Bizzarri, C. L. De, *Inorg. Chem.* 2010, 49, 9891–9901. DOI:10.1021/ic1009253
- F. Monti, F. Kessler, M. Delgado, J. Frey, F. Bazzanini, G. Accorsi, N. Armaroli, H. J. Bolink, E. Ortí, R. Scopelliti, M. K. Nazeeruddin, E. Baranoff, *Inorg. Chem.* 2013, 52, 10292–10305. DOI:10.1021/ic400600d
- T. Y. Li, X. Liang, L. Zhou, C. Wu, S. Zhang, X. Liu, G. Z. Lu, L.
 Xue, Y. X. Zheng, J. L. Zuo, *Inorg. Chem.* 2015, 54, 161–173.
 DOI:10.1021/ic501949h
- S. Okada, K. Okinaka, H. Iwawaki, M. Furugori, M. Hashimoto, T. Mukaide, J. Kamatani, S. Igawa, A. Tsuboyama, T. Takiguchi, K. Ueno, *Dalton Trans.* 2005, 9, 1583–1590.
 DOI:10.1039/b417058j
- 40. Z. G. Niu, T. Zheng, Y. H. Su, P. J. Wang, X. Y. Li, F. Cui, J. Liang, G. N. Li, New J. Chem. 2015, 39, 6025–6033.
 DOI:10.1039/C5NJ00975H
- 41. K. A. King, P. J. Spellane, R. J. Watts, *J. Am. Chem. Soc.* **1985**, *107*, 1431–1432. **DOI:**10.1021/ja00291a064
- 42. C. L. Ho, W. Y. Wong, Q. Wang, D. Ma, L. Wang, Z. Lin, Adv. Funct. Mater. 2008, 18, 928–937.
 DOI:10.1002/adfm.200701115
- 43. Y. Wang, N. Herron, V. V. Grushin, D. LeCloux, V. Petrov, *Appl. Phys. Lett.* **2001**, *79*, 449. **DOI:**10.1063/1.1384903
- 44. W. Lee, T. H. Kwon, J. Kwon, J. Y. Kim, C. Lee, J. I. Hong, *New J. Chem.* **2011**, *35*, 2557–2563. **DOI**:10.1039/c1nj20446g

Povzetek

Sintetizirali smo dva nova bis-ciklometalirana iridijeva(III) kompleksa s tfmpiq ligandom, [(tfmpiq) $_2$ Ir(imdzppo)] (2a) in [(tfmpiq) $_2$ Ir(idzpo)] (2b) (tfmpiq = 1-(4-(trifluorometil)fenil)izokinolin, imdzppo = 2-(imidazo[1,2-a]piridin-2-il) fenol, idzpo = 2-(2H-indazol-2-il)fenol), in ju okarakterizirali. Določili smo monokristalno strukturo 2b. Določili smo razmerje med strukturo in fotofizikalnimi lastnostmi obeh kompleksov podprto tudi z DFT izračuni. Ir(III) kompleksa emitirata rdečo svetlobo s kvantnim izkoristkom 39.9–51.9 % v degaziranem CH_2Cl_2 pri sobni temperaturi. Emisija izvira iz hibridnega 3 MLCT/ 3 LC vzbujenega stanja. Vsi ti rezultati kažejo, da sta iridijeva(III) kompleksa 2a-2b primerna kot rdeča fosforescentna materiala v OLED.



Except when otherwise noted, articles in this journal are published under the terms and conditions of the Creative Commons Attribution 4.0 International License

@creative commons

Scientific paper

Extraction-Chromogenic Systems for Vanadium(V) Based on Azo Dyes and Xylometazoline Hydrochloride

Danail G. Hristov, Nikolina P. Milcheva and Kiril B. Gavazov*

Department of Chemical Sciences, Medical University of Plovdiv, 120 Buxton Brothers St., Plovdiv 4004, Bulgaria

* Corresponding author: E-mail: kgavazov@abv.bg

Received: 05-06-2019

Abstract

Liquid-liquid extraction-chromogenic systems for vanadium(V) based on xylometazoline hydrochloride (XMZ) and azo derivatives of resorcinol (ADRs) were studied. The following ADRs were used: 4-(2-thiazolylazo)resorcinol (TAR), 5-methyl-4-(2-thiazolylazo)resorcinol (MTAR), and 6-hexyl-4-(2-thiazolylazo)resorcinol (HTAR). Concentration of the reagents, pH of the aqueous medium and shaking time were subjects of optimization experiments. The chloroform-extracted ternary complexes were of composition 1:1:1. The molar absorptivity coefficients (ε_{λ}), absorption maxima (λ), constants of extraction (Log K), and fractions extracted (E%) were found to be $\varepsilon_{553} = 2.50 \times 10^4$ dm³ mol⁻¹ cm⁻¹, Log K = 3.5, and E = 96% (ADR = TAR); $\varepsilon_{550} = 1.88 \times 10^4$ dm³ mol⁻¹ cm⁻¹, Log K = 3.4, and E = 98% (ADR = MTAR); and $\varepsilon_{554} = 2.62 \times 10^4$ dm³ mol⁻¹ cm⁻¹, Log K = 5.0, and E = 99.5% (ADR = HTAR). The Sandell's sensitivities and Beer's law limits were determined as well.

Keywords: 6-Hexyl-4-(2-thiazolylazo)resorcinol; 5-Methyl-4-(2-thiazolylazo)resorcinol; 4-(2-Thiazolylazo)resorcinol; xylometazoline hydrochloride; ion-association; ternary complex

1. Introduction

Vanadium, atomic number 23, is the first in the line of essential trace metals (V – Zn) located in the first transition row of the periodic table. It can exist in a variety of oxidation states (-I, 0, I, II, III, IV, and V), in monomeric, oligomeric and polymeric species, and is the fifth most abundant transition element in the Earth's crust. Vanadium can enter the environment because of natural processes, such as rock weathering, sediment leaching, volcanic activity, aeolian dust, marine aerosols formation, and wild forest fires.^{2,3} At the levels, provided by these processes, it is considered to be health-promoting,4 but it can become toxic in accordance with Paracelsus' principle "the dose makes the poison". Serious health hazards are associated with elevated vanadium concentrations;5-7 they are typically related to V(V), the most toxic^{8,9} and one of the most common vanadium's oxidation states in the earth's surface systems.9,10

Large amounts of V(V) have been released in the biosphere because of industrial growth. The main sources of anthropogenic vanadium are the combustion of fossil fuels (especially oil), mining, processing of ores, production of steel alloys, glass, ceramics, rubber, redox batteries and dyes, application in catalysts for large-scale processes, fertilizing and recycling of domestic waste.^{3,9,11,12} At present, vanadi-

um has the highest anthropogenic enrichment factor of all trace elements in the atmosphere; it ranks fourth in this factor for global rivers (after antimony, cadmium and nickel).¹³

Many organic reagents have been applied for vanadium preconcentration and determination. 8,10,14-16 Among the most promising and widely used are the azo dyes. 8,15-24 Azo derivatives of resorcinol (ADR), such as 4-(2-pyridylazo)resorcinol (PAR), 24,25 4-(2-thiazolylazo)resorcinol (TAR), 26,27 and 5-methyl-4-(2-thiazolylazo)resorcinol (MTAR)^{28,29} form ternary complexes it the presence of cationic ion-association reagents (CIAR). Their composition, stability, and extraction-chromogenic characteristics depend on the particular pair of reagents. The composition, for example, can be 1:1:1,26,28 2:2:2,29 1:2:325 or 1:2:130 (V:ADR:CIAR). The differences are explained by the possibility of interactions (H-bonding) between ADR and CIAR or between CIAR and the VO₂ group,²⁹ which is generally stable^{26,31,32} but under certain conditions is prone to lose an oxygen atom. Moreover, V(V) is stereochemically flexible; 33-35 the same is true for ADRs which have many conformers³⁶ and can be tridentate, bidentate, and even monodentate ligands³⁷ depending on the environment.

Xylometazoline hydrochloride (XMZ) is a substance widely used in the pharmaceutical industry and included in WHO Model List of Essential Medicines.³⁸ From a

Table 1. Reagents in the present study.

Formula	Name	CAS number	Molar mass
H ₃ C CH ₃ · HCI	Xylometazoline hydrochloride (XMZ)	1218-35-5	280.84
S N=N OH	4-(2-thiazolylazo)resorcinol (TAR)	2246-46-0	221.24
SNN OH	5-methyl-4-(2-thiazolylazo)resorcinol (MTAR)	37422-56-3	235.26
HO N=N S	6-hexyl-4-(2-thiazolylazo)resorcinol (HTAR)	14383-66-5	305.402

chemical point of view, it can be classified as a cationic ion-association reagent. 39,40 Various extraction-chromogenic systems containing transition metals, XMZ and PAR have been described in the literature. $^{40-44}$ However, to the best of our knowledge, there are no reports involving both XMZ and thiazolylazo reagents. In the present paper, we discuss three liquid-liquid extraction-chromogenic systems containing V(V), XMZ and thiazolylazo dye {TAR, MTAR or 6-hexyl-4-(2-thiazolylazo)resorcinol (HTAR)}. In contrast to TAR and MTAR, which have been the subject of many experimental and theoretical studies, 26,31,36,45 HTAR is unexplored reagent. According to the manufacturer, this reagent is part of a collection of rare and unique chemicals. Its formula, along with the formulae of the other reagents, is shown in Table 1.

2. Experimental

2. 1. Reagents and Apparatus

V(V) solution (2 × 10⁻⁴ mol dm⁻³) was prepared from NH₄VO₃ (puriss. p.a., VEB Laborchemie Apolda, Germany). XMZ and ADRs (TAR, 97%; MTAR, 95%; and HTAR) were purchased from Merck. XMZ was dissolved in water; the obtained solutions (2 × 10⁻² and 2 × 10⁻⁴ mol dm⁻³) were kept in dark-glass vessels. ^{43,44} Aqueous solutions of ADRs (2.0 × 10⁻³ mol dm⁻³) were prepared in the presence of KOH (1–2 pellets per 100 cm³). ²⁸ The acidity

of the aqueous phase was set by ammonium acetate buffer (prepared by mixing 2.0 mol dm⁻³ solutions of CH₃COOH and ammonia). The pH of the buffer solutions was measured using a WTW InoLab 7110 (Germany) instrument with an accuracy of ± 0.001 pH units. Absorbance was read using a Ultrospec3300 pro UV-Vis spectrophotometers (UK), equipped with 1-cm path-length glass cuvettes. Distilled water and additionally distilled commercial chloroform (p. a.) were used throughout the work.

2. 2. General Procedure

Solutions of V(V), buffer (pH 3.8–6.8), ADR and XMZ were placed into a separatory funnel. The resulting mixture was diluted with water to a total volume of 10 cm^3 . Then 10 cm^3 of chloroform were added and the funnel was shaken for a fixed time interval (up to 10 min). After a short wait for phase separation (5–10 seconds), a portion of the chloroform extract was transferred through a filter paper into the cuvette. The absorbance was measured against chloroform or simultaneously prepared blank (containing all the reagents except for vanadium).

2. 3. Determination of the Distribution Ratios and Fractions Extracted

The distribution ratios D were calculated by the formula $D = A_1/(A_3 - A_1)$, where A_1 is the absorbance ob-

Table 2. Optimum operating conditions.

Extraction system	λ _{max} , nm	pН	c _{ADR} , mol dm ⁻³	c _{XMZ} , mol dm ⁻³	Extraction time, min
V(V) – TAR – XMZ	553	4.7	3.0×10^{-4}	6.0×10^{-3}	1.0
V(V) - MTAR - XMZ	550	4.7	4.0×10^{-4}	8.0×10^{-3}	1.5
V(V) – HTAR – XMZ	554	5.1	2.0×10^{-4}	4.0×10^{-3}	8.0

tained after a single extraction (under the optimal extraction conditions, Table 2), and A_3 is the absorbance obtained after a triple extraction under the same conditions. The final volume in both cases (single extraction and triple extraction) was 25 cm³.^{28,29} The fractions extracted were calculated by the formula $E\% = 100 \times D / (D+1)$.

3. Results and Discussion

3. 1. Extraction-Spectrophotometric Optimization

In a slightly acidic aqueous-ethanolic medium (pH 4.5-5.5), TAR and MTAR react with V(V)^{29,46} to give red-colored anionic species. In the presence of CIAR, such as tetraphenylarsonium chloride, triphenylmethylarsonium iodide, tetraphenylphosphonium chloride, and tetrazolium salts^{27,29,47,48} and replacing ethanol with a water-immiscible solvent (e. g., chloroform), ternary ion-association complexes are formed. Preliminary investigations on the V(V) - ADR - XMZ - water - chloroform systems (where ADR = TAR, MTAR or HTAR) confirmed our expectations for hydrophobic, intensely colored and well chloroform-extractable complexes. Spectra of these complexes are shown in Fig. 1. The absorption maxima (λ_{max}) in chloroform are located at 552-553 nm (TAR complex), 549-550 nm (MTAR complex) and 553-554 nm (HTAR complex). One can judge that HTAR (spectrum 3) and TAR (spectrum 1) ensure higher molar absorptivity than MTAR (spectrum 2). The blank at λ_{max} is the lowest when ADR = TAR (spectrum 1') and the highest when ADR = MTAR (spectrum 2'). The latter, however, is significantly lower than the blank for the similar system,²⁸

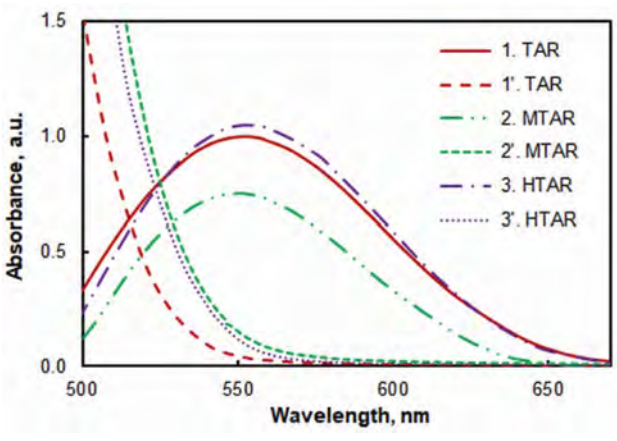


Figure 1. Absorption spectra in chloroform of the V(V) – ADR – XMZ complexes against blanks (1–3; $c_{\text{V(V)}}=4\times10^{-5}$ mol dm⁻³) and blanks (ADR – XMZ) against chloroform (1' – 3'). (1, 1') $c_{\text{TAR}}=3\times10^{-4}$ mol dm⁻³, $c_{\text{XMZ}}=6\times10^{-3}$ mol dm⁻³, pH 4.7, extraction time t = 1 min; (2, 2') $c_{\text{MTAR}}=4\times10^{-4}$ mol dm⁻³, $c_{\text{XMZ}}=8\times10^{-3}$ mol dm⁻³, pH 4.7, extraction time t = 2 min; (3, 3') $c_{\text{HTAR}}=2\times10^{-4}$ mol dm⁻³, $c_{\text{XMZ}}=4\times10^{-3}$ mol dm⁻³, $c_{\text{XMZ}}=4\times10^{-3}$ mol dm⁻³, pH 5.1, extraction time t = 8 min;

containing Aliquat 336 instead of XMZ and isobutanol instead of chloroform.

The effect of pH of the aqueous phase on the complex formation and extraction is shown in Fig. 2. The absorbance is maximal over the broadest pH range (4.1–5.6) for ADR = TAR (curve 1). The left part of this curve resembles the left part of the curve with MTAR (curve 2). Further experiments with TAR and MTAR were performed at pH 4.7. The optimal pH for the system with HTAR appears to be 5.1; the absorbance in this case abruptly decreases at pH > 5.6 (curve 3). In all experiments ammonium acetate buffer (1 cm^3) was used; it exhibits high buffering capacity at the optimal pH values.⁴⁹

The effect of ADR and XMZ concentrations on the absorbance is shown in Fig. 3 and Fig. 4 respectively. The selected optimal concentrations are shown in Table 2. Maximal absorbance is achieved easily (with the lowest re-

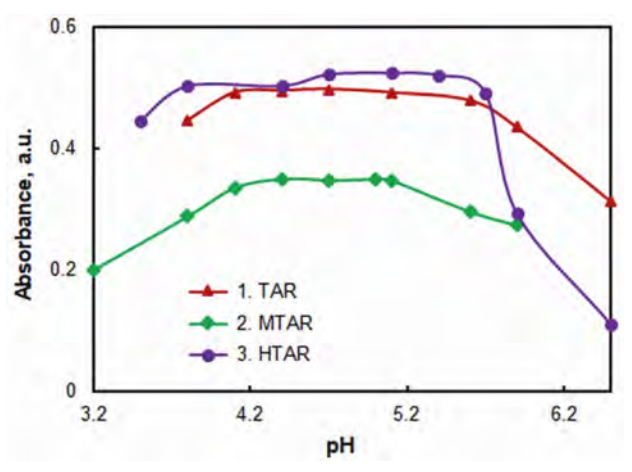


Figure 2. Absorbance of the V(V) – ADR – XMZ complexes vs pH of the aqueous phase, $c_{\rm V}=2\times10^{-5}$ mol dm⁻³. (1) $c_{\rm TAR}=3\times10^{-4}$ mol dm⁻³, $c_{\rm XMZ}=6\times10^{-3}$ mol dm⁻³, extraction time t = 1 min; (2) $c_{\rm MTAR}=4\times10^{-4}$ mol dm⁻³, $c_{\rm XMZ}=8\times10^{-3}$ mol dm⁻³, extraction time t = 2 min; (3) $c_{\rm HTAR}=2\times10^{-4}$ mol dm⁻³, $c_{\rm XMZ}=4\times10^{-3}$ mol dm⁻³, extraction time t = 8 min;

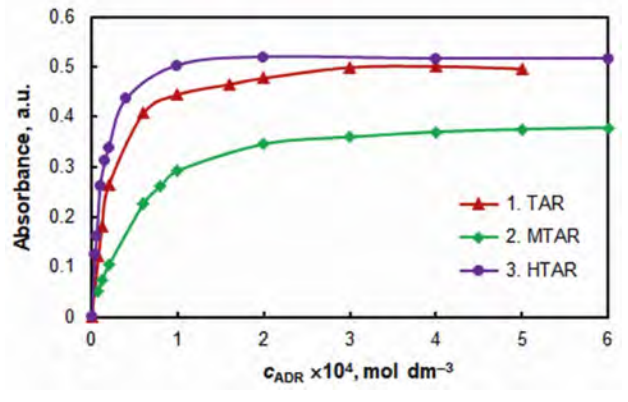


Figure 3. Effect of ADR concentration on the absorbance, $c_{\rm V} = 2 \times 10^{-5}$ mol dm⁻³ (1) $c_{\rm XMZ} = 6 \times 10^{-3}$ mol dm⁻³, pH 4.7, extraction time t = 1 min; (2) $c_{\rm XMZ} = 8 \times 10^{-3}$ mol dm⁻³, pH 4.7, extraction time t = 2 min; (3) $c_{\rm XMZ} = 4 \times 10^{-3}$ mol dm⁻³, pH 5.1, extraction time t = 8 min.

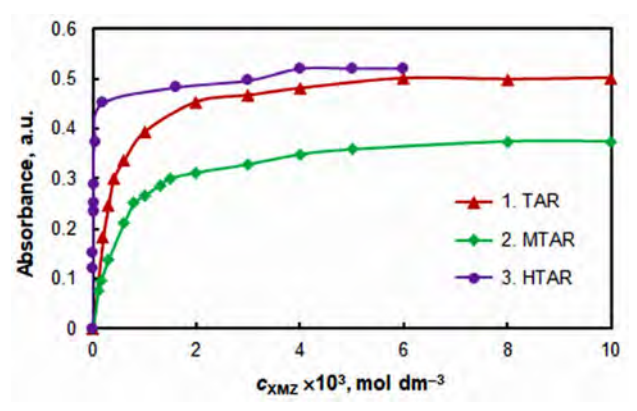


Figure 4. Effect of XMZ concentration on the absorbance, $c_{\rm V}=2\times 10^{-5}$ mol dm⁻³ (1) $c_{\rm TAR}=3\times 10^{-4}$ mol dm⁻³, pH 4.7, extraction time t = 1 min; (2) $c_{\rm MTAR}=4\times 10^{-4}$ mol dm⁻³, pH 4.7, extraction time t = 2 min; (3) $c_{\rm HTAR}=2\times 10^{-4}$ mol dm⁻³, pH 5.1, extraction time t = 8 min.

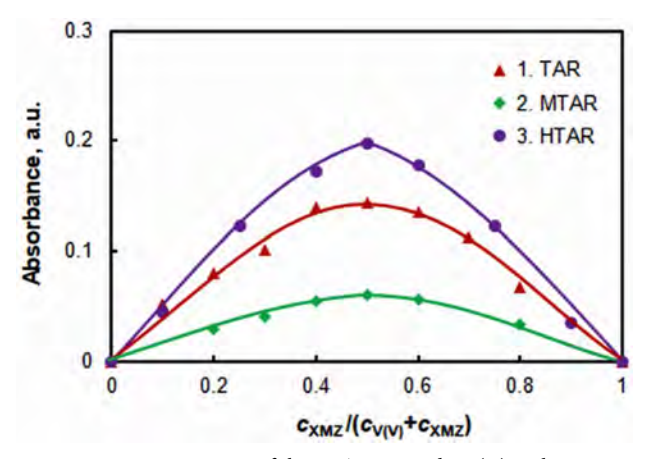


Figure 5. Determination of the XMZ-to-vanadium(V) molar ratio by the Job's method of continuous variations, $c_{\rm XMZ}+c_{\rm V(V)}=1.0\times10^{-4}~{\rm mol~dm^{-3}}$. (1) $c_{\rm TAR}=3\times10^{-4}~{\rm mol~dm^{-3}}$, pH 4.7, extraction time t = 1 min; (2) $c_{\rm MTAR}=4\times10^{-4}~{\rm mol~dm^{-3}}$, pH 4.7, extraction time t = 1.5 min; (3) $c_{\rm HTAR}=2\times10^{-4}~{\rm mol~dm^{-3}}$, pH 5.1, extraction time t = 8 min.

agents concentrations) for the system with HTAR (curves 3 in Figs. 3 and 4). However, the complex with this reagent is extracted most slowly (Table 2). The time required for shaking in this case (8 min) is comparable to that recommended when using tetraphenylphosphonium or tetraphenylarsonium chloride (10 min).⁴⁷

3. 2. Molar Ratios, Composition and Stability

The molar ADR-to-V(V) and XMZ-to-V(V) ratios were determined by different methods from the experimental results presented in Figs. 3–5. The following methods were used: the mobile equilibrium method,⁵⁰ the straight-line method of Asmus,⁵¹ the molar ratio meth-

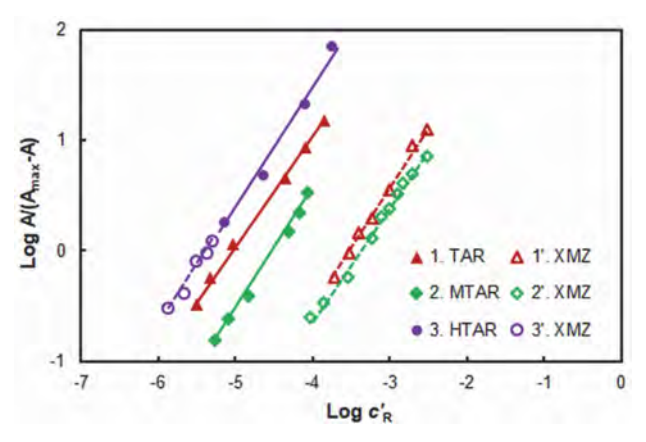


Figure 6. Straight lines obtained by the mobile equilibrium method for ADR-to-V(V) (lines 1–3) and XMZ-to-V(V) (lines 1'–3'). The experimental conditions are given in Fig. 3 and Fig. 4, respectively. Straight lines equations: (1) y=0.98x+4.95, $R^2=0.9984$; (1') y=1.13x+3.97, $R^2=0.9967$; (2) y=1.09x+4.90, $R^2=0.9943$; (2') y=1.01x+3.42, $R^2=0.9940$; (3) y=1.13x+6.01, $R^2=0.9840$; (3') y=1.07x+5.74, $R^2=0.9637$.

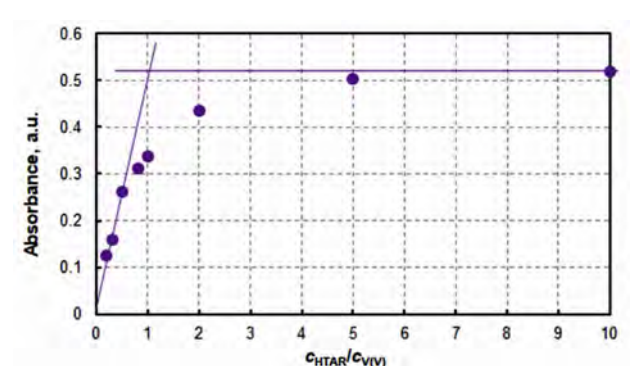


Figure 7. Application of the molar ratio method for the determination of the HTAR-to-V(V) molar ratio. The experimental conditions are given in Fig. 3, line 3.

Table 3. Molar ratios in the ternary V(V) – TAR – XMZ complexes obtained by different methods

Molar ratio	Mobile equilibrium method	Asmus' method	Job's method	Molar ratio method
TAR: V	1:1	1:1	_	Not applicable
MTAR: V	1:1	1:1	_	Not applicable
HTAR: V	1:1	1:1	_	1:1
XMZ : V (V - TAR - XMZ)	1:1	1:1	1:1	Not applicable
XMZ : V (V - MTAR - XMZ)	1:1	1:1	1:1	Not applicable
XMZ : V (V– HTAR – XMZ)	1:1	1:1	1:1	1:1

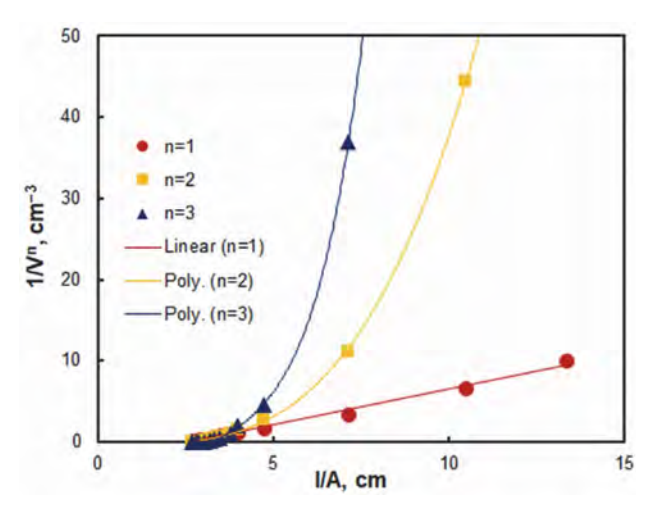


Figure 8. Application of the straight-line method of Asmus for the determination of the XMZ-to-V(V) molar ratio in the extraction system containing MTAR. The experimental conditions are given in Fig. 4, line 2.

od,⁵² and the Job's method of continuous variations.⁵³ As can be concluded from Table 3, and also from Figs. 5–8, all ternary complexes have a composition of 1:1:1. Such a composition was reported for the V(V) ternary complexes with the couples PAR – XMZ,⁴³ TAR – tetraphenylarsonium chloride,⁴⁷ TAR – tetraphenylphosphonium chloride,⁴⁷ and MTAR – Aliquat336.²⁸ The complex involving HTAR appears to be the most stable: the molar ratio method can be applied only to it, Table 3. The isomolar series (Fig. 5) and the straight lines obtained by the mobile equilibrium method (Fig. 6) are also in agreement with this conclusion; curve 3 in Fig. 5 is characterized by a well-defined peak, and curves 3 and 3' in Fig. 6 have the largest y-intercept values.

3.3. Chemical Equations and Extraction Characteristics

The formation and extraction of the ternary complexes can be represented in several successive steps. The first step is the formation of binary V(V) – ADR complexes in aqueous phase (Eq. 1).

$$VO_{3^{-}(aq)} + H_2L_{(aq)} \rightleftharpoons [VO_2L]^{-}_{(aq)} + H_2O$$
 (1)

This equation is based on information concerning the state of $V(V)^{54,55}$ and ADRs (TAR⁵⁶ and MTAR⁵⁷) at the reaction conditions. Although ADRs can stabilize low oxidation state metal centers, 58,59 V(V) is not reduced in their presence. This is evidenced by differences in the spectral characteristics and optimal pH intervals of existence of V(IV)- and V(V)–ARD complexes. 37,46,60 Furthermore, ADRs have been successfully used for V(IV)/V(V) speciation. 8,10,15,61 In this case, the main concern is to prevent the oxidation of V(IV) by the oxygen in air, which starts at ca. pH > 2 and is rather fast in neutral and alkaline medium. 10

TAR and MTAR can be considered as triprotic acids. Deprotonated forms of these ADRs are stable in alkaline media (p K_1 (TAR) = 9.3,^{56,62} p K_1 (MTAR) = 11.8⁵⁷). Monoprotonated forms of TAR and MTAR predominate in neutral and weakly acidic solutions (p K_2 (TAR) = 6.0;^{56,62} p K_2 (MTAR) = 5.6⁵⁷); the proton is bound to the oxygen atom in ortho-position to the azo group. The neutral forms (H₂L) predominate at lower pH values. They attach an additional proton (at the nitrogen atom of the thiazole ring) in a highly acidic environment (p K_{a3} (TAR) = 1.25). There is no information in the literature about the p K_3 (MTAR) nor for the protonation constants of HTAR. However, considering the similar behavior of the blank samples TAR – XMZ, MTAR – XMZ and HTAR – XMZ (Fig. 1), one can assume that these reagents are also in their neutral H₂L forms at the optimum pH.

The next steps, ion-association and extraction can be represented simultaneously by Eq. 2.

$$[VO_{2}L]^{-}_{(aq)} + XMZ^{+}Cl^{-}_{(aq)} \rightleftharpoons (XMZ^{+})[VO_{2}L]_{(org)} + Cl^{-}_{(aq)}$$
 (2)

In it, XMZ and its cation are denoted as XMZ⁺Cl⁻ and XMZ⁺, respectively. The conditional equilibrium constants characterizing Eq. 2 were calculated by two independent methods: the mobile equilibrium method⁵⁰ (Fig. 6, straight lines 1, 2' and 3') and the Likussar-Boltz method.⁶³ The values obtained by these methods are statistically identical (Table 4). The extraction constant K for the system involving HTAR is the highest. The same is true for the other characteristics listed in Table 4, the distribution ratio D and

Table 4. Calculated values of the extraction constants (K), distribution ratios (D) and fractions extracted (E%) at the optimum conditions.

Extraction system	Log K	Log D	E%
V(V) – TAR – XMZ	$3.5 \pm 0.1 (N = 3)^{a}$ $3.52 \pm 0.07 (N = 7)^{b}$	$1.5 \pm 0.3 \text{ (N = 4)}$	$96 \pm 2 \ (N = 4)$
V(V) – MTAR – XMZ	$3.3 \pm 0.1 (N = 3)^{a}$ $3.39 \pm 0.06 (N = 10)^{b}$	$1.6 \pm 0.2 \ (N = 6)$	$98 \pm 1 \ (N = 6)$
V(V) – HTAR – XMZ	$5.0 \pm 0.1 (N = 3)^{a}$ $5.4 \pm 0.5 (N = 5)^{b}$	$2.4 \pm 0.3 \text{ (N = 3)}$	$99.5 \pm 0.3 \text{ (N = 3)}$

^a Calculated by the Likussar-Boltz method ^b Calculated by the molar equilibrium method (Fig. 6)

Analytical characteristics	V(V) - TAR - XMZ	V(V) - MTAR - XMZ	V(V) - HTAR - XMZ
Molar absorptivity (ε), dm ³ mol ⁻¹ cm ⁻¹	2.50×10^{4}	1.88×10^{4}	2.62×10^4
Sandell's sensitivity, ng cm ⁻²	2.0	2.8	2.0
Adherence to Beer's law, μg cm ⁻³	0.03-3.6	0.3-3.1	0.07-5.1
Linear regression equation $y = ax + b$	y = 0.486x + 0.001	y = 0.370x - 0.006	y = 0.513x - 0.013
	$(R^2 = 0.9997; N = 8)$	$(R^2 = 0.9992; N = 8)$	$(R^2 = 0.9991; N = 8)$
Standard deviations of the slope (<i>a</i>) and y-intercept (<i>b</i>)	0.004; 0.007	0.004; 0.007	0.006; 0.017
Limit of detection (LOD), μg cm ⁻³	0.007	0.10	0.019
Limit of quantitation (LOQ), μg cm ⁻³	0.021	0.30	0.058
Standard deviation of the blank	0.001	0.011	0.003

Table 5. Characteristics concerning the application of the ternary complexes for extraction-spectrophotometric determination of vanadium(V).

fraction extracted *E*%. This is related to the highest hydrophobicity and molecular mass (Table 1) of this reagent.

3. 3. Beer's Law and Analytical Characteristics

The dependences between the concentration of V(V) in aqueous phase and absorbance of the extracted ternary complexes were studied under the optimum conditions (Table 2). The linear regression equations and some attendant parameters are listed in Table 5: molar absorptivities, Sandell's sensitivities, Beer's law limits and standard deviation of the slopes, y-intercepts and blanks. The limits of detection (LODs) and quantitation (LOQs) were calculated as 3.3- and 10-times standard deviation of the blank divided by the slope.⁶⁴

4. Conclusions

Ternary well chloroform-extractable complexes are formed in systems containing vanadium(V), thiazolylazo derivatives of resorcinol (TAR, MTAR, HTAR), and xylometazoline hydrochloride. They have a composition of 1:1:1 and can be represented by the general formula (XMZ⁺)[VO₂(ADR)], where ADR is in its doubly deprotonated form (ADR²⁻). The complexes have good extraction-spectrophotometric characteristics. The most extractable (E = 99.5%) and intensively colored ($\varepsilon = 2.62 \times$ 10⁴ dm³ mol⁻¹ cm⁻¹) is the complex of HTAR. The TAR complex is also advantageous. It is formed in the widest pH range, and the absorbance of the blank at λ_{max} for this reagent is the lowest and repeatable. The latter, along with its high molar absorptivity (95% of that for the HTAR complex), provides the lowest LOD and LOQ values. Another advantage of the extraction system containing TAR is the shortest time of extraction.

5. Acknowledgements

This study is part of a project (DPDP-24) within the framework of a scientific competition "Doctoral and

postdoctoral projects-2019" at the Medical University-Plovdiv.

6. References

- 1. A. S. Tracey, G. R. Willsky, E. S. Takeuchi, Vanadium: chemistry, biochemistry, pharmacology and practical applications, CRC press, Boca Raton, **2007**, pp. 1–2.
 - DOI:10.1201/9781420046144
- W.H. Schlesinger, E. M. Klein, A. Vengosh, Proc. Natl. Acad. Sci. 2017, 114, E1109–E11100. DOI:10.1073/pnas.1715500114
- B. Gummow, in: Nriagu, J. O., (Ed.): Encyclopedia of Environmental Health, Elsevier, Burlington, 2011; pp. 628–636.
 DOI:10.1016/B978-0-444-52272-6.00661-9
- K. Marczewski, B. Marczewska, R. Kuzioła, J. Jpn. Soc. Balneol. Climatol. Phys. Med. 2015, 78, 201–208.
 DOI: 10.11390/onki.78.201.
- 5. D. Rehder, ChemTexts **2018**, *4*, 20. **DOI:**10.1007/s40828-018-0074-z
- 6. K. Gruzewska, A. Michno, T. Pawelczyk, H. Bielarczyk, J. Physiol. Pharmacol. **2014**, *65*, 603–611.
- 7. M. R. Awual, M. M. Hasan, A. M. Asiri, M. M. Rahman, J. Mol. Liq. **2019**, *283*, 704–712. **DOI:**10.1016/j.molliq.2019.03.119
- M. J. C. Taylor, J. F. Staden, Analyst 1994, 119, 1263–1276.
 DOI:10.1039/an9941901263
- 9. M. Imtiaz, M. S. Rizwan, S. Xiong, H. Li, M. Ashraf, S. M. Shahzad, M. Shahzad, M. Rizwan, S. Tu, *Environ. Int.* **2015**, *80*, 79–88. **DOI**:10.1016/j.envint.2015.03.018
- K. Pyrzyńska, T. Wierzbicki, Talanta 2004, 64, 823–829.
 DOI:10.1016/j.talanta.2004.05.007
- P. N. Linnik, R. P. Linnik, Russ. J. Gen. Chem. 2018, 88, 2997–3007. DOI:10.1134/S1070363218130273
- 12. H.-I. Kim, G. Moon, I. Choi, J.-Y. Lee, R. K. Jyothi, *J. Clean. Prod.* **2018**, *187*, 449–458. **DOI**:10.1016/j.jclepro.2018.03.247
- J. A. Watt, I. T. Burke, R. A. Edwards, H. M. Malcolm, W. M. Mayes, J. P. Olszewska, G. Pan, M. C. Graham, K. V. Heal, N. L. Rose, S. D. Turner, B. M. Spears, *Environ. Sci. Technol.* 2018, 52, 11973–11974. DOI:10.1021/acs.est.8b05560
- Z. Marczenko, M. Balcerzak, Separation, preconcentration and spectrophotometry in inorganic analysis, Elsevier, Amsterdam, 2000, pp. 456–465. DOI:10.1016/S0926-4345(00)80119-4

- K. Pyrzyńska, Microchim. Acta 2005, 149, 159–164.
 DOI:10.1007/s00604-004-0304-5
- 16. W.-y. He, K.-p. Wang, J.-y. Yang, *Toxicol. Environ. Chem.* **2018**, 1–20. **DOI:** 10.1080/02772248.2018.1428325.
- 17. T. Stefanova-Bahchevanska, N. Milcheva, S. Zaruba, V. Andruch, V. Delchev, K. Simitchiev, K. Gavazov, *J. Mol. Liq.* **2017**, *248*, 135–142. **DOI:**10.1016/j.molliq.2017.10.046
- L. Rostampour, M. A. Taher, *Talanta* 2008, 75, 1279–1283.
 DOI:10.1016/j.talanta.2008.01.045
- 19. S. Chandramouleeswaran, J. Ramkumar, *Der Chemica Sinica* **2018**, *9*, 605–608.
- C. Zhang, J. Liu, B. Yao, L. Zhang, in: 2011 International Symposium on Water Resource and Environmental Protection (ISWREP), Xi'an, China, IEEE, 2011, pp. 1803–1806.
 DOI: 10.1109/ISWREP.2011.5893600.
- 21. A. S. Amin, A. L. Saber, T. Y. Mohammed, *Spectrochim. Acta*, *Part A* **2009**, *73*, 195–200. **DOI:**10.1016/j.saa.2009.02.010
- 22. H. Filik, Z. Yanaz, R. Apak, *Anal. Chim. Acta* **2008**, *620*, 27–33. **DOI**:10.1016/j.aca.2008.05.024
- 23. H. Filik, K. I. Berker, N. Balkis, R. Apak, *Anal. Chim. Acta* **2004**, *518*, 173–179. **DOI**:10.1016/j.aca.2004.05.012
- M. Uslu, H. Ulutürk, A. Yartaşı, S. Döker, *Toxicol. Environ. Chem.* 2014, 95, 1638–1649.
 DOI:10.1080/02772248.2014.896920
- T. S. Stefanova, K. K. Simitchiev, K. B. Gavazov, *Chem. Pap.* 2015, 69, 495–503. DOI:10.1515/chempap-2015-0048
- N. Galesic, M. Siroki, Acta Crystallogr., Sect. C 1984, 40, 378–381. DOI: 10.1107/S0108270184004212.
- K. B. Gavazov, V. D. Lekova, A. N. Dimitrov, G. I. Patronov, *Cent. Eur. J. Chem.* 2007, 5, 257–270.
 DOI:10.2478/s11532-006-0053-x
- G. K. Toncheva, N. P. Milcheva, K. B. Gavazov, Acta Chim. Slov. 2018, 65, 847–852. DOI:10.17344/acsi.2018.4491
- K. B. Gavazov, V. B. Delchev, K. T. Mileva, T. S. Stefanova, G. K. Toncheva, *Acta Chim. Slov.* 2016, 63, 392–398.
 DOI:10.17344/acsi.2016.2431.
- 30. L. M. Dimova, E. A. Morgen, Zavod. Lab. 1984, 50, 7-9.
- 31. M. Široki, L. Marić, Z. Štefanac, J. Inorg. Nucl. Chem. 1981, 43, 1151–1153. DOI:10.1016/0022-1902(81)80008-5
- H. E. Michibata, Vanadium: biochemical and molecular biological approaches. Springer, Dordrecht, 2012.
 DOI:10.1007/978-94-007-0913-3
- S. Kodama, Y. Ueta, J. Yoshida, A. Nomoto, S. Yano, M. Ueshima, A. Ogawa, *Dalton Trans.* 2009, 9708–9711.
 DOI:10.1039/b913823d
- 34. D. C. Crans, J. J. Smee, E. Gaidamauskas, L. Yang, *Chem. Rev.* **2004**, *104*, 849–902. **DOI**:10.1021/cr020607t
- G. K. Toncheva, Z. T. Zhelev, V. B. Delchev, K. B. Gavazov, *Acta Chim. Slov.* 2018, 65, 462–469.
 DOI:10.17344/acsi.2018.4225
- Y. Erdogdu, Ü. C. Başköse, S. Sağlam, Chem. Pap. 2019.
 DOI: 10.1007/s11696-019-00739-4.
- K. B. Gavazov, V. B. Delchev, N. P. Milcheva, G. K. Toncheva, Open Chem. **2019** (in press).
 DOI: 10.1515/chem-2019-0071.
- 38. WHO Model List of Essential Medicines, 20th eddition

- https://www.who.int/medicines/publications/essentialmedicines/en/ (assessed: May 3, 2019)
- S. Khalil, *Microchim. Acta* 1999, 130, 181–184.
 DOI:10.1007/BF01244925
- Y. Anjaneyulu, K. Chandra Sekhar, M. Ravi Prakasa Reddy, R. N. Sarma, *Microchim. Acta* 1985, 87, 23–29.
 DOI:10.1007/BF01201983
- 41. S. N. Bhadani, M. Tewari, A. Agrawal, C. Sekhar, *J. Indian Chem. Soc.* **1998**, *75*, 176–177.
- 42. Y. Anjaneyulu, M. R. Reddy, C. S. Kavipurapu, *Analyst* **1986**, *111*, 1167–1169. **DOI**:10.1039/an9861101167
- 43. A. Yerramilli, C. S. Kavipurapu, R. R. Manda, C. M. Pillutla, *Anal. Chem.* **1986**, *58*, 1451–1453. **DOI:**10.1021/ac00298a040
- C. S. Kavipurapu, S. C. Srivastava, K. K. Gupta, L. P. Pandey, *Mikrochim. Acta* 1993, 111, 127–132.
 DOI:10.1007/BF01240175
- M. Smolinska, O. Korkuna, T. Vrublevska, P. Rudchuk, G. Teslyar, *Open Chem.* 2015, *13*, 1254–1268.
 DOI:10.1515/chem-2015-0139
- M. Langova, I. Klabenesova, K. Kasiura, L. Sommer, Coll. Czech. Chem. Commun. 1976, 41, 2386–2405.
 DOI:10.1135/cccc19762386
- 47. L. Marić, M. Široki, Z. Štefanac, M. J. Herak, *Microchem. J.* **1979**, *24*, 536–544. 3.5, and E = 96% (ADR = TAR); ε550 = 1.88 × 104
- 48. K. B. Gavazov, T. S. Stefanova, *Croat. Chem. Acta* **2014**, *87*, 233–240. **DOI**:10.5562/cca2436
- 49. L. Konermann, *J. Am. Soc. Mass Spectrom.* **2017**, *28*, 1827–1835. **DOI:**10.1007/s13361-017-1739-3
- 50. Z. Zhiming, M. Dongsten, Y. Cunxiao, *J. Rare Earths* **1997**, *15*, 216–219.
- 51. E. Asmus, Fresenius' J. Anal. Chem. **1960**, 178, 104–116. **DOI:**10.1007/BF00467200
- 52. J. H. Yoe, A. L. Jones, *Ind. Eng. Chem. Anal. Ed.* **1944**, *16*, 111–115. **DOI**:10.1021/i560126a015
- 53. P. Job, *Ann. Chim. (Paris)* **1928**, *9*, 113–134. **DOI:**10.3406/bmsap.1928.9218
- L. D. Kurbatova, O. V. Koryakova, M. A. Valova, M. Yu. Yanchenko, Z. Anorg. Allg. Chem. 2015, 641, 617–621.
 DOI:10.1002/zaac.201400426
- N. K. Temel, R. Gürkan, Acta Chim. Slov. 2018, 65, 138–149.
 DOI:10.17344/acsi.2017.3724
- K. Pytlakowska, V. Kozik, M. Dabioch, *Talanta* 2013, 110, 202–228. DOI:10.1016/j.talanta.2013.02.037
- 57. N. Menek, E. Eren, S. Topçu, *Dyes Pigm.* **2006**, *68*, 205–210. **DOI:**10.1016/j.dyepig.2005.01.010.
- F. Karipcin, E. Kabalcilar, S. Ilican, Y. Caglar, M. Caglar, Spectrochim. Acta Part A **2009**, *73*, 174–180.
 DOI:10.1016/j.saa.2009.02.012
- F. Karipcin, E. Kabalcilar, Acta Chim. Slov. 2007, 54, 242– 247.
- N. L. Babenko, A. I. Busev, L. K. Simakova, Zh. Anal. Khim. 1970, 25, 1539–1546.
- 61. K. B. Gavazov, V. D. Lekova, G. I. Patronov, Acta Chim. Slov. **2006**, *53*, 506–511.

- A. Hulanicki, S. Glab, G. Ackermann, Pure Appl. Chem. 1983, 55, 1137–1230.
 - DOI:10.1351/pac198355071137

- W. Likussar, D. F. Boltz, Anal. Chem. 1971, 43, 1265–1272.
 DOI:10.1021/ac60304a006
- A. Shrivastava, V. B. Gupta, Chron. Young Sci. 2011, 2, 21–25.
 DOI:10.4103/2229-5186.79345

Povzetek

Proučevali smo kromogen sistem ekstrakcije tekočina-tekočina za spojine vanadija (V) na osnovi ksilometazolin hidroklorida (XMZ) in azo derivate resorcinola (ADR). Uporabili smo naslednje ADR: 4- (2-tiazolilazo) resorcinol (TAR), 5-metil-4- (2-tiazolilazo) resorcinol (MTAR) in 6-heksil-4- (2-tiazolilazo) resorcinol (HTAR). Koncentracija reagentov, pH vodnega medija in čas stresanja so bili predmet optimizacijskih poskusov. Ternarni kompleksi, ekstrahirani s kloroformom, so bili sestavljeni 1: 1: 1. Določili smo molarne absorbcijske koeficiente (ε_{λ}), absorpcijske maksimume (λ), konstante ekstrakcije (Log K) in delež ekstrahirane frakcije (E%): $\varepsilon_{553} = 2.50 \times 10^4$ dm³ mol $^{-1}$ cm $^{-1}$, Log K = dm³ mol $^{-1}$ cm $^{-1}$, Log K = 3.4, and E = 98% (ADR = MTAR); and $\varepsilon_{554} = 2.62 \times 10^4$ dm³ mol $^{-1}$ cm $^{-1}$, Log K = 5.0, and E = 99.5% (ADR = HTAR). Določili smo tudi Sandellovo občutljivosti in omejitve Beerovega zakona.



Except when otherwise noted, articles in this journal are published under the terms and conditions of the Creative Commons Attribution 4.0 International License

Scientific paper

Synthesis, Characterization, X-Ray Crystal Structures and Antibacterial Activities of Oxidovanadium(V) Complexes with Hydrazone and Hydroxamate Ligands

Heng-Yu Qian

Key Laboratory of Surface & Interface Science of Henan, School of Material & Chemical Engineering, Zhengzhou University of Light Industry, Zhengzhou, 450002 P.R. China

* Corresponding author: E-mail: hengyu_qian@126.com

Received: 05-07-2019

Abstract

Two new oxidovanadium(V) complexes, $[VOL^1L]$ (1) and $[VOL^2L] \cdot CH_3OH$ (2·CH₃OH), where L^1 and L^2 are the dianionic form of N'-(3-bromo-2-hydroxybenzylidene)picolinohydrazide (H_2L^1) and 2-chloro-N'-(2-hydroxy-3-methoxybenzylidene)benzohydrazide (H_2L^2), respectively, and L is the monoanionic form of 2-hydroxybenzohydroxamic acid (HL), were prepared and characterized by elemental analysis, infrared and electronic spectroscopy. Structures of the complexes were further confirmed by single crystal X-ray determination. The V atoms in the complexes are in octahedral coordination. The hydrazone ligands coordinate to the V atoms through the phenolate O, imino N, and enolate O atoms. The hydroxamate ligand coordinates to the V atom through the carbonyl and hydroxy O atoms. The complexes show effective antibacterial activity against B. subtilis, S. aureus and E. coli. The presence of Cl substitute group in the complex may enhance the antibacterial activity.

Keywords: Hydrazone; hydroxamate; oxidovanadium complex; crystal structure; antibacterial activity

1. Introduction

Schiff bases and their metal complexes have received considerable interest in coordination, catalytic, biological and medicinal chemistry. Vanadium acts as essential role in humans and many living organisms. The biological and pharmacological effects of vanadium element include coordination capability and chemical similarity between vanadate and phosphate. Some inorganic vanadates show insulin-mimetic properties, as well as antitumor activities. A number of vanadium complexes with various types of organic ligands are reported to possess interesting antidiabetic activity. In pursuit of new vanadium compounds with decreased toxic side effects and enhanced bioavail-

ability, a great number of organic ligands and vanadium complexes have been investigated.⁴ The metal complexes of vanadium have the ability to normalize blood glucose level, thus, they can act as models of the haloperoxidases.⁵ Moreover, the metal complexes of vanadium possess interesting antimicrobial activities.⁶ In recent years, much attention has been focused on the biological properties of vanadium complexes.⁷ Some metal complexes of vanadium with hydrazone ligands have been reported for their antibacterial activities by our research group.⁸ In pursuit of new vanadium-based biocidal agents, we report here two new vanadium(V) complexes, [VOL¹L] (1) and [VOL²L] · CH₃OH (2 · CH₃OH), with the hydrazone ligands N°-(3-bromo-2-hydroxybenzylidene)picolinohydrazide

$$H_2L^1$$
 H_2L^2 HL

Qian: Synthesis, Characterization, X-Ray Crystal Structures ...

2-chloro-N'-(2-hydroxy-3-methoxyben- (H_2L^1) and zylidene)benzohydrazide (H₂L²), and 2-hydroxybenzohydroxamic acid (HL).

2. Experimental

2. 1. Materials and Measurements

3-Bromo-2-hydroxybenzaldehyde, 2-hydroxy-3-methoxybenzaldehyde, picolinohydrazide and 2-chlorobenzohydrazide were purchased from Aldrich and used as obtained. Other solvents and reagents were made in China and used as received. C, H and N elemental analyses were performed with a Perkin-Elmer 240 elemental analyzer. Infrared spectra were recorded on a Nicolet AVATAR 360 spectrometer as KBr pellets in the 4000-400 cm⁻¹ region. UV-Vis spectra were recorded on a Lambda 900 spectrometer.

2. 2. Synthesis of Complex 1

3-Bromo-2-hydroxybenzaldehyde (0.10 mmol, 20.0 mg) and picolinohydrazide (0.10 mmol, 13.7 mg) were dissolved in ethanol (15 mL). Mixture was stirred at room temperature for 30 min to give a colorless solution. To the solution an ethanolic solution (10 mL) of VO(acac)₂ (0.10 mmol, 26.5 mg) and 2-hydroxybenzoic acid (0.10 mmol, 15.3 mg) was added with stirring. Mixture was further stirred at room temperature for 30 min to give deep brown solution. After keeping the solution in air for a few days, brown block-shaped single crystals, suitable for X-ray crystal structure determination were obtained. The crystals were isolated by filtration and dried in a vacuum desiccator containing anhydrous CaCl₂. Yield 33% (177 mg). IR data (KBr; v_{max}, cm⁻¹): 3453, 3272, 1607, 953. UV-Vis data in ethanol (λ , nm (ϵ , M⁻¹ cm⁻¹)]: 275 (18,200), 305 (17,325), 326 (16,312), 402 (4,535), 580 (1,105). Anal. Calcd. for C₂₀H₁₄BrN₄O₆V (%): C, 44.72; H, 2.63; N, 10.43. Found (%): C, 44.60; H, 2.75; N, 10.32.

2. 3. Synthesis of Complex 2

3-Bromo-2-hydroxybenzaldehyde (0.10 mmol, 20.0 mg) and 2-chlorobenzohydrazide (0.10 mmol, 17.0 mg) were dissolved in ethanol (15 mL). Mixture was stirred at room temperature for 30 min to give a colorless solution. To the solution an ethanolic solution (10 mL) of VO(acac)₂ (0.10 mmol, 26.5 mg) and 2-hydroxybenzoic acid (0.10 mmol, 15.3 mg) was added with stirring. Mixture was further stirred at room temperature for 30 min to give deep brown solution. After keeping the solution in air for a few days, brown block-shaped single crystals, suitable for X-ray crystal structure determination were obtained. The crystals were isolated by filtration and dried in a vacuum desiccator containing anhydrous CaCl2. Yield 41% (227 mg). IR data (KBr; v_{max} , cm⁻¹): 3465, 3252, 1618, 953. UV-Vis data in ethanol (λ , nm (ϵ , M⁻¹ cm⁻¹)]: 272 (19,530), 290 (18,620), 335 (9,755), 420 (1,272), 570 (1,533). Anal. Calcd. for C₂₃H₂₁ClN₃O₈V (%): C, 49.88; H, 3.82; N, 7.59. Found (%): C, 50.12; H, 3.97; N, 7.45.

2. 4. X-ray Crystallography

Diffraction intensities for the complexes were collected at 298(2) K using a Bruker D8 VENTURE PHOTON dif-

Parameters	1	2 · CH ₃ OH	
Molecular formula	C ₂₀ H ₁₄ BrN ₄ O ₆ V	23H21ClN3O8V	
Mr	537.20	553.82	
Crystal color, habit	Brown, block	Brown, block	
Crystal system	Monoclinic	Monoclinic	
Space group	$P2_1/c$	$P2_1/c$	
a, Å	10.811(1)	11.972(1)	
b, Å	17.282(1)	9.583(1)	
c, Å	12.535(1)	21.101(1)	
β, °	95.810(1)	103.792(1)	

Table 1. Crystallographic data and refinement parameters for complexes 1 and 2 ⋅ CH₃OH

Crystal color, habit	Brown, block	Brown, block
Crystal system	Monoclinic	Monoclinic
Space group	$P2_1/c$	$P2_1/c$
a, Å	10.811(1)	11.972(1)
b, Å	17.282(1)	9.583(1)
c, Å	12.535(1)	21.101(1)
β, °	95.810(1)	103.792(1)
V, Å ³	2330.0(3)	2351.1(3)
Z	4	4
$\rho_{calcd}, g \ cm^{-3}$	1.531	1.565
μ, mm ⁻¹	2.182	0.591
F(000)	1072	1136
Number of unique data	4028	4378
Number of observed data $(I > 2\sigma(I))$	3038	3261
Independent parameters	293	332
Restraints	1	1
R_1 , $wR_2(I > 2\sigma(I))$	0.0664, 0.1683	0.0568, 0.1581
R_1 , wR_2 (all data)	0.0899, 0.1838	0.0802, 0.1731
Goodness of fit on F^2	1.040	1.066

Qian: Synthesis, Characterization, X-Ray Crystal Structures ...

fractometer with $MoK\alpha$ radiation ($\lambda = 0.71073$ Å). The collected data were reduced using SAINT,⁹ and multi-scan absorption corrections were performed using SADABS.¹⁰ Structures of the complexes were solved by direct methods and refined against F^2 by full-matrix least-squares methods using SHELXTL.¹¹ All of the non-hydrogen atoms were refined anisotropically. The amino H atoms were located from different Fourier maps and refined isotropically, with N–H distances restrained to 0.90(1) Å. The other hydrogen atoms in both compounds were placed in idealized positions and constrained to ride on their parent atoms. Crystallographic data for the complexes are summarized in Table 1.

2. 5. Antibacterial Assay

The antibacterial activity of the complexes was tested against *B. subtilis*, *S. aureus*, *E. coli*, and *P. aeruginosa* using LB medium (Luria-Bertani medium: Tryptone 10 g, Yeast extract 5 g, NaCl 10 g, distilled water 1000 mL, pH 7.4). The IC $_{50}$ (half inhibitory concentration) of the test compounds were determined by a colorimetric method using the dye MTT (3-(4,5-di-methylthiazol-2-yl)-2,5-diphenyltetrazolium bromide).

A stock solution of the synthesized compound (1000 $\mu g \ mL^{-1}$) in DMSO was prepared and graded quantities of the test compounds were incorporated in specified quantity of sterilized liquid LB medium. Suspension of the microorganism was prepared and applied to 96-well assay plate with serially diluted compounds to be tested. 10 μL of tested samples at pre-set concentrations were added to wells with penicillin as a positive reference and with the solvent control (5% DMSO) in medium and incubated at 37 °C for 24 h.

After 24 h exposure, 10 μ L of PBS (phosphate buffered saline 0.01 mol L⁻¹, pH 7.4) containing 4 mg mL⁻¹ of MTT was added to each well. After 4 h, the medium was replaced by 150 μ L DMSO to dissolve the complexes. The absorbance at 492 nm of each well was measured with an ELISA plate reader. The IC₅₀ value was defined as the concentration at which 50% of the bacterial strain could survive.

3. Results and Discussion

3. 1. Chemistry

The hydrazone ligands H_2L^1 and H_2L^2 were prepared by the reactions of 3-bromo-2-hydroxybenzaldehyde with picolinohydrazide, and 2-hydroxy-3-methoxybenzaldehyde with 2-chlorobenzohydrazide, respectively in ethanol. The two complexes were prepared by the reaction of the hydrazone ligands with $VO(acac)_2$ and 2-hydroxybenzohydroxamic acid in ethanol (Scheme 1). Crystals of the complexes are soluble in DMF, DMSO, methanol, ethanol, and acetonitrile.

3. 2. Structure Description of the Complexes

Molecular structures of complexes 1 and 2 are shown in Figs. 1 and 2, respectively. Selected bond lengths and angles are given in Table 2. The V atoms are in octahedral coordination, with the phenolate O, imino N and enalate O atoms of the hydrazone ligands, and the hydroxy O atom of 2-hydroxybenzohydroxamate ligand defining the equatorial plane, and with the oxido O atom and the carbonyl O atom of the 2-hydroxybenzohydroxamate ligand

Scheme 1. The synthetic method of the complexes.

locating at the axial positions. The V atoms deviate from the least-squares planes defined by the corresponding equatorial atoms by 0.265(1) Å for 1 and 0.277(1) Å for 2. The coordinate bond lengths in the complexes are comparable to each other, and similar to those observed in vanadium complexes with hydrazone ligands. The distortion of the octahedral coordination can be observed from the coordinate bond angles, ranging from 75.01(15)° to 103.70(16)° (1), and 74.98(11)° to 103.59(13)° (2), for the perpendicular angles, and from 154.74(16)° to 170.84(17)° for (1), and from 157.06(11)° to 170.22(13)° (2), for the diagonal angles. The dihedral angles between the two aromatic rings of the hydrazone ligands are 7.2(5)° for 1 and

Table 2. Selected bond distances (Å) and angles (°) for complexes 1 and 2 \cdot CH $_3\text{OH}$

		1	
V1-O1	1.878(4)	V1-O2	1.959(4)
V1-O3	1.854(3)	V1-O4	2.217(4)
V1-O6	1.588(4)	V1-N1	2.072(4)
O6-V1-O3	95.90(18)	O6-V1-O1	100.01(19)
O3-V1-O1	103.70(16)	O6-V1-O2	97.29(18)
O3-V1-O2	92.62(15)	O1-V1-O2	154.74(16)
O6-V1-N1	98.64(18)	O3-V1-N1	161.95(16)
O1-V1-N1	84.28(16)	O2-V1-N1	75.01(15)
O6-V1-O4	170.84(17)	O3-V1-O4	75.41(14)
O1-V1-O4	85.08(15)	O2-V1-O4	80.47(14)
N1-V1-O4	89.39(14)		
	2 · C	H ₃ OH	
V1-O1	1.859(2)	V1-O2	1.971(2)
V1-O3	1.868(3)	V1-O4	2.153(3)
V1-O6	1.593(3)	V1-N1	2.090(3)
O6-V1-O1	99.44(14)	O6-V1-O3	95.72(13)
O1-V1-O3	101.74(12)	O6-V1-O2	95.01(13)
O1-V1-O2	157.06(11)	O3-V1-O2	94.40(11)
O6-V1-N1	103.59(13)	O1-V1-N1	84.32(11)
O3-V1-N1	158.58(12)	O2-V1-N1	74.98(11)
O6-V1-O4	170.22(13)	O1-V1-O4	87.93(11)
O3-V1-O4	76.37(10)	O2-V1-O4	80.09(11)
N1-V1-O4	83.41(11)		

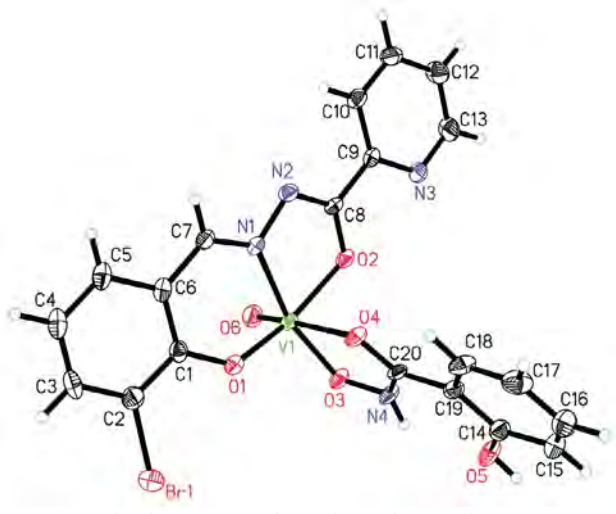


Fig. 1. Molecular structure of complex **1**, showing the atom-numbering scheme. Displacement ellipsoids are drawn at the 30% probability level.

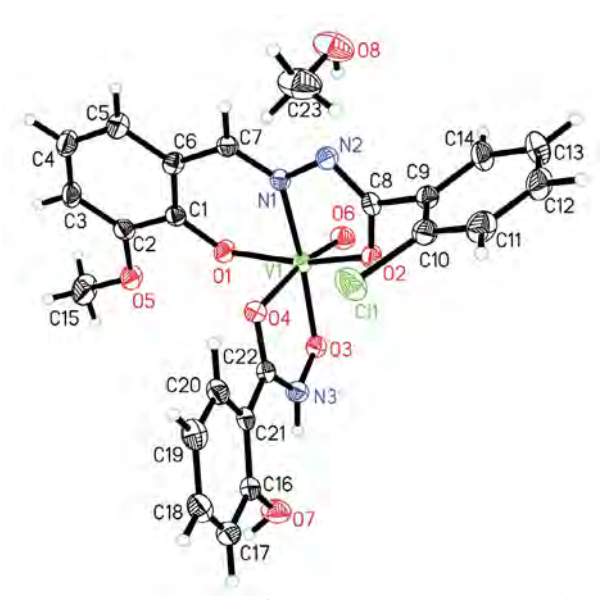


Fig. 2. Molecular structure of compound $2 \cdot \text{CH}_3\text{OH}$, showing the atom-numbering scheme. Displacement ellipsoids are drawn at the 30% probability level.

Table 3. Hydrogen bond distances (Å) and bond angles (°) for the complexes

D-H···A	d(D-H)	d(H···A)	d(D···A)	Angle (D-H···A)
		1		
O5-H5···O2 ⁱ	0.82	2.42	3.051(5)	134.4
O5-H5N3i	0.82	2.04	2.780(6)	150.7
		$2 \cdot CH_3OH$		
N3-H3···O5 ⁱⁱ	0.898(10)	2.50(4)	3.196(4)	134(4)
O7-H7···O8 ⁱⁱⁱ	0.82	1.84	2.621(4)	159.8
O8-H8···N2iv	0.82	2.10	2.874(4)	157.9
C7-H7A···O6 ^v	0.93	2.53	3.1762(3)	127
C18-H18···O5vi	0.93	2.58	3.4652(4)	160
C19-H19···O6 ^{vii}	0.93	2.56	3.4513(4)	160

Symmetry codes for i): 1 - x, - y, 1 - z; ii): - x, 1 - y, - z; iii): - x, $\frac{1}{2} + y$, $\frac{1}{2} - z$; iv): 1 - x, $-\frac{1}{2} + y$, $\frac{1}{2} - z$; v): 1 - x, 1 - y, - z; vii): - x, 2 - y, - z; vii): x, 1 + y, z.

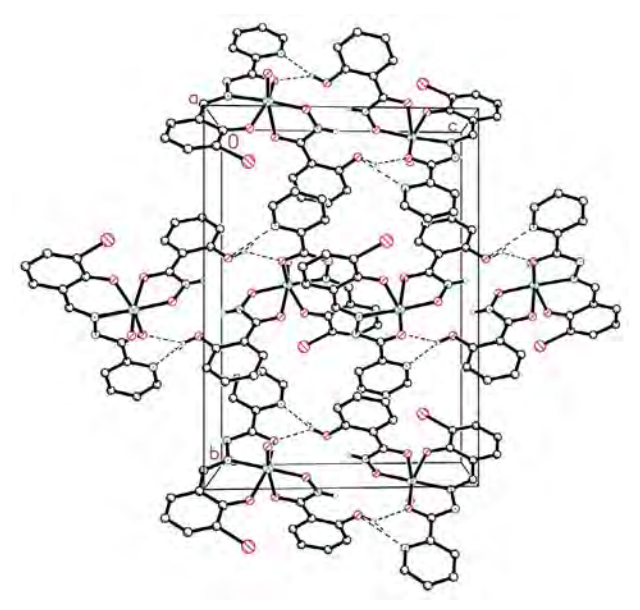


Fig. 3. Crystal packing structure of complex **1**, viewed along the *a* axis. Hydrogen bonds are shown as dashed lines.

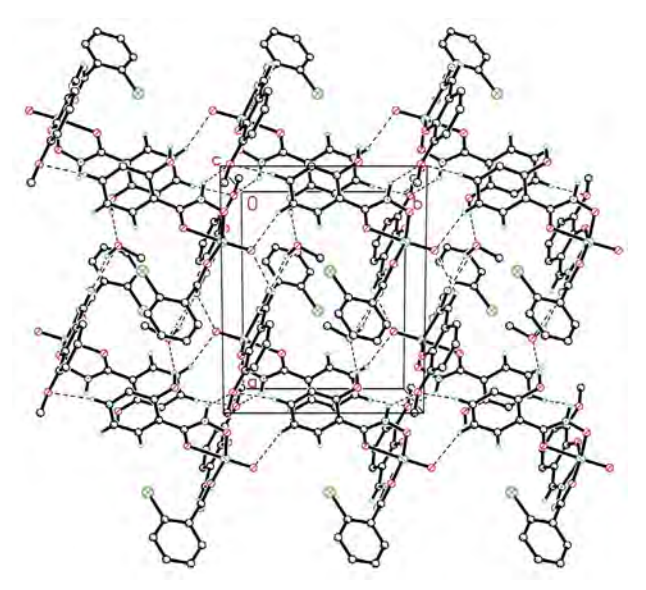


Fig. 4. Crystal packing structure of compound $2 \cdot \text{CH}_3\text{OH}$, viewed along the *c* axis. Hydrogen bonds are shown as dashed lines.

88.9(6)° for **2**. In the crystal structures of the complexes, molecules are linked through hydrogen bonds (Table 3), to form three dimensional networks (Figs. 3 and 4).

3. 3. IR and UV-Vis Spectra of the Complexes

The ν (C=N) absorptions are observed at 1607 cm⁻¹ for complex 1 and 1618 cm⁻¹ for complex 2.¹³ The intense bands indicative of the C=O vibrations are absent in the complexes, indicating the enolization of the hydrazone ligands. The sharp bands indicative of the N-H vibrations are located at 3272 cm⁻¹ for complex 1 and 3252 cm⁻¹ for complex 2. The weak peaks in the low wave numbers in the

region 450–700 cm $^{-1}$ may be attributed to V–O and V–N bonds in the complexes. Complexes 1 and 2 exhibit typical bands at 953 cm $^{-1}$, which are assigned to the V=O vibrations.¹⁴

The UV-Vis spectra of the complexes were recorded in 10^{-5} mol L⁻¹ in ethanol, in the range 200–800 nm. The weak bands centered at 326 nm for complex **1** and 335 nm for complex **2** are attributed to intramolecular charge transfer transitions from the p_{π} orbital on the nitrogen and oxygen to the empty d orbitals of the metal.¹⁵ The intense bands observed at about 275 nm for the complexes are assigned to intraligand π - π * transition.¹⁵ The bands centered at 580 nm for complex **1** and 570 nm for complex **2** are attributed to the ligand-to-metal charge transfer transitions (LMCT).¹⁶

3. 4. Antibacterial Activities

The complexes were screened for antibacterial activities against two Gram-positive bacterial strains (B. subtilis and S. aureus) and two Gram-negative bacterial strains (E. coli and P. aeruginosa) by MTT method. The IC₅₀ values of the complexes against the bacteria are presented in Table 4. Penicillin G was tested as a reference drug. Complex 1 exhibited effective activity against B. subtilis, and weak activity against S. aureus, while no activity against Gram-negative bacteria E. coli and P. aeruginosa. Complex 2 exhibited effective activity against B. subtilis and S. aureus, weak activity against E. coli, while no activity against P. aeruginosa. In general, complex 2 has stronger activity against B. subtilis, S. aureus and E. coli than complex 1, which might be caused by the existence of the biological active substitute group, Cl. Both the free hydrazones H₂L¹ and H₂L², and the hydroxamic acid HL have no or very weak activities on the bacteria. VO(acac)₂ has weak activities on *B. subtilis*, *S.* aureus and E. coli, and no activity on P. aeruginosa.

Table 4. Antibacterial results (IC50, $\mu g \ mL^{-1})$

Compound	Gram-positive		Gram-negative		
-	B. subtilis	S. aureus	E. coli	P. aeruginosa	
1	5.32	13.0	>50	>50	
2	3.10	2.56	21.7	>50	
H_2L^1	35.6	>50	>50	>50	
H_2L^2	22.7	32.9	>50	>50	
HL	>50	>50	>50	>50	
VO(acac) ₂	16.7	25.3	38.2	>50	
Penicillin G	2.35	0.75	17.5	17.5	

4. Conclusion

Two new oxidovanadium(V) complexes were obtained and structurally characterized. The complexes show superior antibacterial activities against *B. subtilis*, *S. aureus* and *E. coli* than the free ligands and VO(acac)₂. Complex 2

has similar activities against *B. subtilis* when compared with penicillin G. The presence of Cl substitute group in the complex may enhance the antibacterial activity.

5. Supplementary Materials

X-ray crystallographic data for the complexes have been deposited with the Cambridge Crystallographic Data Centre (The Director, CCDC, 12 Union Road, Cambridge, CB2 1 EZ, UK; e-mail: deposit@ccdc.cam.ac.uk; http://www.ccdc.cam.ac.uk; fax: +44-(0)1223-336033) and are available free of charge on request, quoting the deposition number CCDC 1914265 for 1, and 1914266 for 2.

6. References

- (a) G. M. Chans, A. Nieto-Camacho, T. Ramirez-Apan, S. Hernandez-Ortega, C. Alvarez-Toledano, E. Gomez, *Aust. J. Chem.* 2016, 69, 279–290; DOI:10.1071/CH15344
 - (b) F. Qureshi, M. Y. Khuhawar, T. M. Jahangir, A. H. Channar, *Acta Chim. Slov.* **2016**, *63*, 113–120;

DOI:10.17344/acsi.2015.1994

- (c) Y.-T. Li, J.-W. Dong, Y. Lu, Y.-T. Gu, C.-N. Shang, F.-Y. Liu, Y. Xin, C.-L. Jing, Z.-L. You, *Chinese J. Inorg. Chem.* **2018**, *34*, 1192–1198;
- (d) Z. You, H. Yu, Z. Li, W. Zhai, Y. Jiang, A. Li, S. Guo, K. Li, C. Lv, C. Zhang, *Inorg. Chim. Acta* **2018**, 480, 120–126; **DOI**:10.1016/j.ica.2018.05.020
- (e) X.-W. Zhu, *Acta Chim. Slov.* **2018**, 65, 939–945; **DOI**:10.17344/acsi.2018.4607
- (f) M. Liang, N. Sun, D.-H. Zou, *Acta Chim. Slov.* **2018**, *65*, 964–969. **DOI**:10.17344/acsi.2018.4625
- J. Tian, D. Li, F. Zhai, X. Wang, R. Li, Med. Chem. Res. 2010, 19, 1162–1173. DOI:10.1007/s00044-009-9260-2
- (a) N. Patel, A. K. Prajapati, R. N. Jadeja, R. N. Patel, S. K. Patel, V. K. Gupta, I. P. Tripathi, N. Dwivedi, *Inorg. Chim. Acta* 2019, 493, 20–28; DOI:10.1016/j.ica.2019.04.050
 - (b) T. Kolesa-Dobravc, K. Maejima, Y. Yoshikawa, A. Meden, H. Yasui, F. Perdih, *New J. Chem.* **2018**, *42*, 3619–3632;

DOI:10.1039/C7NJ04189F

- (c) T. Jakusch, T. Kiss, *Coord. Chem. Rev.* **2017**, *351*, 118–126; **DOI**:10.1016/j.ccr.2017.04.007
- (d) J.-B. Wang, L.-P. Lu, J.-Y. Liu, Y.-S. Li, *Dalton Trans.* **2014**, 43, 12926–12934; **DOI**:10.1039/C4DT01166J
- (e) I. Z. Gundhla, R. S. Walmsley, V. Ugirinema, N. O. Mnonopi, E. Hosten, R. Betz, C. L. Frost, Z. R. Tshentu, *J. Inorg. Biochem.* **2015**, *145*, 11–18.

DOI:10.1016/j.jinorgbio.2014.12.019

(a) A. K. Srivastava, Mol. Cell. Biochem. 2000, 206, 177–182;
 DOI:10.1023/A:1007075204494

- (b) M. Yamaguchi, H. Oishi, Y. Suketa, Res. Exp. Med. 1989, 189, 47–53; DOI:10.1007/BF01856029
- (c) J. Jiang, M. Yang, Y. Gao, J. Wang, D. Li, T. Li, *Chemosphere* **2017**, *180*, 295–301.

DOI:10.1016/j.chemosphere.2017.03.116

- (a) M. Mba, M. Pontini, S. Lovat, C. Zonta, G. Bernardinelli, P. E. Kundig, G. Licini, *Inorg. Chem.* 2008, 47, 8616–8618;
 DOI:10.1021/ic8015113
 - (b) X. A. Zhang, W. D. Woggon, J. Am. Chem. Soc. 2005, 127, 14138–14139; DOI:10.1021/ja053209r
 - (c) X. A. Zhang, M. Meuwly, W. D. Woggon, *J. Inorg. Biochem.* **2004**, 98, 1967–1970. **DOI**:10.1016/j.jinorgbio.2004.07.013
- (a) J. Farzanfar, K. Ghasemi, A. R. Rezvani, H. S. Delarami, A. Ebrahimi, H. Hosseinpoor, A. Eskandari, H. A. Rudbari, G. Bruno, J. Inorg. Biochem. 2015, 147, 54–64;

DOI:10.1016/j.jinorgbio.2015.02.007

- (b) V. Pawar, S. Joshi, V. Uma, *Asian J. Chem.* **2013**, *25*, 1497–1500; (c) I. Sheikhshoaie, S. Y. Ebrahimipour, N. Lotfi, J. T. Mague, M. Khaleghi, *Inorg. Chim. Acta* **2016**, *442*, 151–157. **DOI**:10.1016/j.ica.2015.11.026
- 7. (a) M. He, Q.-Z. Jiao, X.-F. Chen, J. Li, J. Chen, G.-H. Sheng, Z.-L. You, *Chin. J. Inorg. Chem.* **2015**, *31*, 1590–1596;
 - (b) J.-Q. Ren, Q.-Z. Jiao, Y.-N. Wang, F.-Y. Xu, X.-S. Cheng, Z.-L. You, *Chin. J. Inorg. Chem.* **2014**, *30*, 640–648;
 - (c) X. L. Zhao, X. F. Chen, J. Li, J. Chen, G. Sheng, F. Niu, D. Qu, Y. Huo, H. Zhu, Z. You, *Polyhedron* **2015**, *97*, 268–272. **DOI**:10.1016/j.poly.2015.07.012
- H. Y. Qian, Russ. J. Coord. Chem. 2017, 43, 780–786.
 DOI:10.1134/S1070328417110070
- SMART (version 5. 624) and SAINT (version 6.04), Programs
 Using the Windows NT System, Madison (WI, USA): Bruker
 AXS Inc. 2001.
- G. M. Sheldrick, SADABS, Program for Empirical Absorption Correction of Area Detector, Göttingen (Germany): Univ. of Göttingen 1996.
- 11. G. M. Sheldrick, *Acta Crystallogr. A* **2008**, *64*, 112–122. **DOI:**10.1107/S0108767307043930
- (a) D. Qu, F. Niu, X. Zhao, K.-X. Yan, Y.-T. Ye, J. Wang, M. Zhang, Z. You, *Bioorg. Med. Chem.* 2015, 23, 1944–1949;
 DOI:10.1016/j.bmc.2015.03.036
 (b) L.-X. Li, Y. Sun, Q. Xie, Y.-B. Sun, K.-H. Li, W. Li, Z.-L. You, *Chin. J. Inorg. Chem.* 2016, 32, 369–376.
- 13. Z.-L. You, D.-M. Xian, M. Zhang, *CrystEngComm* **2012**, *14*, 7133–7136. **DOI:**10.1039/c2ce26201k
- N. R. Sangeetha, V. Kavita, S. Wocadlo, A. K. Powell, S. Pal, J. Coord. Chem. 2000, 51, 55–66.

DOI:10.1080/00958970008047078

- G. Asgedom, A. Sreedhara, J. Kivikoski, E. Kolehmainen, C. P. Rao, *J. Chem. Soc. Dalton Trans.* 1996, 1, 93–97.
 DOI:10.1039/dt9960000093
- A. Sarkar, S. Pal, *Polyhedron* **2006**, *25*, 1689–1694.
 DOI:10.1016/j.poly.2005.11.009

Povzetek

Sintetizirali smo dva nova oksidovanadijeva(V) kompleksa, [VOL 1 L] (1) in [VOL 2 L] \cdot CH $_3$ OH (2 \cdot CH $_3$ OH), kjer sta L 1 in L 2 dianionski obliki N 2 -(3-bromo-2-hidroksibenziliden)pikolinohidrazida (H $_2$ L 1) in 2-kloro-N 2 -(2-hidroksi-3-metoksibenziliden)benzohidrazida (H $_2$ L 2) ter L monoanionska oblika 2-hidroksibenzohidroksamske kisline (HL). Kompleksa smo okarakterizirali z elementno analizo, infrardečo in elektronsko spektroskopijo. Strukturi kompleksov sta bili potrjeni tudi z monokristalno rentgensko analizo. V kompleksu je V atom koordiniran oktaedrično. Hidrazonski ligand se koordinira na V atom preko fenolatnega O, iminskega N in enolatnega O atoma. Hidroksamatni ligand se koordinira na V atom preko karbonilnega in hidroksilnega O atoma. Kompleksa izražata antibakterijsko aktivnost proti B. subtilis, S. aureus in E. coli. Prisotnost Cl skupine na ligandu verjetno ojača antibakterijsko aktivnost.



Except when otherwise noted, articles in this journal are published under the terms and conditions of the Creative Commons Attribution 4.0 International License

Scientific paper

Syntheses, Characterization, Crystal Structures and Antimicrobial Activity of 4-Bromo-N'- (pyridin-2-ylmethylene)benzohydrazide and Its Cobalt(III) and Manganese(II) Complexes

Yao Tan

School of Environmental and Chemical Engineering, Chongaing Three Gorges University, Chongaing 404000, P. R. China

* Corresponding author: E-mail: 18696838310@163.com

Received: 06-06-2019

Abstract

A new hydrazone compound 4-bromo-N'-(pyridin-2-ylmethylene)benzohydrazide (HL) and its cobalt(III) and manganese(II) complexes, $[CoL_2]NO_3 \cdot 2H_2O$ (1) and $[MnL_2]$ (2) were prepared. They were characterized by a variety of physicochemical techniques. Molecular structures of the compounds were further confirmed by single crystal X-ray crystallography. The coordination geometry around the cobalt atom in complex 1 and the manganese atom in complex 2 are octahedral, with two pyridine N atoms, two imino N atoms, and two enolate O atoms from the ligands. The compounds were evaluated for their antibacterial (*Bacillus subtilis*, *Staphylococcus aureus*, *Escherichia coli*, and *Pseudomonas fluorescence*) and antifungal (*Candida albicans* and *Aspergillus niger*) activities by MTT (3-(4,5-dimethylthiazol-2-yl)-2,5-diphenyltetrazolium bromide) method.

Keywords: Hydrazone; Cobalt complex; Manganese complex; Crystal structure; Antimicrobial activity

1. Introduction

Schiff bases and their metal complexes have been the subject of extensive investigations because of their potential pharmacological properties and a wide variation in their modes of bonding and stereochemistry whereas their hydrazone type complexes received much less attention. Hydrazones prepared by the condensation reaction of carbonyl-containing compounds with hydrazides, have attracted considerable attention for their wide range of biological activities. In recent years, transition metal complexes with various ligands have shown interesting biological especially antibacterial activities.² Also, some metal complexes with hydrazones often exhibit diverse biological and pharmaceutical activities.³ Recent research indicated that hydrazone compounds bearing halido-substituted groups are efficient antimicrobial materials. 4 However, the studies on the antimicrobial activities of metal complexes derived from 4-bromo-N'-(pyridin-2-ylmethylene) benzohydrazide (HL) have not been explored. Aiming at exploring new hydrazone based antimicrobial material, a cobalt(III) complex [CoL₂]NO₃ · 2H₂O (1) and a manganese(II) complex $[MnL_2]$ (2) are reported.

2. Experimental

2. 1. Materials and Physical Methods

2-Pyridinecarboxaldehyde and 4-bromobenzohydrazide were purchased from Merck and used as received. $Co(NO_3)_2 \cdot 6H_2O$ and $MnBr_2$ were purchased from Fluka with AR grade. The solvents and other chemical reagents were commercially available and used without further purification. Analysis of C, H and N were done on Elementar Vario EL III CHNOS elemental analyzer. IR spectra were recorded as KBr discs on Shimadzu IR spectrophotometer. Electronic spectra were recorded on Lambda 35 spectrometer. X-ray diffraction was carried out on a Bruker Smart 1000 CCD diffractometer. 1H NMR and ^{13}C NMR spectra were recorded on a Bruker DRX500 using DMSO- d_6 as

solvent and TMS as standard. Solution electrical conductivities were measured on a DIGISUN DI-909 conductivity meter.

2. 2. Synthesis of 4-bromo-N'-(pyridin-2-ylmethylene)benzohydrazide (HL).

HL was prepared by mixing 2-pyridinecarboxaldehyde (0.100 mol, 10.7 g) and 4-bromobenzohydrazide (0.100 mol, 21.5 g) in methanol (100 mL). The solution was heated to boiling for 20 min, cooled to room temperature. The solution was stand still in air to slow evaporate to give well-shaped single crystals. Yield: 31.2 g (93%). Characteristic IR data (KBr, cm⁻¹): 3485 and 3397 (OH), 3231 (NH), 1653 (C=O), 1589 (C=N). UV-Vis data (methanol, λ /nm): 300, 363. Anal. Calcd for C₁₄H₁₄BrN₃O₂: C, 50.02; H, 4.20; N, 12.50. Found: C, 50.13; H, 4.16; N, 12.41%. ¹H NMR (500 MHz, DMSO- d_6) δ 12.08 (s, 1H, NH), 8.62 (d, 2H, ArH), 8.48 (d, 2H, ArH), 7.98 (d, 1H, PyH), 7.90 (m, 1H, PyH), 7.88 (d, 1H, PyH), 7.77 (m, 1H, PyH), 7.43 (s, 1H, CH=N). ¹³C NMR (126 MHz, DMSO) δ 162.36, 153.18, 149.53, 148.35, 136.88, 131.57, 129.79, 128.32, 125.72, 124.78, 119.94.

2. 3. Synthesis of $[CoL_2]NO_3 \cdot 2H_2O(1)$

To a boiling solution of HL (1.0 mmol, 0.30 g) in methanol (20 mL), a methanolic solution of $Co(NO_3)_2 \cdot 6H_2O$ (1.0 mmol, 0.29 g) was added and refluxed continuously for 3 h, and cooled to room temperature. The filtrate was kept in air for a few days, to form crystals suitable for

single crystal X-ray diffraction. Yield: 0.16 mg (42%). Characteristic IR data (KBr, cm⁻¹): 3458 (OH), 1588 (CH=N). UV–Vis data (methanol, λ /nm): 290, 335, 383. Anal. Calcd for C₂₆H₂₂Br₂CoN₇O₇: C, 40.92; H, 2.91; N, 12.85. Found: C, 40.74; H, 2.86; N, 12.97%. $\Lambda_{\rm M}$ (10⁻³ M in acetonitrile): 122 Ω^{-1} cm² mol⁻¹.

2. 4. Synthesis of $[MnL_2]$ (2)

To a boiling solution of HL (1.0 mmol, 0.30 g) in methanol (20 mL), a methanolic solution of MnBr $_2$ (1.0 mmol, 0.215 g) was added and refluxed continuously for 3 h, and cooled to room temperature. The filtrate was kept in air for a few days, to form crystals suitable for single crystal X-ray diffraction. Yield: 0.17 g (52%). Characteristic IR data (KBr, cm $^{-1}$): 1585 (CH=N). UV-Vis data (methanol, λ /nm): 270, 290, 365. Anal. Calcd for C $_{26}$ H $_{18}$ Br $_{2}$ MnN $_{6}$ O $_{2}$: C, 47.23; H, 2.74; N, 12.71. Found: C, 47.45; H, 2.87; N, 12.63%. $\Lambda_{\rm M}$ (10 $^{-3}$ M in acetonitrile): 20 Ω^{-1} cm 2 mol $^{-1}$.

2. 5. X-ray Crystallography

Single-crystal X-ray diffraction measurements for HL and the complexes were carried out on a Bruker Smart 1000 CCD area diffractometer equipped with a graphite crystal monochromator for data collection at 298(2) K. The determinations of unit cell parameters and data collections were performed with Mo K α radiation (λ = 0.71073 Å) and unit cell dimensions were obtained with least-squares refinements. The program SAINT was used for reduction data.⁵ All structures were solved by direct

Table 1. Crystal data for HL and the complex

	HL	1	2
Formula	C ₁₄ H ₁₄ BrN ₃ O ₂	C ₂₆ H ₂₂ Br ₂ CoN ₇ O ₇	C ₂₆ H ₁₈ Br ₂ MnN ₆ O ₂
FW	336.19	763.25	661.22
Crystal system	Triclinic	Monoclinic	Monoclinic
Space group	P-1	$P2_1/n$	C2/c
a (Å)	6.5606(12)	14.226(1)	22.006(2)
b (Å)	9.8819(18)	10.9197(7)	14.516(1)
c (Å)	23.238(2)	18.770(1)	17.460(2)
α (°)	91.573(2)	90	90
β (°)	95.122(2)	93.898(1)	112.867(2)
γ (°)	92.684(2)	90	90
$V(Å^3)$	1498.1(4)	2909.1(3)	5139.1(8)
Z	4	4	8
$\lambda (\text{MoK}\alpha) (\mathring{A})$	0.71073	0.71073	0.71073
T(K)	298(2)	298(2)	298(2)
μ (Mo $K\alpha$) (cm ⁻¹)	2.748	3.395	3.660
Reflections/parameters	8936/367	15314/388	12849/334
Unique reflections	5547	4060	4767
Observed reflections $[I > 2\sigma(I)]$	3466	5433	3257
Restraints	1	0	0
Goodness of fit on F^2	1.006	1.029	1.030
R_1 , wR_2 [$I > 2\sigma(I)$]	0.0498, 0.1370	0.0427, 0.0983	0.0539, 0.1137
R_1 , wR_2 (all data)	0.0902, 0.1706	0.0662, 0.1098	0.0877, 0.1253

methods using SHELXS-97 and refined with SHELXL-97,6 non-hydrogen atoms were located in successive difference Fourier syntheses. The final refinement was performed by full-matrix least-squares methods with anisotropic thermal parameters for non-hydrogen atoms on F^2 . The hydrogen atoms treated by a mixture of independent and constrained refinement. Hydrogen atoms were placed in calculated positions and constrained to ride on their parent atoms. Crystallographic data and experimental details for structural analyses are summarized in Table 1.

2. 6. Antimicrobial Assay

The antibacterial activities of the hydrazone compounds and the vanadium complexes were tested against B. subtilis, S. aureus, E. coli, and P. fluorescence using MH (Mueller-Hinton) medium. The antifungal activities of the compounds were tested against C. albicans and A. niger using RPMI-1640 medium. The MIC values of the tested compounds were determined by a colorimetric method using the dye MTT.⁷ A stock solution of the compound (150 μ g mL⁻¹) in DMSO was prepared and graded quantities (75 μ g mL^{-1} , 37.5 μ g mL^{-1} , 18.8 μ g mL^{-1} , 9.4 μ g mL^{-1} , 4.7 μ g mL^{-1} , 2.3 μ g mL⁻¹, 1.2 μ g mL⁻¹, 0.59 μ g mL⁻¹) were incorporated in specified quantity of the corresponding sterilized liquid medium. A specified quantity of the medium containing the compound was poured into micro-titration plates. Suspension of the microorganism was prepared to contain approximately 1.0×10^5 cfu mL⁻¹ and applied to microtitration plates with serially diluted compounds in DMSO to be tested and incubated at 37 °C for 24 h and 48 h for bacterial and fungi, respectively. Then the MIC values were visually determined on each of the microtitration plates, 50 µL of PBS (phosphate buffered saline 0.01 mol L^{-1} , pH = 7.4) containing 2 mg of MTT mL⁻¹ was added to each well. Incubation was continued at room temperature for 4-5 h. The content of each well was removed and 100 µL of isopropanol containing 5% 1 M HCl was added to extract the dye. After 12 h of incubation at room temperature, the optical density was measured with a microplate reader at 550 nm.

3. Results and Discussion

3. 1. Chemistry

HL was synthesized from the reaction of pyridine-2-carboxaldehyde and 4-bromobenzohydrazide. The complexes were prepared by reaction of the hydrazone with cobalt nitrate and manganese bromide, respectively. Single crystals of the hydrazone and the complexes were obtained by slow evaporation of the methanolic solution of the compounds. Selected bond lengths and angles are given in Table 2. In both complexes the hydrazones are in deprotonated form. The elemental analyses values are in good agreement with the general formulae of the complexes. Molar conductivities of complexes 1 and 2 measured in

methanol at concentration of 10^{-3} mol L^{-1} are 127 and 32 Ω^{-1} cm² mol⁻¹, respectively, indicating the 1:1 electrolytic nature of **1** and non-electrolytic nature of **2**.8

Table 2. Selected bond lengths (Å) and angles (°) for the complexes

1			
Co1-N1	1.858(3)	Co1-N3	1.938(3)
Co1-N5	1.860(3)	Co1-N6	1.927(3)
Co1-O1	1.919(2)	Co1-O2	1.903(3)
N1-Co1-N3	82.79(12)	N1-Co1-N5	178.94(14)
N1-Co1-N6	97.79(13)	N1-Co1-O1	81.66(11)
N1-Co1-O2	97.58(12)	N5-Co1-N3	96.38(12)
N5-Co1-N6	82.90(13)	N5-Co1-O1	99.16(11)
N5-Co1-O2	81.74(12)	N6-Co1-N3	92.82(12)
O1-Co1-N3	164.43(11)	O1-Co1-N6	90.16(12)
O2-Co1-N3	90.15(12)	O2-Co1-N6	164.59(11)
O2-Co1-O1	91.02(11)		
2			
Mn1-O1	2.144(3)	Mn1-O2	2.133(3)
Mn1-N2	2.179(3)	Mn1-N5	2.205(3)
Mn1-N4	2.298(4)	Mn1-N1	2.362(4)
O2-Mn1-O1	104.52(12)	O2-Mn1-N2	121.25(12)
O1-Mn1-N2	71.89(12)	O2-Mn1-N5	70.93(12)
O1-Mn1-N5	127.79(12)	N2-Mn1-N5	156.08(13)
O2-Mn1-N4	140.41(11)	O1-Mn1-N4	90.64(12)
N2-Mn1-N4	98.12(12)	N5-Mn1-N4	70.93(12)
O2-Mn1-N1	92.71(12)	O1-Mn1-N1	142.55(11)
N2-Mn1-N1	70.75(13)	N5-Mn1-N1	89.09(12)
N4-Mn1-N1	96.89(12)		

3. 2. Structure Description of HL · MeOH

The molecular structure of $HL\cdot MeOH$ is shown in Figure 1. The asymmetric unit contains two HL molecules and two methanol molecules. The molecules of HL adopt E configuration with respect to the methylidene units. The distances of the methylidene bonds, 1.26 Å, confirm them as typical double bonds. The shorter distances of the C-N bonds and the longer distances of the C=O bonds for the -C(O)-NH- units than usual, suggest the presence of conjugation effects in the hydrazone molecules. The remaining bond lengths in the compound are within normal values. The dihedral angles between the pyridine and benzene rings are $35.6(5)^\circ$ and $12.2(5)^\circ$. The crystal structure of the compound is stabilized by intermolecular hydrogen bonds (Table 3, Figure 2).

3. 3. Structure Description of Complex 1

Molecular structure of complex 1 is shown in Figure 3. The compound contains a mononuclear cobalt(III) complex cation, a nitrate anion, and two water molecules of crystallization. The cobalt center exhibits a distorted octahedral geometry comprising two tridentate ligands coordinated in a meridional fashion and positioned very nearly perpendicularly to each other. The hydrazone li-

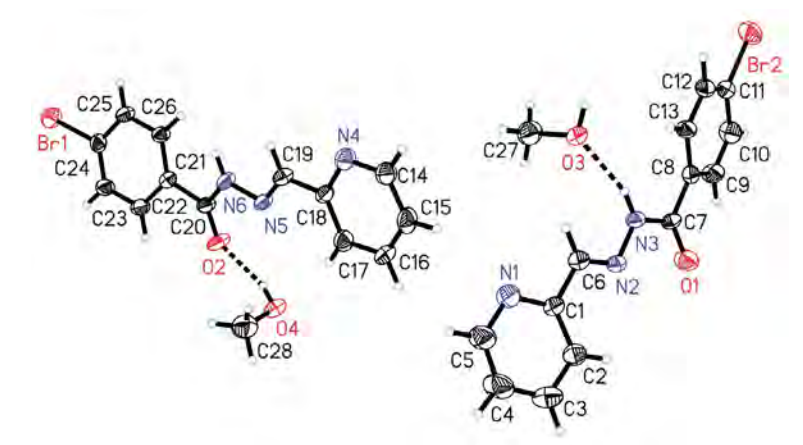


Figure 1. Molecular structure of HL, showing the atom-numbering scheme. Displacement ellipsoids for non-hydrogen atoms are drawn at 30% probability level.

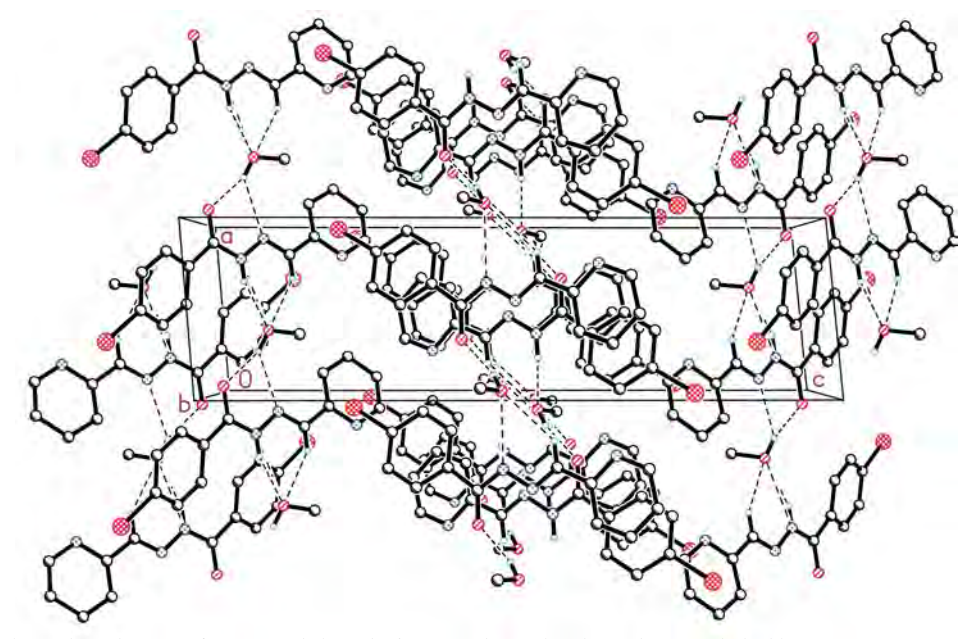


Figure 2. Molecular packing diagram of HL, viewed along the b axis. Hydrogen bonds are shown as dashed lines.

gands coordinate to the cobalt center through the pyridine nitrogen, imino nitrogen and enolate oxygens. The coordinate bond lengths in the complex are comparable to those observed in cobalt(III) complexes with hydrazone ligands. Close inspection of the bond distances reveals that the ligands have undergone keto-enol tautomerization. The deprotonation of the ligands enhances the delocalization of electrons across the ligand framework and increases the basicity of the imine nitrogen and pyridine nitrogen. Like most six-coordinate Schiff base complexes, the imine nitrogens in the complex coordinate to the cobalt center in *trans* positions, while the pyridine nitrogens and enolate oxygens occupy *cis* positions.

In the crystal structure of the compound, the complex molecules are linked by nitrate anions and water molecules through intermolecular hydrogen bonds (Table 3), to form a three-dimensional network (Figure 4).

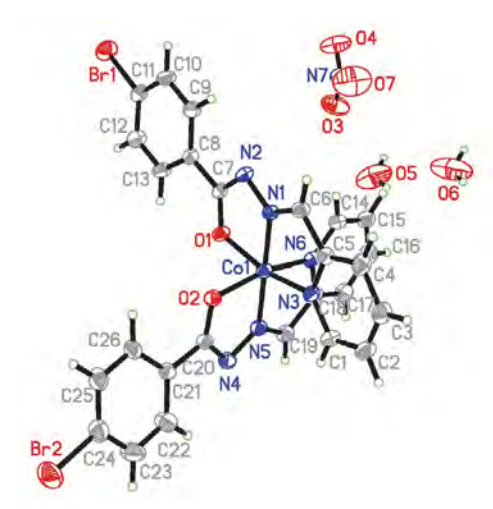


Figure 3. Molecular structure of 1, showing the atom-numbering scheme. Displacement ellipsoids are drawn at 30% probability level.

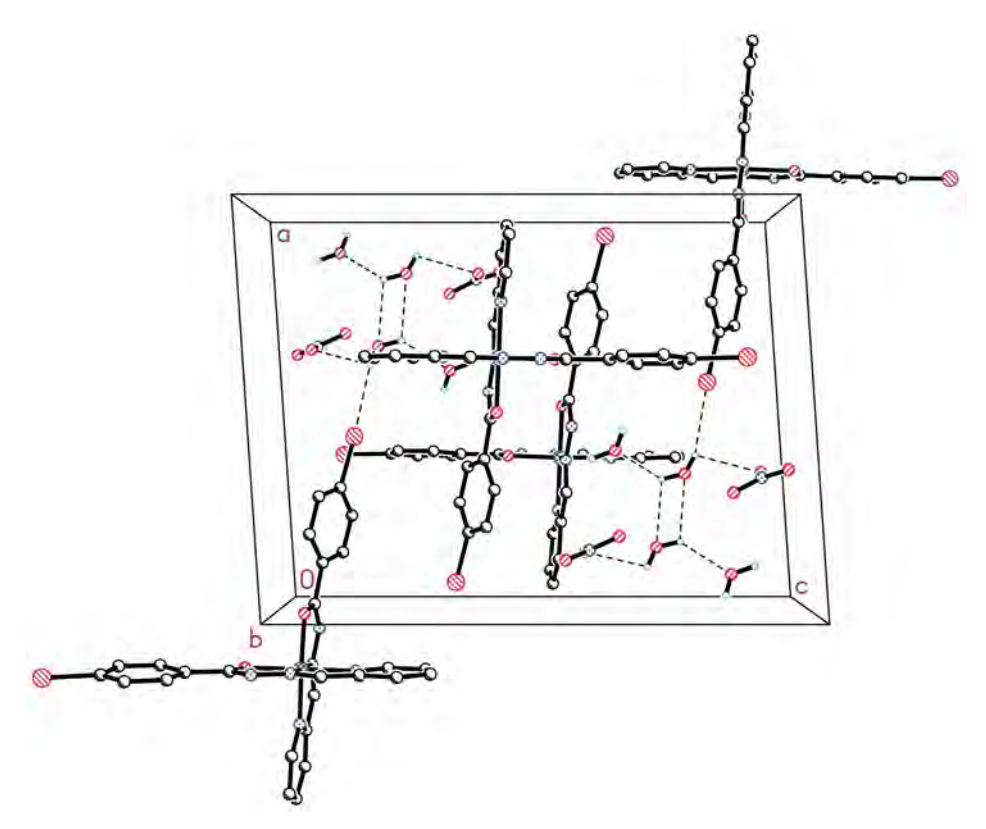


Figure 4. Molecular packing diagram of complex 1, viewed along the b axis. Hydrogen bonds are shown as dashed lines.

3. 4. Structure Description of Complex 2

Molecular structure of complex 2 is shown in Figure 5. The manganese center exhibits a distorted octahedral geometry comprising two tridentate ligands coordinated in a meridional fashion and positioned very nearly perpendicularly to each other. The hydrazone ligands coordinate to the manganese center through the pyridine nitro-

gen, imino nitrogen and enolate oxygens. The coordinate bond lengths in the complex are comparable to those observed in manganese(II) complexes with hydrazone ligands. Close inspection of the bond distances reveals that the ligands have undergone keto-enol tautomerization. The deprotonation of the ligands enhances the delocalization of electrons across the ligand framework and increases the basicity of the imine nitrogen and pyridine

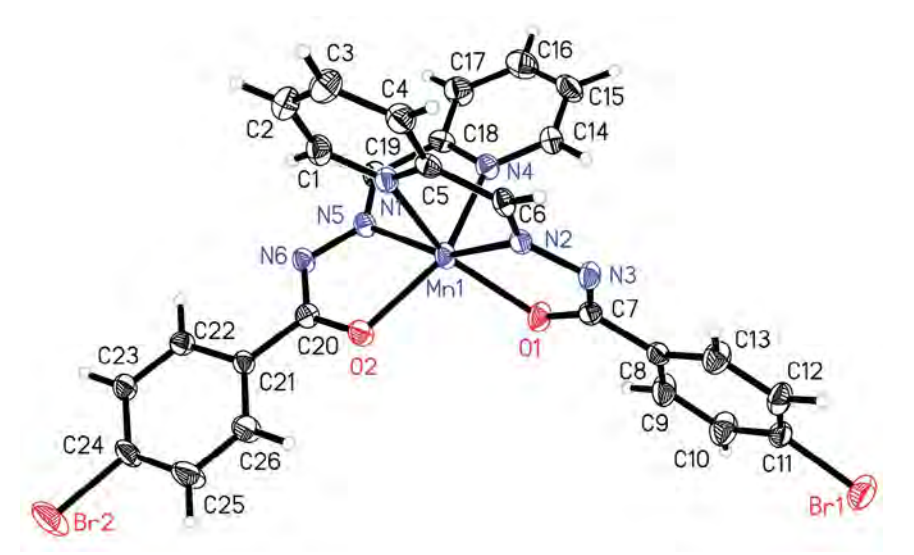


Figure 5. Molecular structure of 2, showing the atom-numbering scheme. Displacement ellipsoids for non-hydrogen atoms are drawn at 30% probability level.

D-H···Ad(D-H) $d(H \cdot \cdot \cdot A)$ $d(D \cdots A)$ Angle $(D-H\cdots A)$ HL. O3-H3B...N2i 0.85(1)2.48(4)3.127(5)133(5)O3-H3B...O1i 0.85(1)1.99(3)2.775(5)151(5) O4-H4A...O2 1.97 2.767(4)0.82 164(5) N6-H6--O4i 2.06 0.86 2.873(5)156(5)N3-H3--O3 0.86 2.05 2.884(5)162(5) O5-H5B···Br2ii 0.85 2.75 3.346(5)129(5)O5-H5B...O3iii 0.85 2.50 2.924(7)112(5) O5-H5A...O6 0.85 2.42 3.031(12) 129(6)

Table 3. Hydrogen bond distances (Å) and bond angles (°) for the compounds

Symmetry codes: (i) 1 + x, y, z; (ii) -1 + x, y, z; (iii) 1 - x, 1 - y, 1 - z.

nitrogen. Like most six-coordinate Schiff base complexes, the imine nitrogens in the complex coordinate to the manganese center in *trans* positions, while the pyridine nitrogens and enolate oxygens occupy *cis* positions.

3. 5. Spectroscopic Studies

The moderate broad bands at 3230 and 3300-3500 cm⁻¹ in the IR spectra of HL and complex 1 are ascribed to the stretching vibrations of N-H and O-H, respectively. Characteristic band of v(C=O) at 1653 cm⁻¹ for the free ligand HL is an indication of the keto-form in the solid state. For the complexes the absorption bands due to v(NH) stretching and the amide band v(C=O) were absent, indicating that the ligands are coordinated in the enolate form.¹² The C=N bonds are represented by intense bands centered at 1588 and 1585 cm⁻¹ for complexes 1 and 2, respectively.¹³ In addition, complex 1 shows an intense band at 1383 cm⁻¹, in agreement with the ionic nitrate.¹⁴ The electronic spectra of HL and the complexes show bands centered at 290–340 nm, due to the $n-\pi^*$ transition of the C=N-NH-CO chromophore. The charge transfer LMCT bands are located in the range 360-390 nm.¹⁵

3. 6. Antimicrobial Activity

The hydrazone HL and the complexes were screened for antibacterial activities against two Gram (+) bacterial strains (*Bacillus subtilis* and *Staphylococcus aureus*) and two Gram (–) bacterial strains (*Escherichia coli* and *Pseudomonas fluorescence*) by MTT method. The MIC (minimum inhibitory concentration, μg mL⁻¹) values of the compounds against four bacteria are listed in Table 4. Penicillin G was used as the standard drug. The hydrazone HL shows medium activities against the bacteria *B. subtilis* and *S. aureus*, and no activity against *E. coli* and *P. fluorescence*. The two complexes, in general, have stronger activities than the free hydrazone. Complex 1 has strong activity against *B. subtilis*, *S. aureus* and *E. coli*, and weak activity against *P. fluorescence*. Complex 2 has strong ac-

tivity against *B. subtilis* and *E. coli*, medium activity against *S. aureus*, and weak activity against *P. fluorescence*. However, both hydrazone and the two complexes have no activity against the two fungal strains (*Candida albicans* and *Aspergillus niger*). It is interesting that complex 1 has even stronger activity against the four bacteria than penicillin *G*.

Table 4. Antimicrobial activities of the compounds

Minimum inhibitory concentrations (μg · mL ⁻¹)							
Tested material	B. subtilis	S. aureus	E. coli	P. fluorescence			
HL	18.8	37.5	> 150	> 150			
1	1.2	2.3	4.7	37.5			
2	4.7	18.8	9.4	37.5			
Penicillin G	2.3	4.7	>150	>150			

4. Conclusion

In summary, a new hydrazone compound 4-bromo-N-(pyridin-2-ylmethylene)benzohydrazide and its two new cobalt(III) and manganese(II) complexes were prepared and structurally characterized. The metal centers are in octahedral geometry. Both complexes have interesting antibacterial activities. The cobalt complex has MIC values of 1.2 and 2.3 μ g mL⁻¹ against B. subtilis and S. aureus, respectively, which are even better than penicillin G. Further work is required to be carried out to explore new and efficient antibacterial drug based on the present models.

5. Supplementary Data

CCDC 1812949 (HL), 1547397 (1) and 1547398 (2) contain the supplementary crystallographic data for this paper. These data can be obtained free of charge *via* http://www.ccdc.cam.ac.uk/conts/retrieving.html, or from the

Cambridge Crystallographic Data Centre, 12 Union Road, Cambridge CB2 1EZ, UK; fax: (+44) 1223-336-033; or e-mail: deposit@ccdc.cam.ac.uk.

6. References

- (a) Z. A. Kaplancikli, M. D. Altintop, A. Ozdemir, G. Turan-Zitouni, G. Goger, F. Demirci, *Lett. Drug Des. Discov.* 2014, 11, 355–362. DOI:10.2174/15701808113109990030
 - (b) R. Narisetty, K. B. Chandrasekhar, S. Mohanty, B. Balram, *Lett. Drug Des. Discov.* **2013**, *10*, 620–624.

DOI:10.2174/1570180811310070009

(c) F. Zhi, N. Shao, Q. Wang, Y. Zhang, R. Wang, Y. Yang, J. Struct. Chem. 2013, 54, 148–154.

DOI:10.1134/S0022476613010216

- (d) A. Ozdemir, G. Turan-Zitouni, Z. A. Kaplancikli, F. Demirci, G. Iscan, *J. Enzyme Inhib. Med. Chem.* **2008**, *23*, 470–475. **DOI:**10.1080/14756360701709094
- (e) C. Loncle, J. M. Brunel, N. Vidal, M. Dherbomez, Y. Letourneux, *Eur. J. Med. Chem.* **2004**, *39*, 1067–1071.

DOI:10.1016/j.ejmech.2004.07.005

- (f) Y.-C. Liu, H.-L. Wang, S.-F. Tang, Z.-F. Chen, H. Liang, *Anticancer Res.* **2014**, *34*, 6034–6035.
- (g) P. Krishnamoorthy, P. Sathyadevi, A. H. Cowley, R. R. Butorac, N. Dharmaraj, *Eur. J. Med. Chem.* **2011**, *46*, 3376–3387. **DOI**:10.1016/j.ejmech.2011.05.001
- (a) M. Gomleksiz, C. Alkan, B. Erdem, Bull. Chem. Soc. Ethiop. 2013, 27, 213–220.
 - (b) L. A. Saghatforoush, F. Chalabian, A. Aminkhani, G. Karimnezhad, S. Ershad, *Eur. J. Med. Chem.* **2009**, *44*, 4490–4495. **DOI**:10.1016/j.ejmech.2009.06.015
 - (c) D. P. Singh, K. Kumar, C. Sharma, Eur. J. Med. Chem. 2009, 44, 3299-3304.

DOI:10.1016/j.ejmech.2009.02.029

(d) S. Mandal, A. K. Rout, A. Ghosh, G. Pilet, D. Bandyopadhyay, *Polyhedron* **2009**, *28*, 3858–3862.

DOI:10.1016/j.poly.2009.08.034

- (e) R. Vafazadeh, N. Abdollahi, A. C. Willis, *Acta Chim. Slov.* **2017**, *64*, 409–414. **DOI**:10.17344/acsi.2017.3263
- (f) D.-L. Peng, N. Sun, *Acta Chim. Slov.* **2018**, *65*, 895–901. **DOI**:10.17344/acsi.2018.4543
- 3. (a) Z.-C. Liu, B.-D. Wang, Z.-Y. Yang, Y. Li, D.-D. Qin, T.-R. Li, Eur. J. Med. Chem. **2009**, 44, 4477–4484.

DOI:10.1016/j.ejmech.2009.06.009

(b) M. J. Hearn, M. H. Cynamon, M. F. Chen, R. Coppins, J. Davis, H. J.-O. Kang, A. Noble, B. Tu-Sekine, M. S. Terrot, D. Trombino, M. Thai, E. R. Webster, R. Wilson, *Eur. J. Med. Chem.* **2009**, *44*, 4169–4178.

DOI:10.1016/j.ejmech.2009.05.009

- (c) L.-Y. He, X.-Y. Qiu, J.-Y. Cheng, S.-J. Liu, S.-M. Wu, *Polyhedron* 2018, *156*, 105–110. DOI:10.1016/j.poly.2018.09.017
 (d) W. Cao, Y. M. Liu, T. Zhang, J. P. Jia, *Polyhedron* 2018, *147*, 62–68. DOI:10.1016/j.poly.2018.03.012
- (a) M. Zhang, D.-M. Xian, H.-H. Li, J.-C. Zhang, Z.-L. You, Aust. J. Chem. 2012, 65, 343–350. DOI:10.1071/CH11424

(b) L. Shi, H.-M. Ge, S.-H. Tan, H.-Q. Li, Y.-C. Song, H.-L. Zhu, R.-X. Tan, *Eur. J. Med. Chem.* **2007**, *42*, 558–564.

DOI:10.1016/j.ejmech.2006.11.010

(c) N. P. Rai, V. K. Narayanaswamy, T. Govender, B. K. Manuprasad, S. Shashikanth, P. N. Arunachalam, *Eur. J. Med. Chem.* **2010**, *45*, 2677–2682.

DOI:10.1016/j.ejmech.2010.02.021

- 5. Bruker, SMART (Version 5.625) and SAINT (Version 6.01). Bruker AXS Inc., Madison, Wisconsin, USA, 2007.
- 6. G. M. Sheldrick, SHELXTL V5.1 Software Reference Manual, Bruker AXS, Inc., Madison, Wisconsin, USA, 1997.
- J. Meletiadis, J. F. G. M. Meis, J. W. Mouton, J. P. Donnelly, P. E. Verweij, *J. Clin. Microbiol.* 2000, 38, 2949–2954.
- W. J. Geary, Coord. Chem. Rev. 1971, 7, 81–122.
 DOI:10.1016/S0010-8545(00)80009-0
- (a) F. Zhi, N. Shao, Q. Wang, Y. Zhang, R. Wang, Y. Yang, J. Struct. Chem. 2013, 54, 148–154.

DOI:10.1134/S0022476613010216

- (b) X. L. Wang, Z. L. You, C. Wang, J. Chem. Crystallogr. 2011, 41, 621–624.
- (c) J. Xu, T. Zhou, Z. Q. Xu, X. N. Gu, W. N. Wu, H. Chen, Y. Wang, L. Jia, T. F. Zhu, R. H. Chen, *J. Mol. Struct.* **2017**, *1128*, 448–454. **DOI**:10.1016/j.molstruc.2016.09.016
- (a) C. Jing, C. Wang, K. Yan, K. Zhao, G. Sheng, D. Qu, F. Niu, H. Zhu, Z. You, *Bioorg. Med. Chem.* **2016**, *24*, 270–276.
 DOI:10.1016/j.bmc.2015.12.013
 - (b) T. Yang, F. Niu, L. X. Li, Z. N. Xia, Y. Zhang, Z. L. You, Russ. J. Coord. Chem. 2016, 42, 402–409.

DOI:10.1134/S1070328416050109

 (a) Z.-L. You, T. Liu, N. Zhang, M. Zhang, D.-M. Xian, H.-H. Li, *Inorg. Chem. Commun.* 2012, 19, 47–50.

DOI:10.1016/j.inoche.2012.01.034

(b) W. Li, Y. Lu, X.-F. Li, Z. You, *Synth. React. Inorg. Met.-Org. Nano-Met. Chem.* **2012**, *42*, 92–97.

DOI:10.7312/li--16274-043

12. (a) M. F. Iskander, T. E. Khalil, R. Werner, W. Haase, I. Svoboda, H. Fuess, *Polyhedron* **2000**, *19*, 1181–1191.

DOI:10.1016/S0277-5387(00)00366-1

(b) Y. Li, L. Xu, M. Duan, J. Wu, Y. Wang, K. Dong, M. Han, Z. You, *Inorg. Chem. Commun.* **2019**, *105*, 212–216.

DOI:10.1016/j.inoche.2019.05.011

(a) R. N. Patel, S. P. Rawat, M. Choudhary, V. P. Sondhiya, D. K. Patel, K. K. Shukla, D. K. Patel, Y. Singh, R. Pandey, *Inorg. Chim. Acta* 2012, 392, 283–291.

DOI:10.1016/j.ica.2012.03.040

(b) L. Xu, Y. Li, M. Duan, Y. Li, M. Han, J. Wu, Y. Wang, K. Dong, Z. You, *Polyhedron* **2019**, *165*, 138–142.

DOI:10.1016/j.poly.2019.03.016

 M. F. Iskander, T. E. Khalil, R. Werner, W. Haase, I. Svoboda, H. Fuess, *Polyhedron* 2000, 19, 949–958.

DOI:10.1016/S0277-5387(00)00340-5

(a) A. Ray, C. Rizzoli, G. Pilet, C. Desplanches, E. Garribba,
 E. Rentschler, S. Mitra, *Eur. J. Inorg. Chem.* **2009**, 2915–2928.
 DOI:10.1002/ejic.200900188

(b) S. Das, S. Pal, J. Mol. Struct. 2005, 753, 68-79.

DOI:10.1016/j.molstruc.2005.05.037

Povzetek

Sintetizirali smo nov hidrazon 4-bromo-N'-(piridin-2-ilmetilen)benzohidrazid (HL) in njegov kobaltov(III) ter manganov(II) kompleks, $[CoL_2]NO_3 \cdot 2H_2O$ (1) in $[MnL_2]$ (2). Spojine smo okarakterizirali z različnimi fizikalno-kemijskimi metodami. Strukture so bile potrjene z rentgensko monokristalno analizo. Koordinacijska geometrija okoli kobaltovega atoma v kompleksu 1 in manganovega atoma v kompleksu 2 je oktaerična z dvema piridinskima N atomoma, dvema imino N atomoma in dvema enolatnima O atomoma hidrazonskega liganda. Protibakterijske (*Bacillus subtilis, Staphylococcus aureus, Escherichia coli, Pseudomonas fluorescence*) in protimikotične (*Candida albicans* in *Aspergillus niger*) lastnosti vseh treh spojin smo testirali z MTT (3-(4,5-dimetiltiazol-2-il)-2,5-difeniltetrazolijev bromid) metodo.



Except when otherwise noted, articles in this journal are published under the terms and conditions of the Creative Commons Attribution 4.0 International License

Scientific paper

Anion Modulated Structural Variations in Copper(II) Complexes with a Flexidentate Ligand Derived from 2-((2-Aminoethyl)Amino)Ethan-1-ol: Synthesis and Spectroscopic and X-ray Structural Characterization

Rasoul Vafazadeh,1,* Abolghasem Kazemi-nasab1 and Anthony C. Willis2

¹ Department of Chemistry, Yazd University, Yazd, Iran

² Research School of Chemistry, Australian National University, Canberra, ACT 2601, Australia

* Corresponding author: E-mail: rvafazadeh@yazd.ac.ir Tel: +98 351 8214778; Fax: +98 351 7250110

Received: 06-17-2019

Abstract

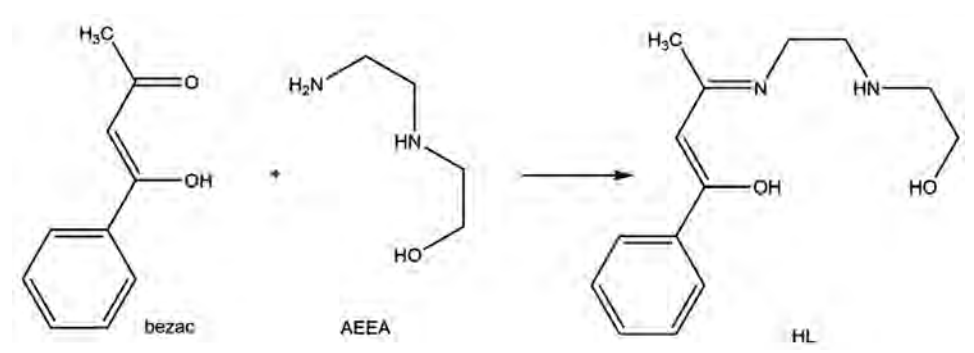
Flexidentate ligand, HL has been prepared by the condensation of aminoethylethanolamine (AEEA) with benzoylacetone (bezac). On reaction with copper(II) salts it gives complexes $CuLClO_4.H_2O$ (1), $CuLN_3$ (2) and $[Cu_3L_3Br]Br_2 \cdot H_2O$ (3). All complexes have been characterized by X-ray crystallography. The results show that the hydroxyl group of the flexidentate ligand can coordinate to the Cu(II) center or remain as an uncoordinated group. In (1), the coordination number around the copper(II) ion is five coordinated and the ligand is tetradentate with the OH group coordinated to the copper(II) ion. Complex (2) has a square planar geometry and the L^- ligand is tridentate with the hydroxyl group left uncoordinated. The X-ray diffraction analysis of the trinuclear complex (3) shows that the copper(II) centers are five-coordinate and L^- is a tetradentate ligand with the hydroxyl group being both terminal and bridging. The Hirshfeld surface analysis and the 2D fingerprint plot were used to analyze all of the intermolecular contacts in the crystal structures.

Keyword: Flexidentate ligand; hydroxyl group; hirshfeld surface; fingerprint plot; tridentate; tetradentate

1. Introduction

The design and synthesis of new transition metal complexes with polynuclating ligands, which represent themselves as potential chelating ligands with more than set of donor atoms, have been of interest for many years.^{1–7} The ability of transition metal ions to bond to possible co-

ordination sites of these ligands depends on the type of the metal ion, the donor atoms of the ligand, the flexibility of the ligand and the counter-anions used. The term "flexidentate" is used to describe the coordination behavior of this type of ligand. Complexes of the transition metal with Schiff base ligands derived from amine-alcohols are



Scheme 1. Synthesis of the flexidentate ligand

probably the best know examples of this. In these compounds, the hydroxyl group coordinates to the metal ions when the other coordination sites of the metal are weakly coordinated (e,g. ClO_4^- and halogens), but the hydroxyl group remains as an uncoordinated OH group when the other coordination sites of the metal ions are occupied by strongly coordinating groups (for example N_3^-). $^{13-17}$

Herein we report the synthesis, spectral characterization and crystal structure of several new copper(II) complexes formed by the reaction of the flexidentate Schiff base ligand aminoethyl ethanolamine benzoylacetone, HL (scheme 1), with Cu(II) in the presence of several counter anions. The Schiff base ligand was obtained by condensation of 2-((2-aminoethyl)amino)ethan-1-ol (aminoethylethanolamine, AEEA) and benzoylacetone (bezac). This flexidentate ligand can be tridentate or tetradentate with copper(II), depending on the coordinating abilities of the other ligands which are present; the hydroxyl group of this ligand may coordinate to Cu(II) or may remain uncoordinated.

2. Experimental Section

2. 1. Starting Materials

All chemicals were of analytical reagent grade and were used without further purification.

Caution! Azide salt is potentially explosive. Only small amounts should be used and it should be handled with great care.

2. 2. Physical Measurements

Infrared spectra were taken with an Equinox 55 Bruker FT-IR spectrometer using KBr pellets in the 400–4000 cm⁻¹ range. Absorption spectra were determined using methanol and dimethylformamide (DMF) solutions in a GBC UV-Visible Cintra 101 spectrophotometer with a 1 cm quartz cell, in the range 200–800 nm. Elemental analyses (C, H, N) were performed by using a CHNS-O 2400II PERKIN-ELMER elemental analyzer.

2. 3. X-ray Crystallography

Diffraction images were measured at 150 K on an Agilent SuperNova diffractometer using Cu Ka (λ = 1.54180 Å) radiation. Data were extracted using the Crys-Alis PRO package. The structures were solved by direct methods with the use of SIR92. The structures were refined on F² by full matrix last-squares techniques using the CRYSTALS program package. Atomic coordinates, bond lengths and angles and displacement parameters have been deposited at the Cambridge Crystallographic Data Centre. The H atoms were initially refined with soft re-

Table 1. Crystallographic data of the complexes 1-3

Compound	1	2	3
Chemical formula	C ₁₄ H ₂₁ ClCu ₄ N ₂ O ₇	C ₁₄ H ₁₉ CuN ₅ O ₂	C ₄₂ H ₅₉ Br ₃ Cu ₃ N ₆ O ₇
Formula weight	428.33	352.88	1190.31
Temperature (K)	150	150	150
Space group	Monoclinic, $P2_1/n$, $Z = 4$	orthorhombic, $Pbca$, $Z = 8$	Monoclinic, $P2_1/n$, $Z = 4$
Unit cell dimensions			
a (Å)	10.2326 (2)	7.2877 (1)	12.2525 (1)
b (Å)	13.2639 (2)	18.1046 (1)	25.5177 (2)
c (Å)	13.1667 (2)	22.1217 (2)	16.5499 (1)
α (°)	90	90	90
β (°)	103.6655 (14)	90	90.0015 (6)
γ (°)	120	90	90
$V(Å^3)$	1736.45 (5)	1178.85 (3)	4566.09 (6)
F(000)	844	1464	2404
D _{Calc} (g cm ⁻³)	1.638	1.606	1.731
Crystal size (mm)	$0.26 \times 0.08 \times 0.06 \text{ mm}$	$0.28 \times 0.06 \times 0.06 \text{ mm}$	$0.30 \times 0.16 \times 0.03 \text{ mm}$
$\mu (mm^{-1})$	3.56	2.25	5.15
θ range (°)	5–73	3–74	3–74
Limiting indices	$-12 \le h \le 11$	$-7 \le h \le 8$	$-15 \le h \le 15$
ū	$-16 \le k \le 16$	$-22 \le k \le 22$	$-24 \le k \le 27$
	$-16 \le l \le 16$	$-27 \le l \le 27$	$-20 \le l \le 20$
$R[F2 > 2\sigma(F2)]$	0.034	0.032	0.0399
wR(F2) (all data)	0.087^{*}	0.087**	0.111***

 $\begin{tabular}{l} $^*w = 1/[\sigma^2(F^2) + (0.05P)^2 + 1.84P], where $P = (max(F_o^2,0) + 2F_c^2)/3$ $^{**w} = 1/[\sigma^2(F^2) + (0.06P)^2 + 1.89P]$, where $P = (max(F_o^2,0) + 2F_c^2)/3$ **m method Chebychev polynomial, [weight] $= 1.0/[A_o^*T_0(x) + A_1^*T_1(x) ... + (A_{n-1})^*T_{n-1}(x)]$, method Robust weighting, $W = [weight]^*[1-(deltaF/6^*sigmaF)^2]^2$ where $A_i = 0.165E + 04 \ 0.171E + 04 \ 708.155$ and $x = F/F_{max}$ $= 1/[A_n^*T_0(x) + A_1^*T_0(x)]$.} \label{eq:max_polynomial}$

straints on the bond lengths and angles to regularize their geometry (C—H in the range 0.93–0.98 Å, N—H = 0.87 Å, O—H = 0.82 Å) and with $U_{\rm iso}(H)$ in the range 1.2–1.5 times $U_{\rm eq}$ of the parent atom. After this, the positions of the H atoms bonded to O and N were refined without constraints whereas those bonded to C ride on the atoms to which they are bonded. Crystallographic data and refinement details for the complexes are given in Table 1.

2. 4. Synthesis of the Schiff-base Ligand Aminoethylethanolaminebenzoylacetone (HL).

The flexidentate Schiff base HL was synthesized by a general method using the condensation reaction of aminoethylethanolamine (1 mmol, 0.10 ml) and benzoylacetone (1 mmol, 0.162 g) in methanol medium (30 mL) under reflux for 2 hours. 21,22 The bright yellow solution containing the Schiff base ligand (HL) was used for synthesis of the complexes without further purification. The IR spectrum of the HL ligand shows a characteristic strong band at 1580 cm $^{-1}$, which is assigned as $\nu C=N$.

2. 5. Synthesis of Copper(II) Complexes

 $\text{CuX}_2.\text{nH}_2\text{O}$, (X = ClO_4 , n = 6, 0.370 g, 1; X = NO_3 , n = 3, 0.242 g, 2 and; X = Br, n = 0, 0.223 g, 3), (1 mmol) was added to a solution of the ligand HL, aminoethylethanol-aminebenzoylacetone (1 mmol) in methanol (30 mL) and the resulting solution was stirred at room temperature for 2 h. The solution's color turned green. For complex 2, after 2 h of continuous stirring of the copper(II) nitrate trihydrate and ligand solution, finely powdered sodium azide (0.065 g, 1.0 mmol) was added to the solution and stirring was continued for a further 2 h.

CuLClO₄.H₂O, 1. The solution was filtered and the clear green filtrate was kept in a beaker to allow slow evaporation of the solvent. A solid green powder was obtained. Dark-green prismatic crystals suitable for X-ray crystallography were obtained from methanol / cyclohexane (3:1 v/v) and were filtered, washed with cold ethanol and dried in the air. Yield: 72%. Anal. Calc. for $C_{14}H_{21}ClCuN_2O_7$: C, 39.26; H, 4.94; N, 6.54%. Found: C, 39.48; H, 4.99; N, 6.60%. IR (KBr, v_{max}/cm^{-1}) bands: 1555, and 1061. UV-Vis, $λ_{max}$ (methanol)/nm: 577 (log ε, 1.88), 281 (4.20) and 211 (4.57).

 CuLN_3 , 2. Stirring was continued for 2 h after addition of sodium azide, The solution was filtered and the filtrate was left aside for crystallization. Dark-green prism crystals suitable for X-ray diffraction appeared at the bottom of the vessel upon slow evaporation of the solvent at room temperature, and were collected by filtration, washed with cold ethanol and dried in the air. Yield: 82%. Anal. Calc. for $C_{14}H_{19}CuN_5O_2$: C, 47.65; H, 5.43; N, 19.85%. Found:

C, 47.73; H, 5.60; N, 19.42%. IR (KBr, v_{max}/cm^{-1}) bands: 2043 and 1556. UV-Vis, λ_{max} (dimethylformamide, DMF)/nm: 567 (log ϵ , 2.19) and 326 (3.18).

[Cu₃L₃Br]Br₂·H₂O, 3. The solution was filtered and the clear green filtrate was kept in a beaker to allow slow evaporation of the solvent. A solid green powder was obtained. Green crystals suitable for X-ray crystallography were obtained from dichloromethane /2-propanol (3:1 v/v) in an open beaker and were filtered, washed with cold ethanol and dried in the air. Yield: 48%. Anal. Calc. for C₄₂H-₅₉Br₃Cu₃N₆O₇: C, 42.38; H, 5.00; N, 7.06%. Found: C, 42.13; H, 5.01; N, 7.01%. IR (KBr, v_{max}/cm^{-1}) band: 1552. UV-Vis, λ_{max} (methanol)/nm: 567 (log ε, 2.58) and 346 (3.70).

Many attempts made to synthesize the CuLX (X= NO₃, Cl, 0.5 SO₄) complexes failed and the sole product isolated from the preparative mixtures was the Cu(bezac)₂ complex which was identified by the X-Ray structure (see Fig. S1).

3. Results and Discussion

3. 1. Synthesis and Characterization of the Complexes

The flexidentate Schiff base HL was obtained by the in-situ condensation of aminoethylethanolamine and benzoylacetone under reflux in methanol solvent. Reactions of appropriate copper(II) salts with an equimolar amount of the ligand HL in methanol solution led to the formation of complexes 1-3. The Schiff base HL can adopt both chelating and bridging modes. The ligand undergoes deprotonation during the reaction and the anionic form of the ligand L^- , coordinates to the metal center.

In the mononuclear CuLClO₄ complex 1, which was formed from copper(II) perchlorate, L⁻ acts as a tetradentate ligand. In mononuclear CuLN₃ complex 2 which was obtained with copper(II) nitrate in the presence of N_3^- . L⁻ act as a tridentate ligand. On the other hand, reaction of HL with CuBr₂ leads to the formation of a trinuclear copper(II) complex where L- acts as a tetradentate ligand with the ligand adopting both chelating and bridging modes (vide infra). However, the green solutions which were obtained by the reaction of HL with Cu(NO₃)₂, CuCl₂ or CuSO₄ contain the Cu(bezac)₂ complex, showing that HL underwent hydrolysis under the same conditions. This complex was characterized by elemental analyses and X-Ray crystallography (SI). Cu(bezac)₂ has been reported previously and can be obtained by directed reaction of Cu(CH₃COO)₂ and benzoylacetone in methanol medium.²³

The IR spectrum of the free HL ligand shows a band at 1580 cm⁻¹, which is assigned as ν C=N. In free Schiff base ligands the frequency of the hydroxyl group (phenol

and alcohol) is observed in the 3200–3400 cm⁻¹ region, due to intramolecular hydrogen bonding between OH and the nitrogen atoms of the ligand. The IR spectra of complexes **1–3** show a decrease in vC=N of about 25 cm⁻¹ in comparison with the free ligand, which indicates coordination of the imine nitrogen atom to the copper ion.^{24–26} Complex **1**, [CuLClO₄], shows strong bands at 1061 cm⁻¹ corresponding to stretching frequencies of the perchlorate group.²⁷ The IR spectra of the complex **2** exhibit a band about 2043 cm⁻¹, which is characteristic of a coordinated azide group ligand.²⁷

3. 2. Crystal Structures

3. 2. 1. Description of the Complex 1

Single crystals of complex 1 suitable for X-ray were obtained from a solution of 1 in methanol/cyclohexane. The complex crystallizes in the monoclinic space group $P2_1/n$. The molecular structure of the complex with labeling of selected atoms is shown in Fig. 1. Selected bond lengths and angles are listed in Table 2. The molecular structure shows that the copper(II) ion is five coordinated. L⁻ acts as a N₂O₂ tetradentate ligand which forms two five-membered and one six-membered chelate rings with the Cu(II) metal center with the hydroxyl group coordinated to the metal ion. The fifth position at the Cu ion is occupied by an O atom of the ClO₄ anion. There is disorder in the packing of the ligand over two positions, which have relative occupancies of 85%:15%. In Fig.1, the molecular structure of the complex shows only the major position for each disordered atom, while Fig. S2 shows both positions of the disordered atoms.

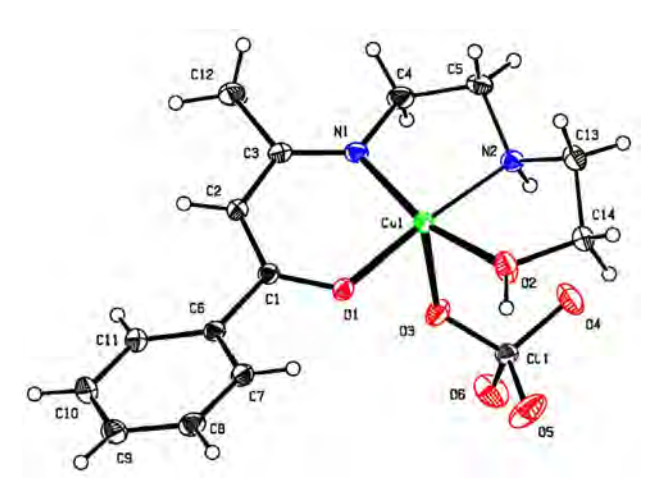


Fig. 1. The molecular structure of $[CuL(ClO_4)]$, 1 with labeling of selected atoms.

The coordination geometry about the copper ion is close to square pyramidal with the Addison parameters $\tau = 0.19$. τ is defined as $\tau = (a-b)/60$, (a > b), where a and b are the two largest angles around the Cu center; $\tau = 1$ for a regular trigonal bipyramid and $\tau = 0$ for a regular square

pyramid.²⁸ According to the bond lengths between the copper and the coordinating atoms (i.e., four bonds with short distances of 1.8935(14)–2.004(2) Å and one bond with a long distance of 2.5173(16) Å) the square base consists of the N2 O2 donors from the flexidentate Schiff base ligand and the apical position is occupied by the oxygen atom from the perchlorate anion and has the longer Cu–O distance. The Cu–O and Co–N bond lengths are in good agreement with analogous Cu(II) complexes previously reported.^{21, 29, 30} The copper atom is displaced from the basal plane of N2O2 by 0.063 Å towards the apical oxygen atom.

The NH amine of Schiff base ligand plays a role in the H bonding network with there being an intramolecular hydrogen bond between the hydrogen atom H1 of the amine with the oxygen atom O4 of the perchlorate anion. Also, there are intramolecular hydrogen bonds between

Table 2. Selected bond lengths (Å) and angles (°) in complexes 1-3

Complex 1			
Cu1-O1	1.894(1)	O1-Cu1-O2	94.36 (6)
Cu1-O2	1.967(2)	O1-Cu1-O3	89.76 (6)
Cu1-O3	2.517(2)	O2-Cu1-O3	99.33 (7)
Cu1-N1	1.911(2)	O1-Cu1-N1	97.09 (7)
Cu1-N2	2.004(2)	O2-Cu2-N1	163.74 (7)
Cu1-N92	2.013 (8)	O1-Cu2-N2	175.08 (8)
Cl1-O3	1.439(2)	O3-Cl1-O6	109.9(1)
Cl1-O6	1.417 (2)	O4-Cl1-O6	109.5 (1)
Complex 2			
Cu1-O1	1.918 (1)	O1-Cu1-N1	93.10 (5)
Cu1-N1	1.940(1)	N1-Cu1-N2	85.25 (6)
Cu1-N2	2.036(1)	N2-Cu1-N3	92.45 (6)
Cu1-N3	1.988 (2)	O1-Cu1-N2	177.68 (6)
O1-C1	1.303(2)	N1-Cu1-N3	167.70 (7)
O2-C14	1.413(2)	Cu1-N3-N4	118.3 (1)
N3-N4	1.195 (2)	N3-N4-N5	176.9 (2)
N4-N5	1.160(2)		
Complex 3			
Cu1-O1	1.887 (2)	O1-Cu1-O2	91.28 (8)
Cu1-O2	2.029(2)	N1-Cu1-N2	86.90 (9)
Cu1-O22	2.508(2)	O2-Cu1-N2	84.55 (9)
Cu1-N2	1.988 (2)	O1-Cu1-N2	175.75 (9)
Cu1-N1	1.905(2)	O2-Cu1-O22	90.07 (7)
Cu2-O21	1.906(2)	N21-Cu2-O22	107.61 (8)
Cu2-O22	2.380(2)	O21-Cu2-O22	98.10 (8)
Cu2-N21	1.948 (2)	O21-Cu2-Br1	159.86 (7)
Cu2-N22	2.017(2)	O21-Cu2-N22	173.2(1)
Cu2-Br1	2.463 (5)	O22-Cu2-Br1	91.85 (5)
Cu3-O31	1.842 (2)	O32-Cu3-N32	84.2 (1)
Cu3-O32	2.008(2)	O31-Cu3-N32	172.7(1)
Cu3-N31	1.910(2)	O31-Cu3-O32	92.04 (8)
Cu3-N32	1.985 (2)	N31-Cu3-N32	86.8 (1)
Cu3-Br1	3.015 (5)	N31-Cu3- Br1	88.32 (7)
Cu1Cu2	4.356	Cu1-O22-Cu2	128.02
Cu2Cu3	3.910	Cu2-Br1-Cu3	90.50

the hydrogen atoms of the uncoordinated water molecule with the oxygen atoms O5 and O1 of the perchlorate anion and with the hydroxyl group. The hydrogen atom of the coordinated hydroxyl group is involved in intermolecular hydrogen bonding interaction with the oxygen atom O7 (-x, -y+1, -z+1) of the uncoordinated water molecule. Full details of the hydrogen bonding are given in Table 3.

3. 2. 2. Description of the Complex 2

The molecular structure of **2** is shown in Fig. 2. Complex **2** is monomeric and crystallizes in orthorhombic space group *Pbca*. The single crystal X-ray diffraction data for compound **2** is listed in Table 1. Selected bond lengths and angles are summarized in Table 2.

The Schiff base ligand acts as a tridentate monoanionic ligand, L⁻. The ligand forms one five-membered and one six-membered chelate ring with the Cu(II) metal center via the two nitrogen atoms of the amine and imine groups and one oxygen atom of one phenoxy group, and the hydroxyl group is left uncoordinated. The coordina-

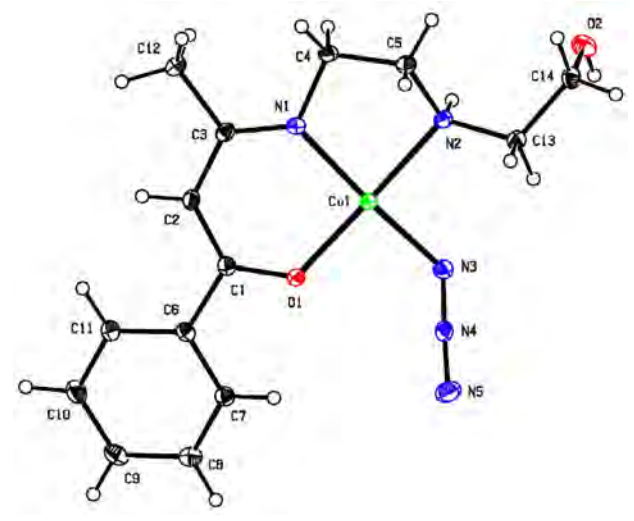


Fig. 2. The molecular structure of [CuL(N₃)], 2 with labeling of selected atoms

tion geometry around the Cu(II) ions is four coordinated with a N3O donor set, N2O from the Schiff base ligand and one nitrogen from the azide ligand. The copper center

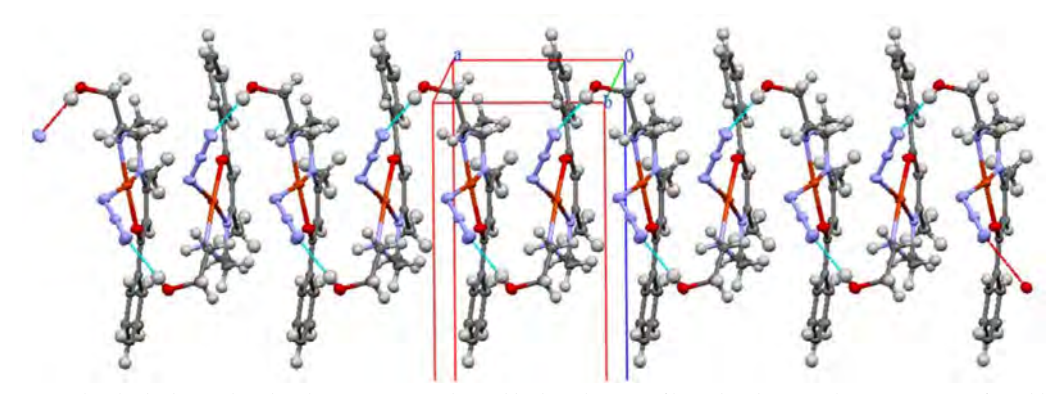


Fig. 3. The intermolecular hydrogen bonding between uncoordinated hydroxyl group of ligand and terminal nitrogen atom of neighboring coordinated azide ligand in complex 1 along a axis.

Table 3. Hydrogen bonding (Å) and angles (°) in copper complexes

	\mathbf{D} - \mathbf{H} A	D-H	\mathbf{H} ··· A	$\mathbf{D}A$	$\mathbf{D}\text{-}\mathbf{H}$ ··· A	Symmetry code
	N2-H1···O4	0.87 (4)	2.32 (4)	3.113 (5)	152 (3)	
	O2-H2···O7*	0.83(4)	1.78 (4)	2.597 (2)	168 (3)	-x, -y+1, -z+1
1	O7-H3···O5	0.74(4)	2.10(4)	2.883 (2)	178 (4)	·
	O7-H4···O1	0.82 (4)	2.05 (4)	2.848 (2)	166 (4)	
	N2-H1···O1*	0.87 (2)	2.43 (2)	3.160 (2)	142 (2)	x-1/2, y, -z+1/2
2	O2-H2···N5*	0.71 (3)	2.22 (3)	2.922 (2)	172 (3)	x-1/2, y, $-z+1/2$
	N2-H1···O21	0.87 (3)	2.22 (3)	3.057 (3)	160 (4)	
	N22-H2···N31	0.88(3)	2.29(2)	3.091(3)	150(3)	
	N32-H3···O1*	0.88(2)	2.46 (3)	3.212 (3)	143 (3)	-x+1/2, $y-1/2$, $-z+3/2$
•	O2-H4···Br2	0.81(2)	2.34(3)	3.141(2)	169 (4)	·
3	O22-H5···Br2	0.85(3)	2.32(3)	3.145 (2)	165 (4)	
	O32-H6···Br3*	0.84(3)	2.28(2)	3.119 (2)	177 (4)	-x+1/2, $y-1/2$, $-z+3/2$
	O41-H7···Br3*	0.86(3)	2.56 (4)	3.393 (3)	166 (3)	-x+1, -y+1, -z+1
	O41-H8···Br1	0.88(4)	2.47 (3)	3.345 (3)	172 (4)	·

has a τ_4 index of 0.104. The τ_4 parameter is $[360^\circ - (\alpha + \beta)]/141^\circ$, where α and β are the largest angles around the central metal in the complex; $\tau_4 = 1$ for a regular tetrahedron and $\tau_4 = 0$ for a regular square planar geometry. In 2, the Cu–O bond length is 1.9184(11) Å and the Cu–N bonds range from 1.9402(13)–2.0363(14) Å. The Cu–N(azide) bond length (1.9879(16) Å), is longer than Cu–N(imine) (1.9402(13) Å) and shorter than Cu–N(amine) (2.0363(14) Å). The Cu–N bond length suggesting that azide ligand interacts with copper(II) center more strongly in comparison to the nitrogen atom of the amine and weaker than the nitrogen atom of the imine. The azide ligand is almost linear with N3-N4-N5 bond angle 176.85(19)°.

The uncoordinated hydroxyl group of the Schiff base ligand plays a significant role in the intermolecular hydrogen bonding. There is an intermolecular hydrogen bonding between the hydrogen atom of the hydroxyl group with the terminal nitrogen atom of a neighboring coordinated azide ligand, with a donor–acceptor distance of 2.922(2) Å and D–H···A angle 172(3)°, which build a 1D chain structure running through the a axis (Fig. 3). Full details of the hydrogen bonding are given in Table 3.

3. 2. 3. Description of the Complex 3

Complex 3 crystallizes in the monoclinic space group $P2_1/c$. The molecular structure of the complex with labeling of selected atoms is shown in Fig. 3. Selected bond lengths and angles are listed in Table 2. From the crystal structure, it has been found that complex 3 is trinuclear, $[Cu_3L_3Br]Br_2$, with a hydroxyl group bridge and one asymmetric Br anion bridge. The copper(II) centers are five-coordinated and L^- acts as a tetradentate ligand with the oxygen atom of the hydroxyl group coordinating in both terminal and bridging ligands. On the basis of atoms donor set around each copper, there are three types of Cu(II)

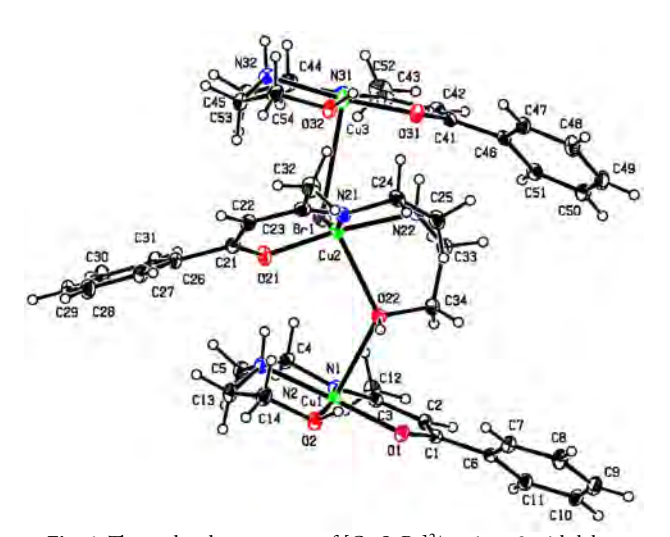


Fig. 4. The molecular structure of $[Cu_3L_3Br]^{2+}$ cations 3 with labeling of selected atoms.

ions, i.e., $[CuN_2O_2(\mu\text{-OH})]$ for Cu1, $[CuN_2O(\mu\text{-OH})(\mu\text{-Br})]$ for Cu2 and $[CuN_2O_2(\mu\text{-Br})]$ for Cu3.

The bond angles at Cu(II) between two donor atoms in the *cis* position are in the range 84.17(10)– $107.61(8)^{\circ}$ and between two donor atoms in the *trans* position they are in the range $159.86(7)^{\circ}$ and $175.75(9)^{\circ}$ (Table 2). The coordination geometry around each of the central copper is distorted square pyramidal, according to Addison τ parameter values of 0.17, 0.22 and 0.06 for Cu1, Cu2, and Cu3, respectively.²⁸ The deviation of copper(II) atoms from the basal plane towards the axially coordinated site are 0.104, 0.135, 0.005 Å for Cu1, Cu2 and Cu3, respectively.

In the case of Cu1 center, the four equatorial positions are occupied by two oxygen (O1 and O2) and two nitrogen atoms (N1 and N2) of the Schiff base and the apical position is occupied by one oxygen atom (O22)

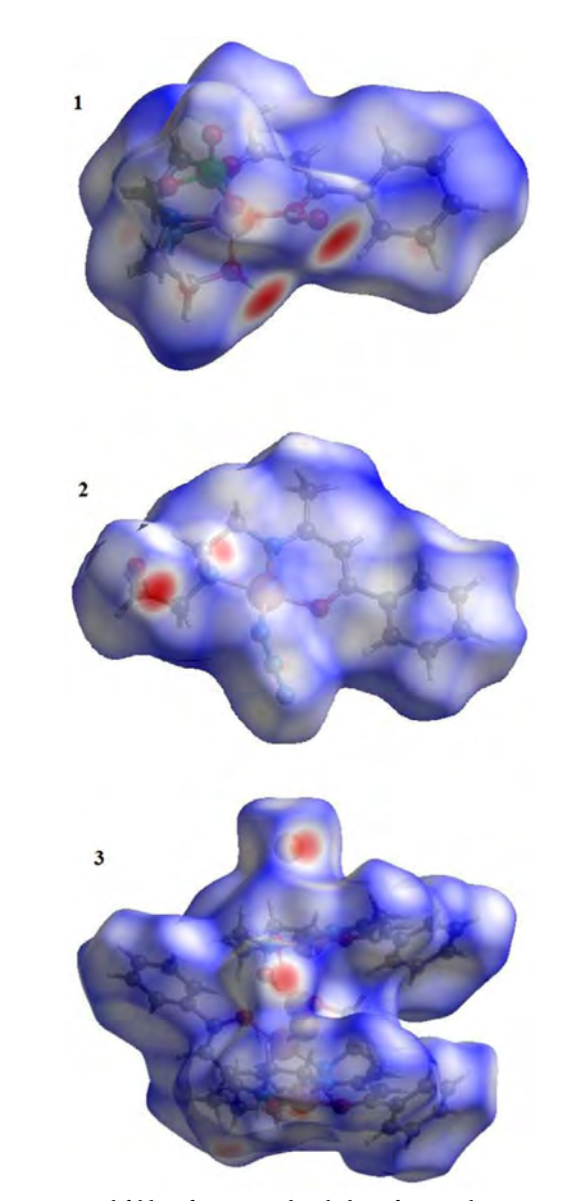


Fig. 5. Hirshfeld surface mapped with d_{norm} for complexes 1–3.

from an adjacent Schiff base ligand of the next unit of the trinuclear complex. In the Cu2, the four equatorial positions are occupied by one oxygen (O21) and two nitrogen atoms (N21 and N22) of the Schiff base and a μ -Br1 anion,

while the apical position is occupied by the oxygen atom (O22) of the hydroxyl group of the Schiff base. The hydroxyl oxygen atom acts as a bridge connecting two Cu1 and Cu2 centers. The remaining copper center, Cu3 is

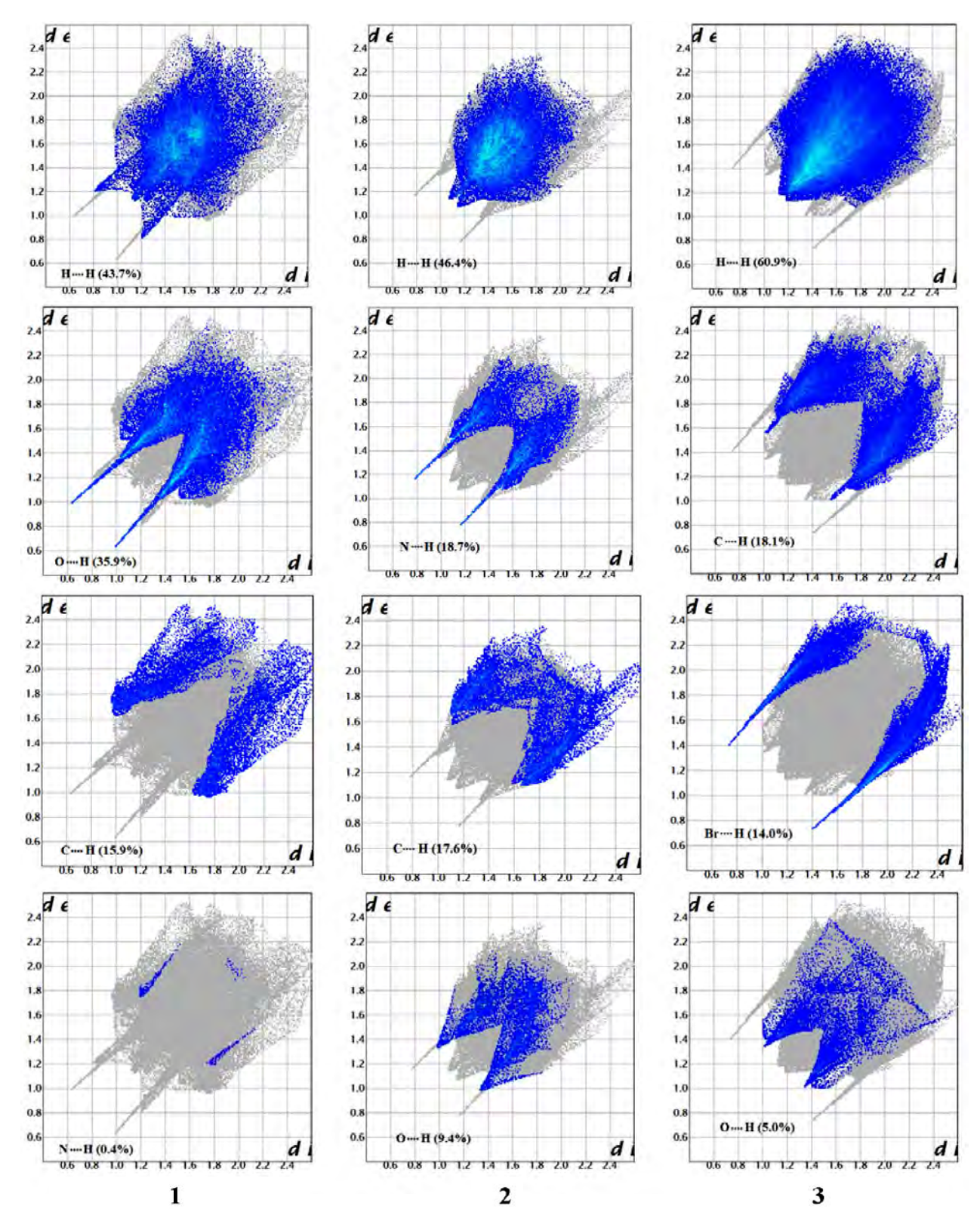


Fig. 6. The 2D fingerprint plots and relative contributions to the percentage of Hirshfeld surface for various interactions in 1-3.

similar to Cu1 in that the four equatorial positions are occupied by the Schiff base with N_2O_2 donor atoms, while the apical position is occupied by a μ -Br1 anion. The bridging Br1 anion connects two Cu2 and Cu3 ions with each other.

The Cu–O and Cu–N bond lengths in the equatorial plane are in the range of 1.872(2)–2.029(2) and 1.905(2) to 2.017(2) Å, respectively (Table 2). As shown in Table 2, the Cu–O(hydroxy) bond lengths in the apical position (Cu1–O22 = 2.508(2) and Cu2–O22 = 2.380(2) Å) are longer than the Cu–O(hydroxy) bond lengths in the equatorial positions (Cu1–O1 = 2.029(2) and Cu3–O32 = 2.008(2)), which is consistent with analogous systems observed in the literature. 17, 22, 26, 32

The NH amine of the Schiff base ligand plays a significant role in the hydrogen bonding. There are intramolecular and intermolecular hydrogen bonds between the hydrogen atoms of the NH groups of the amines with the oxygen atoms of hydroxyl groups. Also, there are intramolecular and intermolecular hydrogen bonding between the hydrogen atoms of the uncoordinated water molecule and hydroxyl groups with the uncoordinated Br anions. Full details of the hydrogen bonding are given in Table 3.

3. 3. Hirshfeld Surface Analysis

In order to profoundly examine the strength and role of the intermolecular contacts, and to estimate their importance for the crystal lattice stability, Hirshfeld surface analysis has been conducted. The Hirshfeld surface of the complexes 1-3 is illustrated in Fig. 5. The normalized contact distance, $d_{\rm norm}$ defined in terms of $d_{\rm e}$ (distance from a point on the surface to the nearest nucleus outside the surface), $d_{\rm i}$ (distance from a point on the surface to the nearest nucleus inside the surface) and the van der Waals radii of the atoms, $r^{\rm vdW}$ given by equation 1:

$$d_{norm} = \frac{d_i - r_i^{vdw}}{r_i^{vdw}} + \frac{d_e - r_e^{vdw}}{r_e^{vdw}}$$
(1)

The value of the d_{norm} can be positive or negative when intermolecular contacts are longer or shorter than the sum of the atoms vdw radii, respectively. The d_{norm} values are mapped onto the Hirshfeld surface using a redblue–white color scheme. Red regions correspond to closer contacts and negative d_{norm} value, the blue regions correspond to longer contacts and positive d_{norm} value. The white-colored regions correspond to weak contacts and the distance of contacts is around the vdW separation $(d_{norm}\approx 0).^{33,34}$

The 2D fingerprint plots are used to analyses all of the intermolecular interactions. The full fingerprint plot for 1–3 and the contribution of each type of interaction are shown in Fig. 6. The highest contribution occurs due to H···H contacts. Fig. 6 shows the percentage of contribution of various intermolecular close contacts which

play an important role in the stabilization of molecular structures.

4. Conclusion

Three complexes have been synthesized by reaction of Cu(II) ion with the flexidentate Schiff base ligand derived from the condensation of aminoethylethanolamine and benzoylacetone. All complexes have been characterized by X-ray crystallography. In complexes 1 and 3, the ClO_4^- and Br^- anions are coordinated to the copper ion, and the hydroxyl group of the flexidentate ligand coordinates to the Cu(II) center such that the ligand is tetradentate. However, in complex 2, the presence of the N_3 anion with its strong coordinating ability, leads to the ligand being tridentate, with the hydroxyl group left uncoordinated.

5. Supplementary Material

The deposition numbers of the studied complexes, 1–3 are CCDC 1912996-1912998, respectively. These data can be obtained free-of-charge via www.ccdc.cam.ac.uk/data_request/cif, by emailing data-request@ccdc.cam. ac.uk, or by contacting The Cambridge Crystallographic Data Centre, 12 Union Road, Cambridge CB2 1EZ, UK; fax +44 1223 336033.

Acknowledgments

The authors are grateful to the Yazd University and the Australian National University for partial support of this work.

6. References

- C. Papatriantafyllopoulou, T. C. Stamatatos, W. Wernsdorfer, S. J. Teat, A. J. Tasiopoulos, A.t Escuer, S. P. Perlepes, *Inorg. Chem.* 2010, 49, 10486–10496. DOI:10.1021/ic1014829
- M. Das, B. N. Ghosh, K. Rissanen, S. Chattopadhyay, *Polyhedron*, 2014, 77, 103–114. DOI:10.1016/j.poly.2014.03.027
- 3. P. Bhowmik, S. Chatterjee, S. Chattopadhyay, *Polyhedron*, **2013**, *63*, 214–221. **DOI:**10.1016/j.poly.2013.07.023
- 4. A. Beheshti, A. Lalegani, G. Bruno, H. A. Rudbari, *J. Mol. Struct.* **2014**, *1071*, 18–22.

DOI:10.1016/j.molstruc.2014.04.048

 K. Bhar, S. Choubey, P. Mitra, G. Rosair, J. Ribas, B. K. Ghosh, J. Mol. Struct. 2011, 988, 128–135.

DOI:10.1016/j.molstruc.2010.12.042

 S. Mondal, S. Hazra, S. Sarkar, S. Sasmal, S. Mohanta, J. Mol. Struct. 2011, 1004, 204–214.

DOI:10.1016/j.molstruc.2011.08.005

7. I. Beloso, J. Borras, J. Castro, J. A. Garcia-Vazquez, P.

- Perez-Lourido, J. Romero, A. Sousa, Eur. J. Inorg. Chem. 2004, 635–645. DOI:10.1002/ejic.200300338
- 8. N. A. I. Hisham, H. Khaledi, H. M. Ali, H. A. Hadi, *J. Coord. Chem.* **2012**, *65*, 2992–3006.
 - DOI:10.1080/00958972.2012.708412
- S. Mukhopadhyay, D. Mandal, D. Ghosh, I. Goldberg, M. Chaudhury, *Inorg. Chem.*, 2003, 42, 8439–8445.
 DOI:10.1021/ic0346174
- H. Y. Wang, H. Y. Liu, Transit. Met. Chem. 2017, 42, 165–173.
 DOI:10.1007/s11243-017-0121-4
- 11. Y. Sunatsukia, R. Kawamotoa, K. Fujita, H. Maruyamaa, T. Suzukia, H. Ishidaa, M. Kojimaa, S. Iijima, N. Matsumoto, *Coord. Chem. Rev.*, **2010**, *254*, 1871–1881.
 - DOI:10.1016/j.ccr.2009.11.016
- S. Mukhopadhyay, D. Mandal, D. Ghosh, I. Goldberg, M. Chaudhury, *Inorg. Chem.*, 2003, 42, 8439–8445.
 DOI:10.1021/ic0346174
- R. Diaz-Torres and S. Alvarez, *Dalton Trans.*, 2011, 40, 10742–10750. DOI:10.1039/c1dt11000d
- 14. H. Keypour, M. Shayesteh, M. Rezaeivala, K. Sayin, *J. Mol. Struct.*, **2016**, *1112*, 110–118.
 - DOI:10.1016/j.molstruc.2016.02.004
- A. S. de Sousa, M. A. Fernandes, K. Padayachy, H. M. Marques, *Inorg. Chem.*, 2010, 49, 8003–8011.
 DOI:10.1021/ic101018b
- S. H. Hsieh, Y. P. Kuo, H. M. Gau, *Dalton Trans.*, 2007, 97– 106. DOI:10.1039/B613212J
- 17. Y. C. Shi, H. J. Cheng, S. H. Zhang, *Polyhedron*, **2008**, *27*, 3331–3136. **DOI:**10.1016/j.poly.2008.04.057
- 18. Z. Otwinowski, W. Minor. Methods in Enzymology, edited by C. W. Carter Jr & R. M.W. Sweet, New York: Academic Pressn, 1997, 276, pp. 307–326.
 - **DOI:**10.1016/S0076-6879(97)76066-X
- A. Altomare, G. Cascarano, G. Giacovazzo, A. Guagliardi, M. C. Burla, G. Polidori, M. Camalli, *J. Appl. Cryst.*, **1994**, *27*, 435–436. **DOI**:10.1107/S0021889894000221
- 20. P. W. Betteridge, J. R. Carruthers, R. I. Cooper, K. Prout, D. J.

- Watkin, *J. Appl. Cryst.*, **2003**, *36*, 1487–1487. **DOI:**10.1107/S0021889803021800
- R. Vafazadeh, Z. Moghadas, A.C. Willis, J. Coord. Chem.,
 2015, 68, 4255–5271. DOI:10.1080/00958972.2015.1096349
- 22. R. Vafazadeh, F. Jafari, M. M. Heidari, A. C. Willis, *J. Coord. Chem.*, **2016**, *69*, 1313–1325.
 - **DOI:**10.1080/00958972.2016.1163547
- S. K. Dey, B. Bag, Z. Zhou, A. S. C. Chan, S. Mitra, *Inorg. Chim. Acta*, 2004, 357, 1991–1996.
 DOI:10.1016/j.ica.2003.12.014
- 24. R. Vafazadeh, M. Alinaghi, A. C. Willis, A. Benvidi, *Acta Chim. Slov.*, **2014**, *61*, 121–125.
- M.T.H. Tarafder, A. Kasbollah, K.A. Crouse, A.M. Ali, B.M. Yamin, H.K. Fun, *Polyhedron*, **2001**, *20*, 2363–2370.
 DOI:10.1016/S0277-5387(01)00817-8
- R. Vafazadeh, A. C. Willis, J. Coord. Chem. 2015, 68, 2240– 2252. DOI:10.1080/00958972.2015.1048688
- K. Nakamoto, Infrared and Raman Spectra of Inorganic and Coordination Compounds, fourth ed., Wiley, New York, 1986.
- A.W. Addison, T.N. Rao, J. Reedijk, J. Vanrijn, G.C. Verschoor. J. Chem. Soc., Dalton Trans., 1984, 1349–1356.
 DOI:10.1039/DT9840001349
- R. Vafazadeh, M. Namazian, M. Chavoshiyan, A. C. Willis, P. D. Carr, *Acta Chim. Slov.*, **2017**, *64*, 613–620.
 DOI:10.17344/acsi.2017.3401
- 30. R. Vafazadeh, N. Abdollahi, A. C. Willis, *Acta Chim. Slov.*, **2017**, *64*, 409–414. **DOI**:10.17344/acsi.2017.3263
- 31. P. Seth, S. Ghosh, A. Figuerola, A. Ghosh, *Dalton Trans.*, **2014**, *43*, 990–998. **DOI:**10.1039/C3DT52012A
- 32. Z. Lu, T. Fan, W. Guo, J. Lu, C. Fan, *Inorg. Chim. Acta*, **2013**, 400, 191–196. **DOI**:10.1016/j.ica.2013.02.030
- 33. N. Khelloul, K. Toubal, N. Benhalima, R. Rahmani, A. Chouaih, A. Djafri, F. Hamzaoui, *Acta Chim. Slov.*, **2016**, *63*, 619–626. **DOI**:10.17344/acsi.2016.2362
- 34. M. A. Spackman, D. Jayatilaka, *CrystEngComm*, **2009**, *11*, 19–32. **DOI**:10.1039/B818330A

Povzetek

Večevezni ligand (HL), smo pripravili s kondenzacijo aminoetiletanolamina (AEEA) z benzoilacetonom (bezac). Pri reakciji z bakrovimi (II) solmi nastanejo kompleksi $CuLClO_4.H_2O$ (1), $CuLN_3$ (2) in $[Cu_3L_3Br]Br_2 \cdot H_2O$ (3). Vse kompleksne smo karakterizirali z rentgensko strukturno analizo monokristalov. Rezultati kažejo, da se hidroksilna skupina liganda lahko koordinira na Cu(II) center ali ostane kot nekoordinirana skupina. V kompleksu (1) je koordinacijsko število bakrovega(II) iona pet, od tega štiri vezavna mesta pripadajo ligandu (HL). V kompleksu (2) najdemo kvadratno ploskovno geometrijo, ligand (HL) je tridentatni, pri čemer hidroksilna skupina ni vezana na Cu(II) center. V kompleksu (3) je Cu(II) koordiniran s petimi atomi, od tega štirje pripadajo ligandu (HL). Za analizo vseh interakcij med molekulami v kristalnih strukturah smo uporabili Hirshfeldovo površinsko analizo in 2D prstni odtis.



Except when otherwise noted, articles in this journal are published under the terms and conditions of the Creative Commons Attribution 4.0 International License

Scientific paper

Copper(II) Coordination Compounds with Methanoato and Pyridine Ligands: Conversion from Mononuclear to Polynuclear in the Presence of Moisture

Amalija Golobič, Fedja Marušič, Primož Šegedin and Marta Počkaj*

Faculty of Chemistry and Chemical Technology, University of Ljubljana, Večna pot 113, 1000 Ljubljana, Slovenia.

* Corresponding author: E-mail: marta.pockaj@fkkt.uni-lj.si.

Received: 08-12-2019

Abstract

Blue prismatic crystals of mononuclear $[Cu^{II}(O_2CH)_2(Py)_3]$ (Py = pyridine, C_5H_5N), **1**, were prepared from reaction solution containing dry pyridine and dinuclear $[Cu_2^{II}(O_2CH)_4(Py)_2]$. When a portion of solution together with crystals was exposed to air moisture, crystals of **1** dissolved in mother liquid. Simultaneously, blue needles of **2**, *i.e.* covalently linked one-dimensional chain structure with formula $[Cu(O_2CH)_2(Py)_2]_n \cdot nH_2O$, grew out of the solution. The process lasted few minutes and was observed under optical microscope. The conversion from **1** to **2** takes place also outside of solution in the solid state. Single crystal X-ray diffraction data were collected at 150 K for **1** and after that for **2**, originating from the same reaction solution. This paper reports the structures of both compounds. Alternative synthesis method of **2** arising from a mixture of copper methanoate and pyridine is also reported.

Keywords: Copper(II) methanoates; pyridine; crystal structure determination; structure conversion

1. Introduction

The coordination chemistry of copper(II) with different carboxylate ligands is very diverse, mainly due to the versatility of coordination modes of carboxylate ligand which with its four lone electron pairs can be coordinated to 1-4 metal centres.1 Additionally, different alkyl chain lengths of different carboxylates represent a greater or lesser sterical obstacle on a way to a formation of complex molecules. However, the smallest carboxylate ligand, i.e. methanoate anion, is thus the one with the least steric influences. If additional N-donor ligand from the family of (substituted) pyridines is introduced besides the methanoato ligand, the diversity of the obtained crystal structures further increases. In this case, mononuclear, dinuclear paddle-wheel like or polynuclear coordination moieties are formed.² Interestingly, only four crystal structures of copper(II) with pyridine and methanoato ligand are listed in CSD, i.e. mononuclear [Cu(O₂CH)₂(Py)₂(H₂O)₂] (refcode AFMPCA)³, dinuclear paddle-wheel [Cu₂(O₂CH)₄ $(Py)_2$] (refcode AFMPCB)³, and polynuclear $[Cu(O_2CH)_2]$ $(Py)_2$ _n · nH_2O (refcodes FORPCU and FORPCU01).^{3,4} Crystal structures with substituted pyridines are more frequent, e.g. with 2-methylpyridine, 5,6 3-methylpyridine, 6,7

4-methylpyridine,⁶ 2,6-dimethylpyridine,⁸ 3-hydroxypyridine,⁹ 4-aminopyridine,¹⁰ etc.

In this paper, the synthesis and characterization of two copper(II) coordination compounds with methanoato and pyridine ligands is described. In both compounds, the coordination number of central copper(II) is five, which is less usual than four- or sixfold coordination.^{11–13}

2. Experimental

2. 1. Materials and Measurements

All reagents and chemicals were purchased from commercial sources and used without further purification. The identity of the intermediate compounds was proven by means of X-ray powder diffraction (see Supplementary Information). CHN elemental analyses were performed with a Perkin-Elmer 2400 CHN Elemental Analyzer. The amount of copper was determined electrogravimetrically with Pt electrodes. The infrared spectra were measured on solid samples using a Perkin-Elmer Spectrum 100 series FT-IR spectrometer equipped with ATR. Electronic spectra were recorded as nujol mulls and also as solutions (water, acetonitrile, methanol, DMSO) on Perkin Elmer UV/VIS/NIR Spectrometer Lambda 19 between 200 and 860

nm. Magnetic susceptibility of the substance was determined at room temperature by the Evans method using powdered sample and a Sherwood Scientific MSB-1 balance with $HgCo(NCS)_4$ as a calibrant. Diamagnetic corrections were estimated from Pascal's constants and the effective magnetic moment was calculated using the equation: $\mu_{eff} = 2.828(\chi MT)^{1/2}$.

2. 2. Syntheses

 α -Cu(O₂CH)₂ was synthesized *via* modified published synthesis pathway.¹⁴ To concentrated HCOOH (11.9 mL), water (0.8 mL) and powdered Cu₂(OH)₂CO₃ (2.0 g, 9.0 mmol) were added. The reaction mixture was refluxed for one hour, and left in the refrigerator at approx. 5 °C overnight. Dark blue crystalline product was filtered off, dried in the air for 20 minutes and additionally in a desiccator over solid KOH for 24 hours. Yield: 95%.

 $[Cu_2(O_2CH)_4(Py)_2]$ was prepared from α -Cu(O₂CH)₂ (1.0 g, 6.5 mmol), pyridine (1.2 mL, 14.9 mmol) and acetonitrile (20 mL). The reaction mixture was stirred at room temperature for two hours. The obtained green powder was filtered off, dried in the air for 20 minutes and additionally in a desiccator over solid KOH for 24 hours. Yield: 88%

 $[Cu(O_2CH)_2(Py)_3]$ (1). The flask with 10 mL of dry pyridine (dried with KOH) was placed in an inert atmosphere and purged with argon. While stirring, 0.40 g of powdered [Cu₂(O₂CH)₄(Py)₂] was added. The flask was put into an oil bath which was heated to 50 °C. After 10 min the reaction solution was poured through the filter paper, the flask with the filtrate was sealed and put in the refrigerator at approx. 5 °C. After one month the blue prisms were obtained, suitable for X-ray structural analysis. The compound 1 is very sensitive to the presence of moisture. Crystals of 1 were stable for several weeks, if they were kept in a hermetically sealed container. Upon exposure to air moisture, the crystals of 1 transformed into 2 very quickly. Thus, the other analyses of 1, with exception of single crystal X-Ray structural analysis could not be performed.

 $[Cu(O_2CH)_2(Py)_2]_n \cdot nH_2O$ (2). Compound 2 was prepared in two different ways:

A) 0,75 g α -Cu(O₂CH)₂ was added into 10 mL of pyridine while stirring. The reaction mixture was cautiously heated until the previously blue solution became dark violet. At that time the hot solution was poured through the filter paper. The filtrate was left to stand in the refrigerator at approx. 5 °C for 24 hours. After that time blue needle like crystals grew in the solution which were filtered off and dried in air. Diffraction image of selected single crystal showed that the unit cell of product corresponded to that of compound 2. This identification was further confirmed by taking powder diffraction pattern using Guinier-De Wolf camera. Yield: 68%. Anal. Calc. for $C_{12}H_{14}CuN_2O_5$: C, 43.70; H, 4.28; N, 8.50; Cu, 19.27.

Found: C, 43.53; H, 4.36; N, 8.46; Cu, 19.15. Magnetic susceptibility (RT): μ_{eff} , 1.83 BM. IR: $\nu_{\text{asym}}(\text{CO}_2)$, 1626, 1589, 1579 cm⁻¹, $\nu_{\text{sym}}(\text{CO}_2)$, 1326 cm⁻¹. UV-VIS (nujol): λ_{max} 638, 270 nm.

B) The single crystals of **2** were obtained also from **1** as follows. Single crystals of **1** together with the mother liquid were left in the open Petri dish. After few minutes, the crystals of **1** dissolved completely and single crystals of **2** grew out of the reaction solution. Such single crystal of **2** was used for structural determination described in this paper.

2. 3. X-Ray Crystallography

For X-ray structure determination, the single crystals of both compounds were surrounded by silicon grease, mounted on the tip of glass fibres and transferred to the goniometer head in the stream of liquid nitrogen. For compound 2, the single crystal obtained by decomposition of 1 as well as the one obtained by procedure B was used to prove that both possess the same crystal structure (the data included in this paper refer to the single crystal of 2 that was prepared from 1). Diffraction data for structure analysis were collected on a Nonius Kappa CCD diffractometer using Nonius COLLECT software and monochromated Mo Kα radiation at 150 K.15 Data reduction and integration were performed with the DENZO-SMN program suite.16 The initial structural model containing coordination molecule was obtained via direct methods using the SIR97 structure solution program. ¹⁷ A full-matrix least-squares refinement on F^2 magnitudes with anisotropic displacement parameters for all non-hydrogen atoms using SHELXL-2013 was employed.¹⁸ All H atoms were initially located in difference Fourier maps and were further treated as riding on their parent atoms with C(aromatic)–H distance of 0.93 Å. The oxygen of water molecule is symmetry disordered due to its position near mirror plane in 2, while the hydrogen atoms bound to it lie on a mirror plane. The positions of both hydrogens were obtained from a difference Fourier map and refined using AFIX 3 command: only their displacement parameters were refined using the $U_{iso}(H) =$ $1.2U_{\rm eq}({\rm O})$ constraint. Details on crystal data, data collection and structure refinement are given in Table 1. Figures depicting the structures were prepared with ORTEP3 and Mercury. 19, 20

3. Results and Discussion

In a symmetrical coordination molecule of 1 (Fig. 1) in which a twofold axis runs through atoms Cu1-N2-C9, the central copper(II) atom is surrounded by three pyridine molecules and two monodentately bound methanoato ligands. Thus the coordination number is five, and the value of τ_5 parameter²¹ (0.29) confirms that

Table 1. Crystal data, data collection and structure refinement.

Crystal data	1	2
Formula	C ₁₇ H ₁₇ CuN ₃ O ₄	C ₁₂ H ₁₄ CuN ₂ O ₅
$M_{ m r}$	390.87	329.79
Cell setting, space group	monoclinic, C2/c	orthorhombic, Pnma
a (Å)	12.2422(2)	9.6528(2)
b (Å)	9.5968(2)	14.1667(3)
c (Å)	15.5626(4)	10.3540(2)
β (°)	108.8790(10)	90
$V(\mathring{A}^3)$	1730.03(6)	1415.89(5)
Z	4	4
$D_{\rm x}$ (Mg m ⁻³)	1.501	1.547
μ (mm ⁻¹)	1.289	1.562
F(000)	804	676
Absorption correction	multi-scan	multi-scan
No. of measured, independent		
and observed reflections	12534, 1975, 1741	20392, 1688, 1454
$R_{\rm int}$	0.045	0.039
R (on F_{obs}), wR (on F_{obs}), S	0.0304, 0.0658, 1.078	0.0265, 0.0669, 1.108
No. of contributing reflections	1975	1688
No. of parameters	115	108
$\Delta ho_{ m max}, \Delta ho_{ m min} \ ({ m e \AA}^{-3})$	0.33, -0.47	0.33, -0.42

the central ion lies in a distorted square pyramidal environment as usual for copper(II) compounds with such coordination number. The two pyridines as well as the two methanoates in a basal plane of the square pyramid are positioned *trans* to each other. The methanoato ligand is slightly closer than the basal pyridine: the corresponding distances are 1.9716(13) Å for Cu1–O1 and 2.0391(15) Å for Cu1–N1. The coordination bond to the apical pyridine ligand is prolonged in comparison with these from basal plane (2.246(2) Å, Cu1–N2). Data on selected bond lengths and angles for 1 are given in Table 2.

Table 2. Selected bond lengths and angles (Å, °) for 1 and 2.

1			
Cu1-O1	1.972(1)	O1-Cu1-N1	92.09(6)
Cu1-N1	2.039(2)	O1-Cu1-N1 ⁱ	88.95(6)
Cu1-N2	2.246(2)	O1-Cu1-N2	87.32(4)
O1-Cu1-O1 ⁱ	174.63(8)	N1-Cu1-N2	101.25(4)
N1-Cu1-N1 ⁱ	157.49(9)		
2			
Cu1-O1	1.954(2)	Cu1-O4ii	1.975(2)
Cu1-O3	2.281(2)	Cu1-N1	2.019(2)
N1-Cu1-N1iii	169.79(8)	O3-Cu1-N1	94.78(4)
O1-Cu1-O4 ⁱⁱ	177.85(7)	O3-Cu1-O4 ⁱⁱ	84.18(6)
O1-Cu1-N1	91.48(4)	O4ii-Cu1-N1	88.70(4)
O1-Cu1-O3	93.67(6)		

Symmetry codes: (*i*) -x, y, $-z + \frac{1}{2}$; (*ii*) $x - \frac{1}{2}$, y, $-z + \frac{1}{2}$; (*iii*) x, $-y + \frac{1}{2}$, z.

When exposed to water, even in traces from the air, the crystal structure 1 converts into more symmetrical 2 with the formula $[Cu(O_2CH)_2(Py)_2]_n \cdot nH_2O$, in which Cu(II) and

both methanoates as well as the hydrogen atoms from water molecule lie on a mirror plane. The central Cu(II) atom in 2 remains five-coordinate in a shape of distorted square pyramid with parameter value $\tau_5 = 0.14$ (Fig. 2). As in 1, the basal plane is defined by two nitrogens from two pyridine molecules and two oxygens from two methanoato ligands. Similarly, pyridines as well as the methanoates are positioned *trans* to each other. The deviations from the basal mean plane are significantly smaller than in 1. One of the two symmetry independent methanoato ligands is monodentate (Cu1–O1 1.954(2) Å), while the other acts as a bidentate bridge between the adjacent Cu(II) atoms in a *syn-anti* mode. The corresponding distances Cu1–O4ⁱ and Cu1–O3

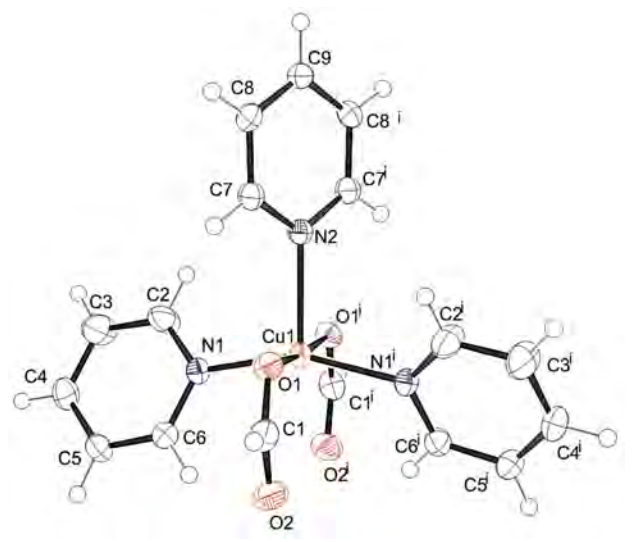


Figure 1. The *ORTEP* representation of coordination molecule in **1**. (*i*) -x, y, $-z + \frac{1}{2}$.

are 1.975(2) and 2.281(2) Å, respectively ($i = x - \frac{1}{2}$, y, $-z + \frac{1}{2}$). As in 1, the distances between Cu1 and equatorial O-ligands are shorter than towards the apical one. With the assistance of the bridging methanoato ligand, infinite chains of $[\text{Cu}(\text{O}_2\text{CH})_2(\text{Py})_2]_n$ running parallel to the crystallographic a axis are formed (Fig. 7d). Water molecules are hydrogen bonded to O atoms of two methanoato ligands from the neighboring coordination moieties of the same chain. In this way the structure is additionally stabilized. The geometry of hydrogen bonds is presented in Table 3.

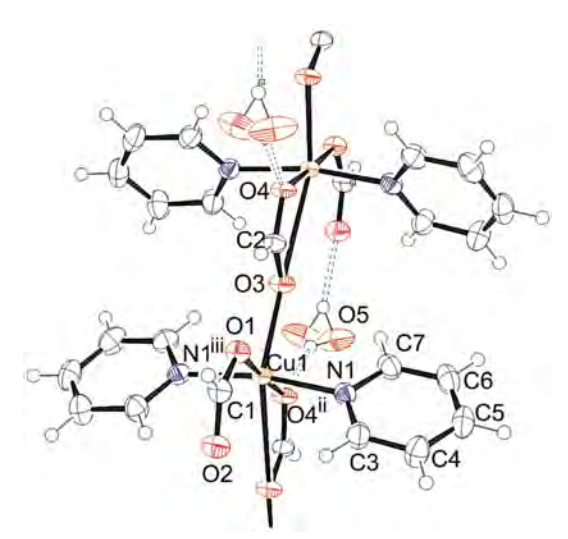


Figure 2. The *ORTEP* representation of coordination environment of Cu(II) in **2** and a formation of chains. ($ii = x - \frac{1}{2}$, y, $-z + \frac{1}{2}$; iii = x, $-y + \frac{1}{2}$, z). Dashed lines represent hydrogen bonds.

on Fig. 4. The single crystal experiment was run on opaque crystal, from which the powder pattern was extracted afterwards. The obtained powder pattern has shown the presence of compound 2 and the absence of 1 very clearly (Fig. 5). The same changes were observed with single crystal of 1, used for data collection at 150 K. The crystal was extensively surrounded by vacuum grease which to some

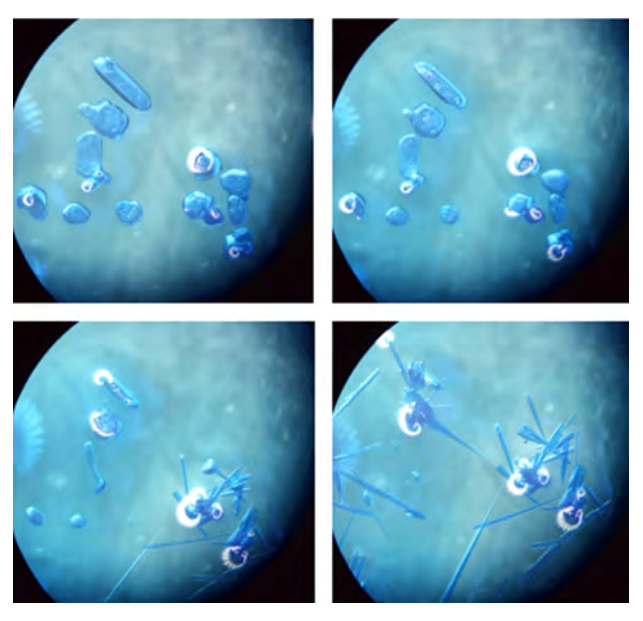


Figure 3. The conversion of blue prisms of **1** to needle-like crystals of **2** in mother liquor. The identity of the crystals was confirmed by the determination of unit cell parameters.

Table 3. Hydrogen bond geometry in **2**.

D-H···A	D-H (Å)	HA (Å)	DA (Å)	D-HA (°)	Symmetry code of A
O5-H5AO4	0.85	2.01	2.757(3)	145.5	$x - \frac{1}{2}, y, -z + \frac{1}{2}$
O5-H5BO2	0.87	1.97	2.749(3)	147.6	$x + \frac{1}{2}, y, -z + \frac{1}{2}$

The structure of **2** was previously described (refcodes FORPCU and FORPCU01)^{3,4} but both crystal structures were determined at room temperature whereas ours was performed at 150 K. Low temperature and room temperature unit cell parameters and atoms' coordinates are similar, consequently the arrangement of atoms is basically the same. Disorder of water molecules is present also at 150 K, probably indicating the static nature of disorder.

The structure conversion process from 1 to 2 was relatively fast. When the mother liquor with the crystals of 1 was exposed to air, it took approximately 15 minutes for the following changes to happen. At first, the prismatic blue crystals of 1 dissolved in mother liquid. At the same time, new needle-like blue crystals of 2 were growing out of the solution (Fig. 3). The conversion from 1 to 2 took place also outside of the solution, i.e. in the solid state, when crystals of 1 were left in air on a filter paper. Visual change from optically clear to opaque crystals can be seen

extent protected its exposure against moisture and thus slowed down the conversion process. After 24 h at ambient temperature, the single crystal experiment was repeated and the powder pattern extracted from it. As shown in Fig. S3, the structure conversion from 1 to 2 can be confirmed.

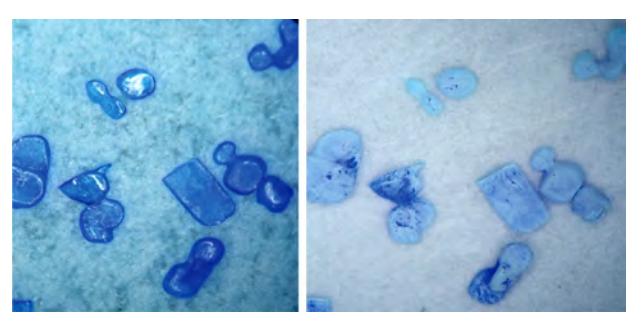


Figure 4. Prismatic crystals of **1** just after taking out of the solution (left) and getting opaque after few minutes (right).

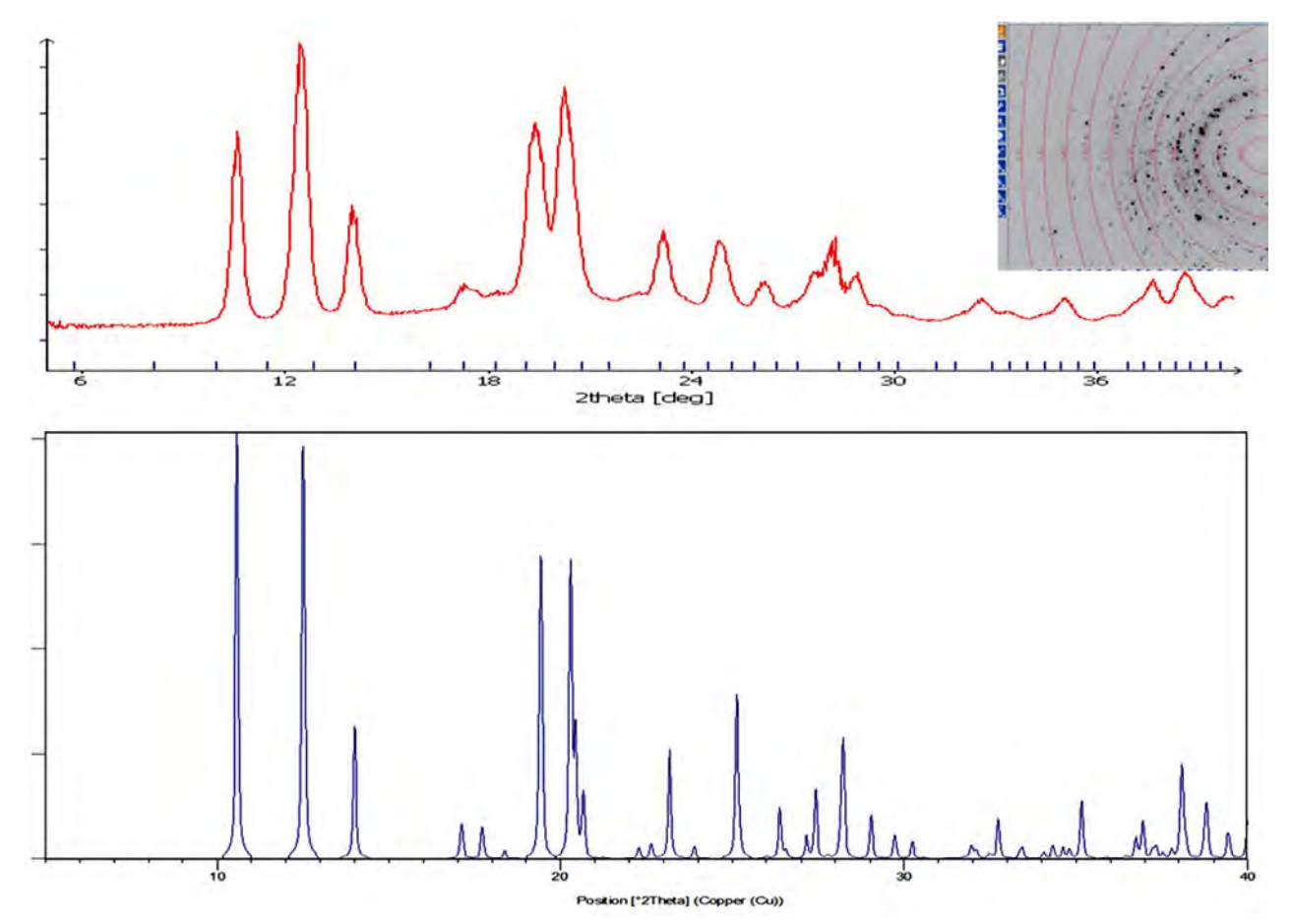


Figure 5. Upper graph represents the extraction of the powder pattern from the single crystal experiment, performed on opaque prism from Fig. S3. The powder pattern below is calculated from the crystal structure **2**. By comparison of both patterns, the formation of **2** from **1** on air can be confirmed. Powder pattern extraction was performed by CrysAlis software.²²

According to the observations, the structure conversion should not require significant reorganization of the atoms and molecules in the crystal. When comparing coordination environment of copper(II) in both title structures (cf. Figs. 1 and 2), the first difference between 1 and 2 can be observed in the apical ligand while the basal planes of the square pyramid remain mostly the same in both compounds; instead of pyridine in apical position in 1, a bridging methanoato ligand is present in 2 which enables the formation of polynuclear complex molecules. The second difference is in the presence of water in 2. One would expect that (i) the crystal packing of 1 should enable apical pyridine to leave the structure, and water to enter the structure simultaneously, and that (ii) monomeric coordination molecules should be arranged and oriented properly that the neighboring molecules can connect into chains via methanoato bridges. A drawing of molecular packing in 1 (Fig. 6) reveals that the apical pyridine ligands (drawn black) are located in virtual channels running along monoclinic c axis. Through the latter the water molecules can enter while the pyridine ones can leave the structure. Crystal packing of 2 is represented in Fig. 7d. Considering the second requirement, at first glance molecules in 1 are not

properly oriented to join themselves into chains as in 2 since the uncoordinated oxygen atoms of methanoato ligands are not oriented towards copper(II) ions. The proposed mechanism for the conversion of 1 to 2 is shown in Fig. 7: after removal of apical pyridines and entering of water the remaining coordination moieties rotate and move slightly to achieve an orientation that enables uncoordinated O atom of (every second) methanato ligand to coordi-

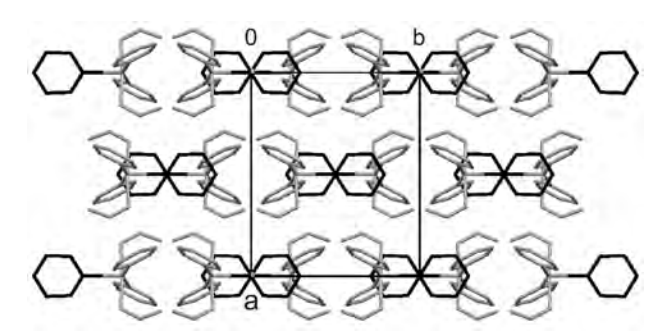


Figure 6. The packing of coordination molecules in 1; a view along c axis. The channels through which the apical pyridine molecules (shown in black) can leave the structure and the water molecules enter it can be observed. Hydrogen atoms are omitted for clarity.

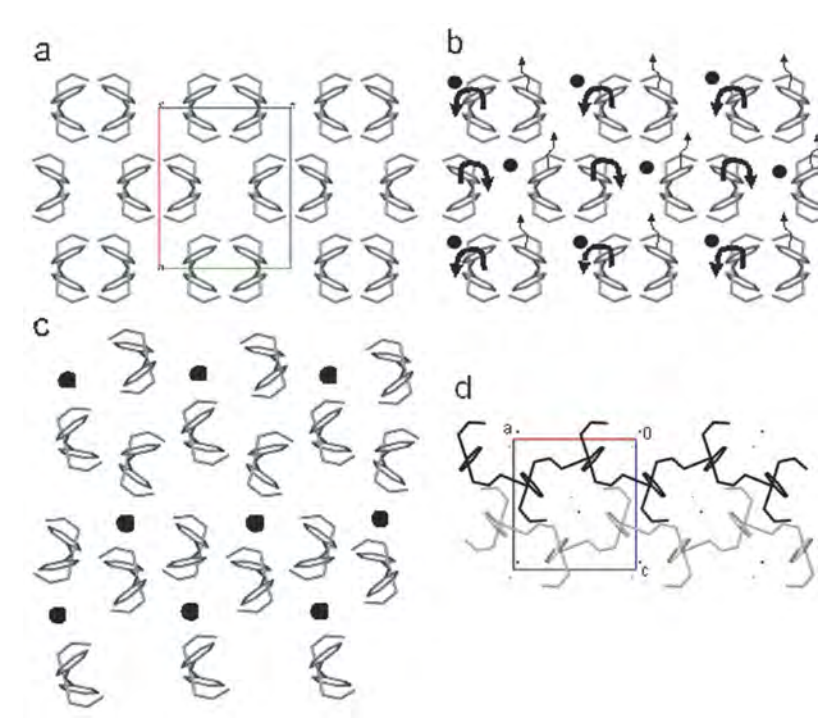


Figure 7. The proposed mechanism of conversion from 1 to 2. a) Pyridine molecules exit the structure of 1 (cf. Fig. 6), b) water molecules shown as black dots enter the structure, c) coordination moieties rearrange and consequently form chains to which water molecules are hydrogen bonded as in 2 (d). Narrow arrows show the direction of movement of complex molecules while the bold ones represent their rotations.

nate to neighboring Cu atom – making this way bridging methanoato ligands from the monodentate ones and consequently chains – to which the water molecules attach. All of proposed steps probably take place simultaneously.

4. Conclusions

Crystal structures of two methanoato copper(II) complexes with pyridine, i.e. [Cu(O2CH)2(Py)3] (1) and $[Cu(O_2CH)_2(Py)_2]_n \cdot nH_2O$ (2) at 150 K were determined by single-crystal X-ray diffraction. In both compounds, central Cu(II) is five-coordinated in a shape of square pyramid. In both complexes, the basal meanplane is formed by two nitrogens from coordinated pyridine molecules and two oxygens from two monodentately bound methanoato ligands. The apical atom is either nitrogen from the third coordinated pyridine molecule in 1 or oxygen from bridging methanoato ligand in 2. The distance Cu-apical is about 0.25 Å longer than the distances Cu-equatorial. In 2 five coordinated copper(II) moieties are connected into chains through bridging methanoato ligands. To such chains water molecules are hydrogen bonded. Compound 2 was prepared in two ways: by heating copper(II) methanoate in pyridine and also from compound 1. The conversion from 1 into 2 was observed in the solution as well as in the solid state at exposure to water from air. Crystal packing in 1 enables entering of water and release of pyridine. Only little further structure reorganization is needed to achieve chain structure of 2.

5. Supplementary Materials

CCDC 1019407 (1) and 1019408 (2) contain the supplementary crystallographic data. These data can be obtained free of charge from The Cambridge Crystallographic Data Centre *via* www.ccdc.cam.ac.uk/data_request/cif.

Acknowledgements

Financial support of the Ministry of Higher Education, Science and Technology of the Republic of Slovenia is gratefully acknowledged (grants P1-0175 and X-2000). The authors also thank Leja Erzin for optimization of syntheses.

6. References

- D. A. Dickie, P. T. K. Lee, O. A. Labeodan, G. Schatte, N. Weinberg, A. R. Lewis, G. M. Bernard, R. E. Wasylishen, J. A. C. Clyburne, *Dalton Trans.* 2007, 2862–2869, and references therein. DOI:10.1039/b704588c
- F. H. Allen, Acta Crystallogr. 2002, B58, 380–388.
 DOI:10.1107/S0108768102003890
- 3. M. A. Bernard, M. M. Borel, F. Busnot, A. Leclaire, *Rev. Chim. Miner.* **1979**, *16*, 124–133.
- B. A. Cartwright, L. Couchman, A. C. Skapski, Acta Crystallogr. 1979, B35, 824–827. DOI:10.1107/S0567740879004982
- B. Kozlevčar, E. Mate, Z. Jagličić, L. Glažar, A. Golobič, P. Strauch, J. Moncol, N. Kitanovski, P. Šegedin, *Polyhedron* 2009, 28, 2759–2765. DOI:10.1016/j.poly.2009.05.066

- M. Yamanaka, H. Uekusa, S. Ohba, Y. Saito, S. Iwata, M. Kato,
 T. Tokii, Y. Muto, O. W. Steward, Acta Crystallogr. 1991, *B47*,
 344–355. DOI:10.1107/S0108768190012459
- M. M. Borel, F. Busnot, A. Leclaire, Rev. Chim. Miner. 1977, 14, 286–294.
- M. M. Borel, A. Busnot, F. Busnot, A. Leclaire, Rev. Chim. Miner. 1980, 17, 202–208.
- B. Kozlevčar, L. Glažar, G. Pirc, Z. Jagličić, A. Golobič, P. Šegedin, *Polyhedron* 2007, 26, 11–16.
 DOI:10.1016/j.poly.2007.08.019
- G. A. van Albada, S. A. Komaei, H. Kooijman, A. L. Spek, J. Reedijk, *Inorg. Chim. Acta* 1999, 287, 226–231.
 DOI:10.1016/S0020-1693(99)00010-9
- M. A. Sharif, M. Tabatabaee, V. Beik, H. R. Khavasi, *Acta Chim. Slov.* 2012, 59, 289–293.
- 12. S. Esmaielzadeh, E. Zarenezhad, *Acta Chim. Slov.* **2018**, *65*, 416–428. **DOI**:10.17344/acsi.2018.4159
- 13. Y.-L. Sang, X.-S. Lin, Acta Chim. Slov. 2019, 66, 168-172.
- N. Burger, H. Fuess, Solid State Commun. 1980, 34, 699–703.
 DOI:10.1016/0038-1098(80)90959-X

- 15. Collect Software. Nonius BV. Delft, The Netherlands, 2000.
- 16. Z. Otwinowski, W. Minor, *Methods Enzymol.* **1997**, *276*, 307–326. **DOI**:10.1016/S0076-6879(97)76066-X
- A. Altomare, M. C. Burla, M. Camalli, G. L. Cascarano, C. Giacovazzo, A. Guagliardi, A. G. G. Moliterni, G. Polidori, R. Spagna, J. Appl. Crystallogr. 1999, 32, 115–119.
 DOI:10.1107/S0021889898007717
- SHELXL2013. G. M. Sheldrick, University of Göttingen, Germany, 2013.
- L. J. Farrugia, J. Appl. Crystallogr. 1997, 30, 565–565.
 DOI:10.1107/S0021889897003117
- C. F. Macrae, P. R. Edgington, P. McCabe, E. Pidcock, G. P. Shields, R. Taylor, M. Towler, J. van de Streek, *J. Appl. Crystallogr.* 2006, 39, 453–457. DOI:10.1107/S002188980600731X
- A. W. Addison, N. T. Rao, J. Reedijk, J. van Rijn, G. C. Verschoor, J. Chem. Soc., Dalton Trans. 1984, 1349–1356.
 DOI:10.1039/DT9840001349
- Agilent (2014). CrysAlis PRO. Agilent Technologies Ltd, Yarnton, Oxfordshire, England.

Povzetek

Iz reakcijske raztopine, ki je vsebovala suh piridin in dvojedrni $[Cu_2^{II}(O_2CH)_4(Py)_2]$, smo pripravili modre prizmatične kristale enojedrne spojine $[Cu^{II}(O_2CH)_2(Py)_3]$ (Py = piridin, C_5H_5N), **1**. Ko smo del reakcijske raztopine izpostavili zračni vlagi, so se kristali **1** najprej raztopili v matični lužini, hkrati pa so iz raztopine zrasli modri igličasti kristali **2**, tj. kristali kovalentno povezane verižne strukture s formulo $[Cu(O_2CH)_2(Py)_2]_n \cdot nH_2O$. Proces, ki je bil zaključen v nekaj minutah, smo opazovali pod optičnim mikroskopom. Pretvorba iz **1** v **2** se zgodi tudi v trdnem stanju izven raztopine. Uklonsko sliko monokristalov smo posneli pri 150 K, in sicer najprej za strukturo **1** ter nato še za **2** iz iste reakcijske raztopine. Opisana je tudi alternativna sintezna metoda iz zmesi bakrovega metanoata in piridina za pripravo **2**.



Except when otherwise noted, articles in this journal are published under the terms and conditions of the Creative Commons Attribution 4.0 International License



Scientific paper

Temperature Dependent Behavior of Isotactic and Atactic Poly(Methacrylic Acid) in the Presence of MgCl₂ and CaCl₂

Patricija Hriberšek¹ and Ksenija Kogej^{1,*}

¹Department of Chemistry and Biochemistry, Faculty of Chemistry and Chemical Technology, University of Ljubljana, SI-1000 Ljubljana, Slovenia

> * Corresponding author: E-mail: ksenija.kogej@fkkt.uni-lj.si Tel.: 01-4798-538;

> > Received: 11-06-2019

Abstract

Temperature (T) induced nanoparticle formation of isotactic (iPMA) and atactic (aPMA) poly(methacrylic acid) chains is investigated in aqueous solutions in the presence of divalent cations (Mg²⁺ and Ca²⁺) by UV spectroscopy, visual observations and pyrene fluorimetry. In aPMA solutions, aggregation and phase separation take place with increasing T. The onset of aPMA aggregation (heating) and re-dissolution of the aggregates (cooling) is shifted to lower Ts with increasing ionic strength of the solutions. iPMA associates partly decompose upon heating, but stable nano-sized particles are present at all Ts. Structural characterization of the aggregates was carried out by dynamic and static light scattering measurements at 25 °C. Results revealed that aggregates of both PMAs with Mg²⁺ ions involve a lot of water and have a rather even mass distribution. This is attributed to strong hydration of Mg²⁺ ions and their preference towards monodentate binding to carboxylate groups. Differently, Ca²⁺ ions bind more strongly and in a bidentate manner, they lose the hydration water and form aggregates with several structural elements, depending on chain tacticity.

Keywords: Temperature-responsive polymers; poly(methacrylic acid) isomers; atactic; isotactic; divalent cations; intermolecular association

1. Introduction

Despite the ubiquitous presence of polyelectrolytes in chemistry, biology and physics, their interactions with numerous species, among those also with oppositely charged and multivalent metal ions, still present one of the most challenging aspects of macromolecule chemistry. These interactions have a significant effect on size, charge and structure of the polymer molecules in solutions, on dynamics of polymer chains, kinetics of eventual phase separation, and furthermore have implications to biological systems, since metal ions perform important functions in biological processes. 1-3 Among the most common cations found in nature and in living systems are divalent Mg²⁺ and Ca²⁺. Since these two ions play a crucial role in stabilizing the structure of many proteins, many studies have been performed on their interactions with macromolecules. 1,4-10 For example, Mg²⁺ is responsible for the DNA replication^{1,5} and Ca²⁺ has a stabilizing function in bones, teeth and shells.^{1,11} They are both so-called hard ions and prefer to bind to hard ligands containing oxygen, such as carboxylates, carbonyls, water,

and hydroxyl groups. 1,12 However, Mg^{2+} and Ca^{2+} each has specific properties that make them different from each other. Apart from small ionic (0.65 Å 13) and significantly larger hydrated radius (4.76 Å 13,14), one of the main characteristics of Mg^{2+} is strong interaction with water molecules leading to a bulky hydration sphere with a hexa-coordinated geometry around this ion. The slow exchange rate of the hydrated water molecules is responsible that Mg^{2+} ions do not readily lose water molecules. $^{1,4,6,12-18}$ These features of Mg^{2+} play a crucial role in stabilizing the monodentate binding of Mg^{2+} to carboxylate group (see Scheme S1 in Supporting Information (SI)). 1,4,12,13,17

 ${\rm Ca^{2+}}$ has quite different properties in comparison to Mg²⁺ and therefore participates in different biochemical processes. ^{11,13} Its ionic radius (0.99¹³) is considerably larger in comparison to Mg²⁺ and this leads to significant flexibility in the coordination number of its complexes with various ligands. The water coordination numbers for ${\rm Ca^{2+}}$ range from 6 to 8, but also up to 12 is possible, which leads to irregular geometry of the ion's coordination sphere. ^{1,11–13} Hydrated radius of ${\rm Ca^{2+}}$ thus depends on the coordination

number, but is always smaller than that of Mg²⁺. For coordination numbers 6–8, the hydrated radius is 2.95.¹³ These properties cause that Ca²⁺ can easily lose water molecules from its hydration sphere.^{13,15,16} Its complexes, in which bidentate binding prevails,¹⁷ are therefore classified as 'dry'. There are two types of bidentate binding of Ca²⁺ to carboxylate groups: chelating bidentate and bridging bidentate binding (see Scheme S1). In chelating coordination, one central Ca²⁺ ion is bound to two oxygen atoms of one carboxyl group, whereas in bridging coordination Ca²⁺ bridges two different carboxyl groups via their oxygen atoms.¹⁹

Interactions of macromolecules and counterions are important also in the (bio)technological, industrial, and pharmaceutical fields, where synthetic polymers are more commonly used.^{2,3} For example, poly(acrylic acid) is a promising candidate for controlling water hardness²⁰ and poly(methacrylic acid) (PMA) is widely studied due to its pH- and temperature dependent behavior, 21-24 which is very appropriate in targeted drug delivery.²⁵ In the case of PMA, chain tacticity brings in qualitatively different solution behavior. For example, the atactic form (aPMA) is known to form intermolecular associates in dilute aqueous solutions²⁶ and gels in concentrated solutions upon heating,^{22–24,27,28} whereas the isotactic form (iPMA) associates upon cooling. ^{26,28,30} These findings are attributed to different distribution of polar (carboxyl) and nonpolar (methyl) groups on aPMA and iPMA chains and consequently within the associates. The favorable isotactic arrangement of carboxyl groups on iPMA favors strong hydrogen bonding between neighboring chains and exposes the methyl groups towards the polar solvent (water), leading to insolubility of unionized iPMA in water. Increasing the temperature destroys the H-bonds, the associates decompose and consequently carboxyl groups become exposed to water. This is different when the distribution of functional groups is irregular, such as in aPMA. In this case, hydrogen bonding is much less advantageous. The mostly free carboxyl groups are exposed to water and the methyl groups can effectively hide from the polar aqueous environment by forming associates with a hydrophobic core. Increasing the temperature would lead to exposure of these methyl groups to water, which is clearly unfavorable. As a result, the polymer chains first form intermolecular associates and finally precipitate from solution at elevated temperatures. Our previous results show that the added simple salt, in particular the cation charge, affects the temperature at which association takes place, either by heating (aPMA) or by cooling (iPMA).²⁸

The main focus of this paper is to compare the effect of biologically relevant divalent Mg²⁺ and Ca²⁺ cations on the temperature-dependent association of iPMA and aPMA chains in aqueous solutions. For this purpose, we first carry out UV spectroscopy measurements supported by visual observations in the temperature range between 0 and 95 °C to clarify the effect of polymer tacticity on the association process. To identify the role that the specific

nature of Mg²⁺ and Ca²⁺ plays in the interaction with carboxylate groups on PMA isomers, fluorescence measurements using pyrene as a polarity probe are used. Finally, the molecular characteristics of the associates are determined by dynamic (DLS) and static light scattering (SLS), which are further supported by pH measurements, both carried out at 25 °C.

2. Experimental

2. 1. Materials

The aPMA sample (product number P2419-MAA) with the weight (M_w) and number average molar masses $(M_{\rm n})$ of $M_{\rm w} = 159~900~{\rm g~mol^{-1}}$ and $M_{\rm n} = 123~000~{\rm g~mol^{-1}}$ and a polydispersity index (PDI) of PDI = 1.3 was purchased from Polymer Source Inc (Montreal, QC, Canada). iPMA was obtained by acidic hydrolysis of its ester form, isotactic poly(methylmetacrylate) (iPMMA), which was synthesized following the procedure reported in the literature^{29,30} at the Catholic University of Leuven. Detailed description of hydrolysis and further purification of iPMA was described previously.^{29,31} The molecular characteristics of the starting iPMMA were the following: the triad content or tacticity was 94% of isotactic, 4% of syndiotactic, and 2% of atactic triads, $M_w = 138\,000\,\mathrm{g}\,\mathrm{mol}^{-1}$, $M_n = 30\,000\,\mathrm{g}\,\mathrm{mol}^{-1}$, and PDI = 4.6. After hydrolysis and purification, the $M_{\rm w}$ and PDI ($M_{\rm w} = 69~500~{\rm g~mol^{-1}}$ and PDI = 3) were determined by size exclusion chromatography, and the degree of hydrolysis (> 98%) was determined from the ¹H nuclear magnetic resonance spectrum of the sample in D_2O .

MgCl₂ (> 98%; Sigma Aldrich, St. Louis, Missouri, USA) and CaCl₂ (in the form CaCl₂ × 2H₂O; pro analysis, Merck KGaA, Darmstadt, Germany) were used to prepare stock salt solutions in water. The exact concentration of salts (c_s) was determined by potentiometric titration using a standardized AgNO₃ solution. Pyrene (optical grade) for fluorimetric measurements was purchased from Aldrich (Darmstadt, Germany). The saturated solutions of pyrene in aqueous MgCl₂ and CaCl₂ were prepared as reported previously. ^{32,33}

2. 2. Preparation of Solutions

Stock solution of aPMA was prepared at a degree of neutralization (α_N) α_N = 0 by dissolving the dry polymer in water. After one day of stirring, the solution was filtered through 0.45 μ m Millex HV filter and the exact polymer concentration (c_m , in g L⁻¹) was determined by potentiometric titration with a standardized NaOH solution.

The iPMA does not dissolve in water at $\alpha_{\rm N}=0.^{29,34,35}$ Therefore, the iPMA stock solution was prepared at a higher $\alpha_{\rm N}$ (> 0.8) to ensure that the polyacid was completely dissolved. A calculated volume of 1 M NaOH was slowly added to the iPMA suspension in water under continuous stirring to obtain the desired $\alpha_{\rm N}$ value. The dissolution process at

room temperature was slow. The iPMA suspension was stirred for several days with occasional heating to ~50 °C, which accelerated the dissolution. When the polymer was visually dissolved, the solution was filtered through 0.45 μm Millex HV filter and the exact α_N and c_m values were determined by potentiometric titration, first with 0.1 M NaOH in the direction of increasing α_N (to determine the concentration of the still protonated COOH groups) and then with 0.1 M HCl in the direction of decreasing α_N (to determine the total concentration of carboxyl groups).

Due to differences in solubility, different procedures were used also for the preparation of aPMA and iPMA solutions with added MgCl₂ and CaCl₂. Solutions of aPMA with a desired salt concentration (c_s) were prepared by adding a calculated volume of concentrated salt solutions to the aPMA stock solution and diluting the solution with triple distilled water to adjust the concentration of aPMA and the ionic strength (I) to the desired values. For all the measurements with aPMA, $\alpha_N = 0$, $c_m = 2$ g L⁻¹ (or in moles of COOH groups per volume, designated as c_p , $c_p =$ 0.023 mol L⁻¹), and the concentration of MgCl₂ and CaCl₂ was $c_s = 0.0333$ and 0.0667 mol L⁻¹, which corresponds to I = 0.1 and 0.2 mol L⁻¹, respectively (these data are collected in Table S1). UV and pH measurements with aPMA were performed also at higher I (or c_s) values, *i.e.* in the range $I = 0.1-0.5 \text{ mol } L^{-1}$.

For the preparation of iPMA solutions with the lowest possible α_N , at which the polyacid was still soluble, a calculated amount of 0.1 M HCl was gradually added to the stock solution with $\alpha_N > 0.8$, which resulted in some NaCl in solution. The NaCl was removed by dialysis using dialysis membranes Float-A-Lyzer G2 with a molecular weight cut-off MWCO = 3.5-5 kDa. Finally, calculated amounts of concentrated MgCl2 or CaCl2 solutions and water were added slowly and under continuous stirring to adjust I and c_p to the desired final values, so as in the case of aPMA. The final I values were 10 times lower in comparison to aPMA, because iPMA precipitated from solutions with $I = 0.1 \text{ mol } L^{-1}$ in the presence of the studied divalent cations. For both, MgCl₂ and CaCl₂, I was 0.01 (or $c_{\rm s} = 0.0033~{
m mol~L^{-1}})$ and 0.02 mol L⁻¹ (or $c_{\rm s} = 0.0067~{
m mol}$ L^{-1}) and α_N was 0.2. In the case of MgCl₂, the iPMA solution with $\alpha_N = 0.2$ and I = 0.02 mol L⁻¹ was stable (no phase separation occurred). However, in the case of CaCl₂, $\alpha_{\rm N}$ in iPMA solution with I=0.02 mol L⁻¹ could not be reduced to $\alpha_N = 0.2$, because the solution became opaque when α_N was decreased from $\alpha_N > 0.8$ to $\alpha_N = 0.63$ and remained cloudy even after prolonged stirring. This solution was therefore studied at $\alpha_N = 0.63$. All I, c_s , and α_N values for iPMA solutions are reported in Table S1.

2. 3. Methods

2. 3. 1. Visual Observations

In order to obtain visual information about temperature-dependent aggregation of a- and iPMA chains in

aqueous solutions, samples were kept in cuvettes and equilibrated at different temperatures (T) (T = 15, 25, 45, 55, 65, 75, 85 and 95 °C) in a Julabo circulator. aPMA in MgCl₂ and CaCl₂ precipitated on a macroscopic scale during heating. The samples were photographed and the photographs are presented in Tables S2 and S3. For iPMA, only pictures at 25 °C are shown (Table S4), because the solutions were transparent in the whole temperature range. Photographs of iPMA in CaCl₂ with I = 0.02 mol L⁻¹ and $\alpha_{\rm N}$ = 0.63 (not shown) resembled the case of aPMA at 75 °C.

2. 3. 2. UV Measurements

The UV absorbance (A) was recorded with a UV-Vis spectrophotometer Cary BIO 100 (Varian, Australia) at a wavelength λ = 280 nm in the temperature range between 0 and 95 °C. To avoid condensation on the cuvette walls, measurements were carried out by blowing dry nitrogen around the cuvette. Samples were degassed prior to measurements. The heating and cooling rate programs were different for a- and iPMA solutions and are reported in Table S5.

2. 3. 3. Fluorimetric Measurements

Fluorimetric measurements were performed by using pyrene as the external fluorophore. The fluorescence emission spectra of pyrene were recorded on a Perkin-Elmer model LS-100 luminescence spectrometer in the direction of increasing temperature (from 15 to 95 °C) with a step of 10 °C, also under nitrogen flow similar to UV measurements. The excitation light wavelength was 330 nm, the recording speed was 100 nm min⁻¹, and 20 emission spectra were collected in the wavelength region 350–450 nm and averaged. From the averaged spectra, the ratio of intensities of the first (I_1) and the third (I_3) vibrational peak in the emission spectrum of pyrene or so-called pyrene polarity ratio (I_1/I_3) was calculated.

2. 3. 4. Light Scattering

In order to obtain the information on size and structure of aPMA and iPMA associates in MgCl₂ and CaCl₂ solutions, dynamic (DLS) and static light scattering (SLS) measurements were performed with the 3D-DLS-SLS cross-correlation spectrometer from LS Instruments GmbH (Fribourg, Switzerland). The measurements were carried out only at 25 °C. The source of incident light was the He-Ne laser with a wavelength λ_0 = 632.8 nm. Intensity of scattered light was collected in the angular range between 40° and 150° with a step of 10° after keeping the samples at 25 °C for 30 min. At each angle, five correlation functions were collected and averaged. For processing the measured correlation functions, CONTIN analysis was used. Prior to light scattering (LS) measurements, all aPMA and iPMA solutions were filtered through hydro-

philic and low protein binding Millex-HV filters (diameter 13 mm, pore size 0.45 µm) directly into the sealable dust-free cylindrical quartz LS sample cells. LS measurements were performed 3 days after filtration. Due to opacity, iPMA solution in 0.0067 mol L⁻¹ CaCl₂ (I = 0.02 mol L⁻¹ and $\alpha_{\rm N} = 0.63$; see above) was studied without being filtered. Note that the 3D cross-correlation technique was designed especially for the characterization of such strongly turbid samples.³⁶ After 2 weeks two phases were observed in the cuvette in this case. The one at the bottom was more turbid than the upper one. By changing the height of the cuvette in the decalin bath, we were able to perform the LS characterization of both phases separately.

LS experiments identified two (in some cases three) populations of particles in iPMA and aPMA solutions (see examples of calculated hydrodynamic radii (R_h) distributions in Figure S1). The R_h values of smaller particles (R_h < 10 nm, assigned to individual chains, and 10 nm $< R_h < 20$ nm, assigned to small pre-associates; not reported) did not depend on the angle. We were interested in the R_h values of larger particles (70-200 nm), which were assigned to inter-chain associates and designated as $R_{h.ass}$. Their values depended considerably on the angle of observation. For further calculations, the $R_{h,ass}$ values at $\theta = 0^{\circ}$ were obtained by extrapolation of the measured $R_{h,ass}$ to zero angle. Due to large size of the associates, their radius of gyration $(R_{g,ass})$ could be determined from the angular dependency of the LS intensity following the procedures reported previously.^{37–39} From $R_{h,ass}$ at $\theta = 0^{\circ}$ and $R_{g,ass}$, the shape parameter (ρ) was calculated as $\rho = R_{g,ass}/R_{h,ass}$. This parameter is often used to characterize mass distribution within the scattering particles.^{37,38} All further details of LS data evaluation were reported previously. 37-40

2. 3. 5. pH Measurements

The pH values of the samples were measured by using the combined glass micro-electrode from Mettler Toledo (type InLab® 423; Schwerzenbach, Switzerland) and the Iskra pH meter model MA 5740 (Ljubljana, Slovenia).

3. Results and Discussion

3. 1. Temperature Dependent Behavior of iPMA and aPMA in the Presence of MgCl₂ and CaCl₂

3. 1. 1. UV Spectroscopy and Visible Observations

In Figure 1, A is presented as a function of temperature for aPMA ($\alpha_{\rm N}=0$) solutions with I=0.1 mol L⁻¹ and for iPMA ($\alpha_{\rm N}=0.2$) solutions with I=0.01 mol L⁻¹ in the presence of both, MgCl₂ and CaCl₂. In addition, measurements for aPMA at higher I (= 0.2–0.5 mol L⁻¹) are shown in Figure 2. The data demonstrate that aqueous aPMA solutions with added MgCl₂ and CaCl₂ behave as polymer

mixtures with so-called lower critical solution temperature (LCST) behavior. The LCST behavior (phase separation induced by heating) is inferred from the fact that UV absorbance is close to zero at low temperatures (below 70 and 80 °C in CaCl₂ and MgCl₂, respectively; Figure 1b) and steeply increases at high temperatures. Strong increase in A indicates the formation of larger particles in solution, which is ultimately followed by phase separation of the polymer-rich phase (see visual observations reported below). Clearly, the increase in A is more pronounced in the presence of Ca^{2+} ions. For the aPMA-CaCl₂ solution, a plateau in A is reached between 80 and 90 °C, followed by a fall as T approaches 95 °C. We anticipate that this final drop in A is a consequence of the fact that the aPMA precipitate in the presence of CaCl₂ is effectively removed from the solution by settling down to the bottom of the cuvette, whereas it still fills the whole cuvette in the MgCl₂ solution at this $I (= 0.1 \text{ mol } L^{-1}; \text{ for more details see photographs in Table})$ S2). The LCST for aPMA-CaCl₂ solution clearly appears at lower Ts in comparison with that in aPMA-MgCl₂ solution (see the LCST values reported in Table S6 and the method for their determination shown in Figure S2).

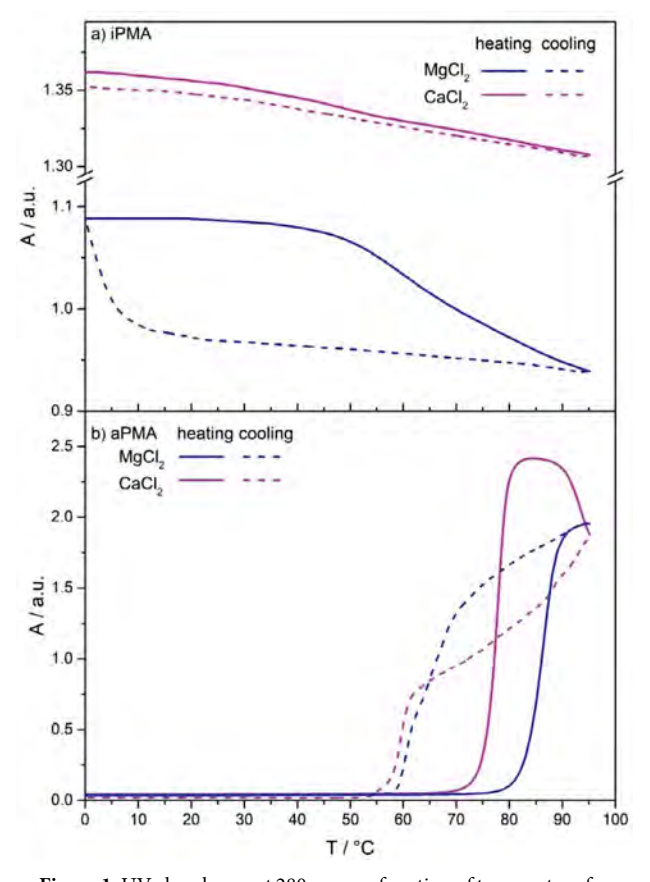


Figure 1. UV absorbance at 280 nm as a function of temperature for a) iPMA ($c_{\rm p}=0.022~{\rm mol~L^{-1}},~\alpha_{\rm N}=0.20$) in MgCl₂ and CaCl₂ with $I=0.01~{\rm mol~L^{-1}},~{\rm and~for~b})$ aPMA ($c_{\rm p}=0.023~{\rm mol~L^{-1}},~\alpha_{\rm N}=0$) in MgCl₂ and CaCl₂ with $I=0.1~{\rm mol~L^{-1}}.$ Heating (solid lines) and cooling (dashed lines) were performed according to the temperature programs reported in Table S5.

During cooling the aPMA-MgCl₂ solution back to the initial temperature, the absorbance first decreases gradually and then drops steeply to 0 at lower temperatures (below approximately 60 °C) as compared to the heating direction. Meanwhile, the initial drop in A upon cooling the aPMA-CaCl₂ solution is steeper, but reaches zero at approximately the same temperature (at around 58 °C) as in MgCl₂ solution. The drop in A to zero indicates that aPMA aggregates, which form in the presence of MgCl₂ and CaCl₂ upon heating, disintegrate upon cooling. We conclude that Mg²⁺ and Ca²⁺ cations induce reversible association of aPMA chains at elevated temperatures. These findings are in agreement with our recent report on intermolecular association of aPMA chains in the presence of cations with increasing charge.²⁸ The occurrence of the aPMA rich phase (the turbid part that eventually forms a precipitate) in the CaCl2 solution is similar to that in LaCl₃.²⁸ This is not surprising, since both cations (Ca²⁺ and La³⁺) are known to bind to carboxylate groups in a bidentate manner. 19 The La³⁺ cations are also recognized as Ca²⁺ analogs in living systems and can thus act as substitutes of Ca²⁺ in many proteins and cell membranes.^{41–43} However, in the case of aPMA the presence of trivalent La^{3+} ions at I = $0.1 \text{ mol } L^{-1}$ induces irreversible precipitation from solution (no re-dissolution takes place upon cooling), whereas Ca^{2+} precipitates re-dissolve at the same *I*.

Visual observations for aPMA ($\alpha_{\rm N}=0$) solutions are in good agreement with the UV results (see photographs presented in Table S2 for the heating and in Table S3 for the cooling direction). When temperature increases above 75 °C, aPMA solutions in MgCl₂ and CaCl₂ first become turbid. Fine flakes of precipitated aPMA are formed in the presence of MgCl₂, which do not readily settle down (the solution remains turbid). In CaCl₂ solutions, on the other hand, the initial turbidity is considerably more pronounced (see for example the photograph taken at 85 °C,

Table S2). The precipitate, which subsequently forms in the aPMA-CaCl₂ system with further heating to 95 °C, finally settles to the bottom of the cuvette or is partially stuck to the glass wall. This explains the plateau in *A* values in aPMA-CaCl₂ solution at 80–90 °C (maximum turbidity) and their steep drop towards 95 °C (partial removal of the precipitate from solution).

The LCST values for aPMA in the presence of MgCl₂ and CaCl₂ were determined in a broader range of I values (up to 0.5 mol L⁻¹). Heating of aPMA-MgCl₂ solution at higher I (> 0.1 mol L⁻¹) leads to a similar plateau and a drop in A values as highlighted above for CaCl₂ solution for all I (c.f. Figure 2). With increasing I, the rise in A shifts to lower LCSTs, whereas the plateau shifts to higher A due to higher turbidity and more extensive precipitation of aPMA from solutions at higher MgCl₂ concentration. An-

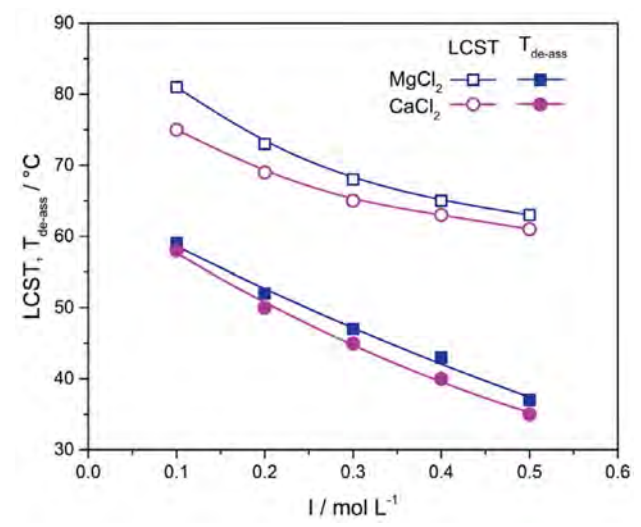


Figure 3. The dependences of LCST and $T_{\text{de-ass}}$ on ionic strength (I) for aPMA ($c_p = 0.023 \text{ mol L}^{-1}$, $\alpha_N = 0$) in MgCl₂ and in CaCl₂ solutions.

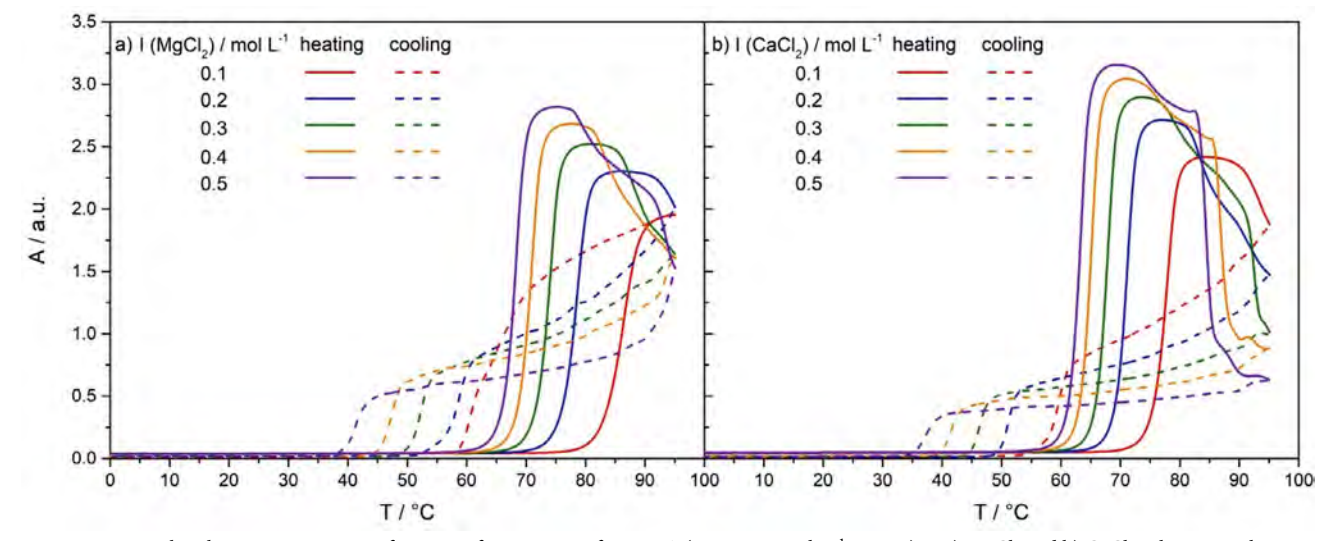


Figure 2. UV absorbance at 280 nm as a function of temperature for aPMA ($c_p = 0.023 \text{ mol L}^{-1}$, $\alpha_N = 0$) in a) MgCl₂ and b) CaCl₂ solutions with I = 0.1, 0.2, 0.3, 0.4 and 0.5 mol L⁻¹. The heating (solid lines) and cooling (dashed lines) were performed with a rate of 1 °C min⁻¹.

other important observation is that upon cooling the plateau, and consequently the associated critical temperature of de-association, designated as $T_{\rm de-ass}$, also shift to lower temperatures with increasing I. A strong hysteresis is clearly seen in the plots in Figure 2, indicating that $T_{\rm de-ass}$ is considerably lower than LCST (see $T_{\rm de-ass}$ and LCST values reported in Table S6 and plotted in Figure 3).

Similar behavior is observed also for aPMA in the presence of CaCl₂. Again, a strong hysteresis is detected along the heating and cooling paths. Nevertheless, some key differences between MgCl₂ and CaCl₂ solutions can be extracted from these plots. During heating, the plateau in A reaches higher values when Ca2+ cations are present, which means that these divalent cations induce more extensive association and consequently more extensive precipitation of aPMA from the solution in comparison to Mg²⁺ cations. This can be inferred also from a much steeper drop in A towards the end of the heating cycle in CaCl₂ solutions (compare Figure 2b with Figure 2a). In agreement with this, the T_{de-ass} and in particular the LCST values, are lower for aPMA in CaCl₂, suggesting a more effective intermolecular association of aPMA induced by Ca²⁺ ions. However, in the case of both divalent chlorides, the LCST and T_{de-ass} decrease with increasing *I*. Interestingly, $T_{\text{de-ass}}$ approaches body temperature at the highest ionic strength of 0.5 mol $\rm L^{-1}$ ($T_{\rm de-ass}$ = 35 and 37 °C in $\rm CaCl_2$ and MgCl₂, respectively). From the obtained results we can conclude that changing I of the solutions strongly affects the LCST and T_{de-ass} values for aPMA in aqueous MgCl₂ and CaCl2 solutions, in spite of the fact that the aPMA chain is almost uncharged at $\alpha_N = 0$.

The opposite effect of temperature is found for the iPMA isomer as demonstrated by the plot of UV absorbance in Figure 1a. It should be emphasized right from the start that α_N (= 0.2) is not negligible in the iPMA case, which puts electrostatic interactions at the forefront in this case. In contrast to aPMA ($\alpha_N = 0$), the UV absorbance is high in iPMA ($\alpha_N = 0.2$) solutions at low temperatures and starts to decrease at higher temperatures, but never drops to zero, so as is the case with aPMA. This is most clearly seen for the iPMA solution with added MgCl₂: A is roughly constant up to 40 °C and starts to decrease more steeply above 50 °C, but does not drop below $A \approx 0.95$ even when approaching 95 °C. In the presence of CaCl₂, the measured A values are even higher ($A \approx 1.3-1.35$), suggesting that the concentration and/or size of the iPMA associates are larger than in MgCl₂ solution. In addition, no significant drop in A values can be identified from the curves for iPMA in CaCl₂ and the hysteresis is almost absent, which suggests stronger interactions and different kinetics of the association process as compared to MgCl₂. However, by inspecting the enlarged plot for iPMA-CaCl₂ solution (Figure S3) we see that the trend in A values is similar to the one in MgCl₂ or in other chlorides.²⁸ This type of behavior of aqueous iPMA solutions was previously ascribed to so-called upper critical solution temperature (UCST) behavior, denoting polymer mixtures where phase separation (or merely association) is achieved upon cooling. The high A values in iPMA ($\alpha_{\rm N}=0.2$) solutions with added MgCl₂ and CaCl₂ are attributed to the presence of intermolecular associates that are abundant in these solutions in the whole temperature range (A stays high even at 95 °C). Similar to these observations, it was found previously that iPMA associates are stable in the whole temperature range in aqueous solutions with added trivalent La³⁺ ions, however they largely decomposed upon heating in the presence of monovalent Na⁺ ions. This again indicates the important role of electrostatics (counterion charge) in intermolecular association of iPMA ($\alpha_{\rm N}=0.2$) chains.

Visual observations of iPMA solutions show that, in spite of high absorbance, no macroscopic phase separation occurs in iPMA ($\alpha_{\rm N}=0.2$) solutions at I=0.01 mol L⁻¹ (therefore only the photograph at 25 °C is presented in Table S4), indicating that iPMA associates are formed on a mesoscopic scale, as already established for iPMA solutions with mono- and trivalent cations under the same conditions (i.e. at I=0.01 mol L⁻¹).²⁸ The iPMA ($\alpha_{\rm N}=0.2$) system is, however, very sensitive to salt concentration as the polymer precipitates from solution when I exceeds 0.01 mol L⁻¹ (see Experimental and discussion below). Again, the relatively high charge of the iPMA chain plays the key role here.

3. 1. 2. Fluorescence Measurements

Pyrene fluorescence measurements were used to follow the micropolarity of the aggregates' interior in aPMA and iPMA solutions. It is expected that pyrene, as a very hydrophobic molecule, would solubilize inside the aggregates if they are composed of a non-polar core. It is well-known that aPMA chains at low α_N adopt a compact con-

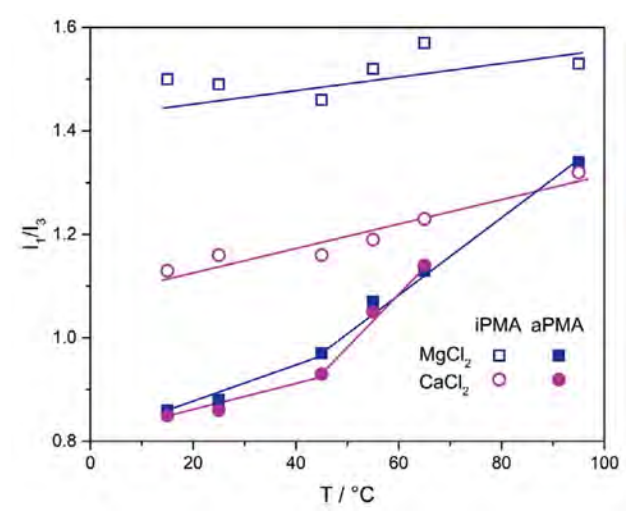


Figure 4. Temperature dependence of the pyrene polarity ratio (I_1/I_3) for iPMA ($c_p=0.022$ mol L⁻¹, $\alpha_N=0.20$) in MgCl₂ and CaCl₂ solutions with I=0.01 mol L⁻¹ and for aPMA ($c_p=0.023$ mol L⁻¹, $\alpha_N=0$) in MgCl₂ and CaCl₂ solutions with I=0.1 mol L⁻¹.

formation with hydrophobic methyl groups forming the interior and offering a suitable solubilization site for pyrene. We were interested in how the tacticity and added divalent metal ions affect the polarity of microenvironment in aPMA ($\alpha_N = 0$) and iPMA ($\alpha_N = 0.2$) solutions.

The emission spectra of pyrene for both PMA isomers in MgCl_2 and CaCl_2 solutions are presented in Figure S4. From these spectra, the pyrene polarity ratio I_1/I_3 was calculated. The obtained values are reported in Table S8 and plotted as a function of temperature in Figure 4. The immediately evident feature of the spectra in Figure S4 is the decrease in fluorescence intensity with increasing temperature, which significantly distorts the spectrum for aPMA in CaCl_2 solution at 95 °C. This is attributed to extensive precipitation of aPMA from this solution, as discussed above. No I_1/I_3 value is therefore reported for aPMA in CaCl_2 at the highest temperature.

The most obvious result of Figure 4 is that I_1/I_3 values are higher in iPMA (above 1.4 in iPMA-MgCl2 and above 1.1 in iPMA-CaCl2 solutions) than in aPMA solutions (here I_1/I_3 values start at around 0.85 at low Ts) and only weakly increase with temperature with no evident change of slope in the iPMA case. The value $I_1/I_3 \approx 1.5$ in iPMA-MgCl₂ solutions points to a rather high polarity of microenvironment where pyrene molecules reside in these solutions. For comparison, I_1/I_3 is 1.3 in methanol, 1.35 in ethyl acetate, and around 1.7 (depending on the presence of eventual ions) in water.³³ These high I_1/I_3 values are attributed to strong interactions of Mg²⁺ ions with water molecules, due to which these cations bring a lot of water into the associates with iPMA. At the same time the monodentate binding of Mg²⁺ is weaker in comparison with cations that release the hydration water (like Ca²⁺).³⁷ However, the iPMA ($\alpha_N = 0.2$) chains must be held rather strongly in these associates, considering that they are charged and thus also repel each other. As proposed previously²⁸ we attribute the stability of the iPMA associates to strong cooperative intermolecular H-bonds between unionized COOH groups on different iPMA chains and in case of Mg²⁺ ions also to H-bonds between COOH groups and the hydration water molecules around the ion. The presence of large amounts of water in the iPMA-MgCl₂ associates contributes to the observed high I_1/I_3 values.

The I_1/I_3 values for iPMA in CaCl₂ are somewhat lower ($I_1/I_3 \approx 1.1-1.3$) than in MgCl₂ solutions, which can be explained by bidentate Ca²⁺ binding to carboxylate groups. This type of binding is accompanied by elimination of water from cation's hydration sphere and thus also from the associates. Consequently, the polarity of these associates is determined mainly by H-bonded COOH groups and is thus expected to be lower. Altogether, fluorescence measurements show that the interior of the iPMA associates is actually rather polar (in contrast to aPMA; see below) and stems from polar COOH groups and/or water in these associates. Strong H-bonding between COOH groups is facilitated by their suitable isotac-

tic orientation on the iPMA chain. Meanwhile, the charged COO⁻ groups are positioned on the surface and grant the solubility of the associates in water.

The pyrene polarity ratio in aPMA solutions at temperatures below 45 °C is $I_1/I_3 \approx 0.85-0.95$ (irrespective of the cation) and demonstrates a considerably less polar microenvironment of the aPMA aggregates. This can be explained by so-called hydrophobic interactions that force the methyl groups to hide inside the cores of the aPMA aggregates, which is well known. The irregular orientation of COOH groups on aPMA actually facilitates the formation of such hydrophobic cores as a result of higher flexibility of the aPMA chain and at the same time does not allow extensive H-bonding (as in the iPMA case). The hydrophilic COOH groups are positioned mostly on the surface and protect the core against the water solvent. Above 45 °C, an increase is observed in I_1/I_3 values for aPMA solutions in both, MgCl₂ and CaCl₂, which is attributed to precipitation of aPMA aggregates from solutions. Some of the pyrene molecules remain accumulated inside these precipitates and are removed from water, whereas the remaining ones detect the polarity of water without aPMA.

The above conclusions apply also to higher I values, however the increasing in I has no significant effect on the I_1/I_3 ratio. Its value depends primarily on chain tacticity (see the I_1/I_3 values measured at 25 °C in Table S9).

3. 2. LS Characterization of aPMA and iPMA Associates at 25 °C

Further structural information about the associates was obtained by LS measurements at 25 °C. In Table 1, the $R_{\rm h,ass}$, $R_{\rm g,ass}$ and ρ values are reported for aPMA ($\alpha_{\rm N}=0$) and iPMA ($\alpha_{\rm N}=0.2$) associates in MgCl₂ and CaCl₂ solutions. The $R_{\rm h,ass}$ values (the dynamic LS data) are shown in Figures 5a and 5b as a function of q^2 (q is the scattering vector given by the relationship $q=(4\pi n_0/\lambda_0)\sin(\theta/2)$, with n_0 the refractive index of the medium and λ_0 the wavelength of the incident light). From these dependencies, the zero angle values were obtained by using either linear function or second order polynomial for extrapolation to $\theta=0^\circ$. In Figures 5c and 5d, the static LS data are presented for both PMA isomers in the form of a Kratky plot (i.e. the dependence of $(qR_{\rm g})^2P(\theta)$ on $qR_{\rm g}$) and compared with the calculated curves for some well-known particle topologies.

The DLS results show that aPMA particles in the presence of both divalent salts have more or less comparable hydrodynamic radii (160–190 nm). However, the radii of gyration (the SLS result) of these particles are considerably smaller in the presence of Ca²⁺ ions, leading to lower ρ values in this case. The value $\rho \approx 0.70$ (aPMA-CaCl₂ with I = 0.1 mol L⁻¹) indicates micro-gel like structure of particles with mass concentrated in the core surrounded by a water swollen corona, whereas $\rho \approx 0.90$ in both aPMA-Mg-Cl₂ solutions points to a more even mass distribution. For comparison, a homogeneous mass distribution, such as in

Table 1. Hydrodynamic radii ($R_{\rm h,ass}$), radii of gyration ($R_{\rm g,ass}$) and parameter ρ (= $R_{\rm g,ass}/R_{\rm h,ass}$) for associates of iPMA ($c_{\rm p}=0.022$ mol L⁻¹, $\alpha_{\rm N}=0.20$) and aPMA ($c_{\rm p}=0.023$ mol L⁻¹, $\alpha_{\rm N}=0$) in the presence of MgCl₂ and CaCl₂ at different I and at 25 °C.

		iPMA			aPMA			
Added salt	$I/\mathrm{mol}\ \mathrm{L}^{-1}$	$R_{\rm h,ass}$ / nm	$R_{\rm g,ass}$ / nm	ρ	$I/\mathrm{mol}\ \mathrm{L}^{-1}$	$R_{\rm h,ass}$ / nm	$R_{\rm g,ass}$ / nm	ρ
MgCl ₂	0.01	75	73	0.97	0.1	178	164	0.92
_	0.02	177	180	1.02	0.2	191	160	0.84
CaCl ₂	$0.01 \\ 0.02^{a)}$	65 111 ^{b)} 184 ^{c)}	76 153 ^{b)} 127 ^{c)}	1.16 1.37 ^{b)} 0.69 ^{c)}	0.1 0.2 ^{b)}	161 178 ^{b)}	109 125 ^{b)}	0.68 0.70 ^{b)}

 $^{^{}a)}\alpha_{N} = 0.63$; $^{b)}$ upper phase; $^{c)}$ lower phase

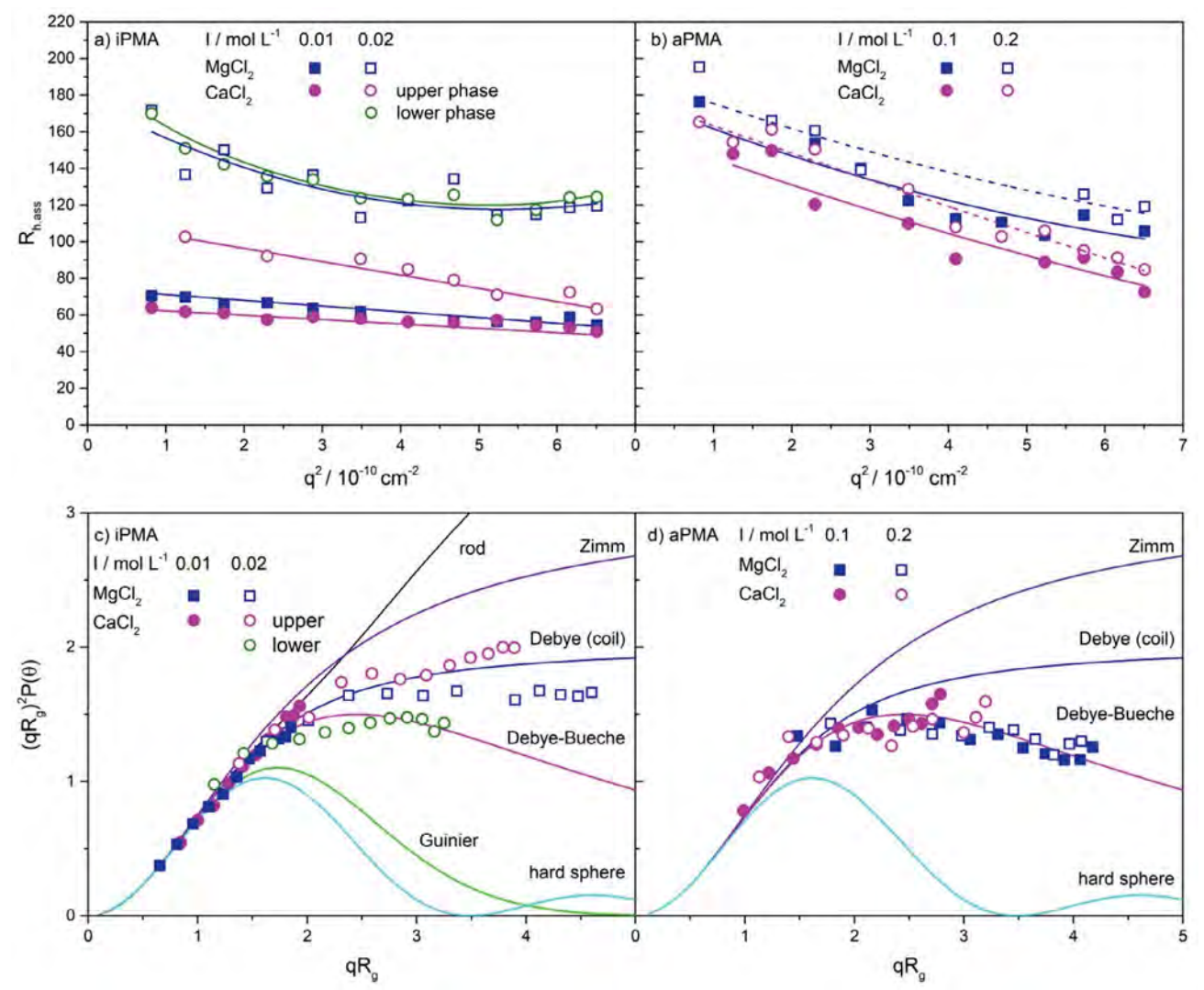


Figure 5. Hydrodynamic radii ($R_{\rm h,ass}$) as a function of q^2 for a) iPMA ($c_{\rm p}=0.022$ mol L⁻¹, $\alpha_{\rm N}=0.20$) in MgCl₂ and CaCl₂ with I=0.01 mol L⁻¹ (full squares) and I=0.02 mol L⁻¹ (open symbols) (note that $\alpha_{\rm N}=0.63$ for iPMA in CaCl₂ with I=0.02 mol L⁻¹) and for b) aPMA ($c_{\rm p}=0.023$ mol L⁻¹, $\alpha_{\rm N}=0$) in the corresponding salt solutions with I=0.1 and 0.2 mol L⁻¹. The Kratky plot (the dependence of $(qR_{\rm g})^2P(\theta)$ on $qR_{\rm g}$) for selected topologies (solid lines; for details on these scattering functions see⁴⁴) and the experimental data for c) iPMA ($\alpha_{\rm N}=0.20$ for all salt solutions, except for CaCl₂ with I=0.02 mol L⁻¹ where $\alpha_{\rm N}=0.63$) and d) aPMA associates ($\alpha_{\rm N}=0$) in aqueous solutions of MgCl₂ and CaCl₂ salt solutions with I=0.1 and 0.2 mol L⁻¹.

a (monodisperse) hard sphere, would result in $\rho = 0.778$. By considering that polydyspersity that is virtually always present in real samples tends to increase ρ , a particle with a measured ρ of 0.70 definitely cannot be a hard sphere.

Lower ρ values in the presence of CaCl₂ are actually expected due to the preference of strong bidentate binding of Ca²⁺ to carboxylate groups as discussed above. Ca²⁺ ions release coordinated water molecules upon binding to car-

boxylate groups, the aggregates' interior is thus 'drier' (leaving only the outer layers hydrated) and therefore more compact. On the other hand, Mg^{2+} ions remain strongly hydrated due to their pronounced inability to dehydrate and thus the aPMA chains in $MgCl_2$ solutions form rather loose and more water swollen aggregates. Such environment offers more mobility to the chains and the structure is more permeable for the solvent, which altogether leads to higher ρ values. Still, $\rho \approx 0.90$ for aPMA-MgCl₂ aggregates is far from values known for random coils of single chains in a θ -solvent ($\rho \approx 1.5$).

The Kratky plots for aPMA aggregates in both metal chlorides (Figure 5d) confirm the suggested structures. The data points coincide with the Debve-Bueche scattering function, which is valid for micro-gel like particles with a core-shell structure and at the same time demonstrate that the increase in *I* does not greatly affect the structure, which is reasonable in case of aPMA ($\alpha_N = 0$) with charge close to zero. The experimental points for aPMA in CaCl₂ solutions show a noticeable upturn from the Debye-Bueche towards the Debye scattering function at high qR_g values. This kind of upturns were previously attributed to the excluded-volume interactions, 37,40 which may be more pronounced in case of Ca2+ ions in view of their stronger interaction with carboxyl groups. We actually demonstrate in the following (see results of pH measurements below), that Ca²⁺ ions replace some H⁺ ions from COOH groups and thus increase the ionization of aPMA.

Different from aPMA, $R_{h,ass}$ and $R_{g,ass}$ values for iPMA associates in $MgCl_2$ and $CaCl_2$ with lower I (= 0.01 mol L^{-1}) are significantly smaller in comparison to those in solutions with higher $I = 0.02 \text{ mol } L^{-1}$). This result is reasonable, because salt concentration should play a more important role in the case of partly charged iPMA (α_N = 0.2) chains: higher salt concentration (higher I) contributes to stronger electrostatic screening and enables more extensive intermolecular association and formation of larger particles. However, ρ values for iPMA-Mg²⁺ associates are not much affected by $I(\rho \approx 1)$, whereas those for iPMA-Ca²⁺ associates range from 0.69 (the lower phase formed in the CaCl₂ solution with $I = 0.02 \text{ mol } L^{-1}$ and α_N = 0.63; see Experimental Section) to 1.37 (the upper phase in the same solution). In the Kratky plot we see that the experimental data for larger particles in iPMA solutions show a systematic positive shift from the Debye-Bueche function at high $qR_{\rm g}$ values. We attribute these observations to a possibility that different structural elements are present in the iPMA-Ca²⁺ associates. Let's assume that the bidentate binding of Ca2+ proceeds predominately via bridging interaction with carboxyl groups on neighboring iPMA chains (i.e. intermolecularly), whereas the chelating (intramolecular) binding is less likely (see a scheme of both binding modes in Figure 6). The bridging bidentate binding with a concomitant pronounced dehydration of Ca²⁺ ions may induce structural elements of higher rigidity within these complexes, in particular considering also

the isotacticty of the chain, and contributes to shifting of the points in the Kratky plot toward more rod-like structures. On the other hand, portions of the iPMA chains that are not involved in this complexation (presumably the more ionized parts) form coil-like outer regions with higher ρ (*c.f.* ρ = 1.16 and 1.37 for the homogeneous sample at I = 0.01 mol L⁻¹ and for the upper phase at I = 0.02 mol L⁻¹, respectively) around the compacted parts.

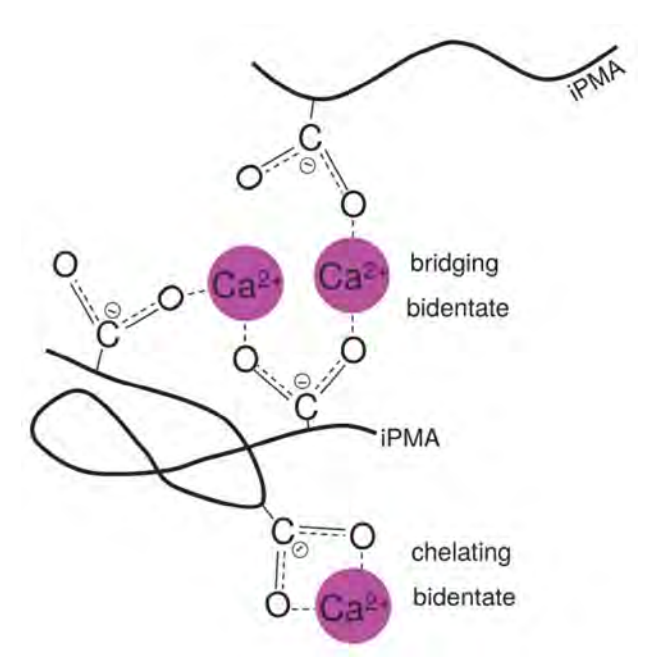


Figure 6. Cartoon depicting proposed ways of bidentate binding (chelate and bridging) of Ca²⁺ to COO⁻ groups on iPMA chains.

At the end we should shortly comment also the result for the lower (polymer rich) phase in iPMA-CaCl₂ solution with I=0.02 mol L⁻¹ and $\alpha_{\rm N}=0.63$ (note that these are average values for the whole sample). Here, ρ (= 0.69) is again very low and the points in the Kratky plot fit the Debye-Bueche function, showing that associates in this phase are much more compact as compared to the upper more solvated and dilute phase. We also presume, that $\alpha_{\rm N}$ in the bottom phase may be lower than the average value ($\alpha_{\rm N}=0.63$).

We conclude the discussion of LS results by proposing that PMA-Ca²⁺ associates could also include interactions in terms of so-called egg-box model, commonly used in interpretation of gelation phenomena of alginates and pectates, which belong to a class of polysaccharides with carboxylate groups.^{7,9,10} According to the egg-box model, interaction between COO⁻ groups on the polysaccharide and divalent cations is cooperative if the ion has an appropriate size to fit into the space in the egg-box, which is formed by the polyion backbone. Ca²⁺ fulfils this criterion, while the hydrated Mg^{2+} is too big.⁷ By proposing the existence of egg-box-like structural elements into which Ca²⁺ ions fit due to their size, one can understand both, the for-

mation of more gel-like polymer-rich phase in aPMA-Ca-Cl₂ and more complex structural observations for iP-MA-CaCl₂ solutions.

3. 2. 1. pH and Degree of Ionization

In support of the above interpretation of differences between MgCl₂ and CaCl₂ solutions, we report the pH values for both PMA solutions, from which the degree of ionization (α_i) of COOH groups was calculated from $\alpha_i = \alpha_N$ + ([H⁺] – [OH⁻])/ c_n (in this equation, [H⁺] and [OH⁻] are the molar hydronium and hydroxide concentrations). These measurements are reasonable only for aPMA solutions with $\alpha_N = 0$, because binding of cations has pronounced effect on ionization of COOH groups if $\alpha_N = 0$, whereas with iPMA with $\alpha_N = 0.2$ (or $\alpha_N = 0.63$) this effect is negligible (see the measured pH and calculated α_i values in Table S10). The α_i values in aPMA solutions are plotted in Figure 7 as a function of I. Clearly, α_i increases (from 0.013 at I = 0.1 to 0.036 at I = 0.5 mol L⁻¹) with increasing I in aPMA-CaCl₂ solutions, but changes negligibly in aP-MA-MgCl₂ solutions. The pronounced (threefold) increase in the presence of CaCl₂ is attributed to the replacement of H+ cations from COOH groups upon bidentate binding of Ca²⁺ as predicted above. As a result, some H⁺ ions are released into the solution, pH decreases, and α_i increases. On the contrary, the monodentate binding of Mg²⁺ ions to COOH groups is weaker and indirect (via hydration water molecules). Mg²⁺ is not able to replace H⁺ from the COOH group and has no (or negligible) effect on α_i . This clearly supports the above interpretations.

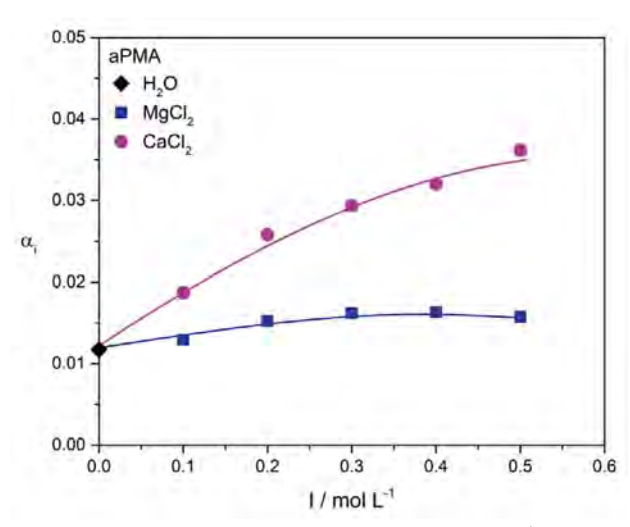


Figure 7. Calculated α_i values for aPMA ($c_p = 0.023 \text{ mol L}^{-1}$, $\alpha_N = 0$) in dependence on I in aqueous MgCl₂ and CaCl₂ solutions.

4. Conclusions

Our main interest in this study was the comparison of temperature induced intermolecular association in dilute aqueous solutions of two chemically identical PMA isomers, aPMA and iPMA, in the presence of divalent cations $\mathrm{Mg^{2+}}$ and $\mathrm{Ca^{2+}}$. UV spectroscopy and visual observations reveal that heating of aPMA solutions from 0 to 95 °C leads to intermolecular association and aggregate growth and finally to precipitation of aPMA from solution. Since the aPMA- $\mathrm{Mg^{2+}}$ and aPMA- $\mathrm{Ca^{2+}}$ precipitates re-dissolve upon cooling it was concluded that the process of association is reversible. Increasing *I* in aPMA solutions $(0.1-0.5 \text{ mol L}^{-1})$ leads to a decrease in the temperature at which phase separation occurs. iPMA behaves oppositely, which means that heating induces partial de-association of the aggregates, but the process is reversible and associates are reformed upon cooling. Nevertheless, iPMA- $\mathrm{Mg^{2+}}$ and iPMA- $\mathrm{Ca^{2+}}$ associates are stable in solution in the whole temperature range.

Considerable differences in micropolarity of the aPMA and iPMA aggregates in the presence of Mg²⁺ and Ca²⁺ ions are found by pyrene fluorescence measurements. The micropolarity of the iPMA associates is higher in comparison with the aPMA ones, which is attributed to different distribution of CH₃ and COOH groups within the associates. It is proposed that the cores of iPMA associates are composed of COOH groups, connected via cooperative H-bonds, in contrast to the aPMA ones where the CH₃ groups reside in the aggregate interior. The polarity of the aggregates' interior in the iPMA-MgCl₂ solutions is the highest and close to that of water due to strong hydration of Mg²⁺ ions.

The LS measurements in iPMA and aPMA solutions in MgCl₂ and CaCl₂ show that both PMAs form intermolecular associates with dimensions in the nanometer range at low α_N values. The values of the shape parameter ρ indicate either micro-gel like particles ($\rho \approx 0.7$) or more water permeable structures ($\rho \approx 0.90$) or even a combination of rod-like and coil-like regions in the same aggregate ($\rho \approx 1.37$). This latter case was identified with iPMA aggregates in the presence of Ca²⁺ ions.

Acknowledgements

This work was financially supported by the Slovenian Research Agency (ARRS), through the Physical Chemistry program P1-0201.

ORCID - Ksenija Kogej: 0000-0002-6291-1032

5. References

- T. Dudev, C. Lim, *Chem. Rev.* 2003, 103, 773–787.
 DOI:10.1021/cr020467n
- M. Muthukumar, *Macromolecules* 2017, 50, 9528–9560.
 DOI:10.1021/acs.macromol.7b01929
- F. Cilurzo, C. G. M. Gennari, F. Selmin, G. Vistoli, *Mol. Pharm.* 2010, 7, 421–430. DOI:10.1021/mp900199a
- T. Dudev, C. Lim, Acc. Chem. Res. 2007, 40, 85–93.
 DOI:10.1021/ar068181i

- Schauss, F. Dahms, B. P. Fingerhut, T. Elsaesser, J. Phys. Chem. Lett. 2019, 10, 238–243. DOI:10.1021/acs.jpclett.8b03568
- Kavitha, P. Deepa, M. Karthika, R. Kanakaraju, J. Mol. Graph. Model. 2018, 85, 13–24.
 - **DOI:**10.1016/j.jmgm.2018.07.004
- J. Mattai, J. C. T. Kwak, J. Phys. Chem. 1984, 88, 2625–2629.
 DOI:10.1021/j150656a040
- Y. Fang, S. Al-Assaf, G. O. Phillips, K. Nishinari, T. Funami,
 P. A. Williams, L. Li, *J. Phys. Chem. B* 2007, *111*, 2456–2462.
 DOI:10.1021/jp0689870
- X. Wang, H. G. Spencer, *Polymer* 1998, 39, 2759–2764.
 DOI:10.1016/S0032-3861(97)00597-1
- L. Q. Wan, J. Jiang, D. E. Arnold, X. E. Guo, H. H. Lu, V. C. Mow, Cell. Mol. Bioeng. 2008, 1, 93–102.
 DOI:10.1007/s12195-008-0014-x
- 11. J. Krebs, in: R. A. Mayers (Ed.): Encyclopedia of Molecular Cell Biology and Molecular Medicine, 2nd Edition, Wiley-VCH Verlag GmbH & Co. KGaA, Weinheim, Germany, 2004, pp. 133–170.
- A. Kaufman Katz, J. P. Glusker, S. A. Beebe, C. W. Bock, J. Am. Chem. Soc. 1996, 118, 5752–5763. DOI:10.1021/ja953943i
- M. E. Maguire, J. A. Cowan, *Biometals* 2002, 15, 203–210.
 DOI:10.1023/A:1016058229972
- W. Johnen-Dechent, M. Kettler, Clin. Kidney J. 2012, 5, i3–i14. DOI:10.1093/ndtplus/sfr163
- 15. M. Eigen, *Pure Appl. Chem.* **1963**, *6*, 97–115. **DOI:**10.1351/pac196306010097
- H. Diebler, M. Eigen, *Pure Appl. Chem.* **1969**, *20*, 93–116.
 DOI:10.1351/pac196920010093
- T. Dudev, C. Lim, J. Phys. Chem. B 2004, 108, 4546–4557.
 DOI:10.1021/jp0310347
- 18. J. V. Needham, T.Y. Chen, J. J. Falke, *Biochemistry* **1993**, *32*, 3363–3367. **DOI**:10.1021/bi00064a020
- R. Konradi, J. Rühe, *Macromolecules* 2004, 37, 6954–6961.
 DOI:10.1021/ma049126x
- 20. D. M. Chang, *JAOCS*, **1983**, *60*, 618–622. **DOI:**10.1007/BF02679800
- 21. A. Silberberg, J. Eliassaf, A. Katchalsky, *J. Polym. Sci.* **1957**, 23, 259–284. **DOI:**10.1002/pol.1957.1202310325
- M. Sedlák, Colloid Polym. Sci. 2017, 295, 1281–1292.
 DOI:10.1007/s00396-016-4003-7
- M. Sedlák, Č. Konňák, Macromolecules 2009, 42, 7430–7438.
 DOI:10.1021/ma9015032
- M. Sedlák, Č. Konňák, *Macromolecules* 2009, 42, 7439–7446.
 DOI:10.1021/ma901504h

- A. K. Bajpai, S. K. Shukla, S. Bhanu, S. Kankane, *Prog. Polym. Sci.* 2008, *33*, 1088–1118.
 DOI:10.1016/j.progpolymsci.2008.07.005
- K. Kogej, *Polymers* **2016**, *8*, 168.
 DOI:10.3390/polym8050168
- J. Eliassaf, A. Silberberg, *Polymer* 1962, 3, 555–564.
 DOI:10.1016/0032-3861(62)90103-9
- P. Hriberšek, K. Kogej, *Macromolecules*, 2019, 52, 7028–7041.
 DOI:10.1021/acs.macromol.9b01467
- E. Van den Bosch, Q. Keil, G. Filipcsei, H. Berghmans, H. Reynaers, *Macromolecules* 2004, *37*, 9673–9675.
 DOI:10.1021/ma047821z
- W. E. Goode, F. H. Owens, R. F. Fellmann, W. H. Snyder, J. E. Moore, *J. Polym. Sci.* 1960, 46, 317–331.
 DOI:10.1002/pol.1960.1204614803
- 31. B. Jerman, K. Kogej, Acta Chim. Slov. 2006, 53, 264-273.
- 32. K. Kogej, J. Škerjanc, *Langmuir* **1999**, *15*, 4251–4258. **DOI:**10.1021/la9811517
- 33. D. Y. Chu, J. K. Thomas, *J. Am. Chem. Soc.* **1986**, *108*, 6270–6276. **DOI:**10.1021/ja00280a026
- E. M. Loebl, J. J. O'Niell, J. Polym. Sci. 1960, 45, 538–540.
 DOI:10.1002/pol.1960.1204514629
- 35. N. Vlachy, J. Dolenc, B. Jerman, K. Kogej, J. *Phys. Chem. B* **2006**, *110*, 9061–9071. **DOI**:10.1021/jp060422g
- C. Urban, P. Schurtenberger, J. Colloid Interface Sci. 1998, 207, 150–158. DOI:10.1006/jcis.1998.5769
- 37. P. Hriberšek, K. Kogej, *Polymers* **2019**, *11*, 605. **DOI:**10.3390/polym11040605
- 38. S. Sitar, V. Aseyev, K. Kogej, *Soft Matter* **2014**, *10*, 7712–7722. **DOI:**10.1039/C4SM01448K
- S. Sitar, V. Aseyev, K. Kogej, *Polymer* 2014, 55, 848–854.
 DOI:10.1016/j.polymer.2014.01.007
- 40. E. V. Tarassova, V. Aseyev, A. Filippov, H. Tenhu, *Polymer* **2007**, *48*, 4503–4510. **DOI:**10.1016/j.polymer.2007.05.069
- 41. H. G. Brittain, F. S. Richardson, R. B. Martin, *J. Am. Chem. Soc.* **1976**, 98, 8255–8260. **DOI:**10.1021/ja00441a060
- 42. R. B. Martin, F. S. Richardson, Q. Rev. Biophys. 1979, 12, 181–209. DOI:10.1017/S0033583500002754
- 43. C. G. Dos Remedios, *Cell Calcium* **1981**, *2*, 29–51. **DOI:**10.1016/0143-4160(81)90044-0
- 44. P. Kratochvil, in: M. B. Huglin (Ed.): Particle scattering functions in light scattering from polymer solutions, Academic Press Inc.: London and New York, **1972**, pp. 333–384.
- E. J. Robertson, A. P. Carpenter, C. M. Olson, R. K. Ciszewski,
 G. L. Richmond, J. Phys. Chem. C 2014, 118, 15260–15273.
 DOI:10.1021/jp503051w

Povzetek

Z UV spektroskopijo, vizualnim opazovanjem in fluorimetrijo na osnovi pirena smo proučevali vpliv temperature na tvorbo asociatov med verigami izotaktične (iPMA) in ataktične poli(metakrilne kisline) (aPMA) v vodnih raztopinah v prisotnosti dvovalentnih kationov (Mg²+ in Ca²+). Gretje raztopin aPMA povzroči agregacijo verig, kar vodi do makroskopske ločitve faz. Z naraščajočo ionsko jakostjo raztopin se nastop agregacije (segrevanje) oziroma de-agregacija (ohlajanje) aPMA verig pomika k nižjim temperaturam. Nasprotno pa asociati iPMA med segrevanjem razpadejo, a le delno, tako da so stabilni delci z nano-dimenzijami prisotni v raztopini v celotnem temperaturnem območju. Strukturno karakterizacijo agregatov smo izvedli z meritvami dinamičnega in statičnega sipanja svetlobe pri 25 °C. Rezultati kažejo, da agregati obeh PMA z Mg²+ vključujejo precej vode, porazdelitev mase znotraj delcev pa je precej enakomerna. To pripisujemo močni hidrataciji Mg²+ ionov, zaradi česar Mg²+ ioni favorizirajo monodentatno vezavo na karboksilatne skupine. Ca²+ ioni pa se vežejo nanje na bidentatni način in zato močneje kot Mg²+ ioni, pri čemer izgubijo hidratno vodo in tvorijo agregate z več strukturnimi elementi, kar je odvisno od taktičnosti verige.



Except when otherwise noted, articles in this journal are published under the terms and conditions of the Creative Commons Attribution 4.0 International License

Acta Chimica Slovenica Vol. 66 (2019)

AUTHOR INDEX

Abbasi Muhammad Athar	. 294	Bratkič Arne	. 239
Abid Obaid Hasan	. 552	Brazhko Olexandr Anatolievich	. 145
Adil Muhammad	. 859	Brovč Ema Valentina	. 934
Afsarian Mohammad Hosein	. 874	Budasheva Hanna	. 814
Afzal Hafiz Usman	. 435	Budasheva Hana	. 239
Aghkand Anila Rahimi	. 344	Çabuk Hasan	. 385
Ågren Hans		Ćadar Oana	
Akbaridilmaghani Karim		Chaban Ihor G.	. 103
Akhondi Maryam		Chaban Taras I.	. 103
Aksuner Nur		Chakraborty Tanmoy	
Akyurekoğlu Ragibe Hulya		Chebotarev Alexander	
Albadi Jalal		Chellappa Joel	
Ali Qamar		Chen Guang-Ying378,	
Aliyev Akif Shikhan		Chen Jia-Yi	414
Aliyeva Yegana Rasul		Chen Qin	
Amiraslanov Imameddin Rajabali		Chen Xia	
An Dongxia		Chen Yan	
Antypenko Lyudmyla		Cheng Xiao-Shan	
Antypenko Oleksii Mykolayovich		Chouaih Abdelkader	
Arsene Cecilia		Christian Orrenius	
Asadi Marziyeh		Cor Darija	
Asgharib Behvar		Coşkun Yasemin İşlek	
Ashraf Muhammad294,		Cui-Lin Zhang,	
Avula Sri Nivas		Cvetanović Aleksandra	
Baara Fayssal Triki		Cvijović Mirjana R Čakarević Jelena	/0
Băbălău-Fuss Vanda			
Babanly Dunya Mahammad		Čolnik Maja	205
Babanly Mahammad Baba		D'Alessio Roberto	
Babapoor Aziz		Dapiaggi Federico	
Bahrani Sonia		Demchuk Inna L.	
Bakić Marina Tranfić		Demetrescu Ioana	
Barbalat Dmytro		Devetak Iztok	
Baryshnikov Glib V		Djafri Ayada.	
Bayrakci Mevlut		Dlouhy Matjaž	. 229
Bayram Esiye Irem		Dodevska Totka	
Behrouz Somayeh		Dogan Ahmet	
Beitollahi Hadi		Dolenc Iztok5,	
Bejaoui Linda		Du Xiu-Li	
Berlec Aleš		Dubovyi Vitaliy	
Beyranvand Narges Safar		Eigner Vaclav	
Bharali Pranjal		El Bour Monia	
Bhat Haamid Rasool		EL-Hawary Ibrahim Ibrahim	. 592
Bhatt Bhupesh S.	. 944	Elrouby Mahmood	. 155
Bitis Leyla	. 831	Esmaeili Hossein 208, 865,	, 888
Boroujeni Kaveh Parvanak	. 542	Fang Lizhen	. 745
Boukabcha Nourdine	. 490	Fang Xiao-Niu	.414
Božič Janja	. 501	Farahani Hadi	
Božić Bojan		Farhadi Saeed	
Božović Štojan		Farjam Mojtaba	
Bratkič Arne		Farokhnia Ahmad	. 542

Fatima Tahzeeb	435	Jamalizadeh Effat	
Felder Eduard	395	Jamir Latonglila	276
Fonovi, Marko	50	Jarrah Afsoon	85
Fonović Urša Pečar.		Javeed Aqeel	
Franko Mladen		Joksović Ljubinka G	70
Franko Mladen		Jukić Marijana	
Gądek-Sobczyńska Joanna		Kanthecha Darshana N	944
Galagan Rostislav L		Karia Parag S.	
Gao Yue		Karmaker Rituparna	
Garbe Leif-Alexander		Karthik Pulluri	
		Karthik Pulluri	
Garvas Maja Gavazov Kiril B		Karvani Jamshid	
Ghafoor Aamir		Kazemi-nasab Abolghasem	
Ghezelbash Zahra Dono		Keskin Sedat	
Glavaš-Obrovac Ljubica		Khan Abdul Muqeet	
Gligorić Emilia		Khoshkerdar Iman	
Globočnik Maja		Khuhawar Muhammad Yar	
Goger Fatih		Khvalbota Liudmyla	
Goljat Leja	814	Knez Hrnčič Maša	
Golobič Amalija	1019	Knez Željko217, 33	7, 732, 751
Gong Chang-Da	421	Koduru Janardhan Reddy	123
Gongadze Ekaterina		Kogej Ksenija	1026
Grassino Antonela Ninčević		Kopp Josef	
Grbavac Daria		Korošec Peter	
Gregor-Svetec Diana		Korte Dorota	
Gruden Kristina		Kos Janko	
Grudić Veselinka		Kotnik Petra	
Grujić-Letić Nevena		Kovalenko Sergii Ivanovich	
Guzenko Elena		Kralj Cigić Irena	059
Hachani Salah Eddine			
		Kralj-Iglič Veronika Kramer Karl J	334
Hamama Wafaa			
Hamzaoui Fodil		Kraševec Ida	
Han Yong-Jun		Kravanja Gregor	33/
Hao Xiao-Yun		Kravos Aleksander	
Hashemi Seyyed Alireza	865	Križni Maja	45
Hassen Rached Ben		Krstić Jovana	
Hatzidimitriou Antonis		Kucukkolbasi Semahat	
He Guo-Xu		Kufelnicki Aleksander	
Hojnik Podrepšek Gordana		Kuotsu Visekhonuo	
Hriberšek Patricija	1026	Labenska Irina Borisivna	
Hristov Danail G	987	Lađarević Jelena	182
Hu Shuyu		Lai Huimin	745
Hu Xiaojing		Lalić Marina Mrđa	913
Humelnicu Doina		Lan Wen-Long	
Humelnic, Ionel		Lazarova Yanna	
Hussain Zakir		Leitgeb Maja21	
Ibrahim Ismail Taha		Lekova Vanya	
Ibrahim Mohd.		Lesar Antonija	
Igić Ružica			
		Leskovšek Mirjam	
Iglič Aleš		Li Gao-Nan	
Iram Fozia		Li Wei	
Irshad Misbah		Li Gao-Nan	
Isacchi Antonella		Li Jia	
Ismail Amel		Li Yang	
Ivić Milka Avramov		Li Yong-Xiu	
Jaafar Nur Farhana		Lin Xue-Song	
Jahandideh Sara	865	Litvin Valentina A	427
Jahangir Taj Muhammad	899	Liu En-Cheng	971
Jalali Mehdi		Liu Kai	
Jamal Syed Babar		Liu Shu-Juan	

Liu Qing-Yun	308	Olari Romeo Iulian	
Liu Yu	308	Oleksiv Lesia	62
Liu Zhi-Ping		Omer Muhammad Ovais	
Lodhi Muhammad Arif	294	Owaid Mustafa Nadhim	552
Longkumer Naruti		Oymak Tülay	78
Lovi Jelena		Ozyilmaz Ozyilmaz Gul	
Lunder Mojca		Pajk Stane	
Luo Xiao-Qiang		Pasternak Beata	
Lu Qi		Patel Mohan N.	
Ma Gang		Patidar Anshul P.	
Ma Zhiguang		Patsay Ihor	
Magallón Cacho Lorena		Pavlovič Irena	
Magnaghi Paola		Pavlović Aleksandra	
Majer Janja	659	Pecev-Marinković Emilija	
Majidzade Vusala Asim	155	Pechousek Jiri	455
Mallick Subrata	923	Pedisić Sandra	367
Mammadov Faig Mamedagha	466	Peng Qin-Long	570, 694
Maou Samira		Peng Hui	
Marco Valerio Di		Perdih Anton	
Martinez Sanja		Pérez Bueno José de Jesús	
Martynenko Yulya Victorivna		Pieraccini Stefano	
		Pisal Mohamad Anis Farith	
Marušič Fedja			
Mashadiyeva Leyla Farkhad		Plavec Tina Vida	
Matiychuk Vasyl S		Počkaj Marta	
Meftah Yazid		Pompe-Novak Maruša	45
Megrouss Youcef	490	Ponikvar-Svet Maja	255
Meye Fatuma		Popović Ljiljana	473
Mihailović Nevena R	70	Posta Katalin	648
Mijin Dušan		Pradhan Sukanta Kumar	
Milcheva Nikolina P		Pramanik Arunima	
Milošev Ingrid		Primožič Mateja21	
Minaev Boris F.		Prosen Helena	
Mišković Špoljarić Katarina		Qian Heng-Yu	
Miti Snežana		Qi Jie	
Mo Zheng-Rong		Qiu Xiao-Yang	
Mobini Mohsen		Qiu Xiao-Yang	
Mojoudi Fatemeh		Qureshi Farah	
Moldovan Ana		Rad Mohammad Navid Soltar	
Moradi Niloofar		Ragimov Sadiyar Sultan	
Motto Ilaria		Rahmati Morteza	
Mousavi Seyyed Mojtaba	865	Rahnema Yaghoub	865
Mravljak Janez	934	Rajaretnam Biju Bennie	196
Mrmošanin Jelena		Rana Malay K	
Muslim Rasim Farraj		Ranjan Prabhat	
Nanda Ashirbad		Rápó Eszter	
Nandi Souvik		Ratković Ana	
Nanut Milica Perišić		Razman Nur Izzatie Hannah.	
		Rebiai Abdelkrim	
Naqvi Tahira Nasti Nataša			
		Reddy Koduri Vasumathi	701
Neag Emilia		Rehman Aziz Ur	
Nebbache Nadia		Renko Miha	
Nedić Zoran P.		Richa Kikoleho	
Nektegayev Ihor A		Rizvi Masood Ahmad	
Nikolić Milena		Rohlíček Jan	603
Niu Zhi-Gang	978	Roman Cecilia	850
Niu Zhi-Gang		Sabotič Jerica	28
Nordin Norazzizi		Sadykova Zhanar	
Novak Petr		Safaei Mohadeseh	
Odak Ilijana		Sahoo Rudra Narayan	
Ogurtsov Volodymyr V		Samiey Babak	
Ogurwov voiouyiliyi v	103	Samily Davak	

Samimi Heshmat Allah		Tehrani Abbas Dadkhah	443
Sang Ya-Li	168	Teofilović Branislava	
Savardashtaki Amir	865	Tomsič Gaja	
Savić Saša	560	Tonk Szende	648
Sayin Serkan	839	Torok Anamaria	850
Seghir Imane	629	Tošić Snežana	802
Selvanayagam Theodore	David	Tuncay Ali	950
Manickam	196	Turk Boris	
Sen Ali		Turk Dušan	
Sert Sema		Turk Vito	
Seyd Abdelkader Hadj		Turk-Sekulić Maja	
Shahid Muhammad		Tymoshuk Oleksandr	
Shahrokh Mansooreh		Urbas Raša	
Shishehbore Masoud Reza		Dragović Uzelac Verica	
Shterey Ivan		Vafazadeh Rasoul	
Shu-Juan Liu		Vardaki Maria	
Si Wei-Jiang		Vekariya Pankaj A.	
Siddique Adil		Verma Lata	
Singh Jiwan		Vidmar Robert	
Sinha Upasana Bora		Vidovic Senka	
Sironi Maurizio		Vizovišek Matej	
Slapničar Miha		Vladić Jelena	
Snigur Denys		Vong Yunny Meas	
Snoj Ekmečič Tina		Vrabič Brodnjak Urška	
Sofan Mamdouh	592	Wang Li-Hang	675
Solomon Daniel Abraham	196	Wang Pan-Pan	570
Soroaga Laurentiu Valentin	326	Wang Pan-Pan	694
Souyei Belgacem	315	Wang Pan-Pan	190
Stankovič Elesini Urška		Willis Anthony C	
Stanković Srboljub J	70	Woźniczka Magdalena	
Stanojković Tatjana		Wu Shui-Xing	
Stefano Rendine		Xiao-Yang Qiu	
Steffens Karl		Xie Long-Yan	
Stoian Andrei Bogdan		Xu Han-Ru	
Stojnova Kirila		Xue Ling-Wei	
Stoka Veronika		Xue Ling-Wei	
Stremsdoerfer Guy		Xue Ling-Wei	
Subramanian Iyyam Pillai		Xue Ling-Wei	
Suciu Maria		Yang Xiao-Han	
Sun Qianqian		Yang Lu	
Sunitha Malladi		Yang Xiao-Han	402
		Yanik, Jale	
Supong Aola		Yeganeh Golan	
Suvajdžić Ljiljana		Yi Xiu-Guang	
Swain Rakesh		Yıldız Elif	
Szép Robert		Yilmaz Mustafa	
Šagud Ivana		Yılmaz Yasemin	
Šegedin Primož		Yuan Ding	
Šink Roman		Zahirović Abida	
Škerget Mojca	732	Zaiz Faouzi	
Škorić Irena	681	Zarenezhad Elham	
Štepec Dona		Zeković Zoran	
Štrancar Janez	668	Zhang Cui-Lin	719
Štrukelj Borut	37	Zhang Cuimiao	
Švarc-Gajić Jaroslava		Zhang Hong	
Świątek Mirosława		Zhang Hui-Jie	
Tagiyev Dilgam Babir		Zhang Hui-Jie	
Tan Yao		Zhang Yu	
Tao Zi-Wen		Zhang Dao-Peng	
Tawfeeq Hiba Maher	552	Zhang Hui-Jie	

Zhang Qian	378	Zidar Nace	58
Zhao Fangfei			
Zhao Zheng	978	Zorić Zoran	367
Zhou Zhen			378
Zhuang Shu-Juan	308	Žižak Željko	473

DRUŠTVENE VESTI IN DRUGE AKTIVNOSTI SOCIETY NEWS, ANNOUNCEMENTS, ACTIVITIES

Vsebina

Mednarodna kemijska olimpijada 2019	S69
Poročilo o delu v letu 2019	S75
Koledar važnejših znanstvenih srečanj s področja kemije,	
kemijske tehnologije in kemijskega inženirstva	S77
Navodila za avtorje	S80
Contents	
International Chemistry Olympiad 2019	S69
Report for 2019	S75
Scientific meetings – chemistry, chemical technology and chemical engineering	S77
Instructions for authors	S80

Acta Chim. Slov. 2019, 66, (4), Su	pplement

S68 ____

Mednarodna kemijska olimpijada 2019

Andrej Godec

UL, FKKT

Letošnja, že 51. mednarodna kemijska olimpijada, je potekala od 21. do 29. 7. 2019 v Parizu. Olimpijade se je udeležila naslednja slovenska dijaška ekipa: Tijan Prijon (gimnazija Bežigrad), Mitja Koderman (gimnazija Ptuj), Aleš Globočnik (gimnazija Kranj) in Dren Gruden (gimnazija Bežigrad). Vsi štirje so dobili bronasto odličje. Vsem čestitamo za res lep uspeh!

Ekipo sva vodila mentorja dr. Berta Košmrlj in dr. Andrej Godec, oba iz Fakultete za kemijo in kemijsko tehnologijo v Ljubljani.

Priprave na olimpijado in izbirna tekmovanja potekajo na Fakulteti za kemijo in kemijsko tehnologijo v Ljubljani. Letos je pri tem sodelovala naslednja ekipa FKKT: dr. Berta Košmrlj, dr. Alojz Demšar, dr. Darko Dolenc, dr. Jernej Markelj, dr. Črtomir Podlipnik in dr. Andrej Godec. Pomagali sta še Branka Miklavčič in Mojca Žitko.

Pri organizaciji udeležbe na olimpijadi sodelujemo z Zvezo za tehniško kulturo Slovenije. Vsem se za pomoč najlepše zahvaljujemo.

Letošnje olimpijade se je udeležilo rekordnih 309 tekmovalcev iz 80 držav. Vsaka država ima lahko največ štiri tekmovalce, in dva mentorja. Zastopani so pravzaprav že vsi kontinenti. Vsako leto pa pridejo tudi države opazo-

valke, ki potem že naslednje leto lahko pripeljejo tudi tekmovalce. Letos so to bile Bangladeš, Oman, Sri Lanka in Trinidad ter Tobago. V prihodnosti lahko tako pričakujemo še več tekmovalcev.

Absolutni zmagovalec letošnje olimpijade je bil He Lyu iz Kitajske (dosežek 97,3 %), drugi je bil prav tako Kitajec Deng Zijie (97,1 %), in tretji Korejec Choi Hyeogkui (96,5 %). Vsega skupaj je bilo podeljenih 37 zlatih, 63 srebrnih in 94 bronastih medalj. Dosežek naših tekmovalcev je bil odličen: Tijan je dosegel 69,1 %, Mitja 67,4 %, Aleš 62,7 % in Dren 61,5 %, kar je zadostovalo za bronasto odličje vseh štirih. Vsi rezultati so sicer objavljeni na spletni strain organizatorja olimpijade (https://icho2019.paris/en/).

Na olimpijadi sta sicer dva tekmovalna dneva: najprej je na vrsti praktično delo v laboratoriju, in kasneje še teoretični test. Vsak traja po pet ur. Ostale dni preživijo dijaki na izletih in raznih aktivnostih.

Vloga mentorjev je usklajevanje in prevajanje besedil nalog, kar nam vzame večino časa. Na koncu naloge svoje ekipe popraviva, in ocene usklajujeva z organizatorjevimi na arbitraži. Letos je bilo najino delo še posebej zahtevno, saj je bilo takrat v Parizu 42 °C, Francozi pa večinoma ne uporabljajo klime.

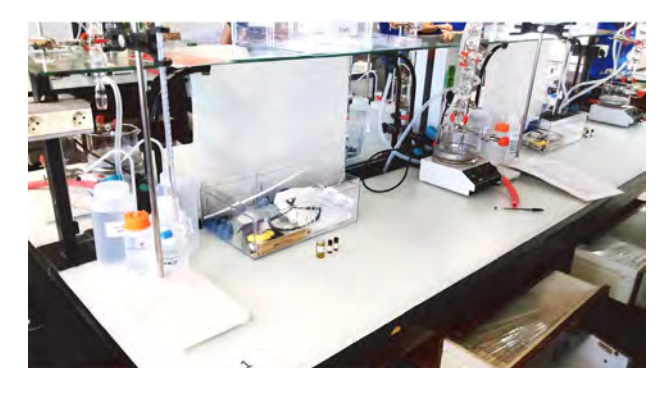


Slovenska ekipa na 51. mednarodni kemijski olimpijadi. Z leve so Berta Košmrlj, Mitja Koderman, Dren Gruden, Tijan Prijon, Aleš Globočnik, ter Andrej Godec.

Otvoritev letošnje olimpijade je bila 22. 7. v dvorani *Amphithéâtre Lavoisier* stavbe *Maison de la Chimie*. V državi organizatorki gre za dogodek najvišjega ranga, zato so tam predstavniki politike, stroke in medijev, otvoritev pa je tudi priložnost, da organizatorji predstavijo svoje dosežke in kulturo. Olimpijado je uradno odprl Jean-Michel Blanquer, francoski minister za izobraževanje in mlade. Med govorniki na otvoritvi je bil tudi eden od dobitnikov Nobelove nagrade za leto 2016 Jean-Pierre Sauvage, ki je v krajšem predavanju o svojih raziskavah na področju molekularnih strojev navduševal udeleženke in udeležence za znanost. Ni naključje, da se je kasneje med teoretičnimi nalogami na olimpijadi ravno ta tema večkrat ponovila.

Po uvodni slovesnosti in pogostitvi smo mentorji odšli na ogled laboratorijev v šoli Lycée Pierre-Gilles de Gennes, kjer so sicer potekala vsa tekmovanja. Mentorja tam preveriva laboratorijski inventar za vsakega našega tekmovalca in preizkusiva delovanje naprav, ki jih bodo uporabljali pri eksperimentalnem delu. Laboratoriji so v tej stavbi zelo prostorni, kar je velika redkost na olimpijadah.

Še isti dan zvečer sledi že prva seja vseh mentorjev in sestavljalcev praktičnih nalog. Na teh srečanjih usklajujemo in pilimo besedila nalog, ki jih bomo potem mentorji prevajali.



tudi strukturo dobljenega produkta (4-nitrobenzojska kislina). Okson se sicer uporablja v plavalnih bazenih in pri tretmanu odpadnih voda.

Druga praktična naloga je bila na temo železa in njegove vloge pri staranju vina. Ko njegova koncentracija preseže 10 do 15 mg na liter, se zaradi oksidacije železa(II) v železo(III) lahko poslabša kvaliteta vina, ker nastanejo oborine. Zato je nujno določevanje vsebnosti železa med proizvodnjo vina. Pri zelo nizkih koncentracijah železa lahko koncentracijo določimo z nastankom obarvanega kompleksa železa(III) s tiocianatom SCN- kot ligandom, pri čemer uporabimo spektrofotometrične meritve. Pri tej nalogi so morali dijaki določiti celotno koncentracijo železa v vzorcu belega vina z uporabo spektrofotometrije, in na podoben način ugotoviti stehiometrijo kompleksa tiocianat – železo(III).

Tretja praktična naloga je bila na temo skladiščenja vina. Žveplov dioksid, SO_2 , se uporablja kot konzervans za vino. Ko vinu dodamo SO_2 , lahko ta reagira z vodo, pri čemer nastanejo ioni HSO_3^- in protoni H^+ . Če odstranimo drugi proton, lahko bisulfit spremenimo v sulfit, SO_3^{3-} .

$$SO_2 + H_2O = H^+ + HSO_3^-$$

 $HSO_3^- = H^+ + SO_3^{2-}$



Laboratorijski pult tekmovalca. Desno je prostor za prevajanje mentoric in mentorjev.

Letos so morali dijaki v laboratoriju izvesti tri praktične naloge, za vse skupaj pa so imeli 5 ur časa. Prva naloga je bila okolju prijaznejša oksidacija nitrobenzaldehida. Kemiki namreč ves čas iščejo nove reagente za oksidacije, saj večina teh reagentov onesnažuje vode. V tej nalogi so dijaki izvedli reakcijo oksidacije 4-nitrobenzaldehida, dobljeni produkt prekristalizirali, primerjali mobilni fazi za TLC in preverili čistočo produkta s TLC. Kot oksidant so uporabili kalijev peroksomonosulfat (Oxone*), ki daje okolju nenevarne in nestrupene sulfatne soli. Reakcijo so izvajali v mešanici vode in etanola, ki tudi veljata za okolju prijazni topili. Dijaki so morali sestaviti aparaturo za segrevanje reakcijske zmesi pod refluksom, in kasneje nučirati. Na koncu so izvedli še TLC analizo produktov, in na kromatogramu označiti ustrezne lise. Opisati so morali

Te tri različne oblike žveplovega dioksida lahko v vodi reagirajo z drugimi spojinami v vinu, na primer acetaldehidom, pigmenti, sladkorji itd., pri čemer nastanejo produkti P. Celotna (totalna) koncentracija žveplovega dioksida je vsota koncentracij »prostih« oblik (SO₂, HSO₃ and SO₃) in P.

Koncentracijo konzervansov nadzorujejo in regulirajo, ker so sulfiti in žveplov dioksid za nekatere ljudi škodljivi. V EU je maksimalna dovoljena celotna koncentracija žveplovega dioksida 100 mg L⁻¹ za rdeče vino in 150 mg L⁻¹ za belo vino ter rozé. Dijaki so morali pri tej nalogi z jodometrično titracijo določiti celotno koncentracijo žveplovega dioksida v vzorcu belega vina.

Tema dveh nalog je bila torej vino, ki je v Franciji zelo popularna alkoholna pijača; poraba te je 42 litrov letno na osebo.





Cité International Universitaire de Paris. Na desni je kemijski šov, ki so ga za nas pripravili v Palais de la Découverte.

Po prevajanju smo imeli mentorji naslednji dan na sporedu prvič ogled mesta. Pravzaprav je s Parizom povezano ime za kemijski element Lutecij. Starodavno galsko pleme Parisii se je namreč v tretjem stoletju pred Kristusom naselilo na otočku mesta, in ga poimenovalo Lutetia. Današnje ime je mesto dobilo v četrtem stoletju.

Najprej smo obiskali *Palais de la Découverte.* Gre za izjemen muzej odkritij, z mnogimi interaktivnimi vsebinami, katerih namen je približati vsa področja znanosti laikom. Tu lahko preverite svoje znanje o zvezdah, pa o matematiki v π sobi, o načinih komunikacije med živalmi, prisostvujete lahko živahni prezentaciji kemijskih principov in tako naprej. En dan v tem muzeju je komaj dovolj, če imate radi naravoslovje.

Mentorji smo sicer prebivali in delali v kampusu Cité International Universitaire de Paris, ki je bila ustanovljena z namenom zagotoviti ustvarjalno okolje tudi za mednarodne študente in raziskovalce. Na olimpijadi imamo dva prosta dneva, ko smo poleg že navedenega obiskali še muzej znanosti Cité des Sciences et de l'Industrie, šli na izlet z ladjo po Seni, ter seveda videli še Versailles ter predvsem tamkajšnje vrtove. V senci dreves smo imeli piknik, ki se je po pohajanju pod vročim pariškim soncem zelo prilegel. Palača predstavlja esenco francoske monarhije, saj so v

njej nekaj čez sto let domovali francoski kralji. To je bilo prizorišče razkošnih zabav in sprejemov. Kot lepo pokaže dokumentarec o zgodovini, ki ga lahko vidite v Versaillesu, pa se je ta zgodba končala leta 1789 s francosko revolucijo.

Del naših aktivnosti je bil tudi na znameniti École Polytechnique, ki je bila ustanovljena med francosko revolucijo, in je kasneje pod Napoleonom postala vojaška šola. Med njenimi študenti so bili odlični znanstveniki, kot naprimer Henri Becquerel, Louis Joseph Gay-Lussac in Henri Le Chatelier.

Več dela smo mentorji (in dijaki!) imeli s teoretičnim testom. Letošnji je vseboval 9 nalog, dijaki pa so imeli pet ur časa za reševanje. Naloge so bile povezane z odkritji francoskih znanstvenikov, ki so dali močan pečat razvoju znanosti. Naloge so sicer v celoti dostopne v spletni učilnici Kemljub, ki je namenjena olimpijadi in dogajanjem okrog nje (https://skupnost.sio.si/course/view.php?id=150).

Prva naloga je bila iz kvantne kemije. Na primeru buta-1,3-diena so morali dijaki obravnavati π elektrone v modelu z lokaliziranimi in delokaliziranimi in za oba primera izračunati celotno energijo π sistema kot funkcijo $h,\,m_{\rm e}$ in d. Nato so morali izračunati še konjugacijsko energijo butadiena, določiti vrednost π valovnih funkcij $\psi_{\rm n}$ v odvisnosti od L za zasedene nivoje, in na koncu še elektronsko gostoto.



Piknik mentoric in mentorjev v Versaillesu. Na desni je pogled z ladje na katedralo Notre-Dame, ki je trenutno zaradi požara v procesu rekonstrukcije.



Druga naloga je bila na temo vodika kot morebitnega vira energije v prihodnosti. Najprej so morali dijaki ovrednotiti reakcijo elektrolize vode, s katero dobijo vodik; izračunali so, ali je termodinamsko ugodna. Nato so morali izračunati teoretično vrednost električne napetosti med elektrodama, ki je potrebna, ter izkoristek moči, ko sta bili uporabljeni Pt katoda in ${\rm Fe}_2{\rm O}_3$ anoda. Alternativa elektrolizi vode je direktni fotokatalitični razcep vode. Pri tem se uporablja polprevodnik, ki se lahko aktivira z absorpcijo svetlobe. Izračunati so morali, kolikšna energija je potrebna za aktivacijo večih izbranih polprevodnikov, ter izkoristek moči tudi za ta primer.

Tretja naloga je bila zgodba o srebrovem kloridu, in je bila posvečena Gay-Lussacu. Ta znanstvenik je bil zelo priljubljen professor na École Polytechnique. Pri nalogi smo tako dobili 6 citatov iz njegovih predavanj o tej spojini in njenih lastnostih, dijaki pa so morali vsak citat napisati v kemijskem jeziku, to je s kemijsko enačbo. Razen tega so morali izračunati topnost spojine, ter določiti strukture kompleksov z amonijakom. Na koncu pa so spoznali še Mohrovo metodo; na osnovi podatkov pri titraciji so morali izračunati neznano koncentracijo kloridnih ionov v raztopini natrijevega klorida, ter utemeljiti, zakaj je CrO_4^{2-} dober pokazatelj končne točke.

Četrta naloga je bila posvečena jodu in njegovem odkritelju, Bernardu Courtoisu. Leta 1811, ko je delal s pepelom alg, je Courtois opazil, da se bakrene posode izrabijo hitreje kot običajno. Ko je študiral ta fenomen, je njegova mačka prišla v laboratorij in polila raztopino koncentrirane žveplove kisline na suh pepel alg. Takoj so nastale vijolične pare; tako je bil odkrit jod (I₂)! Jod je bil tudi vzrok korozije bakra. Zaradi uporabe v medicini je Courtois odprl nov obrat za pridobivanje joda z reakcijo alg s klorom. Dandanes pridobivajo jod iz več setov reaktantov, (NO₃, I⁻, H⁺) ali (IO₃, I⁻, H⁺). Dijaki so morali pri nalogi zapisati urejene enačbe za navedene procese pridobivanja joda. Nato pa so morali proučevati ravnotežje I-(aq) + $I_2(aq) = I_2(aq)$, ki je povezano z naslednjim poskusom: za pripravo začetne raztopine so nekaj kristalov trdnega joda raztopili v 50.0 mL vodne raztopine kalijevega jodida, dodali diklorometan in zmes močno stresali, dokler ni nastalo ravnotežje. Po ločitvi faz so vsako fazo titrirali z standardno vodno raztopino natrijevega tiosulfata pentahidrata. Dijaki so morali uganiti barve med posameznimi stopnjami poskusa, napisati kemijske enačbe, izračunati maso joda za pripravo začetne raztopine ter konstanto ravnotežja za zgornjo reakcijo.

Peta naloga je bila povezana s kompleksi azobenzen – β -cyclodekstrin in njihovo vlogo pri izgradnji nanostrojev. Nanostroji so molekulski skupki, ki omogočajo pretvorbo virov energije v nano-premike, ki pridejo v poštev pri naprimer dostavi zdravilnih učinkovin. Številni nanostroji izrabljajo izomerizacijo azo spojin (R–N=N–R') pod vplivom svetlobe. β -ciklodekstrin (C na sliki spodaj) je ciklični heptamer glukoze, ki lahko tvori inkluzijske komplekse z azo spojinami. Dijaki so morali z uporabo

spektroskopije določati konstanto asociacije K_t , ki ustreza procesu nastanka inkluzijskega kompleksa $\mathrm{CM}_{\mathrm{trans}}$. Potem so izračunali še konstanto K_c za nastanek cis-kompleksa, pri čemer pa so tokrat uporabili kinetične študije procesa. Shema dogajanja je predstavljena na sliki spodaj.

$$C$$
 M_{cis}
 K_c
 CM_{cis}
 K_c
 CM_{cis}
 K_c
 K_c
 K_c
 CM_{cis}
 K_c
 K_c
 K_c
 CM_{cis}
 K_c
 K_c
 K_c
 K_c
 K_c
 K_c
 K_c
 K_c
 K_c
 K_c
 K_c
 K_c
 K_c
 K_c
 K_c
 K_c
 K_c
 K_c
 K_c
 K_c
 K_c
 K_c
 K_c
 K_c
 K_c
 K_c
 K_c
 K_c
 K_c
 K_c
 K_c
 K_c
 K_c
 K_c
 K_c
 K_c
 K_c
 K_c
 K_c
 K_c
 K_c
 K_c
 K_c
 K_c
 K_c
 K_c
 K_c
 K_c
 K_c
 K_c
 K_c
 K_c
 K_c
 K_c
 K_c
 K_c
 K_c
 K_c
 K_c
 K_c
 K_c
 K_c
 K_c
 K_c
 K_c
 K_c
 K_c
 K_c
 K_c
 K_c
 K_c
 K_c
 K_c
 K_c
 K_c
 K_c
 K_c
 K_c
 K_c
 K_c
 K_c
 K_c
 K_c
 K_c
 K_c
 K_c
 K_c
 K_c
 K_c
 K_c

Azobenzen se v povezavi s silikagelom lahko uporablja za »dostavo« raznih snovi na željeno mesto ob določenem času. Pri nalogi je bilo to barvilo, ujeto v pore silikagela, ki pa se sprosti ob osvetlitvi s svetlobo ustrezne valovne dolžine, ko se razcepi kompleks azobenzen-ciklodekstrin. Dijaki so morali določiti še pogoje za omenjeni proces. Ta naloga je bila vsebinsko in časovno precej zahtevna.

Šesta naloga je bila sinteza in karakterizacija blok-kopolimerov, ki jih pripravimo s povezavo različnih polimerov (blokov), zato imajo posebne lastnosti, kot je sposobnost, da se samodejno organizirajo. V prvem delu so morali dijaki izvesti NMR analizo v vodi topnega homopolimera 1 (α -metoksi- ω -aminopolietilenglikol), in nato še mehanizem sinteze drugega blok kopolimera, ki nastane pri reakciji spojine 1 z 2 (ϵ -(benziloksokarbonil)-lizin N-karboksianhidrid). Pri tem nastane blok-kopolimer 3, shema 1.

Za vse tri spojine so morali okarakterizirati tudi IR-spektre, in zatem z uporabo podatkov izključitvene kromatografije določiti še stopnjo polimerizacije drugega bloka. Nazadnje pa so morali narisati še strukture vmesnih spojin pri sintezi triblok kopolimera, ki se uporablja za razne biološke aplikacije, kot je npr. tvorba micelov. Takšni kopolimeri se uporabljajo v medicini, saj se samodejno organizirajo v vodi (pH = 7), zaradi česar lahko služijo kot prenašalci zdravilnih učinkovin. Ta naloga je bila povezana z delovanjem francoskega znanstvenika Pierre-Gilles de Gennesa, ki je leta 1991 dobil Nobelovo nagrado za raziskave polimerov, in po katerem se imenuje šola, na kateri so letos potekala vsa tekmovanja.

Navdih za sedmo nalogo so bile raziskave, ki jih je opravil že omenjeni Pierre Sauvage, častni predsednik znanstvenega odbora letošnje olimpijade. Leta 2016 so namreč Nobelovo nagrado za kemijo dobili J.-P. Sauvage, Sir J. F. Stoddart in B. L. Feringa »za načrtovanje in sintezo

molekularnih strojev«. Primer teh je [2]katenan, molekula, ki ima dva prepletena obroča. Prvi obroč ima en fenantrolinski (bidentatni) ligand, drugi obroč pa dva liganda: fenantrolinski in terpiridinski (tridentatni) ligand. Bakrov ion je koordiniran s po enim ligandom iz vsakega obroča. Glede na oksidacijsko stanje bakra (+I or +II), sta možni dve konfiguraciji:

Dijaki so morali narisati strukture vmesnih produktov, ki nastanejo pri sintezi obročev, ter sklepati o geometriji bakrovega iona, za katerega so morali narisati tudi orbitalni diagram.

Pri osmi nalogi so tako kot pri prvi nalogi sestavljalci mislili na Martina Karplusa, ki je trenutno zaposlen na Univerzi v Strasbourgu. Ta znanstvenik je dobil leta 2013 Nobelovo nagrado za modeliranje v kemiji. Sam sicer pravi, da je edina prava kemija, s katero se ukvarja, v njegovi kuhinji doma. Tema te naloge je bila identifikacija in sinteza inozitolov. Inozitoli so cikloheksan-1,2,3,4,5,6-heksoli. Nekateri od teh 6-členskih karbociklov, predvsem *mio*-inozitol, sodelujejo pri številnih bioloških procesih. Dijaki so morali narisati strukturno formule te snovi, in 3D strukture vseh optično aktivnih stereoizomerov. Na osnovi NMR spektrov so morali določiti molekulsko formulo in

ravnine simetrije spojine. V medicinske namene je uporabna sinteza nekaterih inozitol fosfatov v večjih količinah. Primer je sinteza inozitola 2 iz bromodiola 1.

Inozitol 2 lahko pripravimo iz spojine 1 v 7 stopnjah. Dijaki so morali narisati spojine, ki nastanejo v posameznih stopnjah reakcijskega mehanizma, seveda vse z upoštevanjem stereokemije.

Tema devete naloge je bila sinteza levobupivakaina. Lokalni anestetik bupivakain (tržno ime Marcaine) je Svetovna znanstvena organizacija WHO uvrstila na seznam esencialnih zdravil. Čeprav se v zdravilu trenutno nahaja racemna zmes, pa raziskave kažejo, da je en enatiomer, levobupivakain, manj kardiotoksičen kot racemat, in zato varnejši. Levobupivakain lahko sintetiziramo iz naravne aminokisline L-lisina. Dijaki so morali narisati strukture izhodnih spojin in vmesnih produktov pri sintezi levobupivakaina, pri čemer so tudi tukaj morali pokazati poznavanje stereokemije.

Francozi so pri sestavljanju nalog poskrbeli za dobro promocijo države in francoskih znanstvenikov, ki so veliko doprinesli k razvoju znanosti. To smo tudi pričakovali; naloge so bile res zanimive.

Naslednja mednarodna kemijska olimpijada bo v Istanbulu v Turčiji.

Vabljene in vabljeni!

Tekst in foto: Andrej Godec

S74	Acta Chim. Slov. 2019, 66, (4), Supplement

Poročilo Sekcije za kristalografijo za leto 2019

Sekcija za kristalografijo pri Slovenskem kemijskem društvu je v letu 2019 delovala po ustaljenem programu. Spremljali smo delo in IUCr (mednarodne kristalografske zveze) in ECA (evropske kristalografske zveze), katerih člani smo. Sodelovali smo pri aktivnostih, ki jih promovirata obe organizaciji (letos na primer je nekaj naših članov, ki so tudi člani SKD, sodelovalo pri postavitvi razstave ob mednarodnem letu periodnega sistema. Z obema organizacijama smo v rednem stiku po e-pošti.

Delovanje v Sloveniji je bilo osredotočeno na organizacijo tradicionalne kristalografske konference. Skupaj s hrvaškim kristalografskim društvom iz Zagreba smo organizirala 27. zaporedno srečanje slovenskih in hrvaških kristalografov. Srečanje je potekalo v Rogaški Slatini med 19. in 23 junijem 2019 (https://slocro27.fkkt.uni-lj.si/). Kot vsako leto je bila tudi tokrat udeležba mednarodna, zato je bil uradni jezik srečanja angleščina. S sredstvi donatorjev in sponzorjev ter veliko prostovoljnega dela članov sekcije smo uspeli organizirati srečanje tako, da smo obdržali tradicijo in udeležencem ni bilo treba plačati kotizacije. Velika zahvala za to gre sponzorjem, ki so bili: Renacon, Rigaku, Bruker, Crystal Impact, Dectris, Optik Instruments, Aparatura, Lek-Sandoz, Krka in Scan.

Podobno kot na prejšnjih konferencah, so se tudi tokrat povabilu za sodelovanje odzvali ugledni, mednarodno uveljavljeni plenarni predavatelji. Petra Bombicz iz raziskovalnega centra za naravoslovno znanosti pri madžarski akademiji znanosti in umetnosti iz Budmpešte je predstavila predavanje Synthon/property-engineering of calixarenes (supramolecular interactions, shape and symmetries), prof. Piero Macchi z universe v Bernu v Švici je imel predavanje Are there molecules in crystals?, Martina Vrankić z inštituta Ruđer Bošković iz Zagreba je predstavila

temo Ambient and non-ambient driven X-ray powder diffraction: insights into the structure-property relationship in powders, Matic Lozinšek z UL Fakultete z kemijo in kemijsko tehnologijo in Inštituta Jožef Stefan pa je predaval o Noble-gas chemistry in the 21st century.

Konferenca je bila uspešna, udeležilo se je je 55 prijavljenih udeležencev iz 8 držav (Avstrija, Madžarska, Indija, Italija, Švica, Ukrajina, Hrvaška in Slovenija. Poleg plenarnih predavanj so udeleženci 38 prispevkov v obliki kratkih predavanj, kar je ena od prednosti teh konferenc. Pretežno mladi raziskovalci imajo možnost predavati pred strokovno zahtevnim, vendar naklonjenim občinstvom, kar je dragocena izkušnja. Predavanja so pokrivala sodobne vidike kristalografije kot so: strukturna analiza organskih, bioloških, anorganskih in koordinacijskih spojin, arhitektura in načrtovanje struktur, fazni prehodi, trdne raztopine, povezava med lastnostmi in strukturo, sinergija med kristalografskimi in drugimi metodami karakterizacije, predstavljenih pa je bilo tud nekaj zanimivih utrinkov iz zgodovine kristalografije.

Tudi družabni dogodki, vključeni v program (vodena ekskurzija po muzeju na prostem in Steklarni Rogaška, konferenčna večerja) so bili spet priložnost za izmenjavo spoznanj, navezavo stikov in intenzivno učenje mlajših kolegov.

Že letos pa potekajo tui priprave na tri dogodke, ki bodo v naslednjem letu in jih podpirata IUCr in ECA, to so svetovni kongres IUCr v Pragi avgusta 2020, evropska konferenca o praškovni difrakciji v Šibeniku v maju in 28. Hrvaško-Slovensko kristalografsko srečanje v juniju v Rabcu na Hrvaškem.

prof. dr. Anton Meden

S76	Acta Chim. Slov. 2019, 66, (4), Supplement

KOLEDAR VAŽNEJŠIH ZNANSTVENIH SREČANJ S PODROČJA KEMIJE IN KEMIJSKE TEHNOLOGIJE

SCIENTIFIC MEETINGS – CHEMISTRY AND CHEMICAL ENGINEERING

2019

December 2019

05 IYPT2019 CLOSING CEREMONY

Tokyo, Japan

Information: https://iypt.jp/en.html

15 – 18 12TH INTERNATIONAL SYMPOSIUM ON BIOORGANIC CHEMISTRY (ISBOC-12)

Shenzhen, China

Information: http://www.sz-isboc.com/

16 – 19 CHEMCON 2019

Delhi, India

Information: https://www.chemcon19.com/

2020

February 2020

08 – 12 INTERNATIONAL NATURAL SCIENCES TOURNAMENT

Warsaw, Poland

Information: http://www.scitourn.com/inst/

19 – 21 CHEMISTRY CONFERENCE FOR YOUNG SCIENTISTS (CHEMCYS 2020)

Blankenberge, Belgium

Information: https://www.chemcys.be

March 2020

19 – 20 3RD EUROPEAN CHEMISTRY CONFERENCE

Rome, Italy

Information: https://europeanchemistry.madridge.com/

23 – 27 SNOW COVER, ATMOSPHERIC PRECIPITATION, AEROSOLS: CHEMISTRY AND

CLIMATE

Listvyanka, Russian Federation

Information: http://snow-baikal.tw1.ru/index-eng

April 2020

22 – 24 AUSTRIAN FOOD CHEMISTRY DAYS 2020

Klagenfurt, Austria

Information: https://www.goech.at/lebensmittelchemikertage

26. 4. – 2. 5. XII. INTERNATIONAL MASS SPECTROMETRY CONFERENCE ON PETROCHEMISTRY,

ENVIRONMENTAL AND FOOD CHEMISTRY

Crete, Greece

Information: https://www.petromass2020.com/

May 2020

05 – 10 44TH INTERNATIONAL CONFERENCE ON COORDINATION CHEMISTRY

Rimini, Italy

Information: https://www.iccc2020.com

18 – 22 POLY-CHAR 2020 [VENICE] – INTERNATIONAL POLYMER CHARACTERIZATION

FORUM

Venezia Mestre, Italy

Information: https://www.poly-char2020.org/

24 – 27 THE 30TH EUROPEAN SYMPOSIUM ON COMPUTER AIDED PROCESS ENGINEERING

Milano, Italy

Information: https://www.aidic.it/escape30/enter.php

24 – 29 THE 44TH INTERNATIONAL SYMPOSIUM ON CAPILLARY CHROMATOGRAPHY

Riva del Garda, Italy

Information: http://iscc44.chromaleont.it/slider.htm

26 – 27 FOOD CONTAMINATION AND TRACEABILITY SUMMIT

Stadthalle Erding Centre, Erding

Information: https://contaminationsummit.com/

June 2020

Information:

02-05 14^{TH} MEDITERRANEAN CONGRESS OF CHEMICAL ENGINEERING

Barcelona, Spain https://www.mecce.org/

08 – 12 11TH EUROPEAN CONFERENCE ON SOLAR CHEMISTRY AND PHOTOCATALYSIS:

ENVIRONMENTAL APPLICATIONS (SPEA)

Turin, Italy

Information: http://www.spea11.unito.it/home

14-18 12^{TH} EUROPEAN SYMPOSIUM ON ELECTROCHEMICAL ENGINEERING

Leeuwarden, The Netherlands

Information: http://www.electrochemical-engineering.eu/2020/

July 2020

05 – 09 48TH WORLD POLYMER CONGRESS – MACRO2020

Jeju Island, Republic of Korea

Information: http://www.macro2020.org

06 – 08 EUROPEAN CONFERENCE OF RESEARCH IN CHEMISTRY EDUCATION (ECRICE 2020)

Weizmann Institute of Science, Rehovot

Information: http://www.weizmann.ac.il/st/blonder/

August 2020

30.08. – 03.09. ECC8 – 8^{TH} EUCHEMS CHEMISTRY CONGRESS

Centro de Congressos de Lisboa, Lisbon

Information: https://www.euchems.eu/events/ecc8-8th-euchems-chemistry-congress/

September 2020

09-11 25^{TH} CONFERENCE ON ISOPRENOIDS

The International Research and Production Holding "Phytochemistry", Karaganda

Information: http://www.isoprenoids25.phyto.kz/

Acta Chimica Slovenica

Author Guidelines

Submissions

Submission to ACSi is made with the implicit understanding that neither the manuscript nor the essence of its content has been published in whole or in part and that it is not being considered for publication elsewhere. All the listed authors should have agreed on the content and the corresponding (submitting) author is responsible for having ensured that this agreement has been reached. The acceptance of an article is based entirely on its scientific merit, as judged by peer review. There are no page charges for publishing articles in ACSi. The authors are asked to read the Author Guidelines carefully to gain an overview and assess if their manuscript is suitable for ACSi.

Additional information

- · Citing spectral and analytical data
- · Depositing X-ray data

Submission material

Typical submission consists of:

- full manuscript (PDF file, with title, authors, abstract, keywords, figures and tables embedded, and references)
- supplementary files
 - Full manuscript (original Word file)
 - Statement of novelty (Word file)
 - List of suggested reviewers (Word file)
 - ZIP file containing graphics (figures, illustrations, images, photographs)
 - Graphical abstract (single graphics file)
 - Proposed cover picture (optional, single graphics file)
 - Appendices (optional, Word files, graphics files)

Incomplete or not properly prepared submissions will be rejected.

Submission process

Before submission, authors should go through the checklist at the bottom of the page and prepare for submission.

Submission process consists of 5 steps.

Step 1: Starting the submission

- Choose one of the journal sections.
- · Confirm all the requirements of the checklist.
- Additional plain text comments for the editor can be provided in the relevant text field.

Step 2: Upload submission

 Upload full manuscript in the form of a Word file (with title, authors, abstract, keywords, figures and tables embedded, and references).

Step 3: Enter metadata

 First name, last name, contact email and affiliation for all authors, in relevant order, must be provided. Corresponding author has to be selected. Full postal address and phone number of the corresponding author has to be provided.

- Title and abstract must be provided in plain text.
- Keywords must be provided (max. 6, separated by semicolons).
- Data about contributors and supporting agencies may be entered.
- References in plain text must be provided in the relevant text filed.

Step 4: Upload supplementary files

- Original Word file (original of the PDF uploaded in the step 2)
- Statement of novelty in a Word file must be uploaded
- All graphics have to be uploaded in a single ZIP file. Graphics should be named Figure 1.jpg, Figure 2.eps, etc.
- Graphical abstract image must be uploaded separately
- Proposed cover picture (optional) should be uploaded separately.
- Any additional appendices (optional) to the paper may be uploaded. Appendices may be published as a supplementary material to the paper, if accepted.
- For each uploaded file the author is asked for additional metadata which may be provided. Depending of the type of the file please provide the relevant title (Statement of novelty, List of suggested reviewers, Figures, Graphical abstract, Proposed cover picture, Appendix).

Step 5: Confirmation

Final confirmation is required.

Article Types

Feature Articles are contributions that are written on editor's invitation. They should be clear and concise summaries of the most recent activity of the author and his/her research group written with the broad scope of ACSi in mind. They are intended to be general overviews of the authors' subfield of research but should be written in a way that engages and informs scientists in other areas. They should contain the following (see also general directions for article structure in ACSi below): (1) an introduction that acquaints readers with the authors' research field and outlines the important questions to which answers are being sought; (2) interesting, new, and recent contributions of the author(s) to the field; and (3) a summary that presents possible future directions. Manuscripts normally should not exceed 40 pages of one column format (letter size 12, 33 lines per page). Generally, experts in a field who have made important contribution to a specific topic in recent years will be invited by an editor to contribute such an Invited Feature Article. Individuals may, however, send a proposal (one-page maximum) for an Invited Feature Article to the Editorin-Chief for consideration.

Scientific articles should report significant and innovative achievements in chemistry and related sciences and should exhibit a high level of originality. They

should have the following structure:

- 1. Title (max. 150 characters),
- 2. Authors and affiliations,
- 3. Abstract (max. 1000 characters),
- 4. Keywords (max. 6),
- 5. Introduction,
- Experimental,
- 7. Results and Discussion,
- 8. Conclusions,
- 9. Acknowledgements,

10.References.

The sections should be arranged in the sequence generally accepted for publications in the respective fields and should be successively numbered.

Short communications generally follow the same order of sections as Scientific articles, but should be short (max. 2500 words) and report a significant aspect of research work meriting separate publication. Editors may decide that a Scientific paper is categorized as a Short Communication if its length is short.

Technical articles report applications of an already described innovation. Typically, technical articles are not based on new experiments.

Preparation of Submissions

Text of the submitted articles must be prepared with Microsoft Word. Normal style set to single column, 1.5 line spacing, and 12 pt Times New Roman font is recommended. Line numbering (continuous, for the whole document) must be enabled to simplify the reviewing process. For any other format, please consult the editor. Articles should be written in English. Correct spelling and grammar are the sole responsibility of the author(s). Papers should be written in a concise and succinct manner. The authors shall respect the ISO 80000 standard [1], and IUPAC Green Book [2] rules on the names and symbols of quantities and units. The Système International d'Unités (SI) must be used for all dimensional quantities.

Graphics (figures, graphs, illustrations, digital images, photographs) should be inserted in the text where appropriate. The captions should be self-explanatory. Lettering should be readable (suggested 8 point Arial font) with equal size in all figures. Use common programs such as MS Excel or similar to prepare figures (graphs) and ChemDraw to prepare structures in their final size. Width of graphs in the manuscript should be 8 cm. Only in special cases (in case of numerous data, visibility issues) graphs can be 17 cm wide. All graphs in the manuscript should be inserted in relevant places and aligned left. The same graphs should be provided separately as images of appropriate resolution (see below) and submitted together in a ZIP file (Graphics ZIP). Please do not submit figures as a Word file. In graphs, only the graph area determined by both axes should be in the frame, while a frame around the whole graph should be omitted. The graph area should be white. The legend should be inside the graph area. The style of all graphs should be the same. Figures and illustrations should be of sufficient quality for the printed version, i.e. 300 dpi minimum. Digital images and photographs should be of high quality (minimum 250 dpi resolution). On submission, figures should be of good enough resolution to be assessed by the referees, ideally as JPEGs. High-resolution figures (in JPEG, TIFF, or EPS format) might be required if the paper is accepted for publication.

Tables should be prepared in the Word file of the paper as usual Word tables. The captions should appear above the table and should be self-explanatory.

References should be numbered and ordered sequentially as they appear in the text, likewise methods, tables, figure captions. When cited in the text, reference numbers should be superscripted, following punctuation marks. It is the sole responsibility of authors to cite articles that have been submitted to a journal or were in print at the time of submission to ACSi. Formatting of references to published work should follow the journal style; please also consult a recent issue:

- 1. J. W. Smith, A. G. White, *Acta Chim. Slov.* **2008**, *55*, 1055–1059.
- M. F. Kemmere, T. F. Keurentjes, in: S. P. Nunes, K. V. Peinemann (Ed.): Membrane Technology in the Chemical Industry, Wiley-VCH, Weinheim, Germany, 2008, pp. 229–255.
- J. Levec, Arrangement and process for oxidizing an aqueous medium, US Patent Number 5,928,521, date of patent July 27, 1999.
- 4. L. A. Bursill, J. M. Thomas, in: R. Sersale, C. Collela, R. Aiello (Eds.), Recent Progress Report and Discussions: 5th International Zeolite Conference, Naples, Italy, 1980, Gianini, Naples, 1981, pp. 25–30.
- J. Szegezdi, F. Csizmadia, Prediction of dissociation constant using microconstants, http://www. chemaxon.com/conf/Prediction_of_dissociation _constant_using_microco nstants.pdf, (assessed: March 31, 2008)

Titles of journals should be abbreviated according to Chemical Abstracts Service Source Index (CASSI).

Special Notes

- Complete characterization, including crystal structure, should be given when the synthesis of new compounds in crystal form is reported.
- Numerical data should be reported with the number of significant digits corresponding to the magnitude of experimental uncertainty.
- The SI system of units and IUPAC recommendations for nomenclature, symbols and abbreviations should be followed closely. Additionally, the authors should follow the general guidelines when citing spectral and analytical data, and depositing crystallographic data.
- Characters should be correctly represented throughout the manuscript: for example, 1 (one) and I (ell), 0 (zero) and O (oh), x (ex), D7 (times sign), B0 (degree sign). Use Symbol font for all Greek letters and mathematical symbols.
- The rules and recommendations of the IUBMB and the International Union of Pure and Applied Chemistry (IUPAC) should be used for abbreviation of chemical names, nomenclature of chemical compounds, enzyme nomenclature, isotopic compounds, optically active isomers, and spectroscopic data.
- A conflict of interest occurs when an individual (author, reviewer, editor) or its organization is involved in multiple interests, one of which could possibly corrupt the motivation for an act in the

other. Financial relationships are the most easily identifiable conflicts of interest, while conflicts can occur also as personal relationships, academic competition, etc. The Editors will make effort to ensure that conflicts of interest will not compromise the evaluation process; potential editors and reviewers will be asked to exempt themselves from review process when such conflict of interest exists. When the manuscript is submitted for publication, the authors are expected to disclose any relationships that might pose potential conflict of interest with respect to results reported in that manuscript. In the Acknowledgement section the source of funding support should be mentioned. The statement of disclosure must be provided as Comments to Editor during the submission pro-

- Research described in papers submitted to ACSi must adhere to the principles of the Declaration of Helsinki (http://www.wma.net/e/policy/b3.htm). These studies must be approved by an appropriate institutional review board or committee, and informed consent must be obtained from subjects. The Methods section of the paper must include: 1) a statement of protocol approval from an institutional review board or committee and 2), a statement that informed consent was obtained from the human subjects or their representatives.
- Published Statement of Human and Animal Rights. When reporting experiments on human subjects, authors should indicate whether the procedures followed were in accordance with the ethical standards of the responsible committee on human experimentation (institutional and national) and with the Helsinki Declaration of 1975, as revised in 2008. If doubt exists whether the research was conducted in accordance with the Helsinki Declaration, the authors must explain the rationale for their approach and demonstrate that the institutional review body explicitly approved the doubtful aspects of the study. When reporting experiments on animals, authors should indicate whether the institutional and national guide for the care and use of laboratory animals was followed.
- To avoid conflict of interest between authors and referees we expect that not more than one referee is from the same country as the corresponding author(s), however, not from the same institution.
- Contributions authored by Slovenian scientists are evaluated by non-Slovenian referees.
- Papers describing microwave-assisted reactions performed in domestic microwave ovens are not considered for publication in Acta Chimica Slovenica.
- Manuscripts that are not prepared and submitted in accord with the instructions for authors are not considered for publication.

Appendices

Authors are encouraged to make use of supporting information for publication, which is supplementary material (appendices) that is submitted at the same time as the manuscript. It is made available on the Journal's web site and is linked to the article in the

Journal's Web edition. The use of supporting information is particularly appropriate for presenting additional graphs, spectra, tables and discussion and is more likely to be of interest to specialists than to general readers. When preparing supporting information, authors should keep in mind that the supporting information files will not be edited by the editorial staff. In addition, the files should be not too large (upper limit 10 MB) and should be provided in common widely known file formats to be accessible to readers without difficulty. All files of supplementary materials are loaded separately during the submission process as supplementary files.

Proposed Cover Picture and Graphical Abstract Image

Graphical content: an ideally full-colour illustration of resolution 300 dpi from the manuscript must be proposed with the submission. Graphical abstract pictures are printed in size 6.5×4 cm (hence minimal resolution of 770×470 pixels). Cover picture is printed in size 11×9.5 cm (hence minimal resolution of 1300×1130 pixels)

Authors are encouraged to submit illustrations as candidates for the journal Cover Picture*. The illustration must be related to the subject matter of the paper. Usually both proposed cover picture and graphical abstract are the same, but authors may provide different pictures as well.

* The authors will be asked to contribute to the costs of the cover picture production.

Statement of novelty

Statement of novelty is provided in a Word file and submitted as a supplementary file in step 4 of submission process. Authors should in no more than 100 words emphasize the scientific novelty of the presented research. Do not repeat for this purpose the content of your abstract.

List of suggested reviewers

List of suggested reviewers is a Word file submitted as a supplementary file in step 4 of submission process. Authors should propose the names, full affiliation (department, institution, city and country) and e-mail addresses of three potential referees. Field of expertise and at least two references relevant to the scientific field of the submitted manuscript must be provided for each of the suggested reviewers. The referees should be knowledgeable about the subject but have no close connection with any of the authors. In addition, referees should be from institutions other than (and preferably countries other than) those of any of the authors.

How to Submit

Users registered in the role of author can start submission by choosing USER HOME link on the top of the page, then choosing the role of the Author and follow the relevant link for starting the submission process. Prior to submission we strongly recommend that you familiarize yourself with the ACSi style by browsing the journal, particularly if you have not submitted to the ACSi before or recently.

Correspondence

All correspondence with the ACSi editor regarding the paper goes through this web site and emails. Emails are sent and recorded in the web site database. In the correspondence with the editorial office please provide ID number of your manuscript. All emails you receive from the system contain relevant links. Please do not answer the emails directly but use the embedded links in the emails for carrying out relevant actions. Alternatively, you can carry out all the actions and correspondence through the online system by logging in and selecting relevant options.

Proofs

Proofs will be dispatched via e-mail and corrections should be returned to the editor by e-mail as quickly as possible, normally within 48 hours of receipt. Typing errors should be corrected; other changes of contents will be treated as new submissions.

Submission Preparation Checklist

As part of the submission process, authors are required to check off their submission's compliance with all of the following items, and submissions may be returned to authors that do not adhere to these guidelines.

- The submission has not been previously published, nor is it under consideration for publication in any other journal (or an explanation has been provided in Comments to the Editor).
- All the listed authors have agreed on the content and the corresponding (submitting) author is responsible for having ensured that this agreement has been reached.
- 3. The submission files are in the correct format: manuscript is created in MS Word but will be **submitted in PDF** (for reviewers) as well as in original MS Word format (as a supplementary file for technical editing); diagrams and graphs are created in Excel and saved in one of the file formats: TIFF, EPS or JPG; illustrations are also saved in one of these formats. The preferred position of graphic files in a document is to embed them close to the place where they are mentioned in the text (See **Author guidelines** for details).
- The manuscript has been examined for spelling and grammar (spell checked).
- 5. The *title* (maximum 150 characters) briefly explains the contents of the manuscript.
- 6. Full names (first and last) of all authors together with the affiliation address are provided. Name of author(s) denoted as the corresponding author(s), together with their e-mail address, full postal address and telephone/fax numbers are given.
- The abstract states the objective and conclusions of the research concisely in no more than 150 words.
- 8. Keywords (minimum three, maximum six) are provided.
- Statement of novelty (maximum 100 words) clearly explaining new findings reported in the manuscript should be prepared as a separate Word file.
- The text adheres to the stylistic and bibliographic requirements outlined in the **Author guidelines**.
- 11. Text in normal style is set to single column, 1.5 line spacing, and 12 pt. Times New Roman font is

- recommended. All tables, figures and illustrations have appropriate captions and are placed within the text at the appropriate points.
- 12. Mathematical and chemical equations are provided in separate lines and numbered (Arabic numbers) consecutively in parenthesis at the end of the line. All equation numbers are (if necessary) appropriately included in the text. Corresponding numbers are checked.
- Tables, Figures, illustrations, are prepared in correct format and resolution (see *Author guidelines*).
- 14. The lettering used in the figures and graphs do not vary greatly in size. The recommended lettering size is 8 point Arial.
- 15. Separate files for each figure and illustration are prepared. The names (numbers) of the separate files are the same as they appear in the text. All the figure files are packed for uploading in a single ZIP file.
- 16. Authors have read *special notes* and have accordingly prepared their manuscript (if necessary).
- 17. References in the text and in the References are correctly cited. (see *Author guidelines*). All references mentioned in the Reference list are cited in the text, and vice versa.
- Permission has been obtained for use of copyrighted material from other sources (including the Web).
- 19. The names, full affiliation (department, institution, city and country), e-mail addresses and references of three potential referees from institutions other than (and preferably countries other than) those of any of the authors are prepared in the word file. At least two relevant references (important papers with high impact factor, head positions of departments, labs, research groups, etc.) for each suggested reviewer must be provided.
- 20. Full-colour illustration or graph from the manuscript is proposed for graphical abstract.
- Appendices (if appropriate) as supplementary material are prepared and will be submitted at the same time as the manuscript.

Privacy Statement

The names and email addresses entered in this journal site will be used exclusively for the stated purposes of this journal and will not be made available for any other purpose or to any other party.

ISSN: 1580-3155

Koristni naslovi



Slovensko kemijsko društvo

www.chem-soc.si
e-mail: chem.soc@ki.si



Wessex Institute of Technology

www.wessex.ac.uk



SETAC

www.setac.org



European Water Association

http://www.ewa-online.eu/



European Science Foundation

www.esf.org



European Federation of Chemical Engineering

https://efce.info/



International Union of Pure and Applied Chemistry

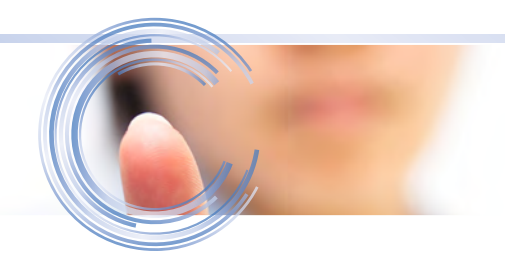
https://iupac.org/



Novice europske zveze kemijskih društev (EuCheMS) najdete na:

EuCheMS: Brussels News Updates

http://www.euchems.eu/newsletters/

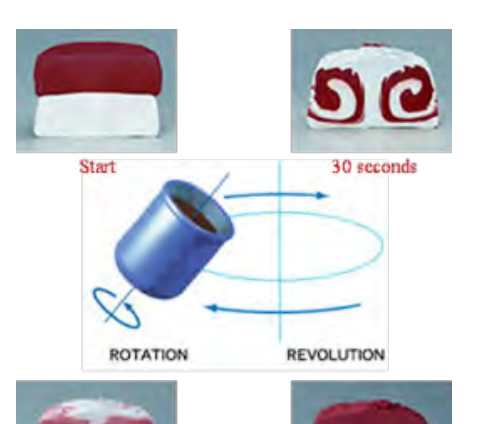




Donau Lab d.o.o., Ljubljana Tbilisijska 85 SI-1000 Ljubljana www.donaulab.si office-si@donaulab.com

Planetarni centrifugalni mikser

ARM-310CE



7 minutes

2 minutes

Brezkontaktno mešanje in disperzija

Tudi za zelo viskozne materiale

Širok spekter uporabe

Atraktivna cena





Izjemen dan se začne z izjemnim spancem.



Odpravite nespečnost in začnite dan spočiti.



ActaChimicaSlovenica ActaChimicaSlovenica

Supercritical fluid extraction of rosehip (*Rosa canina*), red and white grapes skin - a sustainable method to obtain extracts with a high content of phenolic compounds with antioxidant and radical scavenging activities responsible for various health protective effects (see page 751).



Year 2019, Vol. 66, No. 4



